Observation of a Higgs boson and measurement of its mass in the diphoton decay channel with the ATLAS detector at the LHC

Narei Lorenzo Martinez

▶ **To cite this version:**

Narei Lorenzo Martinez. Observation of a Higgs boson and measurement of its mass in the diphoton decay channel with the ATLAS detector at the LHC. Other [cond-mat.other]. Université Paris Sud - Paris XI, 2013. English. NNT : 2013PA112139 . tel-00924105

HAL Id: tel-00924105

https://theses.hal.science/tel-00924105

Submitted on 6 Jan 2014

HAL is a multi-disciplinary open access archive for the deposit and dissemination of scientific research documents, whether they are published or not. The documents may come from teaching and research institutions in France or abroad, or from public or private research centers.

L'archive ouverte pluridisciplinaire **HAL**, est destinée au dépôt et à la diffusion de documents scientifiques de niveau recherche, publiés ou non, émanant des établissements d'enseignement et de recherche français ou étrangers, des laboratoires publics ou privés.

LAL 13-288
Septembre 2013

THÈSE DE DOCTORAT

soutenue le 10 septembre 2013 par

Narei Lorenzo Martinez

pour obtenir le grade de

Docteur en Sciences
de l'Université Paris-Sud XI, Orsay

Observation of a Higgs boson and measurement of its mass in the diphoton decay channel with the ATLAS detector at the LHC.

devant la commission d'examen composée de

Maarten BOONEKAMP	Examinateur
Lance DIXON	Examinateur
Marumi KADO	Directeur de thèse
Markus SCHUMACHER	Rapporteur
Christopher SEEZ	Rapporteur
Achille STOCCHI	Président du jury

Abstract

The Standard Model of particle physics predicts the existence of a massive scalar boson, referred to as the Higgs boson, resulting from the introduction of a doublet of complex scalar fields and the Spontaneous Symmetry Breaking mechanism, needed to generate the mass of the particles. The Higgs boson, whose mass is theoretically undetermined, has been searched for experimentally since almost half a century by various experiments. The search for the Higgs boson is one of the goals of the LHC physics program. One of the most important decay channels at the LHC is the diphoton channel, because the final state can be completely reconstructed with high precision. In this thesis, a detailed study of the photon energy response, using the ATLAS electromagnetic calorimeter has been performed. In particular, the stability and uniformity of the energy response has been tested. This study has provided a better understanding of the photon energy resolution and scale, which are very important for the determination of the systematic uncertainties on the mass and production rate in the diphoton channel. This channel had a prominent role in the discovery of a new particle compatible with the Standard Model Higgs boson by the ATLAS and CMS experiments. Using this channel as well as the improved understanding of the photon energy response, a measurement of the mass of this particle is proposed in this thesis, with the data collected in 2011 and 2012 at a center-of-mass energy of 7 TeV and 8 TeV. A mass of 126.8 $\pm$ 0.2 (stat) $\pm$ 0.7 (syst) GeV/c^2 is found. The calibration of the photon energy measurement with the calorimeter is the source of the largest systematic uncertainty on this measurement. Strategies to reduce this systematic error are discussed. Among them, a method to measure the amount of material upstream of the calorimeter, which provides the largest contribution to the uncertainty on the energy scale, has been developed. The energy scale measurement of the different layers of the electromagnetic calorimeter, that is also a source of uncertainty for the global energy scale, is presented.

Résumé

Le Modèle Standard de la physique des particules prédit l'existence d'un boson scalaire massif, appelé boson de Higgs, comme résultant de l'introduction d'un doublet de champs scalaires complexes et d'un mécanisme de brisure spontanée de symétrie, qui permet de générer la masse des particules. Le boson de Higgs, dont la masse est inconnue théoriquement, est recherché expérimentalement depuis plusieurs décennies par plusieurs expériences. La recherche du boson de Higgs est un des objectifs du programme de physique du collisionneur LHC. Un des canaux de désintégration les plus intéressants à étudier au LHC est le canal en deux photons, car l'état final peut être intégralement reconstruit avec une grande précision. Dans cette thèse une étude approfondie de la réponse en énergie des photons en utilisant le calorimètre électromagnétique d'ATLAS a été faite. En particulier, la stabilité et l'uniformité de la réponse en énergie ont été testées. Ces études ont permis de mieux comprendre la résolution et l'échelle d'énergie des photons, qui sont des paramètres importants dans la détermination des incertitudes systématiques sur la masse et le nombre de signal dans le canal en deux photons. Ce canal a eu un rôle prépondérant dans la découverte d'une nouvelle particule compatible avec le boson de Higgs en Juillet 2012 par les expériences ATLAS et CMS. En utilisant ce canal ainsi que la meilleure compréhension de la réponse en énergie acquise au cours de cette thèse, une mesure de la masse du boson est proposée avec les données collectées durant les années 2011 et 2012 avec une énergie de centre de masse de 7 TeV et 8 TeV. Une masse de 126.8 $\pm$ 0.2 (stat) $\pm$ 0.7 (syst) GeV/c^2 a été trouvée. L'étalonnage de la mesure de l'énergie des photons avec le calorimètre électromagnétique est la plus grande source d'incertitude sur

cette mesure. Une stratégie pour réduire cette erreur systématique sur la masse est également détaillée. Une méthode de mesure de la quantité de matière an amont du calorimètre a notamment été développée. L'échelle d'énergie des différentes couches du calorimètre a aussi été étudiée. Ces deux points constituent une grande source d'incertitude sur l'échelle d'énergie globale des photons.

Synopsis of personal contribution

The work presented in this thesis has been made in collaboration with and is based on previous work of a large number of collaborators in ATLAS. To avoid ambiguities, I summarize below which parts of the analyses presented in this thesis are pertaining to my own work and where I had a significant contribution.

Chapter 4 is dedicated to the discussion of the ATLAS data quality criteria. In particular, a new procedure to assign a noise burst to a calorimeter partition in order to reduce the fraction of data losses in Section 4.2.2, and of an algorithm to discriminate misidentified photons coming from calorimeter noises from real photon candidates in Section 4.3, which corresponds to my contributions, are reported. The performance of additional discriminative variables has also been compared and their dependence to the photon transverse momentum investigated.

Chapter 5 corresponds to the core of the thesis where the calibration of the electron and photon energy is described. The following studies that I have completed are described:

- Study of the calorimeter barrel-endcap transition region calibration in Section 5.2.3.
- Estimation of the energy scale systematic uncertainty: contribution from the presampler scale and the material mismodeling. Extrapolation to different energy ranges and to photons (Sections 5.3.5.3 and 5.3.5.4).
- Measurement of the stability of the electron energy response with respect to time, pileup and location in the bunch train. Study of the uniformity of the energy response as a function of the azimuthal angle and pseudorapidity. Correction of periodic non-uniformities (Section 5.4).
- Check of the energy calibration path with an alternative method based on the Jacobian peak. Estimation of all the related systematic uncertainties, Section 5.5.
- Study of the $Z \rightarrow ee$ lineshape in Section 5.6.
- Measurement of the presampler energy scale and of the strip and middle relative energy scale using the $Z \rightarrow ee$ invariant mass. Definition of the method, estimation of the systematics and comparison with alternative methods. Section 5.7.
- Impact of the layer calibration on the $Z \rightarrow ee$ lineshape, in Section 5.8.

Chapter 6 is dedicated to an overview of the measurement of the material in the ATLAS detector. Different methods are described including the shower shape method that I used to probe material upstream of the calorimeter. With this method, various small simulation problems were solved as described in Section 6.4.

The $H \to \gamma\gamma$ analysis is presented in Chapter 7 in its most recent form. My contribution to this analysis are reported below:

- Study of the effect of the interference between the gluon fusion signal and the background on the $H \to \gamma\gamma$ signal rate in Section 7.4.3.
- Estimation of various systematic uncertainties, related to the mass resolution or signal yield in Sections 7.8.1 and 7.8.3.
- Estimation of the systematic uncertainties on the peak position in Section 7.8.4, and building of a model to take into account the correlations.

Finally, a measurement of the Higgs boson mass is proposed in Chapter 8, using the $H \to \gamma\gamma$ decay channel. In this chapter:

- I provide a full validation of the method chosen for the measurement in Section 8.3,
- I test the robustness of the measurement as a function of various variables in Section 8.5,
- I investigate the effects of the signal resolution on the mass and signal strength measurements in Section 8.6,
- I finally estimate the contribution of the different sources of systematic uncertainties to the total error on the mass in Section 8.8.

Introduction

The spontaneous symmetry breaking and the presence of a scalar boson have been predicted for half a century [1,2,3,4,5,6] as the most compelling mechanism to allow the fermions and bosons to have masses in the Standard Model [7,8,9].

After an unsuccessful search for this boson, referred to as the Higgs boson, at the LEP collider, the LHC machine at CERN, whose construction started in 2000 and ended in 2008, was designed to provide energy in the center of mass of 14 TeV and high luminosity of $1.10^{34} cm^{-2} s^{-1}$. Two of the experiments of the LHC collider, ATLAS and CMS, were designed in part for the search for the Higgs boson. In particular, the electromagnetic calorimeter of ATLAS was designed to optimize the sensitivity to the $H \to \gamma\gamma$ channel which was expected to take a important role in this hunt.

The proton-proton collisions at LHC, with half the design beam energy and a luminosity considerably lowered due to an interconnection problem, started in 2010. The luminosity was continuously increased during this year and the following ones. In December 2011, the ATLAS and CMS experiments reported an excess of events over the background expectation in the diphoton and four-leptons decay channels with a combined local significance of 3.6σ and 2.6σ respectively for a mass around 125 GeV. These two channels both benefit from the complete final state reconstruction and from a high mass resolution resulting from the excellent performance of the electromagnetic calorimeter, tracker and muon spectrometer in these two experiments. The excesses in these two channels have continued to grow with more data recorded. In July 2012 both experiments announced the observation of a new boson, with a significance close to 5σ, again combining these two channels [10,11].

Using the various decay channels available in the low mass region, and the dedicated categories sensitive to the different production modes, the couplings of the neutral boson to gauge bosons and fermions have been measured in ATLAS in September 2012. No deviations with respect to the Standard Model expectation were found [12,13,14]. In December 2012, a preliminary combined measurement of the Higgs boson mass in the $H \to \gamma\gamma$ and $H \to 4l$ channels was provided. A difference in mass between these two channels was found with a statistical significance of about 2.5σ [15] [16]. This has been investigated and has led to a large number of checks and systematic studies. In July 2013, one year after the discovery, an evidence for the spin-0 nature of the new boson was reported by ATLAS, using the three decay channels $H \to \gamma\gamma$, $H \to 4l$ and $H \to WW \to l\nu l\nu$ [17].

I had the privilege to work from 2011 to 2013 in ATLAS on the $H \to \gamma\gamma$ analysis. The sensitivity of the analysis depends mostly on the rejection of the background events and on the photon energy resolution, as the signal would appear as a narrow peak over a large background in the

diphoton invariant mass. The knowledge of the amount of material upstream of the calorimeter is for example an important ingredient, as mismodeling of this material would deteriorate the energy resolution. Local or longer-range non-uniformities in the calorimeter also have an impact on the constant term of the energy resolution. Studies have been carried out in this thesis in order to better understand the photon energy response.

Most of the properties of the Higgs boson have been measured and found to be in agreement with the Standard Model. However, other models provide a similar phenomenology so that much refined studies are still needed to confirm if this is *the* Higgs boson. The measurement of the mass of the Higgs boson is of crucial importance: it is the unique parameter of the Standard Model not yet determined, and once accurately measured, precise predictions can be made about the couplings of the Higgs boson to other particles. Hence, the measurement of the Higgs boson mass is a first step toward the validation of the Standard Model spontaneous symmetry breaking sector.

A first measurement of the mass of the Higgs boson in the $H \to \gamma\gamma$ channel is proposed in this thesis. This measurement is based on the knowledge acquired on the photon energy reconstruction with the ATLAS calorimeter.

Contents

1 The Standard Model and Spontaneous Symmetry Breaking **15**
1.1 Spontaneous Symmetry Breaking and the generation of mass 15
1.1.1 Symmetries 15
1.1.2 $U(1)$ symmetry 16
1.1.3 The electroweak sector and the SSB 19
1.1.3.1 The Electroweak sector 19
1.1.3.2 The SSB in the Electroweak sector 20
1.1.3.3 Masses of the fermions 23
1.2 The constraints on the Higgs boson mass 23
1.2.1 Unitarity of scattering amplitudes 24
1.2.2 Triviality of the Higgs boson self-coupling 24
1.2.3 Vacuum stability 26
1.2.4 Fine tuning: radiative correction to m_H 27
1.3 Consequence of a 125 GeV Higgs boson in the Electroweak fit 28
1.3.1 Electroweak precision data 28
1.3.2 Introducing the Higgs boson mass 30

2 The phenomenology of the Standard Model Higgs Boson at LHC **33**
2.1 Cross sections 33
2.1.1 The production modes 33
2.1.2 Theoretical uncertainties 36
2.1.2.1 PDFs 36
2.1.2.2 PDF4LHC recommendations 37
2.1.2.3 Scale dependence 38
2.2 The decays of the Higgs boson 38
2.2.1 Partial Widths 39
2.2.1.1 Decay to two photons 40
2.2.1.2 Other decays 42
2.2.2 Total width and Branching Ratios 43

3 The LHC and the ATLAS Detector **46**
3.1 The LHC machine 46
3.1.1 Description 46
3.1.1.1 LHC Layout 46
3.1.1.2 Main components of the LHC machine 47
3.1.1.3 The LHC injector Complex 48
3.1.1.4 Beam Structure 48
3.1.2 Performance 49

3.2 The ATLAS detector . . . 52
3.2.1 Overview of the ATLAS detector . . . 53
3.2.1.1 Coordinate System . . . 54
3.2.1.2 Tracking . . . 54
3.2.1.3 Calorimetry . . . 57
3.2.1.4 Magnets . . . 59
3.2.1.5 Muon Systems . . . 59
3.2.1.6 Forward detector . . . 60
3.2.1.7 Trigger system and data acquisition . . . 60
3.2.2 The LAr electromagnetic calorimeter . . . 61
3.2.2.1 Barrel . . . 61
3.2.2.2 Endcap . . . 63
3.2.2.3 Presampler . . . 64
3.2.2.4 The High Voltage settings . . . 65
3.2.2.5 The energy reconstruction . . . 66
3.2.3 Material Distribution . . . 70

4 The ATLAS Data and their Quality 73
4.1 ATLAS Data . . . 73
4.1.1 Distribution of the data . . . 73
4.1.2 Organization of the data . . . 74
4.2 The Quality of Data . . . 74
4.2.1 High voltage power supply trip . . . 75
4.2.2 Burst of coherent noise . . . 75
4.2.2.1 Assignation of a noise burst to a partition . . . 77
4.2.2.2 Time window veto . . . 78
4.2.3 Problematic channels . . . 78
4.2.3.1 The Good Run List . . . 79
4.3 Complementing the offline data quality . . . 81
4.3.1 Impact of a noisy channels on the physics . . . 81
4.3.2 The LAr cleaning variable and the photon cleaning . . . 82
4.3.2.1 LAr Cleaning . . . 82
4.3.2.2 Photon Cleaning . . . 83
4.3.3 Other variables of interest . . . 87
4.3.3.1 Cell-based variables . . . 87

5 The calibration of the electron and photon energy 90
5.1 Electron and photon energy reconstruction . . . 90
5.1.1 Clustering algorithm . . . 90
5.1.2 Electron and Photon Reconstruction . . . 91
5.1.3 Electron and Photon Identification . . . 91
5.1.4 Electron and Photon Energy Calibration . . . 92
5.2 The cluster-based energy calibration using MCs . . . 94
5.2.1 Method . . . 94
5.2.2 Performance . . . 96
5.2.3 Transition Region . . . 96
5.3 The *in situ* energy calibration . . . 98
5.3.1 Samples and Event Selection . . . 99
5.3.2 Background . . . 100

5.3.3 Method . . . 100
5.3.4 Results . . . 101
5.3.5 Systematic uncertainties . . . 101
5.3.5.1 Theoretical uncertainties . . . 101
5.3.5.2 Experimental uncertainties . . . 102
5.3.5.3 The energy scale uncertainty for different p_T regimes . . . 103
5.3.5.4 The energy scale uncertainty for photons . . . 104
5.3.6 Resolution extraction . . . 109
5.3.7 Systematics uncertainties and Results . . . 110
5.4 Uniformity and stability of the energy response . . . 111
5.4.1 The $Z \rightarrow ee$ Method . . . 111
5.4.2 The E/p Method . . . 112
5.4.3 Stability of energy response versus time and pile-up . . . 112
5.4.4 Effect of the location in the bunch train . . . 114
5.4.5 Uniformity along η . . . 115
5.4.6 Comparing $Z \rightarrow ee$ and $W \rightarrow e\nu$ in narrow ϕ bins . . . 117
5.4.7 Intermodule widening effect . . . 117
5.4.8 Summary . . . 123
5.5 Response uniformity using the Jacobian peak . . . 124
5.5.1 Method . . . 124
5.5.2 Results . . . 126
5.5.3 Cross checks . . . 130
5.6 The $Z \rightarrow ee$ lineshape . . . 131
5.6.1 Multiple scattering modeling . . . 135
5.6.2 Other effects . . . 136
5.7 The layer inter-calibration . . . 137
5.7.1 The presampler calibration . . . 137
5.7.1.1 E_0 and E_1/E_2 correlation . . . 138
5.7.1.2 The E_1/E_2 modeling . . . 141
5.7.1.3 Uncertainties on E_1/E_2 modeling . . . 141
5.7.1.4 Presampler energy scale . . . 143
5.7.2 The strip/middle inter-calibration . . . 143
5.7.2.1 Invariant mass method . . . 144
5.7.2.2 Comparison of the results . . . 147
5.8 $Z \rightarrow ee$ lineshape after layer inter-calibration . . . 148

6 Probing the material budget upstream of the calorimeter with shower shapes 151
6.1 Interaction of particles with matter . . . 151
6.1.1 Electron interactions . . . 151
6.1.2 Photons interactions . . . 152
6.1.3 Radiation length . . . 152
6.1.4 Electromagnetic shower development . . . 153
6.1.4.1 Definition . . . 153
6.1.4.2 Modeling . . . 155
6.2 Estimating the material upstream of the calorimeter . . . 155
6.2.1 Secondary Hadronic interactions . . . 155
6.2.2 SCT extensions . . . 156
6.2.3 Conversions . . . 157

6.2.4 K_s^0 mass . . . 157
6.2.5 Energy flow studies . . . 158
6.3 Electromagnetic shower shapes in simulation . . . 159
6.3.1 Variable of interest . . . 160
6.3.2 Geometries . . . 161
6.3.3 Quantifying the sensitivity . . . 161
6.3.4 Analysis . . . 161
6.4 Shower shapes studies with data . . . 163
6.4.1 Probing the material vs ϕ . . . 163
6.4.2 Probing the material vs η . . . 165
6.4.2.1 Calibration coefficients in presampler energy . . . 166
6.4.2.2 The back energy . . . 167
6.4.2.3 f_0 and f_1 . . . 171
6.4.2.4 The region $\eta \sim 1.7$ . . . 172
6.4.3 Quantification of material . . . 178

7 The $H \to \gamma\gamma$ analysis 180
7.1 Event selection . . . 180
7.1.1 Diphoton events selection . . . 180
7.1.2 Object selection . . . 182
7.2 Invariant mass reconstruction . . . 183
7.3 Event categorization . . . 184
7.3.1 2011 data taking . . . 185
7.3.2 2012 data taking . . . 186
7.4 Signal Model Specific Corrections . . . 188
7.4.1 Signal MC description . . . 188
7.4.2 General corrections . . . 189
7.4.3 Interference correction . . . 189
7.4.3.1 Definition . . . 189
7.4.3.2 Application to the analysis . . . 192
7.5 Signal modeling . . . 195
7.5.1 Signal shape . . . 195
7.5.2 Signal yield . . . 196
7.6 Background modeling . . . 197
7.6.1 Background composition . . . 197
7.6.1.1 Reducible and Irreducible background . . . 197
7.6.1.2 Data driven background composition . . . 198
7.6.2 MC samples . . . 199
7.6.3 Background modeling . . . 199
7.7 Summary . . . 200
7.8 Systematic uncertainties . . . 201
7.8.1 Uncertainty on signal yield . . . 201
7.8.1.1 Experimental sources of uncertainties . . . 201
7.8.1.2 Theoretical sources of uncertainties . . . 203
7.8.1.3 Summary . . . 203
7.8.2 Migration uncertainties . . . 203
7.8.3 Uncertainty on signal resolution . . . 206
7.8.4 Uncertainties on signal peak position . . . 209

7.8.4.1 The impact of the energy scale systematic on the peak position . 210
7.9 Statistics Intermezzo . . . 212
7.9.1 Description of the statistical procedure . . . 212
7.9.2 Treatment of systematic uncertainties . . . 216
7.10 Results . . . 219
7.10.1 Comparison to background-only hypothesis . . . 219
7.10.2 Signal strength . . . 220
7.10.3 Couplings and production modes . . . 220
7.10.3.1 Signal strength per production mode . . . 220
7.10.3.2 Couplings . . . 221
7.10.4 Fiducial cross section . . . 223

8 Measurement of the Higgs boson mass 224
8.1 Method . . . 224
8.2 Results . . . 225
8.3 Validation of the method . . . 228
8.3.1 Validation of the mass measurement . . . 228
8.3.2 Validation of the strength parameter measurement . . . 229
8.3.3 Coverage of the error . . . 231
8.3.3.1 Coverage for a given μ . . . 231
8.3.3.2 Dependence of the statistical mass uncertainty on μ . . . 231
8.3.3.3 Dependence of the coverage on μ . . . 232
8.3.3.4 Calibration of the statistical uncertainty . . . 233
8.3.3.5 Checks of the error calibration chain . . . 234
8.4 Checks on the diphoton invariant mass . . . 234
8.4.1 Electronic calibration: LAr cell miscalibration . . . 234
8.4.2 Calibration of converted photons . . . 235
8.4.3 Conversion fraction . . . 236
8.4.4 Presampler scale . . . 236
8.4.5 Relative calibration of layer 1 and 2 . . . 236
8.4.6 Angle reconstruction . . . 237
8.5 Consistency checks for the mass measurement . . . 238
8.5.1 Influence of the Background Models and Fit Ranges . . . 238
8.5.1.1 Influence of the Background Model choice . . . 238
8.5.1.2 Dependence to the fit range . . . 239
8.5.2 Signal model choice . . . 240
8.5.3 Categorized vs. inclusive analysis . . . 240
8.5.4 Consistency checks inside the categories of the analysis . . . 241
8.5.5 Excluding events around the transition region . . . 242
8.5.6 Production process strength parameters . . . 243
8.5.7 Further consistency checks for converted photons . . . 243
8.5.8 Stability with time . . . 244
8.5.9 Dependence on the pileup . . . 247
8.5.10 Dependence on the choice of the primary vertex . . . 247
8.5.11 Dependence on the $\cos(\theta^*)$ angle . . . 247
8.6 Signal resolution effects . . . 249
8.6.1 Impact on the peak position . . . 249
8.6.2 Impact on the strength parameter . . . 250

8.6.3 Impact on the nuisance parameter related to the resolution 251
8.6.4 Validation of the mass resolution 254
8.6.4.1 Validation for the inclusive analysis 254
8.6.4.2 Validation in separated categories 255
8.7 Summary of the checks and validations 256
8.8 Impact of the final mass scale uncertainties 257

Bibliography **264**

Chapter 1

The Standard Model and Spontaneous Symmetry Breaking

1.1 Spontaneous Symmetry Breaking and the generation of mass

The Standard Model of particle physics is governed by symmetry principles, some of which are first described below.

1.1.1 Symmetries

The Noether theorem [18] states that to each continuous symmetry is associated a conserved quantity. For example, the invariance under space translation indicates momentum conservation, the invariance under time translation corresponds to energy conservation, and the invariance under rotations signals angular momentum conservation.
There are global and local symmetries. The first, also referred to as internal symmetry, stands for symmetries that leave the space-time point invariant. One example is the ensemble of wave function phase transformations

$$\begin{cases} \phi & \rightarrow & e^{i\alpha}\phi \\ \phi^* & \rightarrow & e^{-i\alpha}\phi^* \end{cases}$$

where α is constant. These transformations form an unitary Abelian group (i.e where the multiplicative operations commute), called $U(1)$. The Dirac equation

$$\gamma^\mu \partial_\mu \psi = m\psi, \tag{1.1}$$

for example is invariant under global transformations. It is obtained by varying the Lagrangian of a free fermion:

$$L = i\bar{\psi}\gamma_\mu \partial^\mu \psi - m\bar{\psi}\psi,$$

where γ_μ corresponds to the Dirac matrices and where $m\bar{\psi}\psi$ represents the self interaction of the vectorial field of mass m, in the equation of motion

$$\frac{\partial}{\partial x^\mu}\left(\frac{\partial L}{\partial(\frac{\partial \psi}{\partial x^\mu})}\right) - \frac{\partial L}{\partial \psi} = 0.$$

According to the Noether theorem, this indicates the conservation of a quantity:

$$J^\mu = \bar{\psi}\gamma^\mu \psi,$$

which corresponds to the electromagnetic current. The charge of the fermion is written:

$$Q = \int d^3 \times J^0.$$

The local symmetries corresponds to transformations where the parameters are functions of the space-time point: in the previous equation this consists in replacing α by $\alpha(x)$. This kind of transformation are generally improperly referred to as gauge transformations [19].

The Lagrangian described above is not invariant under a local symmetry. To re-establish this invariance, the covariant derivative

$$D_\mu = \partial_\mu - ieA_\mu \tag{1.2}$$

has to be introduced in Equation 1.1 in place of ∂_μ. A_μ is a vectorial gauge field that couples with the Dirac particle.

The kinetic term for the field A_μ should also be introduced by hand in the Lagrangian, and has to be invariant under a transformation of A_μ. This is the case for the expression

$$\frac{1}{4}F_{\mu\nu}F^{\mu\nu} \tag{1.3}$$

with $F_{\mu\nu} = \partial_\mu A_\nu - \partial_\nu A_\mu$.

However, a mass term for the field A_μ cannot be added to this Lagrangian as it would break the gauge invariance.

A symmetry can be broken explicitly or spontaneously. In the example given above, the introduction "by hand" of a mass term in the Lagrangian would break explicitly the symmetry. The spontaneous breaking of a symmetry is a concept that is derived from the phase transition phenomenon observed in solid physics. Indeed, it was noticed by Heisenberg in 1928 [20] that ferro-magnets at a temperature below a critical threshold T_C are in an ordered state where the dipoles are aligned in arbitrary directions. This state spontaneously breaks the rotational symmetry of the system. The term of "Spontaneous Symmetry Breaking" (SSB) in particle physics was first introduced by Baker and Glashow [21] and the transposition of the SSB from condensed matter to particle physics was done by Nambu and Jona-Lasinio [22, 23, 24, 25].

The origin of the mass of particles in the Standard Model is based on symmetry considerations. It will be shown in the following that to introduce mass terms in the Standard Model Lagrangian, one should break spontaneously the gauge symmetry. This is first described in a simple $U(1)$ Abelian symmetry.

1.1.2 $U(1)$ symmetry

Global invariance The Lagrangian for a complex scalar field can be expressed as:

$$L = (\partial_\mu \phi)^*(\partial^\mu \phi) - V(\phi\phi^*) \tag{1.4}$$

with

$$V(\phi\phi^*) = +\mu^2\phi^*\phi + \lambda(\phi^*\phi)^2$$

corresponding to the potential and where μ and λ are constant parameters, with λ positive to have a potential bounded from below. The $(\phi^*\phi)^2$ term symbolises a four-vertex configuration for the self interaction of the field ϕ, with a coupling of size λ. The complex scalar field ϕ is written as

$$\phi = (\frac{\phi_1 + i\phi_2}{\sqrt{2}}).$$

The Lagrangian is invariant under the transformation $\phi \rightarrow e^{i\alpha}\phi$, which is a $U(1)$ global gauge symmetry.

If the sign of μ^2 sign is positive, one gets one minimum for the potential $V(\phi\phi^*)$, by asking $dV(\phi\phi^*) = 0$. If the sign of μ^2 is negative, one gets instead one maximum at $\phi = 0$ which is an unstable solution, and a continuous family

$$\phi_1^2 + \phi_2^2 = v^2, \tag{1.5}$$

which are stable solutions with

$$v^2 = \frac{-\mu^2}{\lambda}. \tag{1.6}$$

This ensemble of solutions corresponds to the equation of a circle of centre 0 and radius v in the (ϕ_1,ϕ_2) frame. The potential in the case $\mu^2 < 0$ is illustrated in Figure 1.1 in the (ϕ_1,ϕ_2) frame.

One can choose arbitrarily the solution $\begin{pmatrix} v \\ 0 \end{pmatrix}$, that fulfils the requirement given in Equation 1.5. Choosing this specific solution spontaneously breaks the $U(1)$ symmetry.

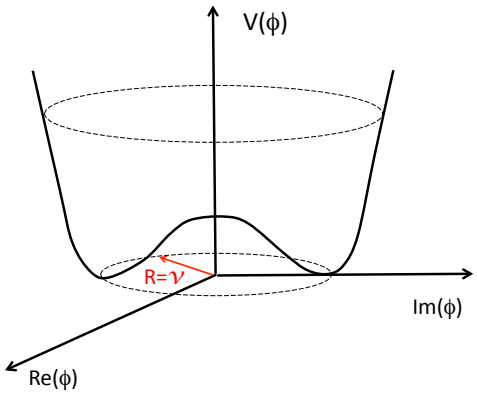

Figure 1.1: Complex Scalar Potential.

The Lagrangian is expanded near this stable minimum to find the spectrum of the theory, using the following expression for the complex scalar field:

$$\phi(x) = \frac{1}{\sqrt{2}}[v + \eta(x) + i\xi(x)] \tag{1.7}$$

with $\eta(x)$ and $\xi(x)$ corresponding to quantum fluctuations around the minimum.

Replacing this expression in the Lagrangian, one gets a new expression:

$$L' = \frac{1}{2}(\partial_\mu \xi)^2 + \frac{1}{2}(\partial_\mu \eta)^2 + \mu^2\eta^2 + A + \mathcal{O}(\eta^3) + \mathcal{O}(\xi^3) + \mathcal{O}(\eta^4) + \mathcal{O}(\xi^4)$$

where A is a constant. The term $\mu^2\eta^2$ corresponds to a mass term for the field η: $m_\eta = \sqrt{-2\mu^2} = \sqrt{2\lambda v^2}$ using Equation 1.6. The field ξ does not get a mass term in this new Lagrangian.

This is an illustration of the Goldstone theorem: in 1960, Goldstone showed that massless scalar bosons appear when a continuous global symmetry is spontaneously broken [26, 27]. The number of Goldstone bosons is equal to the number of broken generators. In the above example, the field ξ corresponds to the massless Goldstone boson expected from this theorem.

Local gauge invariance The Lagrangian given in Equation 1.4 is not invariant under a local transformation like

$$\phi \rightarrow e^{i\alpha(x)}\phi.$$

The covariant derivative defined in Equation 1.2 is used to restore the invariance, and the self-interaction of the field ϕ, with the form given in Equation 1.3, is introduced in the Lagrangian, which is written as

$$L = (D^{\mu}\phi)^{*}(D_{\mu}\phi) - \mu^{2}\phi^{*}\phi - \lambda(\phi^{*}\phi)^{2} - \frac{1}{4}F_{\mu\nu}F^{\mu\nu},$$

with $\lambda > 0$ and $\mu^{2} < 0$. The minima of the potential are the same as the ones detailed previously, and the complex scalar field ϕ is rewritten as in Equation 1.7. Using this new expression of ϕ, the Lagrangian becomes:

$$L' = \frac{1}{2}(\partial_{\mu}\xi)^{2} + \frac{1}{2}(\partial_{\mu}\eta)^{2} - v^{2}\lambda\eta^{2} + \frac{1}{2}e^{2}v^{2}A_{\mu}A^{\mu} - evA_{\mu}\partial^{\mu}\xi - \frac{1}{4}F_{\mu\nu}F^{\mu\nu} + ...$$

The remaining terms not included here correspond to interaction terms. The inspection of this new Lagrangian leads to the following statement:

- A massive scalar particle η appears with a mass $m_{\eta} = \sqrt{2\lambda v^{2}}$
- A massive gauge boson A_{μ} is produced, whose mass is $m_{A_{\mu}} = ev$
- A massless Goldstone boson ξ is generated, $m_{\xi} = 0$

The number of initial degrees of freedom in term of field content is two (for the complex scalar field ϕ) whereas the final number is three, one for the massless Goldstone boson, one for the massive scalar and one for extra longitudinal mode of the massive gauge boson. However, the spontaneous symmetry breaking should not create additional degrees of freedom.

The extra degree of freedom in reality corresponds to the freedom of making a gauge transformation [28]. Hence one should find a particular gauge transformation that allows to eliminate this extra degree of freedom: from Equation 1.7 one can write

$$\phi(x) = \frac{1}{\sqrt{2}}[v + \eta(x) + i\xi(x)] \sim \frac{1}{\sqrt{2}}[v + \eta(x)]e^{i\frac{\xi}{v}}$$

and choose the particular transformation:

$$\phi \rightarrow \frac{1}{\sqrt{2}}[v + h(x)]e^{i\frac{\theta(x)}{v}} \tag{1.8}$$

If $\theta(x)$ is fixed, $h(x)$ is real and then the theory is independent of θ.

Repeating the procedure described above using this transformation, the Lagrangian becomes:

$$L'' = \frac{1}{2}(\partial_{\mu}h)^{2} - v^{2}\lambda h^{2} + \frac{1}{2}e^{2}v^{2}A_{\mu}A^{\mu} - \lambda v h^{3} - \frac{1}{4}\lambda h^{4} + ve^{2}A_{\mu}A^{\mu}h + \frac{1}{2}e^{2}A_{\mu}A^{\mu}h^{2} - \frac{1}{4}F_{\mu\nu}F^{\mu\nu}$$

The conclusions stated before are modified:

- A scalar massive particle h appears with the mass $m_{h} = \sqrt{2\lambda v^{2}}$
- A massive vector A_{μ} is produced, whose mass is $m_{A_{\mu}} = ev$
- The massless Goldstone boson has disappeared

When a Spontaneous Symmetry Breaking (SSB) occurs with a local gauge invariance, there is an exception to the Goldstone theorem: the Goldstone boson is not produced, it is instead absorbed by the longitudinal polarization of the gauge vector. This mechanism corresponds to the so-called "Higgs mechanism" and the scalar massive particle h is referred to as the Higgs boson. The mass of this scalar particle is not determined, as the constant λ is unknown. Then the Higgs boson mass cannot be determined except by measuring it experimentally.

One can notice the presence of interaction terms in h^3, h^4, $hA_\mu A^\mu$, $h^2 A_\mu A^\mu$ with the corresponding strengths λv, $\frac{1}{4}\lambda$, ve^2, $\frac{1}{2}e^2$ which correspond to the self-couplings of the scalar massive boson and its couplings to the gauge boson A_μ. The self-couplings strength are unknown due to the presence of the constant λ but the couplings to the gauge bosons can be determined.

The constant v has been evaluated experimentally from the measurement of the W mass and the constant g or from the measurement of the Fermi constant G_F : $v = 246$ GeV. The mass of a Higgs-like boson has been measured recently at LHC (see Chapter 8). Considering the value $m_H = 126$ GeV, one gets

$$\lambda = \frac{m_H^2}{2v^2} \sim 0.13.$$

This means that the theory can be calculated in a perturbative regime.

1.1.3 The electroweak sector and the SSB

1.1.3.1 The Electroweak sector

The Lagrangian of the Electroweak interactions is invariant under $SU(2)_L \times U(1)_Y$ transformations, where L corresponds to the left-handed components and Y to the weak hyper-charge.

This can be written:

$$-igJ_\mu.W^\mu = -ig\bar{\chi_L}\gamma_\mu\tau.W^\mu\chi_L$$

and

$$-i\frac{g'}{2}j_\mu^Y.B^\mu = -ig'\bar{\psi}\gamma_\mu\frac{Y}{2}.\psi B^\mu$$

where:

- J_μ (j_μ^Y) is an isotriplet of weak current (weak hyper-charge current) of the $SU(2)_L$ ($U(1)_Y$) group of transformation
- W^μ and B^μ are vector bosons
- g ($\frac{g'}{2}$) is the strength of the coupling to W^μ (B^μ)
- χ_L is an isospin doublet used for left-handed fermions.
- τ (Y) are the generators of the $SU(2)_L$ ($U(1)_Y$) group

The generator τ are linear independent traceless matrices 3×3 with $\tau = \frac{\sigma}{2}$ where σ are the Pauli matrices:

$$\sigma^1 = \begin{pmatrix} 0 & 1 \\ 1 & 0 \end{pmatrix}, \sigma^2 = \begin{pmatrix} 0 & -i \\ i & 0 \end{pmatrix}, \sigma^3 = \begin{pmatrix} 1 & 0 \\ 0 & -1 \end{pmatrix}$$

To complete the electroweak theory, one has also to consider the $U(1)_{em}$ group corresponding to the electromagnetic interactions:

$$-iej_\mu^{em}A^\mu = ie(\bar{\psi}\gamma_\mu Q\psi)A^\mu$$

where similarly:

- j_μ^{em} is the electromagnetic current of the $U(1)_{em}$ group of transformations
- Q are the generators of this group
- A^μ corresponds to the associated vector boson
- e is the strength of the coupling to this vector

The generators for these three groups follow the relation:

$$Q = \tau^3 + \frac{Y}{2} \tag{1.9}$$

and then :

$$j_\mu^{em} = J_\mu^3 + \frac{1}{2}j_\mu^Y \tag{1.10}$$

This means that the electromagnetic current is a linear combination of the neutral currents J_μ^3 and j_μ^Y and therefore that the gauge fields associated to these currents W_μ^3 and B_μ are orthogonal linear combination of the physical neutral gauge fields A_μ and Z_μ. This is described in more detail below.

1.1.3.2 The SSB in the Electroweak sector

Four fields are needed to describe the Spontaneous Symmetry Breaking in the Electroweak sector. These fields should belong to the $SU(2) \times U(1)$ multiplet in order to keep the gauge invariance of the Lagrangian. The choice historically made by Weinberg in 1967 [7], is to put them in an isospin doublet, with weak hyper-charge equal to 1:

$$\phi = \begin{pmatrix} \phi^+ \\ \phi^0 \end{pmatrix}$$

with

$$\begin{cases} \phi^+ &= \frac{\phi_1 + i\phi_2}{\sqrt{2}} \\ \phi^0 &= \frac{\phi_3 + i\phi_4}{\sqrt{2}} \end{cases}$$

The Electroweak Lagrangian, invariant under a local $U(1) \times SU(2)$ transformation, can be written as [1]

$$L = (D_\mu\phi)^\dagger(D^\mu\phi) - V(\phi^\dagger\phi) \tag{1.11}$$

with

$$V(\phi^\dagger\phi) = \mu^2\phi^\dagger\phi + \lambda(\phi^\dagger\phi)^2$$

where $\lambda > 0$ and $\mu^2 < 0$ and with

$$D_\mu = \partial_\mu - ig\frac{\boldsymbol{\sigma}}{2} \cdot \boldsymbol{W}_\mu - ig'\frac{Y}{2}B_\mu$$

[1] Setting aside the gauge kinematic terms.

The gauge vector fields $\boldsymbol{W}_\mu$ and B_μ have then been introduced to re-establish the invariance of the Lagrangian.

The stable minima of the potential are solutions of:

$$\frac{1}{2}(\phi_1^2 + \phi_2^2 + \phi_3^2 + \phi_4^2) = \frac{-\mu^2}{2\lambda} \tag{1.12}$$

which is the equation of a sphere in a 4-dimensional space.

The choice $\phi_1 = \phi_2 = \phi_4 = 0$ and $\phi_3^2 = \frac{-\mu^2}{2\lambda} = v^2$ is one particular solution of Equation 1.12, leading to $\phi_0 = \begin{pmatrix} 0 \\ v \end{pmatrix}$. This choice hides the symmetry that resided in the ϕ_i fields.

Each choice of ϕ_0 that breaks a symmetry generates a mass for the corresponding gauge boson. Therefore, if ϕ_0 is left invariant under a group of gauge transformation, the gauge boson associated to this group will be massless. The choice of this solution is then not fortuitous: it should break both $SU(2)_L$ and $U(1)_Y$ and should be invariant under the $U(1)_{em}$ transformation group in order to let the photon massless. If ϕ_0 is neutral, the $U(1)_{em}$ symmetry is not broken. Indeed, the transformation

$$\phi_0 \rightarrow \phi_0' = e^{i\alpha(x)Q\phi_0}$$

leads to $\phi_0' = \phi_0$, whatever the value of $\alpha(x)$. The vacuum is therefore invariant under $U(1)_{em}$, and the photon remains massless. The generator of $U(1)_{em}$ is related to the generators of $SU(2)_L$ and $U(1)_Y$ following the relation 1.9. Then the choice $Y = 1$, $T^3 = -\frac{1}{2}$ and $T = \frac{1}{2}$ both satisfy this relation and breaks at the same time $SU(2)_L$ and $U(1)_Y$.

The Lagrangian is expanded near this particular minimum:

$$\phi(x) = \frac{1}{\sqrt{2}} \begin{pmatrix} 0 \\ v + \eta(x) + i\xi(x) \end{pmatrix}$$

with $\eta(x)$ and $\xi(x)$ corresponding to quantum fluctuations around the minimum.

As described in Section 1.1.2, for the local transformations, there is an extra degree of freedom in the Lagrangian, corresponding to the freedom of making a gauge transformation. Similarly to Equation 1.8, one can choose the transformation:

$$\phi(x) \rightarrow \frac{e^{i\boldsymbol{\sigma}\cdot\boldsymbol{\theta}(x)/v}}{\sqrt{2}} \begin{pmatrix} 0 \\ v + h(x) \end{pmatrix}$$

and substituting this expression into the Lagrangian it is again seen that it becomes independent of $\boldsymbol{\theta}$. The fields $\boldsymbol{\theta}$ corresponds to three massless Goldstone bosons that are absorbed by this transformation.

In the Lagrangian defined in Equation 1.11, the part that will provide the mass term for the fields $\boldsymbol{W}_\mu$ and B_μ corresponds to:

$$\mid (-ig\frac{\boldsymbol{\sigma}}{2} \cdot \boldsymbol{W}_\mu - ig'\frac{Y}{2}B_\mu)\phi \mid^2$$

with the symbol $\mid \quad \mid^2$ representing the product $(\ )^\dagger(\ )$

This leads to

$$\frac{1}{2} \mid \frac{-i}{2} \begin{pmatrix} gW_\mu^3 + g'B_\mu & g(W_\mu^1 - iW_\mu^2) \\ g(W_\mu^1 + iW_\mu^2) & -gW_\mu^3 + g'B_\mu \end{pmatrix} \begin{pmatrix} 0 \\ v \end{pmatrix} \mid^2$$

that can be re-written as:

$$\frac{1}{4}v^2g^2W_\mu^+W_\mu^- + \frac{1}{8}v^2(W_\mu^3, B_\mu)\begin{pmatrix} g^2 & -gg' \\ -gg' & g'^2 \end{pmatrix}\begin{pmatrix} W^{\mu 3} \\ B^\mu \end{pmatrix} \tag{1.13}$$

with

$$W_\mu^\pm = \frac{W_\mu^1 \mp iW_\mu^2}{\sqrt{2}}.$$

This provides a mass term for the gauge boson W:

$$M_W = \frac{1}{2}gv$$

The matrix $\begin{pmatrix} g^2 & -gg' \\ -gg' & g'^2 \end{pmatrix}$ mixes explicitly the states $W^{\mu 3}$ and B^μ. This matrix is diagonalisable, and the eigenvalues corresponds to 0 and $g^2+g'^2$. There are then two linearly independent vectors associated to these eigenvalues which corresponds to

$$a = \begin{pmatrix} g' \\ g \end{pmatrix} \; ; z = \begin{pmatrix} g \\ -g' \end{pmatrix}$$

respectively for the eigenvalues 0 and $g^2 + g'^2$. A_μ and Z_μ diagonalizes the matrix and corresponds respectively to the photon and Z bosons physical states. After normalization of these eigenvectors, one gets the relation

$$\begin{pmatrix} Z_\mu \\ A_\mu \end{pmatrix} = \begin{pmatrix} \cos\theta_W & -\sin\theta_W \\ \sin\theta_W & \cos\theta_W \end{pmatrix}\begin{pmatrix} W_\mu^3 \\ B_\mu \end{pmatrix}$$

with

$$\sin\theta_W = \frac{g'}{\sqrt{g^2+g'^2}} \; ; \; \cos\theta_W = \frac{g}{\sqrt{g^2+g'^2}} \tag{1.14}$$

where θ_W is the mixing angle introduced by Weinberg in 1967 [7].

From the eigenvalues and from Equation 1.13, one can then deduce the mass terms for these two bosons:

$$M_A = 0 \; ; \; M_Z = \frac{1}{2}v\sqrt{g^2+g'^2}$$

The Lagrangian describes then two massive gauge fields with a mass $M_W = \frac{1}{2}gv$, one massive gauge field with a mass $M_Z = \frac{1}{2}v\sqrt{g^2+g'^2}$, one massless gauge field and one scalar h with the mass $m_h = \sqrt{2\lambda v^2}$ (see Section 1.1.2). The massless Goldstone bosons have disappeared, the gauge fields became massive by "eating" them.

From Equation 1.14, one can deduce the relation between the W and Z mass:

$$\frac{M_W}{M_Z} = cos(\theta_W) \tag{1.15}$$

which is a prediction of the Standard Model with a Higgs boson doublet. The W and Z masses are different due to the mixing between W_μ^3 and B_μ. The parameter ρ is defined as:

$$\rho = \frac{M_W^2}{M_Z^2\cos^2(\theta_W)} = 1.$$

This parameter is equal to 1, due to the global (or custodial) $SU(2)_R$ symmetry of the Higgs Lagrangian.

This model, also called the Weinberg-Salam model, corresponds to the minimal model of the electroweak interactions.

Developing the full Lagrangian, one can find terms that represent the interaction between the gauge massive bosons and the Higgs boson. These terms are in the form:

$$g_{HVV} \propto \frac{m_V^2}{v} \tag{1.16}$$

with m_V the gauge boson mass.

1.1.3.3 Masses of the fermions

A mass term for the fermions $m\bar{\psi}\psi$ breaks explicitly the symmetry of the Electroweak Lagrangian. The Higgs mechanism allows to generate the lepton and quark masses using the same Higgs doublet as the one previously described for the generation of the gauge boson masses.

To generate the fermions masses, a Yukawa term invariant under $SU(2) \times U(1)$ is added to the initial Lagrangian. For example for the quarks, this term is written as:

$$L_{quarks} = -G_d^{i,j}(\bar{u_i}, \bar{d_i'})_L \begin{pmatrix} \phi^+ \\ \phi^0 \end{pmatrix} d_{jR} - G_u^{i,j}(\bar{u_i}, \bar{d_i'})_L \begin{pmatrix} -\bar{\phi^0} \\ \phi^- \end{pmatrix} u_{jR} + h.c.$$

with $\phi_L = \begin{pmatrix} \phi^+ \\ \phi^0 \end{pmatrix}$ and $\phi_R = \begin{pmatrix} -\bar{\phi^0} \\ \phi^- \end{pmatrix}$ corresponding respectively to the left-handed and right-handed doublets and where $i, j = 1, ..., N$ with N the number of quark doublets and where the primed states are the linear combination of the flavour eigenstates.

When substituting ϕ_L by $\begin{pmatrix} 0 \\ v + h(x) \end{pmatrix}$ and ϕ_R by $\begin{pmatrix} v + h(x) \\ 0 \end{pmatrix}$ the Lagrangian transforms as:

$$L_{quarks} = -m_d^i \bar{d}_i d_i (1 + \frac{h}{v}) - m_u^i \bar{u}_i u_i (1 + \frac{h}{v})$$

where m_d^i and m_u^i depend on G_d^{ij} and G_u^{ij} which are arbitrary couplings of the theory. Therefore the quark masses are also not predicted by the theory.

Looking at the term that couples the Higgs boson with the quarks, it can be noticed that this coupling is proportional to the quark mass. The same conclusion also apply to leptons, so that:

$$g_{Hf\bar{f}} \propto \frac{m_f}{v} \tag{1.17}$$

with m_f the fermion mass. This property can be checked experimentally.

1.2 The constraints on the Higgs boson mass

The Higgs boson mass is not predicted in the theory, its value depends on two constants, λ and v (see Equation 1.1.2). However this mass has been measured recently at LHC and is about 126 GeV (see Chapter 8). In the following it will be shown in more detail that with this mass, the unitarity of the theory is ensured, but that an uncertainty on the stability of the potential arises. See for more details [29] for example.

1.2.1 Unitarity of scattering amplitudes

In the scattering process $W^+W^- \to W^+W^-$, if one does not consider the presence of a Higgs boson particle in the intermediate loop, the amplitude of the process scales quadratically with the energy. When the Higgs boson is introduced (see Figure 1.2), the amplitude, in the limit of center of mass energies well beyond the W mass, is modified as follows

$$A(W^+W^- \to W^+W^-) \longrightarrow \frac{1}{v^2}\left[s + t - \frac{s^2}{s - m_H^2} - \frac{t^2}{t - m_H^2}\right],$$

with $s = (p_i + p_f)^2$ and $t = (p_i - p_f)^2$, p_i and p_f being the initial and final momentum.

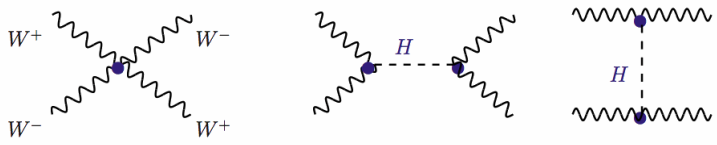

Figure 1.2: Feynman diagrams for the WW scattering, with a Higgs boson exchange.

Requiring that the unitarity conditions are met [30] [31], this gives an approximative condition on the Higgs boson mass: $m_H < 870$ GeV and $m_H < 710$ GeV when including the scattering processes ZZ, HH and ZH [32]. Therefore with a mass $m_H \sim 126$ GeV, and since the couplings of the Higgs-like boson measured are in agreement with the Standard Model expectations [12, 13, 14], the unitarity constraint do not seems to be an issue anymore. However, it is still important to test the couplings with higher precision to check the unitarization.

1.2.2 Triviality of the Higgs boson self-coupling

The evolution of the quartic coupling of the Higgs boson λ with the energy scale is described by the Renormalization Group Equations (RGE) [33]. Taking into account the first loop corrections for the Higgs boson self-interaction (see Figure 1.3 for loops of Higgs bosons and Figure 1.4 for loops of fermions and vector bosons), the evolution of λ with the energy scale Q can then be written as:

$$\frac{d\lambda}{d\log Q^2} \sim \frac{1}{16\pi^2}\left[12\lambda^2 + 6\lambda\lambda_t^2 - 3\lambda_t^4 - \frac{3}{2}\lambda(3g^2 + g'^2) + \frac{3}{16}(2g^4 + (g^2 + g'^2)^2)\right] \tag{1.18}$$

with λ_t the top Yukawa coupling ($\lambda_t = \sqrt{2}\frac{m_t}{v}$) and g, g' the couplings in the electroweak sector. Only the dominant quark and vector boson loops are kept here.

For large values of the Higgs boson mass, the first term dominates in the expression 1.18, corresponding to the case where only Higgs bosons enter in the loops.

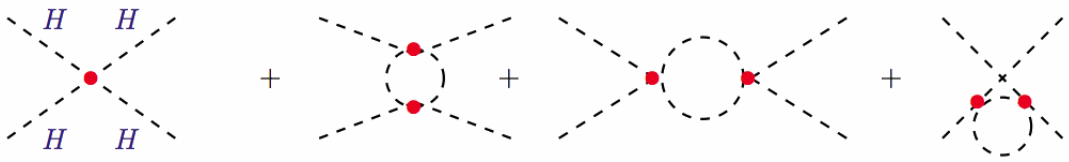

Figure 1.3: Feynman diagrams for Higgs boson self-coupling and 1-loop Higgs boson corrections.

Figure 1.4: Feynman diagrams for Higgs boson self-coupling and 1-loop vector bosons and fermions corrections.

In this case, the solution is:

$$\frac{1}{\lambda(Q^2)} = \frac{1}{\lambda(Q_0^2)} - \frac{3}{4\pi^2}\log(\frac{Q^2}{Q_0^2}).$$

The quartic coupling of the Higgs boson varies logarithmically with the energy scale in this approximation. The pole of this equation, referred to as the Landau pole, is written as

$$Q_{\text{Landau}} = v\exp(\frac{4\pi^2 v^2}{3m_H^2})$$

To avoid this pole, one should ask $Q < Q_{\text{Landau}}$. To have a theory perturbative at all scales, the quartic coupling should vanish, thus rendering the theory non-interacting, i.e trivial [34]. From this equation, one can notice that the smaller the Higgs boson mass, the larger the energy scale until which the theory is valid. In Figure 1.5(a), this bound which is called the "Perturbativity bound" is shown in blue lines. Typically, for a Higgs boson mass $m_H < 170$ GeV, the presence of physics Beyond the Standard Model is not necessary up to the Planck scale [35]. Given the Higgs boson mass of around 126 GeV, the theory does not reach the triviality bound.

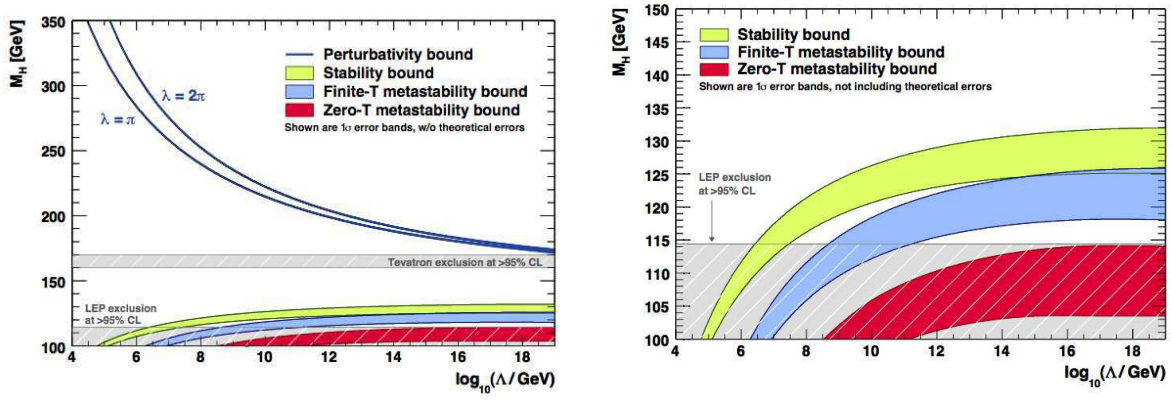

(a) (b)

Figure 1.5: Perturbativity and Stability bounds as a function of the Higgs boson mass and cut-off (a) and enlarging of the curves illustrating the stability bounds (b). Taken from the reference [35].

1.2.3 Vacuum stability

For low Higgs boson mass, the contribution of the Higgs boson to the loops for the Higgs self-coupling becomes sub-dominant with respect to the contribution of the top quark and vector bosons. Neglecting this contribution in the RGE equations and replacing the top Yukawa coupling by its expression as a function of the top mass, Equation 1.18 can be then rewritten as [33]

$$\frac{d\lambda}{d\log Q^2} \sim \frac{1}{16\pi^2}\left[-12\frac{m_t^4}{v^4} + \frac{3}{16}(2g^4 + (g^2+g'^2)^2)\right],$$

where only the dominant contributions of the top quark and of the gauge bosons W,Z are kept. The solution of this equation is

$$\lambda(Q^2) = \lambda(v^2) + \frac{1}{16\pi^2}[-12\frac{m_t^4}{v^4} + \frac{3}{16}(2g^4 + (g^2+g'^2)^2))]\log(\frac{Q^2}{v^2})$$

A negative value of the quartic coupling at the scale Q can be reached, due to the negative sign in front of the dominant top quark term leading to a vacuum which not anymore bounded from below and then to an unstable vacuum. The transition between a negative and positive $\lambda(Q^2)$ value depends on the top mass. The stability argument consists in requiring that the quartic coupling at the scale Q is always larger than 0 [36, 37]. Figure 1.5 shows the stability bound, in yellow curve. On this figure, the mass measured at LHC implies a theory valid up to about $10^9 - 10^{10}$ GeV.

The case where the vacuum is metastable has also been considered. See for more details the references [38, 39, 40]. This configuration relaxes the condition on the mass as seen in Figure 1.5(b) where the blue and red curves show two different models for the metastability [35]. With the Higgs boson mass measured at LHC, there is a preference for a meta-stability of the vacuum for an energy scale above 10^{10} GeV, as seen in Figure 1.6, even if the stability scenario is not excluded [41].

From this figure, one can see that both the precise measurement of the Higgs boson mass and top quark masses are necessary to know the fate of the universe, if the Standard Model is valid up to high energies.

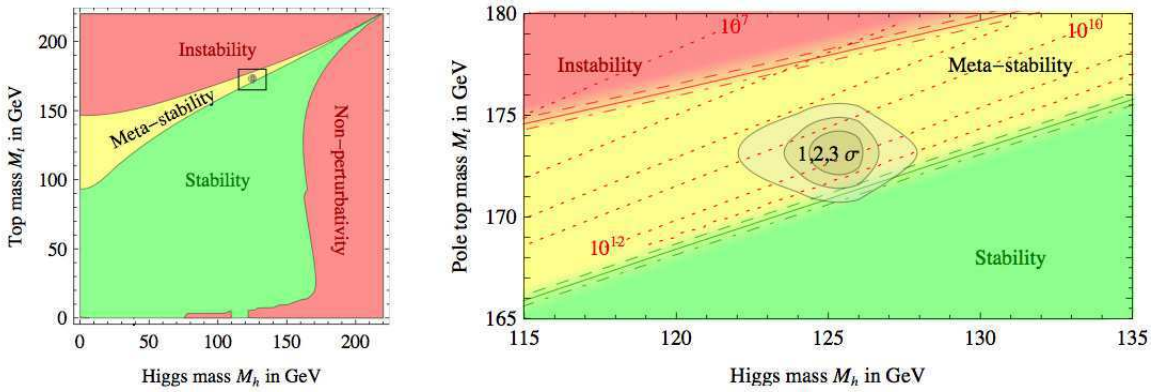

Figure 1.6: Stability, metastability and instability regions as a function of the Higgs boson and top masses [41].

1.2.4 Fine tuning: radiative correction to m_H

Radiative corrections to the Higgs boson mass arise from loop corrections to the Higgs boson propagator. In the loops, fermions, vector bosons and Higgs boson can circulate (see Figure 1.7).

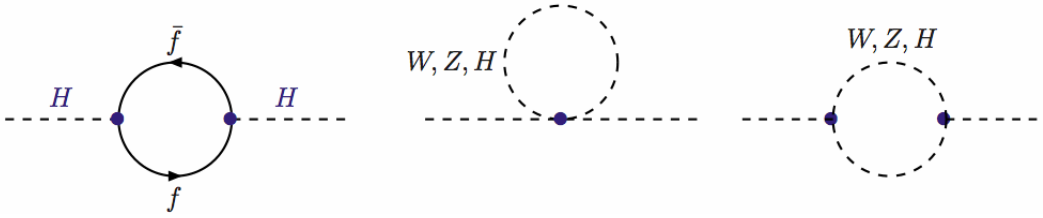

Figure 1.7: Feynman diagrams for the radiative corrections to the Higgs boson propagator, due to fermions, gauge vectors and Higgs bosons.

The physical mass, when keeping only the dominant contribution and cutting off the loop integral at the scale Λ (scale where the new physics is supposed to occur) can be written as:

$$m_H^2 = (m_H^0)^2 + \frac{3\Lambda^2}{8\pi^2 v^2}[m_H^2 + 2m_W^2 + m_Z^2 - 4m_t^2]$$

As can be seen in this expression, the physical mass has a quadratic divergence with the cut-off. In order to suppress this divergence, a compensation between the bare mass m_H^0 and the radiative corrections is needed. If the theory is valid up to the Planck scale, a control of these parameters along 16 orders of magnitude is required. This procedure, called the fine-tuning, is usually considered as inelegant.

Another way to eliminate the divergences would be to have vanishing radiative corrections leading to the relation $m_H^2 + 2m_W^2 + m_Z^2 - 4m_t^2 = 0$. This is referred to as the Veltman condition [42]. Given the W, Z and top mass values, this gives a prediction on the Higgs boson mass: $m_H \sim 320$ GeV.

Only the first order has been added above. Including higher orders one can generally rewrite the previous expression as [43]

$$m_H^2 = (m_H^0)^2 + \Lambda^2 \sum_n c_n(\lambda_i) \log^n(\frac{\Lambda}{Q}), \tag{1.19}$$

where λ_i represents the coupling constants.

To eliminate the divergences, the Veltman condition must be fulfilled at all orders, that is normally impossible given that at each orders the expressions are independent. In reality, one does not need to have the radiative corrections perfectly equal to zero, some fine-tuning is still possible if it is enough small. The amount of fine-tuning which is acceptable is defined as [44]

$$\Delta_{FT} = |\frac{\Delta m_W^2}{m_W^2}| = |\frac{\Delta m_H^2}{m_H^2}|. \tag{1.20}$$

The larger Δ_{FT} is, the more fine-tuning is needed. $\Delta_{FT} \leq 1$ means that there is no fine-tuning. Using the expressions 1.20 and 1.19, the amount of fine-tuning translates:

$$\Delta_{FT} = \frac{2\Lambda^2}{m_H^2} \sum_n c_n(\lambda_i) \log^n(\frac{\Lambda}{m_H})$$

It can be noticed that the fine-tuning increases when Λ increases or m_H decreases.

This sets a lower bound on the value of m_H, in order to have small enough fine tuning up to large scales. This is illustrated in Figure 1.8 where the boundaries for two different allowed amount of fine-tuning $1/\Delta_{FT}$ (10% or 1%) are depicted. This figure summarizes also the previous constraints derived from stability and triviality arguments. A tiny region at large scales

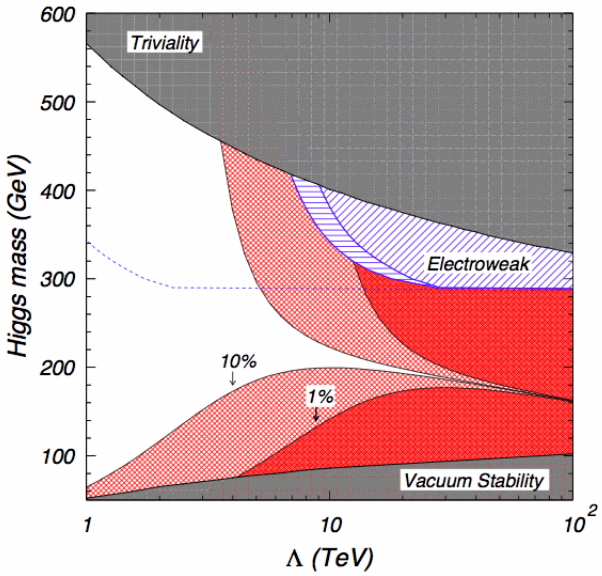

Figure 1.8: Bounds from fine-tuning as a function of the Higgs boson mass and cut-off. Taken from reference [44].

is still allowed around $m_H = 200$ GeV. This region is called the "Veltman throat". Considering $m_H = 125$ GeV, a small tuning of 10 (100) is possible until a scale of around 2 TeV (8 TeV).

This fine-tuning problem raises the question of naturalness: this argument require that the parameters of any physical theory should take reasonable values of order 1. This principle is broken when trying to compensate the divergent radiative corrections of the Higgs boson mass by a fine-tuned value of the bare mass.

1.3 Consequence of a 125 GeV Higgs boson in the Electroweak fit

1.3.1 Electroweak precision data

The Standard Model contains 19 free parameters that are necessary to describe the masses of the particles, the Higgs boson mass and its self-coupling, and the different couplings between the particles.

All the parameters of the Standard Model, even until very recently the Higgs boson mass, have been determined from direct measurements. The Higgs boson mass can also be determined indirectly through radiative corrections to electroweak observables and precision measurement of them.

Indeed, looking at the Fermi constant for example, at leading order it can be written:

$$G_F^{LO} = \frac{\pi\alpha}{\sqrt{2}m_W^2 \sin^2(\theta_W)} = \frac{\pi\alpha}{\sqrt{2}m_W^2(1 - m_W^2/m_Z^2)} \tag{1.21}$$

using Equation 1.15. In addition, there are radiative corrections to the W propagator, due to top and Higgs boson loops (see Figure 1.9).

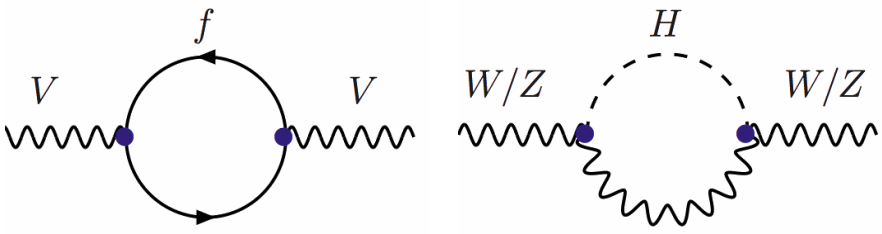

(a) (b)

Figure 1.9: Feynman diagrams for the radiative corrections to the W and Z propagators, due to fermions (a) and Higgs boson (b) loops.

These loops introduce a correction to the Fermi constant which is then modified as:

$$G_F^{NLO} = G_F^{LO} \cdot (1 + \Delta r) \tag{1.22}$$

The correction Δr is proportional to the squared top mass for top contributions in the loop and to the logarithm of m_H/m_W for Higgs boson contribution in the loop:

$$\Delta r \sim c_1 \frac{m_t^2}{m_W^2} + c_2 \log(\frac{m_H}{m_W}) \tag{1.23}$$

with c_1 and c_2 two constants. The weakness of the dependence of the radiative corrections on the Higgs boson mass is explained by the so-called "Veltman screening theorem". The radiative corrections involving a Higgs boson appear only logarithmically and are suppressed due to the small value of the electroweak coupling.

The expression 1.23 describes the correlation between the top, W, Z and Higgs boson masses, the fine structure constant, the Weinberg angle θ_W and the Fermi constant.

Many observables of the electroweak sector have been precisely measured from electron-positron colliders (LEP, SLC) or proton colliders (Tevatron).

Among them, some observables are sensitive to the Higgs boson mass through Equations 1.21, 1.22 and 1.23. These parameters, beside the W mass, are the leptonic left-right asymmetry led by the longitudinal asymmetry A_{LR} (that can be derived for polarized electron beams) and the hadronic asymmetry led by the forward-backward asymmetry for the b quarks A_{FB}^b. There is another parameter which is the ratio of partial widths for Z decay to fermions over the one for decay to hadrons:

$$R_f = \frac{\Gamma(Z \to f\bar{f})}{\Gamma(Z \to hadrons)} \tag{1.24}$$

From all these sensitive parameters, the Higgs boson mass can then be predicted [45, 46, 47]. This can be done with a likelihood fit on the mass, given that the other parameters are

measured elsewhere. The prediction on the Higgs boson mass is then, with the most up-to-date measurements of the electroweak parameters [48],

$$m_H = 94 \pm^{25}_{22} \quad \text{GeV} \tag{1.25}$$

(see Figure 1.11(a), grey band). For the Higgs boson-like resonance observed at LHC, ATLAS and CMS have respectively measured a mass of 126.0 ± 0.4 (stat) ± 0.4 (syst) GeV and 125.3 ± 0.4 (stat) ± 0.5 (syst) GeV. The values are (unofficially) combined assuming uncorrelated uncertainties yielding the combined mass 125.7 ± 0.4 GeV.

This value is consistent with the one given in Equation 1.25 at 1.3σ.

The main part of the uncertainty on the Higgs boson mass prediction comes from the uncertainty on the $\Delta\alpha^{(5)}_{had}(m_Z^2)$ parameter [48]. This parameter is involved when running the value of α (the coupling constant for electromagnetism, normally measured at low energy) to the electroweak mass scale.

In this case the electromagnetic constant is modified as:

$$\alpha(m_Z^2) = \frac{\alpha(0)}{1 - \Delta\alpha_l(m_Z^2) - \Delta\alpha^{(5)}_{had}(m_Z^2) - \Delta\alpha_{top}(m_Z^2)}$$

where $\alpha(0)$ corresponds to the value of α at low energy, and $^{(5)}$ means that only the 5 less massive quarks enter in the loop. The top quark is considered apart, through α_{top}. The contribution from the top is very small ($\sim 10^{-5}$).

The contribution from leptons amounts to around 0.0315 and the contributions from the 5 lightest quarks is of order 0.02761. The world average value of α at the electroweak scale is:

$$\alpha(m_Z^2) = \frac{1}{128.951 \pm 0.027}$$

1.3.2 Introducing the Higgs boson mass

Once the mass of the Higgs boson is measured, all the fundamental parameters of the Standard Model are known. This allows to perform a test of the internal consistency of the Standard Model.

The GFitter group has made such studies [48]. The full electroweak fit gives a $\chi^2_{min} = 21.8$ for 14 free parameters. This translates into a p-value of 0.07 (1.8σ). This result shows a rather good internal consistency of the Standard Model when adding the Higgs boson mass.

In addition, the pulls of the comparison of the fitted values of the electroweak parameters to their direct measurement are always below 3σ. Small tensions of 2.5 σ and 2.4 σ are observed for the forward-backward asymmetry and the ratio of partial width of Z decay into b quarks over the total width for Z boson decay into hadrons R_b (see expression 1.24). These tensions are not due to the introduction of the Higgs boson mass in the fit, but instead observed since a long time.

As seen in Figure 1.10, the A_{LR} (=A_l(SLD) on plot) measurement favours light Higgs boson mass (as the W mass does) whereas the A^b_{FB} measurement prefers a heavy Higgs boson.

The noteworthy result is that the introduction of the measurement of the Higgs boson mass dramatically improves the prediction of the top and W masses as well as the prediction of the effective weak mixing angle (see Figure 1.11). Indeed, the precision on these parameters respectively goes from 6.2 GeV to 2.5 GeV, 28 MeV to 11 MeV and from $2.3 \cdot 10^{-3}$ to $1.0 \cdot 10^{-5}$, while staying in good agreement with the direct measurements. Except for the top mass, these predictions have even a smaller uncertainty than the ones reached by the direct measurements.

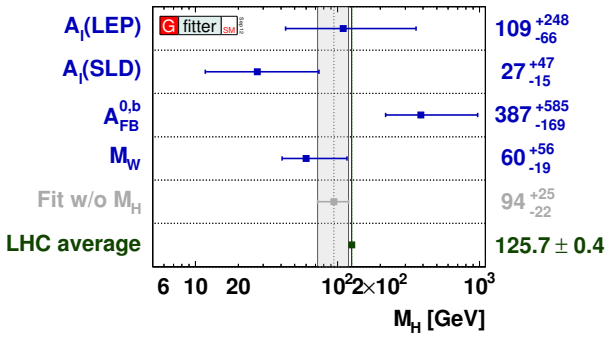

Figure 1.10: Higgs boson mass prediction from leptonic and hadronic asymmetries and comparison to direct measurements [48].

The biggest uncertainty on the prediction of the W mass and on the effective weak mixing angle comes from the uncertainty on the top mass. The uncertainty coming from the unknown higher electroweak corrections contributes around 50%. The uncertainty on the Higgs boson mass contributes very little to the total uncertainty, due to the logarithmic dependence of these parameters on the Higgs boson mass already discussed (Equation 1.23).

The 68% and 95% Confidence Level (CL) for the (m_W,m_t) contour has also been computed, as shown in Figure 1.12. The contours when the Higgs boson mass value is introduced are compared to the direct measurement of these two parameters, as well with the Higgs boson mass prediction. This result demonstrates again a good internal consistency of the Standard Model. It can be noticed from this plot that the uncertainty on the W mass contributes more than the top mass one on the Higgs boson mass uncertainty.

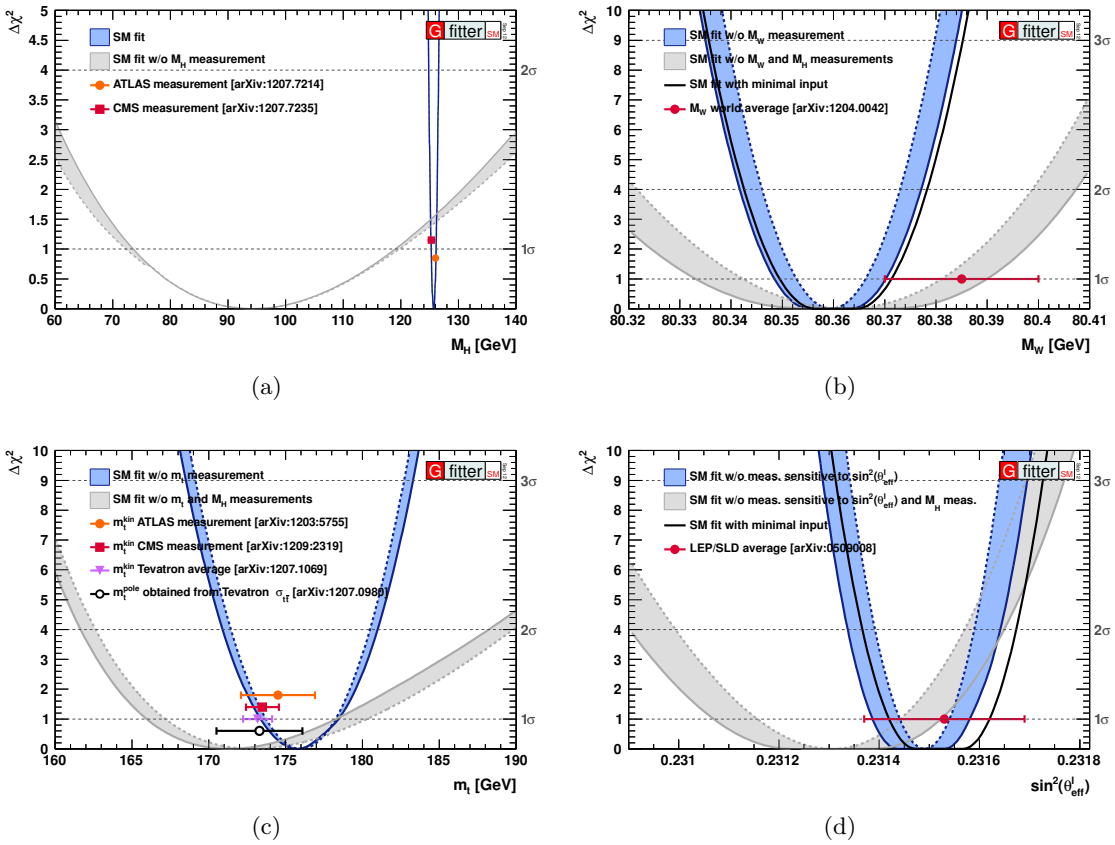

Figure 1.11: $\Delta\chi^2$ for the electroweak fit as a function of m_H (a), m_W (b), m_t (c) and $\sin^2(\theta_{eff})$ (d) [48].

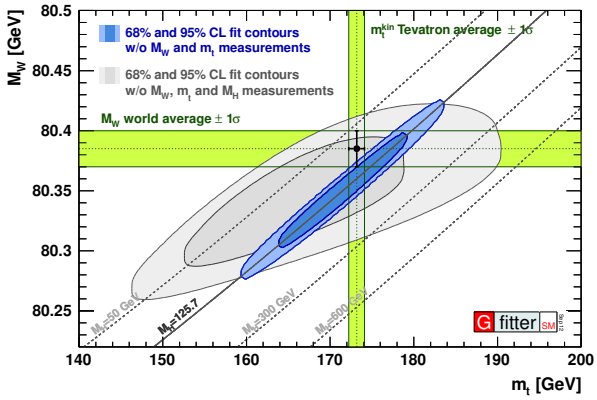

Figure 1.12: (m_W,m_t) contour [48].

Chapter 2

The phenomenology of the Standard Model Higgs Boson at LHC

2.1 Cross sections

2.1.1 The production modes

Gluon Fusion At hadron colliders, the main Higgs boson production process in the Standard Model is the fusion of gluons via a loop of heavy quarks (top, bottom) [49]. Figure 2.1 shows the Feynman diagram for this process. The main contribution comes from the top, because of its large Yukawa couplings to the Higgs boson.

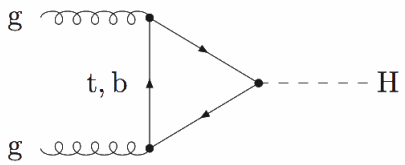

Figure 2.1: Feynman diagram for the Higgs boson production through gluon-gluon fusion.

The gluon fusion cross section has been calculated at next-to-leading order (NLO) [50,51,52] and can be calculated up to the next-to-next-to-leading order (NNLO) in QCD [53, 54, 55].

At next-to-leading order (NLO), the QCD correction reaches 80 to 100% of the cross section, and at the next-to-next leading order (NNLO), an additional 25% correction of the cross section arises, both computed in the limit of large top mass m_t. At NLO, the cross section was also computed exactly (see [50]). This approximation has been shown to describe well the exact calculation at better than 1% for low Higgs boson masses (m_H <300 GeV) [56, 57, 58]. The additional re-summation of soft gluons at next-to-next-leading-logarithm (NNLL) has also been computed. This allows to improve the precision of the cross section [59] and adds an extra 7-9% QCD correction to the cross section.

The electroweak (EW) corrections have also been calculated up to the next-to-leading order [60, 61, 62]. These corrections strongly depend on the Higgs boson mass, going from 5% for $m_H = 120$ GeV to -2% for $m_H = 300$ GeV.

See Table 2.1 for the values of the cross section for this production mode, for $\sqrt{s} = 7,8$ TeV and for a Higgs boson mass of 125 GeV. The evolution of the cross section with the Higgs boson mass is shown in Figure 2.8.

Vector Boson Fusion process The signature of this process corresponds to the production of two forward jets with a large rapidity gap. In addition, there is no colour exchange between the quarks lines, and a very low hadronic radiation activity is therefore expected in the central region of the detector. This process offers thus a possibility of a good background suppression, as the usual QCD background does not produce such a configuration. A set of cuts, like on the jet transverse momentum, on the rapidity gap between the jets or on the jet rapidity are sufficient to obtain a good purity. This production mode is an order of magnitude lower than gluon fusion because this is an electroweak process.

Three channels are available as shown in Figure 2.2, but only the two first, where the Higgs boson is coupled to weak bosons themselves linked to quarks, correspond to the genuine VBF modes. The third channel, the s-channel, is suppressed is suppressed when using the cuts mentioned above. This is why the total production cross section can be generally approximated by the contribution of the t- and u-channels alone [63].

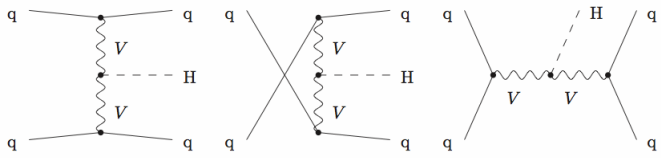

Figure 2.2: Feynman diagrams for the Higgs boson production by Vector Boson Fusion.

In the approximation where only the channels t and u are included, the QCD corrections to the cross section have been fully calculated up to NLO and are of order of 5-10% at NLO [64,65]. Approximate corrections up to NNLO have been also computed [66].

The electroweak corrections to the cross section include contributions with a photon in the initial state. They have been fully computed up to NLO and are of order of -5%, almost as large as the QCD corrections [64, 65].

The values of the cross section for a Higgs boson mass of 125 GeV can be found in Table 2.1. The evolution of the cross section with the Higgs boson mass is shown in Figure 2.8.

The production of a Higgs boson in association with 2 jets, could also come from the gluon fusion process. The cross section for such configuration has been computed theoretically [67] but suffers from quite large uncertainty at NLO [68, 69].

Such QCD production corresponds to a background for the VBF signal. But after applying the VBF-type cuts, they contribute to only $\sim 25\%$ of the Higgs boson + 2 jets production for a Higgs boson mass of 120 GeV (see for example Figure 7.5). The other backgrounds for the VBF process for Higgs decays to τ pairs consist for example in the Z + 2 jets production, where the the Z boson decays to τ pairs.

Associated production WH/ZH This is usually referred to as the "Higgs-strahlung" process. It is characterized at leading-order by the production of an off-shell vector boson *via* the Drell-Yan process and then by the radiation of a Higgs boson by this produced boson. Figure 2.3 shows this process for the W (a) and Z (b) bosons. For the production of a Higgs boson

in association with a Z boson, a third contribution arises at next-to-leading-order. The Higgs boson and Z bosons are produced through a top quark loop from the fusion of two gluons. This is shown in Figure 2.3 (c). This process is involved in 2-6% of the cases for ZH production, for $\sqrt{s} = 7$ TeV in the center of mass [63].

For the first two contributions, the inclusive partonic cross section of the ZH process roughly corresponds to the Drell-Yan cross-section multiplied by the probability that the virtual boson decay into a Higgs boson boson and another vector boson. The hadronic cross section is obtained by convolving the partonic cross section with the parton distribution functions.

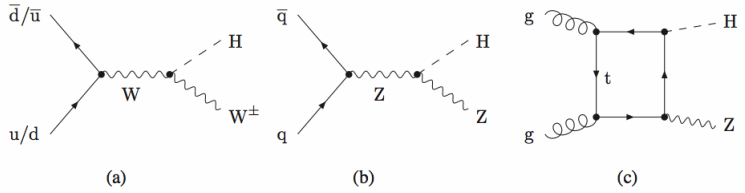

Figure 2.3: Feynman diagram for associated production of a Higgs boson with a boson W,Z

At NLO as well as NNLO, the QCD corrections solely come from the corrections to the Drell-Yan process. The full QCD corrections have been calculated at NLO [70] and at NNLO [71].

The electroweak correction are also derived for this process. Unlike the QCD corrections, there is no factorization of the corrections concerning the Drell-Yan process. The full calculation up to NLO of the EW corrections has been completed [72].

The combination of the electroweak and QCD corrections to the cross section can be treated in different ways. The method adopted for the VH production process is the full factorization of the two effects [73]. This leads to the inclusive cross section at NNLO:

$$\sigma_{WH} = \sigma_{WH}^{NNLO} \times (1 + \delta_{WH,EW}),$$

$$\sigma_{ZH} = \sigma_{ZH}^{NNLO} \times (1 + \delta_{ZH,EW}) + \sigma_{gg \to ZH},$$

where

- σ_{WH}^{NNLO} (σ_{ZH}^{NNLO}) is the WH (ZH) cross section including QCD corrections calculated up to NNLO without including the third process $gg \to ZH$.
- $\sigma_{gg \to ZH}$ is the cross section for the process $gg \to ZH$
- $\delta_{WH,EW}$ ($\delta_{ZH,EW}$) is the relative electroweak correction to the WH (ZH) cross section.

The cross sections for the WH and ZH processes are given in Table 2.1. The evolution of the cross section with the Higgs boson mass is shown in Figure 2.8.

ttH production mode This process corresponds to the production of a Higgs boson in association with a top quark pair, as illustrated in Figure 2.4. This production mode has the smallest cross section which is for example around 100 times smaller than the gluon-gluon fusion one. Moreover the background for this process is large: the dominant ones are for example the $t\bar{t}b\bar{b}$, $t\bar{t}\gamma\gamma$, and $t\bar{t}W^+W^-$ processes. In addition it will be seen in Section 2.1.2 that this process suffers from large uncertainties even at LO.

The measurement of the ttH production cross section is however useful to provide direct information on the Yukawa top-Higgs boson coupling.

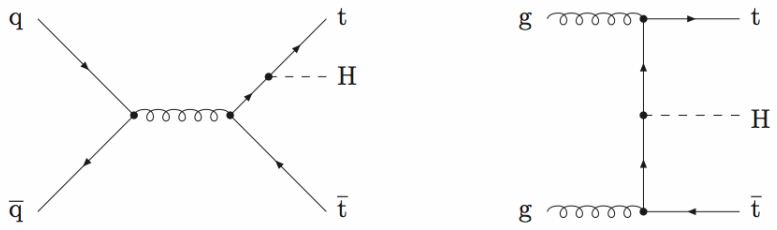

Figure 2.4: Feynman diagram for associated production of a Higgs boson with top quarks.

Only QCD corrections are computed for this process. This has been done up to NLO [74, 75, 76, 77].

The central values and error on the cross section can be found in Table 2.1. The evolution of the cross section with the Higgs boson mass is shown in Figure 2.8.

2.1.2 Theoretical uncertainties

2.1.2.1 PDFs

One of the most important theoretical uncertainties comes from the limited knowledge of the Parton Distribution Functions (PDFs). The PDFs describe the momentum distribution of the partons inside the protons. They are essential in order to predict the production cross section for any process at LHC. The PDFs are obtained from the fit of deep inelastic scattering, jet production or Drell-Yan data, recorded in various experiments like HERA (e-p collider) or Tevatron (hadron collider). Various sets of PDFs are provided by different groups. These functions have differences that come from many sources: the choice of the datasets used, the statistical treatment of the data (experimental uncertainties), the PDF parametrization , the choice of the value of the strong coupling constant α_s and its uncertainty (theoretical uncertainty). Indeed, the PDFs are sensitive to α_s mainly through the gluon distribution.

The LHC experiments use mostly the three sets of PDFs referred to as CTEQ6 [78], MSTW [79] and NNPDF [80].

Their differences are numerous. Among others, mention may be made of [63]:

- The statistical treatment: CTEQ6 and MSTW use Hessian method whereas NNPDF use a Monte Carlo approach.
- The number of functions and free parameters used: CTEQ6 group uses 6 independent PDFs (two to parametrize the lightest flavours and corresponding anti-flavours, one for the total strangeness and the latest models the gluon) and introduces 22 free parameters. Instead, the MSTW group used 7 independent PDFS (three for the lightest favours and corresponding anti-flavours, and one for the gluon) with a total of 28 free parameters. Finally the NNPDF use the same 7 independent PDFs as MSTW, the difference is that it uses 259 free parameters, 37 for each of the PDFs.
- The value of α_s at next-to-leading-order used : 0.118 for CTEQ6, 0.120 for MSTW, and 0.119 for NNPDF.
- The treatment of α_s: CTEQ6 and NNPDF introduce the value of $\alpha_s(M_Z)$ as an external parameter, whereas MSTW group considers the value of $\alpha_s(M_Z)$ as a parameter in the fit.

As seen in Figure 2.5, the relative parton-parton luminosities at NLO are in good agreement for MSTW, NNPDF and CTEQ6 in the low Higgs boson mass region. For other sets of PDFs like HERAPDF1.0, the agreement is less good especially at low and high x. This can be explained by the fact that some of these PDFs do not use the data from Tevatron for the production of jets and W bosons that however allow to constrain respectively the gluon (low x) and light-quarks (high x) distributions. The differences observed between the different sets of PDFs remain when going to next-to-next-to-leading-order calculations, demonstrating that the difference comes either from experimental choices or from the different treatment of charm mass in ep collisions at HERA.

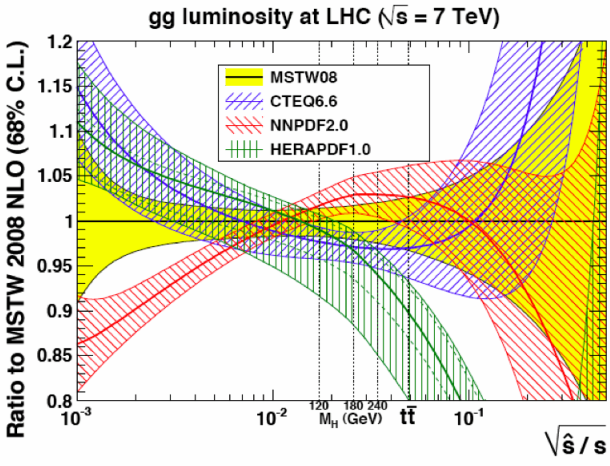

Figure 2.5: Relative gluon-gluon luminosity for different sets of PDFs [81].

2.1.2.2 PDF4LHC recommendations

The predictions can be quite different depending on the set of PDFs used. The full difference between the various PDFs cannot be taken as the total uncertainty because very different inputs enter in these PDFs. This is why a standard procedure for the evaluation of the uncertainty coming from the PDFs has been defined. The PDF4LHC recommendations [82] consist on using the predictions from the three sets of PDFs MSTW, NNPDF and CTEQ6. These PDFs can be compared as they all use data from hadron colliders (Tevatron), fixed target experiments and e-p colliders (HERA). More precisely, the PDF versions that are compared are MSTW2008, NNPDF2.0 and CTEQ6.6. These versions are used because they are the most commonly used by the LHC experiments.

The uncertainty coming from the coupling constant α_s has a strong impact on the PDFs uncertainties as this constant is used in the fits, especially for the gluon-gluon process which starts at the level of α_s^2. An evaluation of the combined PDF + α_s uncertainties has been performed [83, 84].

Figure 2.6, shows the uncertainty band for the total Higgs boson production cross section via gluon fusion at NLO for the three sets of PDFs, normalized to the central MSTW result. At NLO, the central value is taken as the middle point of the envelope provided by the central values and the PDF + α_s errors from these three sets. The error is taken as the full envelope

itself.
At NNLO, the central value is directly given by the prediction from the MSTW2008 PDF set because it includes a larger variety of data from hadron colliders. The error is derived in the same way as described for the NLO prescriptions.

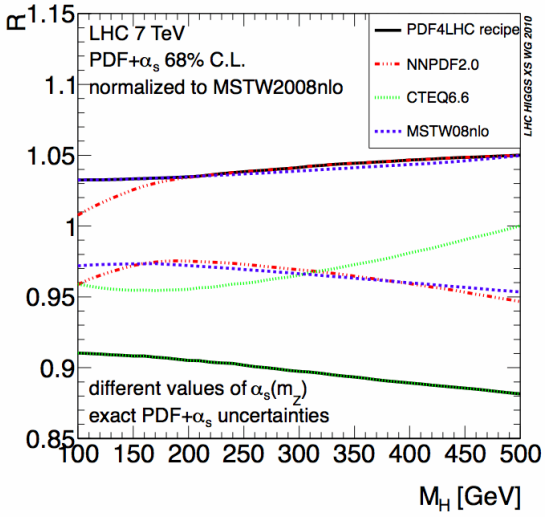

Figure 2.6: Uncertainty band for the total Higgs boson production cross section via gluon fusion at NLO [63].

2.1.2.3 Scale dependence

Another large source of uncertainty comes from the scale dependence. This uncertainty corresponds to the fact that the cross section evaluated at a given order of the QCD perturbative series depends on the factorization and renormalization scales μ_R and μ_F. This variation is not physical, it only reflects the arbitrary truncation in the perturbative series. In most of the cases, going to higher orders allows to decrease this uncertainty. This uncertainty mainly impacts the gluon-gluon fusion process, whereas it is small for the other processes (see Table 2.1).

The uncertainty is estimated by varying the renormalization and factorization scales in an arbitrary window. An example of this scale dependence is that the NLO total cross section for the Higgs boson production is a factor two higher than the LO cross section, and the NNLO cross section is 20% larger than the NLO one [63]. This is illustrated in Figure 2.7. At NLO, the scale dependence is about 15 %, leading to a quite good control of the theoretical uncertainties.

2.2 The decays of the Higgs boson

As seen in Equations 1.17 and 1.16, the couplings of the Higgs boson to fermions are proportional to their masses and the couplings to bosons are proportional to their squared masses. The consequence is that the Higgs boson will preferentially decay into the heaviest particles, given the available phase space. Most of the particle masses are very well known, allowing a precise prediction of the various branching ratios for the decay of the Higgs boson. For Higgs boson search studies and the measurement of the Higgs boson properties, a precise knowledge of the kinematic properties of the final states is needed.

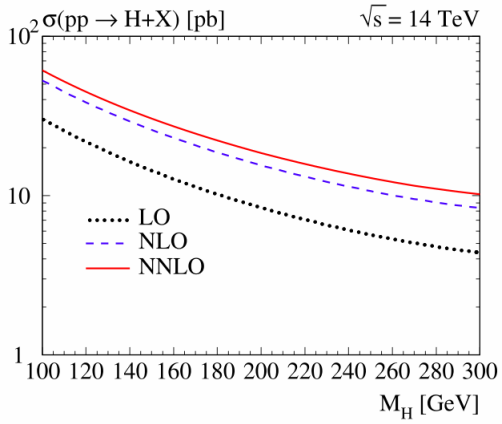

Figure 2.7: Total cross section for Higgs boson production at LHC with $\sqrt{s} = 14$ TeV [63].

Table 2.1: Cross section for the different production modes, at a center-of-mass energy $\sqrt{s} = 7, 8$ TeV at LHC, for a Higgs boson mass of 125 GeV. The highest order reached in the calculation for QCD and EW corrections are given, as well as the uncertainty on these cross sections coming from the scale dependence and from the PDFs following the PDF4LHC recommendation. The total uncertainty corresponds to the linear combination of the QCD and PDF4LHC uncertainties.

Production	QCD	EW	$\sqrt{s}$	σ [pb]	Scale (%)	PDF4LHC (%)
ggH	NNLO + NNLL	NLO	7 TeV	15.32	$^{+7.1}_{-7.8}$	$^{+7.6}_{-7.1}$
			8 TeV	19.52	$^{+7.2}_{-7.8}$	$^{+7.5}_{-6.9}$
VBF	NNLO	NLO	7 TeV	1.22	± 0.3	$^{+2.5}_{-2.1}$
			8 TeV	1.58	± 0.2	$^{+2.6}_{-2.8}$
WH	NNLO	NLO	7 TeV	0.57	$^{+0.2}_{-0.8}$	± 3.5
			8 TeV	0.70	$^{+0.2}_{-0.6}$	± 3.5
ZH	NNLO	NLO	7 TeV	0.32	$^{+1.4}_{-1.6}$	± 3.5
			8 TeV	0.39	$^{+1.6}_{-1.5}$	± 3.5
ttH	NLO	-	7 TeV	0.09	$^{+3.3}_{-9.3}$	± 8.5
			8 TeV	0.13	$^{+3.8}_{-9.3}$	± 7.8

2.2.1 Partial Widths

The Branching Ratios for the various decay modes of the Higgs boson have been calculated. This calculation starts from the derivation of all the partial widths. The branching ratio for the ith mode is defined by:

$$BR_i = \frac{\Gamma_i}{\Gamma_{tot}} \tag{2.1}$$

with Γ_i corresponding to the partial width and Γ_{tot} the total width for the Higgs boson.

The uncertainties on the partial width come from QCD and Electroweak corrections. For QCD, the calculation is up to NLO. The uncertainty coming from missing higher order corrections has been estimated by varying the scale and by looking the impact on the width.

The partial width for the decay into different types of particles and their radiative corrections are detailed below. More attention will be given to the decay into two photons which is the

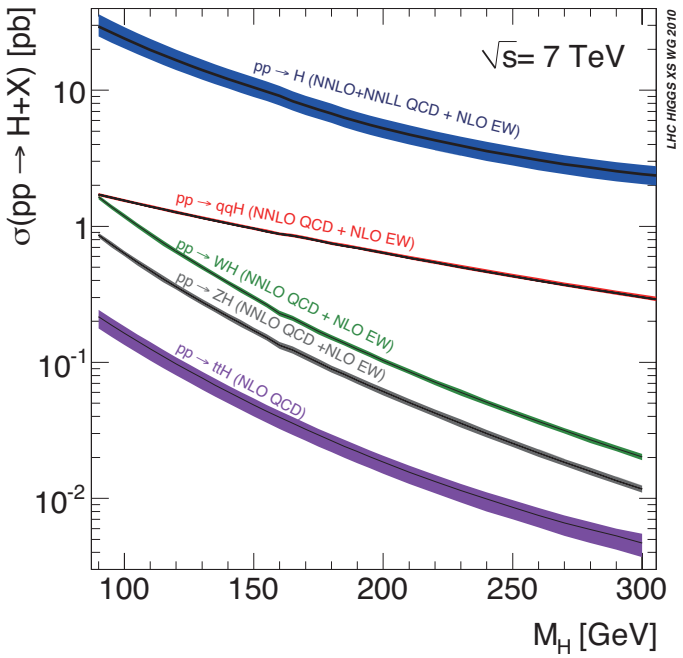

Figure 2.8: Evolution of the cross sections for the different Higgs boson production mode with the Higgs boson mass for a center-of-mass energy $\sqrt{s} = 7$ TeV [63].

channel studied in this thesis.

2.2.1.1 Decay to two photons

The decay into massless photons is made possible thanks to intermediate loops. The particles involved in these loops are either fermions or W vector bosons. This channel provides a clean signature at LHC with two isolated photons with a high transverse momentum.

Massive Beyond Standard Model particles could circulate in the intermediate loop. The test of the effective coupling of the Higgs boson to the photons provides a test of such models and could put constraints on the mass of the unexpected particle circulating in the loops.

The partial width for the decay into photons is [85].

$$\Gamma[H \to \gamma\gamma] = \frac{G_F \alpha^2 m_H^3}{128\sqrt{2}\pi^3} \left| \sum_f N_c Q_f^2 F_{1/2}^H(\tau_f) + F_1^H(\tau_W) \right|^2 \tag{2.2}$$

where Q_f is the charge of the fermion. The squared term corresponds to form factors that depends on the spin of the particle in the loop:

- $F_{1/2}^H(\tau_f)$ for spin 1/2 (fermions, mainly the top quark)
- $F_1^H(\tau_W)$ for spin 1 (W boson)

These form factors are functions of τ_i with $\tau_i = m_H^2/4m_i^2$ and $i = f, W$. They are expressed as:

$$F_{1/2}^H(\tau) = 2[\tau + (\tau - 1)f(\tau)]\tau^{-2}$$

$$F_1^H(\tau) = -[2\tau^2 + 3\tau + 3(2\tau - 1)f(\tau)]\tau^{-2}$$

with the function $f(\tau)$ defined as:

$$f(\tau) = \begin{cases} \arcsin^2 \sqrt{\tau} & \tau \leq 1 \\ -\frac{1}{4}\left[\log \frac{1+\sqrt{1-\tau^{-1}}}{1-\sqrt{1-\tau^{-1}}} - i\pi\right]^2 & \tau > 1 \end{cases}$$

The W and top one-loop contributions interfere destructively. This provides a sensitivity to the relative sign between the W and top coupling to the Higgs boson [86]. The Standard Model predicts the same sign for both couplings, a deviation from this could be interpreted as due to beyond standard model contributions.

The evolution of the real and complex parts of the partial width as a function of the Higgs boson mass has been studied. When the Higgs boson boson mass is lower than $2m_i$, the amplitudes are real as illustrated in Figure 2.9. For low mass Higgs boson (m_H <160 GeV), the dominant amplitude for this decay is then always real [29].

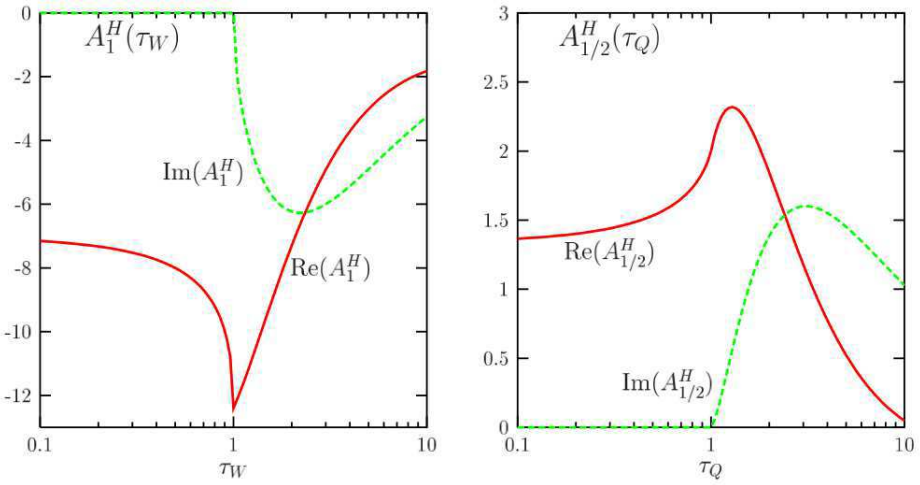

Figure 2.9: Imaginary and real parts of the W boson (left) and heavy fermion (right) amplitudes in the $H \to \gamma\gamma$ decay as a function of the variable $\tau_i = m_H^2/4m_i^2$. Taken from reference [29].

The partial width $\Gamma_{H\to\gamma\gamma}$ evolves rapidly with the Higgs boson mass due to the cubic dependence on m_H seen in Equation 2.2, going from a few keV to ~ 100 keV, when the Higgs boson mass vary from 100 to 300 GeV.

For the $H \to \gamma\gamma$ decay, the NLO QCD corrections consist uniquely in virtual corrections as seen in Figure 2.10. Indeed, the real corrections are forbidden due to color conservation. The correction factor δ to the LO partial width such that $\Gamma_{\gamma\gamma} = \Gamma_{\gamma\gamma}^{LO}(1+\delta)$ is quite small for low masses [29]. These NLO QCD corrections are calculated in references [50, 87, 88, 89].

Two-loop electroweak corrections also arise for this decay. These corrections have been extensively studied in references [60, 90, 91].

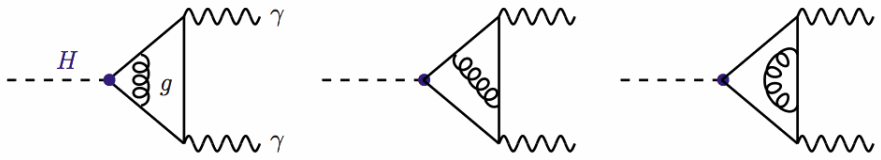

Figure 2.10: Feynman diagrams for Higgs boson decay to photons, and QCD corrections.

2.2.1.2 Other decays

Decay to fermions The study of the Higgs boson decay into fermions is needed to test the Higgs boson couplings to fermions. However in the LHC environment these final states are not easy to detect.

The partial width for decay into fermions at leading order in the Born approximation can be written as [85, 92]

$$\Gamma_{Born}[H \to f\bar{f}] = \frac{G_\mu N_c}{4\sqrt{2}\pi} m_H m_f^2 \beta_f^3 = \frac{g^2 N_c}{32\pi m_W^2} m_H m_f^2 \beta_f^3 \tag{2.3}$$

with $\beta = (1 - 4m_f^2/m_H^2)^{1/2}$, and N_c the color factor (1 for leptons and 3 for quarks).

The partial width increases linearly with the Higgs boson mass m_H and increases quadratically with the fermion mass m_f. Then, below the $t\bar{t}$ threshold, the $b\bar{b}$ channel will be the dominant one.

For the decay into quarks, the QCD NLO corrections are important and have to be taken into account. Figure 2.11 shows these corrections at the first order, which include gluon exchanges and gluon emissions in the final state. With respect to the tree level, in the limit where the quark masses are small compared to the Higgs boson one, at NLO the width is multiplied by a correction factor that depends logarithmically on the ratio between the quark and Higgs boson mass [93, 94, 95, 96]

$$\Gamma[H \to q\bar{q}] = \frac{3G_\mu}{4\sqrt{2}\pi} m_H m_q^2 [1 + \frac{4}{3}\frac{\alpha_s}{\pi}(\frac{9}{4} + \frac{3}{2}\log(\frac{m_q^2}{m_H^2}))].$$

The EW corrections for the decay into bottom and charm quarks are calculated in the approximation of small Higgs boson mass up to NLO [97, 98, 99, 100] (valid with $\sim 1\%$ accuracy for $m_H < 135$ GeV).

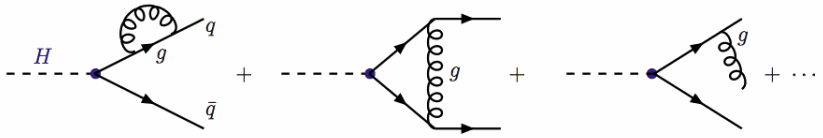

Figure 2.11: Feynman diagram for Higgs boson decay to fermions, and QCD corrections.

Decay to vector bosons The Higgs boson decay to vector boson pairs is expected to have a very clear signature at LHC especially in the decay into two Z bosons decaying consecutively in two leptons each.

The partial width for the decay into electroweak gauge bosons can be written as [101, 92]

$$\Gamma[H \to VV] = \frac{G_\mu m_H^3}{16\sqrt{2}\pi}\delta_V\sqrt{1-4x}(1-4x+12x^2), \tag{2.4}$$

with $x = \frac{m_V^2}{m_H^2}$, $V = W, Z$ and $\delta_W = 2$; $\delta_Z = 1$.

From this equation, one can notice that the partial width grows as m_H^3. This is expected to have an important impact on the total Higgs boson width at high masses.

The difference in the dependence with m_H for the decay into fermions and into vector bosons (m_H vs m_H^3) comes from the fact that the vector boson gets a longitudinal polarization for large Higgs boson mass that grows with the energy [29].

The ZZ and WW channels are open for low Higgs boson mass, even below the mass thresholds $2m_Z$ or $2m_W$, because one of the bosons can be off-shell. However this process is strongly reduced [102, 103, 104].

In addition, when the Higgs boson mass is below the ZZ threshold, the interference for final states with identical fermions becomes important. For a Higgs boson mass of 120 GeV, this interference increases by about 10% the $H \to eeee$ and $H \to \mu\mu\mu\mu$ branching ratios and decrease by about 5% the $H \to e\nu_e e\nu_e$ and $H \to \mu\nu_\mu\mu\nu_\mu$ processes.

The complete QCD and EW NLO corrections for the decay into a pair of vector bosons, with either a 4-leptons final state [105] or a semileptonic and hadronic final state [106] have been computed.

2.2.2 Total width and Branching Ratios

The total width of the Higgs boson is computed as the sum of all the partial widths. Figure 2.12 shows the evolution of the total width as a function of the Higgs boson mass hypothesis. The shoulder observed around $m_H = 160$ GeV corresponds to the vector boson threshold. At $m_H = 125$ GeV, the total width amounts to 4.03 MeV. The mass peak resolution is therefore completely dominated by detector effects.

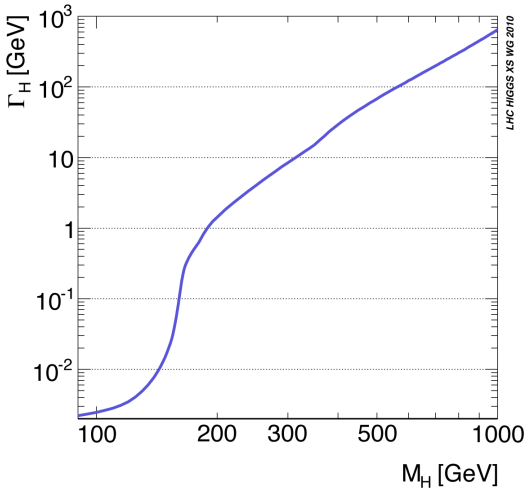

Figure 2.12: Evolution of the total width of the Higgs boson as a function of its mass. Taken from reference [63].

The value of the branching ratios are derived from Equation 2.1 which uses the computation of the partial widths described previously and of the total width.

Figure 2.13 shows the evolution of the branching ratios as a function of the Higgs boson mass for various decay modes.

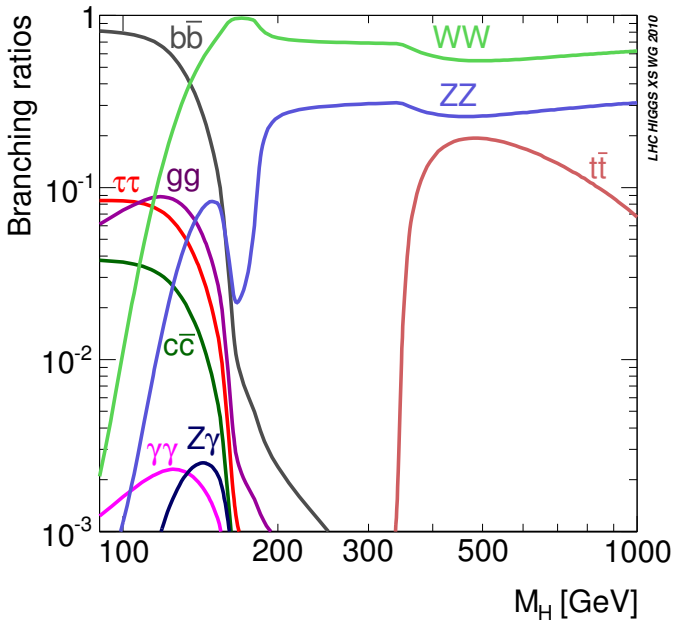

Figure 2.13: Dependence of the Branching Ratios for the different Higgs boson decay modes on the Higgs boson mass. Taken from reference [63].

The branching ratios change rapidly with the Higgs boson mass. Their values for a Higgs boson mass of 125 GeV are summarized in Table 2.2. The QCD and electroweak uncertainties coming from missing higher order terms are also summarized in this table.

Following the mass window which is considered, more or fewer channels are exploitable at LHC. Three windows can be considered: the low mass range $110 < m_H < 160$ GeV, the intermediate mass range $160 < m_H < 250$ GeV and the high mass range $250 < m_H < 1000$ GeV.

Table 2.2: Main branching ratios for a standard model Higgs boson at $m_H = 125$ GeV in fermionic and bosonic final states and the associated systematic uncertainties coming from missing higher orders QCD and EW terms [63]. The highest orders reached for the partial width are indicated.

Decay	Branching ratio	QCD (%)	EW (%)
$H \to t\bar{t}$	$< 5 \cdot 10^{-8}$	$\sim 5\%$ (NLO)	$< 2 - 5\%$ (NLO)
$H \to b\bar{b}$	$5.78 \cdot 10^{-1}$	0.1-0.2% (NNNLO)	1-2% (NLO)
$H \to c\bar{c}$	$2.68 \cdot 10^{-2}$	0.1-0.2% (NNNLO)	1-2% (NLO)
$H \to \tau\tau$	$6.37 \cdot 10^{-2}$	-	1-2% (NLO)
$H \to gg$	$8.6 \cdot 10^{-2}$	10% (NNLO)	1% (NLO)
$H \to \gamma\gamma$	$2.30 \cdot 10^{-3}$	$< 1\%$ (NLO)	$< 1\%$ (NLO)
$H \to WW$	$2.16 \cdot 10^{-1}$	$< 0.5\%$ (NLO)	$\sim 0.5\%$ (NLO)
$H \to ZZ$	$2.67 \cdot 10^{-2}$	$< 0.5\%$ (NLO)	$\sim 0.5\%$ (NLO)

Low mass region In this region, most of the decay channels are accessible. An hypothetical Higgs boson at 125 GeV is then an ideal scenario for studying its couplings to other particles. Typically, the branching ratio for low mass range $m_H < 135$ GeV amounts to around:

- $H \to b\bar{b} \sim 40 - 80\%$
- $H \to WW \sim 0 - 40\%$
- $H \to \tau\tau \sim 4 - 8\%$
- $H \to gg \sim 6 - 7\%$
- $H \to ZZ \sim 0 - 5\%$
- $H \to c\bar{c} \sim 2 - 4\%$

The other are below the percent level in this mass window. The $H \to b\bar{b}$ channel is the dominant one below 130 GeV, and is sensitive only below this mass threshold.

Intermediate mass region In the intermediate mass range, there are only three surviving decay modes: ZZ, WW, and $b\bar{b}$ at the level of a few percent.

High mass region Finally, in the high mass range, the two remaining decay channels are WW and ZZ, that share respectively approximately 2/3 and 1/3 of the total Higgs boson width. The top quark is the heaviest particle, but this channel is not open for Higgs boson masses below around 260 GeV.

At high mass, the $t\bar{t}$ channel does not contribute so much compared to WW and ZZ, because its partial width grows as m_H whereas the WW and ZZ partial widths grows more rapidly, as m_H^3 (see Equations 2.3 and 2.4).

Chapter 3

The LHC and the ATLAS Detector

3.1 The LHC machine

3.1.1 Description

The Large Hadron Collider is a hadron accelerator and collider machine based at CERN near Geneva. This machine uses the 27 km tunnel, located underground between 50 m and 175 m depth, that was built between 1984 and 1989 for the LEP machine. In 2000, LEP stopped operations to give way to the LHC. The approval of the LHC project has been given in December 1994, by the CERN Council [107].

The LHC started its operation on September 10, 2008. It was obliged to stop soon after for more than one year due to serious damages on accelerator components caused by faulty electrical connections, which led to an important helium leakage in the tunnel [108]. The LHC restarted on November 20, 2009 with a center of mass energy well below the nominal 14 TeV. The instantaneous luminosity was also well below the nominal target, but it has increased continuously since. In 2012, the beam energies increased, reaching 4 TeV each.

In February 2013, the LHC stopped again its operation for an expected long period of two years. This long shutdown (LS) is necessary to prepare the machine for going to higher energy, close to the 14 TeV initially targeted.

3.1.1.1 LHC Layout

The tunnel geometry was designed for electron-positron collisions for LEP: it consists of eight long arcs (2.45 km each) and eight insertions also denoted Points. The arcs contain the dipole bending magnets (154 in each arc). An insertion is made of one long straight section (approximately 528 m) plus two transition regions, one at each end. The layout of a straight section is not constant, it depends on the objective of the insertion: it can be for physics, or for beam injection, extraction and cleaning. An octant starts from the middle of an arc and ends in the middle of the following arc, and therefore covers a full insertion, as illustrated in Figure 3.1.

The LHC experiment hosts four experiments: ATLAS [110], CMS [111], LHCb [112] and ALICE [113]. The ATLAS and CMS experiments are located respectively at Points 1 and 5 (diametrically opposite straight sections). These two insertions are identical in term of hardware and optics. However the crossing angles are different: it is in the vertical plane in Point 1 and in the horizontal plane in Point 5. ALICE and LHCb are located at Points 2 and 8 respectively. The Beam 1 going clockwise is injected at Point 2 whereas the Beam 2 going anti-clockwise is injected at Point 8. The four remaining interaction points are not used for physics experiments: the straight section at Point 6 contains the beam extraction system, the one at Point 4 contains two

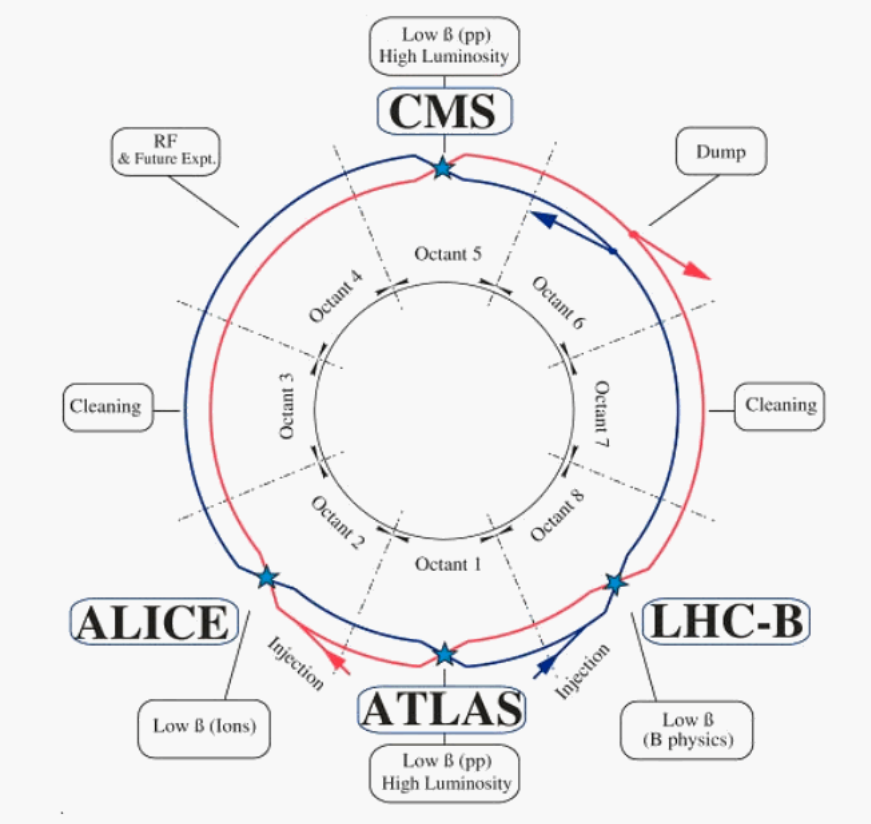

Figure 3.1: LHC layout [109].

Radio-Frequency systems, one for each LHC beam, that allow to compensate for the synchrotron radiation losses, and at Points 3 and 7, collimation systems are installed. The collimation and extraction system are not detailed here. See for example the references [109, 114].

3.1.1.2 Main components of the LHC machine

The Radio-Frequency (RF) cavities consist in an important element of the LHC machine, as they are at the source of the gain of energy of the particles. Indeed, this energy gain is proportional to the delivered voltage, which is a sinusoidal function of the RF. For hadron beams, low frequency RF cavities are used.

The acceleration of bunches of charged particles requires a synchronization, which is achieved by matching the RF with the particle's velocity. The LHC uses eight cavities per beam, each delivering 2 MV at 400 MHz.

Another important element of the LHC machine is the magnet system. Different types of magnets are used [115]. The dipole magnets are used to control the beam orbit, by guiding the charged particle along the desired orbit. Each dipole is 15 m long and weighs around 35 t. There are 1232 units of such magnets in the LHC tunnel. In addition 392 quadrupole magnets are used to control the beam size. In particular, the beam size is required to be very small near the interaction point, to maximize the average number of interactions per bunch crossing. Finally, sextupole and higher order magnets are used to control the chromatic and geometric aberrations.

The peak energy is directly proportional to the strength of the dipole field given a specific acceleration circumference. To reach the high energy target needed at LHC, superconducting technology has been used. The peak dipole field is 8.33 T for a beam energy of 7 TeV in the LHC machine.

3.1.1.3 The LHC injector Complex

The LHC Injector Complex is made of several stages [116, 117]. The protons are initially extracted by stripping electrons from hydrogen atoms. These protons are first accelerated in the Linac2 accelerator, which is 30 meters long, until reaching the energy of 50 MeV. They are then injected into the Proton Synchrotron Booster (PSB), which accelerates them to 1.4 GeV. The PSB is made of four superposed rings, and has a circumference of 157 meters. The protons are then injected into the Proton Synchrotron (PS) where they are accelerated to 26 GeV. The PS has a circumference of 628 meters (this corresponds to four times the PSB circumference), and it forms the bunches spaced by 25 or 50 ns necessary for LHC operation. The protons are then sent to the Super Proton Synchrotron (SPS) that has a circumference of 6911 meters, where they are accelerated to 450 GeV. They are finally transferred to the LHC, through two transfer lines, the TI2 and TI8 lines corresponding to the clockwise and anti-clockwise injections as seen previously. The filling of the LHC ring takes about 4 min.The protons are finally accelerated for about 20 minutes to their nominal energy.

Figure 3.2 summarizes the characteristic of the LHC Injector Complex.

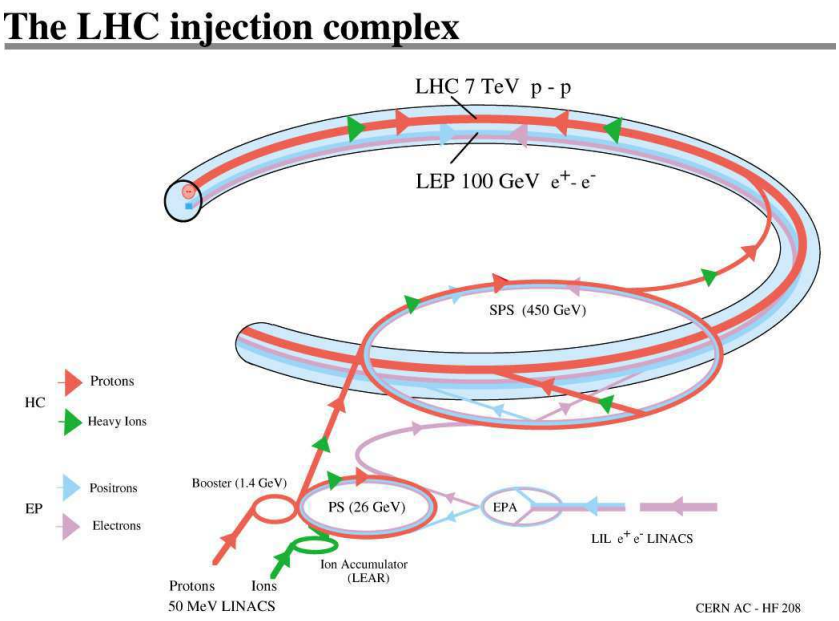

Figure 3.2: LHC Injector Complex.

3.1.1.4 Beam Structure

The LHC 400 MHz Radio-Frequency system provides 35640 possible bunch positions every 2.5 ns (0.75 m) along the LHC circumference. The smallest bunch-to-bunch distance was fixed to 25 ns, that corresponds to a maximal number of bunches of 3564, from which has to be subtracted some dead-time for the beam extraction system (dump kickers). In the nominal LHC pattern,

the beam is composed of 2808 proton bunches, organized into 39 groups of 72 bunches spaced by 25 ns. Between each group there are variable spacings, requested by the different injection and extraction systems.

This bunch organisation inside the LHC ring actually comes from the different steps of injection from the PSB to the LHC. As seen in Section 3.1.1.3, in the PSB two to four bunches are formed and injected into the PS, twice, for a total of 6 booster bunches injected into the PS. Each injection into the PS takes 1.2 s. In the PS, each of the 6 bunches are split into 12 smaller bunches, yielding a total of 72 bunches injected into the SPS. This is repeated two to four times, yielding a total of 144 to 288 bunches injected into the SPS, each injection taking 3.6 s. Finally, these groups of bunches are extracted from the SPS and injected into the LHC. To fill the LHC, 12 cycles of SPS synchrotron are needed, providing at the end the 39 groups of 72 bunches mentioned above. Each SPS cycle takes 21.6 s.

Figure 3.3 summarizes the beam structure.

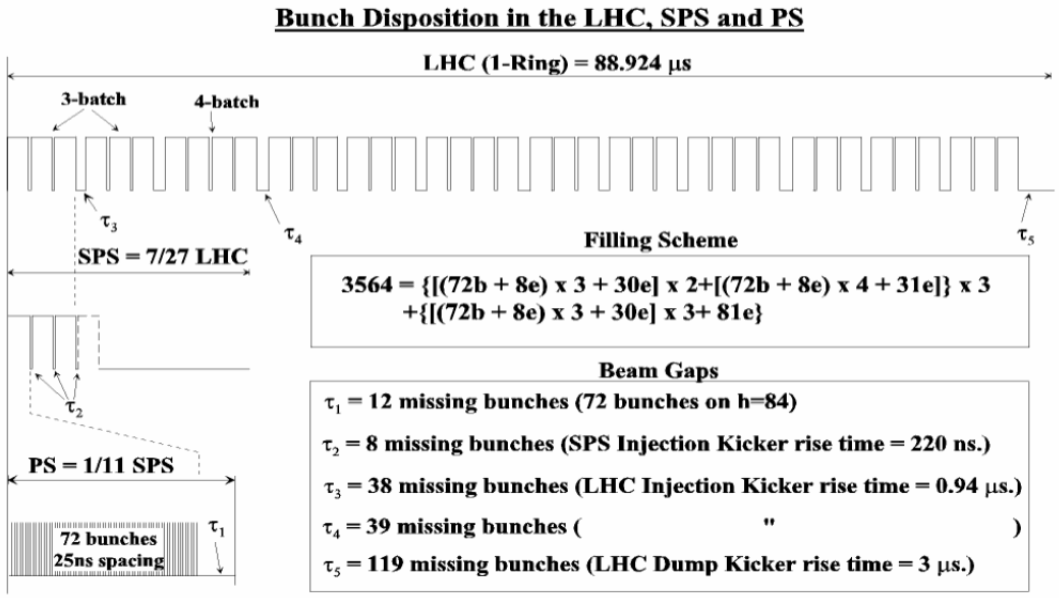

Figure 3.3: Bunch Structure of the LHC. Over a total of 3564 possible bunch positions, 2808 are really filled for a 25 ns beam structure, whereas 756 are free due to the SPS injection kicker rise time (which typically covers 8 positions), the LHC Injection kicker rise time (which typically covers 38-39 positions) and the LHC dump kicker rise time (which typically covers 119 positions). Taken from [109].

In reality, as seen in Table 3.1 which summarizes the evolution of the LHC parameters, for 2011 and 2012 the LHC has operated with a 50 ns bunch spacing, which corresponds to a final number of bunches of 1380. The 50 ns beam structure provides a higher peak luminosity, at the price of a higher pile-up.

3.1.2 Performance

The luminosity is related to the number of events of a given type produced each second at the LHC:

$$N_{event} = L\sigma_{event}$$

where σ_{event} corresponds to the cross section of the event under study and L is the machine luminosity. The luminosity only depends on the machine characteristics:

$$L = \frac{N_b^2 n_b f_{rev}}{4\pi\sigma_x^*\sigma_y^*}F = \frac{N_b^2 n_b f_{rev}\gamma_r}{4\pi\epsilon_n\beta*}F \tag{3.1}$$

where

- N_b is the number of particles per bunch
- n_b is the number of bunches
- f_{rev} is the frequency of revolution. The nominal value is 11.25 kHz.
- σ_x^* and σ_y^* are respectively the horizontal and vertical beam size at the collision point. Their value are typically 16 μm.
- γ_r is the relativistic gamma factor ($\gamma_r = \frac{1}{\sqrt{1-\beta^2}}$, and $\beta = \frac{v}{c}$ with v the particle velocity and c the light speed)
- ϵ_n is the normalized transverse beam emittance which corresponds to the phase space volume occupied by the beam. The transverse emittance of a beam corresponds to the average spread of a particle's coordinates in position and momentum phase space, in the perpendicular plane of the particle's motion. A low emittance means that the particles are confined to a small distance and that they have nearly the same momentum. The interaction with a particle in the opposite bunch will be then more probable, increasing consequently the luminosity.
- β^* is the beta function at the collision point:

  $$\beta^* = \frac{\sigma^2\gamma_r}{\epsilon_n}$$

  This beta function relates the beam size σ to the emittance, it corresponds to the beam envelope.
- F is the geometric luminosity reduction factor due to the crossing angle at the Interaction Point (IP):

  $$F = \left(1 + (\frac{\theta_c\sigma_z}{2\sigma^*})^2\right)^{-1/2}$$

  with θ_c the crossing angle at the IP, σ_z the RMS bunch length, and σ^* the transverse RMS beam size at the IP. This angle is not null in order to avoid unwanted collisions near the interaction points. The angle is typically about 150-200 μrad.

Table 3.1 summarizes the value of these parameters and show their evolution with time [118].

Figure 3.4 shows the peak luminosity in $cm^{-2}s^{-1}$ as a function of the time in 2012, for the ATLAS detector [119]. The peak luminosity has been regularly increased between 2010 and 2012, reaching finally a value close to the one expected at nominal design, as seen in Table 3.1. The integrated luminosity corresponds to the integral of the instantaneous luminosity over a given time period. For the 2012 data taking period the integrated luminosity expressed in fb^{-1} is shown in Figure 3.5.

Table 3.1: Evolution of the LHC parameters.

Parameter	2010	2011	2012	Nominal
Energy (TeV)	3.5	3.5	4.0	7.0
Number of protons per bunch N (10^{11})	1.2	1.45	1.58	1.15
Number of bunches n_b	368	1380	1374/1380	2808
Bunch spacing (ns)	150	75/50	50	25
Emittance ϵ (μm rad)	2.4-4	1.9-2.4	2.2-2.5	3.75
Betatron function $\beta*$ (m)	3.5	1.5→1	0.6	0.55
Luminosity L ($cm^{-2}s^{-1}$)	$2 \cdot 10^{32}$	$3.5 \cdot 10^{33}$	$7.6 \cdot 10^{33}$	$1 \cdot 10^{34}$

Between 2010 and 2012 a total of about 27 fb^{-1} has been recorded by the ATLAS experiment corresponding to about 0.05 fb^{-1} in 2010, 5.25 fb^{-1} in 2011 and 21.74 fb^{-1} for 2012. However not all these data can be used for physics analyses: as will be seen in Chapter 4, the quality of the data is first scrutinized. The data affected by quality problems are removed, corresponding to a fraction of around 8% in 2011 and 5% in 2012.

The final dataset used in physics analyses like Higgs boson searches corresponds then to 4.9 fb^{-1} collected in 2011 and 20.7 fb^{-1} collected in 2012. This dataset corresponds to the so-called Run I dataset.

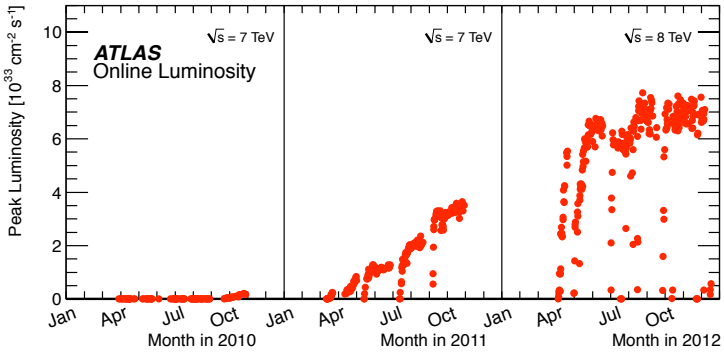

Figure 3.4: Peak Luminosity as a function of time [119].

In order to enhance the number of interesting events produced at the LHC in a given time period, for a fixed bunch spacing of 50 ns like in 2011 and 2012 LHC operation, the number of protons per bunch is increased. One can notice from Table 3.1 that this number was larger than the nominal one for these two years. This led to an average number of collisions per bunch crossing (referred to as $\langle\mu\rangle$) of about 9 in 2011 and 21 in 2012 (see Figure 3.6). The large difference between 2011 and 2012 is in part explained by the lowering of the β^* function in 2012, that is also a factor playing in the luminosity as seen in formula 3.1. The number of collisions per bunch crossing can be approximately measured by counting the number of reconstructed primary vertices. Figure 3.7 shows an illustration of a collision that occurred in 2012 where a Z boson decaying to a pair of muons has been produced. The vertex has to be reconstructed from among 25 other vertices.

In the following, the term "pileup" will refer to the effect of having more than one event at a time interacting within the detector.

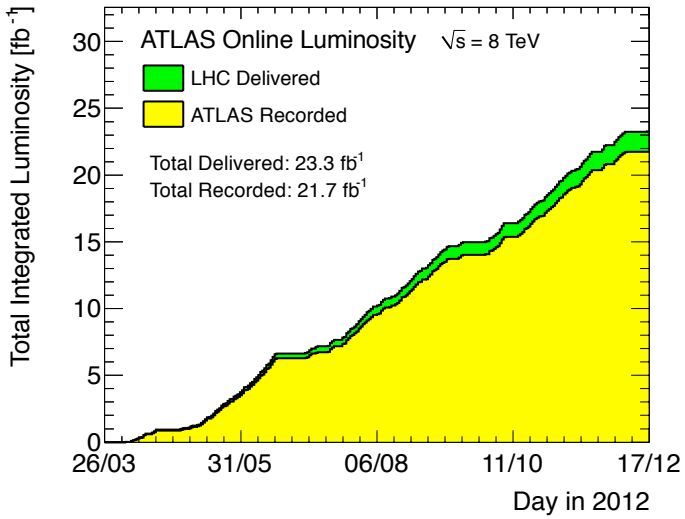

Figure 3.5: Integrated Luminosity for 2012 data taking [119].

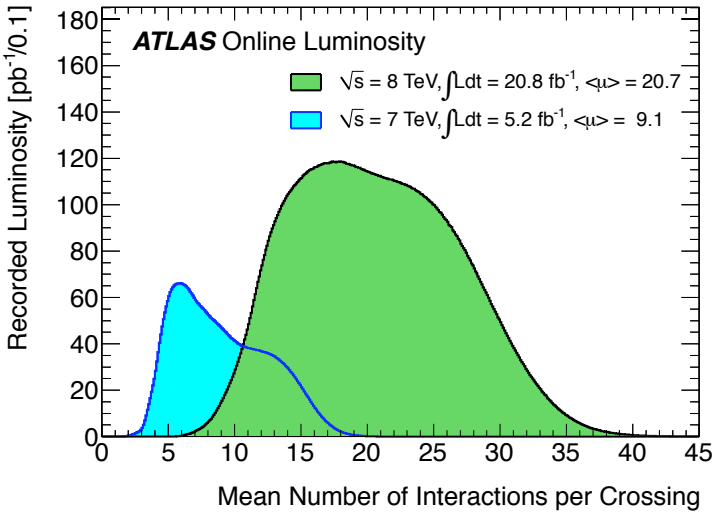

Figure 3.6: Distribution of the mean number of interactions per bunch crossing in 2011 and 2012 data taking [119].

3.2 The ATLAS detector

ATLAS (A Toroidal LHC ApparatuS) is an experiment located at Point 1 in the LHC ring, at CERN near Geneva. It is 25 meters in height, 44 meters in length and weighs about 7000 tons. ATLAS is a forward/backward symmetric detector with respect to the interaction point.

The design of the ATLAS detector was mostly dictated by physics requirements: the search for the Standard Model Higgs boson was used as one of the benchmarks to establish the performance of many of the ATLAS sub-systems. For example, for low masses of the Higgs boson, the natural width is of order of few MeV so that the observed width is dominated by the instrumental resolution. Thus, an excellent resolution has to be reached in the detectors measuring

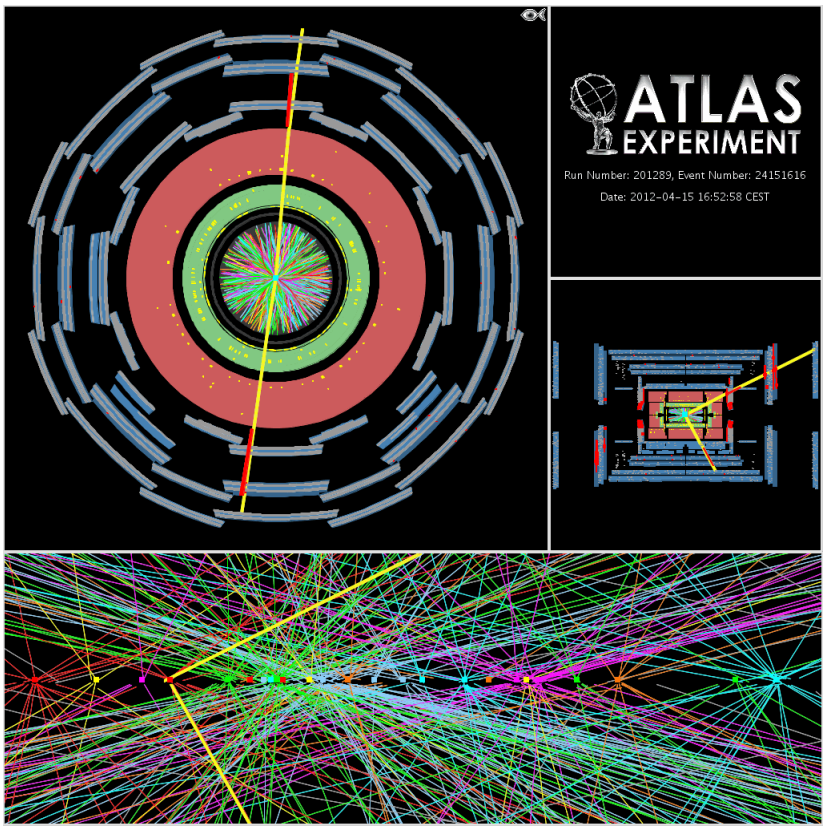

Figure 3.7: Z candidate decaying in two muons, recorded in 2012, inside an environment of 25 other reconstructed vertices.

the energy, in order to provide a good discrimination between the signal and the background. At design luminosity, 40 million bunch crossings are expected to occur per second. With an inelastic proton-proton cross-section of 80 mb, this leads to 10^9 inelastic collisions per second. This can cause radiation damages in the detectors. Fast and robust electronics are required. In addition, an efficient trigger system is needed, as not all the events can be recorded.

The ATLAS detector includes sub-detectors with a high granularity, especially in the central region. It has a large acceptance in pseudorapidity and an almost full coverage for the azimuthal angle.

The ATLAS design is described in more detail below.

3.2.1 Overview of the ATLAS detector

The ATLAS detector geometry follows classical rules for the high energy physics experiments: it is made of various sub-detectors, each having its particular role, in a concentric design: the innermost detector is the tracker for the measurement of particle momentum and charge, then come the calorimeters that measure particle energy and finally the muon system, providing a measurement of the momentum and charge of muons.

It is composed of a barrel section (concentric around the beam axis) and two endcaps (perpendicular to the beam-axis). These sub-detectors are described in more detail in the following.

3.2.1.1 Coordinate System

The origin of the coordinate system used by ATLAS corresponds to the nominal interaction point. The beam direction defines the z-axis, which is used to determine the so called side-A (positive z) and side-C (negative z) of the detector. The transverse plane, perpendicular to the beam axis, is delimited by the (x,y) axis. The positive x coordinate points to the centre of the LHC ring while the positive y coordinate points upward. The pseudorapidity η is defined as

$$\eta = -\log\tan(\frac{\theta}{2}),$$

with θ the polar angle.

Figure 3.8 shows the overall ATLAS detector with the various sub-detectors and its coordinate system.

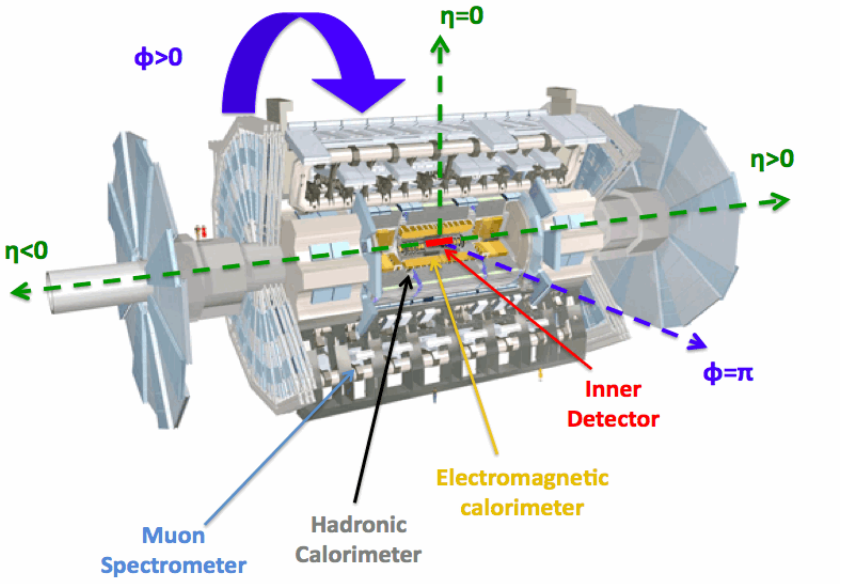

Figure 3.8: The different components of the ATLAS detector and the coordinate system. Modified from [110].

3.2.1.2 Tracking

Within $|\eta| < 2.5$, around 1000 particles emerge from the collision point every 25 ns at design luminosity. This creates a very large density of tracks in the detector. A fine detector granularity has been designed to overcome this difficulty.

The tracker system is made of three sub-detectors: the silicon-pixel detector, the Semiconductor Tracker (SCT) and the Transition Radiation Tracker (TRT) [120, 121]. The full inner detector (ID) is immersed in a 2 T solenoid field, generated by the central solenoid, which extends over a length of 5.3 m with a diameter of 2.5 m (see Section 3.2.1.4). Figures 3.9 and 3.10 show the tracker system structure in barrel and endcap respectively. The intrinsic accuracies of individual hit measurements in the three sub-detectors are given in Table 3.2. The average momentum resolution provided by this tracker system is $\sigma_{p_T}/p_T \sim 0.05\%\, p_T\,(\text{GeV}) \oplus 1\%$.

Pixels The silicon-pixel detector covers the region $|\eta| < 2.5$. This detector is made of 3 concentric cylindrical silicon-pixel layers in the barrel and of 3 silicon-pixel disks perpendicular to the beam axis in the endcap [122]. The layers are segmented in R-ϕ and in the z direction in 1744 identical sensors (also referred to as modules) [123]. The majority of the sensors have a size of 50×400 μm^2 and the remaining ones (mainly in the module's front-end) have a larger size of 50×600 μm^2. Each sensor is made of 47232 pixels. This leads to a total of about 80 million readout channels for the pixel detector. This detector has the highest granularity, especially around the vertex region. It has been designed to enhance the secondary vertex measurement.

Semiconductor Tracker The Semiconductor Tracker (SCT) also covers the region $|\eta| < 2.5$. The barrel of this detector consists of 4 concentric cylindrical silicon microstrip double-layers. One of the layers of each sensor plane is axial (parallel to the beam axis, to measure the R-ϕ coordinate) and the other one has a stereo angle of 40 μrad. This stereo angle enables a complete measurement of the particle coordinates. In the endcap (EC) region, the SCT is made of 9 disks perpendicular to the beam axis, with a set of strips running radially, and a set of stereo strips at an angle of 40 μrad. The SCT detector is segmented into 4088 modules distributed in 2112 modules in the barrel and 1976 modules in the endcap [124, 125]. In the barrel, the silicon microstrip sensors have a typical pitch of 80 μm [126]. The total number of readout channels is approximately 6 million.
All the silicon sensors (from both the pixel and SCT detectors) are maintained at a temperature of about -5° C to -10° C, in order to limit radiation damage effects. A coolant liquid at a temperature of -25° C is then routed up to these sensors through copper cooling pipes running along the cryostat. The cryostat is a thermally insulating vessel used to contain cryogenic detectors and magnets [110].

Transition Radiation Tracker The Transition Radiation Tracker (TRT) has been designed to provide a large number of measured space-points and to enhance the electron identification capabilities up to $|\eta| = 2$. It is made of straw tubes of about 4 mm diameter, that provide a large number of measured points, typically, 36 per track. In the barrel region, there are 73 straw layers, that are parallel to the beam axis; each straw is 144 cm long. In the EC region, there are 160 planes of 768 straws that are arranged radially in wheels; each straw is 37 cm long. The straw tubes are filled with a Xenon-based gas mixture (70% Xe, 27% CO_2, 3% O_2). When an electron crosses the straws, transition radiation is emitted and absorbed in the gas mixture. The amplitude of the signal detected is larger than for other charged particles. Two electronic thresholds exist (low and high) that allow to distinguish between tracking signals and transition radiation [127]. The total number of readout channels for the TRT is approximately 351 000. This detector is much less precise than the pixel or SCT detector (it provides only the R-ϕ information), but this feature is compensated by a larger number of hits, that facilitate pattern recognition.

The TRT detector has been designed to operate at room temperature.

Mechanical structure and Services Carbon-fibre rails, fastened in the barrel cryostat inner wall, have been designed to support the detector and to allow an easy access to sub-detectors. The pixel detector is housed in a octagonal pixel support tube (PST), as shown in Figure 3.11. The PST inner radius is about 230 mm.
The pixel services (cooling services, power cables, monitoring) are routed to the end of the PST, and included inside this structure. The power lines of this detector are connected to four Patch Panels. The Patch Panels 0 and 1 (PP0 and PP1) are located in the cryostat wall in the ID

Table 3.2: Intrinsic accuracy of the different Inner Detector sub-detectors.

Detector	Intrinsic accuracy (μm)
Pixel Barrel	10 $(R-\phi)$ 115 (z)
Pixel Disks	10 $(R-\phi)$ 115 (R)
SCT barrel	17 $(R-\phi)$ 580 (z)
SCT disks	17 $(R-\phi)$ 580 (R)
TRT	130

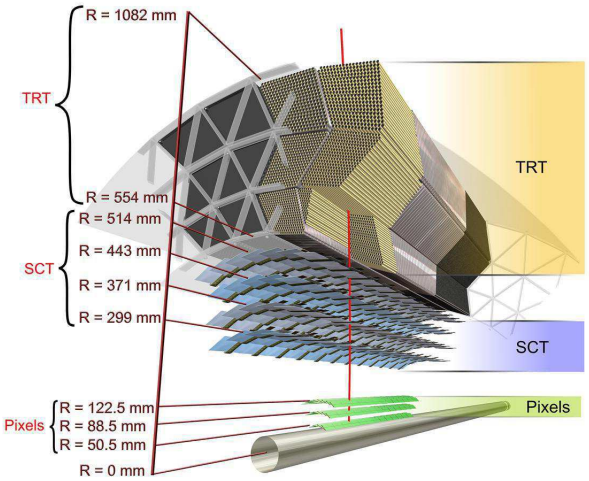

Figure 3.9: Illustration of the Inner Detector, for the barrel part [110].

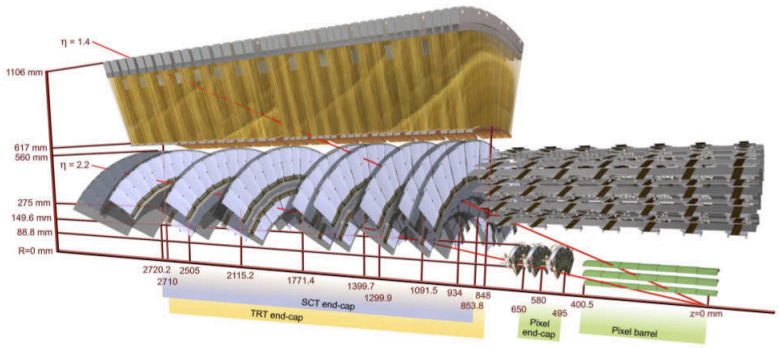

Figure 3.10: Illustration of the Inner Detector, for the EC part [110].

volume, whereas the Patch Panels 2 and 3 (PP2 and PP3) are located outside the ID volume. Figure 3.12 shows a picture of the PP0 region. This region is very complex to simulate because of the high concentration of cables and electronics.

The ID volume is sealed at each end by two large aluminium end-plates. These plates have two skins and the ID services (TRT,SCT) are inserted between these two skins.

Figure 3.11: Schematic view of the pixel detector surrounded by its octagonal supports [128].

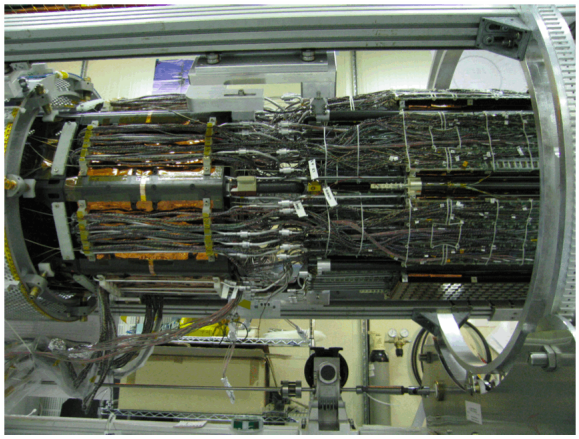

Figure 3.12: Picture of the PP0 region.

3.2.1.3 Calorimetry

The calorimetry system of ATLAS is made of three sampling calorimeters. This kind of detector consist in a succession of active medium and absorber plates. The interaction of the initial particle with the absorbers creates daughter particles that ionize the active medium. The energy of the initial particle is reconstructed from the signal collected from this ionization. Liquid argon has been chosen for most of the ATLAS calorimeters for its intrinsic linear behaviour, its stability of response over time and its intrinsic radiation-hardness.

The first liquid argon calorimeter for the detection of electromagnetic showers in high energy experiments was introduced in 1974 by Willis and Radeka [129]. Their primary detector was composed of a stack of steel plates immersed in a liquid argon medium. A voltage was applied between the steel plates to allow the drift of the electrons. The ATLAS liquid argon calorimeter design is based on a similar concept.

The three different calorimeters correspond to the electromagnetic calorimeter (EM) which is used for the detection and reconstruction of the electrons and photons, the hadronic calorimeter (H) which is dedicated to detecting jets arising from the hadronization of quarks or gluons, and finally the forward calorimeter (FCAL) that both provides the electromagnetic and hadronic measurements in the forward region (see Figure 3.13). The liquid argon technology is used in the EM calorimeters, in the FCAL and in the endcaps of the hadronic calorimeter. The barrel section of the latter uses scintillating tiles, as described in more detail below.

There are in total 182468 readout channels for the liquid argon: 60% and 35% are dedicated to the barrel and endcap electromagnetic calorimeters, 3% to the hadronic endcap and finally 2% to the forward calorimeter. These channels represent 97.2% of the full ATLAS calorimeter

readout system, the remaining 2.8% belong to the scintillating tile hadronic barrel.

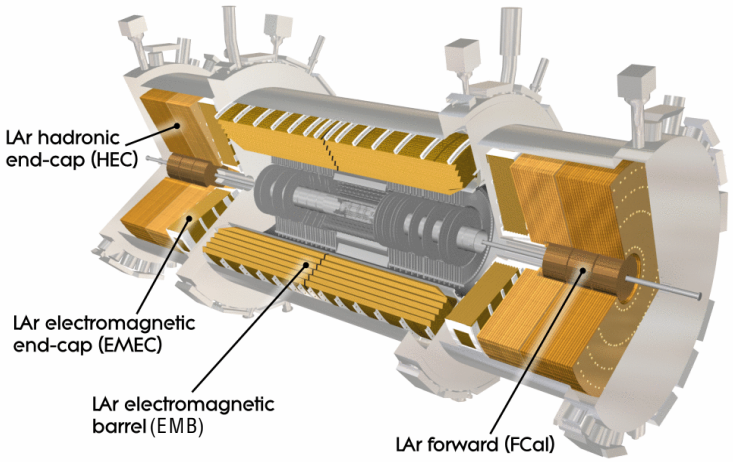

Figure 3.13: Localization of the three calorimeters in ATLAS [110].

For the measurement of the Higgs boson mass in the di-photon channel, the electromagnetic calorimeter plays an important role. It is described in detail in Section 3.2.2, after a quick review of the other calorimeter systems below.

Hadronic calorimeter This detector is a sampling calorimeter made of a large barrel covering $|\eta| < 1.0$, plus two extended barrel cylinders covering $0.8 < |\eta| < 1.7$. The EC region covers the range $1.5 < |\eta| < 3.2$. Two different technologies are used for the barrels and endcaps. In the barrels, the steel is used as absorber and scintillating tiles as active material. They are azimuthally divided into 64 modules, and in depth in three layers. The total thickness of this tile detector in hadronic interaction length is 9.7 λ at $\eta = 0$. Each endcap is made of two independent wheels, each of them made of 32 identical wedge-shaped modules, and divided in depth into two sections, for a total of 4 layers per endcap. The wheels the closest (the furthest) to the interaction point are built from parallel copper plates of 50 mm (25 mm) thickness interleaved with 8.5 mm LAr gaps as active medium. The endcap wheels are placed immediately behind the EM EC calorimeters, and share the same cryostat. The energy resolution provided by this calorimeter is $\sigma_E/E \sim 50\%/\sqrt{E} \oplus 3\%$.

LAr forward calorimeter The LAr forward detector is a sampling calorimeter that provides both electromagnetic and hadronic energy measurement up to $|\eta| = 4.9$. It is made of two parts, housed in the same cryostats as the ones used for the EC hadronic and EM calorimeters, providing a good uniformity along the coverage of the calorimeter. This detector is exposed to high particle flux as it is located at a high pseudorapidity and at a distance of roughly 4.7 m from the interaction point. It is about 10 interaction lengths in depth. Each calorimeter is segmented in 3 modules: the first (FCal1) is composed of copper for the absorbers, and is dedicated to electromagnetic energy measurement, whereas the two other (FCal2 and FCal3) are mainly composed of tungsten for the absorbers and are optimized for hadronic energy measurement. Figure 3.14 shows a schematic view of their location along the z axis, as well as the

relative location of the electromagnetic and hadronic EC. All the modules use liquid-argon as the sensitive medium. This detector provides an energy resolution of $\sigma_E/E \sim 100\%/\sqrt{E} \oplus 10\%$.

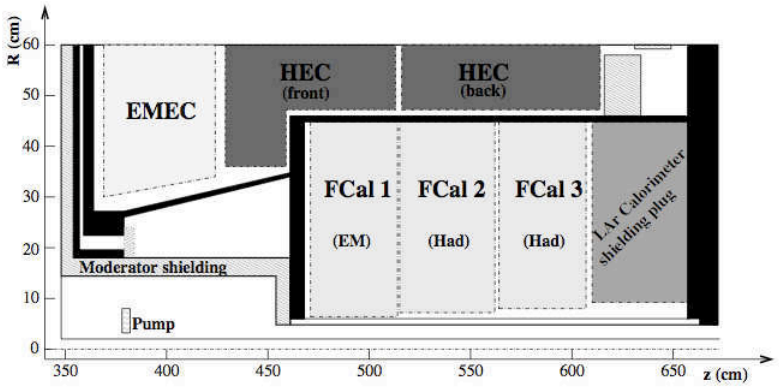

Figure 3.14: Illustration of the structure of the Forward Detector along the z axis [110].

3.2.1.4 Magnets

There are four large magnets in the ATLAS detector. The first one is a thin superconducting solenoid surrounding the Inner Detector cavity, parallel to the beam axis, that provides a 2 T axial field, dedicated to the inner detector for the bending of the tracks. It has been designed with a small thickness in order to reduce the material in front of the calorimeter (~ 0.66 radiation lengths at normal incidence).

There are three superconducting air-core toroids. One is dedicated to the barrel and two other to the endcap regions. The latter are inserted in both ends of the barrel toroid. These magnets are placed concentrically behind the calorimeter and produce a 0.5 T (1 T) toroid magnetic field in the barrel (EC) dedicated to the detection and momentum measurement of muons. They are composed of eight coils, which are arranged radially and symmetrically around the beam axis. In the barrel, the eight coils are each immersed in their own cryostat whereas they are housed all together in in a single large cryostat in each endcap. The endcap toroid coil system is rotated by 22.5 degrees with respect to the barrel one in order to provide a radial overlap and to optimise the bending power.

3.2.1.5 Muon Systems

The muon spectrometer surrounds the calorimeters. It is designed to detect and measure the momentum of charged particles exiting the calorimeters, in the range $|\eta| < 2.7$. It is also designed to trigger on these particles in the region $|\eta| < 2.4$. In the region $|\eta| < 1.4$, the deflection of the muons is provided by the barrel toroid, whereas in the region $1.6 < |\eta| < 2.7$, they are bent by the two EC toroids. In the transition region $1.4 < |\eta| < 1.6$, the magnetic bending is provided by a combination of the barrel and EC toroids' fields. The overall momentum resolution provided by the muon system is $\sigma_{p_T}/p_T = 4\%$ at 50 GeV and $\sigma_{p_T}/p_T = 11\%$ at 1 TeV.

The spectrometer is made of two different kinds of chambers which are arranged in eight octants with an azimuthal symmetry, each octant being divided in two sectors, one small and one larger, that allow a region of overlap in ϕ, thus reducing gaps in detector coverage. This overlap also enables a relative alignment of adjacent sectors. In the barrel, the chambers are

arranged in three concentric shells whereas in the EC region they are arranged in 4 large parallel wheels, perpendicular to the z axis.

The two different muon chambers are the precision tracking chambers which provide a precise measurement of the track coordinates and the fast trigger chambers that allows to trigger on muon tracks by providing information on the track within a few tens of nanoseconds.

The first chambers are located between and on the eight coils of the barrel toroid magnets or in front of and behind the EC toroid magnet. The precision tracking chambers are of two types:

- the Monitored Drift Tube chambers (MDT's), that cover the region $|\eta| < 2.7$, except in the innermost endcap layer where they cover the region $|\eta| < 2.0$. In each chamber there are three to eight tube layers, providing a resolution of 35 μm per chamber.
- the Cathode-Strip-Chambers (CSC) are used instead in the innermost layer of the EC. The resolution of a chamber is about 40 μm in the bending plane and 5 mm in the transverse plane.

The fast trigger chambers cover the region $|\eta| < 2.4$ and enable the track coordinates measurement, in the bending and non bending planes (η and ϕ). These chambers are composed of two systems, the Resistive Plate Chambers (RPC) in the region $|\eta| < 1.05$ and the Thin Gap Chambers (TGC) in the region $1.05 < |\eta| < 2.4$.

The muon spectrometer defines the overall size of the ATLAS detector.

3.2.1.6 Forward detector

There are three small detectors in the forward region whose main purpose is to measure the luminosity seen by the ATLAS detector:

- LUCID (LUminosity measurement using Cerenkov Integrating Detector), located at $\pm$17 m from the interaction point. This is the main relative luminosity monitor in ATLAS. The measurement of the integrated and instantaneous luminosity is made by detecting inelastic p-p scattering in the forward direction.
- ALFA (Absolute Luminosity For ATLAS), located at $\pm$240 m from the interaction point. It estimates the absolute luminosity of ATLAS by measuring the elastic-scattering amplitude in the forward direction and by comparing it to the total p-p cross section. These measurements can only be performed with special beam conditions (high β^* optics and reduced beam emittance) since very small scattering angles are needed (about 3 μrad), smaller than the nominal beam divergence.
- ZDC (Zero-Degree Calorimeter) located at $\pm$140 m from the interaction point is dedicated to the measurement of centrality for heavy-ions collisions by the detection of forward spectator neutrons.

3.2.1.7 Trigger system and data acquisition

The proton-proton interaction rate at the design luminosity ($10^{34} cm^2 s^{-1}$) amounts to approximately 1 GHz, if considering the 40 MHz frequency of collisions of LHC and an average of 25 interactions per bunch crossing. Due to a limited capacity for storage of data this rate has to be lowered to around 200 Hz leading to an overall rejection factor of 5 millions. This rejection

has to be done while maintaining high efficiency for recording events from interesting physics processes. There are three levels of triggers:

- the Level 1 trigger (L1) enables the reduction from 40 MHz to 75 kHz, using a subset of the detector information. It selects mainly high transverse momentum muons (using trigger information coming from the muon spectrometer), electrons and photons (using information from the calorimeters with a broader granularity), jets, large missing energy and large transverse energy. In each event, this trigger defines one or more Regions-of-Interest (ROI's), which corresponds to a (η, ϕ) region where the interesting event occurred. The L1 decision takes about 2.5 μs.

- the Level 2 trigger (L2) is designed to reduce the rate to 3.5 kHz, within 40 ms. This reduction is done using the ROI's and reconstructing the interesting events around this region with the full granularity and precision using all the available detector information.

- the Event Filter (EF) provides the final necessary reduction to 200 Hz. The selection is made using offline reconstruction procedure, within 4 s on average.

The latter two triggers together are called the High Level Trigger (HLT).

After an event is accepted by the L1 trigger, the interesting data are transferred off the detector to ROD's (Readout Drivers), which are elements of the front-end systems. The digitised signals are converted into raw data and transferred to the Data Acquisition (DAQ) system. This system temporally stores the data in local buffers, from which they are solicited by the L2 trigger for the data associated to ROI's. The events selected by the L2 trigger are then sent to the event-building system and finally transferred to the Event Filter. The events that are finally selected by the EF are transferred to the CERN computer center, for permanent storage.

3.2.2 The LAr electromagnetic calorimeter

This detector is a sampling calorimeter which uses lead as absorber and liquid argon as active material and which extends up to $|\eta| < 3.2$. The incident electron or photon interacts with lead and initiates an electromagnetic shower, whose secondary electrons ionize the active medium. An electrode in the middle of the liquid argon gap is powered on both sides with high voltage. The difference of voltage between the electrode and the rest of the gap creates a current. The total energy of the incident particle is proportional to the total ionization.

The EM calorimeter is divided into a barrel part covering the region $|\eta| < 1.475$ and two endcap components covering the region $1.375 < |\eta| < 3.2$. These three parts are each immersed in their own cryostat, shared with the hadronic and forward calorimeters. The electromagnetic calorimeter provides an energy resolution of: $\sigma_E/E = 10\%/\sqrt{E} \oplus 0.7\%$.

3.2.2.1 Barrel

The barrel calorimeter consists of two identical half-barrels, separated by a small gap of 4 mm at $z = 0$. Each half barrel is divided into 16 modules, each covering $\Delta\phi = 22.5^o$. One half-barrel consists of 1024 accordion shaped lead absorbers interleaved with readout kapton electrodes, which are positioned in the middle of the liquid argon gap by honeycomb spacers. The readout electrodes consist of three conductive copper layers separated by insulating polyamide sheets. The two outer layers are at high-voltage potential whereas the inner layer is used for the read-out of the signal via capacitive couplings. Azimuthal segmentation is obtained by ganging together the appropriate number of electrodes. In the region $|\eta| < 0.8$ ($|\eta| > 0.8$) the absorbers have a

thickness of 1.53 mm (1.13 mm). The change in thickness at $|\eta| = 0.8$ was necessary to limit the decrease of the sampling fraction as $|\eta|$ increases. As a consequence, there are two different kind of electrodes, dedicated to these two regions. The size of the drift gaps on each side of the electrodes is 2.1 mm. This leads to a total drift time of 450 ns for an operating voltage of 2000 V.

In the barrel the EM calorimeter is divided into three sections in depth. The very fine segmentation in η of the first layer allows a precise measurement of the shower position and a good rejection of π^0 decaying to two photons. The second layer is the largest, designed to collect the largest fraction of the energy. The third layer is dedicated to the measurement of the tails of the shower, to enhance the discrimination between hadronic and electromagnetic showers. It has a coarser granularity in η. Figure 3.15 depicts these three layers and their segmentation in η and ϕ. Table 3.3 gives the granularity of these layers.

Figure 3.16 shows an illustration of a barrel electrode. The three layers in depth are clearly seen, as well as the change of electrodes at $|\eta| = 0.8$.

The support structure of the barrel is made of seven stainless-steel outer rings that provide the required rigidity. Each ring is made of 16 pieces corresponding to the 16 modules. These pieces are all identical, except for the two pieces at the level of the cryostat rails. Similarly, there are eight inner rings, each being also made of 16 pieces. The absorbers are screwed into these ring-pieces.

The total thickness of a barrel module increases from 22 to 30 electromagnetic radiation length (X_0) between $\eta = 0$ and $|\eta| = 0.8$ and from 24 X_0 to 33 X_0 between $|\eta| = 0.8$ and $|\eta| = 1.3$.

There are in total 101760 readout channels for the barrel.

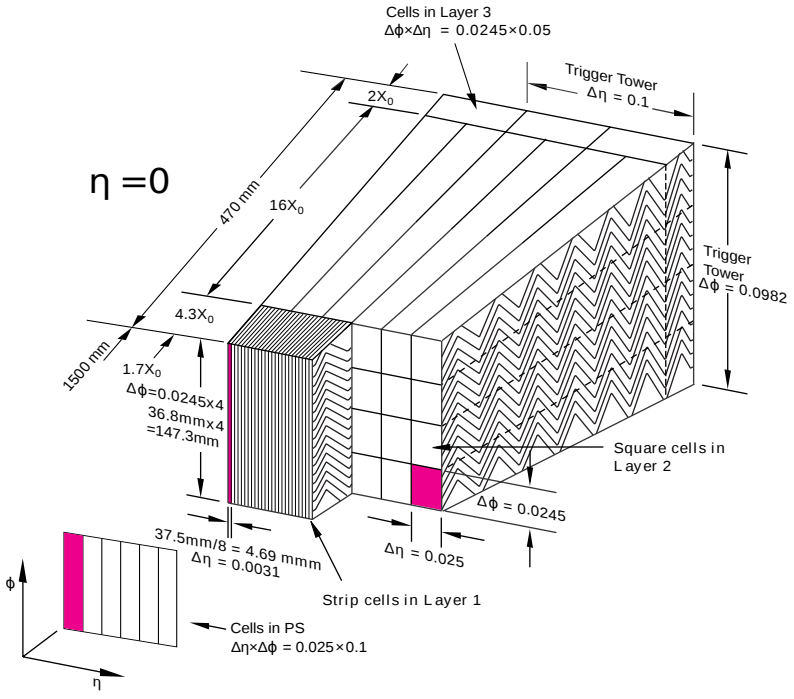

Figure 3.15: Longitudinal segmentation of the accordion detector [110].

Table 3.3: Granularity $\Delta\eta \times \Delta\phi$ of the electromagnetic calorimeter as a function of η

	Barrel	endcap
presampler	0.025×0.1 ($\eta < 1.52$)	0.025×0.1 ($1.5 < \eta < 1.8$)
Layer 1	$0.025/8 \times 0.1$ ($\eta < 1.40$) 0.025×0.025 ($1.40 < \eta < 1.475$)	0.05×0.025 ($1.375 < \eta < 1.425$) 0.025×0.1 ($1.425 < \eta < 1.5$) $0.025/8 \times 0.1$ ($1.5 < \eta < 1.8$) $0.025/6 \times 0.1$ ($1.8 < \eta < 2.0$) $0.025/4 \times 0.1$ ($2.0 < \eta < 2.4$) 0.025×0.1 ($2.4 < \eta < 2.5$) 0.1×0.1 ($2.5 < \eta < 3.2$)
Layer 2	0.025×0.025 ($\eta < 1.40$) 0.075×0.025 ($1.40 < \eta < 1.475$)	0.050×0.025 ($1.375 < \eta < 1.425$) 0.025×0.025 ($1.425 < \eta < 2.5$) 0.1×0.1 ($2.5 < \eta < 3.25$)
Layer 3	0.050×0.025 $\eta < 1.35$	0.050×0.025 $1.5 < \eta < 2.5$

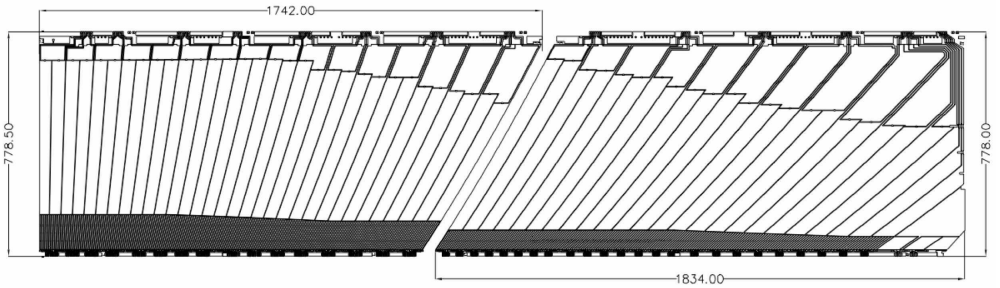

Figure 3.16: Illustration of a barrel electrode [110].

3.2.2.2 Endcap

The EC are divided into two coaxial wheels: an outer wheel covering the region $1.375 < |\eta| < 2.5$ and an inner wheel covering the region $2.5 < |\eta| < 3.2$. The boundary between the inner and outer wheel is 3 mm wide, mostly filled with low density material.

The endcap wheels are divided into eight wedge shaped modules. In the outer (inner) wheel of each endcap, there are 768 (256) absorbers, interleaved with readout electrodes similarly to the barrel. The absorbers have a thickness of 1.7 mm for the precision measurement region ($|\eta| < 2.5$) and of 2.2 mm in the region $|\eta| > 2.5$. As in the barrel, the electrodes are segmented in depth in three layers for the precision region $|\eta| < 2.5$, but only in two layers for $|\eta| > 2.5$. As seen in Table 3.3, the η granularity in front layer varies with η. This is done in order to keep the copper strip width larger than a few millimetres. Indeed, the $\Delta\eta$ =0.025/8 pitch cannot be achieved for $|\eta| > 1.8$ because this would give strips below 5 mm, which is too narrow compared to the shower width and which can induce a too high level of cross talk. As in barrel, the $\Delta\phi$ granularity is obtained by gathering the signals from adjacent electrodes : for the outer wheel, 12 adjacent electrodes are summed for a front cell and 3 for a middle or back cell. An endcap electrode is shown in Figure 3.17.

Unlike in the barrel section, the drift gap is not constant, but is a function of the radius (R). In the outer wheel it decreases from 2.8 mm at R = 200 cm to 0.9 mm at R = 60 cm. In the inner wheel it varies from 3.1 mm at R = 70 cm to 1.8 mm at R = 30 cm.

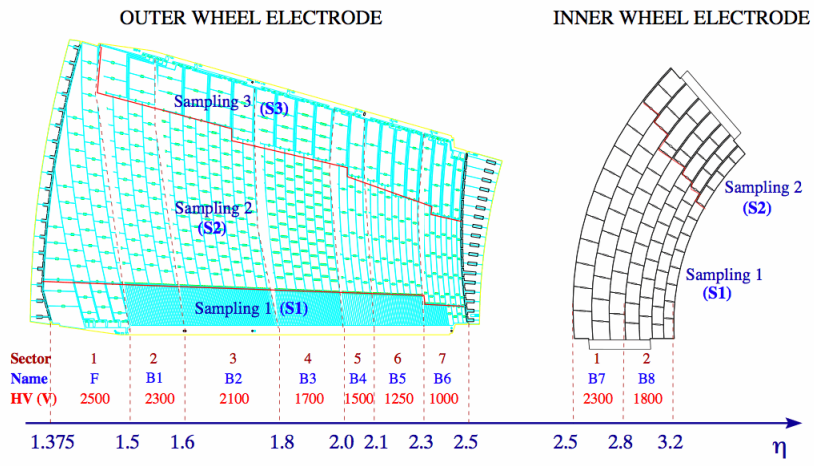

Figure 3.17: Illustration of an endcap electrode [130].

The electromagnetic endcap is supported by six support rings, three in the front and three in the back.

The material thickness increases from 24 to 38 X_0 as $|\eta|$ increases from 1.475 to 2.5 and from 26 X_0 to 36 X_0 as η increases from 2.5 to 3.2.

There are in total 62208 readout channels for the EC region.

For both the barrel and the EC, the accordion geometry provides a full ϕ symmetry without azimuthal cracks and a fast extraction of the signal at the rear or at the front of the electrodes.

3.2.2.3 Presampler

In the region $|\eta| < 1.8$ a fourth section is present in depth, the presampler (PS) detector, which is used to correct for the energy losses upstream of the calorimeter. This detector consists of a layer made uniquely of active LAr, for a thickness of 1.1 cm in the barrel and 0.5 in the EC region [131, 132]. Beyond $|\eta| = 1.8$, this layer is no longer necessary given the more limited amount of dead material in this region (see Section 3.2.3) and the higher energy of particles for a given transverse momentum ($E = p_T \cosh(\eta)$).

In each half-barrel, the presampler is made of 32 identical azimuthal sectors, each of them 3.1 m long and 0.28 m wide, thus covering the half-barrel length. Each sector covers the region $\Delta\eta \times \Delta\phi = 1.52 \times 0.2$. The sectors are mounted on rails which are fixed on the barrel internal rings. Contiguous sectors are mounted with a nominal gap of 0.4 mm at room temperature, which expand up to 1.1 mm in liquid argon due to the thermal transverse shrinkage of the sectors. These sectors each house eight modules, seven of them covering a region of $\Delta\eta \times \Delta\phi = 0.2 \times 0.2$ and the last, located at the edge of the sector, covering a region $\Delta\eta \times \Delta\phi = 0.12 \times 0.2$. Figure 3.18 shows an illustration of a presampler sector. Each module is divided into eight cells in η and two cells in ϕ, leading to a total of 16 cells per module, except at the ends of the barrel where the modules have a reduced size with only ten cells. Therefore the granularity of the barrel presampler is $\Delta\eta \times \Delta\phi = 0.025 \times 0.1$. The required granularity in η is obtained assembling together the appropriate numbers of electrodes. In the ϕ direction, the electrodes are sub-divided into two compartments by etching. In total 7808 read out channels are then needed for the PS.

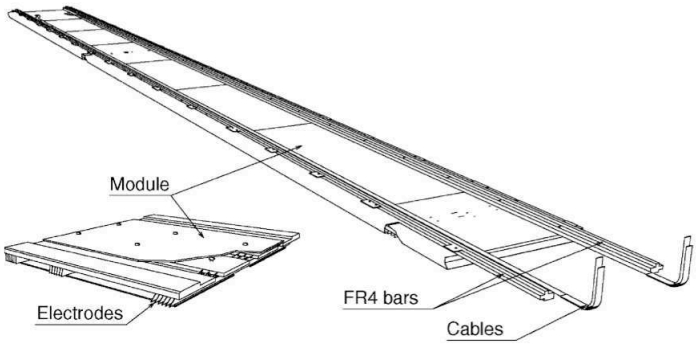

Figure 3.18: Schematic view of a presampler sector [133].

Each endcap has also a PS up to $|\eta| = 1.8$ that is made of 32 identical azimuthal sectors. The PS are placed in a 5 mm deep cavity in the back of the endcap cryostat cold wall, in order to avoid creating a gap in the electromagnetic calorimetry coverage (endcap wheels have to be as close as possible to the barrel modules). The cell granularity is also $\Delta\eta \times \Delta\phi = 0.025 \times 0.1$ corresponding to 768 channels per endcap wheel. A module of the endcap presampler is made of two active liquid-argon layers, each 2 mm thick. Theses modules are formed by three electrodes, which are made from double-sided printed circuit boards, and are separated by honeycomb spaces and glued together with 2 mm thick bars. The bars are used to link the absorbers to the structure; they are parallel to the accordion waves. A negative high voltage is applied to the external electrode, and the signal is read out from the central one as shown in Figure 3.19.

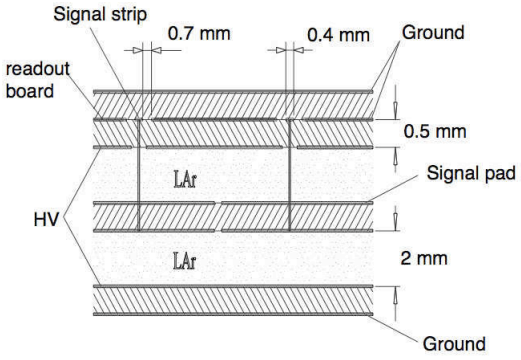

Figure 3.19: Detailed view of a presampler endcap module [133].

3.2.2.4 The High Voltage settings

For the electromagnetic barrel, the high voltage is constant with η, and the granularity of the high-voltage sectors is $\Delta\eta \times \Delta\phi = 0.2 \times 0.2$. The two sides of the electrodes are powered separately at a nominal voltage of 2000 V.

For the endcap calorimeter this is different as the gap thickness varies with η. The collected signal is proportional to the sampling fraction f_{samp} and to the drift velocity v_d while it is

inversely proportional to the liquid argon gap thickness g:

$$E_{tot} \propto \frac{f_{samp}}{g} v_d$$

Therefore, a variation of the gap thickness implies a variation of the signal.

The gap thickness and sampling fraction variations along the detector radius are correlated and, more precisely, they partially compensate. To keep a signal response constant with η an electric field strength almost independent of the radius is then needed. This translates into a continuously decreasing high voltage with respect to η. For technical reasons, a step-varying high voltage has been used instead. The size of the steps is $\Delta\eta \times \Delta\phi = 0.2 \times 0.2$, therefore seven high voltage sectors in the electromagnetic endcap outer wheel and two high voltage sectors for the inner wheel are used. This is shown in Figure 3.20.

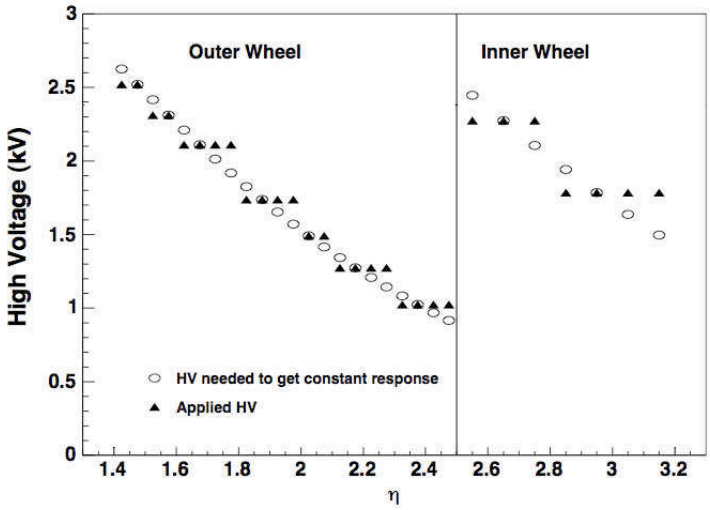

Figure 3.20: High Voltage settings as a function of η in the endcaps [130].

If one side of the electrode is not powered, due to a High Voltage problem, only half of the signal is collected. The total energy can be recovered by applying an offline correction factor. Indeed, the variation of the signal amplitude with the high voltage can be fitted with a function of type $E_{tot} = a.V^b$ with a and b constant and V corresponding to the high voltage. This procedure is efficient and leads to only a small loss of accuracy. Figure 3.21 shows that the variation of the signal amplitude with the high voltage is limited: for example, when decreasing the high-voltage to half its nominal value, 77% of the signal is still collected. In the same way, when electrodes encounters problems like a short-circuit, they can be operated with a lowered voltage. The energy collected is consequently different, but this can again be corrected by the procedure described above.

3.2.2.5 The energy reconstruction

The path from the current created by the ionization of the liquid argon to the final energy is described below.

The raw signals coming from the calorimeters cells are in a first step summed by the Summing Boards. These Summing Boards are placed at the front and back faces of the detector. For the front layer for example, 16 cells in azimuth are integrated.

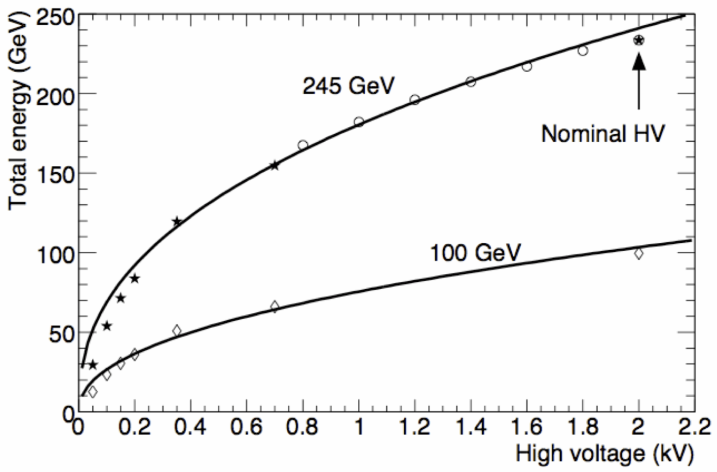

Figure 3.21: Dependence of the collected energy on the high voltage [110].

Then the signals are transferred by cables to the feedthrougth, via the Motherboards (see 3.22). There are 64 feedthroughs each composed of 1920 signal lines. The cryostat feedthroughs allow to transmit the current collected in the electrodes outside the cold vessel to the pre-amplifiers that belong to the Front End Board (FEB) system.

The Front End Boards The Front End Boards (FEBs) read the signal coming from the cells [134]. They are housed inside front-end crates (FEC). There are 1448 FEBs in the electromagnetic calorimeter each containing 128 channels. The location of the FEBs in the detector is such that the access is very difficult during the operation of the LHC. This means that these devices need to be very reliable and robust. The role of the FEBs is to perform an analogue processing, store all signals and digitize accepted signals. They thus contain all the electronics necessary to amplify, shape, sample, and digitize signals. The FEB noise is dominated by the pre-amplifier noise, which reaches 10-50 MeV for one channel. The operation scale of the FEB should thus extend from this pre-amplifier noise up to around 3 TeV, which corresponds to the largest energy deposit in one channel by an electron coming from the hypothetical Z' at 5 TeV. The corresponding scale for the current is then from the nA to the mA (1 GeV $\sim$ 2-3 μA). This is why a pre-amplification is needed. There are 32 pre-amplifiers per FEBs, then one is shared between four channels.

The large scale range of the pre-amplifier cannot be transmitted directly to the digitization step. The amplified signal is directed through three shapers that shapes and amplifies again with three different linear gains: 1, 10 and 100. These three gains corresponds to different energy ranges: the low range is available for energy up to 3 TeV, the medium one for energies up to 300 GeV and finally the high gain for energies up to 30 GeV. The difference between the input and output signal after the signal shaping can be seen in Figure 3.23

Next the signals emerging from these three channels are sampled following the LHC clock (40 MHz or 25 ns). This is done by the switched capacitor array (SCA). For physics studies, the 5 samples that correspond to the peak rise are stored. The third sample corresponds to the maximum of the amplitude. Sometimes 32 samples are also recorded for some dedicated analyses. Finally the signal is stored there waiting for a decision from the L1 trigger. If the signal is accepted, five samples per channel are read from the SCA and the optimal gain is used.

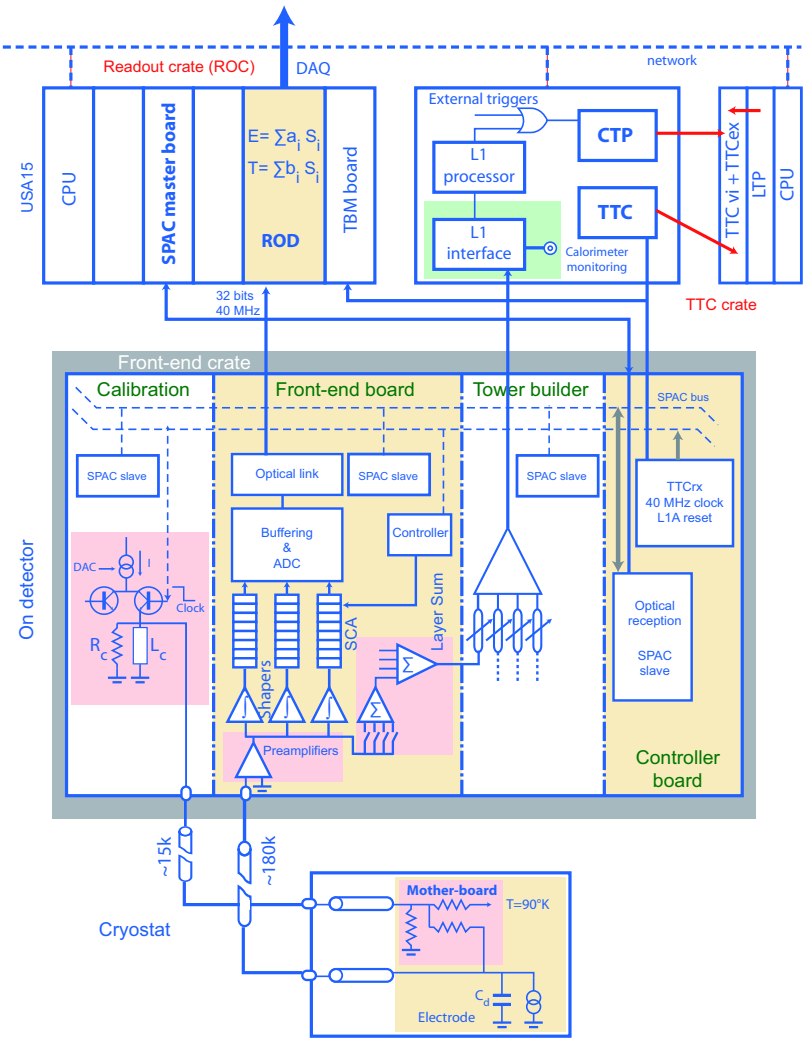

Figure 3.22: Illustration of the Liquid Argon Electronic Readout System [110].

The signal is digitised using 12-bits ADC (Analogue to Digital Converter). An op-amp is used to match between the SCA output and the ADC input. There are 16 ADC devices per FEB, therefore 1 ADC digitizes the signal from 8 channels. A voltage offset is added such that the mean value of the sample amplitudes corresponds to about 1000 ADC counts (the "pedestal"). This allows to measure both the positive and negative part of the pulse. The raw data are also formatted before to be sent outside the detector toward the Read Out Driver (ROD) thanks to an optical link. These links are able to transmit around 1.6 GB per second. Figure 3.24 shows the architecture of a front-end board.

Electronic Calibration The calibration boards allow to monitor the response of the 182468 cells of the liquid argon. They are located in the front end crates. Calibrated current pulses are injected through injection resistors in order to simulate an energy deposition in the calorimeter. The calibration pulse is injected as close as possible to the electrodes, and it is then treated as an ionization pulse. The resistors are placed on the motherboards and are connected to the electrodes through the summing boards. The pulse produced is distributed to a group of nearby channels that have little or no cross-talk in the detector. This calibration pulse has

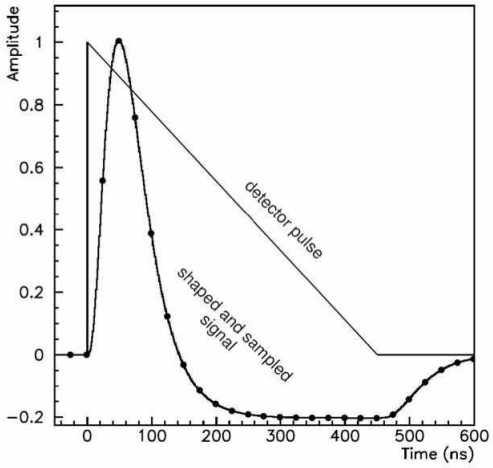

Figure 3.23: Ionization pulse before and after shaping.

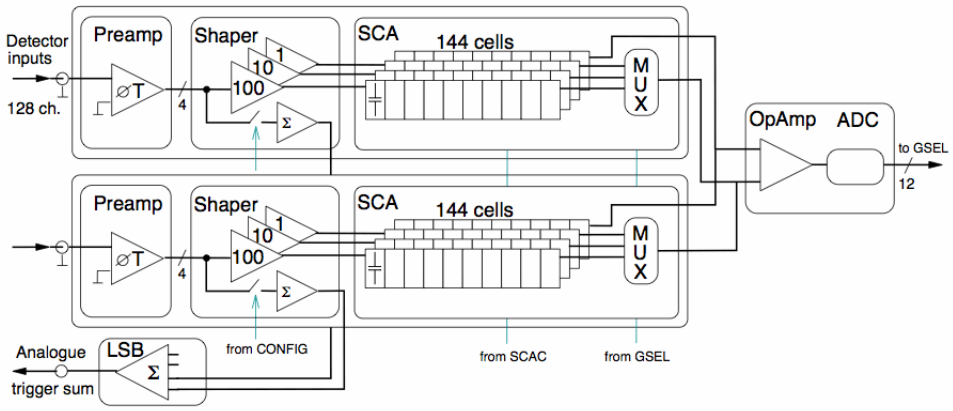

Figure 3.24: Layout of a Front-End-Board.

an exponential shape, that mimics the ionization triangular shape. The calibration pulse is parametrized with f_{step} and τ_{cali}. These parameters are measured for all the calibration boards, and are routinely extracted.

The electronic calibration system is designed to test the current to ADC value conversion, whereas the current to energy conversion is calculated from first principle or simulations, as explained below.

The full path for the energy reconstruction from the electrodes to the ROD and the calibration system are shown in Figure 3.22.

Energy reconstruction The reconstruction of the signal amplitude of the cells in the liquid argon used an Optimal Filtering algorithm applied on the samples s_j. The amplitude in ADC counts for the pulse is:

$$A = \sum_{j=1}^{N_{sample}} a_j(s_j - p)$$

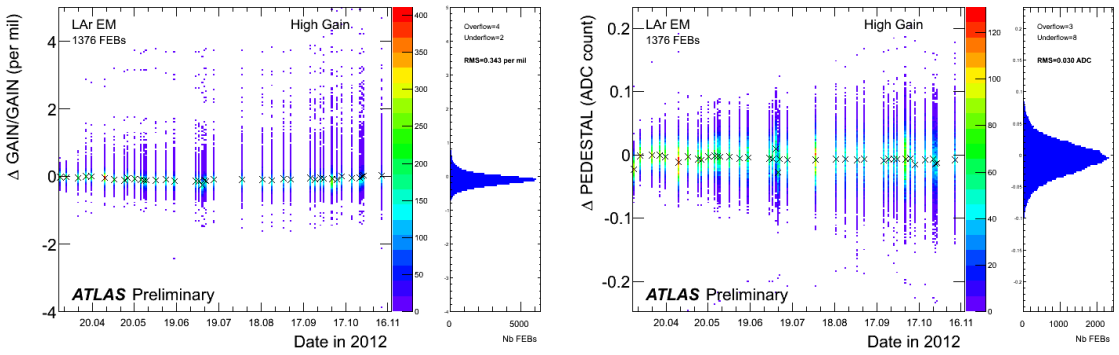

(a) Gain (b) Pedestal

Figure 3.25: (a) Relative variation of the gain and (b) absolute variation of the pedestal over time, for the electromagnetic detector with high gain switch and for data collected over the 2012 running period [135].

where N_{sample} is generally equal to 5, p is the ADC pedestal and a_j the Optimal Filtering Coefficients (OFC). They are calculated for each cell from two inputs: the predicted ionization pulse shape and the measure of the autocorrelation noise in order to minimize the contribution of the noise and the pileup on A. The pedestal corresponds to the mean of the signal sample s_j in ADC counts.

From the amplitude obtained with this algorithm, the energy can be calculated:

$$E_{cell} = F_{DAC\to\mu A} \times F_{\mu A\to MeV} \times \frac{1}{M_{phys}/M_{cal}} \times G \times A$$

where:

- $F_{DAC\to\mu A}$ refers to the conversion from DAC (Digital Analogue Converter) to μA.
- $F_{\mu A\to MeV}$ is the function that converts the μA to MeV. It is estimated from simulations and beam test studies. In case the high voltage setting of the channel is non-nominal, it takes into account the necessary correction.
- M_{phys} and M_{cal} corresponds to the ionization and calibration pulse response. The same current has been used for both pulses.
- G is the cell gain. It is obtained by comparing the amplitude of the pulse to a calibration pulse with a known amplitude, and increasing this amplitude. If there is a bias due to cross talk, for example in the first calorimeter layer, this is corrected here.

The LAr electronic system in the electromagnetic calorimeter is very stable with time, as seen in Figure 3.25 for the pedestal and gain coefficients.

3.2.3 Material Distribution

The total material budget in the ID should be ideally kept very low to allow a precise measurement of the particle tracks. However due to mechanical constraints, the total amount of material is quite large (the overall weight of the ID detector is 4.5 t). Precise studies have been made in order to precisely model the detector geometry. Figure 3.26 shows the simulated integrated

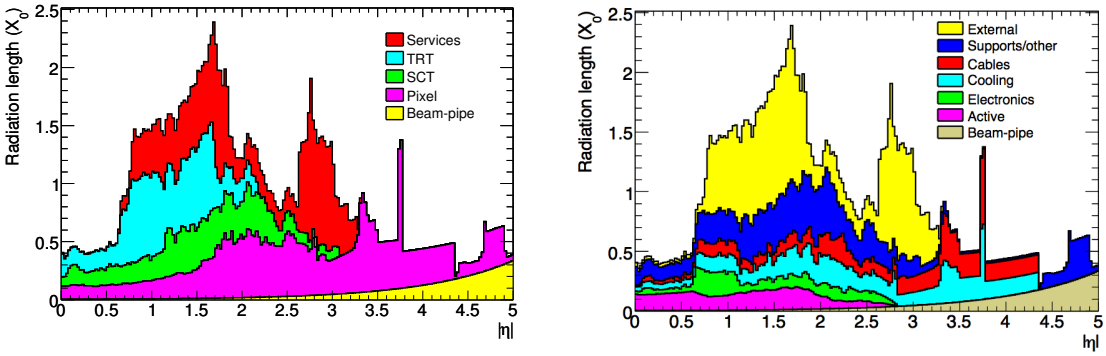

(a) (b)

Figure 3.26: Material budget in the inner detector in radiation length X_0 traversed by a particle existing the Inner Detector as a function of η and integrated over ϕ. The contributions of the different sub-detectors as well of the external services are shown in (a). Figure (b) shows the breakdown of this material budget into ID components [110].

radiation length, X_0, traversed by a particle in the inner detector as a function of η. A large amount of material is present in the barrel endcap transition region. This corresponds mainly to inactive material like the services. Most of the mechanical supports and services are located outside the ID volume, moderating the impact on the track measurement, but worsening the energy resolution as measured in the calorimeter. See Chapter 6 for an example of validation of the material simulation.

The expected integrated amount of material before the calorimeter is also illustrated in Figure 3.27. Locally, the density of material can be important, as for example around the crack transitions between barrel and endcap parts of the detector $|\eta| \sim 1.5$ ($\sim 10X_0$) or in the transition between the inner wheel of the endcap and the forward detector $|\eta| \sim 3.5$ ($\sim 12X_0$). The amount of material increases continuously from $|\eta|$=0 to the end of the barrel, and then it is stable up the end of the electromagnetic calorimeter with an average value of $\sim 3X_0$. The dark and light blue corresponds respectively to the case where we consider material only before the presampler layer or before the accordion detector. The difference between the two corresponds to the cabling services located between the presampler and the first layer of the calorimeter. In

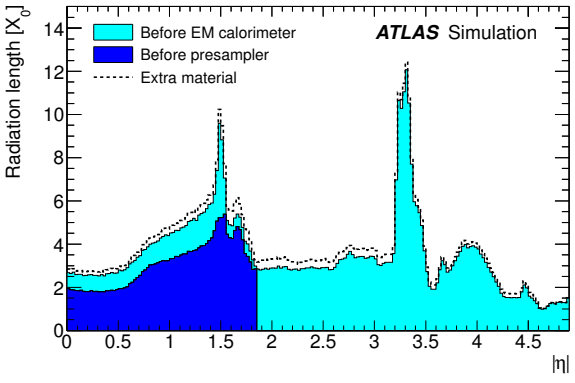

Figure 3.27: Radiation length (X_0) as a function of the pseudorapidity [110].

order to optimize the amount of material in front of the calorimeter, the central solenoid and the LAr calorimeter share a common vacuum vessel. This allows to eliminate two vacuum walls.

The presampler was designed to correct for energy loss in front of the electromagnetic calorimeter, due to interaction with material. Correcting for this effect allows improvement of the energy resolution. See Chapter 6 for a presentation of studies using the presampler to probe the material budget.

Chapter 4

The ATLAS Data and their Quality

The organization and distribution of the data in ATLAS is described below, before presenting details of the quality of the data taken during 2011 and 2012.

4.1 ATLAS Data

4.1.1 Distribution of the data

The rate of data that are stored each second is limited by the storage capacities of the ATLAS computing system, and is about 200 Hz. Each raw selected event has an approximate size of 1.6 Mbytes, leading to a total required storage of around 1 Pbytes per year. A reduction of the size per event is achieved through different steps [136].

At the trigger level, the data are split into different streams, corresponding to physics objects (presence of an electron, muons, jet, photon, ...). The events selected by the triggers are transferred to the CERN Central Tier0 computing center. A set of files in pool (Pool Of persistent Objects for LHC) format called Event Summary Data (ESD) and containing all the reconstruction information about these events is built. The per event size is typically 700 kbytes. A further reduction of the per event size is achieved by keeping only the information related to the objects and not anymore to the detectors (for example the details on the calorimeters cells are removed). This gives again a set of pool files called Analysis Object Data (AOD). This leads to a per event size of around 150 kbytes.

These two steps are realized within 24 hours after the data taking and the associated files are distributed to 10 Tier1 centres. A subsequent distribution of the AODs and a subset of the ESD and raw data is done toward Tier2 centres from the Tier1.

An ultimate per event size reduction is achieved using different techniques: the skimming, which does an event selection and reduces the average per event size, and the trimming, thinning and slimming that respectively remove all objects, selected objects and some parts of an individual object of a certain type. These three techniques ,with increasing reduction of the size of each event, are very efficient to reach a low dataset size.

Datasets more specific to a sub-detector or to physics objects are built, with files in pool format called Derived Physics Data (DPD). The selection of the objects is done using the filtering algorithm described above. The DPD size obtained is only 20% of the ESD size.

From one primary DPD many other derived DPDs can be produced thanks to the filtering algorithm, they are called D2PD, D3PD, following the level of derivation applied.

Two other further processings actually occur: the first one, happening right after the raw data reprocessing, concerns the quality of the data and is described in the following section. The

other may happen a few times per year. It is induced by the fact that the ATLAS reconstruction software evolves continuously and gets at some point better performance than the previous one. A new reprocessing of the data is done with the improved software, followed by the production of new AOD and DPDs, and their distribution to Tier1 and Tier2 centres.

4.1.2 Organization of the data

The possibility for ATLAS to record data depends on the LHC beam conditions. For stable beam conditions, collision data can be recorded. The length of LHC fills varies considerably, it depends on many parameters of the machines such as the ones described in Chapter 3. The average length observed in 2012 was typically 6 hours for each fill, with a record of 23 hours observed the 12th of June 2012 [137].

The standard unit of data in ATLAS is the lumi-block (LB). During the data taking, the events are split into these independent LBs that corresponds to roughly one or two minutes depending on the conditions. This subdivision is made in order to only reject a short period of time, corresponding to a few LBs, in case of data taking problem. The final dataset is obtained by merging the remaining LBs.

The total integrated luminosity for N_{LB} selected lumiblocks corresponds to:

$$L_{tot} = \sum_{i=1}^{N_{LB}} \Delta t_i \cdot L_i$$

where L_i and Δt_i are the average instantaneous luminosity and duration time of the lumi-block i.

The data are also split in time periods, that have coherent detector or trigger configurations. They consist of groups of runs, and they are contiguous and non-overlapping. A significant change in the calibration or configuration of the detector or the trigger leads to the definition of a new period. Tables 4.1 and 4.2 summarize the characteristics of the various periods for 2011 and 2012 respectively [137].

Table 4.1: Characteristic of the 2011 data periods

Data Period	B	C	D	E	F	G	H	I	J	L	M
Start Date	3/21	4/14	4/30	5/15	5/27	6/16	7/13	7/30	8/4	9/7	10/6
Integrated lumi. recorded (fb^{-1})	0.02	0.18	0.05	0.15	0.56	0.28	0.40	0.23	0.66	1.57	1.17
Peak lumi. (10^{33} cm^{-2} s^{-1})	0.2	0.7	0.8	1.1	1.3	1.3	1.9	2.0	2.3	3.3	3.6
Peak events per Bunch crossing	8	7	8	8	8	7	9	10	11	16	32
LAr EM Fraction of good data (%)	94.7	95.3	98.5	97.7	98.2	96.4	98.7	98.7	98.9	98.0	95.3

4.2 The Quality of Data

A Data Quality assessment system has been introduced in order to identify problems that can occur during the data taking. A first level, which corresponds to the on-line data quality system,

allows the stopping of the data taking if a very severe problem occurs. Before restarting the recording of events, the problem should be fixed by the experts present on site. The second level is a more refined study of the quality of the data, which is done offline (after the data have been taken).

This second level is explained below.

Table 4.2: Characteristic of the 2012 data periods

Data Period	A	B	C	D	E	G	H	I	J	L
Start Date	4/4	5/1	7/1	7/24	8/23	9/26	10/13	10/26	11/2	11/30
Integrated lumi. recorded (fb^{-1})	0.86	5.40	1.57	3.43	2.76	1.33	1.58	1.08	2.77	0.91
Peak lumi. (10^{33} cm^{-2} s^{-1})	5.5	6.7	6.2	7.3	7.6	7.3	7.5	7.3	7.4	7.5
Peak events per Bunch crossing	30	32	34	35	36	34	36	35	35	37
LAr EM Fraction of good data (%)	96.5	99.7	97.8	99.5	99.3	99.7	99.7	99.2	99.5	99.8

Before being used for physics analysis, a processing of the data is made, as explained in Section 4.1.1. At the end of this procedure, a further period of 48 hours is allocated to scrutinize the quality of the recorded collisions. When the period comes to its end, a second processing, called the "bulk", occurs and takes into account changes to be made following data quality arguments, closing the so called "calibration loop". Some of the pathologies encountered in the data are summarized below [138].

4.2.1 High voltage power supply trip

In 2011 and 2012 large high voltage instabilities, causing a sudden drop of the high voltage due to a current spike (see Figure 4.1), were observed. As the recorded energy strongly depends on the high voltage applied to the electrodes, the affected data normally cannot be used any more, leading to the exclusion of the corresponding LBs.

In reality, the energy can be corrected, when the high voltage is not at its nominal setting, but only if the other side of the electrode is still supplied (see Section 3.2.2.4). However the correction is not accurate; measuring the energy with the correct HV settings gives much better precision. This is why a recovering of the nominal HV is needed.

Three flags are attributed to the HV status: "Trip" for the drop in HV, "Ramp" for the linearly increase of the HV up to its nominal value, and "OK" when the nominal setting is reached, as seen in Figure 4.1. Only the period "Ramp" can be corrected by the procedure described above. A system allowing an automatic recovering of this nominal HV has been designed. This system allows to increases linearly the voltage up to his nominal setting, in a very short time (the period "Ramp" is strongly reduced).

4.2.2 Burst of coherent noise

With the 40 MHz collision frequency, there is the possibility to place protons bunches every 25 ns all along the LHC ring. In reality, there are gaps due to the delays required for injection and extraction (see Section 3.1.1.4). Moreover, in 2011 and 2012 the LHC mostly ran with a bunch spacing of 50 ns.

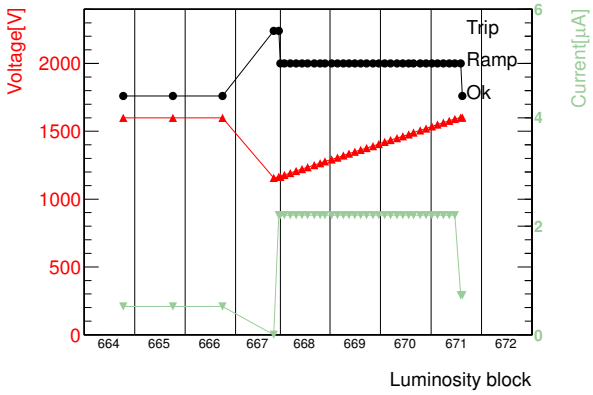

Figure 4.1: Illustration of a high voltage power supply trip [138].

For the data quality assessment, specific triggers are used to select only the collision dead times. A special stream is created for such events, called the CosmicCalo stream. The goal is to check the response of the ATLAS electronic during data taking periods, but without any collision in order to spot the problems. Very low activity in the detectors is expected during these short time periods, mainly due to cosmic muons.

Large depositions of energy in these non-colliding streams have been observed in the calorimeter, reaching sometimes a total energy of up to a few TeVs. Such problems pollute significantly the real collision data. An example of such a burst of noise in the calorimeter is shown in Figure 4.2, where the total energy reaches about 5 TeV.

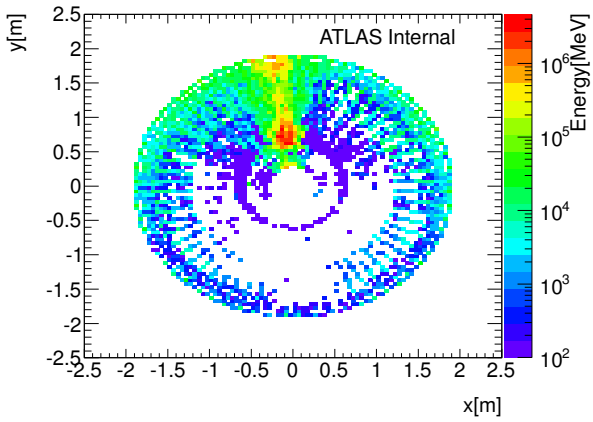

Figure 4.2: Example of a burst of coherent noise in the A side of the electromagnetic calorimeter endcap in the run 205071 [138].

This problem seems to be linked to the high voltage system, as turning-off the power supplies for the HV leads to an extinction of these bursts of noise. More precise studies [139] even show that the noise seems to be radiated by the unshielded high voltage cables inside the cryostat.

This noise can be suppressed by requiring that the ionization pulse be similar to the standard pulse for a physical event. If the energy deposit is produced by the electronic system, it is expected not to have the same shape as a real physics event. The quality of the pulse shape is

parametrized with the Quality factor:

$$Q^2 = \frac{1}{N_{dof}} \sum_{j=1} N_{sample} \frac{(s_f - A g_j^{phys})^2}{\sigma_{noise}^2 + (kA)^2} \tag{4.1}$$

where N_{sample} is the number of pulse samples used (see Chapter 3), s_j the amplitude in ADC counts of each sample, g_j^{phys} is the normalized predicted ionization pulse , A is the maximum amplitude in ADC counts, k is a factor that quantifies the relative accuracy of the amplitude, and N_{dof} is the number of degree of freedom. The k factors are layer dependent and amount to 0.9%, 1.1%, 0.8% and 0.75% [140] for the presampler, layers 1, 2 and 3, respectively. This complete form is not used, instead, the following one:

$$Q^2 = \frac{1}{N_{dof}} \sum_{j=1} N_{sample} \frac{(s_f - A g_j^{phys})^2}{\sigma_{noise}^2} \tag{4.2}$$

where the $(kA)^2$ term is removed, for the analyses presented below.

Two different criteria are established to identify a noise event:

- The standard flag: if more than 5 FEBs contain more than 30 channels having a Quality Factor greater than 4000, then the event is considered as noisy. It is efficient for identifying coherent noise with a large extension.
- The saturated flag: for very different pulses, the Quality Factor can be saturated at 2^{16} (=65536), due to the 16 bits coding of the pulses. If more than 20 channels have a saturated Quality Factor, then the event is tagged as noisy. This condition is more stringent and allow to identify more localized noises.

The procedure adopted in the beginning of the data taking at the LHC was to reject all the LBs where the coherent noise appeared.

4.2.2.1 Assignation of a noise burst to a partition

Using the standard flag, the presence of a noise burst is detected immediately, as the number of affected cells is huge. The problem is then not the detection, but rather the attribution of this noise to a detector, because of its extension.

Many detectors use liquid argon as the active medium, as seen in Chapter 3. These detectors are called "partitions" in the following: the electromagnetic barrel (EMB) and endcaps (EMC), the hadronic endcaps (HEC) and the forward calorimeter (FCAL). These partitions are subdivided in two parts, the negative one with respect to the z axis ("B") and the positive one ("A"). There are thus in total eight partitions.

The bursts of coherent noise were generally assigned to all partitions with a significant fraction of noise. Unnatural correlations were however observed between partitions that don't share the same cryostat. This kind of correlation is suspicious, as the three cryostats are electronically independent.

A more refined procedure, attributing the coherent noise to the noisiest partition, was instead chosen, enabling an important reduction of the correlations. Figure 4.3 illustrates the correlations between the two endcaps' cryostats, and between the barrel and endcaps' cryostats observed with the old and new procedures, for runs in 2011. With the old one, a large fraction of the LBs were assigned at the same time in completely independents partitions. With the new one, this fraction is lowered up to about 10%.

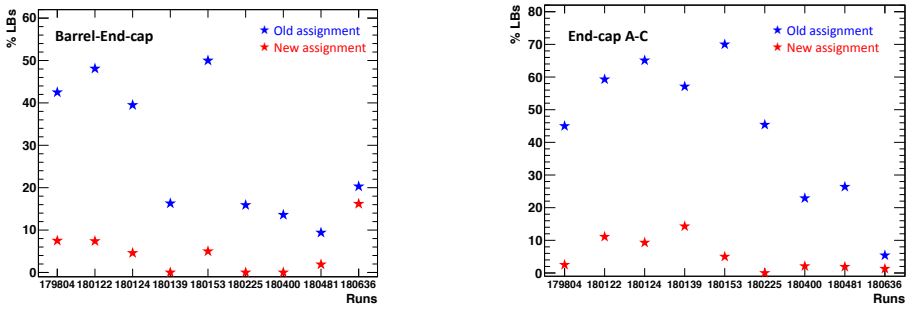

(a) (b)

Figure 4.3: Percentage of LBs where the noise burst is assigned: both to barrel and endcap partitions (a) or both to the A and C partitions of the endcaps (b) with the old and new attribution procedure, for runs in 2011.

4.2.2.2 Time window veto

A dependence of the rate of bursts of coherent noise with the luminosity has been noticed. The fraction of Lumiblocks affected by this issue increases linearly with the instantaneous luminosity. With the restart of the LHC at a peak luminosity of around $1 \cdot 10^{34}\text{cm}^{-2}\text{s}^{-1}$, it is expected that the totality of the LBs of a given data taking period will be rejected due to this problem. To avoid this strong dependence between the rate of noise and the luminosity, an alternative procedure called "time window veto" is used. This method comes from the observation that the lifetime of a noise burst is well below the LB duration, typically less than 5 μs. A window of 250 ms in 2012 and 1 s in 2011 is applied around a group of very noisy events well identified with the standard flag, and this window is rejected. This allow to strongly reduce the rate of data rejected due to noise bursts. For the future data taking with an increased luminosity, the time window will be tuned in order to better match the noise burst duration and then reduce unnecessary data losses. This time window veto cleaning is applied after the 48 hours of the calibration loop, during the second reprocessing mentioned above.

4.2.3 Problematic channels

Regular calibrations of the full LAr electronic allows to identify problematic channels, or channels starting to deviate from their usual operation. Dedicated runs, launched between physics runs several times per week, allow to calibrate the pedestals (noise properties of the readout electronic), the pulse shapes as a function of the time, and the readout gains. This calibration is done on randomly triggered events. However, all the faulty channels are not detected, especially when they have non-Gaussian noise. This has been noticed especially in presence of collisions. Three kind of noisy channels have been listed:

- Non-operational cells: these cells do no read out any more or are permanently noisy. They are always masked offline during the event reconstruction, and they get their energy from the average of neighbouring cells energies.

- Noisy cells: they are a source of background especially for unconverted photons. Indeed, such photons are characterized by localized energy deposition without associated track, which can be mimicked by noisy cells. When the Quality Factor of these cells is above 4000, they are considered as non-operational and selectively masked as in the previous

case. If a given channel is noisy with Q>4000 more than 80 times, it is finally considered as definitively non-operational and is permanently masked.

- Cells for which the calibration constant are not available due to faulty calibration lines: the missing coefficient are recalculated from similar cells.

All these features concern only a low fraction of cells; in total at the beginning of 2012 99.9% of the cells in the liquid argon system are operational.

The burst of coherent noise studied in the previous paragraph can locally fire many cells, giving the impression that they are noisy by themselves. In order to spot correctly genuine problematic cells, the noise bursts first have to be removed. However the cleaning of these events with the time window veto is done only during the second processing, when this is too late to identify the noise. Therefore, for tracking the noisy channels, the LBs where a burst of coherent noise occurred are temporarily rejected, and only the remaining LBs are studied. The masking of the genuine noisy channels is also done during the second processing.

The Presampler issue These problematic channels are usually well distributed all over the acceptance of the calorimeters so that there are no dead regions, and the impact on the physics is negligible. However there is an exception in the presampler of the electromagnetic calorimeter. Figure 4.4(a) shows the (η, ϕ) distribution of events with an energy greater than 800 MeV in the electromagnetic presampler in the CosmicCalo stream. There is a quite dense activity around the region $[-0.3, 0]$. Now looking at the fraction of these events having a quality factor above 4000, in Figure 4.4(c) one can see that almost all this activity comes from noisy channels. The masking procedure explained before is efficient in rejecting such events, as illustrated in Figure 4.4(b) which shows the same events than in Figure 4.4(a) but after the cleaning. The number of events having an energy higher than 800 MeV is significantly reduced.

An energy up to 100 GeV can be recorded in these cells, which can be noisy for only a short time and then come back to a nominal operation. From the detector point of view, there is nothing particular in this region that could explain such concentration of noise.

However, a relation with the HV system has been found: when lowering the high voltage lines for some of the presampler cells, the number of noisy channels decreases significantly.

This solution has been used since the data period H (October 2012, from Run 212619). The result is shown in Figure 4.5 where the percentage of selectively masked channels goes from 7% at the beginning of the 2012 data taking to about 1% at the end of the year. In the same time the number of permanently masked channels did not evolve, it stays around 0.2%.

More precisely, all or some of the lines are progressively lowered from 1600 V to 800 V for the barrel and from 2000 V to 1200 V in the endcaps.

4.2.3.1 The Good Run List

Once the quality of the data for a given period has been assessed and the problems identified, LumiBlocks or even entire runs, that cannot be used for the physics due to a severe problem, are rejected. A list of runs and LBs that are available for physics analysis is established and called the Good Run List.

In this list, not only the LAr electromagnetic detector defects are taken into account but also all the defects from the other systems.

Tables 4.1 and 4.2 (last lines) give the fraction of data that are considered as usable for the physics analysis from the LAr electromagnetic calorimeter point of view. This fraction

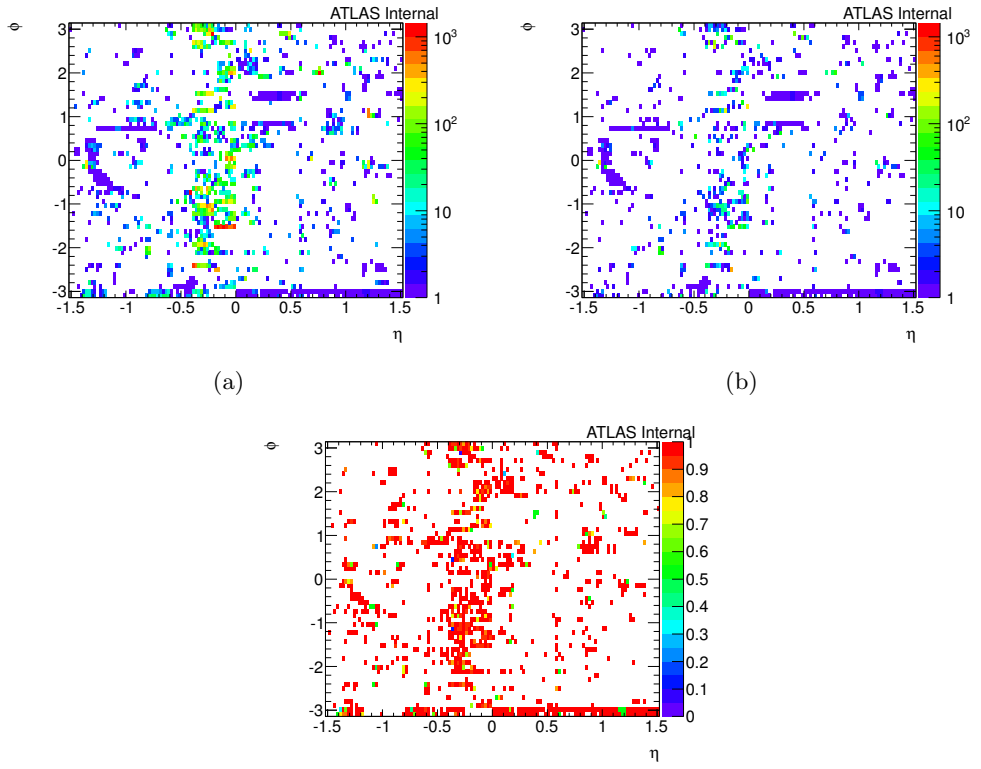

Figure 4.4: Number of events in the run 205071 and in the CosmicCalo stream with an energy greater than 800 MeV in the electromagnetic presampler before (a) and after (b) the offline cleaning. Fraction of the same events with a quality factor above 4000 (c). Taken from [138].

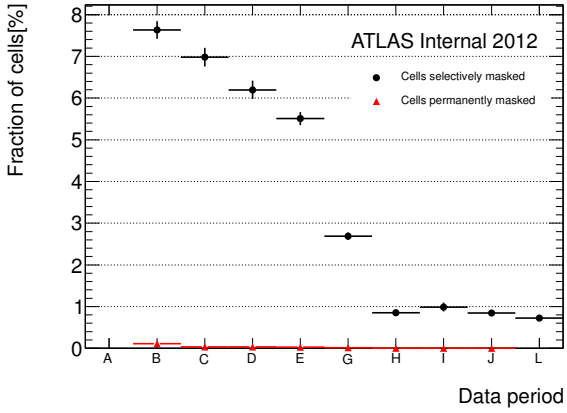

Figure 4.5: Evolution of the fraction of selectively and permanently masked channels with the data period in 2012 [138].

evolves with the time: in 2010, an average of about 9% of data where rejected due to problem in this detector, whereas this quantity amounts to 2% in 2011 and decreases to 1% in 2012. This constant improvement of the quality of the data is due to the huge effort made to better understand the various issues observed and to treat them so that the least amount of data is

lost.

4.3 Complementing the offline data quality

The masking procedure that allows rejection of the noisy channels may fail. For example, this could happen if such cells are noisy during a LB polluted by bursts of coherent noise and rejected during the cell masking procedure.

After the second processing, when all the other cells are masked correctly and the time window veto has rejected the coherent noise, these cells appear clearly as spots in the CosmicCalo stream. All the LBs where these cells are noisy are consequently rejected, to avoid their misidentification as photons.

An additional offline procedure, to be applied after the second reprocessing at the physics analysis level, has been created to solve this issue. It is detailed below.

4.3.1 Impact of a noisy channels on the physics

In order to see if sporadic noise can be misidentified as a photon and in which proportion, a study has been done using non-colliding data samples.

Data samples from the CosmicCalo stream, before and after the second reprocessing are used in ESD format in order to have access to cell information. They correspond to the run 165956 taken in September 2010, with an amount of data of 0.105 pb^{-1}. The sample before the second reprocessing is enriched in problematic channels which provides a sufficient number of events needed for the study.

In these samples, photon candidates with an energy above 10 GeV are selected in the electromagnetic calorimeter acceptance ($\eta < 2.47$). A (η, ϕ) distribution of these photons before and after the masking of the noisy channels is given in Figure 4.6(a) and 4.6(c) respectively.

Two hot spots are seen in Figure 4.6(a). Their coordinates are: (η, ϕ)= (0.012, -0.113) and (η, ϕ)= (-1.521, -1.137). These spots probably correspond to sporadic noisy channels misidentified as photons. This seems to be confirmed by Figure 4.6(c) where these red points have disappeared. For this particular run, the data masking procedure worked perfectly.

One can require some conditions on the photon shower shapes in order to remove noisy channels misidentified as photons. There are two sets of identification criteria for the photons, loose" and "tight", following the hardness of the cuts (see Section 5.1.3). The tight identification is used for example in the $H \rightarrow \gamma\gamma$ analysis that looks for very well identified photons (see Chapter 7).

The map in Figure 4.6(b) shows the distribution of photons selected with the loose criteria, in the CosmicCalo sample before masking of the noisy channels. Among all the photon candidates selected at the beginning, 50% of them pass this criteria. However, the two red spots are still present. Only $\sim 4\%$ of the events belonging to these spots have been removed by this cut. When applying the tight set of cuts instead, the majority of the photon candidates are rejected, and the two hot spots are not any more seen.

For analyses using the loose photon identification set of cuts, the sporadic noise will in certain cases be misidentified as photons. This is the reason why an additional cleaning is needed for the photons.

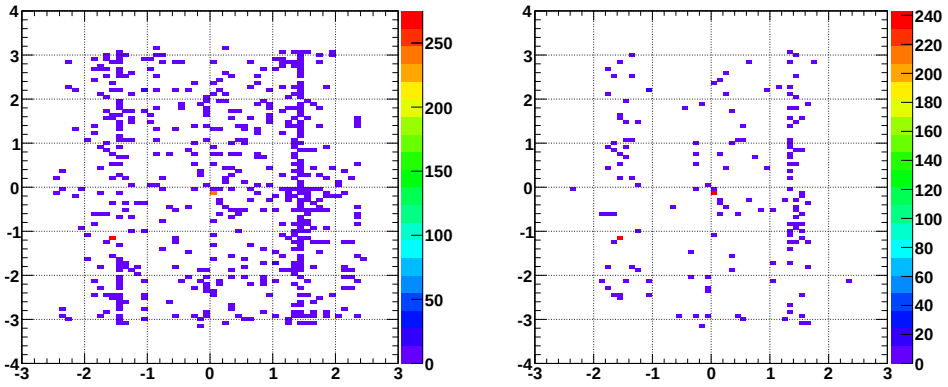

(a) All photons, before masking

(b) Loose photons, before masking

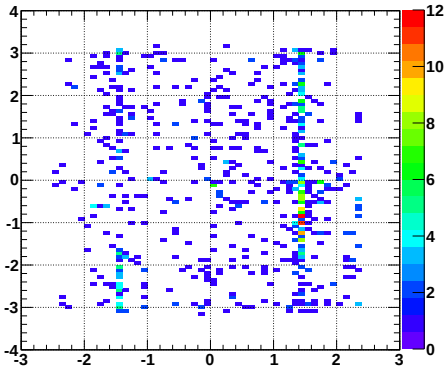

(c) All photons, after masking

Figure 4.6: Map (η, ϕ) for all the photons of the CosmicCalo sample for the run 165956, before (a) and after the bulk processing (c). (b) Same map for photons selected with the loose identification, before masking.

4.3.2 The LAr cleaning variable and the photon cleaning

4.3.2.1 LAr Cleaning

The Quality Factor (Q factor) is used to reject the noisy channels (see 4.2.3). These channels are characterized by large energy deposition in the calorimeter in absence of collisions.

A discriminative variable is built from the Q factor and the cells energies. It is called LarCleaning referencing the JetCleaning variable used to clean the hadronic calorimeter from noise [141]. The difference between the two variables is mainly the size of the clusters used.

The LArCleaning is computed as the sum of the energy of the cells with quality factor greater than 4000 over the sum of all the cells energies in the photon cluster [142] :

$$\text{LarCleaning} = \frac{\sum_{\text{cells}} \text{E}_{\text{cell}}(\text{Q}_{\text{cell}} > 4000)}{\sum_{\text{cells}} \text{E}_{\text{cell}}} \tag{4.3}$$

4.3.2.2 Photon Cleaning

Additional variables In addition to the LAr Cleaning, three other discriminative variables are used to form the photon cleaning procedure. This procedure should be applied on each physics analysis dealing with photons in order to reject efficiently the noise.

First, the recorded collision time of the cells averaged over the photon cluster, is used. This time is obtained by the study of the cell pulse shape. This forms a good indicator because noisy cells are fired sporadically, without any coherence with the collision time.

The other variables used are sensitive to the photon shower development shape. The noisy channels are signified by narrower energy deposition in the calorimeter, compared to the real photons. The variables r_η and r_ϕ, defined as [143]:

$$r_\eta = \frac{E_{cell,3\times7}}{E_{cell,7\times7}} \;\; ; \;\; r_\phi = \frac{E_{cell,3\times3}}{E_{cell,3\times7}}$$

with $E_{cell,x\times y}$ the energy in a cluster of size $x \times y$ in $\eta \times \phi$ in cell units, allow to quantify the η and ϕ size of the energy deposit.

Physics samples An alternative for the CosmiCalo samples before and after the masking of the noisy channels is the use of physics samples dominated either by real or spurious photons. The samples that are expected to contain mostly real photons events are well balanced $\gamma\gamma$ and γ-jet samples, where the sum of the transverse momentum vectors is close to zero. The sample that is expected to be enriched in misidentified photon clusters is the γ-MET sample, where there is no visible object balancing the transverse momentum of the photons.

In these three samples, the photon candidates are selected in the detector acceptance and excluding the transition region between the barrel and endcap of the electromagnetic calorimeter: $|\eta| < 1.37$ or $1.52 < \eta < 2.37$. The photons are required to have a transverse momentum larger than 25 GeV (45 GeV) in the $\gamma\gamma$ and γ-jet samples (γ-MET sample).

The $\gamma\gamma$ and γ-jet samples have a uniform distribution of the photons candidates along η and ϕ, unlike the γ-MET sample where some regions are more densely populated. This is more likely to be noisy channels.

The distribution of the variables defined previously for these three representative samples are shown in Figure 4.7.

The feature of the γ-MET sample is clearly different from the two other ones for these four discriminative variables, confirming the presence of misidentified photons in this sample. More precisely, the amount of candidates having a LArCleaning bigger than 0.8 is much larger than in the other samples, the time distribution is more spread out, reaching up to 40-50 ns delay with respect to the collision, the r_η distribution has very large tails above 1, and r_ϕ has also larger tails above 1.

The photon cleaning cuts These results allow to define a set of cuts efficient in rejecting the misidentified photon electromagnetic clusters. These cuts are defined as:

1. LArCleaning < 0.8
2. $|\tau_{cluster}| < 10$ ns
3. $r_\eta < 0.98$
4. $r_\phi < 1$

A photon is considered as a good candidate, if it passes the cut 1 and at least one of the conditions 2, 3, or 4.

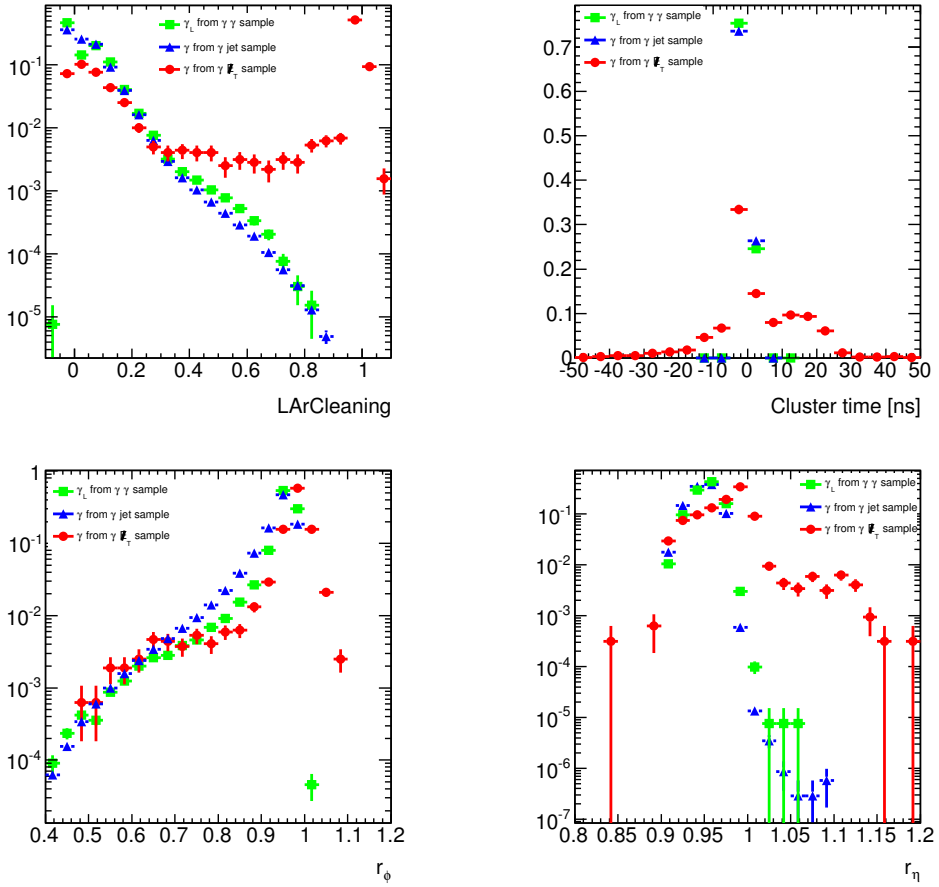

Figure 4.7: Distribution of discriminative variables for the $\gamma\gamma$ (green squares), γ-jet (blue triangular) and γ-MET (red circles) physics samples [142].

Efficiency and rejection The photon cleaning procedure has a good efficiency and rejection in eliminating misidentified photon clusters. This is quantified by comparing the number of photon primarily selected N_{candid} to the number of events rejected once the photon cleaning procedure is applied N_{reject}. This allows to compute the rejection rate: $R_{reject} = N_{reject}/N_{candid}$. The results are shown in Table 4.3.

Table 4.3: Rejection due to the photon cleaning procedure for the three different physic samples.

Sample	$\gamma\gamma$	γ-jet	γ-MET
N_{candid}	237210	3468247	2890
N_{reject}	2	21	1646
R_{reject} (%)	$1.3 \cdot 10^{-3}$	$0.6 \cdot 10^{-3}$	57.0

As foreseen from Figure 4.7, the rejection for the $\gamma\gamma$ and γ-jet samples is very low. On the other hand, the rejection for the γ-MET sample, which is expected to contain mainly misidentified photons due to noise in the calorimeter, reaches almost 60%. Therefore this procedure provides a good rejection of fake photon clusters.

p_T dependence Figure 4.8 shows, for the diphoton sample, the rejection R_{reject} as described previously as a function of the p_T of the photon candidate. A quite strong dependence is observed between these two variables, both for the LArCleaning variable and for the complete photon cleaning selection.

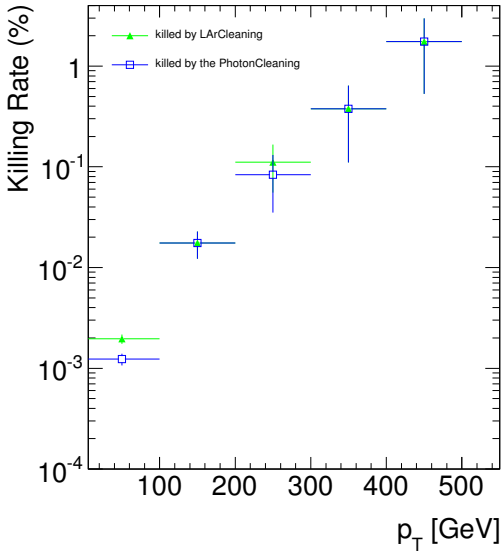

Figure 4.8: Correlation between the transverse momentum of the photons and the rejection achieved either by the LArCleaning variable alone (green triangles) or the photon cleaning procedure (blue squares) in the $\gamma\gamma$ sample [142].

This correlation arises from the cell Quality Factor dependence on the cells' energy. The formula 4.1 corresponding to the original cell Quality Factor has on average no dependence on the energy thanks to the term kA in the denominator. Indeed, the precision on the samples amplitudes increases with the amplitude and so with the energy for a given gain. If the prediction of the LAr ionization pulse is not perfect, the Q factor, similar to a χ^2 test will increase with the energy. The kA factor, that also scales with the energy, allows to compensate this dependence. The formula for the Q-factor actually used is the one given in formula 4.2 where this term is removed. Therefore the dependence of the Quality Factor with the energy is expected.

This could be an issue, as events could be rejected because they have a large energy, and not because they are noisy.

Impact of the LAr Cleaning variable on noisy channels Coming back to the non-colliding sample studied in Section 4.3.1, the performance of the LArCleaning variable is tested. Two sporadic noisy channels have been spotted in this sample, and are successfully masked in the second reprocessing.

Figure 4.9 shows the distribution of the LArCleaning variable for this sample. It can be noticed that a large fraction of the events peaks at 1. These photon candidates have the majority of their cells with a quality factor bigger than 4000. A (η, ϕ) map for the events having a LArCleaning > 0.8 is also shown. In this map, the two spots already mentioned are well seen.

Figure 4.9 shows also the η and ϕ distribution of the photon candidates in the CosmicCalo stream. The sporadically noisy channels are well visible in these distributions as they form very narrow peaks around the coordinates (η, ϕ)= (0.012, -0.113) and (η, ϕ)= (-1.521, -1.137) as seen

previously. When the events having a LArCleaning variable bigger than 0.8 are overlaid, one can see that they correspond mainly to these two hot spots. More quantitatively, this variable has been shown to be as efficient as the masking of the noisy channels during the calibration loop: 100% of the events cleaned with this procedure are also removed by the LArCleaning.

The LArCleaning variable and the photon cleaning procedure have been therefore shown to be efficient in replacing the standard flagging in case it would fail.

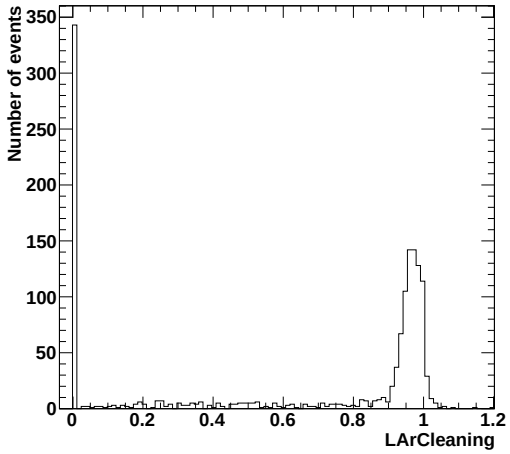

(a) Distribution of the LArCleaning

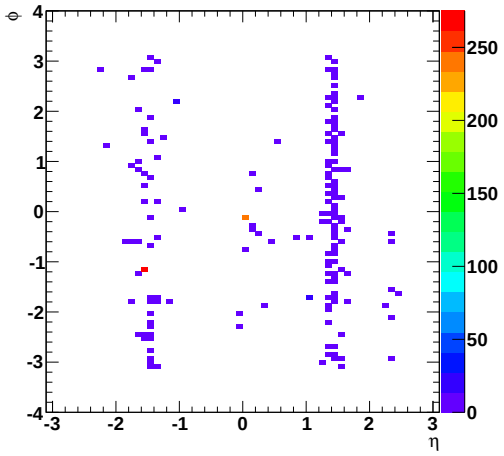

(b) (η, ϕ) map for the photons having $LC > 0.8$

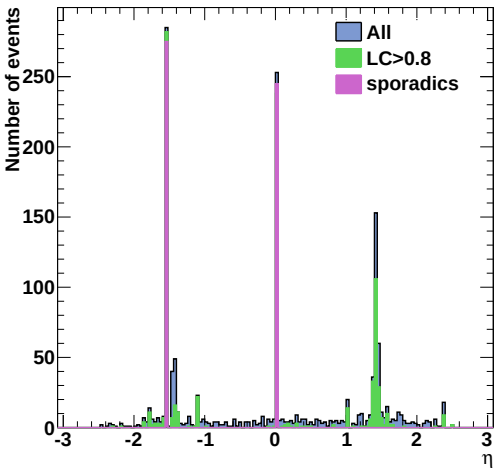

(c) η distribution

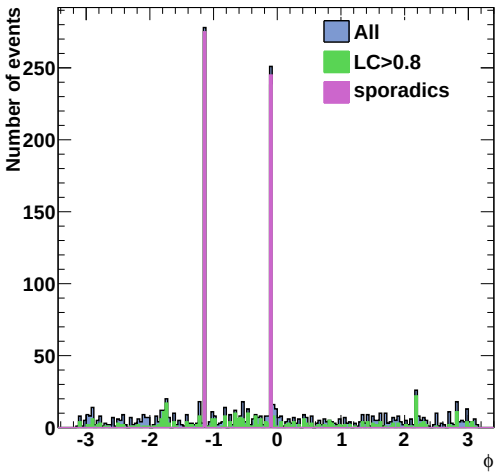

(d) ϕ distribution

Figure 4.9: Figure 4.9(a) shows the distribution of the new variable LArCleaning for the sample studied. A cut like $LC < 0.8$ will remove the peak which seems to correspond to sporadic noise. In Figure 4.9(b), the (η, ϕ) map for the photons having a LArCleaning bigger than 0.8 is shown: one can notice that the two red spots are seen by this cut.

Burst of coherent noise In the η distribution seen in Figure 4.9(c) there is an additional peak at $\eta \sim 1.5$ that is rejected in part by the LarCleaning variable. This corresponds to the

band seen in Figure 4.9(b). These events are noisy and not localized, which is a typical signature of a noise burst (see Section 4.2.2).

4.3.3 Other variables of interest

4.3.3.1 Cell-based variables

The photon cleaning procedure defined previously mainly relies on the Quality Factor of the ionization pulse. However an energy dependence is expected from this variable, artificially increasing the rejection of good photon candidates when increasing the energy.

Moreover, the Quality Factor is very dependent on the time of the cell: when the cell is delayed with respect to collisions, it increases with respect to non-delayed cell. This is an issue when aiming to search for delayed particles coming from long decay chains, as predicted in some Beyond Standard models.

Improvements on the computation of the Q-Factor have been done and are ongoing (see for example [144]). But other variables could also be investigated to replace this variable and eventually be combined with the LArCleaning.

Using information at the cell level, the following variables have been built:

- The maximal cell energy in a cluster. This particular cell is called c_{max}.
- The maximal ADC value (maxADC) of c_{max} and the position of this maximum (index) in term of samples. This gives information about the shape of the pulse (ADC counts where addressed in Section 3.2.2.5).
- The weighted (by the energy) sum of the Q-Factors of the cells in a cluster, called Q_{mean}: $Q_{mean} = \sum_i (E_i Q_i) / \sum_i E_i$. With this variable more weight is given to cells having greater energies and so decreases the impact of the electronic noise. It avoid the case where a cluster would be rejected because of one very noisy cell with low energy, so not contributing so much in the total cluster energy.
- The weighted (by the energy) sum of the Q-Factors of the cells in a cluster in the second sampling of the electromagnetic calorimeter s_2 called Q_{s2}: $Q_{s2} = \sum_i (E_{s2,i} Q_i) / \sum_i E_{s2,i}$.
- The ratio of a given cell energy by the total cluster energy, called R_{cell} or E_{cell}/E_{tot} .

In Figure 4.10 the distribution of these variables for the photon candidates and for the events in the two hot spots are depicted. The distribution of events having a LArCleaning above 0.8 are also overlaid.

Looking at these distributions for the the noisy channel, the following points are noticed:

- The Q_{mean} and Q_{s2} distribution peak at very high values and the pulse shape is very different from the predicted one.
- The MaxADC distribution is centred around high values
- There is a non-negligible amount of events having a maximal value of ADC in the fourth position (this is also illustrated by the pulse shape). However the position of the MaxADC has the same problem than the time variable: a delayed pulse will have its MaxADC at higher value than a "normal" pulse.
- The R_{cell} distribution is strongly peaked at 1, meaning that almost all the energy is concentrated is only one cell.

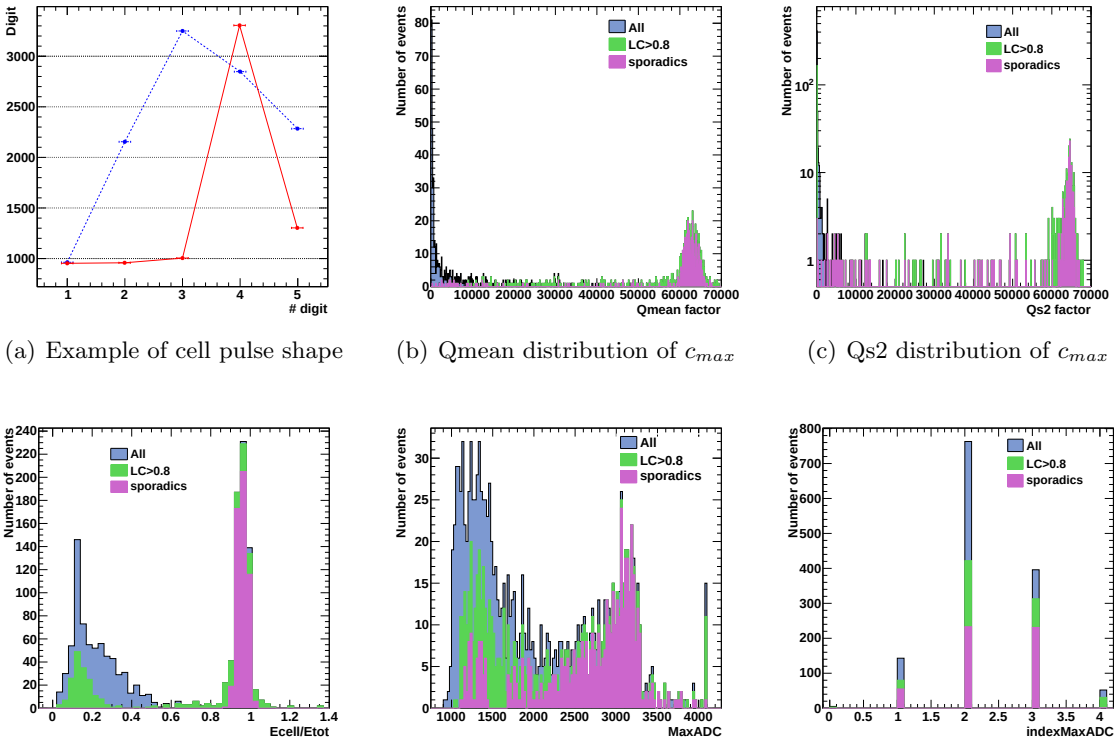

(a) Example of cell pulse shape (b) Qmean distribution of c_{max} (c) Qs2 distribution of c_{max}

(d) R_{cell} distribution of c_{max} (e) MaxADC distribution of c_{max} (f) Index of MaxADC distribution of c_{max}

Figure 4.10: Distributions of different discriminative variables for the cell of maximal energy in a cluster. A comparison between all the photon candidates (blue histogram), the events located in the two hot spots (purple histogram) and the events spotted by the LArCleaning variable (green histogram) is done using the CosmicCalo stream before the second reprocessing. See text for the definition of the variables. On the top left (a) an example of a cell ionization pulse shape for a photon candidate and a event belonging to one the two hot spots is also depicted.

The dependence of these variables on the transverse momentum p_T or energy is investigated, using collision data, where photons with $p_T > 10$ GeV and in the detector acceptance are selected. The conclusions of this study are:

- The maximal ADC value (MaxADC) scales with the energy for a given gain. Figure 4.11(a) illustrates this dependence for this physics sample. The two branches seen in this figure correspond to the two different gains accessible here, i.e high and medium.

- The various Q factors all have a dependence on the energy, even when evaluated in the second sampling or doing an energy weighting.

- The variable R_{cell} has no dependence on energy or transverse momentum as shown in Figure 4.11(b). A cut on this variable such that $R_{cell} > 0.8$ is as efficient as the masking procedure or the LArCleaning cut to remove the noisy channels as seen in Figure 4.10(d) and has in addition the advantage of not scaling with the photon transverse momentum.

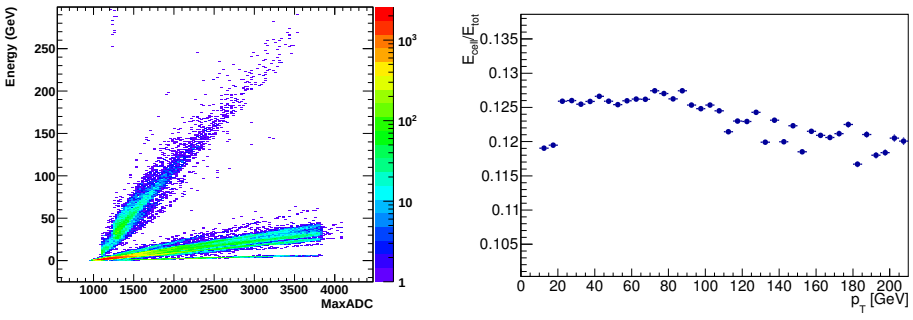

(a) (b)

Figure 4.11: Dependence of the variable MaxADC (a) and E_{cell}/E_{tot} variables with the photon energy or transverse momentum.

Chapter 5

The calibration of the electron and photon energy

In this chapter, the energy response calibration of the electrons and photons is reviewed. Their reconstruction and identification is first described below.

5.1 Electron and photon energy reconstruction

5.1.1 Clustering algorithm

The electrons and photons are reconstructed from a cluster algorithm referred to as the sliding window.

The sliding window algorithm starts by defining a fixed size square window, that moves along a $\Delta\eta \times \Delta\phi$ grid in the electromagnetic calorimeter up to $|\eta| = 2.5$, with a cell size of 0.025×0.025 and a depth corresponding to the three layers of the calorimeter [145]. This fixed size window is optimized to obtain the best efficiency in finding the clusters and highest rejection of fake clusters arising from noise. It corresponds to $\Delta\eta \times \Delta\phi = 5 \times 5$ in cell units. The position of this window is optimized so that it contains the local maximal transverse energy. If this local maximum is above a given threshold ($E_{T,threshold} = 3$ GeV), a pre-cluster is formed.

The pre-cluster is used to find the final electromagnetic cluster. The size of the final cluster depends on the particle type (electron, converted or unconverted photon) and on the detector region: indeed, it should contain most of the energy of the particle to avoid large lateral leakage, while keeping a small size in order to reduce the noise. The magnetic field, for example, curves electron trajectories azimuthally, so that a larger cluster size is necessary in this plane. In the endcap, this field being less pronounced, the size of the cluster can be reduced. The physical cell size in the detector should also be taken into account: in the endcap, for example, this size is smaller than in the barrel along the pseudorapidity direction, so that the number of cells in the cluster should be larger to compensate.

Table 5.1 gives the size in $\Delta\eta \times \Delta\phi$ of the final cluster depending on the particle type and on the detector region in cell units.

The sum of the individual cell energies in a cluster is used to reconstruct the energy of the electromagnetic particle. At this step no calibration is done to recover energy loss laterally or in dead material before the calorimeter. This is the topic of Section 5.2.

Table 5.1: Electromagnetic cluster size for the sliding window method as a function of the particle type and detector region, in units of cells of size $\Delta\eta \times \Delta\phi = 0.025 \times 0.025$.

	Barrel	endcap
Electron	3×7	5×5
Converted photon	3×7	5×5
Unconverted photon	3×5	5×5

5.1.2 Electron and Photon Reconstruction

A cluster is reconstructed as an electron if a track with $p_T > 0.5$ GeV is associated to it. The association requires that the extrapolation of the track up to the calorimeter middle layer is close to the cluster longitudinal barycentre. In case no track matches the cluster, the event is categorized as an unconverted photon. The cluster is reconstructed as a converted photon if a conversion vertex with a radius lower than 800 mm is associated to it. If such a vertex is found, the event is sub-categorized as a single or double track converted photon if one or two tracks are associated to the cluster.

For a transverse energy above 20 GeV, the efficiency of this algorithm is good: only 0.1% (0.9%) of the photons (electrons) are not reconstructed at all and only 2.1% of the photons or electrons are mistakenly reconstructed as electrons or photons respectively [146]. The reconstruction of the electrons has been improved in 2012 with respect to 2011 by using Gaussian Sum Filter methods, which better reconstruct the tracks of the charged particle, in particular in case of conversion and bremsstrahlung [147].

Figure 5.1 shows the electron reconstruction efficiency in the data collected in 2011 (4.7 fb^{-1}) and 2012 (0.8 fb^{-1}) and in the simulation, as a function of the electron transverse energy and pseudorapidity.

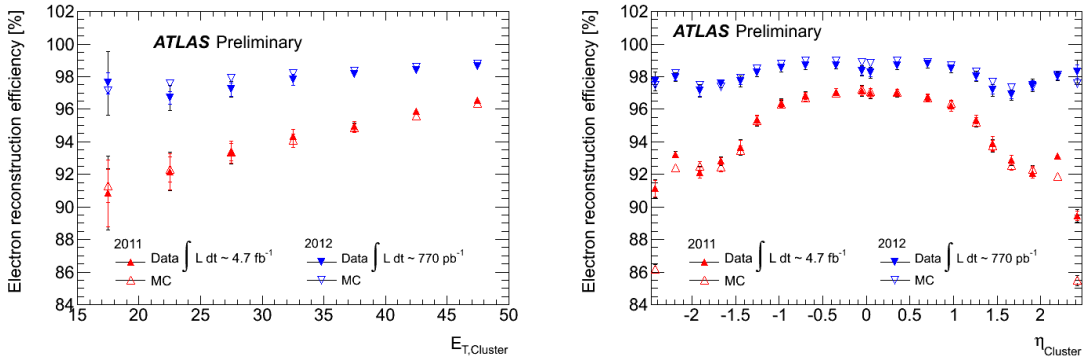

(a) vs E_T (b) vs η

Figure 5.1: Electron reconstruction efficiency in the data collected in 2011 (red) and 2012 (blue) and in the simulation, as a function of the electron transverse energy (a) and pseudorapidity (b). Taken from [148].

5.1.3 Electron and Photon Identification

The identification algorithms allow to discriminate prompt electron and photon events from background. The main background for the photon is the neutral pion decay into two photons

and the main ones for the electron are the QCD jets, the heavy flavour decays leading to non-isolated electrons, and electrons from photon conversion. The discrimination is achieved using information from the calorimeter, the tracker, and also from the quality of the combination of these two quantities. For the calorimeter, a set of rectangular cuts on shower shape variables that are efficient in rejecting events mimicking the electron and photon responses is used.

Three (two) references sets of cuts are designed for the electrons (photons), loose, medium and tight (loose and tight):

- The loose selection has a common set of cuts for the electrons and the photons. This menu is based mainly on the information on the middle layer, on the hadronic leakage and on the energy reconstructed in the hadronic calorimeter. In addition, for the electrons, a track should be matched to the cluster with a loose quality. For the photon, a requirement on the energy in the strip layer is made to reject the π^0.

- In the electron medium menu, a requirement is made on the energy deposited in the strip layer, as well as on the quality of the track and on the track-cluster matching.

- Finally, the tight menu for electrons is used to further reject the background: the quality cuts on the track-cluster matching are tightened and a cut on the impact parameter is done. To reject more specifically the charged hadrons the ratio of the energy measured in the cluster over the one measured in the tracker E/p and the fraction of tight threshold hits in the TRT are used. The photon conversions are rejected by asking at least one hit in the pixel layer and by removing candidates that match a conversion vertex. The tight menu for photons uses the same variables as defined for the loose one, with tighter cuts. In addition cuts on middle and strips layer variables are made.

Table 5.2 summarizes the different variables and cuts used for the different identification selections for the electrons and photons.

The cuts are optimized in bins of p_T and η. Variables like the fraction of energy that leaks in the hadronic calorimeter are very sensitive to pileup effects. In order to have a pileup-independent identification the cuts on these variables are relaxed and the cuts on pileup insensitive variables are tightened (for example the variables related to energy in the strips). This improvement has been achieved in 2012. Figure 5.2 shows the evolution of the identification efficiency for electrons as a function of the number of reconstructed primary vertices for the 2011 and 2012 identifications.

The photon identification efficiency was measured in 2011 with 4.9 fb^{-1} [149]. For the tight criteria it is typically 85 % at low transverse momentum and reaches a plateau of 95% at around $E_T = 100$ GeV.

5.1.4 Electron and Photon Energy Calibration

The calibration of the photon and electron energies starts with an electronic calibration, done at the cell level, which was described in Section 3.2.2.5. This calibration converts the observed signal in ADC counts to a measured energy in GeV.

A calibration based on the clusters is made in a second step with the use of single electron simulation samples. This step allows to correct separately the electrons, converted and unconverted photon energies for energy losses in material upstream of the calorimeter or out of the fixed-size cluster. This calibration relies on the actual knowledge of the material and geometry of the ATLAS detector, and on the interaction of the particles with material, through the GEANT 4 simulation [150].

Table 5.2: Definition of variables used for all electron and photon identification cuts. Taken from [146].

Type	Description	Name
Loose electron and photon cuts		
Acceptance of the detector	$\|\eta\| < 2.47$ for electrons, $\|\eta\| < 2.37$ for photons ($1.37 < \|\eta\| < 1.52$ excluded)	-
Hadronic leakage	Ratio of E_T in the 1st sampling of the hadronic calorimeter to E_T of the EM cluster (used over the range $\|\eta\| < 0.8$ and $\|\eta\| > 1.37$)	R_{had1}
	Ratio of E_T in the hadronic calorimeter to E_T of the EM cluster (used over the range $\|\eta\| > 0.8$ and $\|\eta\| < 1.37$)	R_{had}
Middle layer of the EM calorimeter	Ratio in η of cell energies in 3×7 versus 7×7 cells.	R_η
	Lateral width of the shower	w_2
Medium electron cuts (in addition to the loose cuts)		
Strip layer of the EM calorimeter	Total lateral shower width (20 strips)	w_{stot}
	Ratio of the energy difference between the largest and second largest energy deposits over the sum of these energies	E_{ratio}
Track quality	Number of hits in the pixel detector (at least one)	-
	Number of hits in the pixels and SCT (at least seven)	-
	Transverse impact parameter (<5 mm)	d_0
Track matching	$\Delta\eta$ between the cluster and the track in the strip layer of the EM calorimeter	$\Delta\eta_1$
Tight electron cuts (in addition to the medium electron cuts)		
B-layer	Number of hits in the B-layer (at least one)	
Track matching	$\Delta\phi$ between the cluster and the track in the middle layer of the EM calorimeter	$\Delta\phi_2$
	Ratio of the cluster energy to the track momentum	E/p
TRT	Total number of hits in the TRT (used over the acceptance of the TRT, $\|\eta\| < 2.0$)	-
	Ratio of the number of high-threshold hits to the total number of TRT hits (used over the acceptance of the TRT, $\|\eta\| < 2.0$)	-
Tight photon cuts (in addition to the loose cuts, applied with stricter thresholds)		
Middle layer of the EM calorimeter	Ratio in ϕ of cell energies in 3×3 and 3×7 cells	R_ϕ
Strip layer of the EM calorimeter	Shower width for three strips around maximum strip	w_{s3}
	Total lateral shower width	w_{stot}
	Fraction of energy outside core of three central strips but within seven strips	F_{side}
	Difference between the energy of the strip with the second largest energy deposit and the energy of the strip with the smallest energy deposit between the two leading strips	ΔE
	Ratio of the energy difference associated with the largest and second largest energy deposits over the sum of these energies	E_{ratio}

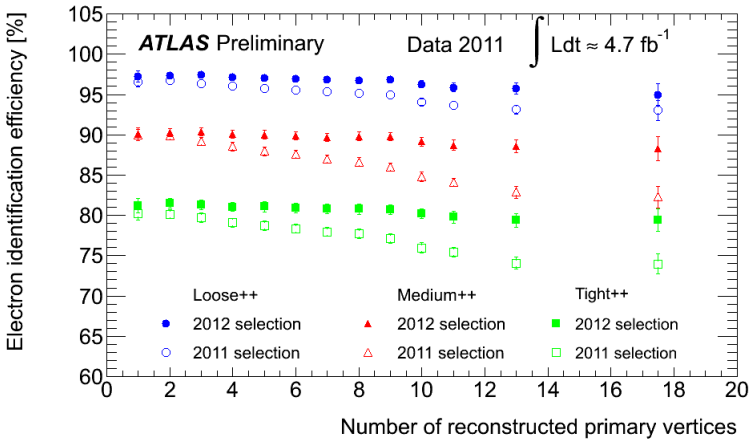

Figure 5.2: Evolution of the identification efficiency for electrons as a function of the number of reconstructed primary vertices for the 2011 and 2012 identification optimizations, using data collected in 2011 [148].

Finally, a *in situ* calibration is performed, coming from the comparison of the $Z \rightarrow ee$ invariant mass peak position in the data and the simulation. This last step allows to correct for unexpected features in the data like non-uniformities or material mismodeling .

The second and third steps are further detailed below.

5.2 The cluster-based energy calibration using MCs

5.2.1 Method

The total energy of a single particle, can be divided in four contributions [151]: the energy deposited in the calorimeter (E_{calo}) which can be inside or outside the cluster (lateral leakage), behind the calorimeter (longitudinal leakage, E_{behind}), or in dead material in front of the calorimeter (E_{front}) like in the inner detector, the cryostat, the coils or the material between the presampler and the strips.

The total energy is written [152] :

$$E_{tot} = [E_{front} + E_{calo} + E_{behind}] \cdot F(\eta, \phi)$$

where $F(\eta, \phi)$ is a correction factor for the energy modulation depending on the impact point of the particle in the cell [153].

The total energy deposited in the accordion calorimeter is written as:

$$E_{calo} = f_{calo}(\eta, X) \cdot (1 + f_{out}(\eta, X)) \sum_{i=1,3} E_i$$

where

- E_i corresponds to the energy deposited only in the active medium (LAr) in the layer i, with i = 1,2,3 for the strip, middle and back respectively.
- X is the shower depth, i.e the longitudinal barycentre of the shower, expressed as:

$$X = \frac{\sum_{i=1,3} E_i \cdot X_i}{\sum_{i=1,3} E_i \cdot}$$

where X_i is the depth in radiation length of each layer, from the interaction point. These depths depend on η, see Figure 5.3.

- f_{calo} is a correction factor to the accordion sampling fraction in the cluster, depending on X and η. The sampling fraction corresponds to the ratio of the energy deposited in the active (LAr) to the inactive (lead) mediums. Its typical value is around 0.2.
- f_{out} is a correction parameter, depending on X and η, for the energy loss outside the cluster.

The energy loss in dead material in front of the calorimeter is expressed as:

$$\begin{cases} E_{front} = a(E_{calo},\eta) + b(E_{calo},\eta)\cdot E_{PS} + c(E_{calo},\eta)\cdot E_{PS}^2 & \eta < 1.8 \\ E_{front} = a(E_{calo},\eta) + b(E_{calo},\eta)\cdot X + c(E_{calo},\eta)\cdot X^2 & \eta > 1.8 \end{cases}$$

where

- E_{PS} is the energy deposited in the presampler
- a, b and c are parameters which depend on E^{calo} and η; they parametrize the dependence of the front energy on the presampler energy when it is present or with the shower depth otherwise. An attempt to parametrize this energy loss in the region without presampler with the front energy was made [152] but it did not show better performance than the use of the shower depth.

Finally, the energy deposited behind the calorimeter is written as:

$$E_{behind} = E_{calo}\cdot f_{leak}(\eta, X)$$

where f_{leak} is a correction parameter, depending on X and η, for the energy loss longitudinally.

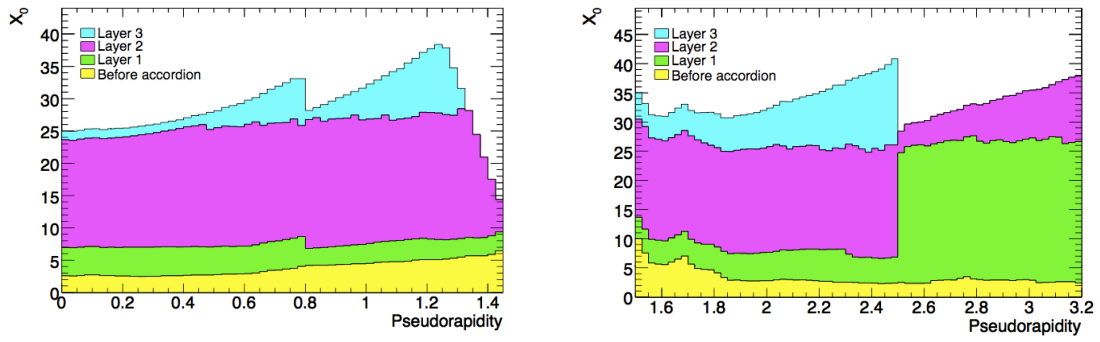

(a) (b)

Figure 5.3: Depth in radiation length of each layer, from the interaction point as a function of the probe pseudorapidity in the barrel (a) and the endcap (b). Taken from [110].

An azimuthal symmetry and a positive/negative symmetry in pseudorapidity are assumed in this procedure. The range of energy and pseudorapidity considered are: $10 < E < 1000$ GeV for $0 < |\eta| < 1.425$ and $25 < E < 1000$ GeV for $1.55 < |\eta| < 2.5$. No coefficients are available in the region between the two cryostats: $1.425 < |\eta| < 1.55$. All the factors are derived separately for the three kinds of particles (electrons, converted and unconverted photons).

5.2.2 Performance

The energy resolution is expressed as:

$$\frac{\sigma_E}{E} = \frac{a}{\sqrt{E}} \oplus \frac{b}{E} \oplus c \tag{5.1}$$

where E is the energy, a the stochastic (or sampling) term, b the noise term, and c the constant term and where $\oplus$ corresponds to the quadratic sum.

Figure 5.4 shows the resolution measured in the single particles simulations for electrons, converted (CV) and unconverted (UC) photons as a function of the pseudorapidity of the particles and for different particles energies. The worsening of the relative resolution for electrons and converted photons with respect to unconverted photons especially at low energy is due to bremsstrahlung effects and to the bending of the trajectories in the ϕ direction. The deterioration of the relative resolution in the region $1.5 < |\eta| < 1.8$ is due to a rapid increase of the material budget in this region.

From dedicated studies, the main contribution to the resolution for electrons and converted photons appears to come from the energy lost in front of the calorimeter, whereas for unconverted photons it appears to come from the sampling fraction [154].
For unconverted photons, the constant term is around 0.4% almost everywhere except in the region between $1.5 < |\eta| < 1.8$ where it increases up to roughly 1%. For converted photons, the constant term is around 0.6%, and for electrons, the constant term is below 0.4% expect in the region $1.5 < |\eta| < 1.8$ where it increases up to 1.3%.

The comparison of the reconstructed energy, after the calibration described above is applied to the generated ones in MC samples, $\frac{E_{reco}}{E_{true}}$, is shown in Figure 5.4 for the three types of particles as a function of the pseudorapidity and for different energies. A good calibration of the energy is achieved, inside $\sim \pm 0.5\%$ for electrons and unconverted photons almost everywhere. The performance is worst for converted photons at low energy. The same conclusion as draw previously arises here: the performance is better for large particle energy, for unconverted photons and outside the region $1.5 < |\eta| < 1.8$.

5.2.3 Transition Region

The region $1.425 < |\eta| < 1.55$ corresponds to the transition region between the barrel and endcap calorimeters. This region is not used in the $H \to \gamma\gamma$ analysis, as the performance of the photon reconstruction, identification and calibration is very poor there. It is however described below, for completeness.

The energy in this region is reconstructed differently by using both the energy collected in the scintillators present in the gaps E_{scint} and in the cluster E_{cl}. The energy calibration is not covered by the above procedure; a different method called the Longitudinal Weights Method [154] is used. The total energy is written as the weighted sum of the energies in these two detectors:

$$E_{tot} = \lambda(\alpha + E_{cl} + \beta E_{scint})$$

where λ, α, and β are parameters determined by a χ^2 fit minimizing the ratio $\frac{(E_{tot}-E_{true})^2}{\sigma^2}$ with σ the expected uncertainty on the reconstructed energy.

The performance in the transition region is much worse than the one obtained in other regions of the calorimeter, with a constant term of approximately 4% [156].

An improvement of the performance has been achieved, using a slightly different method. The transition region is defined as $1.425 \leq |\eta| \leq 1.55$ with η defined in the ATLAS frame

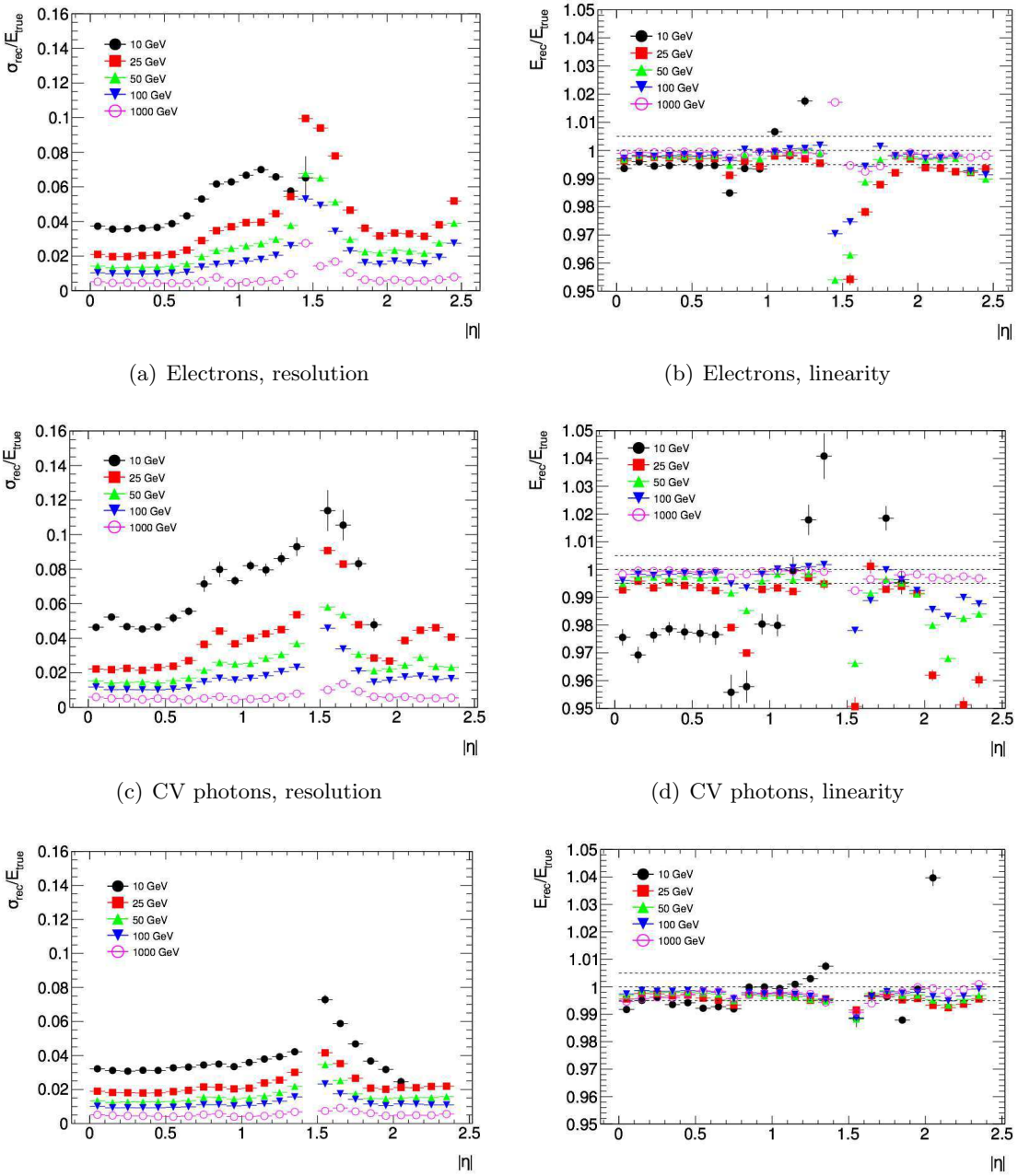

(a) Electrons, resolution

(b) Electrons, linearity

(c) CV photons, resolution

(d) CV photons, linearity

(e) UC photons, resolution

(f) UC photons, linearity

Figure 5.4: Resolution and linearity performance of the MC-based calibration, for the electron (a,b), converted (c,d) and unconverted photons (e,f) using single particles simulations, as a function of the pseudorapidity probe and for different particles energies. Taken from [155].

(which is defined with respect to the nominal vertex (0,0,0)) and calibrated with the longitudinal weights as defined above. The rest of the detector is calibrated with the method described in Section 5.2.1, but using the calorimeter frame to define the pseudorapidity. The pseudorapidity is computed in the second sampling of the accordion: $\eta = \eta_{s2}$. In the transition region, η_{s2} cannot be used because it is not well defined due to the small number of middle cells, whereas outside this region, this definition gives the best accuracy.

This difference of frame definition for the pseudorapidity definition leads to small inconsistencies near to the boundaries, when small misalignments between the different detectors occur. The consequence is that a small fraction of the clusters are calibrated by none of the two methods, resulting in uncalibrated energies (called "raw" energies).

Changing the frame for one of the two calibrations in order to match the pseudorapidity definition would worsen the energy response, due to reason evoked above. It is found better to stay with this small inconsistency.

In the transition region, along the azimuthal direction, 16 scintillators cells have been removed to facilitate the routing of cables. This creates a non-uniformity of the energy response in ϕ. A modified calibration is designed, where the regions with and without scintillator cells are optimized separately. In addition, the calibration is run in the extended region $1.4 < |\eta| < 1.6$, to avoid boundary problems as the ones mentioned above. This new calibration improves the energy linearity by a few percent and the resolution by 10% to 30 % [157].

This calibration is extrapolated to photons (using the same weights). This leads to a slight improvement of the energy linearity and resolution, even if the energy tends to be over-estimated.

Figure 5.5 shows the invariant mass distribution of $Z \rightarrow ee$ events, with the nominal and improved transition region calibration. The resolution of the distribution is improved by 40% and the peak position is increased by 3%, getting closer to the expected Z boson mass.

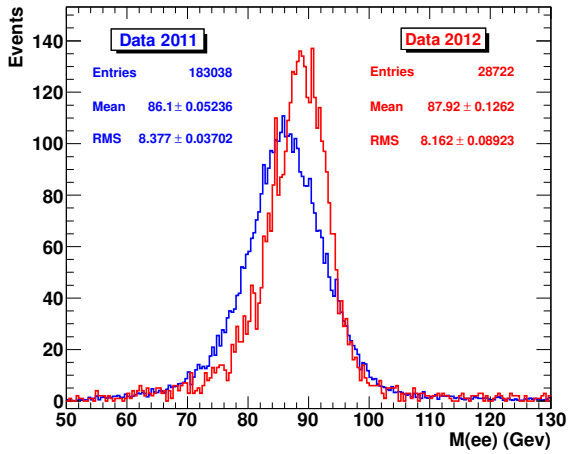

Figure 5.5: Invariant mass distribution for $Z \rightarrow ee$ events with at least one electron in the transition region $1.37 < |\eta| < 1.52$, selected in the data collected in 2011 and reconstructed with the nominal transition region calibration scheme (blue) and collected in 2012 and reconstructed with the the improved calibration scheme (red). The two histograms are normalized to the same number of events. The means and rms values of the distributions in the range [50,130] GeV are given for indication.

5.3 The *in situ* energy calibration

The last step of the energy reconstruction and calibration is the comparison of the position of the $Z \rightarrow ee$ invariant mass peak between the data and the simulation after the MC-based calibration is applied.

5.3.1 Samples and Event Selection

The simulation of this process is done using two generators: PYTHIA 6 [158] mainly in 2010 and 2011 or PYTHIA 8 [159] associated to POWHEG that allows to implement NLO calculations [160] with the tune AU2CT10 (mainly in 2012).

Then the events generated are submitted to a full simulation of the ATLAS detector with the GEANT4 program.

The data used corresponds to the full dataset collected in 2011 with $\sqrt{s} = 7$ TeV corresponding to 4.9 fb^{-1}, as well as the dataset collected in 2012 with $\sqrt{s} = 8$ TeV (20.7 fb^{-1}).

The selection of this process for the data and the simulation is similar:

- the event should be selected by specific triggers, requiring one electron with a medium identification criteria, and with transverse momentum larger than at least 20 GeV and up to 45 GeV. A veto in the energy deposited on the hadronic calorimeter can be also done, usually it should be lower than 1 GeV [161]. The trigger used to make the selection changes with the time, becoming more stringent when the peak luminosity increases.
- The electrons should be reconstructed in the detector acceptance, i.e. $|\eta| < 2.47$
- Exactly two electron candidates with opposite charge reconstructed in the fiducial region of the calorimeter are required.
- The transverse momentum of the electrons should be larger than 27 GeV.
- The "medium" level of identification selection cuts is used for the two electrons.
- Only the events entering in the window $80 < m_{ee} < 100$ GeV are selected.
- Finally a cut on the position of the primary vertex is done: $|z_0| < 150$ mm.

The MC is in addition corrected for various imperfect simulations of the data:

- The efficiency of the trigger, electron identification and reconstruction are corrected to match the ones in data.
- The width of the z distribution of the primary vertices simulated in the MC does not correspond to the one actually observed in data (7.5 cm vs 5.6 cm in 2011 and 6.6 cm vs 4.8 cm in 2012). The events are reweighted in order to better simulate the data.
- The distribution of the average number of interactions per bunch crossing μ in the simulation does not corresponds to the one observed in data. The events are reweighted in order to better simulate the data.
- The Z boson transverse momentum is not well simulated in the MC used in 2011. This MC is based on the PYTHIA generator with modifications with respect to the 2010 version. The 2011 version fails in simulating the Z p_T so that a correction is made to recover the one simulated in the 2010 PYTHIA version. The 2012 MC which is based on the generator POWHEG+PYTHIA simulates this variable well, and no correction is made for this MC.

5.3.2 Background

The main backgrounds for the $Z \to ee$ process are of two types [162]:

- The QCD background that consists in jet events, where the jets are misidentified as electrons. It gives an uniform dielectron invariant mass falling with the increasing of the mass. This background is extracted with data-driven methods described in references [162, 163]. A small fraction of such background enters in the $Z \to ee$ invariant mass distribution (around 1%).

- The electroweak background corresponds to real electrons in the final states, for example coming from W, top, τ, or diboson's (WW, WZ, ZZ) electronic decays. It is simulated with MC samples, and extracted with two Gaussian functions having a common mean. There is very small fraction of such events in the $Z \to ee$ selection (around 0.1%).

5.3.3 Method

Two methods to extract the comparison between the data and the simulation for the peak position of the dielectron invariant mass for the $Z \to ee$ process are designed: the lineshape or template method. Both methods assume a good uniformity in the azimuthal direction, and make the comparison only as a function of pseudorapidity in a small numbers of bin:

$$0, 0.2, 0.4, 0.6, 0.8, 1.0, 1.2, 1.37, 1.47, 1.55, 1.63, 1.74, 1.82, 2.0, 2.1, 2.3, 2.4, 2.47$$

The binning is dictated by the non-uniformities observed in the data (see Section 5.4) and by hardware and high-voltage structures of the calorimeter. It also follows the boundaries of the transition region. In addition, the measurement of the angle between the two electrons $\theta_{1,2}$ is assumed to be perfectly modeled.

The lineshape method is described here, see references [164, 165] for a description of the template method.

The energy of the electrons measured in the data is assumed to have a small bias α_i with respect to the true energy of the electrons generated in the simulation:

$$E^{meas} = E^{true}(1 + \alpha_i)$$

assuming the electron being in a η bin i.

The measured invariant mass:

$$m_{ee}^{meas} = \sqrt{2E_1^{meas}E_2^{meas}(1 - \cos\theta_{1,2})} \tag{5.2}$$

is rewritten as:

$$m_{ee}^{meas} \sim m_{ee}^{true}\left(1 + \frac{\alpha_i + \alpha_j}{2}\right)$$

when neglecting second order terms.

An unbinned likelihood is built:

$$-L_{tot} = \sum_{k=1}^{N_{i,j}} -L_{i,j}\left(\frac{m_k^{meas}}{1 + \frac{\alpha_i+\alpha_j}{2}}\right)$$

with $N_{i,j}$ the number of events selected in the regions i, j and $L_{i,j}$ the probability density function (pdf) quantifying the compatibility of an event with the Z lineshape [166]. The pdfs

come from simulated samples in the mass range [70,110] GeV, which are expected to contain all known theoretical and experimental effects.

The minimization of the likelihood L_{tot} leads to the determination of $\alpha_i + \alpha_j$. Repeating this procedure in all the regions i and j yields an unique determination of the scale factors in each bin.

A small non-closure of the method arises from the different mass ranges for the pdf determination and the fit. A correction is provided for this effect.

5.3.4 Results

For the 2011 dataset, the data energy scale factor extracted with the two methods as a function of η are compared in Figure 5.6(a). A good agreement is found everywhere except in the transition region. The results for the 2011 and 2012 datasets obtained with the template method are compared in Figure 5.6(b). Sizeable differences are observed between the two years, arising from various sources like a modified electronic calibration, a new electron reconstruction, or changes in the calorimeter cells high voltage settings.

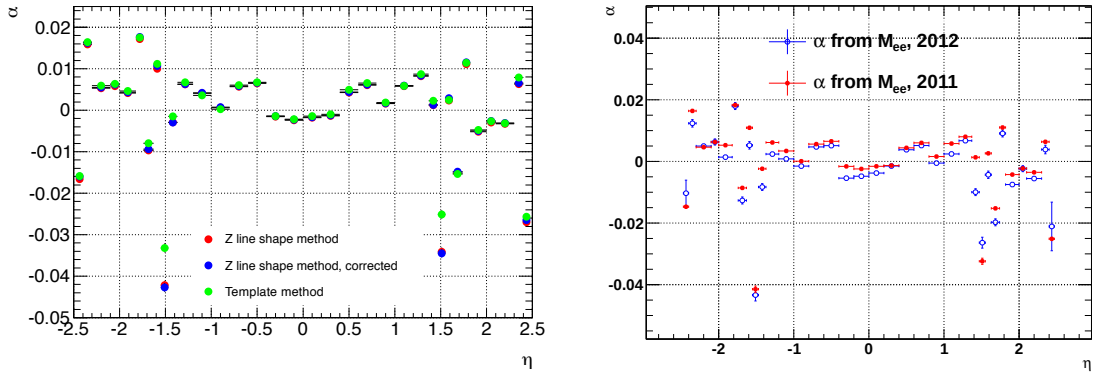

(a) Methods comparison

(b) Datasets comparison

Figure 5.6: Comparison of the energy calibration scale factor as a function of η between the two methods (with and without corrections for the lineshape method) [157] (a) and between the two datasets collected in 2011 and 2012 (b).

Only statistical errors are indicated in these figures, the systematic ones are discussed below.

5.3.5 Systematic uncertainties

The uncertainty on the energy scale for the data come from various theoretical and experimental sources. The evaluation of these uncertainties is described in references [156] and [157].

5.3.5.1 Theoretical uncertainties

- The simulation of the Z lineshape in the MC relies on various theoretical aspects like the relativistic Breit Wigner model for the Z decay, the interference with the Drell-Yan process $\gamma^* \rightarrow ee$, the parton distribution function, and the final state radiation (FSR). All these aspects are not modeled in the same way in the different generators programs. This uncertainty is thus taken as the difference between two typical generators: Pythia 8 and Powheg. This results in an uncertainty of 2.1×10^{-4} independent of η.

- The Z transverse momentum model can also affect the computation of the energy scale. The uncertainty coming from this modeling is computed by switching on/off the correction made in the MC to better match the data. This leads to an uncertainty of 0.9×10^{-4}.

5.3.5.2 Experimental uncertainties

There are two kinds of experimental uncertainties: ones are related to the analysis and the other to the extrapolation of the energy scale to other kinematic ranges and to photons.

Uncertainty related to the analysis

- The use of the medium identification to select the electron leads to a small bias in the extraction of the energy scale. This bias is estimated by using tighter identification cuts, leading to a difference of 0.8×10^{-4} with respect to the standard case.

- The uncertainty on the identification and reconstruction efficiencies is propagated to the uncertainty on the energy scale by varying within one standard deviation these efficiencies and recomputing the scale factors. A η-dependent uncertainty is found varying from 0.04×10^{-4} (0.03×10^{-4}) in the central region and up to 1.4×10^{-4} (1.4×10^{-4}) in some regions like the barrel-endcap transition for the identification (reconstruction). The trigger efficiency is close to 100% and the related uncertainty is then neglected.

- The uncertainty on the background is evaluated by changing its normalization by $\pm$ 10% for the EW component and $\pm$ 40% for the QCD one. This gives a η-dependent uncertainty on the energy scale going from 0.001×10^{-4} (0.002×10^{-4}) in the central region up to 5.5×10^{-4} (4.6×10^{-4}) in the transition regions for the EW (QCD) background.

- The effects of the corrections applied to the MC is estimated by switching on/off these corrections. For the pile-up reweighting this leads to an uncertainty of 0.4×10^{-4}. The z vertex reweighting is supposed to be sufficiently well known not to give an uncertainty on the scale extraction.

- The uncertainty on the methods used to extract the energy scales is evaluated by varying the mass window in which they are extracted, and by comparing the results of the two methods. This gives respectively the uncertainty on the scale factors of 1.1×10^{-4} and 2.7×10^{-4}

Uncertainty on the extrapolation to photons and to different p_T regimes The energy calibration scale factors are extracted using the $Z \to ee$ lineshape and used for a large energy range and for electrons, converted and unconverted photons. Other methods dedicated to lower energies or to photons exist, but they are not yet ready. For the low energy electrons, a method is investigated to extract the calibration coefficients using the J/Ψ decay into two electrons and using a similar procedure as the one described in Section 5.3.3 [156, 166]. This method encounters some difficulties due to the poor electron reconstruction performance at low energy. For the photons, a method could allow to extract their calibration scale factors using the $Z \to ee\gamma$ or $Z \to \mu\mu\gamma$ radiative processes. In this method, the scale factors obtained with the procedure described in Section 5.3.3 are applied to the electrons and photons energies coming from these decays. Then a template fit is used to extract the best scale factor α_γ that provides the best agreement between the MC and the data distributions [157]. This method currently suffers from low statistics.

Applying the scale factors obtained with the standard method to different energy ranges or to photons could lead to a bias. This bias is estimated below.

5.3.5.3 The energy scale uncertainty for different p_T regimes

The different sources of systematic uncertainties are given in the following:

- The uncertainty on the linearity of the response of the readout electronics has been estimated to be 0.1% for the high and medium cell gains [167]. This number is taken as an uncertainty for the energy scale systematic uncertainty extrapolation to different p_T regimes.

- The comparison between the scale factors extracted with low p_T electrons from the J/Ψ decay agrees within 1% with the ones extracted from the Z decay: an uncertainty of $\pm 1\%$ is added for electrons with $p_T = 10$ GeV and a linearly decreasing uncertainty is added for larger energies, until reaching $p_T = 20$ GeV where the systematic uncertainty is taken as null [156].

- The impact of a material mismodeling varies with the electron energy: low energy electrons loss relatively more energy in material than high energy electrons. This will then induce a bias when extrapolating the standard scale factors to different electron energies. This bias is estimated in three steps:

  1. The scale factors α_{mat} arising from the comparison between the energy response in a nominal MC simulation and in a MC with a distorted geometry with additional material in the Inner Detector and in the calorimeter (see also Table 5.6, configuration G') are first extracted. The configuration G' represents the current uncertainty on the material budget in data, even if further studies (see Chapter 6) will show that this uncertainty is much smaller. The distorted geometry is used as pseudo-data and the scale factors α_{mat} are extracted following the procedure presented in Section 5.3.3. Figure 5.7(a) shows these scale factors as a function of η.
  2. Then the electron energies in the distorted MC are corrected with these scale factors α_{mat}.
  3. Finally, the ratio E_{reco}/E_{true} for the nominal and distorted MC are compared along p_T. By construction, the two ratios agree well for p_T around 40 GeV (the average electron p_T for the $Z \to ee$ decay) but disagree when going to different p_T ranges. The discrepancies are taken as an uncertainty (see Table 5.3 and Figure 5.8).

- An uncertainty of $\pm 5\%$ ($\pm 10\%$) in the barrel (endcap) on the presampler energy scale has been extracted from the comparison of the energy deposited in this layer in data and MC [156]. A more precise measurement of the presampler energy scale is proposed in Section 5.7.1. The fraction of energy deposited in the presampler for the same material configuration varies with the electron energy: it is relatively larger for lower energies. Similarly as in the previous item, this induces a bias on the extrapolation which is evaluated in three steps:

  1. The scale factors α_{PS} arising from the comparison between the energy response in a nominal MC and in a MC where the presampler energy is biased by 5% in the barrel and 10% in the endcap are first extracted. The biased MC is used as pseudo-data and the scale factors α_{PS} are extracted following the procedure presented in Section 5.3.3. Figure 5.7(b) shows these scale factors as a function of η.

2. Then the electron energies in the biased MC are corrected with these scale factors α_{PS}.
3. Finally, the ratio E_{reco}/E_{true} for the nominal and biased MC are compared as a function of p_T. By construction, the two ratios agree well for p_T around 40 GeV but disagree when going to different p_T ranges. The discrepancies are taken as an uncertainty (see Table 5.3 and Figure 5.8).

- The different accordion layers can have a different energy scale due to longitudinal cross talk and imperfect determination of the electronic calibration. The electronic calibration difference between the middle and third (first) layer has been measured to be 2% (1%) [168]. As the fraction of energy deposited in the different layers depends on the electron energy, this induces a bias on the extrapolation. This bias is estimated using the same three-steps method described above. The back layer contains a tiny fraction of the shower energy, so that the related bias is found to be negligible. For the front layer, the impact on the energy scale is found to be ±0.1% which is taken as an uncertainty. A measurement of the relative layer energy scale is proposed in Section 5.7.2.

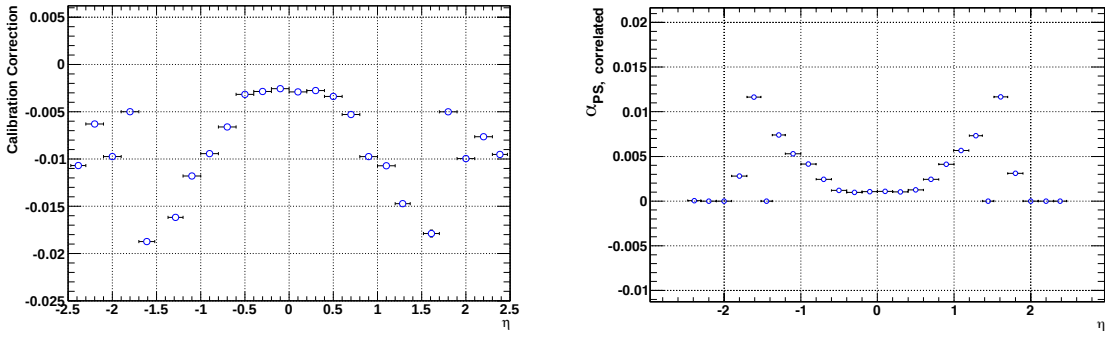

(a) α_{mat} (b) α_{PS}

Figure 5.7: Calibration coefficients resulting from the comparison between a distorted and a nominal MC sample (α_{mat}, (a)), and between a MC where the PS energy scale has been modified and a nominal MC sample (α_{PS}, (b)) for $Z \to ee$ events.

Table 5.3 summarizes all the uncertainties on the electron energy scale, and Figure 5.8 illustrates the evolution of these uncertainties as a function of p_T and η.

5.3.5.4 The energy scale uncertainty for photons

Until a sizeable sample of $Z\gamma$ events is available, especially at a high photon p_T, the photon energy scale must rely on the energy scale measured from electrons, with dedicated systematics estimated from Monte-Carlo.

Most of the energy scale uncertainties derived for electrons are identical for photons. This is the case for the theoretical and experimental uncertainties related to the analysis.

In addition, the systematic from the front energy scale is taken as similar for electrons and photons, due to its small contribution.

All these uncertainties are quadratically summed and somewhat misleadingly called "Uncertainties from the method" in the following.

Table 5.3: Summary of uncertainty on electron energy scale in %, taken from ATL-COM-PHYS-2011-263.

Statistical	η-dependent from $2.6 \cdot 10^{-4}$ to $8.4 \cdot 10^{-4}$
Background EW	η-dependent from $0.001 \cdot 10^{-4}$ to $5.5 \cdot 10^{-4}$
Background QCD	η-dependent from $0.002 \cdot 10^{-4}$ to $4.6 \cdot 10^{-4}$
$\epsilon(ID)$	η-dependent from $0.04 \cdot 10^{-4}$ to $1.4 \cdot 10^{-4}$
$\epsilon(reco)$	η-dependent from $0.03 \cdot 10^{-4}$ to $1.4 \cdot 10^{-4}$
ID	$0.8 \cdot 10^{-4}$
Pile-up	$0.4 \cdot 10^{-4}$
Mass window	$1.1 \cdot 10^{-4}$
Method Comparison	$2.7 \cdot 10^{-4}$
Front energy scale	$\pm 0.1\%$
Electronic non-linearity	$\pm 0.1\%$
Presampler energy scale	p_T-dependent, from -1% to $+1\%$ for $\eta < 1.8$
Extra-material	p_T-dependent, from -1.5% to $+2\%$

The other source of uncertainty, the presampler energy scale or the material mismodeling, are common sources for electrons and photons, but have a different impact on them due to their different interaction with material and their different longitudinal shower shapes.

Impact of material upstream of the calorimeter mismodeling The extrapolation of the scale factor to photons, when the discrepancy between the data and MC energy scale arises from material mismodeling is evaluated here.

A sample simulating the Higgs boson decay to two photons is used as a source of high energy and well identified photons. A second sample simulating the same process, and with a distorted geometry where additional material is added in the inner detector and calorimeter, is also used (symmetrical results are obtained if considering a deficit of material instead).

The following procedure is run:

- The ratio E^{nom}_{reco}/E_{true} and E^{dist}_{reco}/E_{true} are built from the photon sample in the different η bins of the analysis, and separately for converted and unconverted photons, with E^{nom}_{reco} and E^{dist}_{reco} the energy reconstructed in the nominal and distorted MC samples respectively.
- The energy E^{dist}_{reco} is corrected with the scale factors derived in the previous section (see Figure 5.7(a)) and is called $E^{dist'}_{reco}$
- The nominal energy and the distorted one after correction are compared through the variable δ_{MAT}:

$$\delta_{MAT} = \frac{E^{dist'}_{reco}/E_{true}}{E^{nom}_{reco}/E_{true}} - 1$$

The results is shown in Figure 5.9 as a function of the photon pseudorapidity, and of the conversion status. A large dependence on η is observed, coinciding with the material distribution in the detector. The difference is positive, meaning that the scale factors from electrons over-correct the photon energy (which lose less energy upstream of the calorimeter), and is larger for unconverted photons than converted ones. The p_T dependence was checked and found to be small; it is then neglected. These values are taken as an uncertainty on the photon energy scale due to material mismodeling

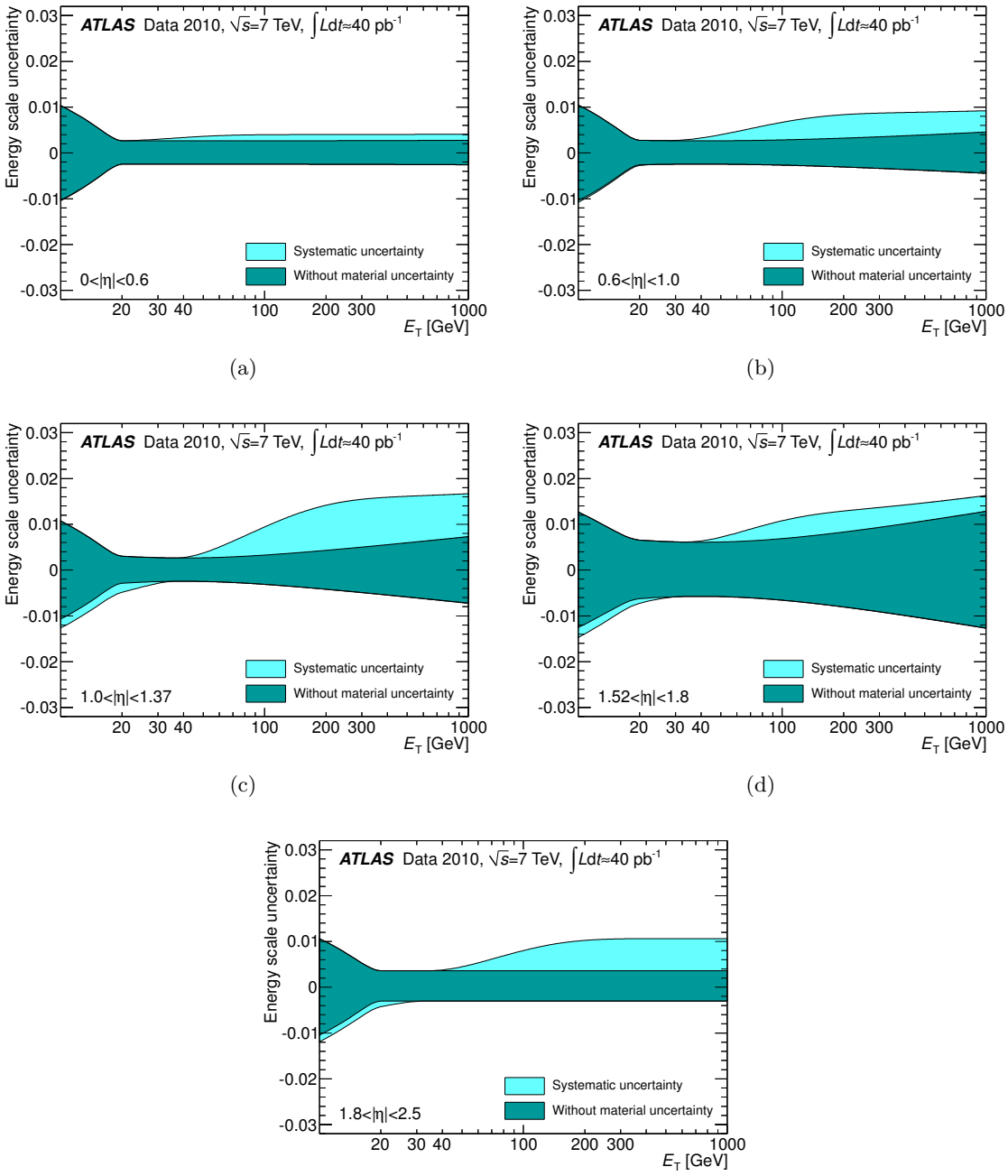

Figure 5.8: Uncertainty on the electron energy scale as a function of the electron transverse momentum, for different bins of pseudorapidity. The contribution from the material is drawn in light blue whereas all the other contributions are drawn in dark blue [166].

Uncertainty from Presampler Energy Scale The extrapolation of the scale factor to photons, when the discrepancy between the data and MC energy scale arises from a +5% (+10%) mismodeling of the presampler scale in barrel (endcap) is evaluated here (symmetrical results are obtained for the opposite sign biases).

The samples and the procedure described in the previous paragraph are used. The distorted

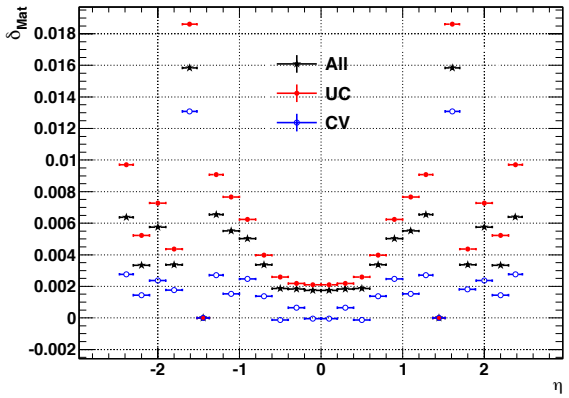

Figure 5.9: Residuals difference between reconstructed nominal energy and reconstructed distorted energy -corrected by the appropriate scale factors-, for converted (CV), unconverted (UC) and both (All) photons as a function of the pseudorapidity.

MC sample with additional material is replaced by a MC where a bias of 5% (10%) of the presampler energy in the barrel (endcap) is injected. The resulting reconstructed energy $E_{reco}^{bias\,PS}$ is corrected with the scale factors α_{PS} defined in Section 5.3.5.2. The residual difference between the nominal energy and this corrected energy can be written as:

$$\delta_{PS} = \frac{E_{reco}^{bias\,PS'}/E_{true}}{E_{reco}^{nom}/E_{true}} - 1$$

The result is shown in Figure 5.7(b) as a function of η.

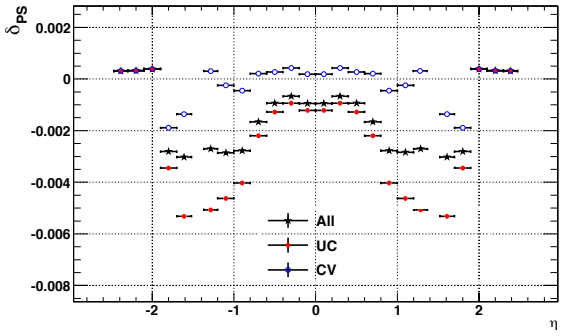

Figure 5.10: Residuals difference between reconstructed nominal energy and reconstructed modified energy (by the change of the presampler energy scale) -corrected by the appropriate scale factors-, for converted, unconverted and both photons, as a function of the pseudorapidity

This difference is negative, meaning that the scale factors from electrons over-correct the photon energy: the photons deposit less energy in the presampler, and the $+5-10\%$ shift gives then smaller biases of their energies. As for the material mismodeling, the difference is larger for unconverted photons than converted ones. A large dependence on the pseudorapidity is observed, resulting from the different biases applied in the barrel and endcap, but also from the material distribution in the detector.

These residual differences are found to be p_T-dependant as seen in Figure 5.11, where an additional binning is p_T is done:

$$[30, 40, 50, 60, 70, 80, 100, 150, \infty] \text{ GeV}$$

The dependence is observed for both converted and unconverted photons.

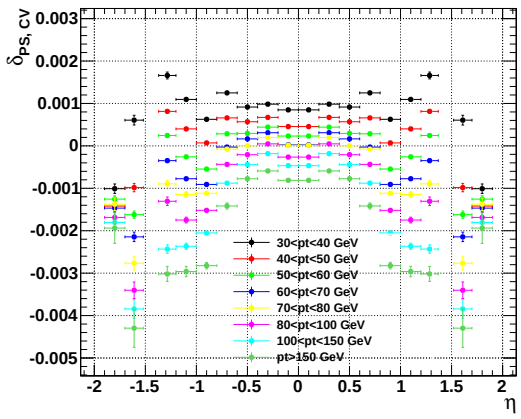

(a) Converted photons

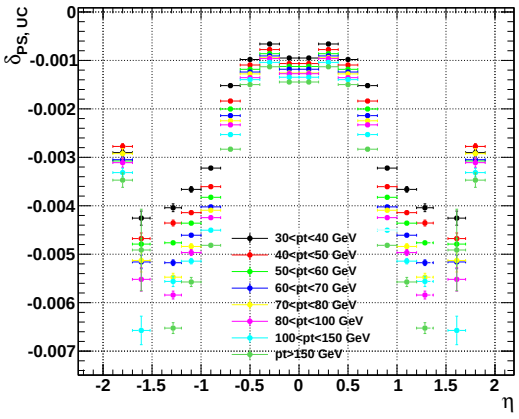

(b) Unconverted photons

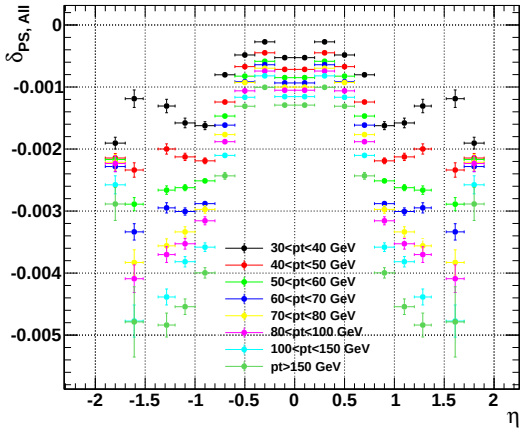

(c) All photons

Figure 5.11: Residuals difference between reconstructed nominal energy and reconstructed modified energy (by the change of the presampler energy scale) -corrected by the appropriate scale factors-, for converted, unconverted and both photons, as a function of the pseudorapidity and for different p_T bins.

However, as one can see, the shapes of the distributions for converted and unconverted photons is very different: for the unconverted case, the difference δ_{PS} is always negative for all the p_T ranges, whereas for the converted photons this is not always the case. For a given η bin, the difference is positive at low p_T and become negative when increasing the transverse momentum. The uncertainty on the photon energy scale due to an uncertainty on the presampler energy scale is then p_T and η dependent.

5.3.6 Resolution extraction

Figure 5.12 shows the $Z \rightarrow ee$ invariant mass distribution for the data and the MC for the inclusive case and separately for the cases where both electrons are in the barrel or in the endcap. The full calibration of the energy is applied resulting in a good agreement of the peak positions. However, the widths of the data distribution are larger than the MC one. More quantitatively, the resolution is extracted with a fit using a relativistic Breit-Wigner convoluted with a Crystal Ball function [169], [170], [171]. The Crystal Ball function corresponds to a Gaussian core up to a certain threshold after which it is replaced by a power-law function for the tails. The parameters of the Breit Wigner are fixed to the PDG values, and the resolution corresponds to the σ of the Crystal Ball. The values are indicated in the figure and show a discrepancy of around 10% (20%) in the barrel (endcap) between the data and MC.

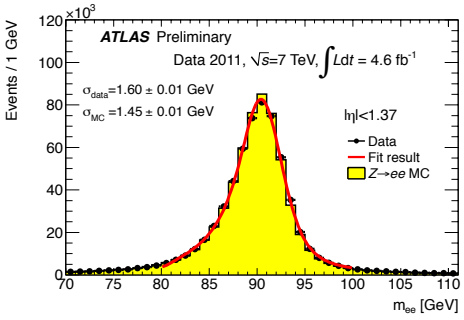

(a) Barrel

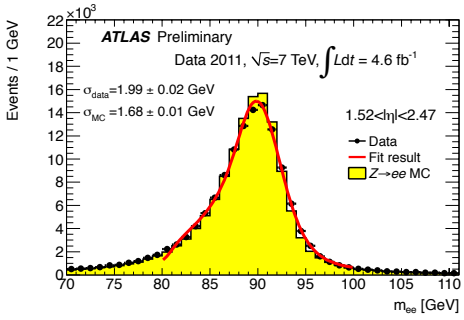

(b) endcap

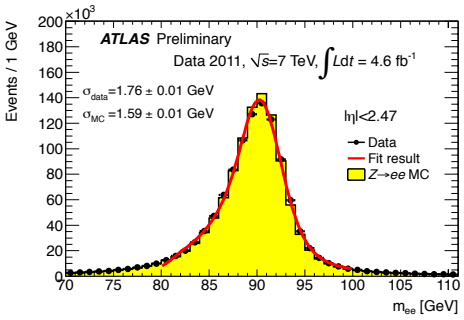

(c) All

Figure 5.12: $Z \rightarrow ee$ invariant mass distribution for the data (black points) and the MC (yellow histogram), separately when both electrons are in the barrel (a) or in the endcap (b) and for the inclusive case (c). The resolution is extracted with a fit using a relativistic Breit-Wigner convoluted with a Crystal Ball shown in red line. The fitted resolutions are indicated in the figures for both data and MC. Taken from [172].

The discrepancy is assumed to come only from different constant terms; the sampling term and noise terms are assumed to be well modeled by the MC (see in Equation 5.1 the expression for the resolution). An additional constant term is thus added to the MC in order to match the resolution observed in the data.

The mass resolution measured in the data for electrons in the regions i and j is approximated

[1] by:

$$\frac{\sigma^{i,j}_{m_{ee}}}{m^{i,j}_{ee}} = \frac{1}{2} \{ \frac{\sigma^{i}_{E}}{E^{i}} \oplus \frac{\sigma^{j}_{E}}{E^{j}} \}$$

This can be rewritten as:

$$\frac{\sigma^{i,j}_{m_{ee}}}{m^{i,j}_{ee}} = \frac{1}{2} \{ ([\frac{\sigma^{i}_{E}}{E^{i}}]_{MC} \oplus c_i) \oplus ([\frac{\sigma^{j}_{E}}{E^{j}}]_{MC} \oplus c_j) \}$$

where c_i and c_j are corrections introduced to the MC resolution. From this one can deduce:

$$c^2_{i,j} = 2 \cdot [(\frac{\sigma^{i,j}_{m^{i,j}_{ee}}}{m_{ee}})^2 - (\frac{\sigma^{i,j}_{m_{ee}}}{m^{i,j}_{ee}})^2_{MC}] \tag{5.3}$$

with

$$c^2_{i,j} = \frac{1}{2}(c^2_i + c^2_j) = (c^2_{i,j})_{data} - (c^2_{i,j})_{MC} \tag{5.4}$$

Two methods exist for the extraction of the additional constant term $c_{i,j}$:

- The subtraction method uses Equations 5.3 and 5.4 and the lineshape method as described in Section 5.3.3 to extract this correction and the constant term in data.
- The template method uses a nominal template coming from the MC simulation and inject biases in the constant term, from 0% to 5%. A χ^2 minimization is then made on data using these biased templates and the constant term in data is extracted as the minimum of the χ^2.

5.3.7 Systematics uncertainties and Results

The constant term for the data derived from the two methods is shown in Figure 5.13 for the 2011 and 2012 data for the lineshape method. The template method gives similar results [157]. The constant term in data reaches around 1% almost everywhere, except in the region $1.37 < \eta < 1.82$ where it reaches 3%. The two datasets collected in 2011 and 2012 are found to have a similar constant term for the energy resolution. From the formula 5.3, a smearing factor for the electron energies in the MC is derived and applied such that:

$$E^i_{smear} = E^i \cdot (1 + c_i \cdot \text{Gaus}(0, 1))$$

The correction factor is multiplied by a Gaussian probability function centred in 0 and of unit width.

Two main uncertainties come from:

- The assumption of a well modeled sampling term: varying this term by ±10% leads to a variation of ±0.006 of the constant term, which is taken as an uncertainty.
- The method comparison: the differences between the two methods is η-dependent and goes from 0.0006 to 0.0069. This is taken as an uncertainty.

The statistical error is the dominant uncertainty, it is η-dependent and goes from 0.0006 to 0.0069.

[1] Assuming that the measurement of the angle is well simulated by the MC and that the resolution is small compared to the mass

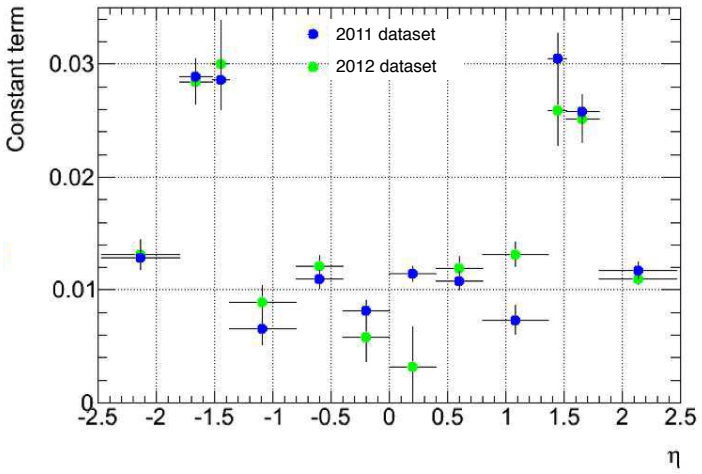

Figure 5.13: Constant term in the data extracted with the subtraction (blue) and template (black) methods (see text).

5.4 Uniformity and stability of the energy response

The mass resolution difference between the data and the MC is assumed to come only from the constant term. This difference is quite large, especially in the endcap. The non-uniformities of the energy response have a direct impact on the constant term. There are local non-uniformities like the gap and absorber structure variations and fine material variation upstream of the calorimeter, and long-range non-uniformities like calibration issues or cross talk.

Uniformity studies from test beams and cosmic muon data did not show any large effect responsible for the sizeable difference observed between the MC and the data for the constant term [173, 174]. The main purpose of the study presented here is to verify a possible impact of the non-uniformities along the η and ϕ directions measured in the data on the constant term. The stability of the energy response as a function of the time and pileup is also evaluated, as this could also deteriorate the resolution.

This is investigated in the following using two different methods, based on the distribution of the $Z \rightarrow ee$ invariant mass and the variable E/p from $W \rightarrow e\nu$ events.

5.4.1 The $Z \rightarrow ee$ Method

In this method, one of the electrons is used as a probe. The second electron pseudorapidity is correlated with the first one, due to the kinematics, as seen in Figure 5.14. The two electrons tend to be both either in positive η region or in negative one. This will lead to a reduction of the size of the non-uniformity measured, due to the averaging from the second electron.

The events selected for this study follow the baseline cut defined in Section 5.3.1. Additionally, the transition region ($1.37 < |\eta| < 1.52$) is removed. The peak position of the invariant mass is determined with two methods:

1. The mean value M in the mass range $[80 - 100$ GeV$]$ is taken as the representative for the peak. This method is quite sensitive to the tails of the distribution.

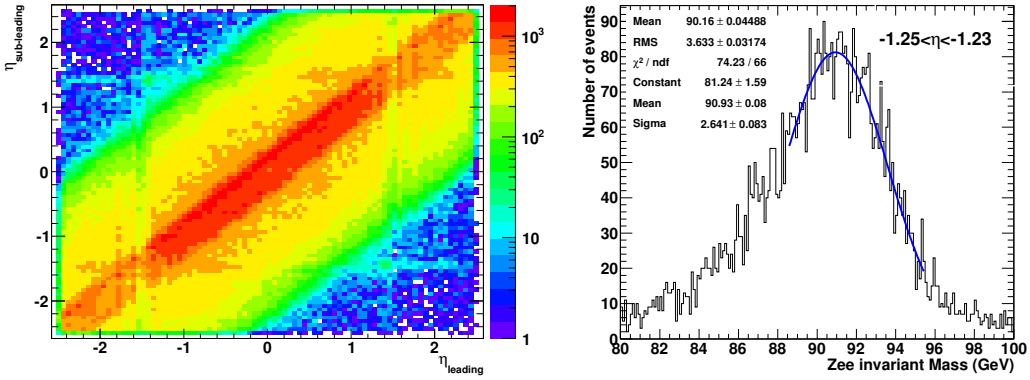

Figure 5.14: The left plot shows the kinematics in η of the two electrons coming from $Z \to ee$ events. The right plot shows an example of a $Z \to ee$ distribution and its fit to the peak with a Gaussian function in η region: $-1.25 < \eta < -1.23$.

2. A Gaussian fit to the peak in a window $[M - 0.5\ \sigma, M + 1.5\ \sigma]$ gives another estimation of the mass peak, less sensitive to the tails. (see Figure 5.14).

The second method is generally used unless otherwise stated.

5.4.2 The E/p Method

In this method all the electrons are used as a probe.

Selection of $W \to e\nu$ The selection of the events is as following:

- Same pre-selection as the one used for the $Z \to ee$ events (see Section 5.3.1).
- The candidates are required to have $p_T > 20$ GeV
- The missing transverse energy defined as $E_{\mathrm{T}}^{\mathrm{miss}} = -\sum_{i=1}^{N} p_T^i$ with N the number of tracks in the event should be larger than 25 GeV.
- A set of tight identification criteria is applied.
- The transverse mass of the W, defined as $m_T = \sqrt{2p_T E^{miss}(1 - \cos(\phi - \phi^{miss}))}$ where ϕ^{miss} corresponds to the azimuthal angle associated to the missing energy, is required to be larger than 40 GeV.

A Crystal Ball fit is used in the region $E/p \in [0.9, 2.2]$ to extract the Most Probable Value (MPV). See Figure 5.4.2 where the MPV is called "mean" and where "alpha", "n", and "sigma" are the other parameters of the Crystal Ball fit).

5.4.3 Stability of energy response versus time and pile-up

The electron energy response using the full 2011 and 2012 datasets, as a function of time and average interaction per bunch crossing is shown in Fig. 5.16. The two methods presented above are compared, after the response is normalized to one. Within the uncertainties, the two methods agree well and the obtained results are stable in a range of ± 0.1 %.

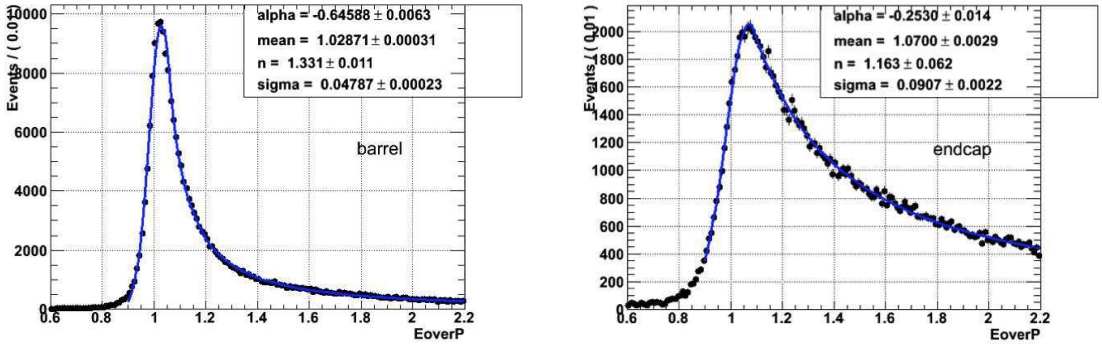

Figure 5.15: Examples of E/p distribution for $e^{\pm}$ from W decays and their Crystal Ball fits with two different η regions, $0.0 < |\eta| < 1.37$ and $1.52 < |\eta| < 2.47$. Taken from [157].

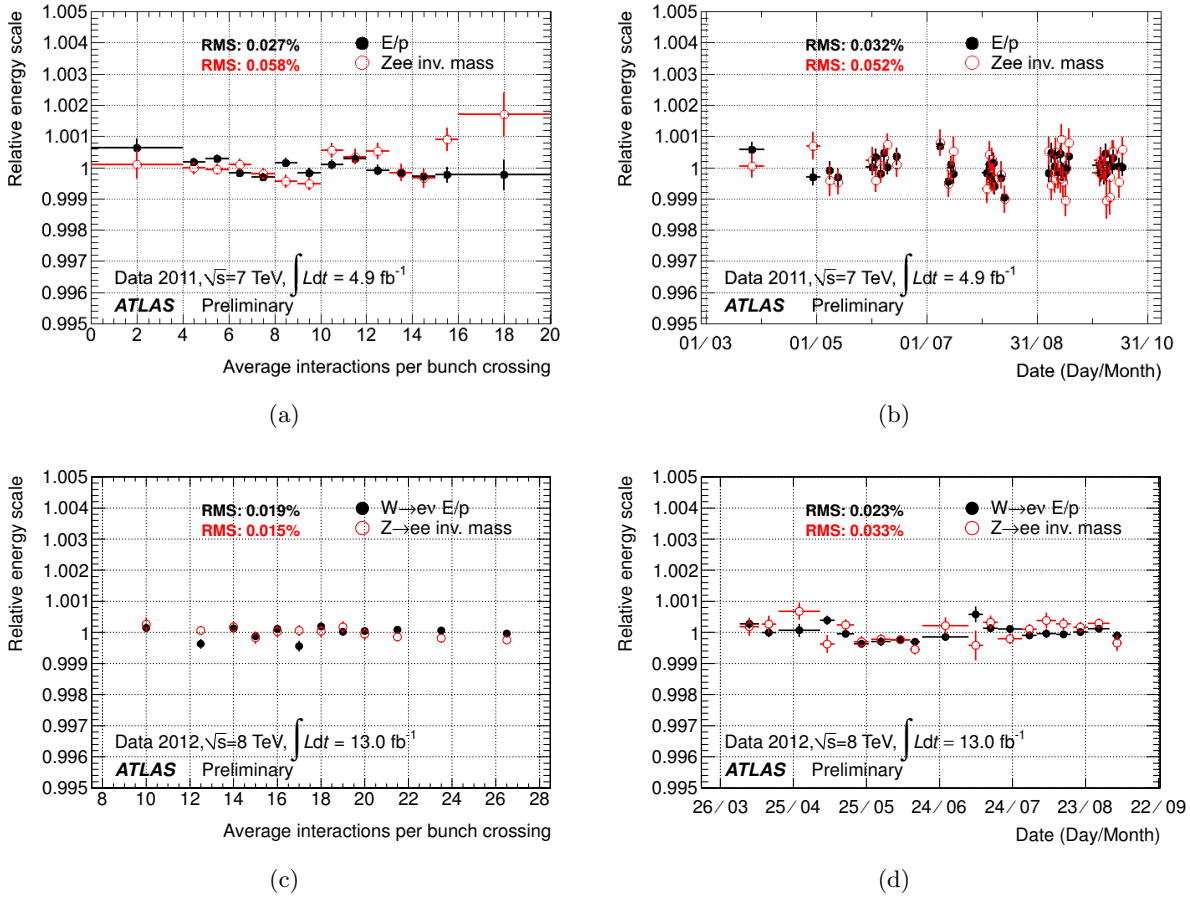

Figure 5.16: Fitted peak value of the $Z \to ee$ invariant mass and E/p most probable value for electrons from $W \to e\nu$ decays, normalized to one, as a function of the average interaction per bunch crossing in 2011 (a) and 2012 (c) and as a function of the time in 2011 (b) and 2012 (d). The quoted RMS are the sum of statistical fluctuations and $< \mu >$ (time) dependence, providing an upper bound on the energy response uniformity with $< \mu >$ (time).

5.4.4 Effect of the location in the bunch train

The relative location of an electron in a bunch train is identified with the Bunch Crossing Identification variable (BCID). The structure of the bunches into trains is not always the same, an identification number (Bunch Group Key (BGK)) is thus given to identify the different structures.

Figure 5.17 shows the stability of E/p and $Z \rightarrow ee$ invariant mass with respect to the BCID. The BGK number (308) for the dataset used corresponds to the bunch structure adopted during the periods H to M in the 2011 data taking period (see Chapter 4), and illustrated in Figure 5.17, left. Among the different trains, six have exactly the same structure, i.e are composed of 4 sub-trains, separated by a time intervals of 8 BCIDs (200 ns).

These six trains are overlaid in order to increase the statistical precision of the test, and compared to the MC with the same bunch structure in Figure 5.17, right. At the beginning of each sub-train, the energy response varies both in Data and MC. This comes from the shape of the LAr ionization pulse with a high amplitude positive part and a long negative tail. The pulse lasts 600 ns and its integral is null. It is sampled every 25 ns whereas the collisions occur every 50 ns in 2011 and 2012 data taking conditions. Each sample is thus the result of an average of several collisions. This effect is generally referred to as the out-of-time pileup in contrast to the in-time pileup which corresponds to several interactions occurring in the *same* bunch crossing. The integral of this average is in general equal to zero, due to the compensation of the different LAr pulses averaged at different times. When a time gap separates the collisions, the compensation is not anymore achieved. This explain the rising of the energy response after each gap, even greater for the larger gap of 36 BCIDs (900 ns) ahead of the first sub-train.
The stability of the energy response along the position in the bunch is better than 0.5% in agreement with the predicted stability. The fluctuations observed after the rising parts are due to a bunch luminosity variation.

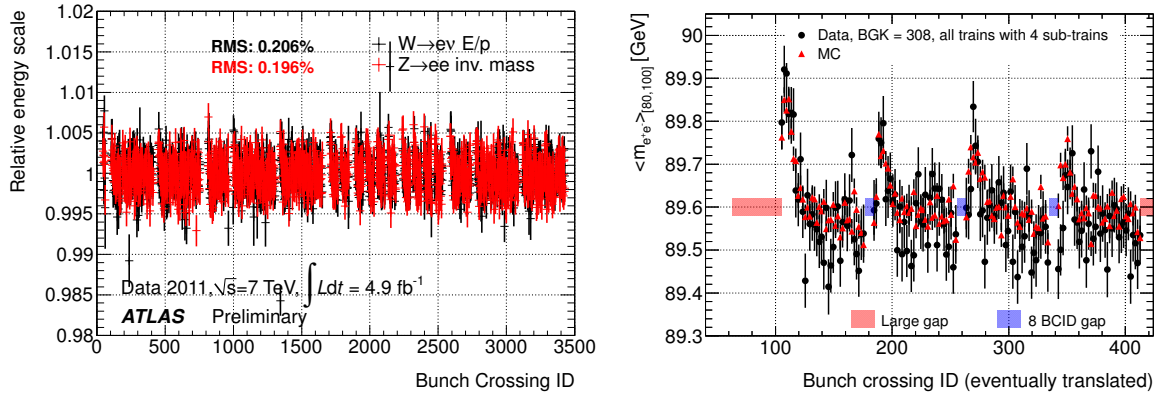

Figure 5.17: $Z \rightarrow ee$ invariant mass and E/p most probable value normalized to one, as a function of the BCID for the data with $BGK = 308$ (left). Data vs MC comparison for the invariant mass, with the six trains having the same structure overlaid [157] (right).

Figure 5.18 shows the stability of the $Z \rightarrow ee$ invariant mass versus the variable FBX. This variable counts the number of filled BCIDs before a given BCID, in a range time of 600 ns. All FBX greater or equal to 12 are superimposed in the last point. The invariant mass is not stable with respect to the FBX, as a consequence of the feature observed previously.

A correction has been designed to handle this effect. It uses the $Z \rightarrow ee$ invariant mass versus FBX variation, in order to take advantage of the larger statistics offered by this variable.

The correction is based on the prediction of the energy from the knowledge of the luminosity per BCID, and from the prediction of the out-of-time pile up. The corrected energy corresponds to:

$$E^{corr}_{BCID} = E^{meas}_{BCID} - E^{pred}_{BCID,\mu 1,\mu 2,...\mu N}$$

with E^{corr}_{BCID} the corrected energy for a given BCID, E^{meas}_{BCID} the measured energy for a given BCID, and $E^{pred}_{BCID,\mu 1,\mu 2,...\mu N}$ the predicted additional energy due to out of time pile up for a given BCID, depending on the luminosity of all BCID before and after the one considered (μi with i the BCID number).

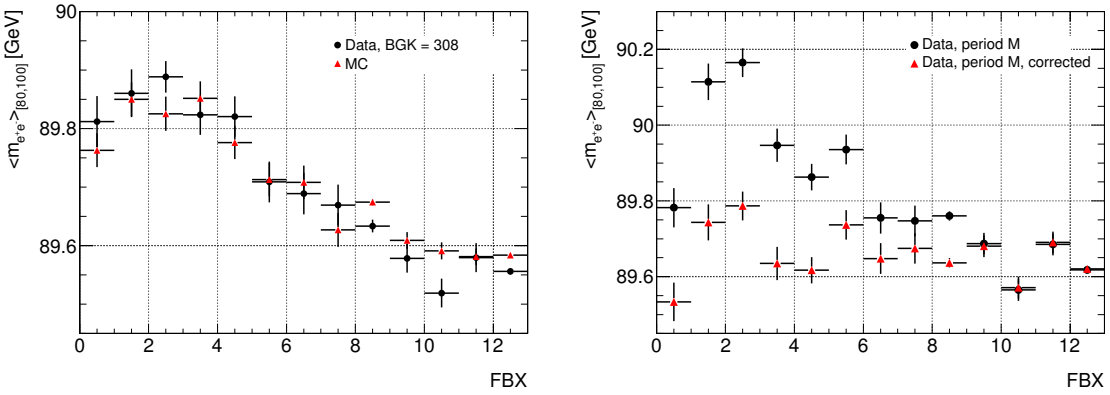

Figure 5.18: $Z \rightarrow ee$ invariant mass for the data and the MC (left) and for the data only before and after the BCID-dependent correction based on the prediction of the additional energy due to out of time pile up (right) [157].

5.4.5 Uniformity along η

The uniformity along η is measured in narrow bins of size of one cell of the second layer of the calorimeter ($\Delta\eta \sim 0.025$), and integrated over ϕ. The variables $\alpha_{E/p}$ and α_{Zee} defined as:

$$\alpha_{E/p} = \frac{MPV^{DATA}_{E/p}}{MPV^{MC}_{E/p}} - 1 \quad (5.5)$$

$$\alpha_{Zee} = \frac{M^{DATA}_{ee}}{M^{MC}_{ee}} - 1 \quad (5.6)$$

are compared in Figure 5.19.

The two methods agree well and see common structures in the following areas:

- $|\eta| \sim 0.6$: an excess is observed in data ($\sim 1\%$)
- $|\eta| \sim 1.52 - 1.55$: a negative scale is observed in both methods up to -6%.
- $|\eta| \sim 1.68$: a negative scale is measured with both methods ($\sim 3\%$)
- $|\eta| \sim 1.8$: an excess is observed in data ($\sim 2 - 3\%$)

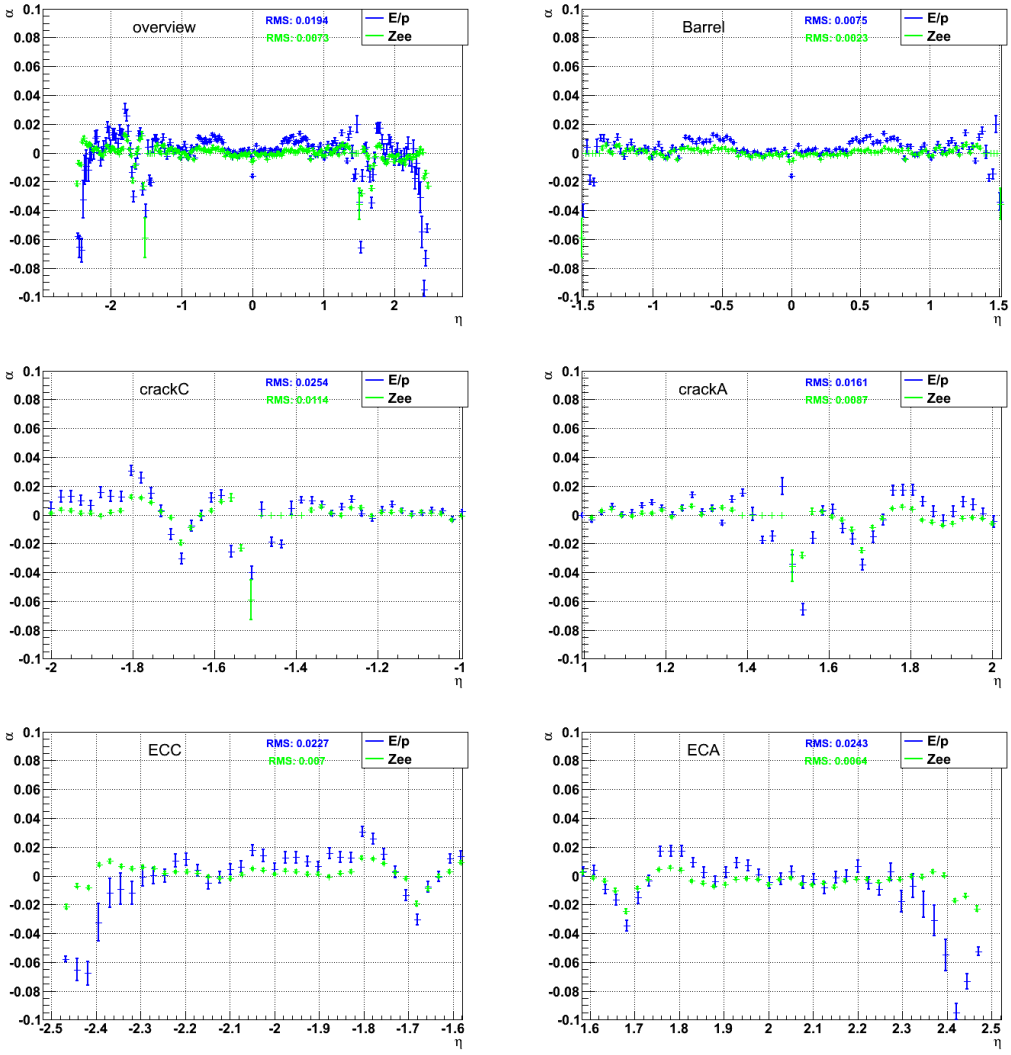

Figure 5.19: Uniformity along η, with a one-cell binning - ϕ integrated. The overview plot is followed by five zooms in different η regions.

- $|\eta| > 2.4$: a negative scale is measured with both methods (up to $\sim 3\%$ for the Z method and $\sim 6\%$ for W one)

The overall non-uniformity for this narrow η binning, calculated as the spread of the points (rms) is:

- $\sim 1.9\%$ for E/p from $W \to e\nu$
- $\sim 0.7\%$ for $Z \to ee$ invariant mass

The difference of a factor two between the methods is expected from the averaging effect in the invariant mass method (see above).

The binning that was proposed for the *in situ* calibration 5.3 deals with the non-uniformities observed here as well with the HV sectors.

5.4.6 Comparing $Z \to ee$ and $W \to e\nu$ in narrow ϕ bins

The uniformity in ϕ is expected to be good from the accordion geometry. This is tested for the 2011 and 2012 datasets.

Along the pseudorapidity axis, various non-uniformities have been observed. To not bias the uniformity on the azimuthal axis, the detector is divided in six η bins (excluding the cracks):

$$[-2.4, -1.6], [-1.3, -0.8], [-0.8, 0], [0, 0.8], [0.8, 1.3], [1.6, 2.4]$$

A narrow binning in ϕ is chosen, corresponding to one cell of the second layer of the calorimeter ($\Delta\phi = 0.025$).

The normalized energy responses in the data for the two methods are compared and shown in Figure 5.20. For this comparison, it should be kept in mind that a factor of about 2 in the measured non-uniformities is expected between the two methods. The comparison of data and MC energy response for both methods, using Equation (5.6) is also shown in Figure 5.21.

This figure shows that the two methods agree very well in the full azimuthal range and in all η regions. In the region $\eta > 1.6$, the E/p method sees however much larger fluctuations, probably due to the worsening of the tracking performance in this region. The following structures are seen along the ϕ range for both methods:

- In most of the η regions in the barrel, narrow dips are seen at $\phi = -\pi$, 0, π. This indicates an energy loss in the data not well modeled by the MC. This could be produced by a material mismodeling. The inner detector rails are good candidates, as they are located in these precise regions and extend up to a radius of around 1144-1152 mm. This is more developed in Chapter 6.

- For $0.0 < \eta < 0.8$, and $\phi \sim -0.8$, a structure is seen. In this region, some Front End Boards are known to be defective in the back layer of the calorimeter. This issue covers the region $(\eta, \phi) \sim (0.5, -0.8)$ and could induce a small loss of energy. In addition, in this region the High-Voltage settings are problematic.

- In the region $1.6 < |\eta| < 2.4$, in the full ϕ range a large oscillation is seen with a periodicity of $\sim 2\pi$. The effect is more pronounced with the E/p method. A sinusoidal function with the form $A + B \cdot \sin(\phi)$ is used to fit this shape with this method, with A and B two constants determined in the fit. The result of the fit in the data gives the following numbers: $A = 1.0002 \pm 0.0004$ and $B = -0.0060 \pm 0.0005$ for the negative side and $A = 1.0001 \pm 0.0004$ and $B = -0.0052 \pm 0.0005$ for the negative side, where the uncertainty is statistical only. The fluctuation is then significant and maximal at $\phi = \pm\pi/2$ with a size of $\sim 0.5 - 0.6\%$. A mechanical sagging effect of the electrodes and absorbers is a good candidate to explain this feature. A gradient of temperature of the liquid argon in the endcap has been also considered, but this temperature is controlled over the time and in different points. This monitoring has shown a good homogeneity of the temperature of the liquid argon [175, 176].

- Structures with periodicity $\Delta\phi \sim 0.4$ can be seen in the region $|\eta| < 0.8$ with both methods. This fine effect is investigated in the next section.

5.4.7 Intermodule widening effect

The periodicity of the structure observed with the two methods in the previous section is typical of the calorimeter modules pattern. The electromagnetic calorimeter is divided in 16 modules in

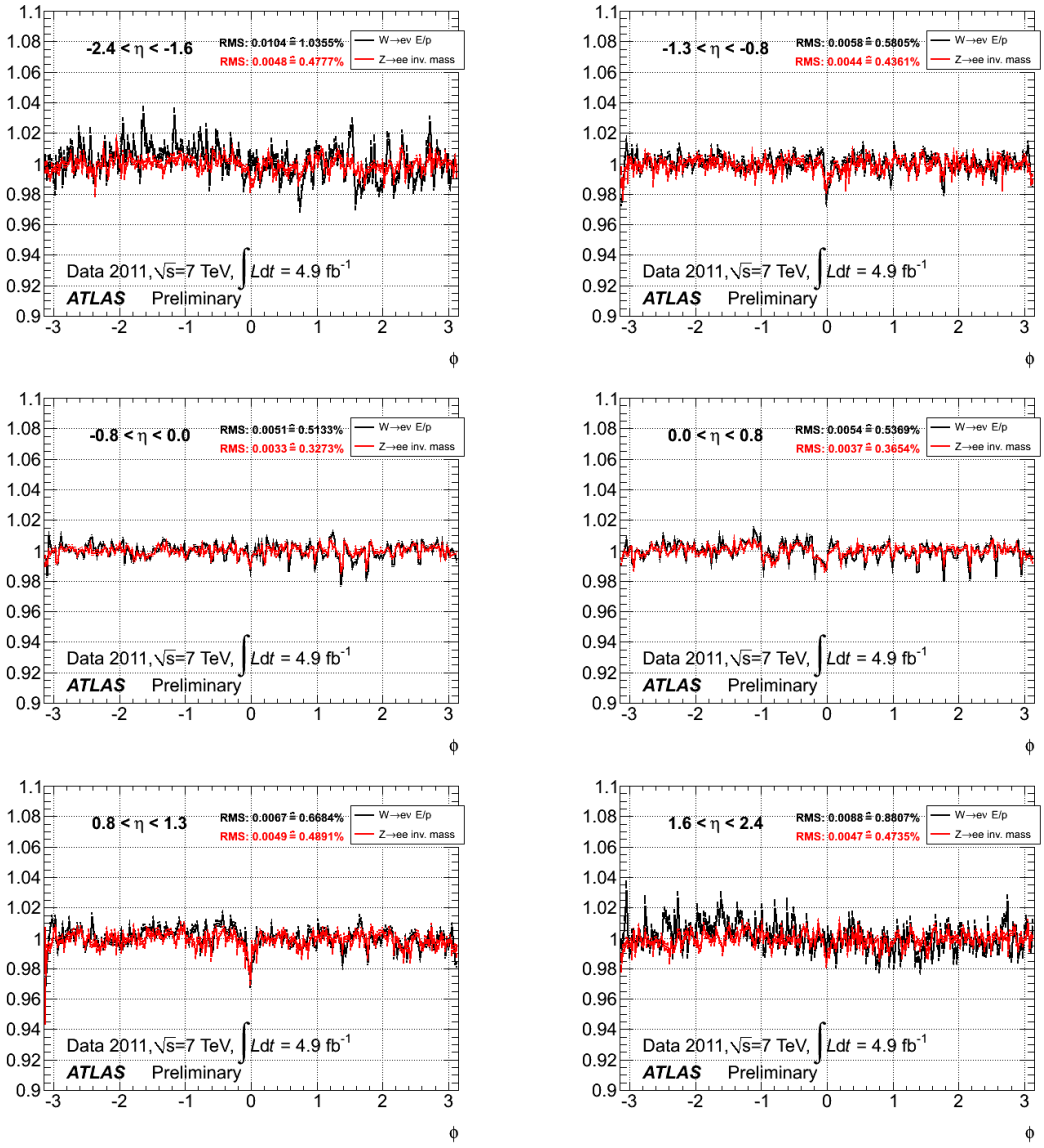

Figure 5.20: Uniformity in data in narrow ϕ bins and in six η regions, using the $Z \to ee$ invariant mass and E/p methods.

the barrel and 8 modules in each endcap. In the barrel each module is subdivided into 16 cells of size $\Delta\phi = 0.025$. The center of the first module is located at $\phi = 0$ and the two edges at $\phi = \pm 0.2$.

In Figure 5.22 the most probable value of the variable E/p and the $Z \to ee$ invariant mass are drawn as a function of the azimuth of the electron probe. The modules of the barrel calorimeter are folded to increase the statistical precision. The ϕ-bin size is $2\pi/1024$, in order to see more precisely any cell-structure. The positive and negative azimuths are separated.

The data and MC disagree in the region $\phi \sim 0.2$, both in positive and negative ϕ. The size of the discrepancy is different: $\sim 3.5\%$ resp. $\sim 1.5\%$ for $\phi > 0$ resp. $\phi < 0$. The drop in E/p follows the typical inter-modules localization, and this suggests a loss of energy in the data due to non-instrumented gaps between the modules.

The gap size uniformity has been probed with the measurement of the electron drift time

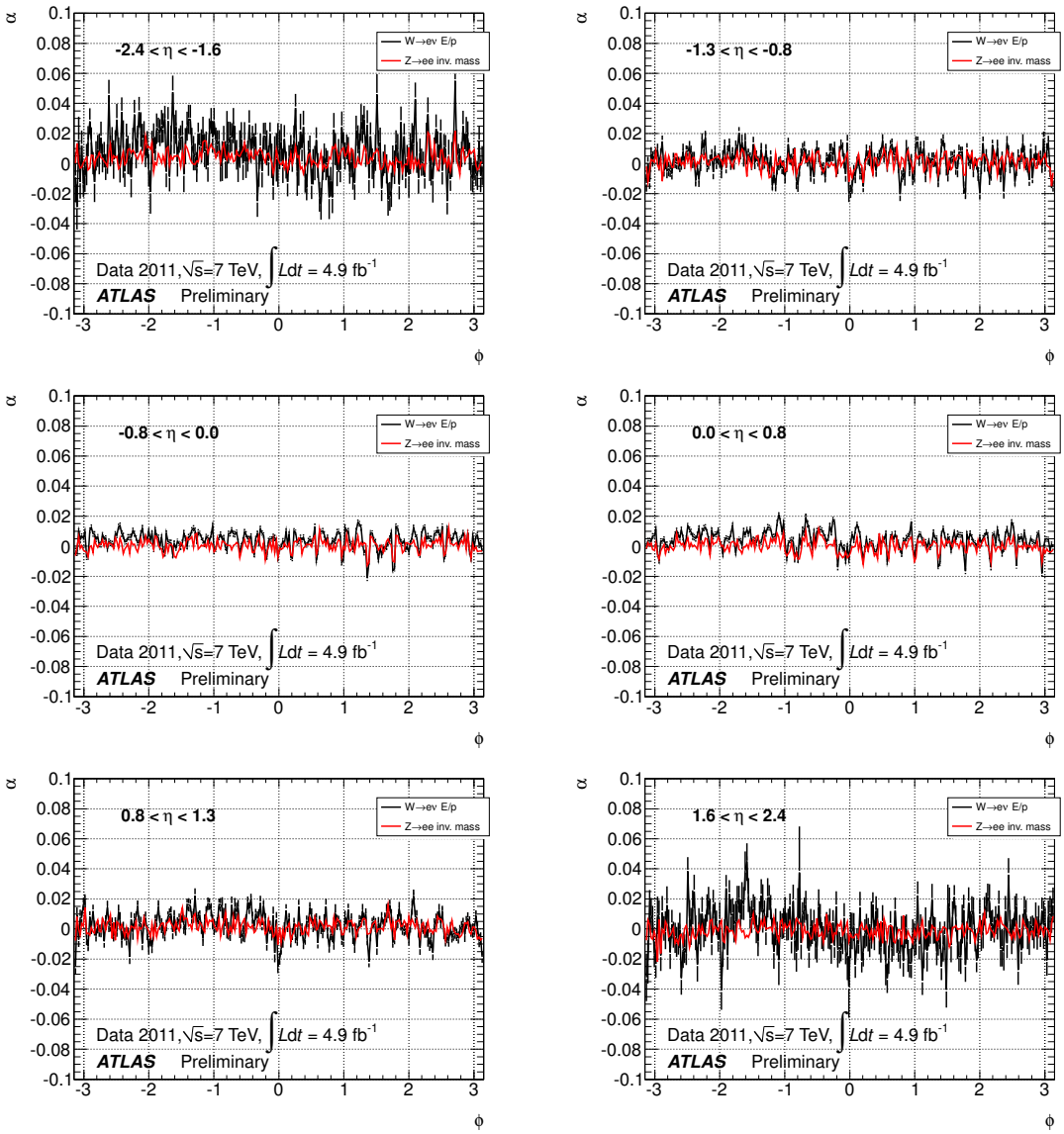

Figure 5.21: This figure compares MC with Data using the α (Eq. 5.6) parameter.

in the liquid argon from cosmic events and found to be good along pseudorapidity [174]. The uniformity of the drift time along the azimuthal angle has also been checked with cosmic muons and collision data [177]. A similar periodical ϕ asymmetry has been found as shown in Figure 5.23(a), for the second sampling of the calorimeter. The dashed lines corresponds to the barrel inter-modules. The drops in E/p or invariant mass corresponds to peaks in drift time, since an enlargement of the gaps induces a larger drift time and a smaller collection of energy.

The ϕ dependence This effect has a ϕ-dependence as already observed in Figure 5.22 with E/p. Figure 5.23(b) shows the evolution of the drift time deviations along ϕ. A sinusoidal shape is found, that can be fitted to extract a correction. The drift time allow precise measurement of the effect because of the large number of measured events available. //

A check of the ϕ-dependence is made with E/p, in larger regions. The barrel is divided in four parts each containing four modules: $\pi/4 < \phi < 3\pi/4$ (top), $-3\pi/4 < \phi < -\pi/4$ (bottom),

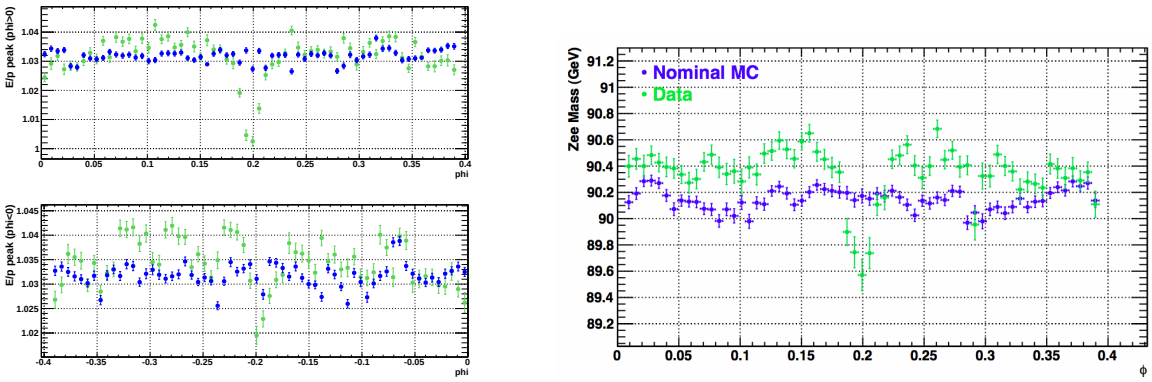

(a) E/p (b) $Z \rightarrow ee$ invariant mass

Figure 5.22: Evolution of the E/p most probable value - for positive (top) or negative (bottom) azimuths - (a) and of the Z invariant mass (b) for the data (green) and nominal MC (blue) as a function of ϕ in the barrel calorimeter when the 16 modules are folded.

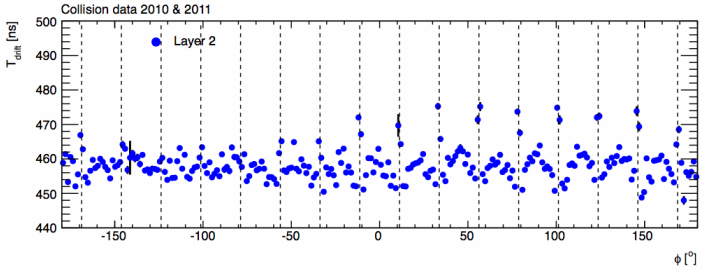

(a)

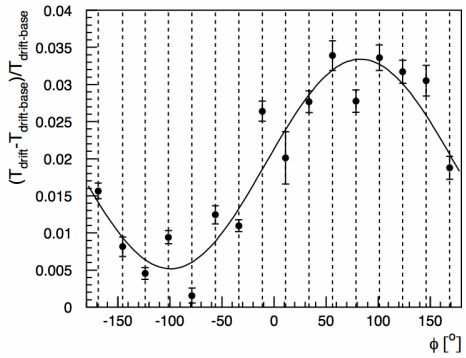

(b)

Figure 5.23: Drift time measurement in the second layer of the calorimeter as a function of ϕ using collision data (a) and evolution of the deviations observed at the inter-module with respect to ϕ (b). Taken from [177].

$-\pi/4 < \phi < \pi/4$ (right) and $-3\pi/4 < \phi < 3\pi/4$ (left). The E/p extracted in these four regions for the data is shown in Figure 5.24.

The top and bottom parts of the calorimeter have respectively the maximal ($\sim 3.5\%$) and minimal ($\sim 1.5\%$) deviations in the inter-modules, whereas the two sides have intermediate deviations ($\sim 2.5\%$). This confirms the effect seen in the drift time measurement. This is

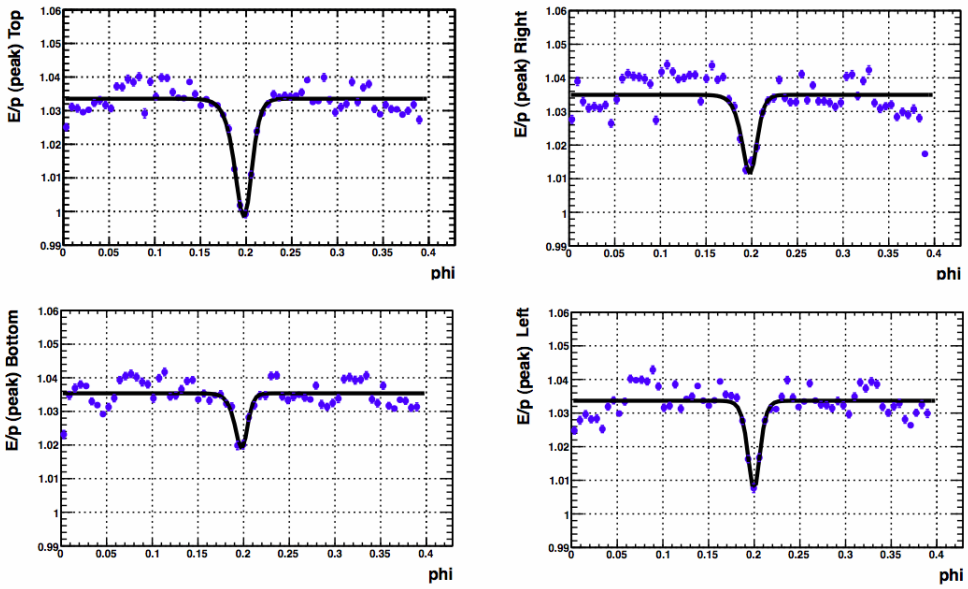

Figure 5.24: Evolution of the most probable value of E/p for the data (blue) as a function of ϕ in the barrel calorimeter. The 16 modules are folded and grouped in four regions: $\pi/4 < \phi < 3\pi/4$ (top left), $-3\pi/4 < \phi < -\pi/4$ (bottom left), $-\pi/4 < \phi < \pi/4$ (top right) and $-3\pi/4 < \phi < 3\pi/4$ (bottom right). The black line corresponds to the Double Fermi-Dirac fit of the data (see text).

interpreted as a widening of the barrel inter-module gaps, modulated by a mechanical sagging effect. The top part of the calorimeter has larger gaps because the sagging under gravity tends to widen them.

Correction of the effect Even if very localized, the impact of this fine effect on the total energy and in the constant term is not negligible. Figure 5.22(b) shows that at the inter-module, the mass decreases by around 1%.

Given that this drop concerns around 1 cell in 16, a global effect of around 0.1% is expected on the total energy in the barrel.

A correction for this effect is derived, using the E/p variable. The holes observed in data are fitted with a Double Fermi-Dirac (DFD) function:

$$f(\phi) = A - B \cdot \frac{1}{1 + e^{(C \cdot (\phi - 0.2))}} \cdot \frac{1}{1 + e^{(D \cdot (\phi - 0.2))}}$$

with A the averaged value on either sides of the hole, B the hole depth and C and D the hole width. This provides four sets of coefficients (A,B,C,D). The result of the fit is seen in Figure 5.24, in black line.

The electron energy is corrected with this function $f(\phi)$, and the correction size in GeV as a function of ϕ is illustrated in Figure 5.25 for electrons with $p_T = 40$ GeV.

A tool has been provided that returns automatically the corrected energy, given the ϕ and η coordinates and the energy of the electrons or photons [178].

The impact of the correction is evaluated at around +0.1% for the mean value of the $Z \rightarrow$ invariant mass while the rms stays unchanged. The change in the mean value corresponds to

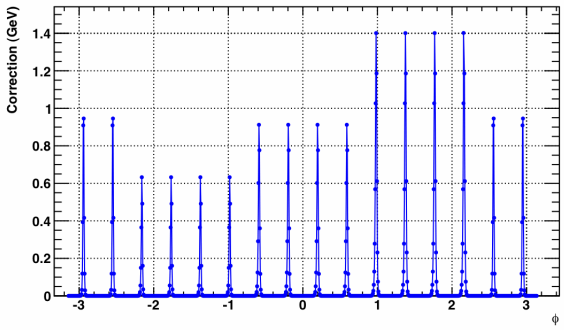

Figure 5.25: Size of the correction of the energy in GeV as a function of ϕ, for an electron with $p_T = 40$ GeV.

the loss of energy expected.

The η dependence Inside the barrel, the evolution of the energy loss due to the intermodule widening along η has been checked. Using the E/p method, it is shown that in the four different regions: $0 < |\eta| < 0.34$, $0.34 < |\eta| < 0.68$, $0.68 < |\eta| < 1.03$ and $1.03 < |\eta| < 1.37$, integrated over ϕ, the energy loss in the inter-modules varies. It is respectively 2.45%, 1.94%, 1.92%, 1.87%. A check is done with the drift time variable. Figure 5.26 shows a map (η, ϕ) of the drift time values in collision data [2]. The inter-module effect is clearly seen in this plot, corresponding to the yellow/red band for $\phi \sim 0.2$ [3]. The increasing of the drift time is larger in the very central region of the calorimeter in η, for $\eta < 0.3$, as seen from the E/p study. This η-dependence is not yet taken into account in the correction for the effect.

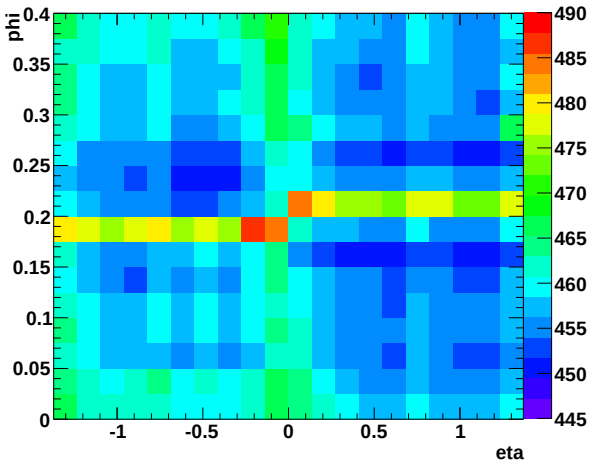

Figure 5.26: Map (η, ϕ) of the drift time in the second layer of the calorimeter from collisions data. The modules are folded along ϕ.

[2] The data samples have been kindly provided by the authors cited in reference [177].

[3] The small shift observed between the 2 barrel sides corresponds to one absorber shift simply arising from the binning.

Overview A more accurate correction is planed, using drift time measurements that are more sensitive to the gap size variations and taking into account the η-dependence.

The same effect has been investigated in the endcaps (using the appropriate size of the modules), but nothing similar has been found.

Figure 5.27 shows the variable $\alpha_{E/p}$, as a function of ϕ, in the four barrel bins, before and after the correction for the Intermodule Widening Effect is applied. The uniformity and the agreement with the MC is improved with this correction.

Table 5.4 shows the rms in each η bins before and after the correction, for both methods.

η-bin	Before Correction [%]		After Correction [%]	
	E/p	$Z \to ee$	E/p	$Z \to ee$
$-2.4 < \eta < -1.6$	1.04	0.48	1.04	0.50
$-1.3 < \eta < -0.8$	0.58	0.44	0.57	0.46
$-0.8 < \eta < 0$	0.51	0.33	0.42	0.29
$0 < \eta < 0.8$	0.54	0.37	0.43	0.34
$0.8 < \eta < 1.3$	0.67	0.49	0.67	0.52
$1.6 < \eta < 2.4$	0.88	0.47	0.88	0.49

Table 5.4: This table shows the impact of the Intermodule Widening Effect in narrow ϕ binning.

As expected, a factor ~ 2 between the E/p and $Z \to ee$ invariant mass non-uniformities arises and no effect on endcap regions rms is observed after the correction. The average improvement due to the intermodule widening correction is $\sim 12\%$ for the E/p case and $\sim 9\%$ for the Z invariant mass one.

The final rms are quite small in the barrel regions (below 0.5%), demonstrating that the residual effects do not contribute much to the large constant term measured in the data. A large positive/negative asymmetry for the E/p variable is seen in the bin $1.6 < |\eta| < 2.4$: the spread of the points is larger in the negative side. This effect is not yet understood.

5.4.8 Summary

Table 5.5 summarizes the non-uniformities observed in data coming from the time dependence of the energy response, the stability against pile-up (μ), and the bunch-position dependence of the energy response. The numbers quoted corresponds to the sum of statistical fluctuations and non-uniformity, which explain partly the differences between the two methods. They give then an upper bound on the non-uniformity of the energy response which is in total about 0.1%.

	Data (M_{ee})	Data (E/p)
Time	0.052	0.032
$< \mu >$	0.058	0.027
FBX	0.09	-

Table 5.5: Non-uniformities observed in data as a function of the time, pile-up and bunch position for the E/p and Z invariant mass methods, extracted from the rms of these profiles. The results are given in percent.

The non-uniformity contribution to the constant term has been also evaluated along ϕ in η-bins of size $\Delta\eta \sim 0.2$. A level of uniformity of typically 0.5% is found. Larger effects occur very

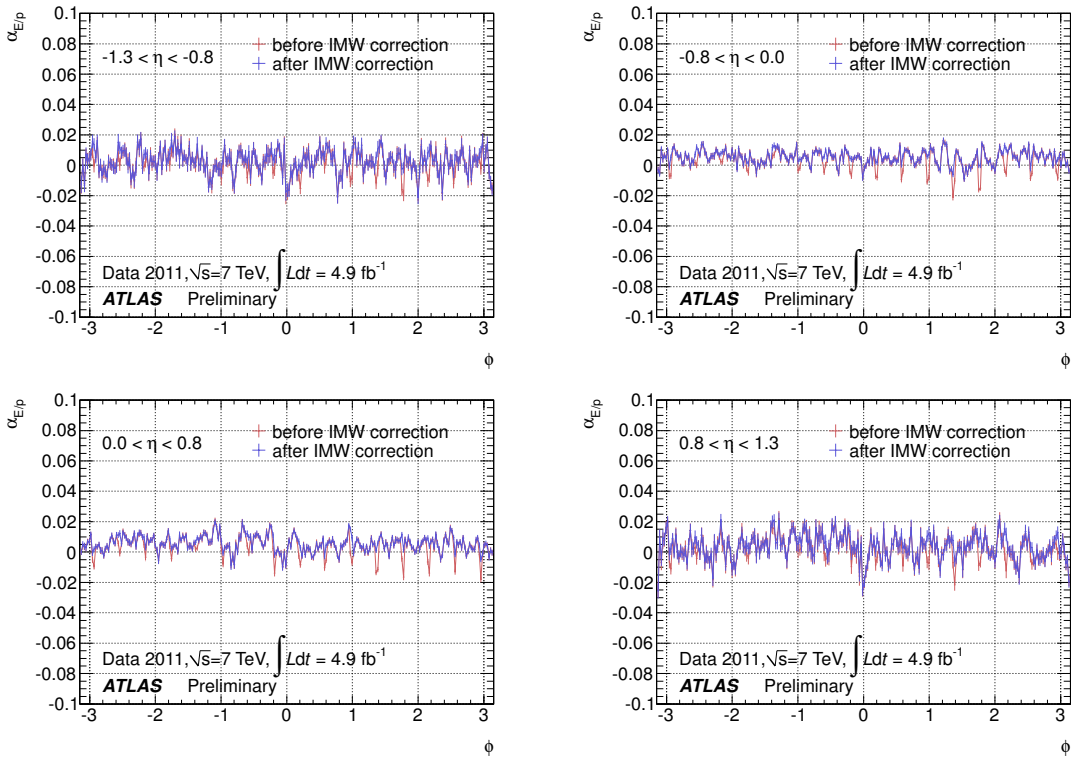

Figure 5.27: $\alpha_{E/p}$ from Eq. 5.6 as a function of ϕ in the four barrel bins, after the Intermodule Widening Effect (IMWE) is corrected [157].

locally (as the intermodule widening effect or near the transition regions), but do not contribute significantly to the quality of the intercalibration. Performing an absolute calibration as a function of pseudorapidity only is then justified.

5.5 Response uniformity using the Jacobian peak

An alternative method is used to probe the electron calibration and is described below. This method relies on the transverse momentum of electrons from $Z \to ee$ and $W \to e\nu$ decays. The p_T distribution for such electrons forms a Jacobian peak, which is characterized by a sharp edge located at half the W or Z mass. Most of the electrons have a p_T less than this value, as shown in Figure 5.28 for the $W \to e\nu$ process and in Figure 5.29 for the $Z \to ee$ one.

The measurement of the edge position gives access to the relative energy scale. The advantage of this method is that it relies only on the electron p_T mainly measured in the calorimeter detector. However, the theoretical uncertainties for the modeling of the Z or W p_T distribution are quite large due to emission of additional partons in the final state. This gives on average an uncertainty on the p_T distribution of around 10% corresponding to the size of the strong coupling constant [179].

5.5.1 Method

The method is based on the comparison of the electron p_T distribution for the data with a set of MC templates taken from a nominal distribution. The energy in data is not corrected with

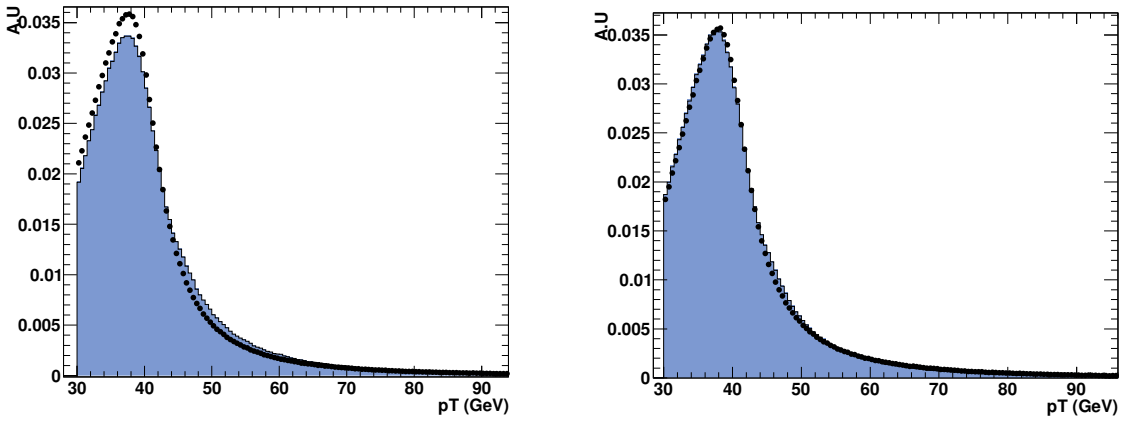

(a) $W^+ \to e^+\nu$ (b) $W^- \to e^-\nu$

Figure 5.28: Electron p_T distribution for the $W \to e\nu$ process for the data (black points) and the nominal MC (blue histogram) for the positrons only (a) and the electrons only (b).

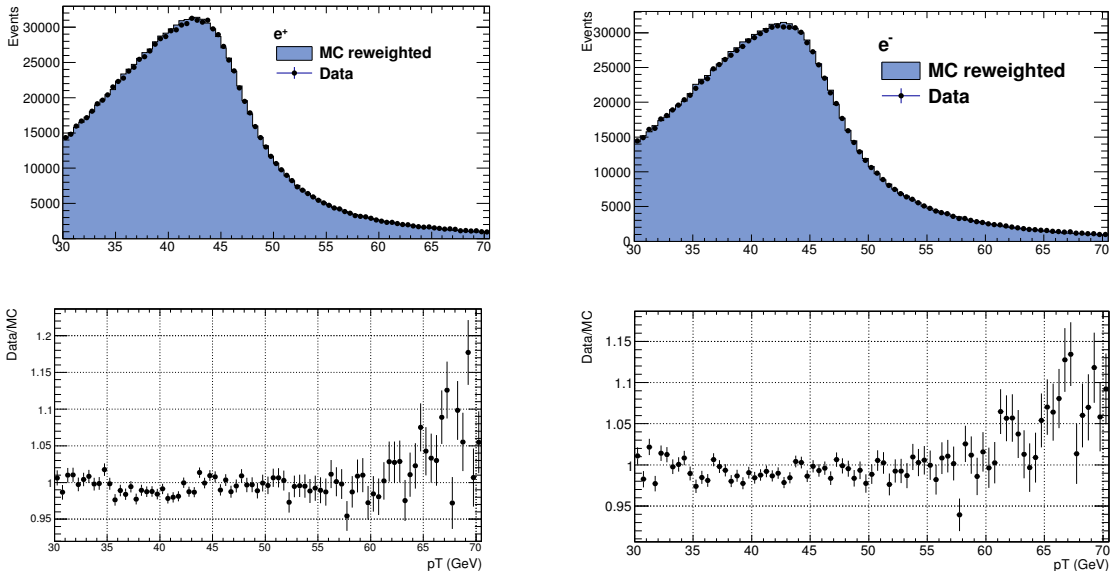

(a) $Z \to ee$, e^+ (b) $Z \to ee$, e^-

Figure 5.29: Electron p_T distribution for the $Z \to ee$ process for the data (black points) and the nominal MC (blue histogram) for the positrons only (a) and the electrons only (b).

the scale factors derived from the *in situ* calibration and the energy in MC is not smeared with the correction factor derived from the same calibration (see Section 5.3.6).

The electrons from the $Z \to ee$ and $W \to e\nu$ processes are selected following the procedure described in Section 5.3.1. All the corrections for the MC listed in Section 5.3.1 are applied, particularly the Z p_T reweighting for the 2011 MC.

The MC does not well model the lepton p_T distribution for the $W \to e\nu$ process, especially for the positrons (see Figure 5.28). Such a discrepancy could arise from background contamination in this channel which is not negligible [180]. As the method is fully based on shape comparisons

between data and MC, this process cannot be used until the disagreements are better understood and a deeper study of the background contribution for this process is done.

The $Z \to ee$ process is used instead, as it has less background contamination and because the MC better model the lepton p_T distribution: as shown in Figure 5.29, the agreement is within ±2% up to $p_T = 60$ GeV where it starts to worsen up to 15% at $p_T = 70$ GeV. The range chosen for the study is then [35,55] GeV, so that the discrepancy observed from $p_T = 60$ GeV does not affect the comparison.

The Z p_T distribution is shown in Figure 5.30 for the data and MC and for the two years 2011 and 2012, after reweighting for the 2011 MC sample. The two MC distributions agree well with the observation, except in the low p_T range where they both have difficulty to simulate the data. The discrepancy amounts around 10% for $p_{T,Z} < 5$ GeV. The effect of this discrepancy will be checked in the following.

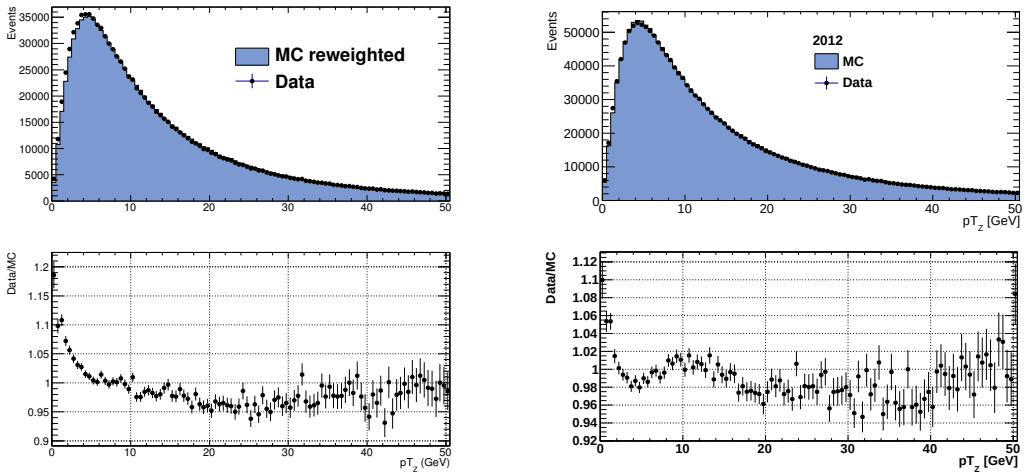

(a) 2011 (b) 2012

Figure 5.30: Z boson p_T distribution for the data (black points) and the nominal MC (blue histogram) for the inclusive dataset collected in 2011 (a), and in 2012 (b).

The MC templates are created by scaling the electron p_T by a factor α_{jac}:

$$p_{T,bias} = p_T(1 + \alpha_{jac})$$

with α_{jac} taking values between -4% and +4% with a step of 0.2%. Three initial templates are created, with $\alpha_{jac} = -4\%, 0, +4\%$, the others are obtained by linearly interpolating these histograms following a technique described in reference [181]. For illustration, Figure 5.31(a) shows a typical interpolation between -4% and +4% with a step of 2%.

A χ^2 minimization is done between the templates and the data distribution, leading to a parabola as a function of the bias injected. The minimum of the parabola gives the scale factor in the data and its width the error on this factor. Figure 5.31(b) shows a typical parabola and the associated fit with a second order polynomial to extract the minimum.

5.5.2 Results

Inter-calibration along η The Jacobian peak method is used to probe the relative inter-calibration along the pseudorapidity. Two different binnings are used in this study: the one

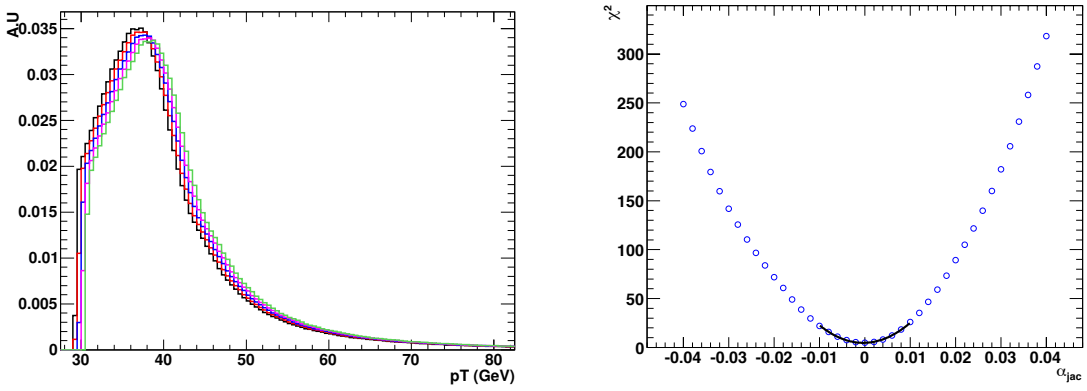

(a) Interpolation

(b) χ^2 minimization

Figure 5.31: (a) Linear interpolation of histograms for α_{jac} between -4% (black line) and 4% (green line) around the nominal template (blue line) with a step of 2% (-2%: red line and +2% pink line). (b) χ^2 minimization between the interpolated histograms and the data distribution, as a function of the injected bias (blue empty dots). The black line shows the second order polynomial function used to extract the minimum and its error.

defined in Section 5.3 and a narrower binning with $\Delta\eta = 0.025$. The Jacobian method is run separately for the electrons and positrons, in order to check their compatibility, and the final result is given as an average of the two sets of scale factors. The compatibility of the results is found to be good. In some narrow regions, like near the barrel-endcap transition, or at the end of the endcap, a small difference is observed. This has been understood as coming from the bad energy resolution in these points, which smears out the p_T distribution and leads to a loss of sensitivity to the energy scale.

The result for a large η binning is shown in Figures 5.32(a) and 5.32(b) for the 2011 and 2012 datasets. The scale factors obtained with the *in situ* calibration method are overlaid for comparison. A good agreement of the general shape for the two methods is obtained. A global shift of the Jacobian scale factors with respect to the reference in the barrel is seen for the 2011 dataset. The bin-by-bin difference between the two methods is shown in Figure 5.32(d) for the two years. The average of the differences for the two years is: 0.0002 ± 0.0002 (0.0000 ± 0.0002 in the barrel) in 2012 and -0.0021 ± 0.0002 (-0.0030 ± 0.0002) in 2011. Then a much better agreement is found in 2012 than in 2011 between the two methods. This could come from various reasons, both from the detector and simulation side. In Section 5.5.3 the robustness of the result against various parameters is tested.

The goodness of the minimization has been also checked. No obvious structure was found, for both electrons and positrons. The typical value is $\chi^2/NDF \sim 1$, and is no larger than 3, demonstrating the good behaviour of the fit.

The same study has been made with a finer binning, as seen in Figure 5.33. The positive and negative pseudorapidities are averaged to increase the statistical precision. The scale factors obtained with the *in situ* method are overlaid. The structures seen in both methods are in good agreement and the Jacobian method with its finer binning shows in more details these structures. This study demonstrates the good sensitivity of this method to the relative energy scale, even with a small granularity.

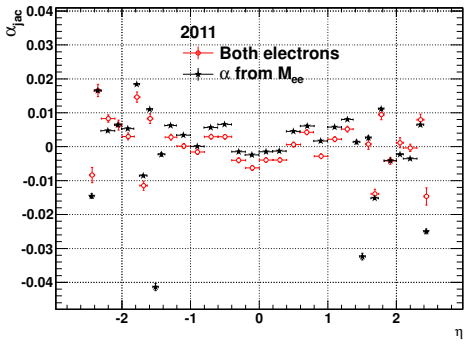

(a) α_{jac}, 2011

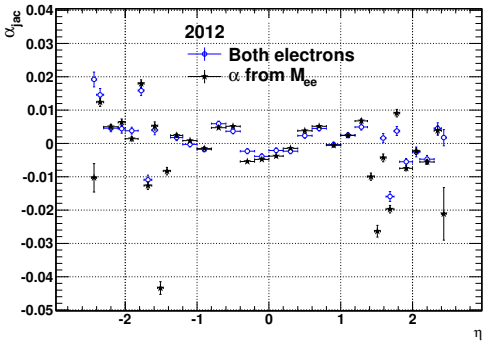

(b) α_{jac}, 2012

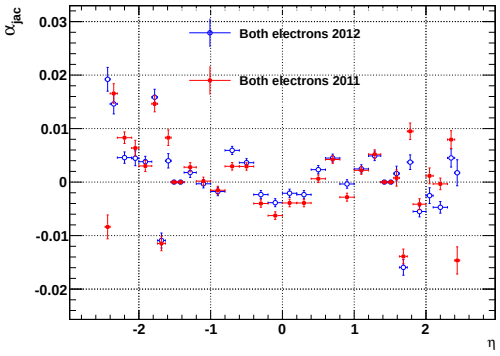

(c) α_{jac}, 2011 vs 2012

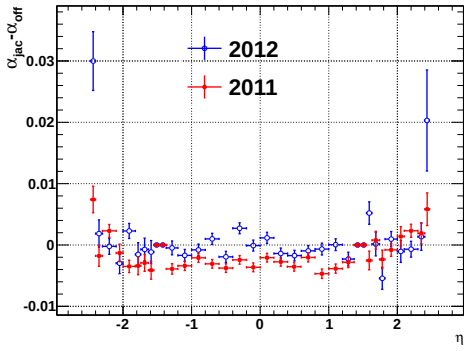

(d) α_{jac} - α_{off} 2011 vs 2012

Figure 5.32: Inter-calibration scale factors from the Jacobian method compared to the official scale factors obtained with the *in situ* method (black line) using the 2011 (a) and 2012 (b) datasets. Comparison of the results for the two years (c) and difference between the two methods for the two years (d).

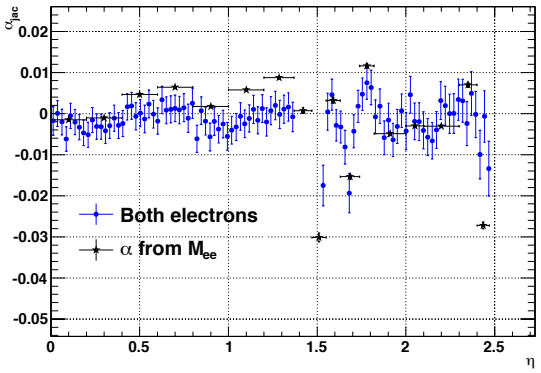

Figure 5.33: Inter-calibration scale factors for the Jacobian method (blue line) compared to the official scale factors obtained with the *in situ* method (black line). Only the dataset collected in 2011 is used here.

Uniformity vs ϕ The uniformity along the azimuthal angle is checked with the Jacobian peak method. The binning used corresponds to $\Delta\phi = 0.1$, thus corresponding to four cells of the second layer of the calorimeter. The results for the 2011 and 2012 datasets inclusively are shown in Figure 5.34(a).

The global inter-calibration scale factors are found to be close to 0, within $\pm 0.5\%$ except in some points:

- At $\phi = 0$, a hole is present for both years. It is more pronounced in the barrel region. This could arise from the ID rail modeling in the MC (see Section 5.4 and Chapter 6).

- A sinusoidal shape of the scale factors, with a maximum and a minimum at $\phi = -\pi/2$ and $\phi = +\pi/2$ respectively is observed. This is more pronounced in the endcap region (see Figure 5.34(b)), in agreement with the effect observed using the E/p method (see Section 5.4). The regions $\eta < 2$ and $\eta > 2$ for the endcap have been tested separately, but did not shown obvious differences. This sinusoidal shapes have been fitted for the Jacobian method in 2011 and 2012 in the endcaps with a function of type $A + B \cdot \sin(\phi)$ with A and B two constants determined in the fit. The result of the fit in the data gives the following numbers: $A = 0.0026 \pm 0.0003$ and $B = -0.0040 \pm 0.0005$ for the 2011 dataset and $A = -0.0017 \pm 0.0002$ and $B = -0.0045 \pm 0.0005$ for the 2012 dataset, where the uncertainty is statistical only. The constants A are significantly different from 0 because no energy scale corrections are applied in this study.

  The amplitudes of the sinusoidal shapes have been compared for the Jacobian method in 2011 and 2012 and for the E/p method presented in Section 5.4. The constants A have been all put to zero and an average of the positive and negative ϕ sides for the E/p method has been done. Figure 5.35 shows this comparison, without including the statistical uncertainties. The amplitudes are comparable within these uncertainties.

  This effect was also observed with drift time measurements in endcaps with a comparable amplitude [182].

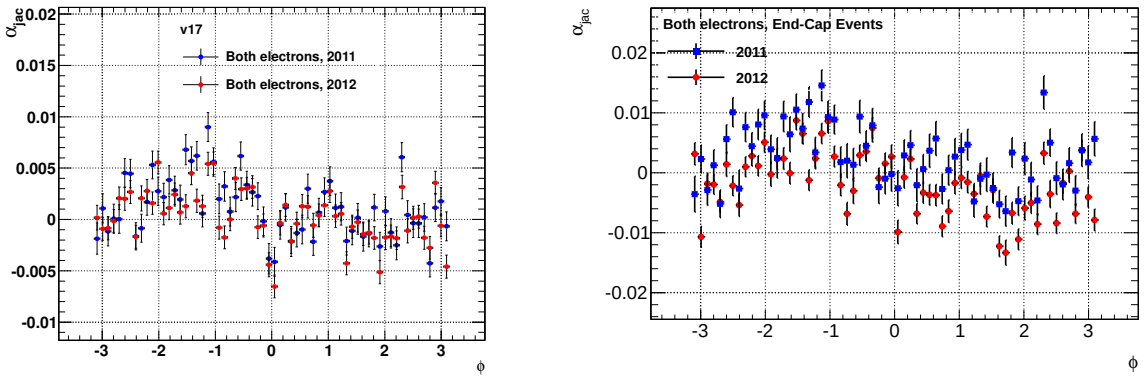

(a) α_{jac}, 2011 vs 2012

(b) α_{jac}, endcap, 2011 vs 2012

Figure 5.34: (a) Inter-calibration scale factors from the Jacobian method as a function of ϕ using the 2011 (blue dots) and 2012 (red dots) datasets. (b) Same scale factors, selecting events in the endcap only.

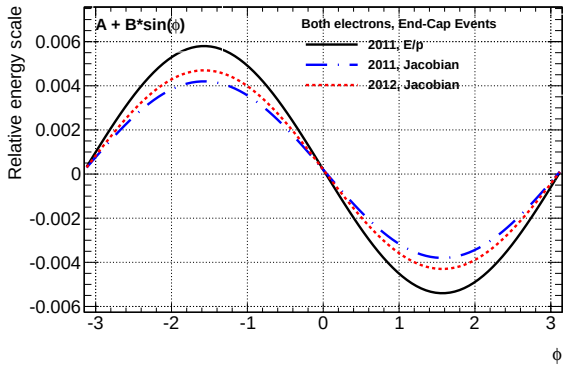

Figure 5.35: Sinusoidal functions corresponding to the fit of the scale factors extracted from the E/p method (black line) and the Jacobian method for the 2011 (blue dashed line) and 2012 (red dotted line) datasets.

5.5.3 Cross checks

The robustness of the Jacobian peak method has been tested in various studies. The first check is the closure of the method: a nominal MC template without bias, is compared to the set of templates used to extract the scale factors in the data. The best scale factor is estimated with the same method as described above. Figure 5.36(a) shows the result as a function of the pseudorapidity. It demonstrates a good closure of the method.

The same exercise is done with an injection of a bias of +3% in the initial MC template. Figure 5.36(b) shows the resulting scale factors extracted using the Jacobian peak method. Again, the method shows a good accuracy.

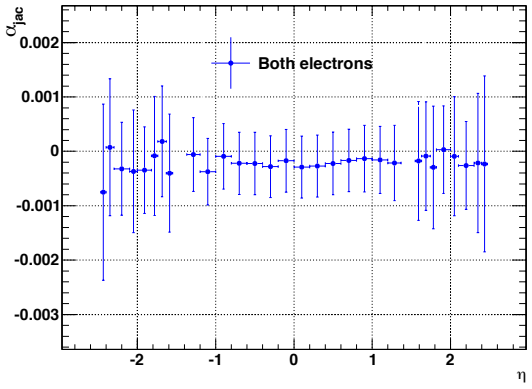

(a) α_{jac}, closure check

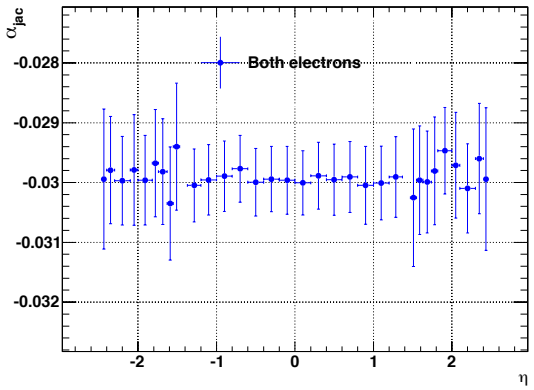

(b) α_{jac}, injection of a +3% bias

Figure 5.36: Inter-calibration scale factors from the Jacobian method using the nominal MC as pseudo-data (a) and a MC template with +3% bias of the energy scale as pseudo-data (b)

In order to understand the differences between the *in situ* and Jacobian methods, other tests are done.

Impact of the background The background in the $Z \to ee$ process can be further rejected by requiring a tight electron identification criteria. The scale factor obtained with an electron medium (reference case) and tight identification criteria are compared to test the impact of the residual background on the energy response with the Jacobian method and how the agreement with the reference results evolves. No sizeable differences are found between the two identifications, showing that the method is quite robust with respect to the background.

Impact of the Z p_T modeling As seen in Section 5.5.1, the Z p_T is not perfectly modeled in the low p_T regime, even after the reweighting for the 2011 MC is applied. The impact of such mismodeling is evaluated by removing all the events having a Z p_T lower than 5 GeV. No obvious differences are seen with this selection.

Impact of the modeling of $\cos\theta^*$ The distributions of the Cosine of the angle $\theta*$ in the Collins-Soper frame for the data and the MC are in good agreement everywhere except in the region $\cos\theta^* > 0.7$ where the MC has some difficulties to model the data. The two regions $\cos\theta^* > 0.7$ and $\cos\theta^* < 0.7$ have very different kinematic characteristics, especially for the p_T of the Z. A mismodeling of the region $\cos\theta^* > 0.7$ could then have an impact on the extraction of the Jacobian scale factors. The scale factors are computed by removing the events having $\cos\theta^* > 0.7$, and compared to the nominal scale factors. A small difference of about 0.1% in average in the barrel is found. This number is then taken as an uncertainty on these scale factors.

Impact of the MC energy smearing For each η bin, the agreement between the p_T distributions in data and MC is checked, after scaling the energies with the best fitted α_{jac}. Figure 5.37 shows the ratio of the p_T distributions, for the barrel and the endcap, when adding the results of all the bins. A structure around 45 GeV is observed only in the barrel, typical of a resolution effect. The resolutions of data and MC do not agree, as expected (no correction was applied) and create this effect. The impact of the smearing correction is tested, by comparing the Jacobian scale factor extracted with and without the smearing, and how the agreement between the two methods evolves. A small difference of about 0.1% in average in the barrel is found. This number is then taken as an uncertainty on these scale factors.

PDFs The uncertainty on the Z p_T modeling, mainly arises from the uncertainty on the parton distribution functions (PDFs). The set of PDFs involved in the MC used for the study corresponds to the CT10 scheme [183]. The impact of this particular choice on the inter-calibration scale factors is tested rerunning the analysis with a different set of PDFs. The HERAPDF 1.0 [184] set is chosen.

Figure 5.38 shows the impact of the change of PDF set on the electron p_T distribution. No obvious difference is observed.

Here only two sets of PDF are compared. A more accurate study is needed, to fully understand the effect of the PDFs on the result. One could use additional sets of PDFs like MSTW 2008 [79] to pursue the comparison or use the CT10 set alone, playing with the uncertainties on this specific set.

5.6 The $Z \to ee$ lineshape

After the scale factor and smearing correction from the *in situ* calibration are applied respectively to the data and the MC, the final step consists in comparing the $Z \to ee$ lineshape itself in the

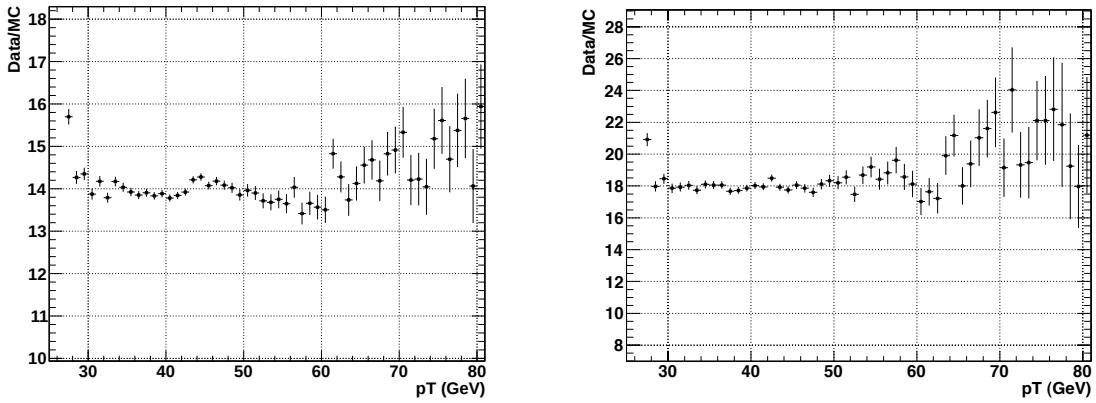

(a) Barrel (b) endcap

Figure 5.37: Ratios of the p_T distributions in data and MC after scaling the energies with the best fitted α_{jac} in barrel (a) and endcap (b), and adding the results of all the η bins. The y axis shows the sum of the individual bins ratio, this is why it is far from 1.

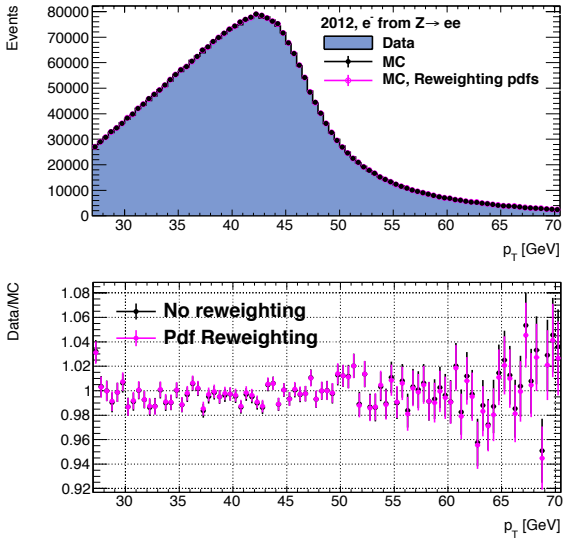

Figure 5.38: Distribution of the electron p_T for the data (blue histogram) and the MC with the set of PDF CT10 (black points) and HERAPDF10 (pink points). The 2012 dataset is used here.

data and the MC. This lineshape can eventually reveal residual discrepancies not addressed by the calibration chain. Figure 5.39 shows the data to MC ratio along the $Z \to ee$ invariant mass after each step of the calibration for the 2011 and 2012 datasets. The agreement between the final lineshapes in data and MC is fairly good in 2011, whereas a 10% discrepancy is seen at low
2795 invariant mass in 2012.

The modification of the low mass tails between the two years is observed only in the MC, the data being stable with time. To understand the origin of this issue, the main modifications to the MC in 2012 are listed below:

- A new electron reconstruction (seeded track, GSF for electrons, crack calibration).

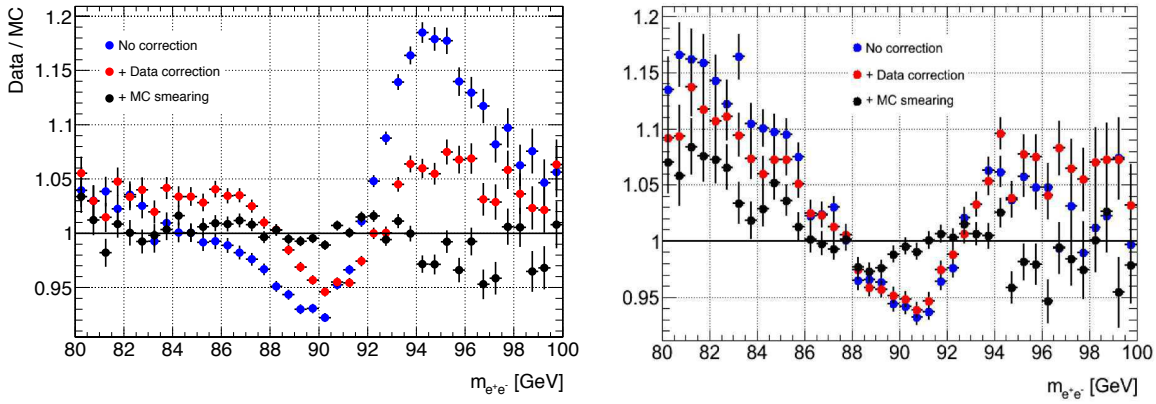

(a) 2011 (b) 2012

Figure 5.39: Data to MC ratio as a function of the $Z \to ee$ invariant mass for the different steps of the calibration: no correction (blue), after the rescaling of the energies in data (red) and the smearing of the energies in the MC (black) for the 2011 [157] (a) and 2012 [185] (b) dataset.

- A larger number of interactions per bunch crossing simulated to follow the increasing pileup in data in 2012.
- A change in GEANT 4 concerning the multiple scattering modeling. An inconsistency was found in the 2011 modeling, leading to unexpected back scattering for high energy electron. The change consisted in removing those unexpected back-scattering events cutting on the angular deflection.

Dedicated MC samples have been produced in order to test separately the impact of these changes.

Pile up The nominal 2011 MC sample is compared with a sample having identical conditions except the pileup, which is not simulated. This allows to test its impact on the lineshape. Figure 5.40(a) shows the invariant mass distribution for these two samples: no obvious discrepancy is seen in particular in the low mass range. In the following, all the MCs used do not contain pileup.

Reconstruction A nominal 2011 MC sample without pileup is compared with a sample having identical conditions except the reconstruction, which corresponds to part of the improved 2012 one (the seeded tracking is not integrated). Changing the reconstruction leads to a shift of the peak position, by around 100 MeV. As this is not the issue being investigated here, this shift is corrected so that the two peaks are aligned. After this alignment, no discrepancy is seen between the two lineshapes, especially in the low mass range, as seen in Figure 5.40(b). The sample with part of the 2012 improved reconstruction is compared with a similar MC where the full 2012 reconstruction is applied, in order to test the impact of the seeded tracking. Figure 5.40(c) shows the comparison of the two lineshapes, and again no obvious effect is noticed.

Multiple Scattering The nominal 2011 MC sample with the old multiple scattering modeling is compared with an identical sample where the new modeling is implemented. A shift of the peak position is induced by this modification, which is corrected so that the two peaks are aligned. Figure 5.40(d) shows the comparison of the two lineshapes after this correction. A

discrepancy of about 10% is seen in the low mass range tails. The 2012 modeling of the multiple scattering yields a reduction of the low mass tails with respect to the 2011 modeling.

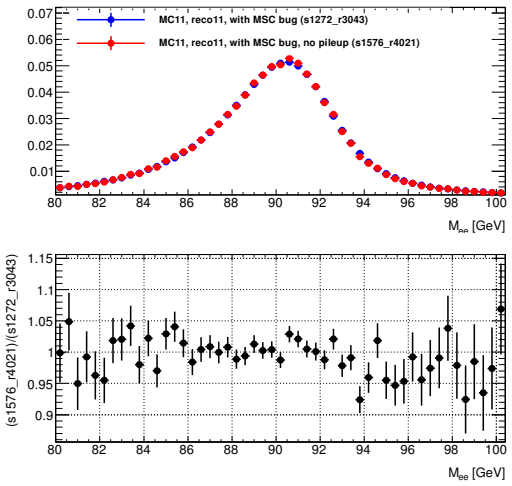

(a) Pileup

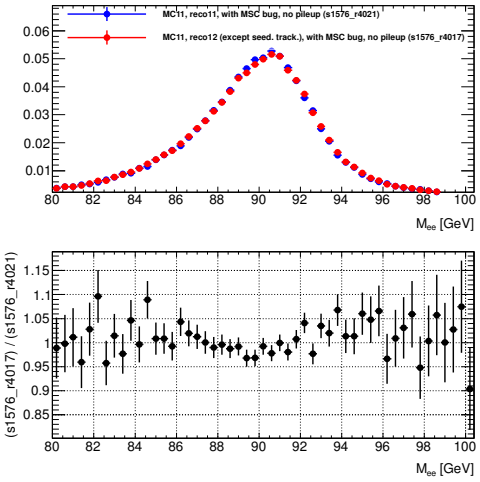

(b) Reconstruction (without seeded tracking)

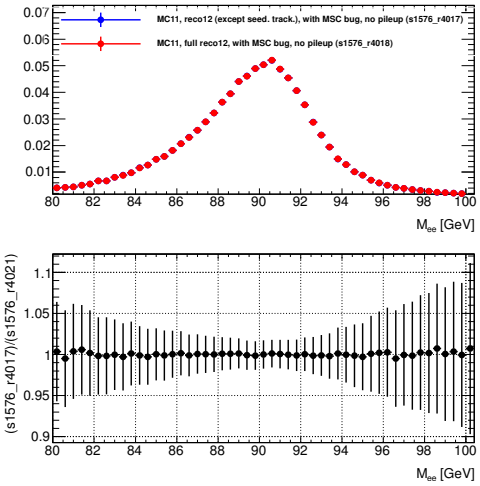

(c) Reconstruction (with seeded tracking)

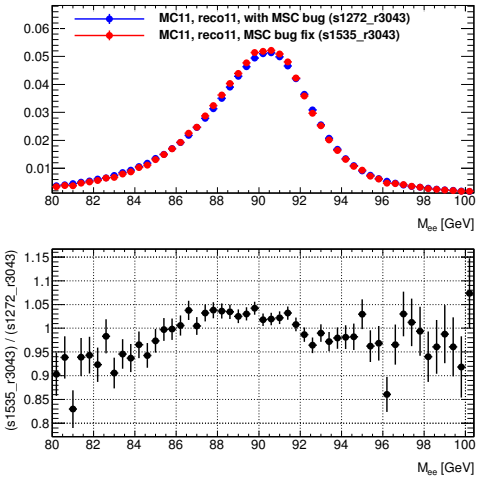

(d) Multiple Scattering

Figure 5.40: $Z \rightarrow ee$ invariant mass distributions for different configurations of the MC (see text) and ratio as a function of the invariant mass.

Two possibilities are tested in the following to explain the difference between the 2011 and 2012 MC:

1 The angular cut introduced in the multiple scattering modeling in 2012 removes artificially a fraction of the low mass tails and creates a discrepancy of $\sim +10\%$ with respect to the data in this region.

2 Not introducing this angular cut leads to a wrong modeling of the lineshape, with too much low mass tails with respect to the data. However another effect with similar size and opposite sign would have to be present to compensate it and make the agreement good

as seen in Figure 5.39(a). For example, a mismodeling of the material could create such tails. This compensation effect would have to be constant in time.

Figure 5.41 illustrates schematically these two configurations.

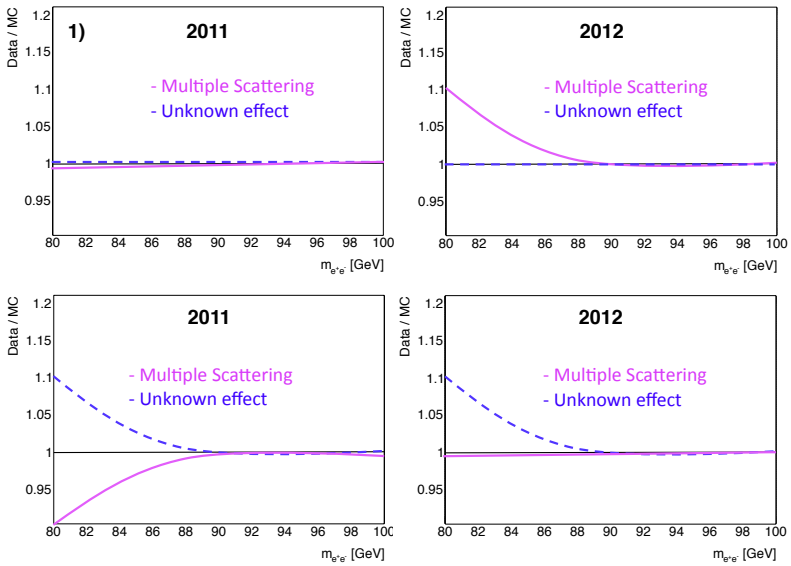

Figure 5.41: Schematic view of the data over MC ratio for the 2011 (left) and 2012 (right) samples, for the two options (top and bottom) considered in the text to explain the discrepancy in the tails in the low mass range, playing with the multiple scattering effect (pink, plain line) and with another unknown effect (blue dashed line).

5.6.1 Multiple scattering modeling

The simulation of the multiple scattering process in 2011 in GEANT 4 is covered by the URBAN93 framework. In order to understand the origin of the backscattering issue, many checks were performed. A numerical instability possibly causing this problem was found and corrected and the angular cut introduced initially was consequently removed. The checks have highlighted the existence of another problem: as the step size in gas become smaller, the scattering angle becomes larger, that is an unexpected feature (defect of the model for small steps in gas). Another correction was included, correcting for this effect by introducing a cut on the parameter that governs the large angular deflection [186].

In order to test the impact of these new fixes on the $Z \rightarrow ee$ lineshape, and to test the robustness of the multiple scattering modeling, special MC simulations were generated, for the $Z \rightarrow ee$ process. All these simulations have no pileup, and use the reconstruction designed in 2011, but different versions of GEANT 4. Two simulations use the nominal GEANT4 versions used in 2011 and 2012 and are called *mc11-like* and *mc12-like*.

An alternative multiple scattering model has been also tested, covered by the URBAN 95 framework (in the nominal version, the framework used is URBAN 93). In addition, a new relativistic modeling for the bremsstrahlung (based on the Seltzer-Berger model [187]) and a new model for the conversion process has been also tested. These two changes are called in

the following BremConv95. The old modeling of bremsstrahlung and conversion is called BremConv93.

The $Z \to ee$ invariant mass distribution is built from all the simulations described above, after the usual selection of the events as described in Section 5.3.1. These distributions are shown in Figure 5.42 top. To compare the low mass tails, the ratios of all the lineshapes to the *mc11-like* simulation is done and shown in Figure 5.42 bottom.

These ratios show a discrepancy at low mass for all the simulations with respect to the *mc11-like* one, even if attenuated using the Urban 93 model associated with the BremConv95 one.

The correction of the numerical instability and of the problematic model for small steps in gas did not modify the lineshape.

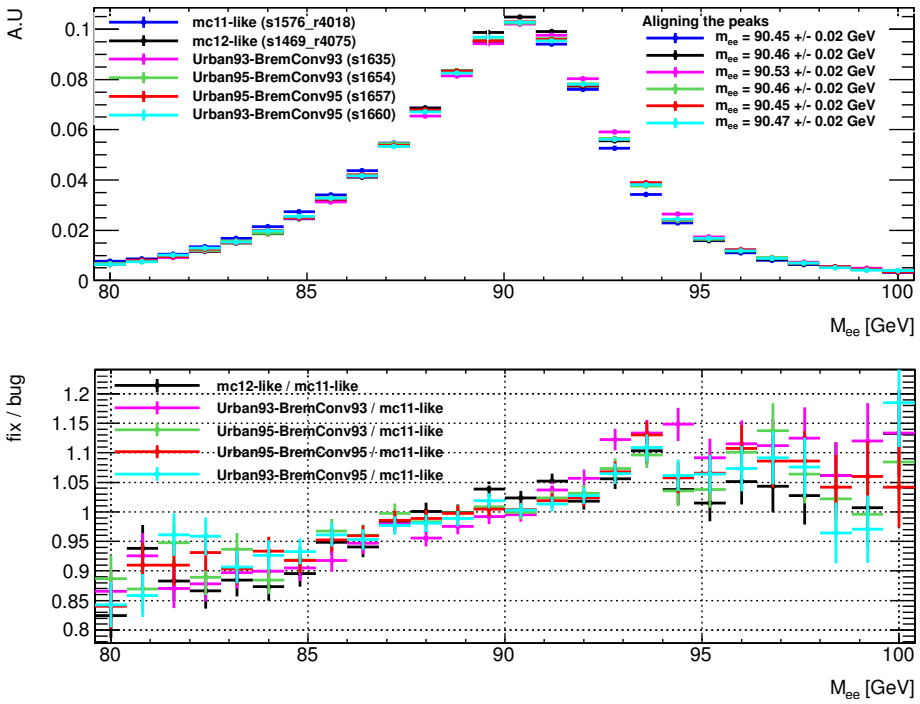

Figure 5.42: $Z \to ee$ invariant mass for the nominal 2011 (blue line) and 2012 MC (black). The other distributions corresponds to alternative versions of Geant4 as explained in the text.

This study has demonstrated a good stability of the multiple scattering modeling in term of its impact on the lineshape.

5.6.2 Other effects

In the previous section, the impact of multiple scattering modeling modifications on the lineshape has been shown to be negligible, after the correction of the numerical instability. The second scenario is thus tested in the following.

The impact of a material mismodeling on the lineshape is tested. The lineshapes of a MC with additional material in the inner detector and in the calorimeter (following the G' configuration, see Table 5.6) and of the nominal MC are compared in Figure 5.43. The MC with the distorted geometry is treated as pseudo-data and energy scale factor and smearing corrections are derived from the comparison to the nominal MC following the method described in Section 5.3.3. The

different steps of the calibrations are shown in this figure. After all the corrections are applied, an effect of around 10% in the low mass tails is visible in the ratio between the distorted and nominal lineshapes.

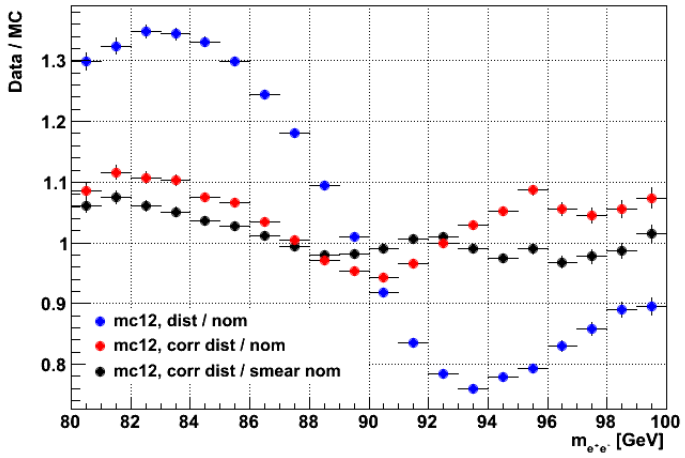

Figure 5.43: Ratios between a distorted and nominal MC lineshapes from the $Z \rightarrow ee$ invariant mass, using the 2012 dataset. The different calibrations steps are shown: no correction (blue dots), after applying the energy scale factor in the distorted MC (red dots) and applying also the smearing correction in the nominal MC (black dots) [185].

If the data have additional material in some regions one could thus expect an increasing of the low mass tails. However the amount of material added in the distorted MC is very large, and many studies have shown the data to be quite similar to the nominal MC except in some localized regions (see Chapter 6). Some other effects are expected to have an impact on the lineshape. Among them, the layer inter-calibration will be tested in Section 5.8, after a full measurement of the relative layers scales which will be discussed in Sections 5.7.1 and 5.7.2.

5.7 The layer inter-calibration

The electromagnetic calorimeter is divided into three layers and a presampler. The inter-calibration of these four layers is necessary before any more global calibration, using the energy fractions in these layers, is done.

5.7.1 The presampler calibration

The presampler layer is a system which is mainly used to recover the energy lost in front of the accordion and is a separated layer independent of the accordion system. An inter-calibration between this layer and the accordion is needed.

The presampler energy scale is defined as the ratio between the data and the MC of the energy deposited in the presampler layer. However, due to the sensitivity of the presampler to the material, a bias on this ratio could come from different sources:

- A material mismodeling in the MC
- A presampler energy scale difference between data and MC

These two effects can be decorrelated using an extra variable, also sensitive to material mismodeling. The variable chosen is E_1/E_2, corresponding to the ratio of energy deposited in the first and second sampling of the accordion. It was shown in Chapter 6 to be very powerful in probing the material distribution. Figure 5.44 shows the response of the presampler energy and E_1/E_2 in data compared to the nominal MC, as a function of pseudorapidity. The responses are clearly correlated. This variable has been also chosen because the E_1 and E_2 energies have been shown to be quite well modeled from tests with cosmic muons [174].

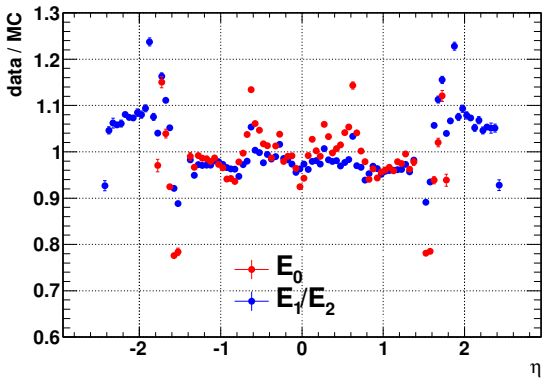

Figure 5.44: Comparison between the data over MC ratios for the presampler energy (red line) and for the E_1/E_2 variable (blue line) as a function of the pseudorapidity for $Z \rightarrow ee$ events.

5.7.1.1 E_0 and E_1/E_2 correlation

The correlation between the presampler energy E_0 and E_1/E_2 is investigated using simulations with additional material in different places of the detector.

Table 5.6 gives the characteristic of these different simulations. Different kind of geometries are used, with additional material:

1) In the Inner Detector,

2) Just before the calorimeter in the cryostat,

3) Between the presampler and the accordion,

4) Just after the calorimeter, in the cryostat.

The energy deposited in the presampler is only sensitive to material added before this detector (categories 1 and 2). The energy deposited in the layers 1 and 2 is only sensitive to material added before the accordion (categories 1, 2 and 3). A bias is therefore expected from this method, due to the third geometry category, that is not seen by both variables. An uncertainty will be derived for this.

The analysis is performed in pseudorapidity bins, as the material distribution varies rapidly with this variable. The binning used is similar to the one used for the *in situ* method:

$$0, 0.2, 0.4, 0.6, 0.7, 0.8, 0.9, 1.0, 1.1, 1.2, 1.3, 1.37, 1.55, 1.63, 1.74, 1.8$$

excluding the complicated transition region $[1.37, 1.55]$ and averaging the positive and negative sides.

Table 5.6: Fraction of radiation lengths (X_0) added in various places of the detectors, for the different MC geometries configurations. The different places are in the whole Inner Detector (ID), in the pixel or SCT services (Pixel S, SCT S), at the end of SCT/TRT endcaps (SCT/TRT EC), in the Inner Detector end-plate (ID e.p), in the pixels or SCT only (Pixel, SCT), radially in barrel cryostat before the calorimeter (Cryost. 1), radially between the presampler and the strips in barrel (PS/S1), and radially in the cryostat after the barrel calorimeter (Cryost. 2).

Config.	ID	Pixel S.	SCT S.	SCT/TRT EC	ID e.p	Pixel	SCT	Cryost. 1	PS/S1	Cryost. 2
A (16-02)	5%	-	-	-	-	-	-	-	-	-
B (16-03)	10%	-	-	-	-	-	-	-	-	-
C (16-04)	-	20%	-	-	-	-	-	-	-	-
D (16-05)	-	-	20%	-	-	-	-	-	-	-
E (16-06)	-	-	-	15%	-	-	-	-	-	-
F (16-07)	-	-	-	-	15%	-	-	-	-	-
G' (16-11)	5%	20%	20%	15%	15%	-	-	0.1	0.05	0.1
I' (16-12)	5%	20%	20%	15%	-	-	-	-	-	-
J (16-13)	-	-	-	-	-	5%	-	-	-	-
K (16-14)	-	-	-	-	-	-	5%	-	-	-
L (16-15)	-	-	-	-	-	-	-	0.1	-	-
M (16-16)	-	-	-	-	-	-	-	-	0.05	-

For each of these bins, for the data and for the different distorted MC geometries, the distribution of the E_0 and E_1/E_2 variables are made, and their means are extracted: E_0^{data}, E_0^{dist}, $(E_1/E_2)^{data}$, $(E_1/E_2)^{dist}$. The ratios with the mean extracted from the nominal MC geometry: E_0^{nom}, $(E_1/E_2)^{nom}$, are computed. In order not to be influenced by the MC-based calibration, the uncalibrated (raw) energies, are used.

Figure 5.45 shows the ratios, simultaneously for the two variables and for the representative bin $1.0 < |\eta| < 1.1$.

In this figure, the geometries belonging to the categories 1 and 2 are depicted with full circles, whereas the ones belonging to the categories 3 and 4 are depicted with empty circles. The data are depicted with the green diamond.

A linear correlation is observed between the two variables, for all the geometries used. The slope is the same for the two kind of geometries illustrated, even if the second one is shifted by $\delta(E_1/E_2) = 3\%$ along the $(E_1/E_2)/(E_1/E_2)^{nom}$ axis, as expected (the energy in presampler is insensitive to this kind of material). The same behaviour is observed for all the other bins.

The correlation between the two variables is then expressed as:

$$\frac{E_0}{E_0^{nom}} = 1 + A \cdot \left(\frac{E_1/E_2}{(E_1/E_2)^{nom}} - 1\right) \tag{5.7}$$

for the different geometries, with A the slope fitted through the points representing the geometries with material *before* the presampler.

If the presampler energy scale in MC is well simulated, the data point should be aligned with the other geometries. The difference, illustrated in the figure with the green arrow, is interpreted as coming from a different energy scale in data and MC.

More analytically, the ratio of the presampler energy observed to the one predicted is written:

$$\frac{E_0^{data,\,obs}}{E_0^{nom}} = \frac{E_0^{data,\,mat.}}{E_0^{nom}} \cdot \frac{E_0^{data,\,calib}}{E_0^{nom}} = \alpha_{mat}^{PS} \cdot \alpha_{calib}^{PS}$$

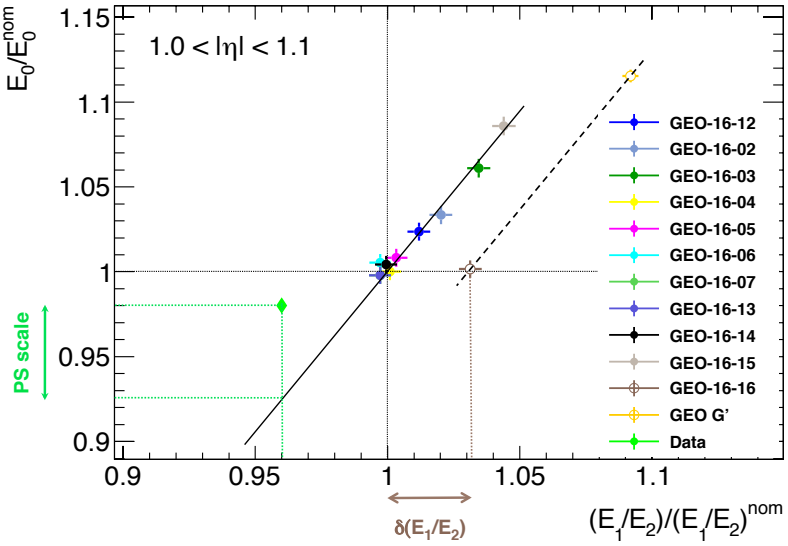

Figure 5.45: Ratio of the mean of the presampler energy distribution in data or in distorted MC geometries over the nominal MC as a function of the same ratio for the E_1/E_2 variable, using $Z \rightarrow ee$ events, for the bin $1.0 < \eta < 1.1$.

where α^{PS}_{mat} and α^{PS}_{calib} are the presampler energy response in data only due to material mismodeling and presampler scale mismodeling respectively.

Similarly, one can write:

$$\frac{(E_1/E_2)^{data,\,obs}}{(E_1/E_2)^{nom}} = \frac{(E_1/E_2)^{data,\,mat.}}{(E_1/E_2)^{nom}} \cdot \frac{(E_1/E_2)^{data,\,calib}}{(E_1/E_2)^{nom}} = \alpha^{E12}_{mat} \cdot \alpha^{E12}_{calib}$$

with α^{E12}_{mat} and α^{E12}_{calib} the E_1/E_2 energy response in data only due to material mismodeling and to inter-calibration between the first and second layer respectively.

From Equation 5.7, one can write:

$$\alpha^{PS}_{mat} = 1 + A \cdot (\alpha^{E12}_{mat} - 1)$$

Given that:

$$\alpha^{PS}_{calib} = \frac{E_0^{data,\,obs}}{E_0^{nom}} \cdot \frac{1}{\alpha^{PS}_{mat}}$$

and that

$$\alpha^{E12}_{mat} = \frac{(E_1/E_2)^{data,\,obs}}{(E_1/E_2)^{nom}} \cdot \frac{1}{\alpha^{E12}_{calib}}$$

one gets finally:

$$\alpha^{PS}_{calib} = \frac{E_0^{data,\,obs}}{E_0^{nom}} \cdot \frac{1}{1 + A \cdot (\frac{(E_1/E_2)^{data,\,obs}}{(E_1/E_2)^{nom}} \cdot \frac{1}{\alpha^{E12}_{calib}} - 1)} \tag{5.8}$$

In this equation, all the quantities are measurable directly from Figure **??**, except α^{E12}_{calib} which represents the inter-calibration difference between data and MC of the layers 1 and 2. This quantity can be determined with an separate study which is presented below.

5.7.1.2 The E_1/E_2 modeling

Despite the good agreement between data and MC of the E_1/E_2 response found during the test beams, a study is done to determine more precisely the quantity α_{calib}^{E12}.

In order to test only the relative layer scales and to be insensitive to the material before the accordion, a sample of radiative unconverted photons is used. The unconverted photon are such that the conversion radius is larger than 800 mm, ensuring a non-interaction with the material up to this radius. In addition the transverse energy deposited in the presampler is required to be below 0.5 GeV, reducing strongly the number of events having interacted with material upstream the presampler [4].

The fraction E_1/E_2 for these photons is compared between the data and MC. This ratio should be only sensitive to the relative layer scale.

Figure 5.46 shows this ratio as a function of the pseudorapidity.

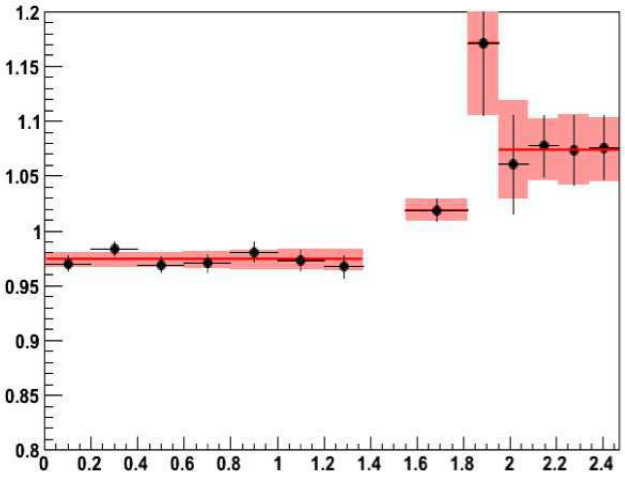

Figure 5.46: E_1/E_2 comparison between data and MC for radiative unconverted photons with low energy deposited in the PS as a function of the pseudorapidity of the photons for the 2011 and 2012 datasets. The red lines corresponds to a linear fit of the points in large η regions and the red filled regions the uncertainties on this fit.

A relative E_1/E_2 scale different from 1 for the data to MC comparison is observed everywhere, leading to around -3% in the barrel, +2% in the region $1.55 < |\eta| < 1.8$ and +7% in the end of the endcap. There is a point where the data/MC ratio differs from 1 by 17% at $|\eta| \sim 1.9$. These numbers are used for the presampler scale measurement. The uncertainties on these values are estimated below.

5.7.1.3 Uncertainties on E_1/E_2 modeling

Three different sources of uncertainties arise from the measurement of α_{calib}^{E12}:

1) The statistical error.

2) The uncertainty on the purity of the sample used: if converted photons contaminate it, this can leads to a bias on the E_1/E_2 response due to material effects.

[4] This selection does not allow to remove events having interacted with material located between the presampler and the strips

3) The uncertainty on the material after the PS.

Uncertainty from material before presampler This uncertainty is evaluated using simulated single photon events with additional material only before the presampler, typically the configuration L defined in Table 5.6. In this configuration the material is added in the cryostat just before the PS. The same selection as the one described previously is made, in order to select only photons interacting very little with the material. The distorted to nominal MC ratio of the variable E_1/E_2 is shown in Figure 5.47(a) as a function of the pseudorapidity in three large bins (barrel, $1.55 < |\eta| < 1.8$ and end of the endcap). Two kind of photons are shown: ones having the cut on the PS energy $E_{PS,T} < 0.5$ GeV and the others with this constraint inverted. The value of E_1/E_2 from a single electrons MC simulation is overlaid as a comparison. No cut on the presampler energy is done on these electrons, as this removes the majority of the events. This figure shows that the cut on the PS energy for photons is efficient in reducing material effects. A residual effect is however observed for these events, that is interpreted as the impact of the contamination of converted photons in the sample. The effect is around 0.5% and taken as an uncertainty on the α^{E12}_{calib} variable.

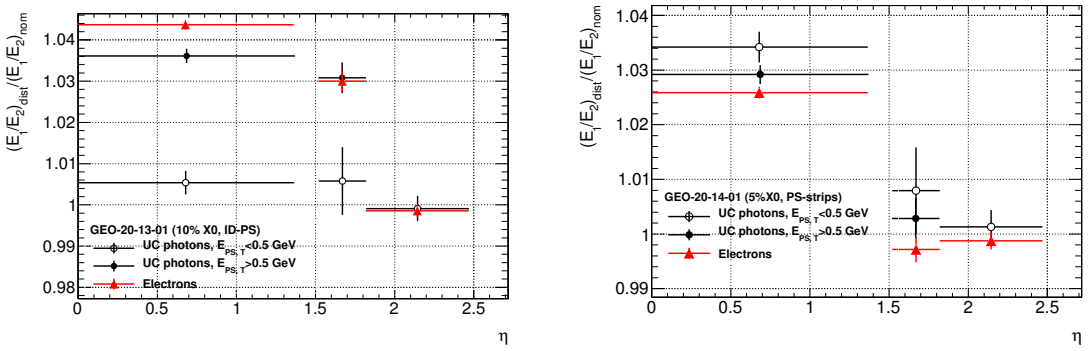

(a) Material before PS

(b) Material between PS and strips

Figure 5.47: Distorted over nominal MC ratio for the variable E_1/E_2 as a function of the pseudorapidity with the distorted geometry corresponding to additional material in cryostat before the presampler (a) or between the presampler and the strips (b). Three different populations are depicted: single unconverted photons with the cut $E_{0,T} < 0.5$ GeV (black open circles), or $E_{0,T} > 0.5$ GeV (black full circles) and single electrons (red triangles).

Uncertainty from material between presampler and strips The presence of material just after the presampler could bias the measurement of the layer inter-calibration. For the presampler scale measurement, the dependence of E_1/E_2 to this late material is already contained in the ratio $\frac{(E_1/E_2)^{data,\,obs}}{(E_1/E_2)^{nom}}$ as seen in Equation 5.8. The variable α^{E12}_{calib} estimated with the method presented above, also indirectly measures the contribution of such material. From Equation 5.8, one can thus see that this dependence washes out. In reality, one needs to take into account the difference of response between radiative unconverted photons and electrons from $Z \to ee$.

Again this is achieved with a MC with a distorted geometry where material is added only between the presampler and the strips (see configuration M in Table 5.6).

Figure 5.47(b) shows the ratio of the distorted MC response to the nominal one for the E_1/E_2 variable for single unconverted photons with a cut on presampler transverse energy. This is compared with the single electrons without cut on the presampler energy. The difference along

the pseudorapidity is at worst around 1%. This difference is taken as an uncertainty coming from material located after the presampler.

5.7.1.4 Presampler energy scale

All the quantities from Equation 5.8 are now determined. Figure 5.48 shows the variable α_{calib}^{PS} as a function of the pseudorapidity. The binning used correspond to $\Delta\eta = 0.05$. The uncertainties coming from the statistical errors and the uncertainty on the α_{calib}^{E12} measurement are also depicted. Two different results are presented: using a fitted estimation of the variable α_{calib}^{E12} as seen in Figure **??** in large η regions or using the values determined in each η-bin. This has an impact on the presampler scale shape along η, but the results are compatible within the uncertainties. Using the unfitted evaluation, the presampler scale is flattened in the barrel. The typical values of this scale are around -2% in the barrel and -14% in the endcap. The uncertainty in the barrel and endcap is typically 3%. The presampler is composed of 16 modules (14 modules of size $\Delta\eta = 0.2$ in the barrel and 2 modules of size $\Delta\eta = 0.3$ in the endcap). The energy scale is thus extracted in each modules. Within a presampler module, the energy scales evaluated with a binning of 0.05 well agree each other, except in the endcap.

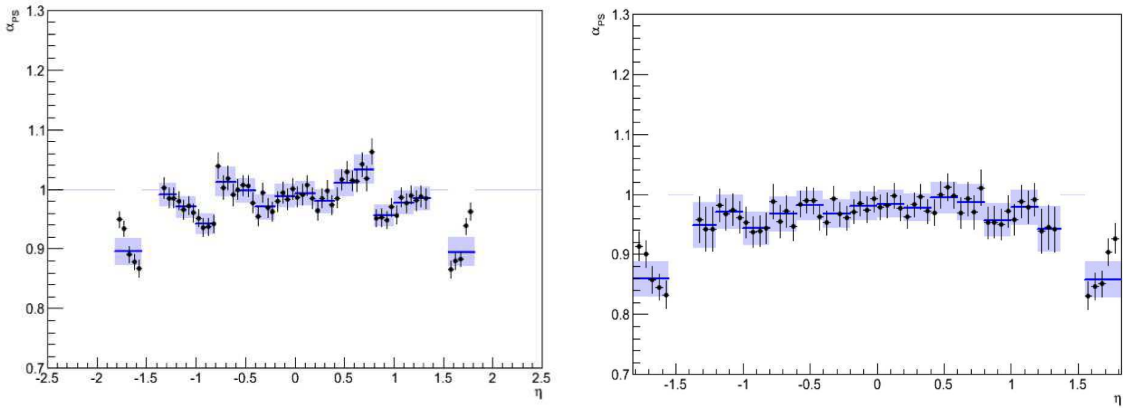

(a) Fitted α_{calib}^{E12} (b) Unfitted α_{calib}^{E12}

Figure 5.48: Presampler energy scale in the data, as a function of the pseudorapidity for electrons from the $Z \rightarrow ee$ decay using a fitted (a) or unfitted (b) estimation of the variable α_{calib}^{E12}. The blue line corresponds to the fit through presampler modules and the blue band corresponds to the uncertainty.

Figure 5.49(a) shows the ratios $\frac{E_0^{data,\,obs}}{E_0^{nom}}$ and $\frac{E_0^{data,\,calib}}{E_0^{nom}}$, corresponding to the data to MC ratio of the presampler energy before and after the material correction. In this plot, no miscalibration of the E_1/E_2 in the data is assumed. The difference between this figure and Figure 5.48 shows therefore the impact of the inter-calibration of the layers 1 and 2 on the measurement of the presampler energy scale. Figure 5.49(b) illustrates the material correction itself, i.e $\frac{E_0^{data,\,mat.}}{E_0^{nom}}$. It is an indirect representation of the mismodeling of the material in the nominal MC.

5.7.2 The strip/middle inter-calibration

The different accordion layers may have different energy scale due to longitudinal cross talk and imperfect determination of the electronic calibration. In Section 5.3.5.2, it has been shown that only the inter-calibration between the first and second layer is relevant.

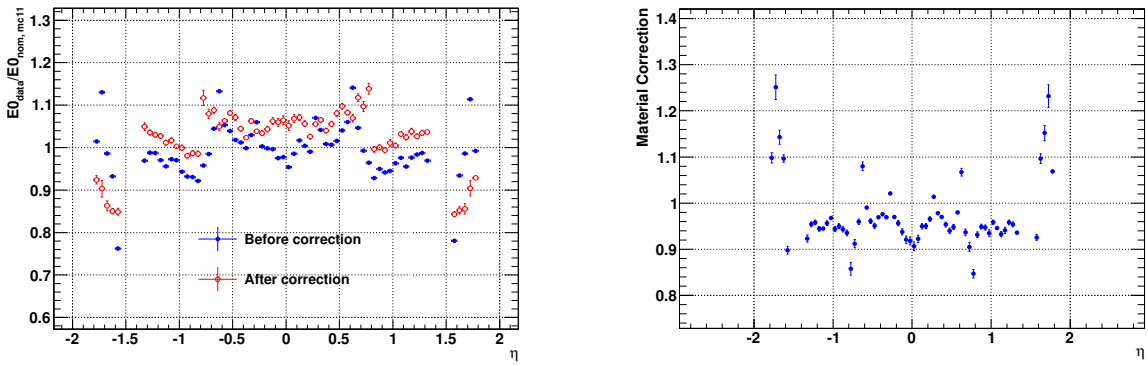

(a) (b)

Figure 5.49: (a) Data to MC ratio of the presampler energy before (blue full circles) and after (red empty circles) the material correction, as a function of the pseudorapidity for electrons from the $Z \to ee$ decay and assuming $\alpha_{calib}^{E12} = 1$. (b) Material correction as a function of the pseudorapidity.

This inter-calibration has been already measured in Section 5.7.1.2, using unconverted photons interacting little with the material as it was needed for the presampler calibration. However, this method suffers from the uncertainty on the material located after the presampler. This uncertainty was factorized and eliminated in the presampler scale measurement, but for the layer inter-calibration this cannot be done.

Other methods free from such material effects are used to probe this inter-calibration. The one presented here relies on the dependence of the Z invariant mass to the fraction E_1/E_2.

5.7.2.1 Invariant mass method

Method The ratio E_1/E_2 is related to the amount of energy lost upstream of the calorimeter and then to a quantity like the $Z \to ee$ invariant mass. A nominal MC simulating the $Z \to ee$ process and the 2012 datasets are used in this study. The Z candidates are selected as described in Section 5.3.3.

Figure 5.50(b) shows the correlation between the invariant mass of the events selected and the variable E_1/E_2 for the representative bin $0.4 < |\eta| < 0.6$. The analysis is performed in all the other regions with the binning:

$$0, 0.2, 0.4, 0.6, 0.8, 1.0, 1.2, 1.37, 1.52, 1.8, 1.9, 2.1, 2.3, 2.47$$

The data over MC ratio should be stable against the variation of E_1/E_2, if the MC well simulates the data. This is not the case, as seen in Figure 5.50(c), where the ratio decreases as a function of E_1/E_2.

The origin of this mismodeling may be:

- A material mismodeling: a MC simulating the $Z \to ee$ process with additional material following the configuration G' (see Table 5.6) is used to test this possibility. The distorted to nominal MC ratio for the invariant mass is shown in Figure **??**. It is stable against E_1/E_2 so that it cannot be the cause of the effect observed in the data to MC ratio.

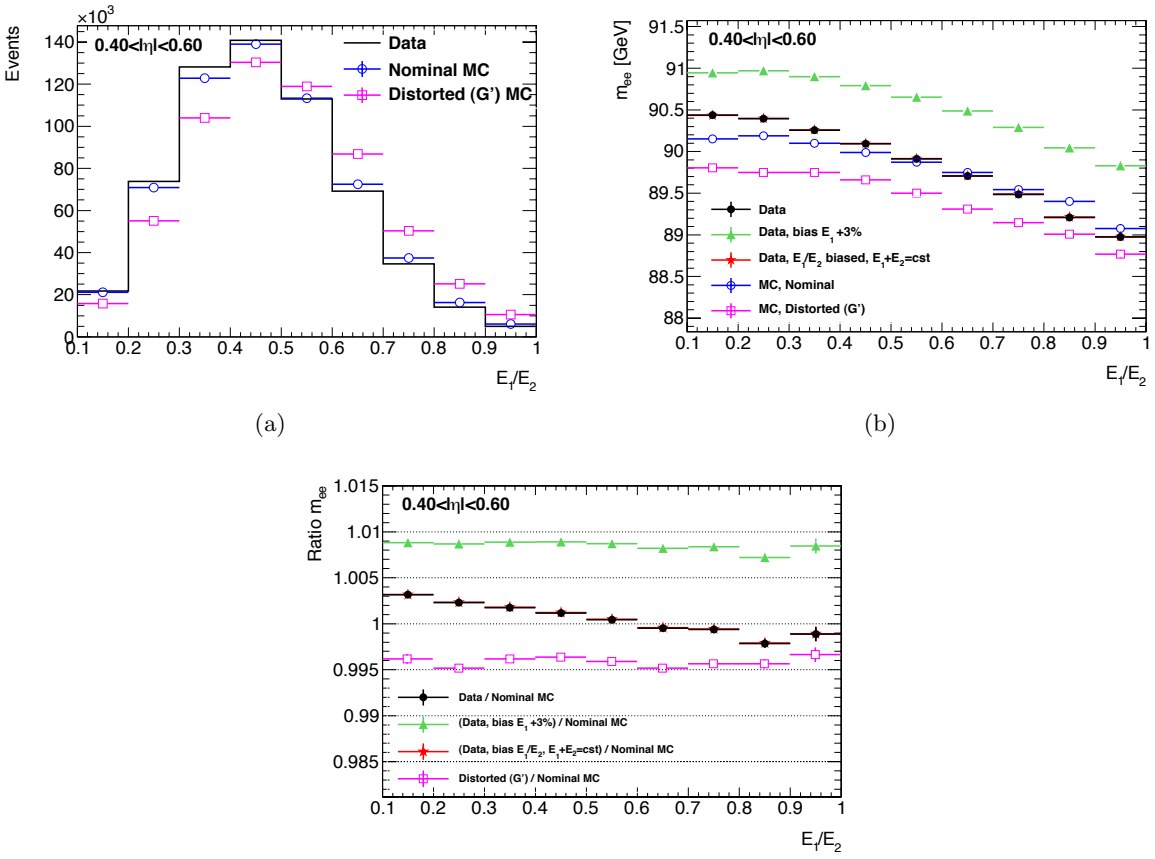

Figure 5.50: (a) E_1/E_2 distribution for the data (black histogram), the nominal MC (blue open circles) and the MC with additional geometry following configuration G' (pink open squares). (b) $Z \rightarrow ee$ invariant mass as a function of E_1/E_2 for the data (black points), the nominal MC (blue open circles), the MC with additional geometry following configuration G' (pink open squares), the data with a 3% scale of the strips energy keeping (red stars) or not (green triangles) the sum of strips and middle energy constant. (c) Ratios of the previous curves to the nominal MC one. The bin shown is $0.4 < |\eta| < 0.6$.

- A layer 1 and 2 relative miscalibration as seen in Section 5.7.1.2: this is tested by an arbitrary rescaling of the strips energy by +3%. The MC-based calibration described in Section 5.2 is rerun because the scaling of the strip energy changes the repartition of the total energy in the different layers. Only an approximative calibration is performed, using a dedicated tool (Offline Calibration Tool [188]). The resulting energy is used to compute the invariant mass, which is compared to the one in the nominal MC. As seen in Figure **??**, the scaling of the strip layer energy has an impact on the MC description of the evolution of the invariant mass with E_1/E_2. Therefore this could be at the origin of the effect seen in the data to MC ratio.

- Cross talk between the strips and middle layers: this can be probed using the procedure described in the previous item, requiring in addition that the sum of the layer 1 and 2 energies be constant, to describe a transfer of energy between these two layers. The ratio of the resulting invariant mass, recomputed using the same calibration tool, to the mass

from the nominal MC is shown in Figure **??**. It is not different from the simple data over MC ratio. The discrepancy between data and MC can therefore not be explained by a cross talk effect.

The method is therefore sensitive to layer inter-calibration, and is free from effects like cross-talk or material mismodeling.

The inter-calibration between the two layers is measured by varying the strip energy scale α_1 from 0.89 to 1.16 in 0.01 steps, leaving the middle layer energy unchanged. For each variation of α_1, the procedure explained above is repeated. A χ^2 minimization is done to find the best value of α_1 that renders the invariant mass data to MC ratio the most compatible with a flat line. The χ^2 as a function of the factor α_1 is fitted with a parabola whose minimum and width give the best value of α_1 and its statistical uncertainty.

The result of this minimization for all the η bins is shown in Figure 5.51(a).

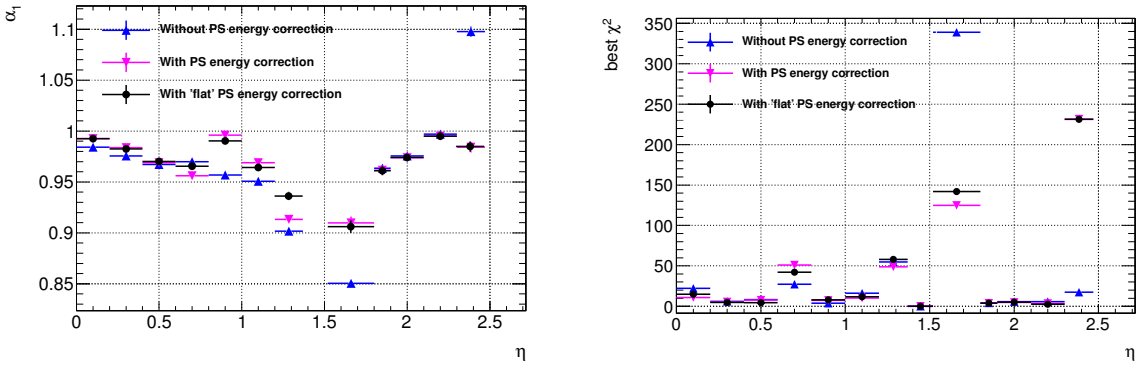

(a) (b)

Figure 5.51: Strip/middle inter-calibration (a) and best fitted χ^2 associated to this inter-calibration when the presampler scale is not corrected (blue up triangles), when it is corrected using a fitted (pink down triangles) or unfitted (black dots) estimation of the variable α_{calib}^{E12} as a function of the pseudorapidity for electrons from the $Z \to ee$ decay.

In addition, the impact of the presampler calibration is tested: the two sets of presampler scale factors derived in the Section 5.7.1.4 are used to correct for the presampler energy. As for the scaling of the strip energy, the approached MC-based calibration tool is used. The full procedure presented above is rerun with this correction.

Figure 5.51(a) presents the comparison with the case where no PS correction is made. This has a large impact in the endcap, where the presampler scale factor is around 14% and a small effect in the barrel up to $|\eta| = 0.8$. For $|\eta| > 0.8$ the impact is slightly larger.

The two different sets of presampler scale give compatible results except in the bin $1.2 < |\eta| < 1.37$.

Figure 5.51(b) shows the best fitted χ^2 associated to the strip scale extracted. This shows up pathological regions, where this number is very large, indicating that no appropriate scale factor for the strips was found to flatten the data to MC ratio. This is the case for the regions $1.5 < |\eta| < 1.8$ and $2.3 < |\eta| < 2.47$.

In the barrel, the E_1/E_2 inter-calibration results are similar to the ones found with the unconverted radiative photons. However the measured inter-calibration from the photons was

flat in this region which is not the case with the present method. More particularly, a step at $\eta = 0.8$ is seen.

In the endcap, the two methods disagree.

Systematic The systematic uncertainties associated with this method are evaluated below. First the robustness of the method is tested by closure. The nominal MC is treated as pseudo-data and the full analysis is rerun with it. The result is shown in Figure 5.52(a). The biggest deviations are around 1%. This number is taken as an uncertainty coming from the method.

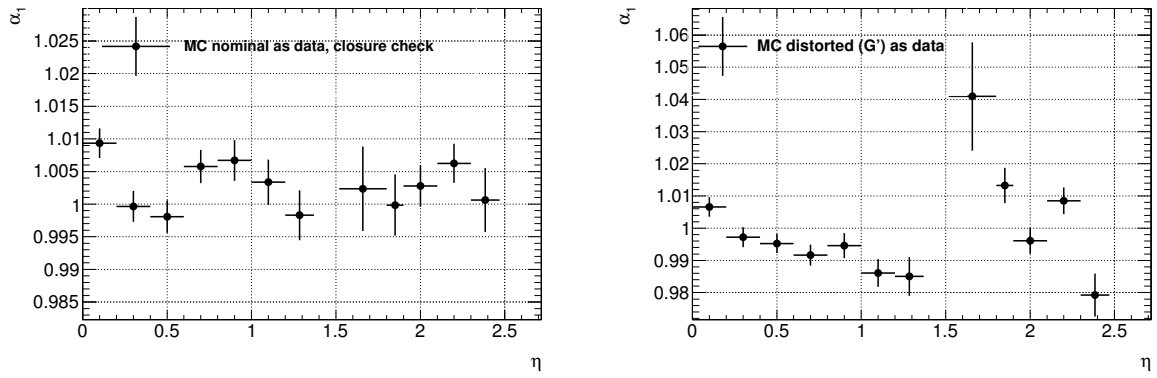

(a) (b)

Figure 5.52: (a) Closure check for the method, using a nominal MC as pseudo-data. (b) Evaluation of the impact of the material mismodeling in the layer intercalibration, using a distorted geometry following the configuration G' as pseudo-data.

The second test concerns the material mismodeling. Even though the method is found to be insensitive to the presence of extra-material, the full analysis is rerun with the distorted MC geometry following configuration G' treated as the pseudo-data. The result is shown in Figure 5.52(b). In the barrel and in the endcap with $\eta > 1.8$, the closure works well, and the biggest deviations are 1.5% and 2% respectively. In the region $1.52 < \eta < 1.8$, a larger deviation of $\sim 4\%$ is found. These three numbers are taken as an uncertainty coming from material mismodeling.

As seen from Figure 5.51(b), this particular region is complicated, the method fails to find an appropriate scale factor.

5.7.2.2 Comparison of the results

This method is compared with two other procedures:

- The same analysis is rerun, using the variable E/p as a probe instead of the $Z \to ee$ invariant mass. However this method is effective only in the barrel, as the track measurement is less accurate in the endcap, especially for large E_1/E_2 fractions.

- The muons traversing the detector are insensitive to the material. The energy loss in the calorimeter is used as a direct probe of the layer scales. The ratio E_1/E_2 provides directly a measurement of the the layer strip/middle inter-calibration. However, due to very low fraction of energy loss in the calorimeter, this method is sensitive to cross talk and

electronic noise. Two different methods to extract the mean of the energy loss distribution are tried: using a convoluted fit of a Landau and a Gaussian function or a truncated mean estimator from 50% to 90%.

The results obtained with all the methods are overlaid and shown in Figure 5.53.

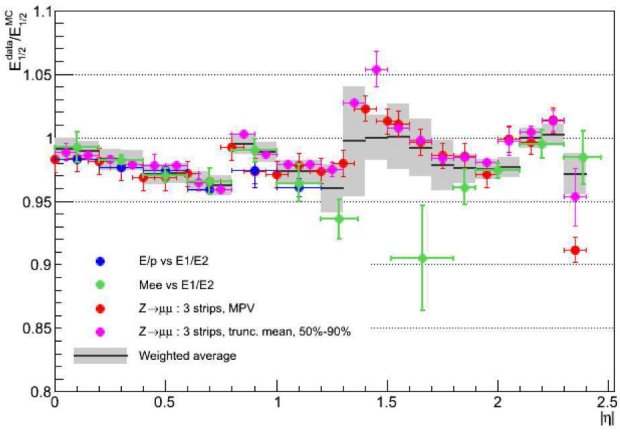

Figure 5.53: Relative layer 1 and 2 calibration as a function of the pseudorapidity of the probe, as measured with different methods. The black horizontal lines and grey filled area correspond to the weighted average with a χ^2 penalty of all the methods and the associated uncertainty.

All the methods agree well in the barrel and in the endcap except in the bins $1.2 < |\eta| < 1.4$ and $1.5 < |\eta| < 1.8$ for the invariant mass method. The structure is the same, especially the step at $\eta = 0.8$. In this figure, all the statistic and systematic errors for the different methods are shown. The precision on the layer relative scale is around 1-4% depending on the region. The difference between the result found with these methods and the one found with unconverted radiative photons can be interpreted as an effect of material located after the presampler.

5.8 $Z \to ee$ lineshape after layer inter-calibration

As discussed in Section 5.6, it has been found that the discrepancy observed in the $Z \to ee$ lineshape might be due to material mismodeling. However, from the actual knowledge of the material distribution in the data (see Chapter 6), this source is not sufficient to explain the full discrepancy. In this section other possibilities are investigated. In particular, the layer miscalibration that has been measured in Sections 5.7.1 and 5.7.2 is tested.

Figure 5.54 shows the impact on the lineshape of rescaling the presampler and strips energy according to their energy scale measured previously. For the strips rescaling, two options are tested: the sum of of the strip and middle energies are kept constant or not. From this figure, it can be seen that only the modification of the presampler scale has a sizeable impact on the low mass tails: around 5% more tails are expected when applying the scale modification. This goes in the right direction to explain the discrepancy seen in data.

However, the presampler extends only up to $|\eta = 1.8|$ so that it is not expected to be the only source. A test has been made to estimate the effect of the strip miscalibration and the material mismodeling in the region $|\eta| > 1.8$.

The discrepancy observed in the lineshape as seen in Figure 5.39 has been derived from an inclusive sample (no η selection). It has been then first checked that selecting exclusively events in the region $|\eta| > 1.8$ gives a similar effect. A study has shown that 10% more low mass tails

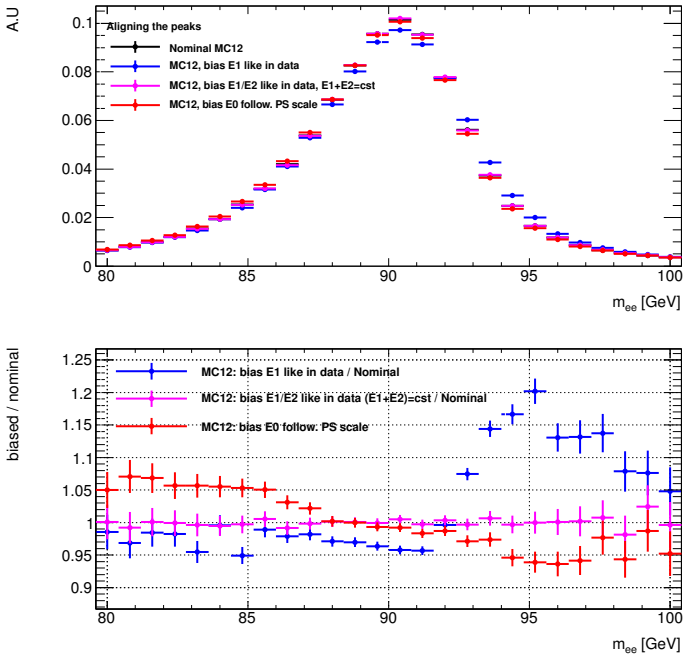

Figure 5.54: $Z \rightarrow ee$ lineshape comparisons for the nominal MC (black line), a MC where the strips energy has been scaled according to scale measured in data and where the middle energy is kept constant (blue line), a MC where the strips energy has been scaled according to scale measured in data and where the middle energy has been modified so that the sum of strip and middle energy remain constant (pink line), and a MC where the presampler energy has been scaled according to scale measured in data (red line). The ratios of each of these configurations to the nominal MC is shown on the bottom.

are again seen in the data to MC comparison after all corrections, when selecting only electrons with $|\eta| > 1.8$ [185].

Figure 5.55(a) shows the $Z \rightarrow ee$ lineshape for both electrons in the region $|\eta| > 1.8$ for the nominal MC and for a MC where the strips energy has been scaled accordingly to the scale measurement in data. On can see that even in this region, the strips miscalibration cannot explain the lineshape discrepancies. In Figure 5.55(b), the nominal MC lineshape is compared to a MC with additional material in the detector following the configuration G'. In this case, the discrepancy in the low mass tails is still present and amounts to about 15%.

The region $|\eta| > 1.8$ is precisely where a large discrepancy arises between data and MC in the longitudinal shower shapes variable E_1/E_2 used for the measurement of the material budget in data (see Figure 6.24). This discrepancy amounted to about 10% in this region. More particularly, it is shown from this Figure 6.24 that in this region, the material budget in data seem to be closer to the G' configuration than to the nominal one.

All this leads to the conclusion that the lineshape discrepancy observed between the data and the MC could, at least in the region $|\eta| > 1.8$, be explained by a material mismodeling. For the region $|\eta| < 1.8$, two sources have been highlighted, the material mismodeling and the presampler scale miscalibration. In reality other effects have also been found to have an impact on the low mass tails, for example the lateral shower shape discrepancies between data and MC, arising from a lateral leakage (out-of cluster energy) mismodeling [189]. The full understanding

of the $Z \rightarrow ee$ lineshape is thus not yet complete, and more studies will be needed to understand
3165 all the effects and model them well.

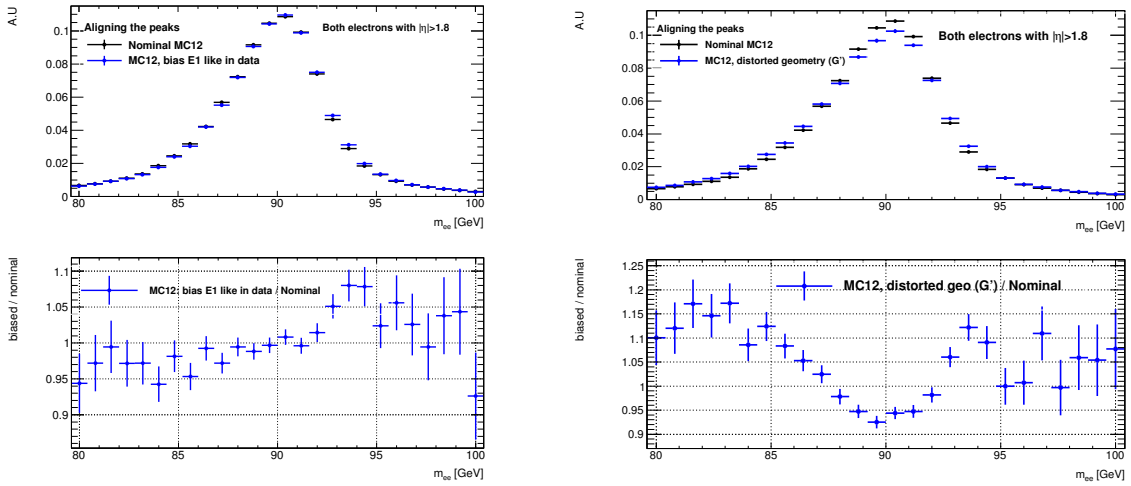

(a) (b)

Figure 5.55: $Z \rightarrow ee$ lineshape comparisons between the nominal MC (black line) and (a) a MC where the strips energy has been scaled according to scale measured in data and where the middle energy is kept constant (blue line) (b) and a MC with additional material in the detector following the configuration G'. The ratios of each of this configuration to the nominal MC is shown on the bottom.

Chapter 6

Probing the material budget upstream of the calorimeter with shower shapes

From Chapter 3 it has been seen that the amount of material in front of the electromagnetic calorimeter is quite substantial. This may lead to energy losses upstream of the calorimeters. As seen in Chapter 5, such energy losses are corrected for with a MC-based simulation. The corrections are valid if the material description in the simulation well corresponds to the one in data.

A method developed to compare the material budget in data and MC is described below.

6.1 Interaction of particles with matter

6.1.1 Electron interactions

The electrons or positrons can interact with the detector material through different processes: ionization, Moller scattering ($e^-e^- \rightarrow e^-e^-$), Bhabha scattering ($e^+e^- \rightarrow e^+e^-$), positron annihilation, elastic Coulomb scattering, or radiation of a photon in presence of an electric field coming for example from a nucleus. This last process is usually called bremsstrahlung. The evolution of the energy loss due to these processes as a function of the electron energy is shown in Figure 6.1 [190].

The two dominant processes are the ionization and the photon radiation for low energy [1] and high electron energy respectively. The electrons from the Z decay that are used to calibrate the energy will then mainly interact by bremsstrahlung. In this process, the energy loss is due to the emission of a braking photon when the electron passes close to the electric field of the atom. The probability of the photon emission is inversely proportional to the squared mass of the particle, meaning that for muons for example, the radiation will be like 40000 less important than for the electrons.

A single Coulomb scattering differential cross section is described by the Rutherford formula [191], which goes in $1/\sin^4(\theta/2)$ where θ corresponds to the scattering angle. This implies that large angular deflections of the incident charged particle will be in general suppressed. Successive scatterings (multiple scattering) along the particle path lead to many random small deflections with respect to the initial direction. After several steps, a big deflection can arise from the

[1] below around 10 MeV.

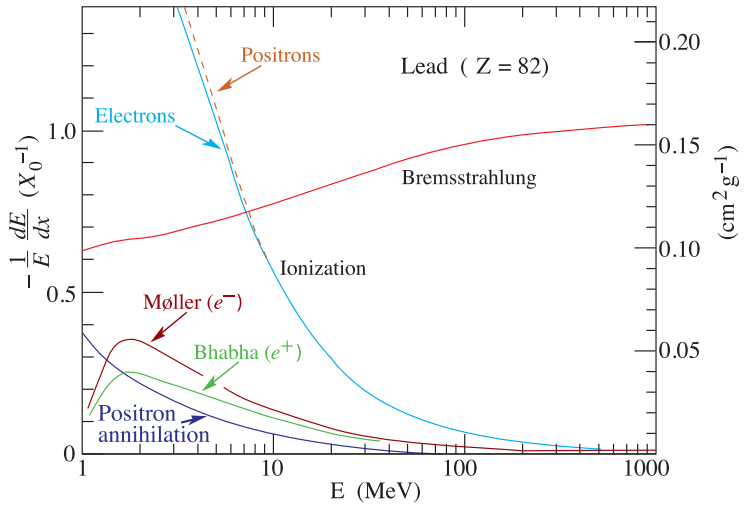

Figure 6.1: Energy loss induced by different processes for electrons in Lead, as a function of its energy [190].

cumulation of these small scatterings. A back scattering of the charged particle with respect to its initial direction can happen. This particularity depends on the particle energy (the smallest is this energy the most probable is the phenomenon) and on the atomic number of the material crossed (the probability increase with Z). It also depends on the incidence angle of the particle.

6.1.2 Photons interactions

Three main processes can affect a photon passing through material: the photoelectric effect, the Compton scattering and the pair production. The photoelectric effect is dominant at low energy, whereas the pair production is the leading process at high energy as seen in Figure 6.2) [190]. The pair production process, also called the photon conversion corresponds to the transformation of a photon into an electron-positron pair in presence of a nuclear (or electric) field . The condition for this pair production is that the photon energy be above the threshold $2 * m_e = 1.022$ MeV.

6.1.3 Radiation length

The probability for a particle not suffering an interaction with the medium over a distance x can be written as $P(x) = e^{-\alpha x}$ where α is the probability to have an interaction between x and $x + dx$. The mean free path λ can be calculated, it actually corresponds to $1/\alpha$. For an electron interacting by photon radiation, the energy after a distance x can be expressed as $E(x) = E_0 \exp(-x/X_0)$ where E_0 is the initial energy. The radiation length X_0 is defined as the distance over which the electron energy is reduced by a factor $1/e$ with e the Euler number. The radiation lengths have been tabulated for various common material and relevant numbers as the one concerning the lead and liquid argon are given in Table 6.1. The radiation length for the lead is very small, for comparison, the one in air is $X_{0,air} = 300.50$ cm $= 36.20$ g·cm^{-2} [192].

The mean free path λ_{pair} correspond to the average distance travelled by a photon before it converts into an electron-position pair. This quantity is related to the radiation length because these two processes are related by a simple substitution rule. Thus, it can be expressed as: $\lambda_{pair} = \frac{9}{7}X_0$. In others words, the probability of conversion of a photon in a material of

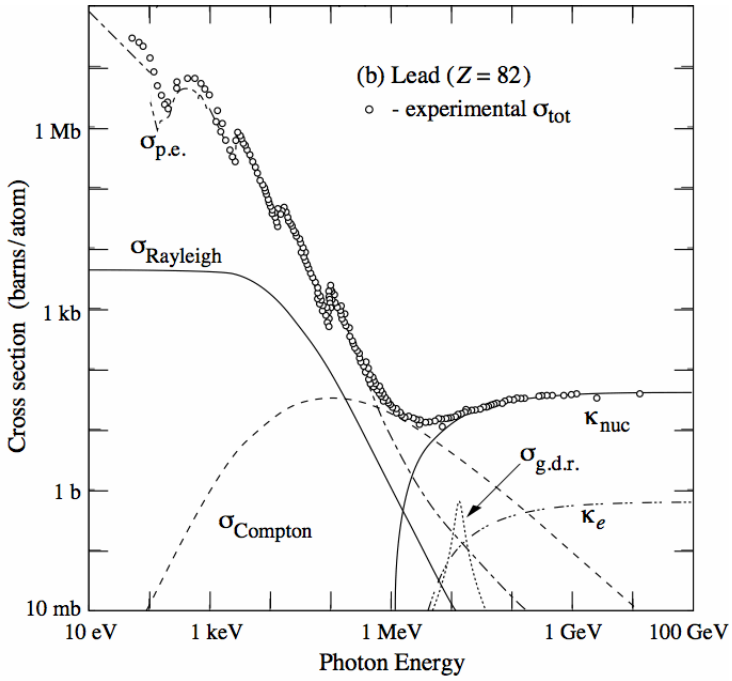

Figure 6.2: Energy loss induced by different processes for photons in Lead, as a function of its energy. The symbols $\sigma_{p.e}$ designates the photoelectric effect, κ_{nuc} and κ_e represent the pair production in a nuclear and electron field respectively and finally σ_{gdr} is for the giant dipole resonance [190].

thickness x by unit of radiation length is expressed as:

$$P(x, X_0) = 1 - \exp(\frac{7}{9}\frac{x}{X_0}) \tag{6.1}$$

Table 6.1: Some atomic and nuclear properties of the liquid argon and lead [193].

Quantity	Liquid Argon	Lead
Atomic number	18	82
Radiation length (g·cm^{-2})	19.55	6.37
Radiation length (cm)	14.00	0.56
Critical energy (MeV)	32.84	7.43
Molière radius (g·cm^{-2})	12.62	18.18
Molière radius (cm)	9.04	1.60

6.1.4 Electromagnetic shower development

6.1.4.1 Definition

An electromagnetic shower in the EM calorimeter can either be formed from an electron or a photon. The incident particle interacts with the lead absorber as described above (photon

radiation or pair production), leading thus either to a photon or to an electron-positron pair. The daughter particles at their turn interact with another lead absorber and creates new photons and electrons. Figure 6.3 shows a schematic view of an electromagnetic shower development starting from an electron. This process continues until the electrons reach the critical energy E_c. The critical energy corresponds to the electron energy for which the loss due to radiation and ionization are roughly equivalent. It can be approximated by: $E_c = \frac{1600\ m_e c^2}{Z}$ [194]. Another approximation of the critical energy, more often used, uses the fact that the critical energy corresponds to the point where losses due to ionization per radiation length is equal to the electron energy [195]. The expression of this energy can be approximated by $E_c \sim \frac{610}{Z+1.24}$ MeV for solids. The critical energies for lead and liquid argon are given in Table 6.1. Figure 6.4 shows the evolution of the critical energy with the atomic number.

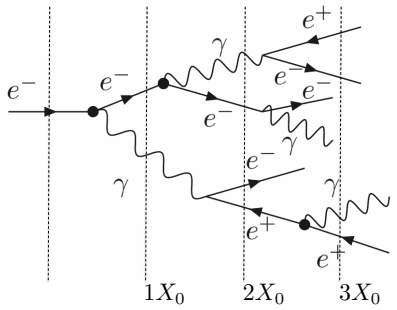

Figure 6.3: Electromagnetic shower development.

Beyond the critical energy, the electron interact with the material mainly through ionization. The lead used in the absorbers of the ATLAS electromagnetic calorimeter has a critical energy of around 7 MeV.

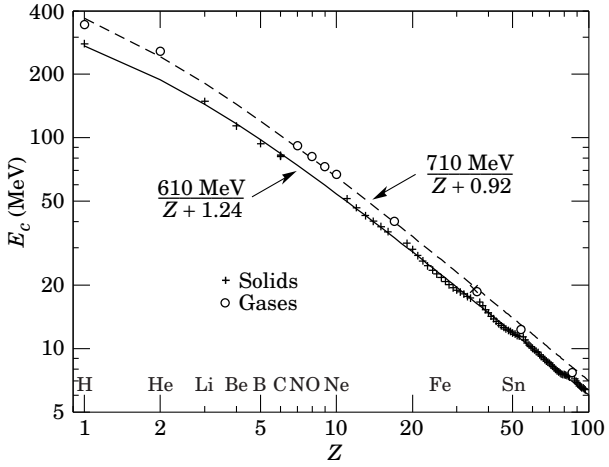

Figure 6.4: Critical energy as a function of the atomic number for electrons [190].

6.1.4.2 Modeling

The cascade of electrons, positrons and photons is a process that can be modeled in a simplified way assuming that in average, the electron (photon) radiates (converts) over one radiation length (see Figure 6.3). In this model the energy of the daughter particles is assumed to be $E(x) \sim E_0/2^x$ with 2^x corresponding to the number of particles produced at the step x. From this, one can deduces over which number of radiation lengths the shower will stops, given the transition energy. This is given by

$$x_{max} = \frac{\ln(\mathrm{E_0/E_c})}{\ln 2},$$

that allows to determine the size of the calorimeter in order to contain the full shower development.

More realistic modelings are also developed, based on Monte Carlo simulations. The transverse development of the electromagnetic shower scales with the Molière radius R_M [196]. This quantity is defined such that in average, only 10% (1%) of the total energy of the incident particle goes outside a cylinder of radius R_M ($3.5{\cdot}R_M$) [190]. Typical values of the Molière radius for liquid argon and lead are given in Table 6.1.

6.2 Estimating the material upstream of the calorimeter

Many different methods exist in order to probe the material distribution in the ATLAS detector. These methods are complementary either for the regions they can probe, or for the precision they can reach. Combining the information from these methods can be used to test the accuracy of the material simulation in MCs.

Most of the studies use the 2009 or 2010 first data with a center of mass energy of $\sqrt{s} = 900$ GeV and $\sqrt{s} = 7$ TeV respectively, because of the low amount of pileup events in these early data. Minimum bias events triggered with the Minimum Bias Trigger Scintillators (MBTS) are mostly used. A transverse momentum larger that about 100 MeV is required in these studies.

6.2.1 Secondary Hadronic interactions

Hadrons also interact with the matter *via* strong interactions. They have been used to probe the material distribution in the detector. The technique used for this study is based on the reconstruction of the secondary vertices due to interaction of primary hadrons with the detector material. This method allows to probe only the inner detector material. The data described above have been used (corresponding to about 0.2 $nb^{-}1$) and compared to the simulation. A selection on the quality of the tracks and on the impact parameter allows to reject most of the background. Excellent resolution on the position in R and z is reached, up to 200-300 μm for low radius ($R < 100$ mm) and 1 mm for larger ones [197] as seen in Figure 6.5(a) where distribution of reconstructed secondary vertices as a function of the transverse position (x,y) is shown. An uncertainty on the amount of material of around 7% arises from the different source of systematic uncertainties for this method.

From this study, two main issues are highlighted:

- The beam pipe is found to be not centred around the nominal origin (0,0) (the displacement is found to be $(x, y) = (0.22 \pm 0.04, -2.01 \pm 0.04)$ mm and explained by the mechanical flexibility of the beam-pipe [197])

- Some of the pixel support structures [2] at radius $R \sim 190$ mm and $R \sim 235$ mm seems to be in wrong place (about 1 cm displacement in opposite directions). This last point is illustrated in the R profile of these secondary vertices in Figure 6.5(b).

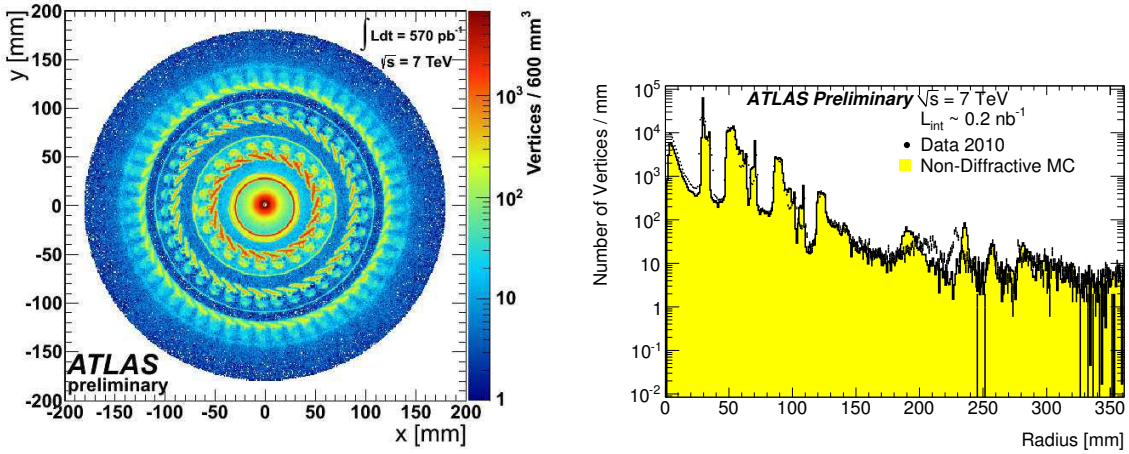

(a) (b)

Figure 6.5: Distribution of the reconstructed secondary vertices as a function of the transverse positions (x, y) for minimum bias events data collected in 2010 [198] (a) and of the radius R for the same data (black points) compared to the simulation (yellow histogram) [199] (b).

The issues have been taken into account and a newer version of the Monte Carlo contains all these modifications. Except for these two issues, the material description in the inner detector is found to be well modeled by the simulation.

6.2.2 SCT extensions

This method is based on the rate of tracks of charged pions reconstructed in the pixels, that are matched to hits in the SCT [200] [201]. This method allows to probe material outside the pixel volumes, especially the inactive material between the pixel and the SCT. The presence of material in this region deviates the particle trajectory and results in a degraded matching between pixel and SCT hits. Using a similar dataset to the one presented above, material mismodelings in the regions $\eta \sim 1.8$ and $\eta > 2.2$ can be seen in Figure 6.6 which shows the distribution of the SCT extension efficiency as a function of the pseudorapidity. This is interpreted as coming from the Patch Panel 0 region [3] which appears to suffer from an underestimation of the material budget.

The material description has been improved by adding an octagonal structure just behind the pixels endcaps in the simulation. The impact of this modification is shown in Figure 6.6, red line. The agreement between data and MC is improved but the regions $\eta \sim 1.9$ and $\eta > 2.3$ are still not well described. The MC simulation of this geometry is still being refined in order to match the data.

[2] See Section 3.2.1.2.
[3] See Chapter 3.

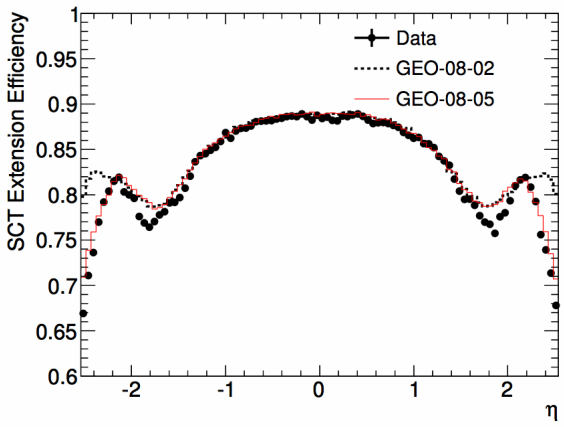

Figure 6.6: SCT extension efficiency as a function of η for the data collected in 2010 (black points) and for the MC before (black dotted line) and after (red line) the addition of an octagonal structure in the PP0 region [201].

6.2.3 Conversions

The photon conversion probability depends on the amount of material traversed (see Equation 6.1). The rate of photon conversions provides a probe of the material distribution.

This method uses photons from π_0 decays selected [4] in a dataset similar to the ones described previously. The sample of selected converted photons has a very high purity of about 90% [202] in most of the regions probed. This method is only sensitive to the material in the inner detector, because the conversion vertices cannot be seen beyond, and has the best accuracy for $R < 400mm$. The radial resolution for the vertex position is about 4 mm [202].

Figure 6.7(a) shows the distribution of the reconstructed conversions in data as a function of the transverse positions (x, y). The three pixel layers, the octagonal shape of the pixel support tubes and the first two SCT layers can be seen clearly. The same material mismodeling as highlighted in Section 6.2.1 are also seen with this method: the beam pipe position deviation is confirmed and the pixel octagonal supports and pixel support tube are found to be slightly displaced. After the modification in the simulation according to these observation mentioned in this section, the data to MC agreement is improved, as seen in Figure 6.7(b), for the region $-0.6 < \eta < -0.1$ which shows the distribution of the number of converted photons as a function of the radius.

6.2.4 K_s^0 mass

The K_s^0 particles are abundantly produced in pp colliders. Their main decay mode is $K_s^0 \rightarrow \pi^+\pi^-$. The charged pions can interact electromagnetically with the material through ionization and multiple scattering. Any unaccounted material would then bias the reconstruction of the track momenta and then the K_s^0 invariant mass. Two oppositely charged tracks coming from the same vertex with a transverse momentum of about 100 MeV each are selected, with in addition requirements on the vertex and track reconstruction quality [204]. The K_s^0 has a decay length of about 2.7 cm (5 cm taking into account the relativistic factor), and a selection on the distance between the primary vertex and the decay vertex of the K_s^0 is made. The peak of the reconstructed mass of the K_s^0 is fitted in order to extract the most probable value. This method

[4] See reference [202] for a description of this selection.

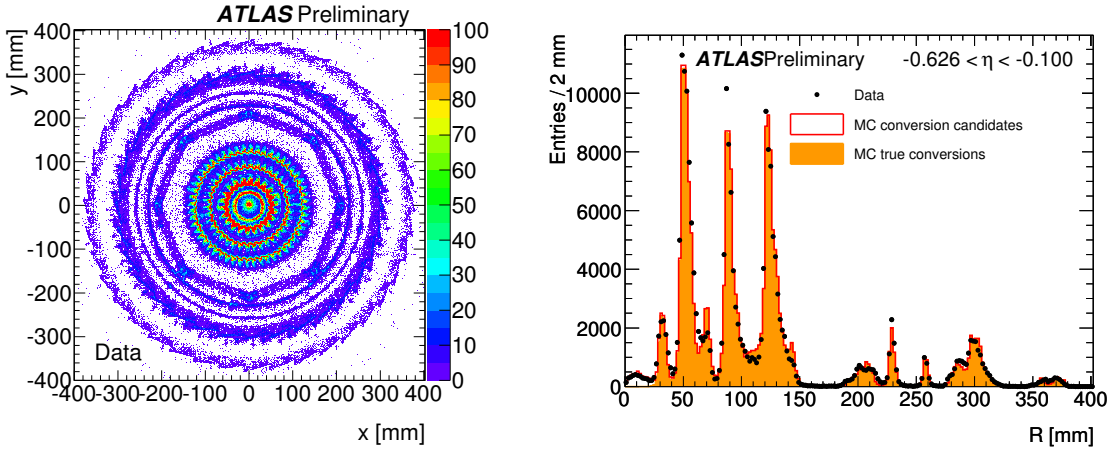

(a) (b)

Figure 6.7: Distribution of the reconstructed photon conversions as a function of the transverse position (a) for the data and as a function of the radius (b) for the data and the simulation [203].

is sensitive only to pixel material, as the number of K_s^0 decaying outside this detector is too low to constrain SCT material. The ratio of the extracted mass in the data and in the simulation as a function of the radius is shown in Figure 6.8. No obvious deviations are found along the radius, neither along the azimuth or the pseudorapidity up to $\eta = 2$. The sensitivity of the method is tested by using simulations where the nominal inner detector volume is scaled by 10% or 20%. As seen in Figure 6.8(b), this additional material compared to the nominal simulation induces significant biases on the K_s^0 invariant mass especially at low radius.

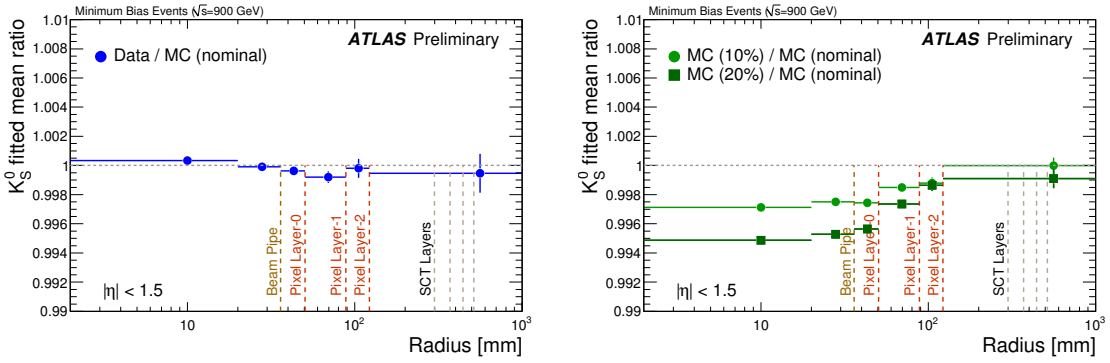

(a) (b)

Figure 6.8: Relative variation of the most probable value of the K_s^0 mass in data (a) or in MC with additional material in the inner detector (b) with respect to the nominal MC as a function of the radius R [204].

6.2.5 Energy flow studies

This method is based on the sensitivity of the electromagnetic calorimeter occupancy to the total amount of material in front of the calorimeter. The occupancy is defined as the fraction of

events having an energy above five times the electronic noise [205] [5]. The presence of material in front of the calorimeter reduces its occupancy, and this can be tested to probe the material simulation. The interest of this method is that it enables a scan of the whole detector up to the electromagnetic detector, thus complementing the methods described in the previous sections which are not sensitive to material beyond the inner detector. Similar data as that used previously are used.

This method has been used to probe the material as a function of the azimuth, as seen in Figure 6.9 that shows the number of measured radiation lengths as a function of ϕ in the interval $-0.1 < \phi < 0.1$ for the two regions $\eta < 0.6$ and $0.6 < \eta < 1.4$. In the first region, the agreement between the simulation and the data is very good, whereas there is a clear lack of material in the second region, up to 1 X_0, affecting the whole interval $-0.1 < \phi < 0.1$. This is interpreted as being due to mismodelling of the inner detector rails. They are located in the inner wall of the calorimeter cryostat, at $\phi = 0, \pi$ and extend up to $\eta = 1.7$. These rails are very narrow ($\Delta\phi = 0.005$) and represent about 0.45 (0.7) X_0 of material in the region $\eta < 0.6$ ($0.6 < \eta < 1.4$). This discrepancy has been taken into account in the Monte Carlo simulation and the amount of material in this particular regions has been increased.

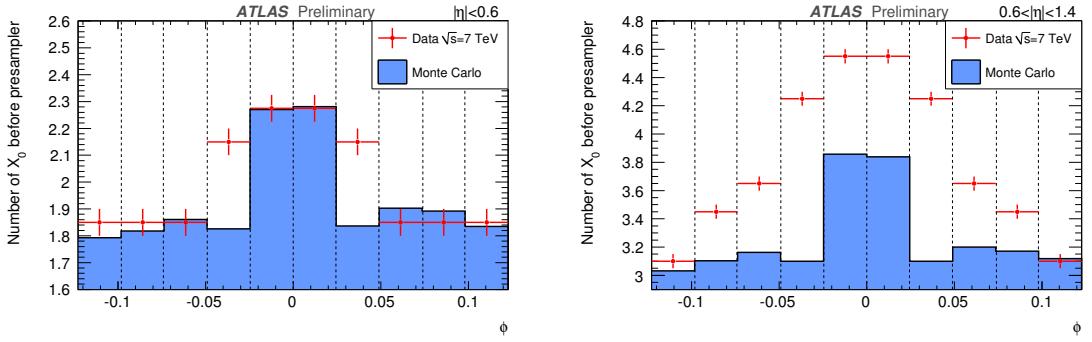

(a) (b)

Figure 6.9: Material distribution in radiation length as a function of ϕ, restricted to $-0.1 < \phi < 0.1$, for two regions in pseudorapidity: $\eta < 0.6$ (a) and $0.6 < \eta < 1.4$ (b) [205].

6.3 Electromagnetic shower shapes in simulation

The material in the detector has been probed with the previous studies, mainly in the inner detector volume and up to radius not exceeding 400 mm. In the following, the material description is tested using shower shape variables that probe the integrated material distribution up to the electromagnetic calorimeter.

A full MC study has been performed before the first collisions at LHC in order to test the possibility to detect and quantify biases in material description thanks to high p_T electrons [206]. More particularly, the sensitivity of various electromagnetic shower shapes variables and track variables has been tested. The results of this study are given below, before applying this method to data recorded in 2010 and 2011.

[5] The electronic noise is typically 25 MeV for the second sampling [205]

6.3.1 Variable of interest

The energy collected in each of the four calorimeter layers will be called E_0, E_1, E_2 and E_3 for the presampler, strips, middle and back layers. The total reconstructed energy from these four layers is called E_{tot} (see Chapter 5 for the details of the energy reconstruction and calibration). The variables used in this study are:

- The fraction of energy collected in the presampler or in the first layer of the accordion detector: $f_0 = E_0/E_{tot}$ and $f_1 = E_1/E_{tot}$. As seen in Figure 6.10, the middle layer collects most of the shower, whereas the strips and the back collect respectively the begin and the end of this shower. The presampler collects the energy loss upstream. Additional material in front of the calorimeter leads to a premature development of the shower that deposits then more energy in the strips and presampler and less in the middle.

- The shower width along η, $w_{4\,strips}$ calculated with the $\pm$ 4 strips around the strips containing the maximum energy and the relative difference between the amount of energy deposited in $\pm$ 3 cells and $\pm$ 1 cell around the strip of maximal energy $f_{out\,1}$. When the shower development is early, its width at the level of the strips is larger than expected and these two variables increase.

- The shower width along ϕ in the sampling 2, w_{s2}. In case of a bremsstrahlung emission, the electron and the emitted photon are separated in azimuth due to the magnetic field. This leads to an enlarged shower shape in ϕ and then to the increasing of this variable.

- The comparison E/p between the energy reconstructed in the cluster, E and the momentum reconstructed from the track, p. An electron emitting a photon has its track momentum reduced, whereas the full energy of the initial electron is reconstructed in the calorimeter clusters [6], see Figure 6.11. This leads to a ratio E/p larger than 1. The tails of the distribution of this variable are especially sensitive to material.

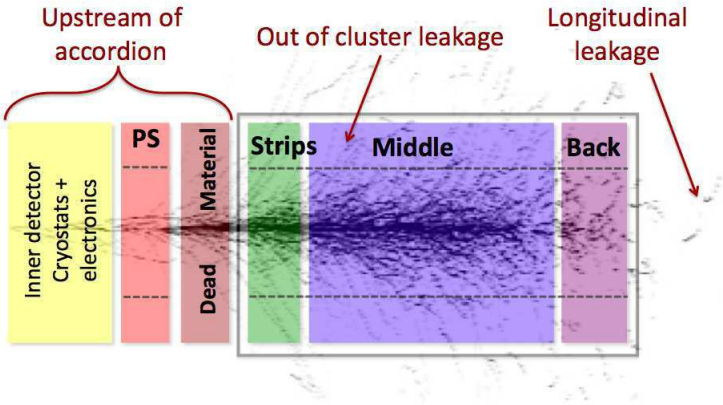

Figure 6.10: Illustration of an electromagnetic shower developing in the ATLAS electromagnetic calorimeter, i.e, in the four compartments that are the presampler (red), the strips (green), the middle (blue) and the back (purple) layers. Dead material is present both before the presampler (yellow) and between the presampler and the strips (brown).

[6] The cluster size are optimized to contain both the emitted photon and the electron, see Chapter 5.

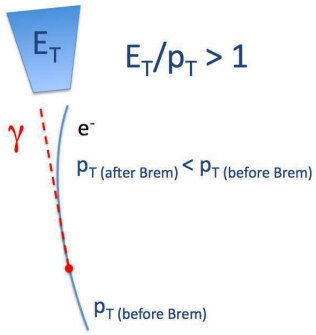

Figure 6.11: The construction of the E/p variable: when an electron radiates a photon, its momentum decreases, whereas the total energy of the electron and the photon and electron is collected in the calorimeter, thus leading to $E/p > 1$.

6.3.2 Geometries

To quantify the sensitivity of the variables defined above under material variations, different simulations are used. One contains the nominal simulation of the material in ATLAS, whereas the others contain extra material at various places of the detector. These distorted MC have: $0.05X_0$ extra material added as a cylinder between the presampler and the strips (referred to as GEO1), 0.10 X_0 extra material added as a cylinder in the cryostat (referred to as GEO2) or extra material in the inner detector:

- In the silicon ID (1% and $1-3\%$ added as a cylinder in pixel and SCT respectively, for $\eta < 0.6$, referred to as GEO3),
- Between the SCT and the TRT (0.025 to 0.05 X_0 added as a cylinder, referred to as GEO4),
- Between the barrel and endcap TRT (0.03 X_0 added as a disk, to account for the silicon and TRT cables and services, referred to as GEO5),
- At the end of the ID, before the cryostat (0.15 X_0, referred to as GEO6).

6.3.3 Quantifying the sensitivity

In order to test the sensitivity of the different variables defined above, the quantity R^x_{geo} is built. It corresponds to the ratio of the averaged value of one of these variables x in a modified geometry *geo* to the nominal one. The significance S^x_{geo} of a deviation of R^x_{geo} is also quantified, it corresponds to $S^x_{geo} = \frac{|R^x_{geo}-1|}{\sigma^{stat}_R \oplus \sigma^{syst}_R}$, with $\sigma^{syst}_R = 0$ in simulation.

6.3.4 Analysis

Well identified electrons from the $W \rightarrow e\nu$ decay with $pT > 15$ GeV and $\eta < 2.47$ are selected and used in this study. The number of events in the MC samples corresponds to $250pb^{-1}$.

Sensitivity to material added between the presampler and the strips This is tested using the MC sample with the geometry GEO1. As the material is added after the presampler, the variable f_0 cannot be used. The ones used in this study are f_1 and $w_{4\,strips}$.

The ratios R^x_{PS-S1} for these two variables are measured along η with a binning of $\Delta\eta = 0.1$. Calculating the sensitivity as described in Section 6.3.3, f_1 is found to be more sensitive over η than $w_{4\,strips}$. In the particular bin $-1 < \eta < -0.9$, $S^{f_1}_{PS-S1} = 5\sigma$ and $S^{w_{4\,strips}}_{PS-S1} = 4\sigma$. The evolution of the ratio R^x_{PS-S1} can be also depicted as a function of the material crossed in radiation lengths. The response of $R^{f_1}_{PS-S1}$ is found to be linear with the amount of material seen, allowing then a quantification of this extra material.

Sensitivity to material added in the cryostat This is done using the geometry GEO2. The variable f_0 can be used as the material is placed before the presampler. In addition $f_{out\,1}$, $w_{4\,strips}$ and f_1 are also tested. The distribution of $f_{out\,1}$ and f_0 for the nominal and distorted geometries can be seen in Figure 6.12.

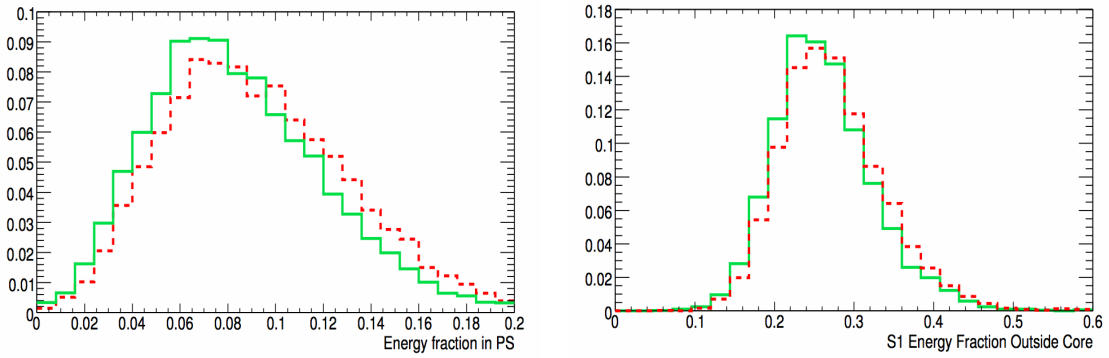

(a) f_0 (b) $f_{out\,1}$

Figure 6.12: Distribution of the two variables f_0 (a) and $f_{out\,1}$ (b) for the nominal (green, full line) and distorted with extra material in the cryostat (red, dashed lines) geometries. See text for more precise definitions of the variables. Taken from [206].

The ratios R and significances S are calculated for these four variables as a function of η They are all found to be very sensitive to an addition of material in this place, with a significance always larger than 4σ, the most sensitive one being f_0.

Sensitivity to material added in the inner detector For this study, the geometries GEO3, GE04, GEO5 and GEO6 are used. The longitudinal shower shapes variables f_0 and f_1 and the shower width along η $w_{4\,strips}$ are shown to be less sensitive than the other ones to this kind of material. The variables related to the tracks or to the shower width in the ϕ direction are found to be more sensitive.

For the material added only inside the silicon ID (GEO3), the two variables E/p and the w_{s2} are very sensitive. The percentage of events having $E/p > 1.2$ provides the most sensitive variable with a significance of about 10 σ for seeing the 1% to 3% X_0 added in the silicon detectors. For comparison, the w_{s2} variable gives a significance of about 7 σ.

When the material is added between the barrel and endcaps of the TRT (GEO5) or between the SCT and TRT (GEO4), the variables described above become less sensitive than variables based on the track quality, like the fraction of tracks reconstructed in the silicon detectors that do not match TRT hits, or the percentage of outliers [7] in a given ID silicon layer.

[7] A outlier is a hit that deviates from the fit of the other hits, indicating the place where a photon may have been radiated [206].

6.4 Shower shapes studies with data

The material study with shower shapes was done with different datasets, depending on the specific analyses. Both data with a center of mass energy $\sqrt{s} = 7$ TeV (2010, 2011) and $\sqrt{s} = 8$ TeV (2012) were used. High p_T electrons coming from the $Z \to ee$ or $W \to e\nu$ decays are used in this analysis. The selection of the events and the MC samples for these two processes have been described in Sections 5.3.1 and 5.4.2. In addition, simulations of single electrons will be used. This kind of simulation provides a source of well-known electrons that have interacted with the material of the detector. Simulations with additional material in some places of the detector are also used. Some of the geometries used were described in Section 6.3.2, the other ones were detailed in Table 5.6.

The events generated for the MC samples are submitted to a full simulation of the ATLAS detector thanks to the GEANT4 program [150]. This program simulates the interaction of the particles with the detector. This simulation evolves continuously following improvements in the geometry, as the ones detailed before. A tag is given to the different geometries, that is ATLAS-GEO-XX-YY-ZZ. The letters XX indicates the major version number of the ATLAS geometry included in GEANT4. It corresponds to important changes in the ATLAS geometry. To give an example, more than 10 official versions have circulated between 2010 and 2013. The YY letters (also called "minor version numbers") are used mainly for the type of geometry used: the nominal description of the detector or the distorted ones with additional material in various places. It can also be used for a change in the detector alignment. Here again up to twenty different geometries can be counted for certain versions. Some of them are also denoted with a letter. Finally the ZZ letters are used to designate further sub-releases of a given version.

Sensitive variables The following variables will be used in the studies:

- f_0 (see description in Section 6.3)
- f_1 the definition is a bit modified with respect to Section 6.3: $f_1 = E_1/E_2$
- the track-cluster matching variable E/p. Both the peak of this quantity (fitted with different functions) and the tails (generally defined as the percentage of events with $E/p > 1.4$) will be used.
- the shower depth χ defined in Section 5.2. It corresponds to a kind of shower longitudinal barycentre. A low (large) depth means that the shower starts early (late). Figure 6.13 shows its distribution, for the data, the nominal and distorted simulations following the configuration G' (see Table 5.6), in four pseudorapidity regions.

6.4.1 Probing the material vs ϕ

For this study, electrons from $W \to e\nu$ events are used. About 760 000 events are selected from the 2011 data.

The longitudinal shower shape variable f_0 is used to probe the material as a function of ϕ. The region is decomposed in bins of size $\Delta\phi = 0.025$ corresponding to the cell size in the middle layer. The profile of the f_0 variable along the azimuthal position of the electron is shown in Figure 6.14 for the data and the nominal MC, and for two η regions: $|\eta| < 0.8$ and $0.8 < |\eta| < 1.4$. Common structures are seen in data and MC, for $\phi = 0, -\pi, +\pi$ interpreted as arising from the ID rails (see Section 6.2.5).

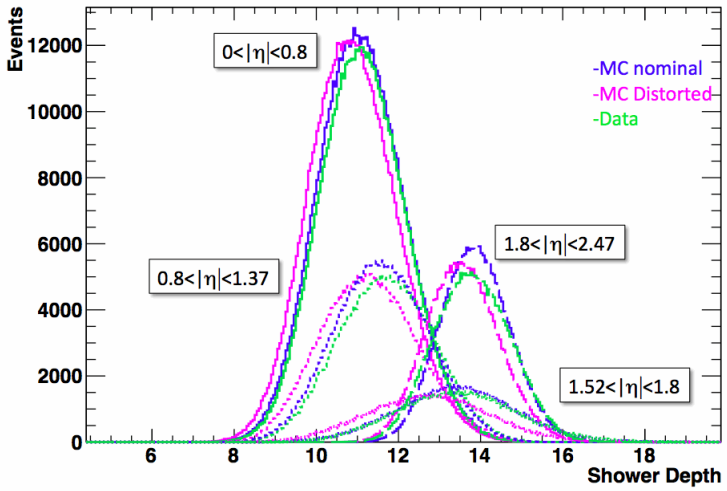

Figure 6.13: Distribution of the shower depth variable for the data (green), nominal MC (blue) and the distorted geometry (pink), were material is added following configuration G'. Four sets of curves corresponds to the four different η regions, as labelled.

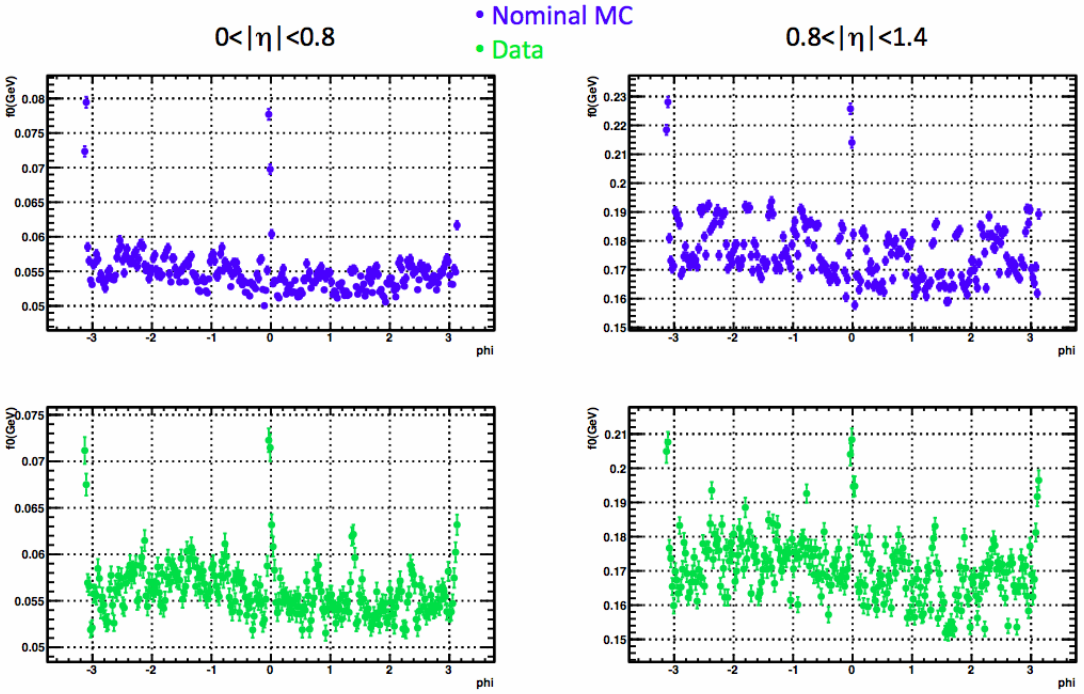

Figure 6.14: Profile of the f_0 variable along ϕ for the data (green) and the nominal Monte-Carlo (blue) and for two η regions: $|\eta| < 0.8$ (left) and $0.8 < |\eta| < 1.4$ (right).

Figure 6.15 shows the comparison between the data and the MC. In the region $|\eta| < 0.8$, there is a quite good agreement, whereas in the region $0.8 < |\eta| < 1.4$, the structures mentioned earlier are still seen, deviating by 20% with respect to the nominal MC. One interpretation is that the amount of material added in the MC after the discovery of a problem in this region

with the energy flow study (see Section 6.2.5) is not sufficient.

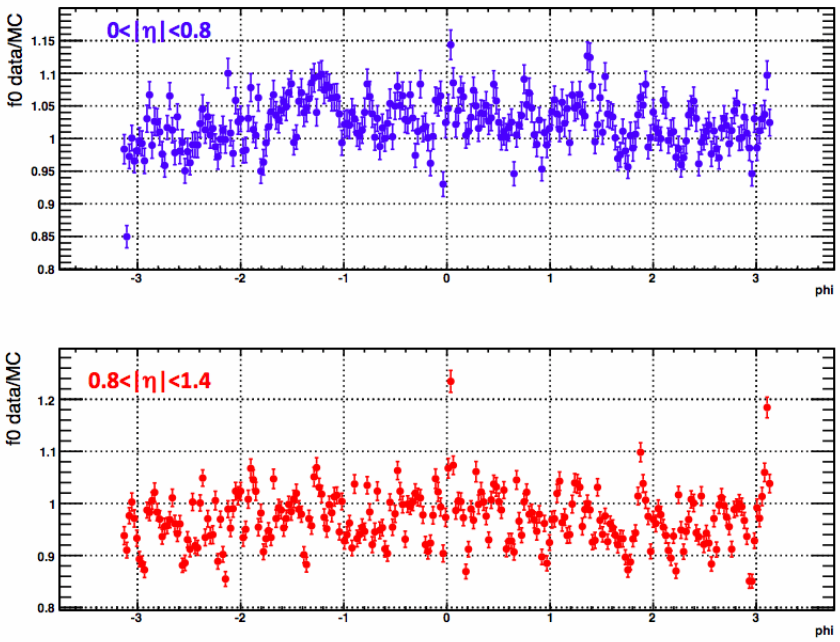

Figure 6.15: Profile of the ratio between data and nominal MC of the f_0 variable along ϕ for the two different η regions: $|\eta| < 0.8$ (blue) and $0.8 < |\eta| < 1.4$ (red).

A sinusoidal shape of the f_0 response is observed both in the data and MC, being more pronounced in the data. Several possibilities exist to explain such effect: a barrel displacement in the cryostat, a mechanical sagging effect, or a LAr temperature non-uniformity. This shape as well as the spikes in $\phi = 0, -\pi, +\pi$ were already observed with the uniformity studies presented in Chapter 5. The barrel displacement has to be excluded because in the uniformity studies, the shape was also observed in the endcap. Mechanical sagging of the calorimeter is also rejected as an explanation. The reason of such effect is not yet understood.

The variable f_1 has been also looked at and found to give similar results than the f_0 one.

6.4.2 Probing the material vs η

The shower shape variables f_0 and f_1 for electrons from the W decay are used to probe the material along the pseudorapidity. The same dataset as described previously is used. The acceptance region $[-2.47, +2.47]$ is decomposed in bins of size $\Delta\eta = 0.025$ corresponding to the cell size in the middle layer.

The profiles of the variables as a function of the pseudorapidity are shown in Figure 6.16. Large discrepancies arise in the data to MC ratio along η.

To understand these discrepancies the variations of the individual energies with η in the four layers is studied. The energy profiles of these four individual layers as a function of the pseudorapidity obtained using a version of the reconstruction software of early 2011 (Release 16) are shown in Figure 6.17. Both data and the nominal MC are shown.

The repartition of the total energy into the four different layers is seen from these plots. A fraction of $\sim 60\%$ is collected in the middle layer, $\sim 30\%$ in the first layer and less than 1% in

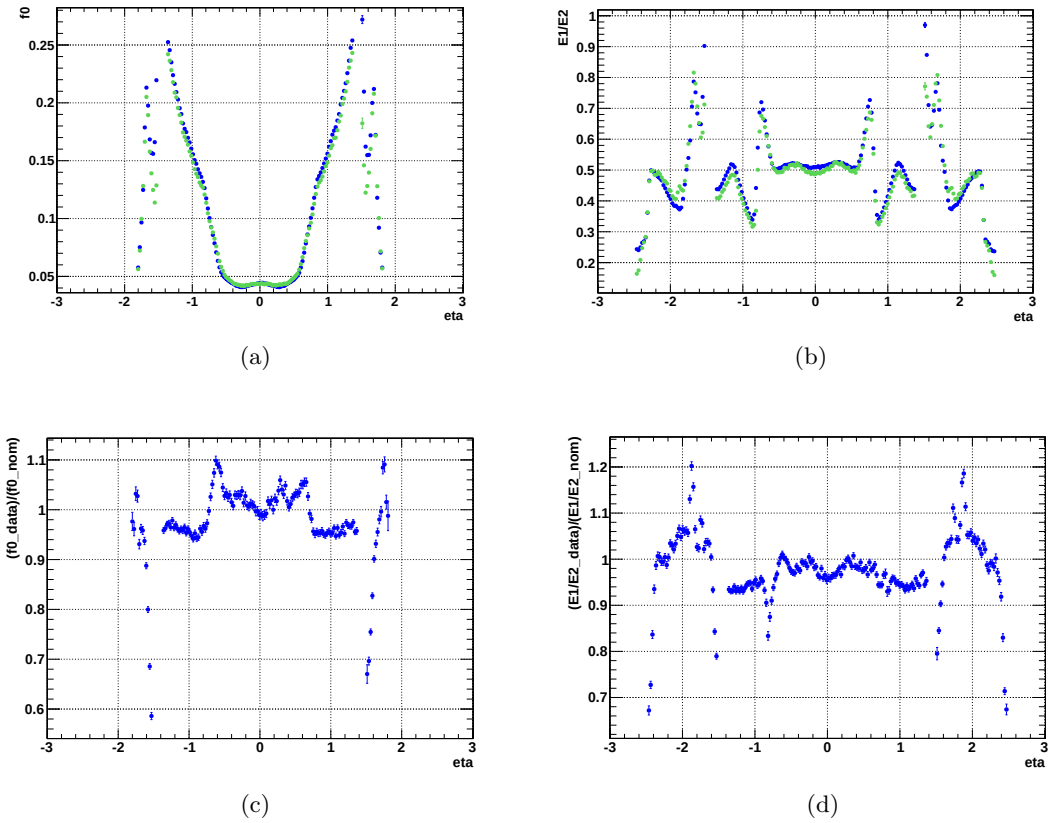

(a) (b)

(c) (d)

Figure 6.16: Profile of the f_0 (a) and f_1 (b) variables as a function of η, for the data (green dots) and the MC (blue dots). Data over MC ratio of the f_0 (c) and f_1 (d) variables as a function of η.

the back layer. The presampler collects about 10% of the total energy.

The change of the absorber widths at $\eta = 0.8$ are seen in the first and second layer as small drops in the energy response. Overall, a good agreement between the data and the simulation is observed in the barrel part for the four layers. In the endcap however, discrepancies are seen in almost all the layers.

6.4.2.1 Calibration coefficients in presampler energy

Looking in more detail at the E_0 profile, a discrepancy between the data and the simulation appears at around $\eta = 0.3$ (see Figure 6.18). This discrepancy is very localized (about 1 cell), and seems to be a feature in the MC (the energy in this region varies smoothly and there is nothing in the geometry that could explain such a drop). In order to understand this, many checks have been done, including a test on the calibration coefficients was performed.

From the MC-based calibration described in Chapter 5, two different sets of coefficients, for the data and the simulation, are attributed to the energies in the different samplings. Comparing the energies before and after this calibration, it was noticed that the discrepancy observed in Figure 6.18 only arises after calibration of the energies. The calibration coefficients in the MC have been checked. The extraction of some coefficients has been found to have failed, creating wrong calibration coefficients for the MC in this region. This feature has been corrected, and a

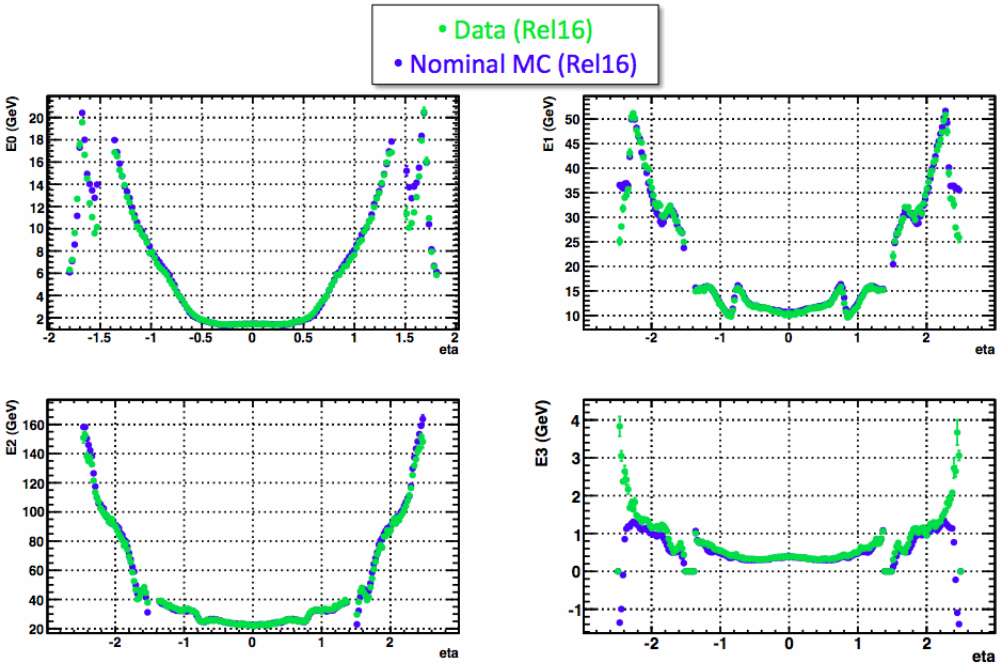

Figure 6.17: Profile of the energy in the different layers: presampler (top left), strips (top right), middle (bottom left) and back (bottom right) as a function of η, for data (green) and MC (blue).

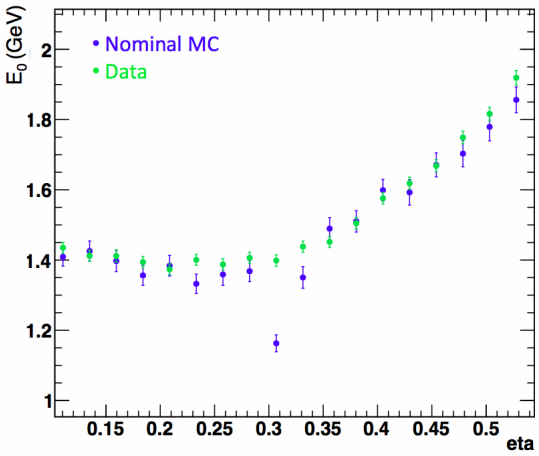

Figure 6.18: Profile of the energy in presampler layer as a function of η, in the range $0.10 < \eta < 0.55$ for the data (green) and the MC (blue).

new set of coefficients produced. After this correction, the discrepancy is no longer seen.

6.4.2.2 The back energy

One of the biggest disagreements observed in Figure 6.17 concerns the back layer energy profile, in the endcap regions. In the MC, it can be seen that the value of E_3 becomes negative at the ends of the pseudorapidity range. This is typical of a cross talk effect, i.e of a signal leakage from middle cells to back cells. Cross-talk modifies the signal pulse shape and consequently the

energy computed using the optimal filtering coefficients (see Chapter 3). The cross talk between the different layers of the LAr calorimeter has been studied [207, 208, 209].

Three different types of crosstalk are found: the capacitive one which is dominant in strips cells, the resistive one between strips and middle cells, which comes from the ink resistor connecting the high voltage between these two layers, and finally the inductive one, which is dominant between the middle and back cells and that comes from a mutual inductance between these cells.

Figure 6.19 illustrates schematically a signal pulse accompanied by its related cross talk signal.

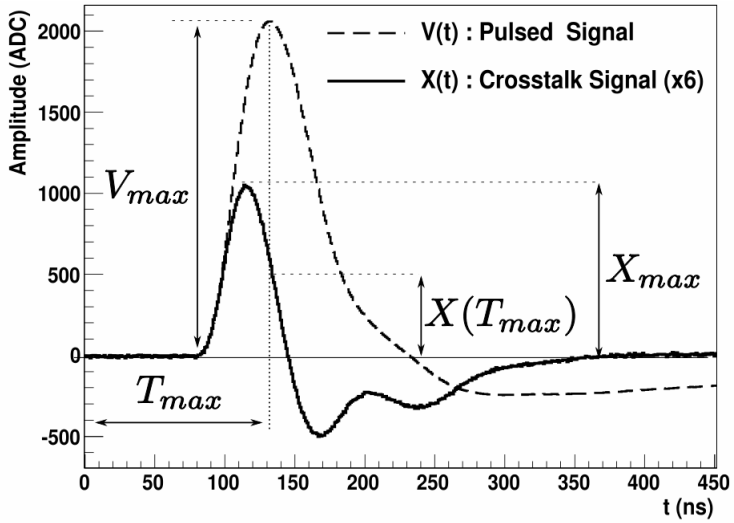

Figure 6.19: Illustration of a physic signal pulse and the resulting cross talk signal pulse magnified in ADC counts as a function of the time. The definition of X_{max}, V_{max}, T_{max} and $X(T_{max})$ are drawn in this figure. Taken from [208].

Two definitions of the magnitude of the cross talk are usually derived:

- the peak-to-peak cross talk, which is the ratio between the maximum amplitude of the cross talk and the physics signal amplitude (X_{max}/V_{max} in Figure 6.19).
- the cross talk under-the-peak which corresponds to the ratio between the cross talk pulse amplitude taken at the signal peak time and the peak amplitude of the signal ($X(T_{max})/V_{max}$ in Figure 6.19).

The under-the-peak measure is more relevant because it directly gives the impact of the cross talk on the physics signal peak amplitude. However, this is very sensitive to the shape of the cross talk pulse. The peak-to-peak measure in general overestimates the real effect of the cross talk on the peak amplitude, but it is a more robust variable. It can be considered as an upper limit on the cross talk effect.

In previous software releases, the under-the-peak definition was used. The negative values observed in the layer 3 energy profile can be understood from the definition of this crosstalk: if the rising of the crosstalk signal is very short, it may happen than the negative part of the cross talk signal be under the peak of the real signal thus leading to a negative ratio.

From this observation, the definition of the crosstalk has been modified in the software. A third model has been implemented, which is based on the crosstalk shape after application of the OFC method. In this method, the amplitudes are not anymore used, instead, the energies

computed from the OFC algorithm are compared. These energies for the real and cross talk signals are written respectively $E_V = \sum a_i v_i$ and $E_X = \sum a_i x_i$ where a_i are the coefficients derived from the OFC method and where v_i and x_i are the sampling amplitudes for the real and cross talk amplitudes. The cross talk is given by the ratio E_X/E_V [210].

This corresponds then to an effective cross-talk, which will depends on the computation of the OFCs.

With the new definition of the cross talk, the profile of the back energy as a function of η is shown in Figure 6.20. The negative values seen in the nominal MC are no longer present for the large values of η. However, the agreement with the data is still very poor.

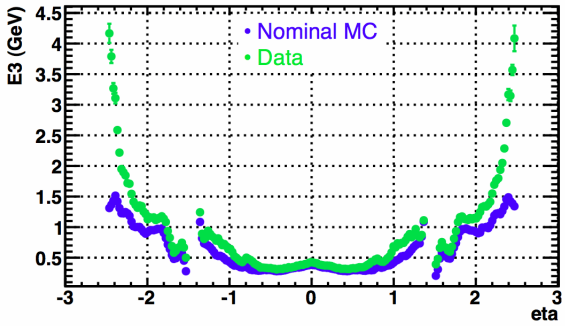

Figure 6.20: Profile of the energy in the back layer as a function of η, after the modification of the definition of the cross talk, for the $W \to e\nu$ channel.

Background The $W \to e\nu$ decay suffers from quite large QCD background. Figure 6.21 shows a distribution of the transverse momentum of the electron from the W, for the signal and the background events [180]. The background contamination is the largest at low p_T and becomes insignificant for large p_T.

One can see from this figure that increasing the value of the cut on the transverse momentum from 20 GeV to 30 GeV would eliminate most of the background contamination. The analysis has been redone using this new selection of the electrons. No difference is found in this layer with respect to the previous analysis.

$W \to e\nu$ and $Z \to ee$ comparison Comparing the back energy profile for the electrons coming from the $Z \to ee$ and $W \to e\nu$ processes, no difference in the discrepant points at high η can be noticed.

Pile-up Another potential source of energy bias is the superimposition of signals from multiple collisions, also called pileup (see Chapter 3). A check is performed to test the dependence of the back energy with the pileup. To perform this test, data samples with different values of the pileup have been used. For this study the full 2011 dataset is used and divided in two blocks: one from period B to J where the average measured number of interactions per bunch crossing is 8-10 and the other from period L to M where the average measured number of interactions per bunch crossing is 15-30 (see Table 4.1). Figure 6.22 shows the profile of the back layer energy normalized to the total one: E_3/E_{tot}, as a function of η for the two different groups of data and for the nominal simulation. The compatibility between the two datasets is very

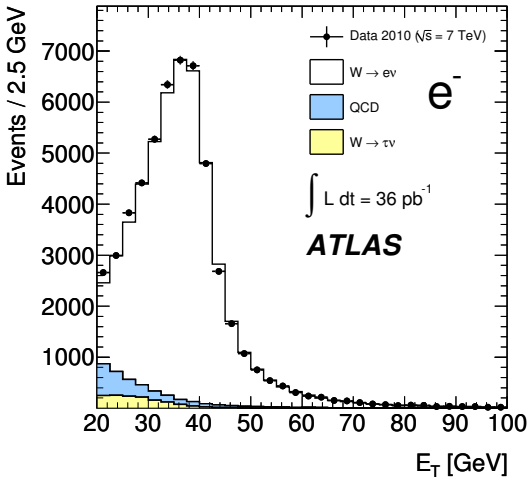

Figure 6.21: Distribution of the transverse energy for the $W \to e^{-}\nu$ process for the 2010 dataset (back dots) and the nominal MC (white histogram). The same distributions for QCD (blue) and $W \to \tau\nu$ (yellow) backgrounds are also depicted. Taken from [180].

good, demonstrating a good robustness of the energy computation with respect to the pileup, as already shown in Section 5.4.

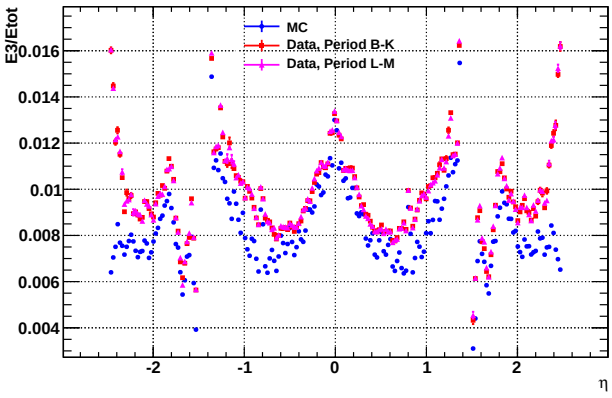

Figure 6.22: Profile of the back layer energy normalized to the total energy as a function of η, for different datasets of 2011 data: period B to J in red and L to M in pink. The nominal MC is also drawn in blue for comparison.

Cross talk Various possibilities have been tested to understand the discrepancies in the back layer at high η. A material effect could be considered: too much amount of material in the simulation could lead to a shower propagating more deeply in the calorimeter, thus increasing the back energy. But the effect seen in Figure 6.20 is very large, the discrepancy with respect to the MC is about 170% which cannot be explained by any realistic amount of material

Another possibility is to consider again a cross talk effect between the middle and back layers. In order to assess this hypothesis, the correlation between the middle and back energy

is looked at. For a cross-talk between these two layers one would see a correlation between the two layers energies different from the natural correlation arising form the shower development. In Figure 6.23(a) the differences observed between the data and MC energies in the back layer is drawn as a function of the energy in the middle layer in data. The energy is proportional to $\cosh(\eta)$ then the x axis can be interpreted also as the pseudorapidity evolution.

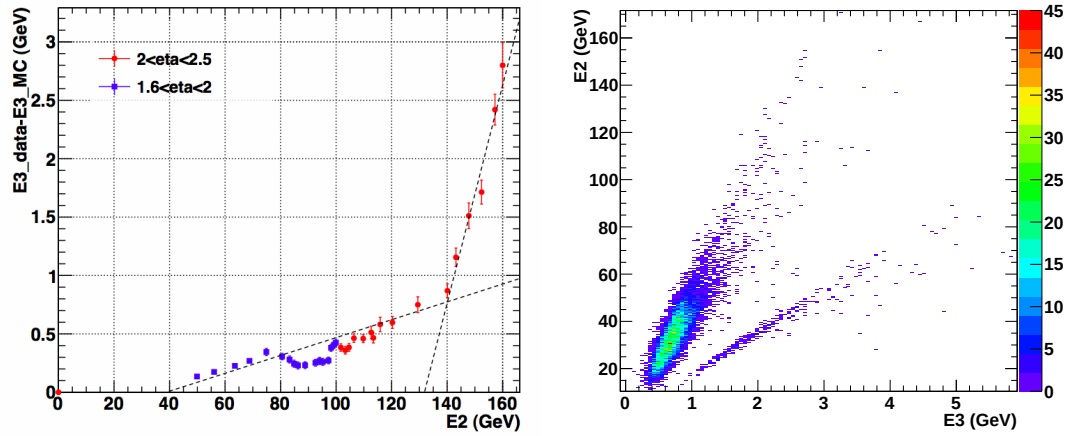

(a) (b)

Figure 6.23: Correlation between: the discrepancy of the energy back layer of data with respect to MC and the the energy in second sampling in data (a) ; the energy in back and middle layers in data (b).

The discrepancy between data and MC evolves in two steps: the first step, up to $\eta \sim 2.3$, is a slow variation of the difference with the energy in middle. In the second step, the variation of the discrepancy is very fast with respect to the middle energy. For both steps, a linear feature can be approximatively considered, and the slopes can be compared. This gives a slope for the second region which is more than ten times larger that the one for the first region.

Figure 6.23(b) shows the variation of the middle energy with respect to the back energy for the data. Once again, two regimes are highlighted: one where the energy in third layers evolves quite linearly with the second one. This concerns the majority of the events. In the other branch, the correlation between the two is also quite linear but the back energy increases much more rapidly.

The presence of these two regimes in both plots, and such sharp variations between the two cannot be explained easily for example by longitudinal shower development arguments. Assuming instead that at $\eta \sim 2.3$ a cross talk not accounted for between the two layers arises, could match better with the previous observations. More refined studies on this are needed, for example by looking at the pulse shapes.

6.4.2.3 f_0 and f_1

The individual layer energy dependence on η are better understood. Returning to the f_0 and f_1 energy profiles shown in Figure 6.16, various discrepancies between the data and the MC are still unexplained. Some of these discrepancies are correlated between the two variables.

The common and larger disagreements are found in these regions:

- η ∼0.6, both variables are larger in data than in MC, which is typical of the presence of additional material upstream of the presampler.
- η ∼0.8, both variables are lower in data than MC. This could arise from a small crack between two electrodes.
- η ∼1.7, similar effect as for η ∼0.6
- η ∼1.9 , similar effect as for η ∼0.6

In Figure 6.24 a comparison is made between the two ratios f_1^{data}/f_1^{MC} and f_1^{dist}/f_1^{MC} where f_1^{dist} corresponds to the variable f_1 evaluated in a MC with additional material following configuration G' (see Table 5.6). This configuration corresponds to a geometry where the material budget of the inner detector and services has been increased by one standard deviation of its uncertainty. The figure shows that the data to MC ratio is close to 1 almost everywhere, and significantly different from the G' to nominal configuration ratio. The points where the f_1^{data}/f_1^{MC} ratio significantly deviates from 1 are the four mentioned above as well as those in the region $|\eta| > 1.8$.

This leads to the conclusion that except from the points raised above, the geometry is quite well simulated in the nominal MC. Taking the G' geometry as it is done currently in various analyses when wanting to estimate the impact of material mismodeling, would provide then clearly a large overestimation of the real effects. A study is ongoing to build a new geometry with additional material in the detector, according to the differences observed between the ratios f_1^{data}/f_1^{MC} and f_1^{dist}/f_1^{MC}. This new geometry would better reflect the reduced uncertainty on the material budget resulting from the studies described above.

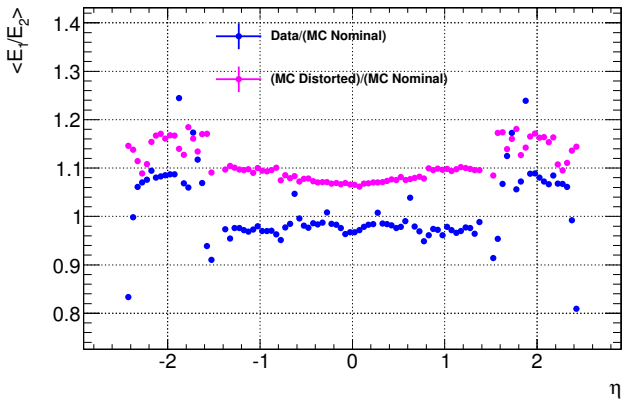

Figure 6.24: Profile of the f_1^{data}/f_1^{MC} (blue line) and f_1^{dist}/f_1^{MC} (pink line) as a function of η.

6.4.2.4 The region $\eta \sim 1.7$

As seen previously, the agreement between the shower shape response in data and MC is very poor in the region $\eta \sim 1.7$. This has been already noticed with the uniformity studies presented in Chapter 5: a 3% drop of the $Z \rightarrow ee$ invariant mass in data with respect to the MC was seen at $\eta = 1.68$. In this region where the material in the tracker and the services have a maximum some features were noticed like a very large constant term and rapidly varying calibration scale factors (see Chapter 5).

In addition the electron reconstruction efficiency is found to be low in this region, as illustrated in Figure 6.25, that shows the η distribution for electrons from the Z decay, for the data and the MC, normalized to 1. The fraction of electrons reconstructed in the region $\eta \sim 1.7$ is about 20% lower in data that in MC. Various tests have been done to understand the origin of this efficiency loss in the data.

The variable used for the pseudorapidity can be either calculated from the cluster barycentre or from the track extrapolation to the calorimeter. To possibly obtain a clue to the origin of the effect, the electron pseudorapidity is plotted with the pseudorapidity computed in both ways, and the two distributions are compared. The same efficiency losses are found, as shown in Figure 6.26(a). The dependence on the electronic charge has been also checked and no obvious differences between electrons and positron was found from this study.

The stability of the effect as a function of the time was investigated: the η distribution in data is compared between the 2011 and 2012 datasets collected at a center of mass energy $\sqrt{s} = 7$ TeV and $\sqrt{s} = 8$ TeV. The results are shown in Figure 6.26(b). No difference is observed between these two datasets in the region $\eta \sim 1.7$.

The dependence with the electron transverse momentum was also tested. The Figure 6.26(c) shows that the efficiency loss is quite stable with respect to the electron p_T.

To localize this effect in the detector, its response along the azimuth was tested. The Figure 6.26(d) shows that no further structures are seen in ϕ.

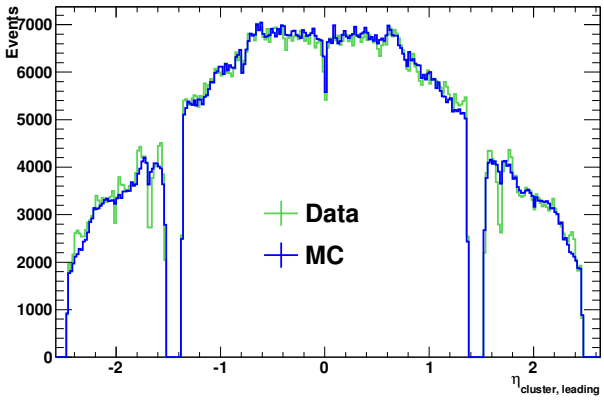

Figure 6.25: Normalized distributions of the pseudorapidity as computed from the cluster barycentre for the data collected in 2011 (green line) and the MC (blue line).

This discrepancy between data and MC could at least be explained by two different possibilities: a large material mismodeling in this region, or a MC-based calibration feature.

The first possibility is tested using the shower depth variable. Figure 6.27(a) shows the profile of this variable as a function of η, with a binning of $\Delta\eta = 0.1$ for the full dataset collected in 2012 and for the MC. The shower depth is quite well described by the MC in the barrel region, however large discrepancies are seen in the endcap parts. Figure 6.27(b) shows more particularly the region $1.5 < \eta < 2$. Discrepancies arise in three regions: $\eta \sim 1.68$ with about $0.2X_0$ difference between the data and the MC, $\eta \sim 1.73$ with a difference of about $0.8X_0$ and $\eta \sim 1.88$ with a difference of about $0.6X_0$. These three pathological regions were also spotted by the shower shape variables f_0 and f_1.

For the region $\eta \sim 1.7$, structures in ϕ are looked for. To be more sensitive, the four detector

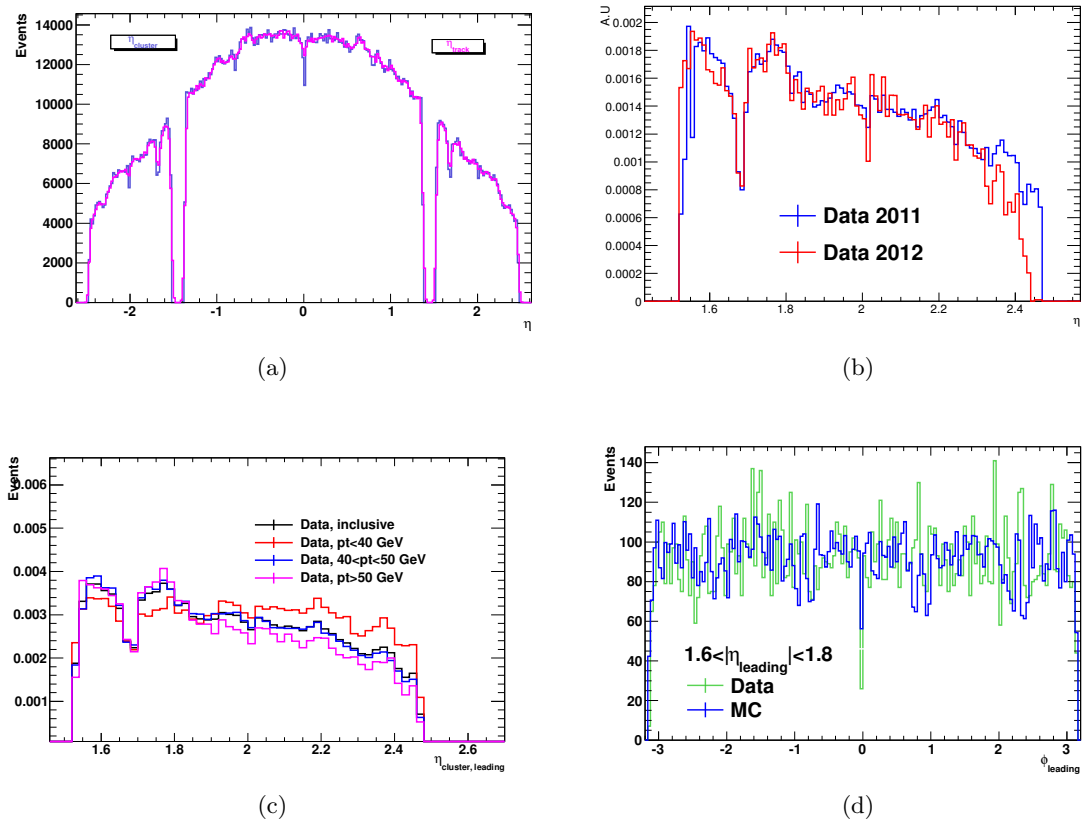

Figure 6.26: (a) Normalized distributions of the pseudorapidity as computed from the cluster barycentre (blue line) or from the track extrapolation to the calorimeter (pink line), for the data collected in 2011. (b) Normalized distributions of the pseudorapidity comparing the data collected in 2011 (blue line) and in 2012 (red line). (c) Normalized distributions of the pseudorapidity for different electrons p_T ranges: $p_T < 40$ GeV (red line) $40 < p_T < 50$ (blue line) and $p_T > 50$ (pink line) compared to the inclusive distribution (black line). (d) Normalized distribution of the azimuth in the region $1.6 < |\eta| < 1.8$ for the data (blue line) and the MC (green line).

quarters $-\pi < \phi < -\pi/2$, $-\pi/2 < \phi < 0$, $0 < \phi < \pi/2$ and $\pi/2 < \phi < \pi$ are folded on each others. Small pseudorapidity regions of size $\Delta\eta = 0.025$ are scanned. Figure 6.29, the distribution of the shower depth as a function of the folded azimuthal direction, for the bin $1.725 < \eta < 1.750$ is shown for the data and the MC. Very different structures are found in this bin: the MC has a two-holes structure whereas the data shows only small fluctuations and has a broader distribution of the shower depth. The structures seen in the MC shower-depth at $\phi_{folded} = 30$ and 40, correspond to a quantity of material of about $2X_0$.

The study was repeated in other η bins, and the structures observed in the MC are present from about $\eta = 1.68$ up to $\eta = 1.8$. Similar results have been found from an independent study using electrons from the W decay [211].

From discussions with inner detector geometry experts [212,213] this problem was interpreted as due to a mismodeling of the SCT endcap cooling pipes running along the cryostat. Indeed, looking at Figure 6.28(a) that shows the material budget for the inner detector services in the region $1.725 < \eta < 1.750$, four double-spikes can be seen, located in the middle of each detector

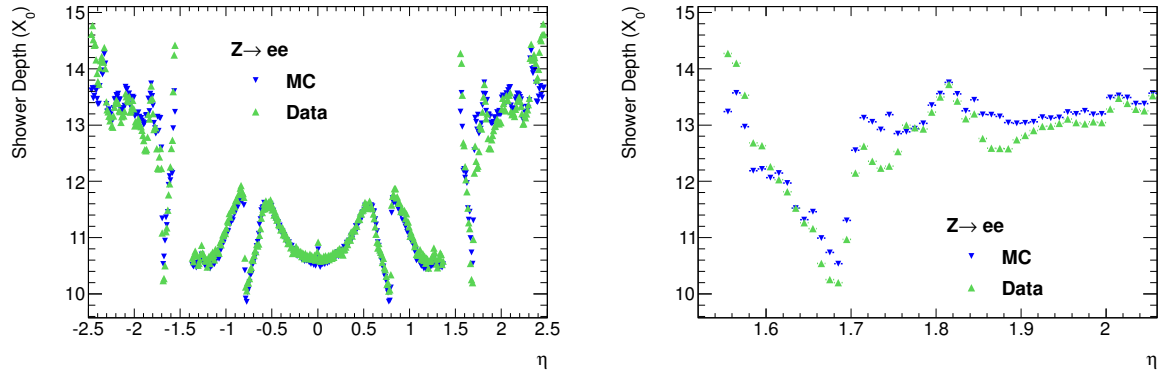

(a) (b)

Figure 6.27: Profile of the shower depth for $Z \rightarrow ee$ events in data (green up triangles) and MC (blue down triangles) as a function of η in the full acceptance (a) and in the range $1.5 < \eta < 2$ (b).

quarter. These structures represent an amount of material of about 2 X_0. This well corresponds to the structures observed previously in the $Z \rightarrow ee$ MC.

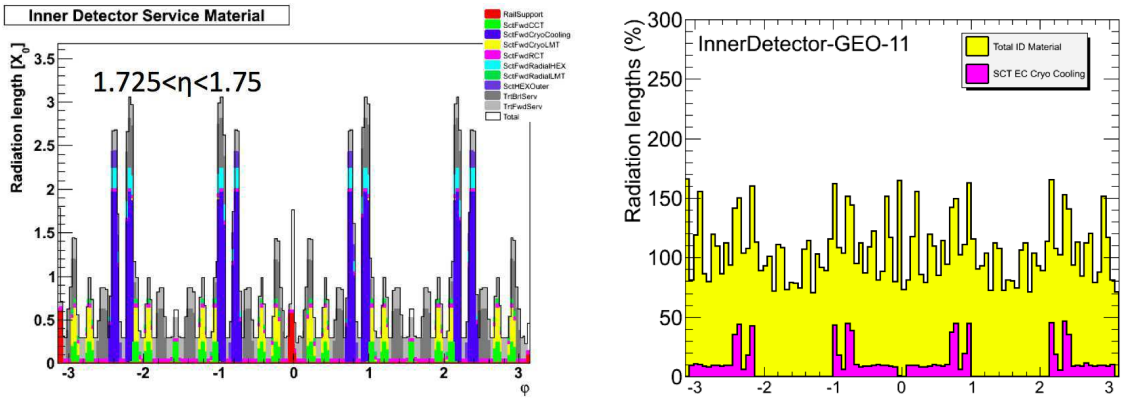

(a) (b)

Figure 6.28: (a) Simulation of the amount of material in radiation length from the inner detector services in the region $1.725 < \eta < 1.750$ as a function of ϕ. The different colors corresponds to the different TRT and SCT services as well as the rails supports. The double-spikes in blue color referred to as "SctFwdCryoCooling" corresponds to the SCT endcap cooling pipes running along the cryostat [214]. (b) New simulation of the amount of material in the SCT endcap cooling pipes volumes in radiation length in the region $1.6 < \eta < 1.8$ [215].

The simulation of the total material in this region was found to be correct but not its distribution [215]. A new model was proposed, where about 40% of the material volume is left at its initial position whereas 40% of this material is spread around the initial position within $\pm 49^o$ around the horizontal plane and 20% is moved radially outside the ID volume in barrel-endcap transition regions. The new distribution of the material is shown in Figure 6.28(b) for the region $1.6 < \eta < 1.8$. A new geometry tag referred to as GEO-21 (with respect to the tag GEO-20 for the nominal geometry) has been created including this new model.

To test the impact of these modifications, MC samples of single electrons have been produced with this tag. The single electrons have been produced with different p_T (20, 40, 90 GeV) and in the region $1.6 < \eta < 1.8$.

A comparison between the new and actual geometry is performed using these samples and a single electron sample with the nominal geometry. In order to be compatible with the results obtained with the $Z \rightarrow ee$ MC, the single electrons are selected in the range $40 < p_T < 50$ GeV.

The study performed previously for the $Z \rightarrow ee$ samples is repeated here for these single electrons samples. Figures 6.29(c) and 6.29(d) shows the distribution of the shower depth as a function of the folded azimuth for the new and nominal geometry.

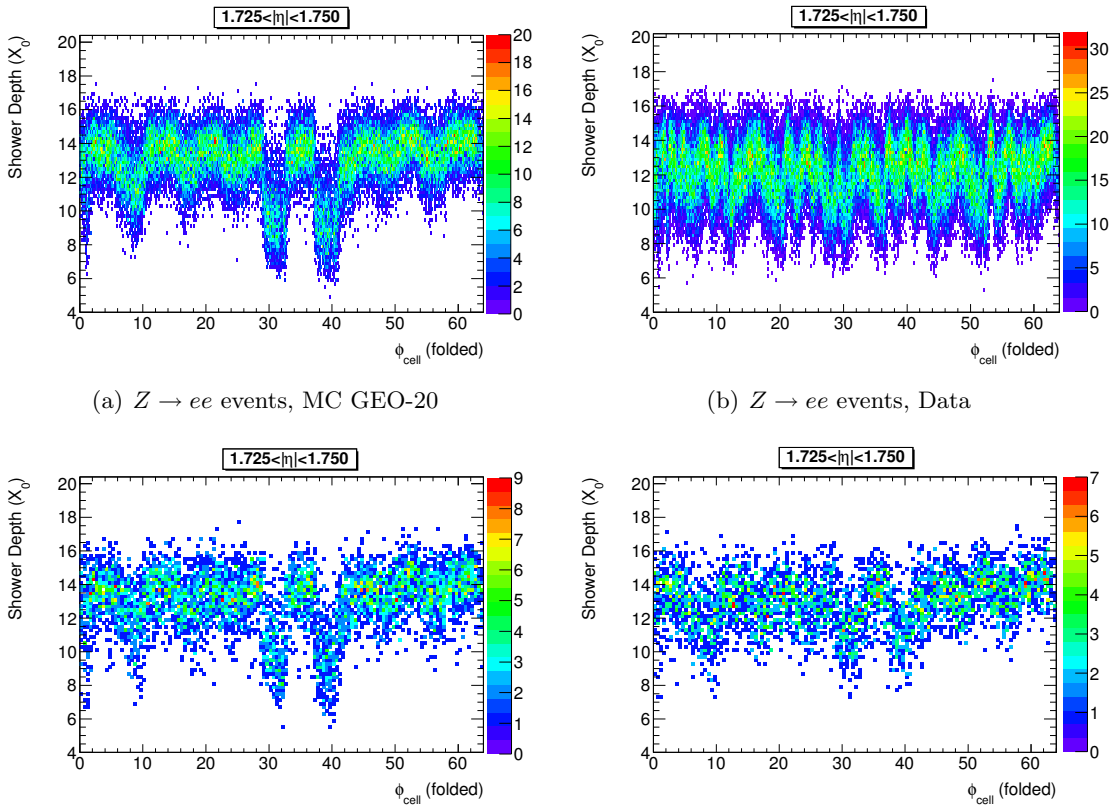

(a) $Z \rightarrow ee$ events, MC GEO-20

(b) $Z \rightarrow ee$ events, Data

(c) Single electrons, GEO-20

(d) Single electrons, GEO-21

Figure 6.29: Distribution of the shower depth for $Z \rightarrow ee$ events in MC (a) and data (b) as a function of the folded azimuthal direction, for the bin $1.725 < \eta < 1.750$. Distribution of the shower depth for single electrons with $40 < p_T < 50$ GeV in the nominal geometry (c) and with the improved modeling of the SCT services (d) as a function of the folded azimuthal direction, in the region $1.6 < \eta < 1.8$.

The structures seen in the single electron sample with the current geometry are similar to the ones observed with the $Z \rightarrow ee$ sample. With the new geometry, the dips in shower depth are almost halved and the distribution of the shower depth has broaden elsewhere. This provides a distribution which is more similar to the data even if the overall agreement is not perfect.

The new tag GE0-21 will be used to generate the next generation of $Z \rightarrow ee$ MC samples. Once these samples will be ready, it will be possible to test the agreement with the data and to evaluate which impact this modification has on the constant term for example.

It is however expected that this effect is not sufficient to explain the poor performance of this region. Beside the shower shape study, in order to understand if other material mismodeling could affect the shower shapes, drawings and mockups of the detector have been studied. From discussions with experts [210, 211], small mismodelings have been found:

- The bolts between the inner warm cylinder and the warm bulkhead are missing in the simulation and the thickness of the flange in this region is underestimated. This concerns a small region around $\eta = 1.7$. Steel bolts have been added and the thickness has been increased from 35 to 50 mm in the simulation. The result of these modifications can be seen in Figure 6.30 where a Geantino scan [8] is made for the standard geometry and for the improved one as a function of *phi*. In this Figure, the structures observed previously are present, because the same region is scanned. The addition of the steel bolts has a visible impact, it broadens the distribution of X_0 along ϕ. The small structures that were seen in data (see Figure 6.29(b)) could be due to these bolts and their addition in the MC could improve the data to MC agreement.

- Coil supports are misplaced and incorrectly described in the region $1.63 < \eta < 1.68$. There are 24 such pieces along ϕ for each side of the detector, corresponding to a maximal thickness along the trajectory of about 1 X_0. In the standard positioning, these supports are equidistant, whereas they are in reality grouped by two. The size of these supports is also mismodeled. The simulation has since been corrected.

Both problems have been noted the problem is noted and will be fixed in future. A test will be performed once simulation samples integrating all these effects will be ready.

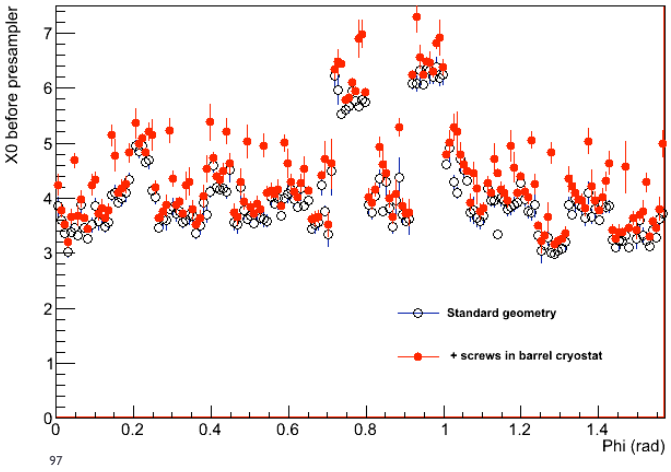

Figure 6.30: Simulation of the amount of material in radiation length before the presampler in the region $1.7 < \eta < 1.73$, for the nominal geometry (open circles) and for a new geometry where the screw barrel cryostat are added (red points), using a Geantino scan [210].

[8] Geantino are virtual particles for simulation which do not interact with materials and undertake transportation processes only [150].

6.4.3 Quantification of material

The shower shape variables f_0 and f_1 are used to quantify deviations in the material budget with respect to the MC. This method is described here but not used due to two issues. First, as seen in Chapter 5, the presampler and strips energy are miscalibrated. The variables f_0 and f_1 cannot then be used to quantify the amount of material, they should be before corrected for with the calibration scale factors derived in this chapter. This is an ongoing work. Then, as seen in most of the studies previously, the shower shapes are not only sensitive to the material mismodeling but also to calibration and simulation problems. All the effects seen in the f_0 and f_1 should then be first understood, in order to only quantify effects coming from material mismodeling.

This method is based on the linear response of these two variables under a variation of the amount of material, as already noticed in Section 6.3.

Single electrons MC samples have been used in this study. The variation of the amount of material are provided by the use of the geometries described below.

- Configurations A1,2,3: Add $1, 2, 4\%$ extra X_0 after the first pixel layer (ATLAS-GEO-06). The energies E=25,50 GeV are simulated with η in [0.65-0.75] and [1.25-1.35],
- Configurations B1,2,3: Add $1-3, 2-6, 4-12\%$ extra X_0 in the SCT Layer 1 (ATLAS-GEO-06). The energies E=25,50 GeV are simulated with η in [0.65-0.75],
- Configuration C1,2,3: Add 3,6,10 % extra X_0 between TRT Barrel and Endcap (ATLAS-GEO-06). The energies E=25,50 GeV are simulated with η in [0.65-0.75],
- Configuration E1,2,3: Add 1,2.5,5,7.5 % extra X_0 between SCT Endcap and TRT Endcap (r=60cm) (ATLAS-GEO-06), with η in [1.25-1.35] and [1.9-2.14],
- Configuration F1,2,3. Add 1,3,4 % extra X_0 between Pixel Barrel and endcap (ATLAS-GEO-06),
- Configuration G1,2,3: Add $0.6-1.2, 1.2-2.4, 2.4-4.8\%$ extra X_0 between pixel forward services along z (ATLAS-GEO-06).

These geometries corresponds to the general tag ATLAS-GEO-06 designed in 2010. The single electrons are simulated with different energies (25, 50, 100 GeV) and in different η regions ($0.65 < \eta < 0.75$,$1.25 < \eta < 1.35$ and $1.9 < \eta < 2.1$). There are about 90000 single electrons generated by sample.

The variable R^x_{geo} defined in Section 6.3 and corresponding to the ratio of the averaged value of one of the variables x in a modified geometry *geo* to the nominal one is used here.

Figure 6.31 shows the evolution of $R^{f_0}_{b\,layer}$ and $R^{f_1}_{b\,layer}$ as a function of the amount of material added in the b-layer (first pixel layer), for electron of 25 GeV and in the regions $0.65 < \eta < 0.75$ and $1.25 < \eta < 1.35$.

A dependence is observed with the pseudorapidity region. A difference of response is also seen between these two variables. This arises from the calibration of the presampler with respect to the accordion which is not corrected here. The linear behaviour can be fitted for each variable and each region, and the slopes extracted.

This study has been repeated for all the different geometries described above, for the three η regions, and the three energies. A qualitative comparison has been made between the slopes extracted in all these configurations. It has been found that the slopes depends on the η region

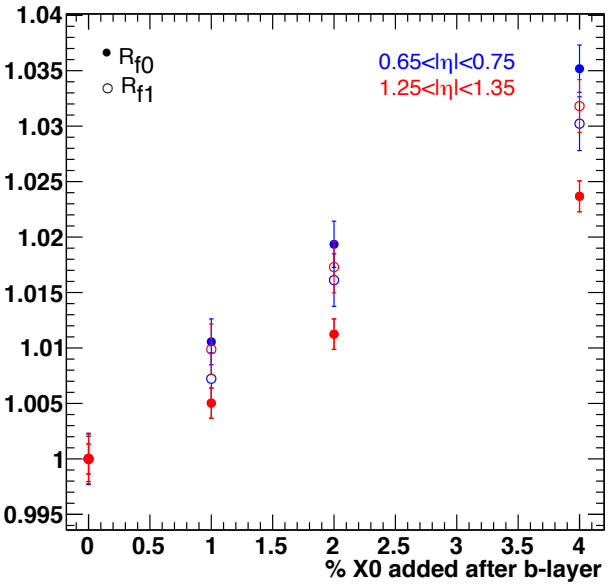

Figure 6.31: Evolution of the ratio R_{f_0} (full dot) and R_{f_1} (empty circle) as a function of the amount of material in radiation length added in the b-layer, for electrons of 25 GeV and in the regions $0.65 < \eta < 0.75$ (blue) and $1.25 < \eta < 1.35$ (red).

and on the radius at which the material has been added. More precisely, going from smaller radius (e.g the b-layer) to larger radius (e.g the TRT), the slope extracted from the linear fits decrease by about 60%. This is true for different energies and for both variables. The variation of the slope with η is less clear, it depends on the geometry considered. Almost no dependence has been found with respect to the energy.

To conclude, measuring of the amount of material is really possible but would require to know the location of the material when using the shower shape method. This is an issue when using the shower shapes method, were only an integral of all the material crossed is provided. Instead, an upper limit on the amount of material can be putted, by using the largest slopes to measure the material budget. At least, it is possible to test if the amount of material seen in the data is in agreement which what is modeled in the simulation.

Chapter 7

The $H \rightarrow \gamma\gamma$ analysis

The ATLAS collaboration has performed a search for the Higgs boson in the diphoton channel. The evolution of this analysis is described in [216, 217, 218, 219, 220, 221, 222, 223].
The latest analysis is described here. It uses the full dataset of the ATLAS Run I (see Chapter 3) i.e up to the Long Shut Down 1 (LS1) that started on the 16th of February 2013. This corresponds to 4.8 fb^{-1} of data recorded by ATLAS at a center of mass energy of $\sqrt{s}$ =7 TeV in 2011 and 20.7 fb^{-1} at a center of mass energy of $\sqrt{s}$ =8 TeV in 2012.

7.1 Event selection

7.1.1 Diphoton events selection

The candidates are first preselected with the following criteria:

- The run and Luminosity Block need to be contained in the Good Run List (GRL, see Chapter 4) to ensure data of good quality from the inner detector, electromagnetic and hadronic calorimeters.
- The events need to pass specific trigger chains requiring at least two photons with loose identification criteria and with transverse momentum of at least 20 GeV for both photons in 2011 and at least 35 and 25 GeV for the leading and sub-leading photon in 2012. These triggers are respectively denoted `2g20_loose` and `g35_loose_g25_loose`. The efficiencies of these triggers is measured from the data recorded by ATLAS using a bootstrap approach where the efficiency of the Event Filter selection with respect to tight photons triggered by the L1 times the efficiency of the L1 selection on tight photons triggered by the Minimum Bias triggers is computed [161]. The measured efficiency of these triggers with respect to the $H \rightarrow \gamma\gamma$ selection is $98.9^{+0.2}_{-0.3}$% for early 2011 and $98.8^{+0.3}_{-0.4}$% for later 2011 and 99.4% in 2012 [224, 225].
- In order to reject candidates from non-collision backgrounds, the events are required to have at least one reconstructed primary vertex. This selection applies only for low luminosity data samples as the ones recorded in early 2011.
- Photon clusters mistakenly built from LAr noisy channels are removed using the LAr Cleaning procedure described in Chapter 4 and in reference [142].
- The converted photon candidates reconstructed in a region where the first pixel layer is not working properly are rejected. This strongly decreases the misidentification of electrons as photons.

- Photons are considered as candidates only if reconstructed in the fiducial region of the calorimeter $|\eta_{s2}| < 1.37$ or $1.52 < |\eta_{s2}| < 2.37$ (where η_{s2} corresponds to the photon pseudorapidity in the second sampling of the calorimeter). The barrel to endcap transition region is excluded, as photons in this region suffer from a worse reconstruction due to the large amount of material (see Chapter 5).

- At least two reconstructed photons with a tight identification criteria are required.

The candidates are then selected following the signature of a Higgs boson decaying into two photons:

- $p_{T1} > 40$ GeV and $p_{T2} > 30$ GeV for the leading and sub-leading photons respectively. These values have been tuned in order to yield the highest sensitivity. The energy of the photons has been calibrated following the procedure reviewed in Chapter 5. In addition, a specific tool for correcting converted photon energy is used. This correction enables an improvement of the RMS of the diphoton invariant mass using the photon conversion radius that brings an important information about material in the detector. A sizeable improvement of 6% on the mass resolution is for example achieved when both photons are converted [226].

- The selection of the primary vertex of the event is crucial as it has an impact on the accuracy of the invariant diphoton mass and then on the signal resolution. In a high pileup environment (typically an average of 9 and 21 interactions per bunch crossing in 2011 and 2012 respectively), a Neural Network algorithm is used to determine the correct primary vertex. This algorithm combines several quantities:

  - The longitudinal segmentation of the calorimeter, that allows to measure the pseudorapidity of the photons. This method is called the calorimeter pointing.
  - The conversion vertex in silicon detectors if available for converted photons
  - The scalar or squared sum of transverse momenta which depart from the considered vertex
  - The azimuthal angle difference between the sum of the tracks p_T associated to a vertex and the diphoton system

  The two latest variables are related to the kinematic properties of hard scattering events where a non-zero Higgs boson p_T and an angular deviation in the transverse plane are expected, due to gluon production in the initial state. This method has been studied with simulation samples and compared to other methods. It has been demonstrated to give one of the best resolutions on the diphoton invariant mass and to be more robust against harsh pileup conditions. The efficiency of choosing a reconstructed vertex, in $H \to \gamma\gamma$ events, that is within 0.3 mm of the true $H \to \gamma\gamma$ vertex position has been evaluated to be 75% using $Z \to ee$ events from data and MC where the electrons track have been removed and after applying the necessary extrapolations to mimic the Higgs boson to diphoton decay signal [223].

- The clusters (and tracks for converted photons) should be isolated in order to remove the indirect or fake photons coming from hadronic decays.

  - The track isolation requires that the sum of transverse momentum of the tracks inside a cone of size $\Delta R = \sqrt{(\Delta\eta)^2 + (\Delta\phi)^2} = 0.2$ around the photon is lower than 2.6 GeV.

– The calorimeter isolation then requires that the sum of energy reconstructed in topological clusters with positive energy in a cone of size $\Delta R = 0.4$ around the photon is lower than 6 GeV. This isolation is corrected for underlying event and pileup noise and is almost pileup-independent [227]. This is illustrated in Figure 7.1 where the isolation is very stable as a function of the bunch position in a train of bunches, which is sensitive to the out-of-time pileup (see Chapter 5).

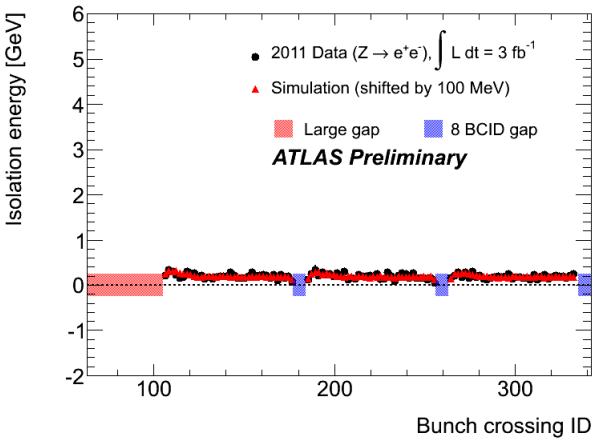

Figure 7.1: Isolation energy as defined in the text, as a function of the position of the bunch in the train, for $Z \to ee$ events selected in a data sample corresponding to 3 fb^{-1} recorded by ATLAS at a center of mass energy $\sqrt{s}$ =7 TeV in 2011 (black points) and in a MC simulating the $Z \to ee$ process (red triangles). The blue and red bands corresponds respectively to small and large gaps without any bunches corresponding to 8 and 36 standard bunch positions (BCID). This is equivalent to 200 ns and 900 ns. Taken from [228].

7.1.2 Object selection

With the relatively large statistics accumulated during the 2011 and 2012 data taking periods, distinguishing between the different production modes for the Higgs boson production becomes achievable. As reviewed in Chapter 2 the five main production processes are the fusion of gluons (ggF), the Vector-Boson-Fusion (VBF), the associated production of a Higgs boson with a W (WH) or a Z (ZH) boson and finally the associated production of a Higgs boson with top quarks (ttH). The specific signatures of these processes are used to build an analysis where at least the four main processes are distinguished. The lepton, jet and neutrino selections are described below.

Electrons The electrons are reconstructed from clusters in the calorimeter and identified with a set of cuts on shower shapes, track quality, and track-cluster matching variables as reviewed in Chapter 5. The electrons are asked to have $p_T > 15$ GeV and $\eta_{cluster} < 2.47$. As for the photons, the electrons should be isolated both in the tracking and calorimeter environments.

Muons The muons are reconstructed by combining tracks in the inner detector and either a complete track or a track-segment in the muon spectrometer [1] [229]. The muon candidates

[1] In the forward region outside the Inner Detector coverage ($2.5 < |\eta| < 2.7$), they are reconstructed from the muon spectrometer alone.

are required to pass the kinematic cuts: $p_T > 10$ GeV and $\eta_\mu < 2.7$ and to be isolated. The muons are selected only if hits could be reconstructed in the three Inner Detector compartments (pixels, SCT, TRT). In addition, the muon vertex should have transverse and longitudinal impact parameters smaller than 1 and 10 mm respectively.

Jets The jets are reconstructed from topological clusters in the calorimeters using the anti-k_t algorithm with a distance parameter of R = 0.4 [230]. To avoid a dependence of the jet energy response on pileup, a subtraction scheme based on the jet area algorithm is applied [231]. Finally, jets from pileup events are avoided using the fraction of the tracks transverse momenta associated to a jet of at least 30 GeV coming from the diphoton vertex. This fraction denoted JVF (Jet Vertex Fraction) should be larger than 0.25 (0.50) in 2012 (2011). The reconstructed jet should satisfy the following kinematic cuts: $\eta_{jet} < 4.5$ and $p_{T,jet} > 25$ GeV ($p_{T,jet} > 30$ GeV) for $\eta_{jet} < 2.4$ ($\eta_{jet} > 2.4$).

Missing transverse energy $E_{\mathrm{T}}^{\mathrm{miss}}$ is reconstructed as the complement of the visible transverse energy (i.e the sum of all calibrated objects in the detector) in an event. The performance of the reconstruction and calibration of this quantity for the 2011 and 2012 data taking period are detailed in references [232, 233, 234]. The measurement of the missing transverse energy is very sensitive to the pileup. Methods have been designed to suppress the pileup contribution [233]. However the resolution of the $E_{\mathrm{T}}^{\mathrm{miss}}$ deteriorates proportionally to the squared total energy deposited in the calorimeter. The significance of the missing energy $S_{E_T^{miss}}$ defined as the ratio of the missing transverse energy over its resolution, is used instead.

7.2 Invariant mass reconstruction

The analysis is based on the search for a resonance in the diphoton invariant mass distribution over a large monotonic falling background. The diphoton invariant mass is reconstructed with:

$$m_{\gamma\gamma} = \sqrt{2E_{T1}E_{T2}(\cosh\Delta\eta - \cos\Delta\phi)} \tag{7.1}$$

where E_{T1} and E_{T2} are the corrected transverse energies of the leading and subleading photons, $\Delta\phi$ is the difference in azimuthal angle between the two photons as determined from the second calorimeter layer and $\Delta\eta$ is the difference in pseudorapidity between the two photons as measured from the extrapolation of the first calorimeter layer position to the primary vertex one.

The resolution on the mass depends then on the primary vertex selection efficiency and on the precision on the photon energy.

Both the energy response [2] and the calorimeter pointing method are stable against pileup. The invariant mass reconstruction is therefore expected to be stable when varying the number of average interactions per bunch crossing. This is illustrated in Figure 7.2.

The explored range in invariant mass is [100,150] GeV but events in the range [100,160] GeV are used in the analysis for background fitting. The presence of a $Z \to ee$ background peaking at 91 GeV, with electrons misidentified as photons, makes the lower mass range difficult to analyse. With the statistics accumulated in the Run I, the higher mass ranges are not yet usable (see Chapter 2).

The number of candidates selected in this mass window with the data sample described previously is respectively 23788 and 118893 in 2011 and 2012.

[2] See Section 5.4.

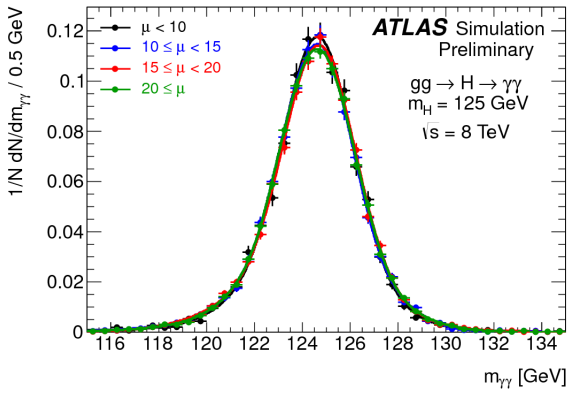

Figure 7.2: Diphoton invariant mass distribution for sets of events having different average number of interactions per bunch crossing μ for a MC simulating the $H \to \gamma\gamma$ process at 125 GeV [10].

7.3 Event categorization

The events passing the above selections are classified mainly according to:

- Their signal over background ratio
- Their resolution

which are two correlated quantities. This classification further increases the sensitivity to a potential signal [235]. As reviewed in Chapter 5, the resolution of the photons is the best in the central barrel region and the worst around the transition region, and is better for unconverted photon than converted ones. Therefore, categories based on the photon pseudorapidity as measured in the second sampling of the calorimeter (η_{s2}) and conversion status are built.

In addition, the variable p_{Tt} is defined. It corresponds to the component of the p_{T} vector transverse to the improperly called "thrust axis". The thrust vector is defined as follows:

$$\begin{aligned} p_{x,thrust} &= p_{x1} - p_{x2}, \\ p_{y,thrust} &= p_{y1} - p_{y2}. \end{aligned} \tag{7.2}$$

$$p_{Tt} = 2 \cdot \left| p_{x1} \cdot \hat{p}_{y,thrust} - p_{y1} \cdot \hat{p}_{x,thrust} \right| . \tag{7.3}$$

with the indices 1 and 2 denoting the leading and sub-leading photons, and $\hat{p}_{thrust}$ the thrust vector normalized to unit vector. See Fig 7.3.

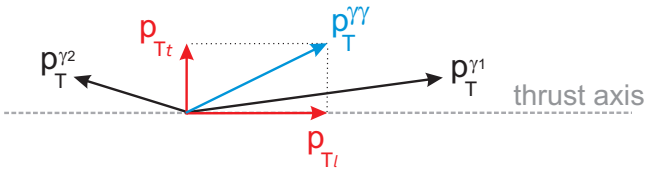

Figure 7.3: Sketch of the p_{Tt} definition.

This variable allows classification of the events according to their signal over background, as the signal is expected to have a harder p_T distribution, especially in the VBF process, as seen

in Figure 7.4.

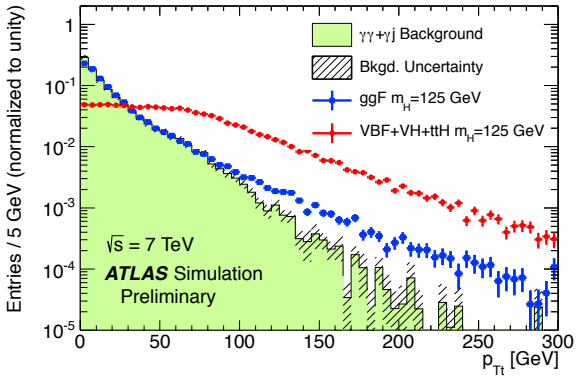

Figure 7.4: Distribution of the p_{Tt} variable for the background (green filled histogram) and for the signal produced with the gluon-gluon fusion (blue dots) and the Vector Boson Fusion (red dots) processes, in the simulation [10].

Additional categories are created for separating the different production processes. This separation is built from the following topological variables:

- the invariant mass of the two leading jets $m_{\mathrm{j_1 j_2}}$
- their pseudorapidity separation $\Delta\eta_{j_1 j_2}$
- the azimuthal angle difference between the diphoton and the dijet systems $\Delta\phi(\gamma_1\gamma_2 - \mathrm{j_1 j_2})$,
- the diphoton system pseudorapidity in the frame of the tagging jet pseudorapidity, usually called Zeppenfeld variable [236]: $\eta^* = |\eta_{\gamma_1\gamma_2} - \frac{\eta_{j_1}+\eta_{j_2}}{2}|$
- the minimal ΔR between one of the photons and one of the two leading jets $\Delta R_{min}^{\gamma_{1,2} j_{1,2}}$.

A more detailed description of the categories for the two analyses performed with the data collected in 2011 and 2012 respectively is given in the next section.

7.3.1 2011 data taking

The analysis is made of ten categories, with one exclusively dedicated to the VBF process. This category is the first filled, by asking for events with two reconstructed jets in addition to the photons. The events that fail this condition are then classified in the remaining 9 categories.

- **C1:** Both photon candidates are unconverted, and have $|\eta_{s2}| < 0.75$; the diphoton system has $p_{\mathrm{Tt}} < 60$ GeV.
- **C2:** Both photon candidates are unconverted, and have $|\eta_{s2}| < 0.75$; the diphoton system has $p_{\mathrm{Tt}} > 60$ GeV.
- **C3:** Both photon candidates are unconverted and at least one candidate has $|\eta_{s2}| > 0.75$; the diphoton system has $p_{\mathrm{Tt}} < 60$ GeV.

- **C4:** Both photon candidates are unconverted and at least one candidate has $|\eta_{s2}| > 0.75$; the diphoton system has $p_{\mathrm{Tt}} > 60$ GeV.

- **C5:** At least one photon candidate is converted and both photon candidates have $|\eta_{s2}| < 0.75$; the diphoton system has $p_{\mathrm{Tt}} < 60$ GeV.

- **C6:** At least one photon candidate is converted and both photon candidates have $|\eta_{s2}| < 0.75$; the diphoton system has $p_{\mathrm{Tt}} > 60$ GeV.

- **C7:** At least one photon candidate is converted and both photon candidates have $|\eta_{s2}| < 1.3$ or $|\eta_{s2}| > 1.75$, but at least one photon candidate has $|\eta_{s2}| > 0.75$. The diphoton system has $p_{\mathrm{Tt}} < 60$ GeV.

- **C8:** At least one photon candidate is converted and both photon candidates have $|\eta_{s2}| < 1.3$ or $|\eta_{s2}| > 1.75$, but at least one photon candidate has $|\eta_{s2}| > 0.75$. The diphoton system has $p_{\mathrm{Tt}} > 60$ GeV.

- **C9:** At least one photon candidate is converted and at least one photon candidate is in the range $1.3 < |\eta_{s2}| < 1.37$ or $1.52 < |\eta_{s2}| < 1.75$.

- **C10:** VBF category. The two leading jets passing the selection cuts must pass in addition the following cuts: $\Delta\eta_{\mathrm{j_1j_2}} > 2.8$, $m_{\mathrm{j_1j_2}} > 400$ GeV and $\Delta\phi(\gamma_1\gamma_2 - \mathrm{j_1j_2}) > 2.6$.

7.3.2 2012 data taking

For the 2012 dataset, the events selected are classified into 14 categories of which 5 are dedicated to the VBF and VH processes. The nine others are defined exactly as the 2011 case, except for C9 where the selection in pseudorapidity is slightly different: $1.3 < |\eta_{s2}| < 1.37$ or $1.56 < |\eta_{s2}| < 1.75$.

The five categories dedicated to VBF and WH or ZH (VH) production process are further presented below [237]:

- **C14:** Lepton category (VH). At least one electron or one muon is required. If the invariant mass computed with the electron and one of the two selected photons is contained in the window [84,94] GeV, the candidate is removed.

- **C13:** $E_{\mathrm{T}}^{\mathrm{miss}}$ category (VH). The candidate should not be selected by the previous category, and should have $S_{E_{\mathrm{T}}^{\mathrm{miss}}} > 5$.

- **C12:** Low mass 2-jets category (VH). The candidate should not be selected by the previous categories, and should pass the following criteria: at least two reconstructed jets, such that $\Delta\eta_{\mathrm{j_1j_2}} < 3.5$, $60 < m_{\mathrm{j_1j_2}} < 110$ GeV and $\Delta\eta(\gamma_1\gamma_2 - \mathrm{j_1j_2}) < 1$. The diphoton system should have $p_{\mathrm{Tt}} > 70$ GeV.

- **C11-C10:** High mass 2-jets categories (VBF). The candidate should not be selected by the previous categories and contain at least two reconstructed jets. The C11-C10 separation, corresponding to a loose and tight selection of the VBF candidates is done in two ways: using a cut-based method or a Multi-Variate-Analysis that classify the events according to a Boosted-Decision-Tree (BDT) [238].

  - **Cut-based:** the two jets should satisfy: $\Delta\eta_{\mathrm{j_1j_2}} > 2.8$, $m_{\mathrm{j_1j_2}} > 400$ GeV and $\Delta\phi(\gamma_1\gamma_2 - \mathrm{j_1j_2}) > 2.6$.

* **C11:** a tighter cut is applied on the 2-jets invariant mass $m_{\mathrm{j_1 j_2}} > 520$ GeV. In addition, two additional criteria are requested: $\Delta R_{min}^{\gamma_{1,2} j_{1,2}} > 2$ for jets with a transverse momentum above 30 GeV, and $\eta^* < 2.4$.
* **C10:** all the preselected events that do not pass the criteria for the C11 category.

– **MVA:**

Eight discriminating variables are used to build the BDT: the jets pseudorapidity η_{j_1} and η_{j_2}, $m_{\mathrm{j_1 j_2}}$, $\Delta\eta_{j_1 j_2}$, the p_{Tt} of the diphoton system, $\Delta\phi(\gamma_1\gamma_2 - \mathrm{j_1 j_2})$, η^*, and $\Delta R_{min}^{\gamma j_1}$.

The two jets are preselected with: $\Delta\eta_{\mathrm{j_1 j_2}} > 2$, $\eta^* < 5$ and with the output of the BDT which should be larger than 0.44.

* **C11:** $BDT > 0.74$
* **C10:** $0.44 < BDT < 0.74$

The C10 category in 2011 does not correspond perfectly to the one defined in 2012, neither with the cut-based method nor with the MVA. The MVA is used as the default method, the Cut-Based is used only as a cross-check. All the results and numbers given in the following use the MVA method unless otherwise stated.

The categories dedicated to the VBF and VH production modes have been optimized in order to get the highest purity and to increase the sensitivity. This optimization is documented in reference [239].

Table 7.1 summarizes the repartition of the selected events into the 10 (14) categories of the analysis performed in 2011 (2012) in the [100,160] GeV mass window.

Table 7.1: Repartition of the selected events into the 10 (14) categories of the analysis performed in 2011 (2012) with 4.9 fb^{-1} (20.7 fb^{-1}) collected at a center of mass energy $\sqrt{s} = 7$ TeV ($\sqrt{s} = 8$ TeV) in the mass window [100,160] GeV.

Category	2011	2012
Unconverted central, low p_{Tt}	2054	10900
Unconverted central, high p_{Tt}	97	553
Unconverted rest, low p_{Tt}	7129	41236
Unconverted rest, high p_{Tt}	444	2558
Converted central, low p_{Tt}	1493	7109
Converted central, high p_{Tt}	77	363
Converted rest, low p_{Tt}	8313	38156
Converted rest, high p_{Tt}	501	2360
Converted transition	3591	14864
VBF	89	-
VBF loose	-	276
VBF tight	-	136
VH(had)	-	210
$E_{\mathrm{T}}^{\mathrm{miss}}$	-	49
VH(lep)	-	123
Inclusive	32788	118893

Figure 7.5 shows, from a MC study, the signal composition of the categories in terms of the different production processes. A high purity is achieved for the categories dedicated to the VH process with leptonic and missing transverse energy signatures (around $80 - 85\%$). The VH

hadronic category is less efficient and contaminated by gluon fusion production process (almost 50%). In the tight (loose) high-mass two-jet category 75% (55%) of the signal is from VBF.

Finally the untagged category has a large fraction of events produced with the gluon fusion process as expected.

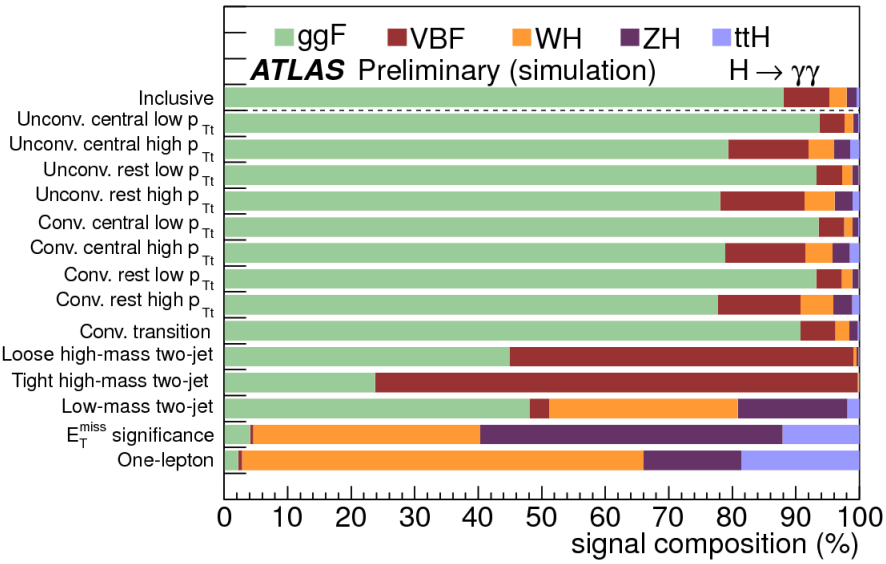

Figure 7.5: Signal decomposition of the different production modes, for the 14 categories built for the 2012 analysis, computed from a $H \to \gamma\gamma$ MC sample at the mass $m_H = 126.5$ GeV [223].

7.4 Signal Model Specific Corrections

The $H \to \gamma\gamma$ simulation is mostly used to extract a signal parametrization (which will be presented in Section 7.5). Its description is given below.

7.4.1 Signal MC description

The production of a Standard Model Higgs boson through the gluon-gluon fusion and the Vector Boson Fusion processes is modeled with the generator POWHEG [240,241] interfaced with PYTHIA [158] for the generation of the parton showers and their hadronization. The production of the Higgs boson in association with vector bosons or top quark pairs is modeled with the PYTHIA generator.

The Higgs boson Branching Ratio into two photons and its uncertainty as a function of the Higgs boson mass are calculated using the HDECAY program [242] and are taken from references [63, 243].

The sets of parton distribution functions used correspond to CT10 [183] for the POWHEG generator and to CTEQ6L1 [78] or MRSTMCAL [244] for the PYTHIA generator.

The pileup is modeled in these simulations following the conditions observed in data by summing up additional simulated inelastic proton-proton collisions. A 50 ns bunch spacing is simulated.

The full simulation of the ATLAS detector is made using the GEANT4 [150] program. An additional simulation with extra material in the detector for the gluon-gluon fusion process and

for a Higgs boson mass of 120 GeV has been also used in order to study the effect of additional material on the yields, resolution and peak position.

7.4.2 General corrections

Some features are not taken into account in the simulation described above and are accounted for as follows:

- Discrepancies in the distribution of variables describing the lateral electromagnetic shower shape have been observed between data and MC especially for the variables $w_{\eta 2}$, R_η and f_{side}. These variables are used to perform the photon identification cuts; their definition is given in Chapter 5. The MC events have been reweighted to simulate the data following a method described for example in reference [245].

- The photon energy in MC is smeared to account for differences in resolution between data and simulation. This smearing has been derived from the comparison of the width of the $Z \to ee$ invariant mass in data and in simulation as described in Chapter 5.

- The beam-spot size in z simulated in the MC does not correspond to the one actually observed in data (7.5 cm vs 5.6 cm in 2011 and 6.6 cm vs 4.8 cm in 2012 [246]). The MC events have been reweighted to simulate the data.

- The distribution of the average number of interactions per bunch crossings μ in the simulation does not correspond to the one observed in data. The MC events have been reweighted to simulate the data.

- The Higgs boson p_T distribution in the MC simulating the gluon fusion process is corrected to match the one obtained with the HQT program [247] which gives a more accurate prediction. Indeed HQT includes QCD soft-gluon re-summations up to NNLL, unlike the MC which contains only LL re-summation.

7.4.3 Interference correction

7.4.3.1 Definition

The two-loops process $gg \to H \to \gamma\gamma$ can interfere with the one-loop [3] process $gg \to \gamma\gamma$ that corresponds to the irreducible continuum background for this channel (see Section 7.6.1). This is illustrated in Figure 7.6.

This interference was first studied for intermediate Higgs boson masses at leading order. Its effect on the signal yield was found to be negligible [249]. The effect on the cross section at next-to-leading order has been also considered in reference [248]. The calculation made in this reference is quickly summarized below as it will be necessary for the following discussion.

The amplitude of the $gg \to \gamma\gamma$ process can be written as the sum of the resonance and continuum amplitudes:

$$A_{gg\to\gamma\gamma} = \frac{-A_{gg\to H}A_{H\to\gamma\gamma}}{\hat{s} - m_H^2 + im_H\Gamma_H} + A_{cont},$$

where $\hat{s}$ corresponds to the gluon-gluon invariant mass and m_H and Γ_H stand for the Higgs boson mass and width respectively. The cross section can be computed from the term $|A_{gg\to\gamma\gamma}|^2$. An

[3] or two-loops if considering the QCD NLO corrections.

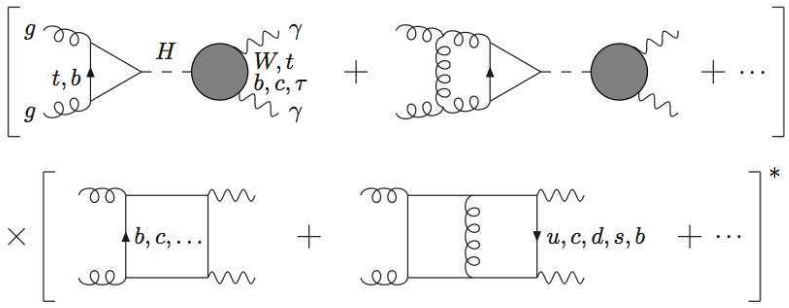

Figure 7.6: Feynman diagrams of the process contributing to the interference between the continuum and the resonance. Taken from reference [248].

interference term arises in this computation:

$$\sigma^{interf}_{gg\to H\to\gamma\gamma} = -2(\hat{s}-m_H^2)\frac{Re(A_{gg\to H}A_{H\to\gamma\gamma}A^*_{cont})}{(\hat{s}-m_H^2)^2+m_H^2\Gamma_H^2} - 2m_H\Gamma_H\frac{Im(A_{gg\to H}A_{H\to\gamma\gamma}A^*_{cont})}{(\hat{s}-m_H^2)^2+m_H^2\Gamma_H^2} \quad (7.4)$$

The hadronic cross section is obtained by integrating this partonic cross section over $\hat{s}$:

$$\sigma^{interf}_{pp\to H\to\gamma\gamma} = \int \frac{d\hat{s}}{s} G(\hat{s})\sigma^{interf}_{gg\to H\to\gamma\gamma} \quad (7.5)$$

where $G(\hat{s})$ corresponds to the gluon-gluon luminosity function which depends on the gluon distribution functions.

The term $(\hat{s}-m_H^2)$ in the real part of the interference term in Equation 7.4 is odd about the Higgs boson peak as illustrated in Figure 7.7, so that it vanishes in the integration. The real part thus contribute negligibly to the interference yield.

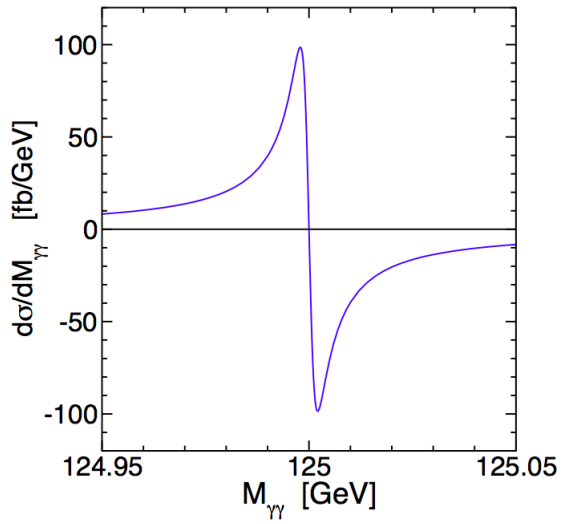

Figure 7.7: Real part of the interference term given in Equation 7.4, as a function of the diphoton invariant mass ($M_{\gamma\gamma} = \sqrt{\hat{s}}$). Taken from [250].

For low Higgs boson masses (below the WW threshold) the resonant amplitude is mainly real (see Chapter 2). In addition, the imaginary part of the term A_{cont} vanishes at one loop due to helicity selection rules and to the quark-mass suppression [249], so that at LO, the interference term of Equation 7.4 is very small.

When the computation is done at the two-loop level, the imaginary part of the interference term arising from the term A_{cont} is not anymore negligible.

The fractional interference correction to the resonance can be written as:

$$\delta = \frac{\sigma^{interf}_{gg\to H\to\gamma\gamma}}{\sigma_{gg\to H\to\gamma\gamma}}$$

where $\sigma_{gg\to H\to\gamma\gamma}$ is the total cross section. In the case where the photons and gluons are unpolarized, and neglecting some sub-dominant terms (see reference [248] for more details), an analytical approximate expression for the fractional interference is :

$$\delta \sim \frac{2\alpha\alpha_s^2(m_H)m_H\Gamma_H \sum_{q=u,c,d,s} e_q^2}{\pi Re(A^{(1)}_{gg\to H})Re(A^{(1)}_{H\to\gamma\gamma})} \times (3ImF^{L}_{--++}(\theta) - \frac{1}{3}ImF^{SL}_{--++}(\theta)) \tag{7.6}$$

where α and α_s correspond to the coupling constants, $A^{(1)}_{gg\to H}$ and $A^{(1)}_{H\to\gamma\gamma}$ correspond to the amplitude terms for the two processes $gg \to H$ and $H \to \gamma\gamma$ at the first order (see Chapter 1), $F^{L}_{--++}(\theta)$ and $F^{SL}_{--++}(\theta)$ are functions which describe the leading and sub-leading color contributions [251] and finally θ designates the angle between one of the photons and the proton-proton beam-line in the Higgs boson Center of Mass frame. In this approximate expression, only virtual corrections such as the one represented in Figure 7.6 are considered. This leads then to the constraint that the Higgs boson is in a small p_T regime.

This formula has been included in a program built and kindly provided by the authors of reference [248]. This program uses an energy in the center of mass of $\sqrt{s} = 7$ TeV. In Figures 7.8(a) and 7.8(b), the evolution of the interference term computed from this program as a function of the Higgs boson mass and the θ angle are shown.

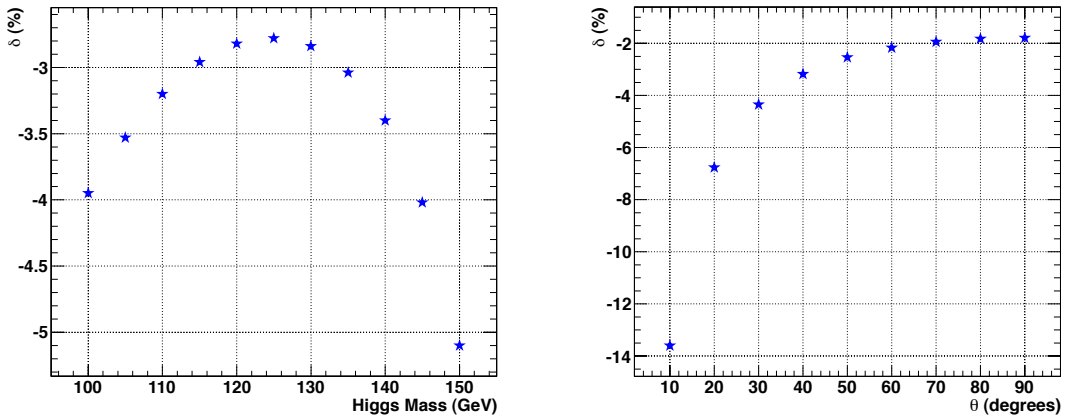

(a) (b)

Figure 7.8: Evolution of the interference term (in %) as a function of m_H for $\theta = 45^o$ (a) and as a function of θ for $m_H = 120$ GeV.

The interference is destructive between the two processes for any mass or angle.
It is the smallest in the signal region. From Equation 7.6 one can see that the fractional correction depends on the Higgs boson width. This explains why the correction increases strongly when approaching $m_H = 160$ GeV, which corresponds to the threshold where the WW channel opens. The interference correction is the biggest in the forward region (small values of θ) because the imaginary part of the continuum amplitude $gg \to \gamma\gamma$ at two-loops (whose phase dominates the interference effect) is peaked forward.

7.4.3.2 Application to the analysis

The impact of the interference on the signal yield has been studied using MC simulations for the $gg \to H \to \gamma\gamma$ process at $\sqrt{s} = 7$ TeV, with different Higgs boson masses and using the expression given in Equation 7.6. The selection and categorization performed in 2011 are used for this study.

This study is done in the Collins-Soper frame [4] [252]. In this frame, the Y-axis is perpendicular to the plane generated by the two photons momenta $\mathbf{P}_1$ and $\mathbf{P}_2$, the X-axis is contained in this plane but is perpendicular to the two photons momenta and the Z-axis is such that it cuts in two identical parts the angle between $\mathbf{P}_1$ and -$\mathbf{P}_2$. Finally, any vector in this frame can be localized thanks to two angles: ϕ and θ as shown in Figure 7.9.

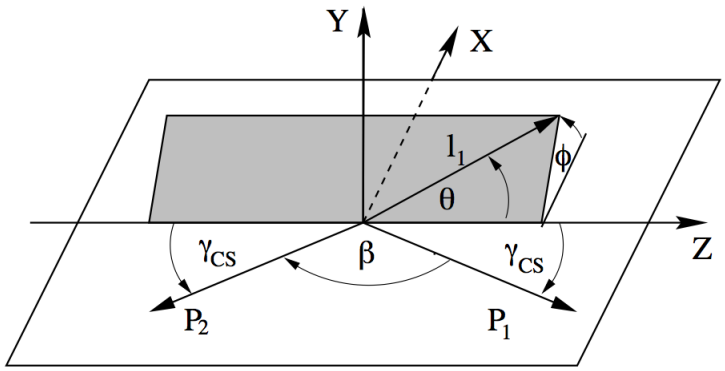

Figure 7.9: Illustration of the (X, Y, Z) Collins-Soper frame for the Higgs boson decaying to two photons of momenta $\mathbf{P}_1$ and $\mathbf{P}_2$ and definition of the angles ϕ and θ in this frame. Figure taken from reference [253].

In order to see the impact of the destructive interference on the $H \to \gamma\gamma$ search analysis, δ is computed for various mass hypotheses (100 to 150 GeV by steps of 5 GeV). For each event, depending on its production angle θ and mass m_H, an interference weight is calculated and the final global correction to the signal yield is obtained by doing a simple average of the corrections obtained for each candidate.

In Figure 7.10(a) the distribution of the angle θ for the simulated events after the full analysis selection is shown for a Higgs boson mass hypothesis of 120 GeV. This distribution peaks at around $\theta = 90^o$.

The distribution of the interference term, for a Higgs boson mass of 120 GeV, is shown in Figure 7.10(b). The most probable value of this distribution is $\delta \sim -2\%$ as expected from Figure 7.8(b) and the major part (more than 80%) of the candidates have $\delta > -5\%$.

[4] Choice positively received by the authors of reference [248].

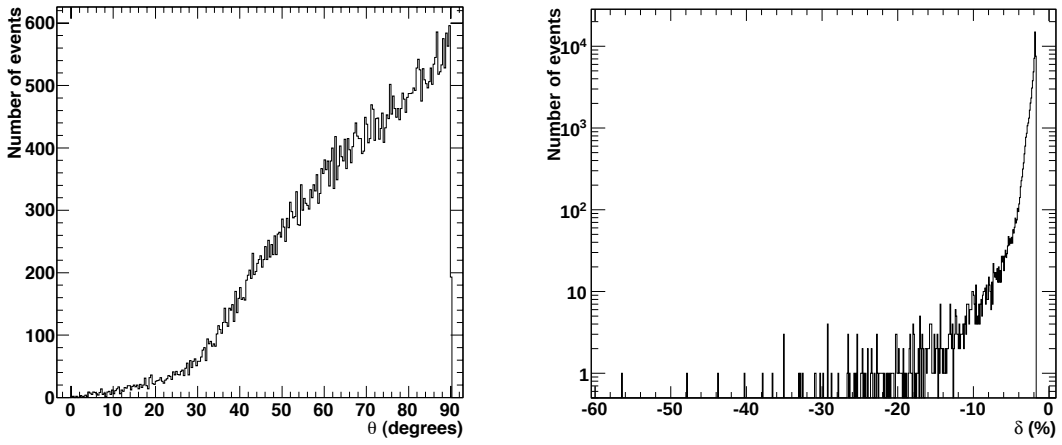

(a) (b)

Figure 7.10: Distributions of the angle θ (a) and δ (b) for $m_H = 120GeV$

Inclusive Analysis Table 7.2 gives the fractional interference correction to the resonance for various masses hypotheses, for an inclusive $gg \to H \to \gamma\gamma$ MC analysis.

Table 7.2: Interference term computed from MCs samples simulating the $gg \to H \to \gamma\gamma$ process with $100 < m_H < 150$ GeV in %

Mass (GeV)	100	105	110	115	120	125	130	135	140	145	150
δ(%)	-3.16	-2.84	-2.60	-2.44	-2.34	-2.32	-2.38	-2.57	-2.90	-3.46	-4.41

A term of order [-2.3%,-4.4%], depending on the mass, is considered as a correction to the $H \to \gamma\gamma$ signal for the gluon fusion production. More particularly a value of -2.32% is found for $m_H = 125$ GeV which is approximately the mass measured for the Higgs-like particle (see Chapter 8).

Categorization The interference term can also be computed taking into account the specificities of each category. Among the four kinds of categorizations which are performed in the 2011 analysis (pseudorapidity, status conversion, Higgs boson p_{Tt} and production process), only the one based on the photon localization in the detector is relevant. Indeed, the interference correction is independent of the p_{Tt} variable [5] and of the conversion status, so that these categories can be merged in this study.

The correction δ is given in Table 7.3 for several Higgs boson mass hypotheses and for the three repartitions of the photons in the detector. The three categories are:

- Central: both photons are required to have $|\eta_{s2}| < 0.75$, corresponding to the categories C1, C2, C5, C6.
- Transition: at least one photon is required to have $1.3 < |\eta_{s2}| < 1.75$: corresponding to the category C9.

[5] The calculation has been performed in the approximation of small p_T regimes, and the events with high p_{Tt} deviates from this approximation. Such events are in the minority (there are typically 15 to 20 times more low-p_{Tt} events) and are then merged with low p_{Tt} events.

- Rest: at least one photon is required to have $|\eta_{s2}| > 0.75$, (and both have $|\eta_{s2}| < 1.3$ or $|\eta_{s2}| > 1.75$), corresponding to the categories C3, C4, (C7, C8).

Table 7.3: Interference term for $100 < m_H < 150$ GeV in %

η Category	100	105	110	115	120	125	130	135	140	145	150
Central	-2.76	-2.44	-2.23	-2.04	-1.94	-1.91	-1.96	-2.09	-2.33	-2.75	-3.50
Rest	-3.34	-2.98	-2.73	-2.56	-2.45	-2.41	-2.50	-2.69	-3.04	-3.60	-4.59
Transition	-3.20	-2.90	-2.68	-2.47	-2.38	-2.38	-2.48	-2.69	-3.04	-3.61	-4.59

The "central" category has the smallest interference correction whereas the "rest" category has the biggest one. This is expected as the events with smaller pseudorapidities are in reality events which are produced almost perpendicularly to the beam axis. As an illustration, Figure 7.11 shows the correlation between $\cos\theta^*$ and the pseudorapidity of the leading photon from the MC sample.

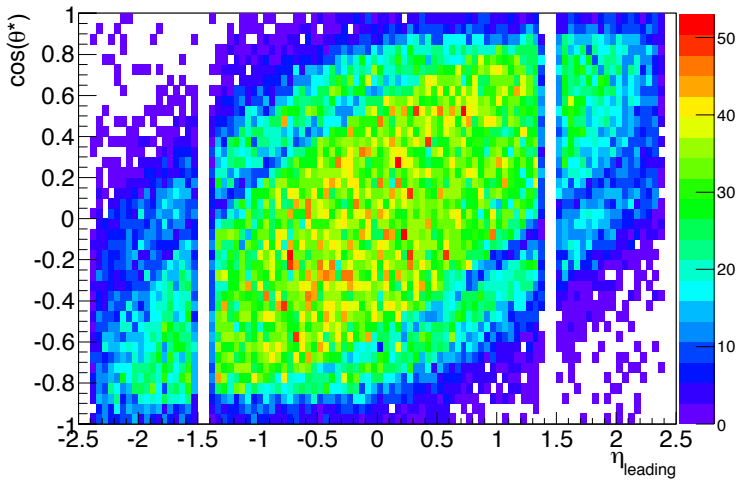

Figure 7.11: Distribution of the $\cos\theta^*$ variable as a function of the pseudorapidity of the leading photon, for a MC simulating the $H \to \gamma\gamma$ process at 120 GeV.

Discussion

The calculation is based on the assumption that the system has $p_T \sim 0$. Using this correction with generators dealing with diagrams having real corrections is not completely obvious.

The calculation was performed with a center of mass energy of $\sqrt{s} = 7$ TeV. The extrapolation of this study to the analysis made in 2012, with $\sqrt{s} = 8$ TeV was considered. The only difference with respect to the 7 TeV analysis is that the beam energy changes. This has an influence on the parton distributions, in particular on the gluon one, $g(x)$ with x the fraction of proton momentum carried by the gluon. For a higher beam energy, the gluons are expected to be sampled at a lower value of x for a fixed Higgs boson mass and this could have an influence on the interference calculation. However, the correction δ is expressed as a fraction of the normal Higgs boson production cross section (see Equation 7.6). The gluon luminosity $G(\hat{s})$ function defined in Equation 7.5 enters both at the numerator and at the denominator of the fraction in

the same way and therefore is eliminated in the ratio [254]. So the same numbers are taken for the 8 TeVanalysis, as referenced in Table 7.3.

In reference [250], a shift of the Higgs boson peak with respect to the expected position when the interference is neglected has been reported. The shift arises from the real part of the interference term given in Equation 7.4 and represented in Figure 7.7, when detector resolution effects are considered by smearing out the invariant mass distribution. The shift arises because this real part is odd about the Higgs boson mass peak. This effect has been further investigated in references [255, 256] for example. The size of the shift depends on various parameters like the method used to fit the diphoton invariant mass distribution in the data, and the transverse momentum and the width of the Higgs boson. These dependences could allow to measure indirectly the width of the Higgs boson [255]. The typical size of this shift is about 100 MeV, which is small compared to the size of the current total error for the mass measurement (see Chapter 8), but which could become significant with higher statistics samples, and reduced systematic uncertainties.

7.5 Signal modeling

7.5.1 Signal shape

A model for the signal is needed for the statistical studies, and this model is derived thanks to MC samples where the $H \to \gamma\gamma$ process is simulated at different masses. The full selection and categorization presented above is applied to these MC samples, in order to get similar conditions than in the data.

The Higgs boson to diphoton invariant mass peak is described with a composite model of a Crystal Ball (CB) function for the core of the distribution and a small wide Gaussian (Ga) component, used to model the tails. The analytical form of the Gaussian and Crystal Ball functions respectively are given below:

$$F_{Ga}(t_{Ga}, N_{Ga}) = N_{Ga} \cdot e^{-t_{Ga}^2/2}$$

$$F_{CB}(t_{CB}, \alpha_{CB}, n_{CB}, N_{CB}) = N_{CB} \cdot \begin{cases} e^{-t_{CB}^2/2} & \text{if } t_{CB} > -\alpha_{CB} \\ (\frac{n_{CB}}{|\alpha_{CB}|})^{n_{CB}} \cdot e^{-|\alpha_{CB}|^2/2} \cdot (\frac{n_{CB}}{|\alpha_{CB}|} - |\alpha_{CB}| - t_{CB})^{-n_{CB}} & \text{if } t_{CB} \leq -\alpha_{CB} \end{cases}$$

with $t_{xx} = \frac{m_{\gamma\gamma} - \mu_{xx}}{\sigma_{xx}}$ and N_{xx} the normalization. The variables μ_{xx} and σ_{xx} correspond respectively to the mean and resolution of the diphoton invariant mass.

The composition of these two functions is written as:

$$C(F_{CB}, F_{Ga}, f_{CB}) = f_{CB} \cdot F_{CB} + (1 - f_{CB}) \cdot F_{Ga} \tag{7.7}$$

The following constraints are set in the fit:

- $\mu_{CB} = \mu_{Ga}$
- n_{CB} is arbitrarily fixed at 10 to help the fit convergence.
- the width of the Gaussian for the non-Gaussian tails is parametrized as $\sigma_{Ga} = \kappa_{Ga} \cdot \sigma_{CB}$.

Then Equation 7.7 can be expressed in the simpler form:

$$C(\mu_{CB}, \sigma_{CB}, \alpha_{CB}, f_{CB}, \kappa_{Ga}) = f_{CB} \cdot F_{CB}(m_{\gamma\gamma}, \mu_{CB}, \sigma_{CB}, \alpha_{CB}) + (1 - f_{CB}) \cdot F_{Ga}(m_{\gamma\gamma}, \mu_{CB}, \kappa_{Ga} \cdot \sigma_{CB}) \quad (7.8)$$

The MCs simulating the process $H \to \gamma\gamma$ for masses from 100 to 150 GeV with steps of 5 GeV are fitted simultaneously with this model, for all the categories of the analysis.

In order to get a model valid for any mass value (necessary for the statistical studies), the dependence of the parameters fitted on the mass has been investigated.

The parameters $\mu_{CB}, \sigma_{CB}, \alpha_{CB}$ have a linear dependence on the mass whereas the parameters f_{CB}, κ_{Ga} have a only a small dependence on the mass. A linear fit is then performed for the first case, providing an interpolation for any mass value, whereas a constant value is considered for the second case. The linear relation between the parameters and the mass is expressed as:

$$\mu_{CB}(m) = \mu_{CB}(m = 125 \text{ GeV}) + s_\mu \cdot (m - 125) \quad (7.9)$$

and similarly for the two other parameters, so that three new parameters arise to take into account the mass dependence: $s_\mu, s_\alpha, s_\sigma$ corresponding to the slopes of the linear fits.

Therefore, eight parameters are considered for the signal model for each of the categories of the analysis: 3 dependent of the mass $\mu_{CB}, \sigma_{CB}, \alpha_{CB}$ with the 3 associated slopes $s_\mu, s_\alpha, s_\sigma$ and 2 independent of the mass f_{CB}, k_{Ga}.

Figure 7.12 shows an example of such fit, for two categories, the one with the best resolution and one with a lower resolution.

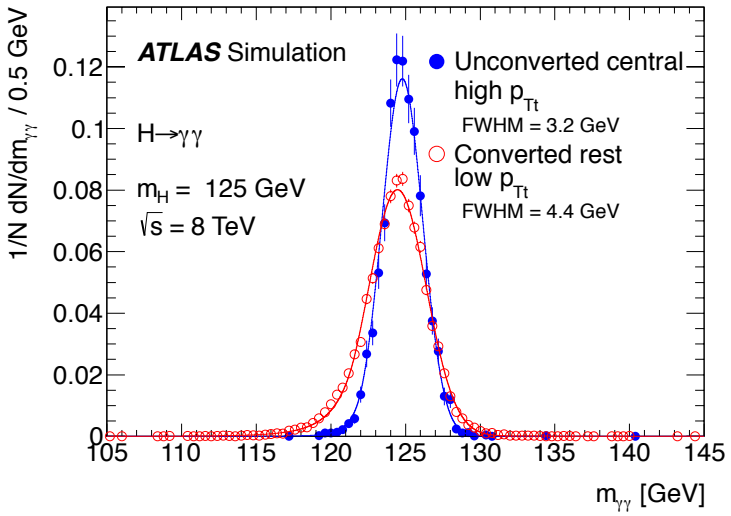

Figure 7.12: Invariant mass distribution for a simulation of the $H \to \gamma\gamma$ process at 125 GeV. The fit described in the text is superimposed. Taken from [10].

7.5.2 Signal yield

The fit described previously can also be used to extract the selection efficiency [6] of the Higgs boson decaying into two photons, and then predict a signal yield, for a given mass, production

[6] Here the word "efficiency" includes the acceptance of the kinematic cuts.

Table 7.4: Efficiency (including the acceptance of the kinematic cuts) of the selection and expected number of signal events for the different production processes at $m_H = 125$ GeV, for the 2011 (4.9 fb^{-1}) and 2012 (20.7 fb^{-1}) analyses.

$\sqrt{s}$	$gg \to H$		VBF		WH		ZH		ttH		Total
	$\epsilon(\%)$	N_{evt}	$\epsilon(\%)$	N_{evt}	$\epsilon(\%)$	N_{evt}	$\epsilon(\%)$	N_{evt}	$\epsilon(\%)$	N_{evt}	N_{evt}
7 TeV	42.3	71.83	43.18	5.87	37.83	2.43	38.02	1.35	36.69	0.32	81.8
8 TeV	35.7	352.9	36.3	28.8	30.9	11	32.4	6.29	28.4	1.87	401

process or category. For a given category and production process, the evolution of the yield extracted from these fits as a function of the Higgs boson mass is well modeled by a 3rd order polynomial. This dependence simply reproduces the $H \to \gamma\gamma$ branching ratio dependence on the mass already seen in Chapter 2. In Table 7.4 an example of these signal yields and efficiency is given for the mass $m_H = 125$ GeV for the inclusive case and for the two analyses performed in 2011 and 2012.

7.6 Background modeling

Proper understanding of the diphoton background is important to correctly assess its impact on the analysis.

7.6.1 Background composition

7.6.1.1 Reducible and Irreducible background

After all the selection cuts, the background composition is estimated using MC and data-driven studies [257], [258]. The main background is of two types:

- Irreducible background: it is characterized by two real isolated photons that come from the following processes:
  - the Born process (see Figure 7.13(a))
  - the fragmentation process (see Figure 7.13(b))
  - the box process (see Figure 7.13(c))

  This background is dominant and corresponds to about 80% of the total background for this channel.

- Reducible background: it is made mainly of jets fragmenting into leading π^0 decaying to two photons. The isolation criteria defined in Section 7.1 rejects most of this background unless the neutral pion carries most of the initial transverse momentum. Further rejection, beyond isolation, is possible thanks to the fine granularity of the first layer of the electromagnetic calorimeter, which allows to distinguish between two very close clusters (as expected from a neutral pion decay with high transverse momentum) and a unique cluster. This last type of background is composed of γ-jet, jet-γ and jet-jet events.

The Drell-Yan process where the two electrons from the Z boson decay are misidentified as photons makes a small contribution to the total background at the lower end of the diphoton mass range.

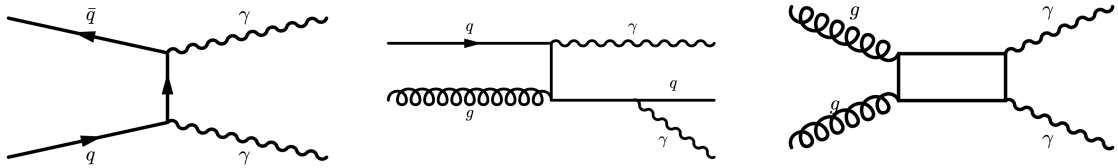

(a) Born process (b) Fragmentation process (c) Box process

Figure 7.13: Feynman diagrams for the three main background processes for the $H \to \gamma\gamma$ analysis.

7.6.1.2 Data driven background composition

The different types of backgrounds and their relative weights have been estimated with different data-driven methods [257, 258]. This decomposition is not used in the analysis but it allows to check the background shape and magnitude simulated in the MC samples.

Non Drell-Yan background One of these methods, denoted the 4×4 matrix method, relies on the classification of the diphotons candidates according to their isolation (see Section 7.1 and reference [227]). Prompt photons are expected to have a smaller isolation energy than jets faking photons. This property allows to distinguish between the four types of backgrounds $\gamma\gamma$, γ-jet, jet-γ and jet-jet. The probabilities ϵ (f) that a prompt (fake) photon passes the isolation criteria is taken into account and calculated either directly from the data or from diphoton MC samples. These probabilities are evaluated using control regions. For example a control region is built by selecting all the photons that fail the tight identification criteria but pass a looser identification where the cuts on strip shower shape are not applied. This control region is expected to be enriched in fake photons. The number of candidates going into each of the four kinds of background is indicated in Table 7.5. The uncertainties quoted in this table come from the definition of the control regions.

Table 7.5: Decomposition of the background for the $H \to \gamma\gamma$ analysis, using the data-driven 4×4 matrix method. The systematics come from the uncertainties of the number of selected events when changing the definition of the control regions.

	Yield ($\pm$ ($stat$) $^{+syst}_{-syst}$)	Relative yield [%] ($\pm$ ($stat$) $^{+syst}_{-syst}$)
$\gamma\gamma$	$97691 \pm 379^{+7211}_{-5021}$	$82.2 \pm 0.3^{+6.1}_{-4.2}$
γ-jet	$14712 \pm 88^{+2735}_{-4817}$	$12.4 \pm 0.1^{+2.3}_{-4.1}$
jet-γ	$3714 \pm 62^{+1729}_{-1630}$	$3.1 \pm 0.1^{+1.5}_{-1.4}$
jet-jet	$2776 \pm 21^{+1289}_{-1473}$	$2.3 \pm 0.0^{+1.1}_{-1.2}$

The invariant mass distributions of γ-jet and jet-jet events as well as of the $\gamma\gamma$ events are illustrated in Figure 7.14(a) for a subset of the 2012 data. Unlike for the invariant mass distribution of the irreducible background component, no peak is observed at $m_{\gamma\gamma} \sim 125$ GeV for the reducible one. The background coming from the Drell-Yan process is not separated from the irreducible $\gamma\gamma$ one.

Drell-Yan background The number of Drell-Yan events in the final $\gamma\gamma$ sample is expressed as a function of the rate of mis-identification of $Z \to ee$ as diphoton events, ρ_{12}. In the data

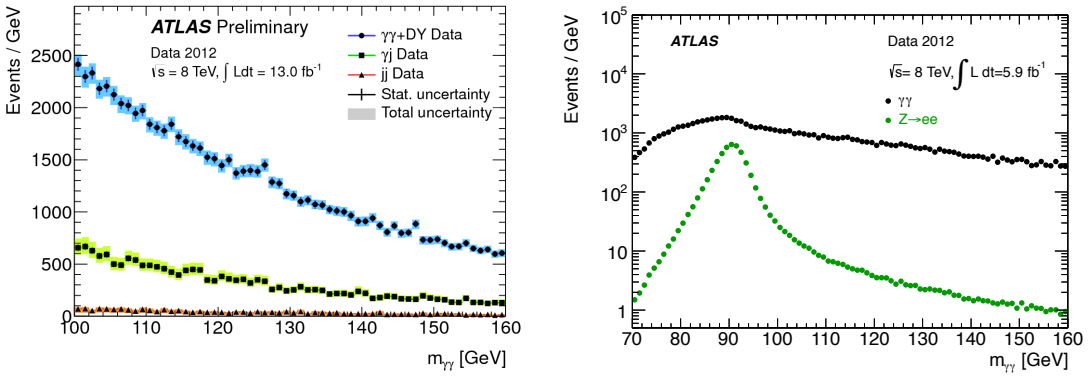

(a) (b)

Figure 7.14: (a) Invariant mass distribution of γ-jet (green) jet-jet (red) and $\gamma\gamma$ events (blue) for the 2012 data [222]. (b) Decomposition of the background for the $H \to \gamma\gamma$ analysis into the $\gamma\gamma$ (black) and $Z \to ee$ (green) components for the 2012 data, as a function of the diphoton invariant mass [10].

the Z invariant mass peak is reconstructed for two cases: using two electrons, and using one electron and one photon, the photon being either leading or sub-leading. Fitting these distributions, the number of Drell-Yan events mis-identified as diphoton events is then estimated to be $403.4 \pm 10.8\ (stat) \pm 81.1\ (syst)$ in the region $100 < m_{\gamma\gamma} < 160$. The systematics come mainly from the extrapolation of the $m_{\gamma\gamma} \sim m_{Z\to ee}$ region to higher $m_{\gamma\gamma}$ regions.

Figure 7.14(b) shows the decomposition of the background into the $\gamma\gamma$ and $Z \to ee$ components for the 2012 data.

7.6.2 MC samples

Simulations are needed to model the background invariant mass distribution (see Section 7.6.3 for the description of this modeling).

The irreducible background is simulated with the generators SHERPA [259], DIPHOX [260] and MADGRAPH [261]. The generator SHERPA is used for the γ-jet background whereas PYTHIA [262] models the jet-jet and Drell-Yann backgrounds.

7.6.3 Background modeling

In order to accurately extract the number of signal events, the number of background events has to be known with a good precision. This is achieved by modeling the background shape with an analytic function relating the background in the side bands to that in the signal region. The choice of the fit function is made on background MC samples, by minimizing any potential bias introduced by this function. The bias for a given parametrization is estimated by fitting the MC samples with a function combining the signal and background models. A given parametrization is kept, if the number of signal events extracted from this fit (called the "spurious" signal) N_{sp} satisfy at least one the two criteria:

- $N_{sp} < 10\%\ N_{S,exp.}$
- $N_{sp} < 20\%\ \sigma_{backg}$

where $N_{S,exp.}$ is the expected number of signal and σ_{backg} is the statistical uncertainty on the number of background events. The tightness of the criteria depends on the luminosity, because the statistical uncertainty on the number of background events decrease when the luminosity increases. The choice of the background model has been therefore done separately for the 2011 and 2012 datasets.

After these criteria are satisfied, a few functions are in general still allowed. The model which is chosen is the one giving the best expected sensitivity, taking the systematics into account.

Exponential decreasing function, 4th order Bernstein polynomial and exponential of a 2nd order polynomial functions have been selected for the 2011 and 2012 analyses. See Table 7.6.

Table 7.6: List of the functions chosen to fit the background and the associated systematic uncertainties for the different categories and for the two analyses performed in 2011 and 2012.

Category	Year	Parametrization	Uncertainty $[N_{event}]$	
			2011	2012
Unconverted central, low p_{Tt}	2011 & 2012	Exp. of 2nd order pol.	2.1	4.6
Unconverted central, high p_{Tt}	2011 & 2012	Exponential	0.2	0.8
Unconverted rest, low p_{Tt}	2011 & 2012	4th order pol.	2.2	11.4
Unconverted rest, high p_{Tt}	2011 & 2012	Exponential	0.5	2.0
Converted central, low p_{Tt}	2011 & 2012	Exp. of 2nd order pol.	1.6	2.4
Converted central, high p_{Tt}	2011 & 2012	Exponential	0.3	0.8
Converted rest, low p_{Tt}	2011 & 2012	4th order pol.	4.6	8.0
Converted rest, high p_{Tt}	2011 & 2012	Exponential	0.5	1.1
Converted transition	2011 & 2012	Exp. of 2nd order pol.	3.2	9.1
VBF	2011	Exponential	0.4	-
VBF loose	2012	Exponential	-	1.1
VBF tight	2012	Exponential	-	0.3
VH(had)	2012	Exponential	-	0.6
$E_{\mathrm{T}}^{\mathrm{miss}}$	2012	Exponential	-	0.1
VH(lep)	2012	Exponential	-	0.3
Inclusive	2011 & 2012	4th order pol.	7.3	12.0

The systematic uncertainty introduced by the choice of a given function corresponds simply to N_{sp}. This number is given in Table 7.6. As illustrated in this table, the number of spurious signal events is larger in 2012, due to the larger statistics gathered by this dataset.

7.7 Summary

Figure 7.15 shows the invariant mass distribution of all the diphoton events selected in the mass range [110, 160] GeV for the 2011 and 2012 datasets. A background-only fit as well as the composition of the signal and background fits are overlaid, based on the models defined in Sections 7.5 and 7.6.3.

Table 7.7 summarizes the general characteristic of the different categories like their resolution or their signal over background ratio. The categories that have the better S/B ratio correspond to the VBF categories. This is explained by the clear signature of this process.

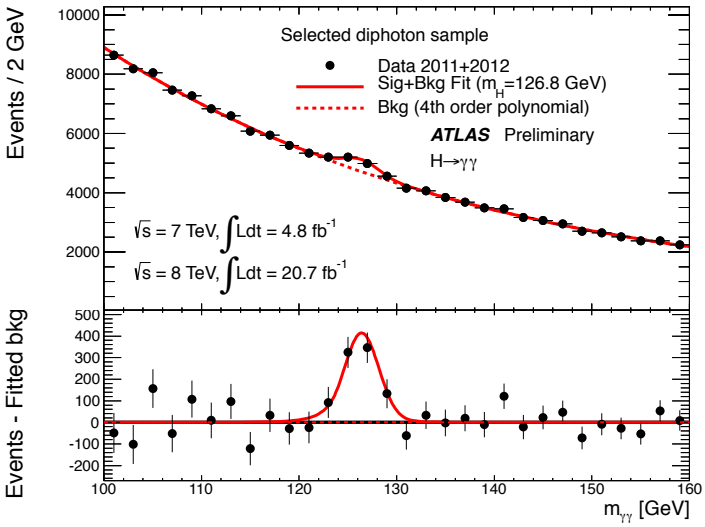

Figure 7.15: Diphoton invariant mass distribution in the range $110 < m_{\gamma\gamma} < 160$ GeV for the events selected in the data (black points) with the 2011 and 2012 datasets, fitted with a background-only fit (dashed red line) and a signal+background fit (red line). On the bottom, the difference between the total number of events and the number of events extracted from the background only fit as a function of the mass is shown, and fitted with a signal-only model. Taken from reference [223].

7.8 Systematic uncertainties

The systematic uncertainties can be classified into five different types: uncertainty on the signal yield, on the signal yield per category (migrations), on the background estimation, on the signal resolution and on the signal position. The background uncertainty arises from the choice of the background model and has been already described in Section 7.6.3. The signal yield and signal yield per category uncertainties are reviewed below. Unlike the uncertainties on the signal resolution and peak position which are also described in the following, they are not expected to have an impact on the mass measurement.

7.8.1 Uncertainty on signal yield

7.8.1.1 Experimental sources of uncertainties

Luminosity The luminosity recorded by the ATLAS detector is extracted from the measurement of the inelastic or elastic proton-proton scattering cross section in the forward direction with the LUCID and ALFA detectors (see Chapter 3). This measurement has an uncertainty of $\pm 1.8\%$ in 2011 [263] and $\pm 3.6\%$ in 2012 [264], and has an impact on all the analyses.

Trigger The triggers used to select diphoton events `2g20_loose` and `g35_loose_g25_loose` have an efficiency close to 100% (see Section 7.1). The uncertainty on this efficiency estimated to be $\pm 0.5\%$ [161] directly induces an uncertainty on the signal yield.

Photon identification The efficiency of the photon identification cut was measured with data-driven techniques and has an uncertainty that depends on the conversion status, the pseu-

Table 7.7: Signal resolution fitted from the Crystal Ball function in the MC (σ_{CB}), Full Width at Half the Maximum (FWHM), number of expected signal events (N_S), number of background events (N_B) and signal to background ratio (N_S/N_B) in a mass window around $m_H = 126.5$ GeV containing 90% of the expected signal events for each of the 14 categories and for the inclusive case for the 2012 analysis.

$\sqrt{s}$	Category	σ_{CB} [GeV]	FWHM [GeV]	Observed	N_S	N_B	N_S/N_B
7 TeV	Inclusive	1.63	3.84	2653	71.5	2557.6	0.028
	Unconv. central, low p_{Tt}	1.45	3.41	161	9.4	154.9	0.061
	Unconv. central, high p_{Tt}	1.37	3.22	7	1.3	7.2	0.181
	Unconv. rest, low p_{Tt}	1.57	3.71	700	19.5	669.7	0.029
	Unconv. rest, high p_{Tt}	1.43	3.36	57	2.5	37.7	0.066
	Conv. central, low p_{Tt}	1.63	3.84	166	6	136.4	0.044
	Conv. central, high p_{Tt}	1.48	3.48	2	0.9	6.4	0.141
	Conv. rest, low p_{Tt}	1.79	4.23	986	18.9	967.3	0.02
	Conv. rest, high p_{Tt}	1.61	3.8	48	2.5	51.2	0.049
	Conv. transition	2.27	5.52	709	8.5	703.9	0.012
	VBF	1.52	3.59	12	2	8.7	0.23
8 TeV	Inclusive	1.77	4.23	14025	355.5	13279.8	0.027
	Unconv. central, low p_{Tt}	1.5	3.53	911	46.6	881.2	0.053
	Unconv. central, high p_{Tt}	1.4	3.3	49	7.1	44.1	0.161
	Unconv. rest, low p_{Tt}	1.74	4.18	4611	97.1	4347.3	0.022
	Unconv. rest, high p_{Tt}	1.69	3.99	292	14.4	247.5	0.058
	Conv. central, low p_{Tt}	1.68	3.96	722	29.8	687	0.043
	Conv. central, high p_{Tt}	1.54	3.64	39	4.6	31.5	0.146
	Conv. rest, low p_{Tt}	2.01	4.78	4865	88	4657.4	0.019
	Conv. rest, high p_{Tt}	1.87	4.41	276	12.9	266.3	0.048
	Conv. transition	2.52	6.04	2554	36.1	2499.1	0.014
	VBF loose	1.71	4.06	40	4.8	28	0.171
	VBF tight	1.64	3.89	24	7.3	12.8	0.57
	VH (had)	1.62	3.83	21	3	21	0.143
	$E_{\mathrm{T}}^{\mathrm{miss}}$	1.74	4.11	8	1.1	4.6	0.239
	VH (lep)	1.75	4.13	19	2.6	12.8	0.203

dorapidity and the transverse momentum of the photons [149]. This uncertainty is propagated to the signal yield by reweighting all the events in a MC signal sample by a Gaussian fluctuation within the photon identification uncertainty. The correlations and anti-correlations between the different η and p_T regions are taken into account [237]. The resulting spread on the signal yield is taken as an uncertainty on the Higgs boson signal yield and amounts to $\pm 8.46\%$ in 2011 and $\pm 2.4\%$ in 2012.

Isolation The uncertainty on the efficiency of the isolation selection is evaluated using $Z \to ee$ events, by comparing data and MC results. The photon isolation variables described in Section 7.1, are slightly modified to be applied instead on electrons. The difference on efficiency between the data and the simulation, amounting to $\pm 0.4\%$ in 2011 and $\pm 1\%$ in 2012 is taken as an uncertainty.

Photon Energy Scale The uncertainty on the energy scale described in Chapter 5 gives an uncertainty on the p_T scale used to select the photons.

For each category the selection efficiency is evaluated varying the energy scale within the uncertainty

The variation in efficiency can be written as:

$$\delta_{eff} = \frac{N'_A + N'_B}{N_A + N_B} - 1$$

with N_A and N_B being the number of selected events respectively in a category with $p_{\mathrm{Tt}} < 60$ GeV and $p_{\mathrm{Tt}} > 60$ GeV, and N'_A and N'_B being the number of selected events in the same categories, when varying the energy scale. These two categories are complementary due to their definition; they share any difference of efficiency due to the energy scale variation.

The inclusive impact of the systematics from energy scale on the total yield was found to be $\pm 0.30\%$ in 2011 and $\pm 0.25\%$ in 2012 .

7.8.1.2 Theoretical sources of uncertainties

Branching Ratio The branching ratio of Standard Model Higgs boson decaying into two photons has a theoretical uncertainty of $\sim \pm 5\%$ for a Higgs boson mass around 126 GeV, and this uncertainty depends on the mass (from $\pm 5.9\%$ at $m_H = 110$ GeV to $\pm 2.1\%$ at $m_H = 150$ GeV) [265].

Scale The Higgs boson production cross sections for the different processes have an uncertainty coming from the variation of the renormalization and factorization scales (Table 2.1 for the values). This uncertainty is the largest for the gluon fusion process and amounts to around $\pm 7\%$ both for $\sqrt{s} = 7$ TeV and $\sqrt{s} = 8$ TeV.

PDF+α_s The variation of the set of parton distribution functions chosen to compute the cross section also leads to an uncertainty as already seen in Chapter 2. The uncertainties for each production mode following the PDF4LHC recommendations were given in Table 2.1. It is again the largest for the gluon fusion production and amounts to around $\pm 7\%$ both for $\sqrt{s} = 7$ TeV and $\sqrt{s} = 8$ TeV.

Theory Cross section on gluon fusion A Higgs boson resulting from the gluon fusion process can be mis-identified as a VBF-type event, when two jets are produced in the final state. The cross section of this configuration is calculated theoretically but has a large uncertainty at NLO (see Section 2.1.1). This uncertainty leads to migration within the 2-jets categories, namely the tight and loose high-mass two jets (C10 and C11: $\pm 48\%$ and $\pm 28\%$) and the low-mass two jets (C12: $\pm 30\%$) for the 2012 analysis, and the VBF category (C10: $\pm 25\%$) for the 2011 period.

7.8.1.3 Summary

Table 7.8 summarizes all the uncertainties on the signal yield for the 2011 and 2012 analyses. The models chosen to parametrize statistically these uncertainties are given in this table and commented with more details in Section 7.9. All the uncertainties are correlated between the two years except for the luminosity.

7.8.2 Migration uncertainties

This systematic impacts the repartition into the different categories of the analysis and comes from uncertainties on the variables used to build the categories.

Table 7.8: Summary of the impact of systematic uncertainties on the signal yields for the analysis of the 7 TeVand 8 TeV data.

$\sqrt{s}$	Systematic uncertainties	Value(%)			Constraint
7 TeV	Luminosity	± 1.8			
	Photon Identification	± 8.46			Log-normal
	Isolation	± 0.4			
	Photon Energy Scale	± 0.3			
	Branching ratio	$\pm 5.9\% - \pm 2.1\%$ (m_H = 110 - 150 GeV)			Asymmetric Log-normal
	Scale	ggF: $^{+7.1}_{-7.8}$	VBF: $^{+0.2}_{-0.3}$	WH: $^{+0.2}_{-0.8}$	Asymmetric
		ZH: $^{+1.4}_{-1.6}$	ttH: $^{+3.3}_{-9.3}$		Log-normal
	PDF+α_s	ggF: $^{+7.6}_{-7.1}$	VBF: $^{+2.5}_{-2.1}$	WH: ± 3.5	Asymmetric
		ZH: ± 3.6	ttH: ± 8.5		Log-normal
	Theory cross section on ggF	2-jets category	± 25		Log-normal
8 TeV	Luminosity	± 3.6			
	Trigger	± 0.5			
	Photon Identification	± 2.4			Log-normal
	Isolation	± 1.0			
	Photon Energy Scale	± 0.25			
	Branching ratio	$\pm 5.9\% - \pm 2.1\%$ (m_H = 110 - 150 GeV)			Asymmetric Log-normal
	Scale	ggF: $^{+7.2}_{-7.8}$	VBF: $^{+0.2}_{-0.2}$	WH: $^{+0.2}_{-0.6}$	Asymmetric
		ZH: $^{+1.6}_{-1.5}$	ttH: $^{+3.8}_{-9.3}$		Log-normal
	PDF+α_s	ggF: $^{+7.5}_{-6.9}$	VBF: $^{+2.6}_{-2.7}$	WH: ± 3.5	Asymmetric
		ZH: ± 3.6	ttH: ± 7.8		Log-normal
	Theory cross section on ggF	Tight VBF	± 48		Log-normal
		Loose VBF	± 28		
		VH (had)	± 30		

Underlying event In some cases underlying events can be misidentified as jets coming from the diphoton vertex and contaminate the VBF or hadronic VH categories. A change in the distribution of the underlying events has then an impact on the repartition of the events within the three related categories. The uncertainty on the underlying events distribution and kinematic is estimated by comparing simulations where the multi-parton interaction is simulated or not. The subsequent uncertainty on the event yield per category is given in Tables 7.10 and 7.9 for different production processes and for the two years 2011 and 2012.

Jet Energy Scale and Resolution Like the electron and photon energy responses, the jet energy scale and resolution are corrected using *in situ* techniques [266]. These corrections introduce a new uncertainty coming from different sources: the comparison between different methods, the pileup conditions and the jets topologies (flavour response, close-by jets). These uncertainties have an impact on the signal yield per category, depending on the production process, because of the kinematic cut applied on the jets. The overall migration uncertainty for the different categories and production processes are summarized in Tables 7.10 and 7.9 for the two years 2011 and 2012.

η^* **modeling** The topological variable η^* defined in Section 7.3 serves as a tighter cut on the VBF candidates and then participates in the separation between the loose and tight VBF categories for the Cut-Based method. It is an initial requirement for categorizing the events in one of the VBF categories in the MVA method. An uncertainty on this variable then induces a migration of events, either within these two categories or between these categories and the other ones. This migration has been estimated by varying η^* within its uncertainty and found to be $+7.6\%$ ($+6.2\%$) in the tight (loose) VBF category.

Dijet angular modeling The variable $\Delta\phi(\gamma_1\gamma_2 - \mathrm{j}_1\mathrm{j}_2)$ is used in the MVA method as a discriminant variable for the VBF process. An uncertainty on its modeling then leads to migrations between these two categories and other categories. The uncertainty on the tight (loose) category yield is found to be $+7.6\%$ ($+6.2\%$) whereas it is negligible for the other categories.

Higgs boson p_T The Higgs boson transverse momentum modeling is important for predicting the numbers of jets produced in the final state as well as for the $E_{\mathrm{T}}^{\mathrm{miss}}$. Moreover, it is correlated with the variable $p_{\mathtt{Tt}}$ that is used to categorize events. An uncertainty on the Higgs boson p_T leads then to migrations between the categories. The uncertainty on the categories yield is given in Tables 7.10 and 7.9 for the two years 2011 and 2012.

Material Mis-modeling The probability of conversion for a photon interacting with the detector depends on the amount of crossed material (see Chapter 6). Consequently, an uncertainty on the amount of material leads to an uncertainty on the number of converted photons with respect to the number of unconverted ones and then on the population of the various categories. This has been estimated using a MC with additional material (the G' geometry). The migration of events from unconverted to converted categories and *vice versa* are respectively -4% and $+3.5\%$.

JVF The JVF variable, defined in Section 7.1.2 is used to select the jets objects accompanying diphoton events. If no jet pass the criteria on the JVF, the event considered is categorized within the $\eta - p_{\mathtt{Tt}}-$conversion categories. Then an uncertainty on the JVF variable leads to migrations within the categories. The uncertainty values are given in Table 7.9 for the different production

process and the 2-jets categories. The uncertainty on the VBF-tight category is negligible (due to the hardness of the jets) and then neglected here.

$E_{\mathrm{T}}^{\mathrm{miss}}$ An uncertainty on the missing transverse energy also leads to migrations between categories, because of the cut on the significance of this variable and of the way events are categorized. The sources of uncertainties on the $E_{\mathrm{T}}^{\mathrm{miss}}$ are numerous, as this variable corresponds to the complement to all the objects' transverse momenta. For example, the uncertainty on the Jet Energy Scale or Resolution leads to an uncertainty on the missing energy. The impact on the yield of the category tagged with the $E_{\mathrm{T}}^{\mathrm{miss}}$ significance is looked at and the uncertainty due to the migrations is referenced in Table 7.9, for different production processes. The migrations within the other categories are found to be negligible.

Lepton reconstruction, identification, energy scale and resolution For the leptonic decay of the VH process, the uncertainties on the variables used to select the lepton could lead to changes in its selection and then cause a migration between this category and the other ones. The uncertainty on the identification, reconstruction, resolution and calibration of the electron and muons are then considered. All these uncertainties lead to migration uncertainties in the lepton category less than 1% and negligible for the other categories.

Photon Energy Scale The uncertainty on the energy scale leads to an uncertainty on the boundary between low and high p_{Tt} categories. The systematic on the migration of candidates between these two categories is evaluated as:

$$\delta_{mig} = \frac{\alpha'}{\alpha} - 1$$

with $\alpha = \dfrac{N_A}{N_A + N_B}$, $\alpha' = \dfrac{N_{A'}}{N_{A'} + N_{B'}}$ and N_A, N_B, N'_A and N'_B defined in Section 7.8.1. The δ_{mig} is computed for the different categories and found to be lower than $\pm 0.10\%$. It is therefore neglected.

Summary The systematic uncertainties on the per-categories yield for the 2011 and 2012 analyses are given in Tables 7.10 and 7.9.

7.8.3 Uncertainty on signal resolution

Constant term The diphoton invariant mass in the MC simulation is smeared to take into account discrepancies with the data. This smearing has an uncertainty coming from the parametrization of the constant term in the data (as given in Chapter 5) and mainly relies on the assumption that the sampling term is well modeled in the simulation. In order to test the impact of a wrong model of the sampling term, the sampling term is varied within +10% and the propagation of the associated variation of the constant term into the width of the $H \to \gamma\gamma$ peak is taken as an uncertainty on the signal resolution. This uncertainty has been derived inclusively in 2011 and found to be $\pm 12\%$, and for each category of the analysis in 2012. The values can be found in Table 7.11. The increasing of the uncertainty in 2012 with respect to 2011 is related to the increase of the constant term in 2012 (see Chapter 5).

Table 7.9: Systematic uncertainties on the signal assignment to categories (migration) for the analysis of the 8 TeV data.

Systematic uncertainties	Category	Value(%)			Constraint
Underlying Event	Tight high-mass two-jet	ggF: ±8.8	VBF: ±2.0	VH, ttH: ±8.8	Log-normal
	Loose high-mass two-jet	ggF: ±12.8	VBF: ±3.3	VH, ttH: ±12.8	
	Low-mass two-jet	ggF: ±12	VBF: ±3.9	VH, ttH: ±12	
Jet Energy Scale	Low p_{Tt}	ggF: −0.1	VBF: −1.0	Others: −0.1	Gaussian
	High p_{Tt}	ggF: −0.7	VBF: −1.3	Others: +0.4	
	Tight high-mass two-jet	ggF: +11.8	VBF: +6.7	Others: +20.2	
	Loose high-mass two-jet	ggF: +10.7	VBF: +4.0	Others: +5.7	
	Low-mass two-jet	ggF: +4.7	VBF: +2.6	Others: 1.4	
	$E_{\mathrm{T}}^{\mathrm{miss}}$significance	ggF: 0.0	VBF: 0.0	Others: 0.0	
	one-lepton	ggF: 0.0	VBF: 0.0	Others: −0.1	
Jet Energy Resolution	Low p_{Tt}	ggF: 0.0	VBF: 0.2	Others: 0.0	Gaussian
	High p_{Tt}	ggF: −0.2	VBF: 0.2	Others: 0.6	
	Tight high-mass two-jet	ggF: 3.8	VBF: −1.3	Others: 7.0	
	Loose high-mass two-jet	ggF: 3.4	VBF: −0.7	Others: 1.2	
	Low-mass two-jet	ggF: 0.5	VBF: 3.4	Others: −1.3	
	$E_{\mathrm{T}}^{\mathrm{miss}}$significance	ggF: 0.0	VBF: 0.0	Others: 0.0	
	one-lepton	ggF: −0.9	VBF: −0.5	Others: −0.1	
η^* modeling	Tight high-mass two-jet: +7.6 Loose high-mass two-jet: +6.2				Gaussian
Dijet angular modeling	Tight high-mass two-jet: +12.1 Loose high-mass two-jet: +8.5				Gaussian
Higgs boson p_{T}	Low p_{Tt}: +1.3 High p_{Tt}: −10.2 Tight high-mass two-jet: −10.4 Loose high-mass two-jet: −8.5 Low-mass two-jet: −12.5 $E_{\mathrm{T}}^{\mathrm{miss}}$significance: −2.0 one-lepton : −4.0				Gaussian
Material Mismodeling		Unconv: −4.0	Conv: +3.5		Gaussian
JVF	Loose High-mass two-jet	ggF: −1.2	VBF: −0.3	Others: −1.2	Gaussian
	Low-mass two-jet	ggF: −2.3	VBF: −2.4	Others: −2.3	
$E_{\mathrm{T}}^{\mathrm{miss}}$	$E_{\mathrm{T}}^{\mathrm{miss}}$significance	ggF: +66.4	VBF: +30.7	VH, ttH: +1.2	Gaussian
e reco and identification	one-lepton: < 1				Gaussian
e Escale and resolution	one-lepton: < 1				Gaussian
μ reco, ID resolution	one-lepton: < 1				Gaussian
μ spectrometer resolution	one-lepton: 0				Gaussian

Table 7.10: Systematic uncertainties on the signal assignment to categories (migration) for the analysis of the 7 TeV data.

Systematic uncertainties	Category	Value(%)			Constraint
Underlying Event	VBF-tagged category	ggF: ±30.0	VBF: ±6.0	VH, ttH: ±30	Log-normal
Jet Energy Scale	Low p_{Tt}	ggF: −0.1	VBF: −1.0	Others: 0.0	Gaussian
	High p_{Tt}	ggF: −0.4	VBF: −2.5	Others: −0.1	
	VBF-tagged category	ggF: +15.1	VBF: +6.4	Others: +12.1	
Higgs boson p_{T}	Low p_{Tt}: +1.1				Gaussian
	High p_{Tt}: −12.5				
	VBF-tagged category: −9.0				
Material Mismodeling		Unconv: −4.0	Conv: +3.5		Gaussian

Table 7.11: Systematic uncertainty on the signal resolution coming from the uncertainty on the constant term for each category of the 2012 analysis.

$\sqrt{s}$	Category	Systematic [%]
7 TeV	Inclusive	12.00
8 TeV	Inclusive	20.00
	Unconv. central, low p_{Tt}	17.91
	Unconv. central, high p_{Tt}	20.70
	Unconv. rest, low p_{Tt}	22.41
	Unconv. rest, high p_{Tt}	22.49
	Conv. central, low p_{Tt}	18.39
	Conv. central, high p_{Tt}	26.48
	Conv. rest, low p_{Tt}	18.63
	Conv. rest, high p_{Tt}	21.00
	Conv. transition	13.08
	Other categories	20.00

Electron to photon extrapolation The smearing of the MC photon and electron energy is made on the basis of the comparison of the resolution observed in data and in the simulation. If the source of the largest effective constant term observed in data is specific to the electrons, applying the same correction for photons and electrons could lead to a bias on photon energy in the MC. For example, the presence of extra material in data leads to an increase of the resolution, but this source will have a lower impact on photons (the unconverted photons do not interact with the material). The uncertainty (coming from this resolution extrapolation from electrons to photons) is estimated to be ±6%.

Pileup In general the pileup deteriorates the energy resolution. The impact of the pileup on the diphoton invariant mass distributions from MC samples is evaluated by comparing the resolution in the two following cases: $\mu < 10$ and $\mu > 10$ with μ the average number of

Table 7.12: Summary of the uncertainties on the mass $H \to \gamma\gamma$ mass resolution for the 2011 and 2012 analyses.

Source	Systematic		Constraint
	$\sqrt{s} = 7$ TeV	$\sqrt{s} = 8$ TeV	
Constant term	$\pm 12\%$	$\pm 20\%$	-
Pileup	$\pm 3\%$	$\pm 3\%$	-
e^-/γ extrapolation	$\pm 6\%$	$\pm 6\%$	-
Total	$\pm 14\%$	$\pm 21\%$	Log-normal

interactions per bunch crossing . The average deterioration of the resolution when going from the low to the high pileup category is estimated to be $\pm 3\%$.

Primary vertex selection The mass resolution is sensitive to the primary vertex position measurement. The method to select the primary vertex is varied to test the impact on the uncertainty on the vertex position on the mass resolution. No obvious effect is observed and this source is then neglected.

Summary A summary of the uncertainty on the mass resolution is given in Table 7.12 for the 2011 and 2012 analyses.

7.8.4 Uncertainties on signal peak position

The uncertainty on the electron and photon energy scale has been reviewed in Chapter 5. Three main sources of uncertainties have been highlighted, namely the limited knowledge on the amount of material in the detector, the energy scale response of the presampler layer and the method to extract the scale factor for the *in situ* calibration. These uncertainties depend on the particle pseudorapidity, on its transverse momentum, on its type (electron or photon) and for the photon on its conversion status.

These uncertainties induce an error on the position of the $H \to \gamma\gamma$ peak, that has been evaluated for each category both for the 2011 and 2012 analyses.

A model for taking properly into account the possible correlations has been built. The possible correlations are:

- between the two photons,
- between the electrons and the photons when considering a combination of the $H \to \gamma\gamma$ channel with $H \to llll$ one,
- between the three different sources of uncertainties,
- within the categories.

The three sources are un-correlated because they do not have the same origin. The uncertainties are chosen to be correlated within the categories. For each of these three sources, the way the two photons are correlated is explained in the following.

Uncertainty from the Method The "Method" uncertainty (defined in Chapter 5) is the quadratic sum of small uncertainties that are for most of them common to electrons and photons and that slightly depend on η. It is then correlated for the two photons and for the photons and electrons.

Uncertainty from extra-material For the material uncertainty, the treatment is more complex because there is a strong η dependence and the effect is not small. Fully correlating the two photons would give an estimation too conservative: the geometry chosen for the study is obviously too pessimistic, many studies have already shown this (see Chapter 6). For the combination of several channels for the Higgs boson search, a too large systematic on the energy scale could give too much freedom to the peak position in one channel to be aligned with a peak in another one, thus artificially increasing the sensitivity.

To be more realistic, the detector is divided into two parts: $|\eta| < 1.8$ and $|\eta| > 1.8$. This separation is justified by the distribution of the inactive material of the Inner Detector but not by the distribution of material in cryostat (see Chapter 6). This is a simplified model, not realistic enough and is only a temporary choice until the amount of material in the detector is better known.

These two regions are then taken as uncorrelated: two sub-sources of uncertainties are built to take into account this decorrelation: one deals with the uncertainty due to extra-material for $|\eta| < 1.8$, whereas the other one deals with the uncertainty due to extra-material for $|\eta| > 1.8$.

Uncertainty from presampler The systematic coming from the uncertainty on the presampler energy scale is also quite important and dependent on η (see Chapter 5). For this reason, the same kind of model as the one addressing the uncertainty from extra-material is used. The presampler is composed of three sub-detectors, one for the barrel and two for the endcaps. The barrel and the endcaps form three different detectors, and the uncertainty can be taken as decorrelated in these three parts. To build a simple model, the two endcaps are assumed to have a correlated uncertainty. Two sub-sources are then considered: the presampler energy scale in the barrel and the one in the endcaps.

7.8.4.1 The impact of the energy scale systematic on the peak position

A MC sample simulating the $gg \rightarrow H \rightarrow \gamma\gamma$ process at 120 GeV is used, and the candidates are selected as described in Section 7.1. For this study, the peak position is defined as the mean of the distribution of the invariant mass $m_{\gamma\gamma}$ in a window [MPV-1.5σ, MPV$+2\sigma$], where "MPV" corresponds to the most probable value of the distribution in the initial window [95, 145 GeV] and "σ" corresponds to the RMS of the same distribution in the same window (see Figure 7.16). Various other methods have been tried (for example fitting the peak with a Crystal Ball convoluted with a Gaussian function) but the results have been found to be very similar. The first method has been chosen for its stability especially when there are few events.

The impact of the energy scale systematic on the peak position is studied as follow: the energy of the photon is biased by a factor which corresponds to the energy scale uncertainty, and this procedure is applied separately for each of the 5 components of the energy scale systematic for photons described above (method, material at low and high η, presampler energy scale in barrel and in endcap). The peak positions of the resulting distributions are extracted and called P_{method}, $P_{material\ \eta<1.8}$, $P_{material\ \eta>1.8}$, $P_{PS\ barrel}$ and $P_{PS\ endcap}$. The nominal peak position is called P_{nom}. For a given systematic xx, the uncertainty on the peak position due to the energy scale systematic is computed as : $\delta P_{xx} = \dfrac{P_{nom} - P_{xx}}{P_{nom}}$.

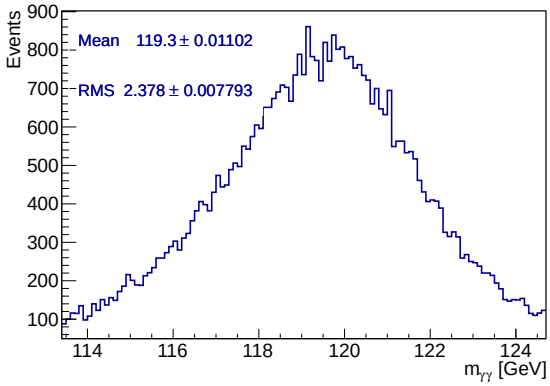

Figure 7.16: Distribution of the invariant mass for a MC simulation the $H \to \gamma\gamma$ process, after selection of the events, in the range [MPV-1.5σ, MPV$+2\sigma$].

The uncertainty on the peak position can be calculated either for an inclusive analysis (no distinction between the candidates) or for an analysis with categories. This is described in the following sections.

Inclusive analysis In Table 7.13 the values of the uncertainty on peak position δP_i (i=1,...,5 for the 5 systematics) are given.

The overall inclusive uncertainty on the peak position is simply the quadratic sum of the five numbers in this table, as the five sources are assumed to be un-correlated: $\delta P_{inclusive} = \pm 0.5\%$. This number is not negligible: for a Higgs boson mass of around 120 GeV, this gives an uncertainty of about 600 MeV on the peak position. The main contributors to this uncertainty are the systematic from the method and the one from the material in $\eta < 1.8$.

Analysis with categories The analysis has been repeated, estimating the uncertainty in each of the categories.

The results are summarized in Table 7.13. For each of the five sources, the inclusive result seen previously can be recovered doing a weighted (by the number of events in the category) sum of the numbers over a column, as the categories are assumed to be correlated.

As expected, the photons that are in the central part of the barrel ($\eta < 0.75$, C1, C2, C5, C6) are unaffected by the systematic due to material at high η or by the presampler energy scale uncertainty in endcap. Moreover the uncertainty in converted photons categories (C5, C6, C7, C8) due to material or presampler energy scale is smaller than in the unconverted ones. This is due to the extrapolation if the energy scale from electrons to photons which is more accurate for photons (see Chapter 5). For the category C9 where at least one photon is in the transition region ($1.3 < \eta < 1.75$ excluding the crack), the systematics are very high due to the huge amount of material in this region. Only one category has non-zero value coming from the presampler energy scale uncertainty in the endcap. The endcap presampler has a small extension ($1.52 < \eta < 1.8$) and thus concerns very few candidates.

Table 7.13: 2012 uncertainty on peak position due to energy scale uncertainties, in different categories Uncertainty on peak position due to energy scale uncertainties, in different categories

$\sqrt{s}$	Category	Method	Mat. $\|\eta\| < 1.8$	Mat. $\|\eta\| > 1.8$	PS Barrel	PS endcap
7 TeV	Inclusive	±0.30%	±0.30%	±0.10%	±0.10%	±0.0%
	C1	±0.30%	±0.30%	-	±0.10%	-
	C2	±0.30%	±0.30%	-	±0.10%	-
	C3	±0.30%	±0.50%	±0.10%	±0.20%	-
	C4	±0.30%	±0.50%	±0.10%	±0.30%	-
	C5	±0.30%	±0.10%	-	-	-
	C6	±0.30%	±0.10%	-	-	-
	C7	±0.30%	±0.20%	±0.10%	±0.10%	-
	C8	±0.30%	±0.20%	±0.10%	±0.10%	-
	C9	±0.40%	±0.60%	-	-	±0.10%
	C10	±0.30%	±0.30%	-	±0.10%	-
8 TeV	Inclusive	±0.34%	±0.39%	±0.06%	±0.10%	±0.01%
	C1	±0.30%	±0.26%	-	±0.10%	-
	C2	±0.31%	±0.26%	-	±0.11%	-
	C3	±0.35%	±0.47%	±0.10%	±0.16%	±0.02%
	C4	±0.35%	±0.49%	±0.08%	±0.18%	±0.01%
	C5	±0.31%	±0.19%	-	±0.03%	-
	C6	±0.31%	±0.20%	-	±0.07%	-
	C7	±0.35%	±0.31%	±0.09%	±0.05%	-
	C8	±0.35%	±0.39%	±0.11%	±0.08%	-
	C9	±0.38%	±0.71%	±0.07%	±0.05%	±0.06%
	C10	±0.33%	±0.41%	±0.07%	±0.10%	-
	C11	±0.33%	±0.38%	±0.03%	±0.13%	-
	C12	±0.33%	±0.43%	±0.06%	±0.12%	-
	C13	±0.34%	±0.39%	±0.05%	±0.12%	-
	C14	±0.34%	±0.40%	±0.07%	±0.10%	-
Constraint	All	Gaussian				

7.9 Statistics Intermezzo

7.9.1 Description of the statistical procedure

Statistical methods are needed to evaluate the properties of a signal when it is observed, like the mass m_H, the signal strength μ, the couplings to other particles or the spin. The signal strength corresponds to the ratio of the number of signal events observed to the number of signal predicted for a Standard Model Higgs boson,

$$\mu = \frac{N_s}{N_s^{SM}}. \tag{7.10}$$

Likelihood The likelihood contains the parameters of interest, i.e. the variables that are tested (μ, m_H,...). It contains other parameters referred to as *nuisance parameters* that model the impact of the systematic uncertainties of the analysis on the accuracy of the measurement of the parameters of interest. The nuisance parameters are denoted with the vector $\boldsymbol{\theta}$. The diphoton channel uses a single side-band-type fit with an extended unbinned likelihood. For the sake of clarity, the fit technique will be detailed in a binned fashion.

Let us consider a variable x measured both in the signal and background samples. From these measurements, one can build an histogram. The probability s_i (b_i) for a signal (background) event to be found in the bin i of the histogram corresponds to

$$s_i = s_{tot} \cdot \int_{bin\ i} f_s(x, \theta_s) dx,$$

$$b_i = b_{tot} \cdot \int_{bin\ i} f_b(x, \theta_b) dx,$$

where s_{tot} (b_{tot}) represents the total number of signal (background) events, f_s (f_b) the probability density function (pdf) of the variable x for the signal (background) and θ_s (θ_b) are the parameters that characterize the signal (background) pdf shapes.

The mean value ν_i of the number of events n_i in each bin i can simply be written as:

$$\nu_i \equiv \langle n_i \rangle = \mu s_i + b_i. \tag{7.11}$$

Then the likelihood corresponds to the product of Poisson probabilities in each bin, and can be written as [267]

$$L(\mu, \theta) = \prod_{i=1}^{N} \frac{(\mu s_i + b_i)^{n_i}}{n_i!} e^{-(\mu s_i + b_i)}, \tag{7.12}$$

where N is the number of bins and θ the set of the nuisance parameters.

For an unbinned analysis, the likelihood is instead expressed in term of events

$$L(\mu, \theta) = \frac{(\mu N_s^{SM} + N_b)^N}{N'!} e^{-(\mu \cdot N_s^{SM} + N_b)} \prod_{k=1}^{N'} \frac{\mu \cdot N_s^{SM}}{\mu N_s^{SM} + N_b} \Psi_s^k + \frac{N_b}{\mu N_s^{SM} + N_b} \Psi_b^k, \tag{7.13}$$

where N' is the total number of events, μN_s^{SM} and N_b the number of signal and background observed and Ψ_s^k and Ψ_b^k are the probability density functions for the event k respectively for the signal and the background.

Profile Likelihood Ratio The unbinned likelihood is used to perform the statistical studies. A statistical test based on the ratio of the profiled likelihood for the variable of interest μ to the likelihood maximizer $\lambda(\mu)$ is used and defined as:

$$\lambda(\mu) = \frac{L(\mu, \hat{\hat{\theta}}(\mu))}{L(\hat{\mu}, \hat{\theta})}, \tag{7.14}$$

where $\hat{\theta}$ and $\hat{\mu}$ are the values of θ and μ that unconditionally maximize the likelihood function: they are called Unconditional Maximal Likelihood Estimators (MLE) of θ and μ; and where $\hat{\hat{\theta}}(\mu)$ corresponds to the value of θ that maximizes the likelihood function for a given value of μ: it is called the Conditional Maximal Likelihood Estimator of θ. The presence of the nuisance parameters, when they are not fixed, will broaden the profile likelihood ratio, reflecting the systematic uncertainty on the number of signal events measured. By allowing the nuisance parameters to vary, the corresponding systematic error is converted into a statistical error. The value of $\lambda(\mu)$ lies between 0 and 1, where 1 signifies a good agreement between the observed data and the value of μ.

Statistical test The statistical test itself is carried out using a statistic expressed as

$$t_\mu = -2 \log \lambda(\mu), \tag{7.15}$$

and then takes values from 0 to infinity, with 0 meaning again a good agreement. A higher value of t_μ indicates more incompatibility between the observed data and the value of μ tested. To quantify more accurately this incompatibility, the p-value variable is built as:

$$p_\mu = \int_{t_{\mu,\text{obs}}}^{\infty} f(t_\mu|\mu) dt_\mu,$$

where $t_{\mu,\text{obs}}$ is the value of t_μ observed in the data using the formula 7.15 and $f(t_\mu|\mu)$ is the probability density function of t_μ under the hypothesis of μ.

With this method, the tested hypothesis can be excluded if the measured p_μ is below a certain threshold that varies following the level of confidence one wants to set on the result. For setting limits, this threshold is generally 0.05, corresponding to providing an exclusion within 95% Confidence Level (CL).

Significance This variable can also be converted into a significance Z: the probability that a Gaussian distributed variable be found at Z standard deviations above the Gaussian mean is equal to the upper-tail probability p_μ. Analytically, this can be expressed as

$$Z = \Phi^{-1}(1 - p_\mu), \tag{7.16}$$

with Φ^{-1} corresponding to the inverse of the cumulative distribution function (also called the quantile function) for the standard Gaussian (with zero mean and unit variance). This corresponds to a one-sided definition.

Discovery The above corresponds to a general case for μ. An particular case is when one wants to test the compatibility of the observed data with the background only hypothesis, then with $\mu = 0$. This test is important because when the case $\mu = 0$ is excluded, this corresponds to the discovery of a new signal. In this particular case, repeating the procedure discussed above, one can build a test statistic: $t_0 = -2 \log \lambda(0)$. An issue arises with this test due to the fact that any large upward or downward fluctuation could reject the $\mu = 0$ hypothesis. When searching for a signal from the the Higgs boson decay, having $\hat{\mu} < 0$ does not mean that a signal has been found, but rather that the background largely fluctuated downward. To prevent from excluding the background-only hypothesis due to background downward fluctuation, the test t_0 is slightly modified and called q_0

$$q_0 = \begin{cases} -2 \log \lambda(0) & \hat{\mu} \geq 0 \\ +2 \log \lambda(0) & \hat{\mu} < 0 \end{cases} \tag{7.17}$$

where the negative fluctuations are conserved but assigned to large values of q_0 for large fluctuations.

Again, to quantify the level of incompatibility of the data observed with the background-only hypothesis, the p_0 quantity is built

$$p_0 = \int_{q_0,obs.}^{\infty} f(q_0|0) dq0, \tag{7.18}$$

and the significance can be calculated from the formula 7.16.

It is customary to claim the discovery of a signal when $Z \geq 5$, corresponding then to $p_0 = 2.87 \cdot 10^{-7}$.

Asymptotic formulae To access this p_0 value, one has to know the distribution of the test statistic q_0 under the $\mu = 0$ hypothesis. This distribution can be built from MC pseudo-experiments, by generating a background only dataset. However this procedure is really time and CPU consuming, as one has to reach p_0 values of order of 10^{-7} to match with the discovery level. Approximated methods called "Asymptotic formulae" have been introduced, that allows to generate this distribution in a much faster way. These methods are in general exact in the limit of large sample size, that is the case in the $H \to \gamma\gamma$ analysis. One of these methods is based on the results of A. Wald [268]: for the general $f(q_\mu|\mu')$ probability density function of the variable q_μ under the hypothesis μ', the test statistic can be approximated by

$$t_\mu = -2\log\lambda(\mu) \sim \frac{(\mu-\hat{\mu})^2}{\sigma^2} + \mathcal{O}(\frac{1}{\sqrt{N}}), \tag{7.19}$$

where N corresponds to the sample size and where $\hat{\mu}$ is distributed following a Gaussian function, of mean μ' and standard deviation σ. If $\hat{\mu}$ is really distributed following a Gaussian function and the term $\mathcal{O}(\frac{1}{\sqrt{N}})$ can really be neglected, then this provides a good estimation of the test statistic. In this case, t_μ is shown to be distributed following a non-central χ^2 function for d degree of freedom, corresponding to the number of parameters of interest.

The particular case for which the mean $\mu' = \mu$, corresponds to a well known case, already demonstrated by S.S Wilks [269], where the distribution of the test statistic follows a simple χ^2 function for d degrees of freedom.

Asimov Dataset Another method is useful in order to get the distribution of the test statistic in a very rapid and accurate way. This method allows to replace many sets of simulated events obtained with MC techniques by a simple representative set called "Asimov dataset" by reference to a short story by Isaac Asimov [270] [267]. This dataset is such that for each parameter of the likelihood (nuisance parameter or parameter of interest), the Maximum Likelihood Estimator (MLE) defined previously is equal to the true value of the parameter: for example $\hat{\mu} = \mu$ or $\hat{\theta} = \theta$. More precisely, to get the MLE, one has to minimize the likelihood defined in Equation 7.12. Using Equations 7.11 and 7.12 the binned likelihood is rewritten as

$$L(\mu,\theta) = \prod_{i=1}^{N} \frac{\nu_i^{n_i}}{n_i!} e^{-\nu_i},$$

and then

$$\log[L(\mu,\theta)] = \sum_{i=1}^{N} \left(\log(\frac{\nu_i^{n_i}}{n_i!}) - \nu_i \right) \sim \sum_{i=1}^{N} \left(n_i \log\nu_i - n_i \log n_i - \nu_i \right),$$

using the Stirling approximation [271].

Finally the minimization is expressed as

$$\frac{\partial \log L}{\partial \theta_i} = 0 = \frac{\partial \log L}{\partial \nu_i}\frac{\partial \nu_i}{\partial \theta_i} = \sum_{i=1}^{N} (\frac{n_i}{\nu_i} - 1)\frac{\partial \nu_i}{\partial \theta_i},$$

with $\theta_i = (\mu, \boldsymbol{\theta})$

The solutions of this Equation $n_{i,Asimov}$ are

$$n_{i,Asimov} = \nu_i = \mu \cdot s_i + b_i.$$

The set of the solutions $n_{i,Asimov}$ form the Asimov dataset.

p_0 and Z_0 Using the approximation defined in Equation 7.19 in the case where the background only hypothesis is tested, one finds from Equation 7.17

$$q_0 = \begin{cases} \frac{\hat{\mu}^2}{\sigma^2} & \hat{\mu} \geq 0 \\ 0 & \hat{\mu} < 0 \end{cases}$$

and one can show that the function $f(q_0|0)$ can be written as [267]

$$f(q_0|0) = \frac{1}{2} + \frac{1}{2} \cdot \frac{1}{\sqrt{2\pi}} \cdot \frac{1}{\sqrt{q_0}} \cdot e^{-\sqrt{q_0}^2/2},$$

where one can recognize the delta function and the χ^2 function for one degree of freedom.

Following Equation 7.18, one can rewrite:

$$p_0 = 1 - \int_{-\infty}^{q_0,obs.} f(q_0|0)dq0 = 1 - \Phi(\sqrt{q_0}).$$

Finally using Equation 7.16, one finds

$$Z_0 = \Phi^{-1}(1 - p_0) = \Phi^{-1}(\Phi(\sqrt{q_0})) = \sqrt{q_0}. \tag{7.20}$$

Combining multiple channels or categories In the $H \to \gamma\gamma$ analysis, categories are made in order to increase the sensitivity (see Section 7.3). Statistically, each category c has its own likelihood $L_i(\mu, \theta_c)$, with the parameter of interest (here μ) common to all the categories, whereas the nuisance parameters $\boldsymbol{\theta_c}$ can be different for each channel. In case of correlated uncertainties within several channels, a common associated nuisance parameter is used.

If all the categories are independent (this is generally the case), the full likelihood is simply the product of the individual likelihoods over all the categories:

$$L(\mu, \theta) = \prod_{c=1}^{N_c} L_c(\mu, \theta_c)$$

where $\theta = \cup\, \theta_c = (\theta_1, \theta_2, ...)$ is the complete set of nuisance parameters, and N_c is the total number of categories. Following Equation 7.14, the profile likelihood ratio then corresponds to:

$$\lambda(\mu) = \frac{\prod_c L_c(\mu, \hat{\hat{\theta}}_c)}{\prod_c L_c(\hat{\mu}, \hat{\theta}_c)}$$

The same procedure is applied when combining different channels, like $H \to \gamma\gamma$ and $H \to llll$ or different analyses like $H \to \gamma\gamma$ at $\sqrt{s} = 7$ TeV and $\sqrt{s} = 8$ TeV.

7.9.2 Treatment of systematic uncertainties

The systematic uncertainties are taken into account through the use of nuisance parameters in the likelihood.

Signal normalization For the systematic affecting the event yield, the systematic uncertainties are carried out by the parameter K^c in the expression [272] [273]

$$N_s^c = \mu N_s^{SM,c} = \mu[N^{ggH,c} + N^{VBF,c} + N^{WH,c} + N^{ZH,c} + N^{ttH,c}] \cdot K^c + n_{spurious} \cdot K_{spurious},$$

where N_s^c is the number of signal observed in the category c.

For example for the $\sqrt{s} = 8$ TeV analysis:

$$K^c = K_{Lumi} \cdot K_{ID} \cdot K_{Iso} \cdot K_{ES} \cdot K_{BR} \cdot K^c_{\sigma^{theor}_{ggH}} \cdot K^c_{\eta^*} \cdot K^c_{\Delta\phi} \cdot K^c_{p_T} \cdot K^c_{mat} \cdot K^c_{e^-} \cdot K^c_{\mu}$$

and

$$N^{X,c} = N^{X,SM}[K_{X,scale} \cdot K_{X,PDF} \cdot K^c_{X,UE} \cdot K^c_{X,JES} \cdot K^c_{X,JER} \cdot K^c_{X,JVF} \cdot K^c_{X,E_{\mathrm{T}}^{\mathrm{miss}}}]$$

In these formulae:

- $n_{spurious}$ is the number of signal measured in background-only sample with a signal+background fit (see Section 7.6.3). This is more detailed in next paragraphs.
- $N^{X,SM}$ corresponds to the number of signal expected in the Standard Model for a Higgs boson production *via* the X process, $X = ggH,\ VBF,\ WH,\ VH,\ ttH$
- the terms K_{yy} correspond to the function that models the systematic uncertainty associated with the source yy (see Tables 7.8, 7.9 and 7.10 and Section 7.8 for the definitions and values of these systematic uncertainties)
- the terms K^c_{yy} have the same definition than the K_{yy} except that they depend on the category c.
- the terms $K_{X,yy}$ or $K^c_{X,yy}$ have the same definition than the K_{yy} or K^c_{yy} except that they depend on the production process X

Signal width and position The signal shape is modeled with a composition of a Crystal Ball and a Gaussian functions as detailed in Section 7.5. Taking now the systematic uncertainties into account, Equation 7.8 can be rewritten as:

$$C = f_{CB} \cdot F_{CB}(m_{\gamma\gamma}, \mu_{CB} \cdot K_\mu, \sigma_{CB} \cdot K_\sigma, \alpha_{CB}) + (1 - f_{CB}) \cdot F_{Ga}(m_{\gamma\gamma}, \mu_{CB} \cdot K_\mu, \kappa_{Ga} \cdot \sigma_{CB} \cdot K_\sigma) \quad (7.21)$$

where K_μ and K_σ are functions that model the systematic uncertainties on the signal position and resolution and with K_μ defined as:

$$K_\mu = K_{method} \cdot K_{mat,low\,\eta} \cdot K_{mat,high\,\eta} \cdot K_{PS,barrel} \cdot K_{PS,EC} \quad (7.22)$$

following the five uncorrelated sources of uncertainties for the signal position determined in Section 7.8

Background The number of background events, N_b, also has a systematic uncertainty coming from the fit model chosen (see 7.6.3). Table 7.6 gives the functional forms chosen for the modeling of the background shape in the various categories and summarizes the uncertainty on the number of background events referred to as "spurious signal". The parameters of the background fit functions are considered as nuisance parameters and determined in the likelihood fit. The spurious signal is modeled as a real signal, it is fitted with the same function.

K modeling and the constraints The functions K defined above have different modeling, depending on the source of uncertainties they represent. Two main cases are:

1. $$K = 1 + \delta\theta,$$

2. $$K = e^{\sqrt{\log(1+\delta^2)}\theta},$$

   where δ is the value of the uncertainty and θ is the nuisance parameter associated to the uncertainty.

The systematic uncertainty as experimentally or theoretically determined δ is not used directly as an uncertainty in these models. Instead, the factor θ gives more or less weight to this uncertainty. This is the frequentist approach for treating the systematic uncertainties. The θ parameters are directly determined during the fit, so that they minimize the likelihood as already seen previously. Their value is not free to vary. The constraint can take different forms:

a) Gaussian constraint G: $G = \frac{1}{N}e^{(x-\delta)^2/2}$. The fit is allowed to find a value of θ inside a Gaussian function having for mean the value of the uncertainty itself δ and a width of unity. It is then less probable to find a value far from the mean.

b) Bifurcated Gaussian constraint G':

$$G' = \begin{cases} \frac{1}{N}e^{(x-\delta)^2/2\sigma_L^2} & x < \delta \\ \frac{1}{N}e^{(x-\delta)^2/2\sigma_R^2} & x > \delta \end{cases}$$

   The parameter θ is constrained by a Gaussian function that has different widths on the left and on the right sides of the mean of the distribution. This allows to take into account asymmetrical errors.

For example for the uncertainty on the peak position, taking Equation 7.22:

$$K_\mu = (1 + \theta_1\delta_{method}).(1 + \theta_2\delta_{mat,low\,\eta}).(1 + \theta_3\delta_{mat,high\,\eta}).(1 + \theta_4\delta_{PS,barrel}).(1 + \theta_5\delta_{PS,EC})$$

where θ_1, θ_2, θ_3, θ_4, θ_5 are 5 nuisances parameters constrained with a Gaussian form G and where δ_{method}, $\delta_{mat,low\,\eta}$, $\delta_{mat,high\,\eta}$, $\delta_{PS,barrel}$, and $\delta_{PS,EC}$ correspond to the different systematics uncertainties values associated to the peak position.

The same form is used for the uncertainty coming from the background model $K_{spurious}$ These forms are called Gaussian constraints.

Another representative example concerns the uncertainty on the resolution:

$$K_\sigma = e^{\sqrt{\log(1+\delta_\sigma^2)}\theta_\sigma}$$

where θ_σ is constrained with a Gaussian function G. This form is called a lognormal constraint.

Finally if the Gaussian function is replaced by a bifurcated one, the form is called an Asymmetric Log-normal constraint.

The constraints taken for each source of systematic are reported in the tables of the Section 7.8.

Nuisance parameters in the framework A total of 119 nuisance parameters are used in the combined likelihood for the 2011 and 2012 analyses for the modeling of the systematic uncertainties, and for the background parametrization and normalization. Two parameters of interest add up, dedicated to the Higgs boson mass and signal strength, leading to 121 parameters to be fitted.

More precisely, 66 parameters are dedicated to the background parametrization and normalization (29 for 2011 and 37 for 2012), 14 to the uncertainty on the background parametrization, 6 and 10 for the experimental and theoretical uncertainties on the signal yield, 17 for the uncertainty on the signal yield per category, 1 for the uncertainty on the signal resolution and 5 for the uncertainty on the signal peak position.

The unconditional ensemble The systematic uncertainties reviewed earlier are mostly measured directly in the data and the statistical procedure used to fit the parameter of interest, in general does not allow to constrain these systematics. Their direct measurement in the data using the knowledge of the detector performance is called an auxiliary measurement. When generating pseudo-experiments, there is an issue for this kind of systematic, as there is not anymore the possibility to extract them from the data. For example, for the systematic uncertainties coming from the photon energy scale, the associated nuisance parameters are constrained with a Gaussian function of mean δ_{ES} (the value of the uncertainty itself) and of unit width. For the pseudo-experiments, to mimic a measurement in the data, the mean of the Gaussian function is not anymore fixed at δ_{ES} but rather randomized around this value [274]. This procedure is referred to as the unconditional ensemble.

7.10 Results

The RooStat tool [275] is used to compute the statistical results, with the help of the RooFit tool for fitting [276, 277]. All the aspects of the $H \to \gamma\gamma$ analysis have been reviewed in the previous sections. Now the final results obtained using the statistical tools defined previously are discussed.

7.10.1 Comparison to background-only hypothesis

Figure 7.17 shows the local p_0 value for the data as defined in Equation 7.20, then corresponding to a test of the background-only hypothesis. The signal is such that the compatibility with a background only hypothesis is about 10^{-13}, and the conversion into a significance (Equation 7.16) leads to the value of 7.4σ for a mass of 126.5 GeV.

The expected value, obtained from a MC analysis with $\mu = 1$, shown with dashed lines, is smaller: $p_0 \sim 10^{-4}$ and leads to the significance 4.1σ at the same mass.

The level of significance measured in the data is sufficient to state that a signal of a particle decaying into two photons is observed. No other significant deviation is seen within the mass range of the analysis.

Looking more precisely at Figure 7.17(a), one can see the difference of expected sensitivity when doing an inclusive (black line) or categorized (red line) analysis.

Figure 7.17(b) shows the difference of p_0 value for the two analyses performed with the data collected in 2011 and 2012. The large difference on the statistical size of the dataset (around four times larger for 2012) is one of the reasons explaining the difference in sensitivity. The minimum of the p_0 value peaks at around the same values for the two years, that demonstrates a good stability of the excess observed (this will be studied in more detail in Chapter 8).

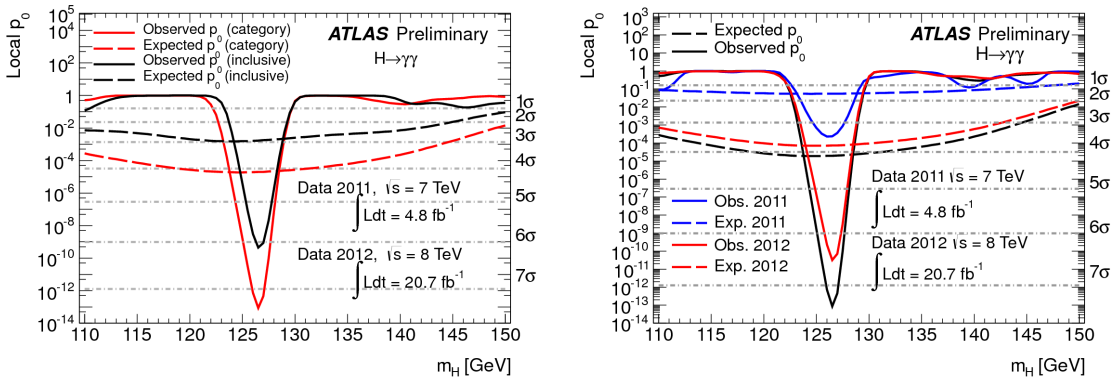

(a) (b)

Figure 7.17: (a) Observed (full line) and expected (dashed line) p_0 value as a function of the Higgs boson mass hypothesis, comparing the analyses with categories (red line) and inclusive (black line) for the full dataset collected in 2011 and 2012. (b) Comparison of the p_0 value for the 2011 (blue line) and 2012 analyses (red line). The black line corresponds to the combination of the two datasets. Taken from [223].

7.10.2 Signal strength

From the previous discussion, it appears that the size of the excess observed is larger than the expectation for a Standard Model Higgs boson. The signal strength μ (Equation 7.10) is measured using the profile likelihood ratio defined in Equation 7.14. The statistical test t_μ defined in Equation 7.15 is evaluated for different values of μ. The value that minimizes t_μ, for a mass of $m_H = 126.8$ GeV is

$$\mu = 1.64^{+0.34}_{-0.30} = 1.64 \pm 0.24 \text{ (stat) } ^{+0.25}_{-0.18} \text{ (syst)},$$

where "stat" denotes the statistical uncertainty and "syst" the systematic one. The errors on the signal strength are given by the width of t_μ: the values of the signal strength for which $t_\mu = 1$ corresponds to two times the total error on the signal strength.

This measurement can also be made in individual categories in order to test the compatibility of the signal strength in the different categories. The evolution of the best fitted signal strength value as a function of the category is shown in Figure 7.18.

The values found in the different categories, inside their uncertainty, are really stable and well distributed around the combined value. The large errors for the categories dedicated to the VH production process reflect the small number of signal events expected in these categories.

More studies on the measurement of the signal strength and its dependence on the signal resolution can be found in the next chapter.

7.10.3 Couplings and production modes

7.10.3.1 Signal strength per production mode

Due to the dedicated categories designed to capture the VBF and VH processes, the signal strength can also be measured for the different production modes. This measurement is of course approximative as some contamination from other production processes is expected (see Figure 7.5). Moreover, from the number of signal events observed one cannot disentangle the

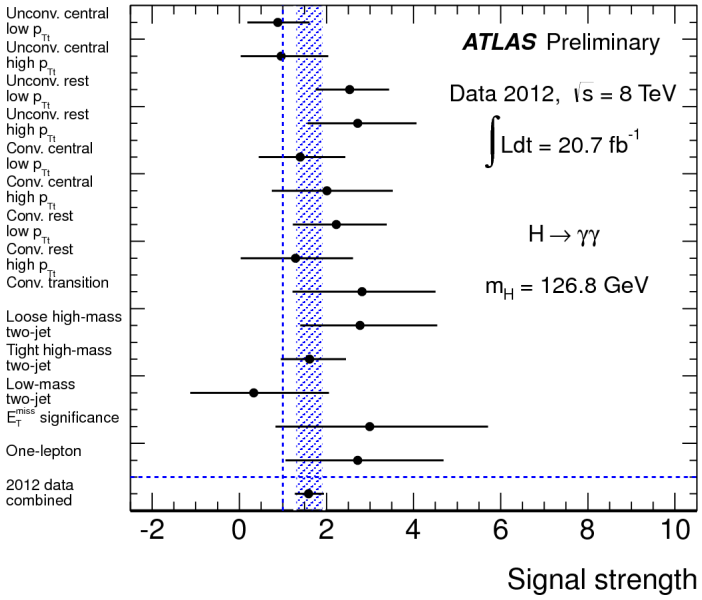

Figure 7.18: Evolution of the best fitted signal strength value as a function of the category of the analysis, for the 2012 dataset. The blue rectangle area shows the combined value with its uncertainty and the vertical dashed blue line depicts the Standard Model expectation $\mu = 1$. Taken from [223].

production and decay processes. Figure 7.19 illustrates the best fitted signal strength values for the three different processes : $\mu_{VH} \times \frac{Br}{Br_{SM}}$ (categories C12, C13, C14), $\mu_{VBF} \times \frac{Br}{Br_{SM}}$ (categories C10,C11) and $\mu_{ggH+ttH} \times \frac{Br}{Br_{SM}}$ (all the other categories).

The values found for these three different signal strengths are

$$\mu_{ggF+ttH} \times \frac{Br}{Br_{SM}} = 1.6 \pm 0.3 \text{ (stat) } ^{+0.3}_{0.2} \text{ (syst)},$$

$$\mu_{VBF} \times \frac{Br}{Br_{SM}} = 1.7 \pm 0.8 \text{ (stat) } ^{+0.5}_{0.4} \text{ (syst)},$$

$$\mu_{VH} \times \frac{Br}{Br_{SM}} = 1.8^{+1.5}_{-1.3} \text{ (stat) } \pm 0.3 \text{ (syst)}.$$

These three values show a good compatibility.

7.10.3.2 Couplings

The couplings of the signal observed with the bosons and fermions can be tested. From the decay mode into two photons *via* fermions and W loops, the Higgs boson couples to both fermions and bosons in an indirect way. However, the particles circulating in the loops could be Beyond Standard Model particles. From the production mode, more information can be gathered as most of them do not contain loops. This is the case for example for the VBF, WH and ZH processes that are mediated by vector bosons. The ttH process, mediated by quarks, is also unambiguous but it cannot be probed alone yet. The fusion of gluons is mediated by a loop of fermions. Therefore the couplings to vector bosons and to fermions can be tested grouping the

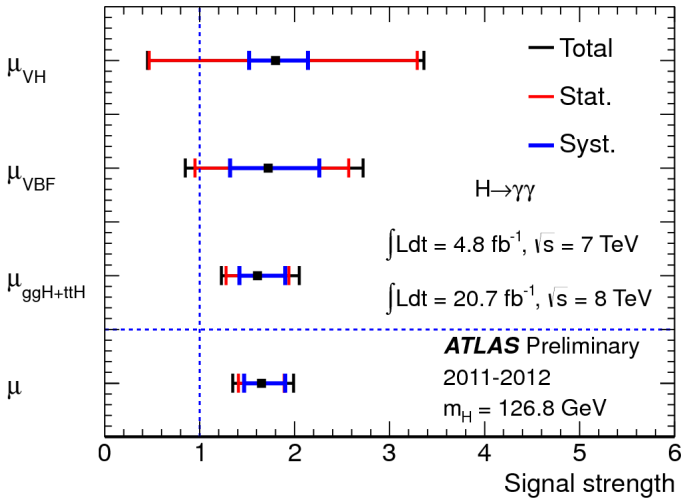

Figure 7.19: Evolution of the best fitted signal strength value as a function of the production process-tagged categories, for the 2011 and 2012 datasets. The blue, red and black lines corresponds respectively to the systematic, statistical and total uncertainties. The vertical blue dashed line corresponds to $\mu = 1$. Taken from [223].

signal strength in the following way: $\mu_{VBF+VH} \times \frac{Br}{Br_{SM}}$ and $\mu_{ggH+ttH} \times \frac{Br}{Br_{SM}}$. The simultaneous fit of these two quantities using the 2011 and 2012 datasets is shown in Figure 7.20. The best two-
4750 dimensional fit value is slightly larger than the Standard Model point (1,1), which is contained in the 95% CL contour.

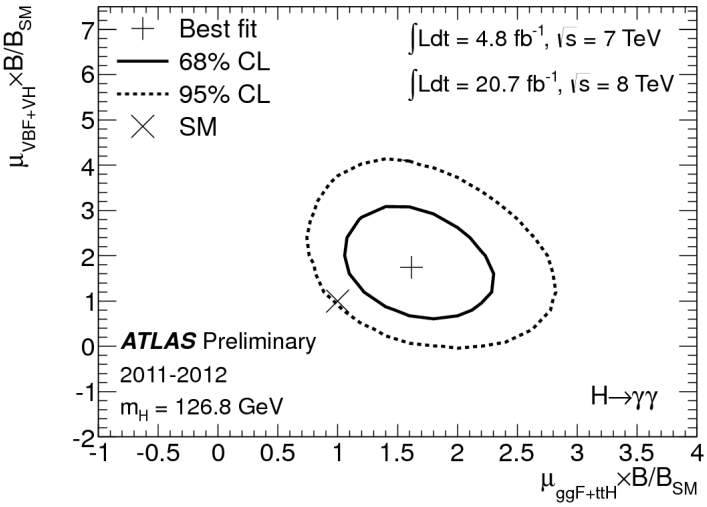

Figure 7.20: Best fitted signal strength values $\mu_{VBF+VH} \times \frac{Br}{Br_{SM}}$ and $\mu_{ggH+ttH} \times \frac{Br}{Br_{SM}}$ for the 2011 and 2012 datasets. The best two-dimensional fit value is shown with the black cross, and the 68% and 95% CL contours are also shown in plain and dashed lines. Taken from [223].

7.10.4 Fiducial cross section

The fiducial cross section corresponds to the cross section measured in a well defined phase space, determined by the pseudorapidity and transverse momentum of the photons: $\eta < 2.37$ and $p_{T1} > 40$ GeV and $p_{T2} > 30$ GeV. No extrapolation to the rest of the acceptance is done.

The measurement is performed with the inclusive analysis and with the 2012 dataset at $\sqrt{s} = 8$ TeV.

The fiducial cross section is measured from the formula:

$$\sigma_{fid} \times Br = \frac{N_{signal}}{C.L}$$

where L is the integrated luminosity, N_{signal} the total number of signal events measured with a signal+background fit on the diphoton invariant mass distribution and C is a factor that allows to correct for detector effects, like the trigger, reconstruction, identification or isolation efficiencies. It is determined using MC simulations of the $H \to \gamma\gamma$ process, for each production mode, by comparing the total number of events generated and selected by the analysis to the total number of events generated and falling inside the fiducial region.

The fiducial cross section is measured:

$$\sigma_{fid} \times Br = 56.2 \pm 10.5 \text{ (stat)} \pm 6.5 \text{ (syst)} \pm 2.0 \text{ (lumi) fb}$$

The main source of systematic uncertainty on the measured number of signal is the photon identification, the isolation, the trigger and the energy scale (see values in Tables 7.8).

Chapter 8

Measurement of the Higgs boson mass

8.1 Method

For the purpose of the mass measurement, the Likelihood $L(m_H, \mu, \theta)$ is built with m_H the mass of the Higgs boson as the parameter of interest, μ the signal strength treated as a nuisance parameter without any constraint and θ the vector of nuisance parameters represents the systematic uncertainties for this channel as described in Section 7.8.

The profile likelihood ratio as defined in Equation 7.14 is computed

$$\lambda(m_H) = \frac{L(m_H, \hat{\hat{\mu}}, \hat{\hat{\theta}})}{L(\hat{m_H}, \hat{\mu}, \hat{\theta})}, \tag{8.1}$$

with $\hat{\hat{\mu}}$ and $\hat{\hat{\theta}}$ being respectively the values of the strength parameter and of the nuisance parameters that maximize the likelihood for the mass hypothesis m_H, and the denominator corresponding to the unconditional maximum of the likelihood.

Then the expression

$$-2\log\lambda(m_H), \tag{8.2}$$

is evaluated at each tested mass point: the parameter m_H is varied from 110 GeV to 135 GeV in steps of 0.1 GeV.

A mass-dependent signal parametrization is then needed, as the one described in Section 7.5, and for example in Equation 7.9. This parametrization is based on a composite model of a Crystal Ball function for the core of the distribution and a small wide Gaussian component, used to model the tails.

Given their small dependence on the mass, the theoretical uncertainties are assumed to be constant, and their values are taken at the mass 126.5 GeV.

The minimum of the likelihood given in Equation 8.2 gives the central value of the resonance mass and the width defined by the crossing of this curve with the line $-2\log\lambda(m_H) = 1$ gives two times the total uncertainty on the mass. This total uncertainty can be decomposed into the statistical and systematic parts.

In order to test the impact of one or more nuisance parameters on the mass measurement, one can choose to fix these parameters so that they do not contribute to the fit. These parameters are not fixed to their nominal value (which is in general 0) but rather to their *profiled* value

i.e $\hat{\theta}$: this corresponds to the value obtained when doing a fit with all the parameters free. This procedure produces what is called the Maximum Likelihood Estimate (MLE) (see Section 7.9).

8.2 Results

Figure 8.1 shows the likelihood defined in Equation 8.2 as a function of the tested mass. The two curves with the smaller and larger width give a measurement of the mass and respectively of the statistical and total uncertainties.

The measured mass and its statistical uncertainty are

$$m_H = 126.8 \pm 0.7 \ \text{GeV} = 126.8 \pm 0.2(\text{stat}) \pm 0.7(\text{syst}) \ \text{GeV}$$

where the systematic error is obtained by quadratically subtracting the statistical uncertainty from the total uncertainty.

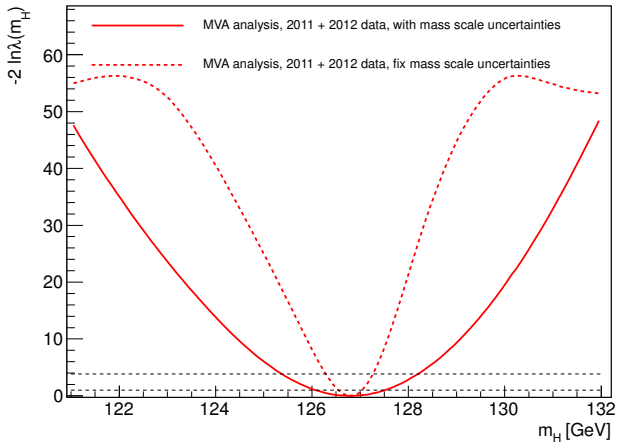

Figure 8.1: Likelihood $-2\ \ln\lambda(\mathrm{m_H})$ as a function of the Higgs boson mass hypothesis, using the full 2011 and 2012 datasets and the running the analysis described in Chapter 7. The dashed (full) line corresponds to the likelihood ratio when the systematic uncertainties related to the peak position are fixed (not fixed) to their profiled value.

To assess the influence of the strength parameter μ on the mass measurement, the correlation between these two quantities is tested. The 68% and 95% CL contours of the likelihood versus (m_H, μ) are shown in Figure 8.2, this time including μ as a parameter of interest in the profile likelihood, i.e. using the likelihood

$$\lambda(m_H, \mu) = \frac{L(m_H, \mu, \hat{\hat{\theta}})}{L(\hat{m_H}, \hat{\mu}, \hat{\theta})}. \tag{8.3}$$

No obvious correlation is found between the mass and the signal strength.

The measurement of the signal strength using the likelihood defined in Equation 8.3 gives

$$\hat{\mu} = 1.64 \pm 0.32.$$

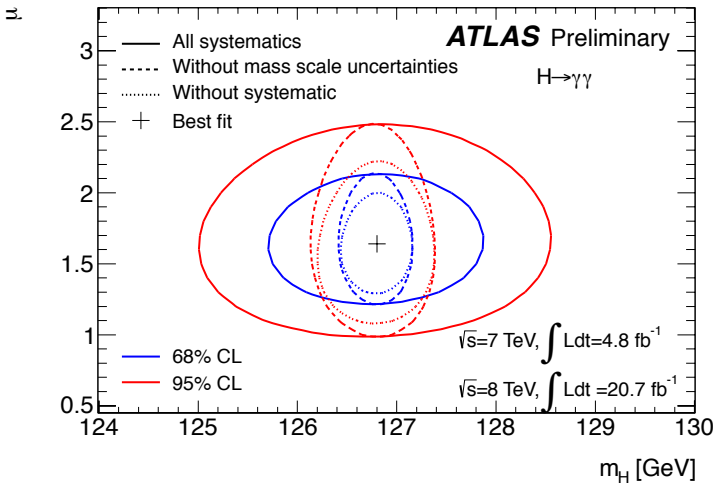

Figure 8.2: The best-fit values of m_H and μ, and their 68% (blue) and 95 % (red) CL contours when all the systematics are included (full line). Results when all the systematics (tight dotted line) or only the mass scale systematics (loose dotted line) are fixed to their profiled values are also shown.

This is compatible with the result detailed in the previous chapter.

The nuisance parameters introduced in the statistical model are used to model the systematic uncertainties of the analysis and the background fit parameters. There are different kinds of systematics as already reported in the previous chapter: theoretical uncertainties, systematics on the yield, migrations, background estimation, signal resolution or peak position. Only one category significantly contributes to the mass measurement: the systematic on the peak position.

The uncertainty on the signal resolution does not have a sizeable impact on the likelihood width, as illustrated in Figure 8.3(a). In this figure, the likelihood ratio as defined in Equation 8.2 is drawn for a dataset of 13 fb^{-1} recorded at $\sqrt{s} = 8$ TeV [1] combined with the full dataset collected at $\sqrt{s} = 7$ TeV, following the analysis procedure described in Chapter 7. In these curves, the nuisance parameter associated to the uncertainty on the signal resolution is fixed (dashed line) or not (full line) to its MLE, all the other parameters being kept free and fitted. No difference is seen between these two curves.

The other nuisance parameters do not have either an effect on the mass uncertainty as demonstrated in Figure 8.3(b) which shows the difference on the likelihood ratio width when all the uncertainties of the analysis or only those related to the peak position are fixed (the related nuisance parameters are fixed to their MLE). No difference can be seen between the two curves up to 2-3 standard deviations illustrating the negligible impact of the other systematic on the uncertainty on the mass in the vicinity of the minimum. At higher masses, the profile where only the uncertainty on the peak position are fixed is widening, which reflects the impact of all the other nuisance parameters in this region.

The impact of the systematic uncertainties on the μ and m_H measurements was shown in Figure 8.2: fixing the uncertainty from mass scale has a very large impact on the total uncertainty on the mass, but no impact on the signal strength uncertainty. On the contrary, fixing all the other systematic uncertainties does not change the uncertainty on the mass, whereas for

[1] Not the full dataset of 20.7 fb^{-1} was available when this test was done.

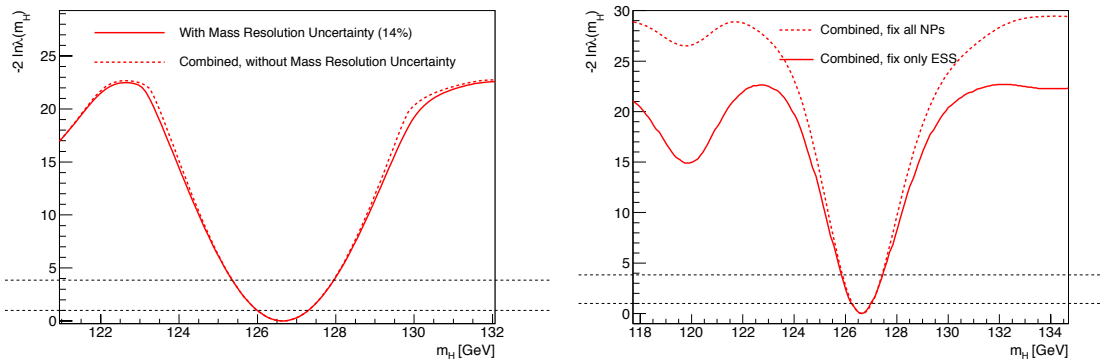

(a) (b)

Figure 8.3: (a) Comparison of the likelihood $-2\ \ln\lambda$ when all the nuisance parameters are fixed to their MLE, including (solid line) or excluding (dashed line) the one related to the mass resolution for the full 2011 dataset combined with a subset of the 2012 dataset corresponding to 13 fb^{-1}. (b) Comparison of the profile likelihood ratio when all the nuisance parameters (dashed line) or only the ones related to the uncertainty on peak position (solid line) are fixed to their profiled value. The same datasets are used.

the signal strength the impact is significant.

The statistical uncertainty is defined as the uncertainty obtained when all the nuisance parameters of the statistical model are fixed to their MLE except the signal strength and the nuisance parameters related to the background fit parameters. Since only the uncertainties related to the peak position have an impact on the likelihood width in the vicinity of the minimum, one can consider that the statistical uncertainty is equivalent to the uncertainty obtained when only the parameters related to the peak position are fixed. This approximation will be used in the following to calculate the statistical uncertainty, unless stated otherwise.

In the ATLAS experiment, the $H \rightarrow llll$ channel has also observed a resonance in the low mass region [10, 278] and measured its mass. This channel benefits from the high mass resolution, even if is suffers from a small number of expected signal events. A comparison with the measurement made in the $H \rightarrow \gamma\gamma$ channel has been done and these two channels have been combined [16, 12]. This comparison is shown in Figure 8.4.

A large discrepancy between these two channels is observed. This has provoked very deep investigations on all the possible aspects of the mass measurement. First a validation of the mass measurement method itself has been performed, as described in Section 8.3, then investigations on the reconstruction of the diphoton invariant mass have been performed, as reviewed in Section 8.4, implying the calibration of the photons and the reconstruction of the primary vertex. Consistency checks on the mass measurement have been made, as reported in Section 8.5, and finally the impact of the signal resolution on the mass measurement was also checked as described in Section 8.6.

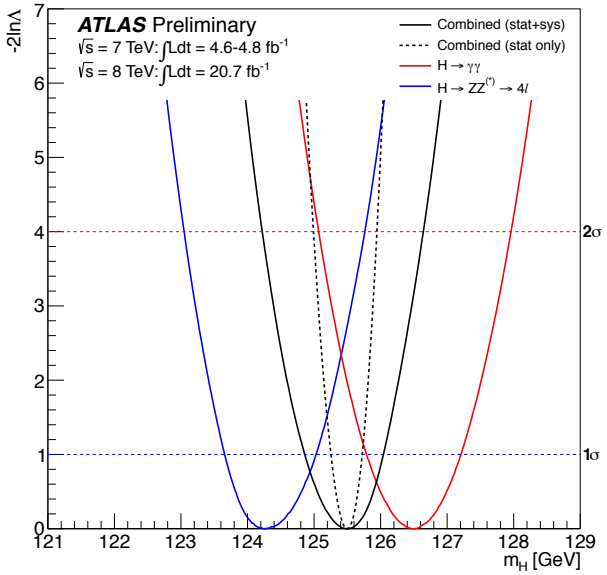

Figure 8.4: Mass measurement in the channels $H \to \gamma\gamma$ (red line) and $H \to 4l$ and combination of the two measurements (black line), for the full Run I dataset. The dashed black line corresponds to the likelihood curve with all systematic uncertainties fixed in the fit. Taken from [12].

8.3 Validation of the method

8.3.1 Validation of the mass measurement

The method is validated using pseudo-experiments, generated by randomly drawing the number of background events from a Poisson distribution around the fitted values in the data and the number of signal events also from a Poisson distribution around the expected values for a given signal strength and mass. Different pseudo-datasets are generated, for different hypotheses on the mass and signal strength of the signal: the two values $\mu = 1$ and $\mu = 2$ and masses in the [120,130] GeV range with a mass step of 1 GeV are tested. An average of 1000 pseudo-experiments are performed to obtain a good accuracy on this measurement. The number of events used for the pseudo-experiments corresponds to 4.9 fb^{-1} at $\sqrt{s} = 7$ TeV in 2011 and 13 fb^{-1} at $\sqrt{s} = 8$ TeV in 2012. The resulting mass of the signal generated is measured with the method described in Section 8.1: the statistical test defined in Equation 8.2 is evaluated for each mass and signal strength hypothesis and the mass that minimizes the likelihood is extracted. All the parameters are free in this fit.

The measured mass is then compared to the injected value in order to test the goodness of the method closure. In Figure 8.5, the mean value of the distribution of the mass obtained with all the pseudo-experiments for each mass hypothesis when considering $\mu = 2$ is drawn as a function of the injected mass value. The agreement is very good: fitting with a first order polynomial gives a slope extremely close to 1. The same result is found for $\mu = 1$. Including or not the systematic uncertainties of the analysis in the fit leads to the same result.

The procedure described above leads then to an unbiased estimate of the Higgs boson mass.

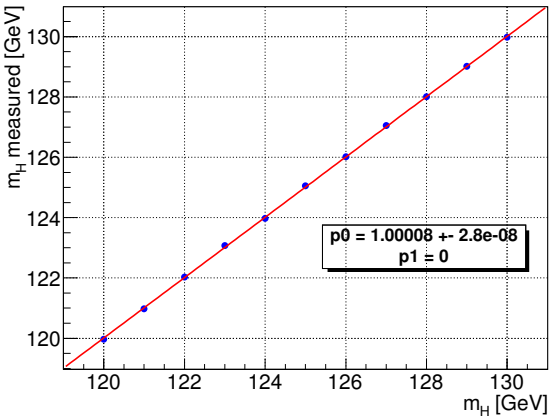

Figure 8.5: Average of the measured Higgs boson mass in pseudo-experiments as a function of the injected mass m_H, for a signal strength of $\mu = 2$. The result of a linear fit is shown in red and the values of the fit parameters (slope p_0 and intercept p_1) are indicated.

8.3.2 Validation of the strength parameter measurement

The measurement of the mass and signal strength are related because the signal strength corresponds to a nuisance parameter in the mass measurement likelihood. The measurement of the signal strength is then also checked in the following.

The same test as the one described previously for the mass is carried out but this time with the signal strength as parameter of interest in the fit. This parameter is scanned from μ=0.5 to μ=2.5 with a step of 0.5, and the mass value is set to 126 GeV, using a similar number of pseudoexperiments and generated events.

Without systematic uncertainties In a first study, all the systematic uncertainties of the analysis are fixed to their profiled value, in order to check only the impact of the statistical fluctuations. The correlation between the best fitted signal strength $\hat{\mu}$ and the injected one is shown in Figure 8.6(a). The method tends to slightly overestimate the value of μ especially for low values. This bias decreases as μ increases. Typically, the bias is about $8 - 10\%$ for $\mu = 1$ and falls to $\sim 3\%$ for $\mu = 2$. This is expected from the procedure chosen: when searching a signal over a large background, the tendency is always to fit the largest fluctuation. When the significance of the signal increases (or equivalently, for the same dataset, if the signal strength is higher), there is less probability to find a background fluctuation as big (or bigger) than the one corresponding to the signal and so the real signal is fitted. This explains the trend observed in Figure 8.6(a).

With systematic uncertainties A more realistic study which includes all the systematics of the analysis is carried. Figure 8.6(b) shows the resulting correlation between the injected signal strength and the measured one with the procedure described above, using pseudo-experiments. The general overestimation of the signal strength by the method is not anymore a constant feature. It appears only for μ below 1, switching on the contrary to an underestimation for μ above 1. This bias slightly decreases when μ increases, and it is typically about -3.5% for $\mu = 2$ and $\sim +2\%$ for $\mu = 1$.

This feature is tested with dedicated pseudo-experiments having different nuisance parameter

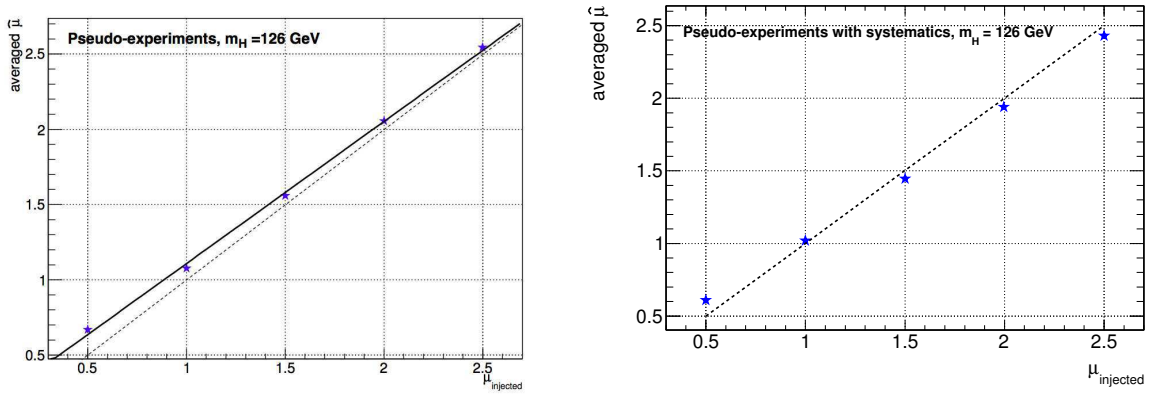

(a) Without systematic

(b) With systematic

Figure 8.6: Average of the measured strength parameter in pseudo-experiments as a function of the injected μ, when all the systematic uncertainties of the analysis are fixed to their MLE (a) or freely fitted (b). The result of a linear fit is shown in black solid line (a) and the line $x = y$ is shown in black dashed line (a,b).

settings. As an example, the distribution of the measured signal strength for a set of pseudo-data with $\mu = 2$ and a mass of 126 GeV for the different settings is shown in Figure 8.7.

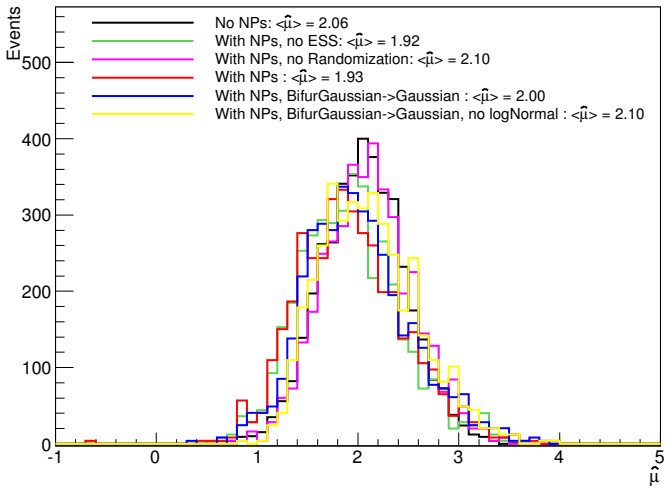

Figure 8.7: Distribution of the best fit of the signal strength for pseudo-experiments generated with $\mu = 2$ and $m_H = 126$ GeV. The red and black lines correspond to the case where all the nuisance parameters are free and fixed respectively. The green line illustrates the case where the nuisance parameters related to the peak position are fixed. The blue and yellow lines correspond to the cases where the bifurcated Gaussian and lognormal functions in the likelihood (see Section 7.9.2) are replaced by simple Gaussian functions. Finally the pink line corresponds to the case where the auxiliary measurement in the pseudo-experiments (see Section 7.9.2) is not anymore randomized. The mean values of the distributions are given in each case.

From the different nuisance parameters settings illustrated in this figure and the resulting mean value for the signal strength measurement, it is noticed that both the randomization of the auxiliary measurement and the presence of bifurcated Gaussian (corresponding to an asymmetric lognormal constraint, see Section 7.9.2) and lognormal functions in the likelihood lead to the negative bias observed in the measurement of the signal strength. This effect seems then to be related to the asymmetric functions.

8.3.3 Coverage of the error

The coverage of a statistical measurement is usually defined as the percentage of events for which the measured quantity x is included in the interval [x-δx, x+δx] with δx being the statistical uncertainty associated to the measurement of x. For a quantity behaving as a Gaussian function, the expected value of this coverage is then 68%. In the studies described below, it is assumed that the parameter of interest m_H has Gaussian properties.

8.3.3.1 Coverage for a given μ

The coverage is computed for the mass m_H measured following the method described in Section 8.1. The evolution of the coverage of the error for the mass is tested as a function of the mass, for a given μ.

For this study, 1000 pseudo-experiments generated with a fixed signal strength of $\mu = 2$ and with masses in the range [120,130] GeV with a 1 GeV step are used. The statistic used corresponds to the full 2011 dataset as well as a subset corresponding to $13fb^{-1}$ of the 2012 dataset. Two different definitions of the coverage are tested: the fraction of pseudo-experiments resulting in measured masses within one standard deviation

1- from the average mass (percentage of events in [$< \hat{m_H} >$ - $< \delta m_H >$, $< \hat{m_H} >$ + $< \delta m_H >$]),

2- from the injected mass (percentage of events such that $\hat{m_H} - \delta m_H < m_H < \hat{m_H} + \delta m_H$).

The evolution of the coverage of the error following these two definitions as a function of the generated mass is shown in Figure 8.8(a). The statistical uncertainty on the coverage measurement is not indicated in this figure, it corresponds roughly to 1.5% [2]. Given this uncertainty, the statistical uncertainty on the mass measurement is close to 68% for both definitions, and for the full mass range, as expected for Gaussian errors.

8.3.3.2 Dependence of the statistical mass uncertainty on μ

Even if it is profiled in the likelihood estimation, the signal strength has an influence on the statistical uncertainty δm_H on the mass since larger signals will result in smaller uncertainties on the mass. Pseudo-experiments are generated with a fixed mass $m_H = 126$ GeV and for μ taking values in the range [0.5,2.5] with a step of 0.5. In Figure 8.8(b), the correlation between the statistical uncertainty on the mass measurement and the measured signal strength for the different μ hypotheses is shown. The mean values of the distributions of δm_H and $\hat{\mu}$ obtained with all the pseudo-experiments are shown. The dependence observed between the two quantities is the same regardless the true value of μ. This dependence is as expected, δm_H decreases when μ increases.

[2] Calculated from the usual formula for the statistic uncertainty on an efficiency ϵ for N events : $\frac{\delta\epsilon}{N} = \sqrt{\frac{\epsilon(1-\epsilon)}{N}}$ [279].

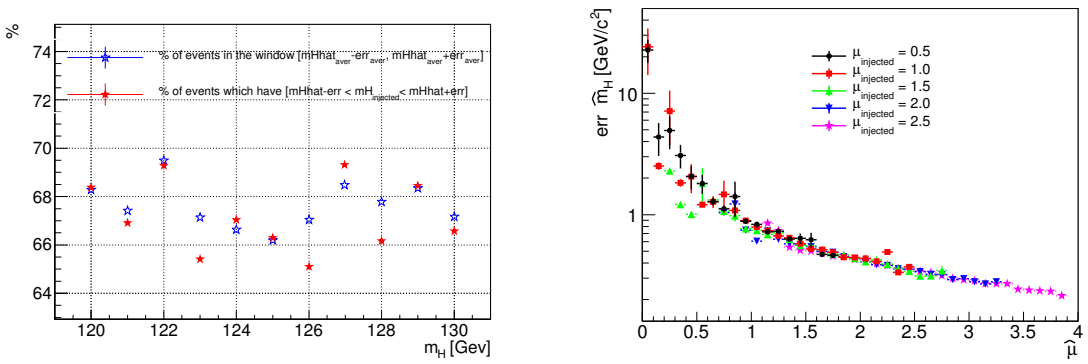

(a) (b)

Figure 8.8: (a) Fraction of pseudo-experiments resulting in measured masses within one standard deviation from the average measured mass (blue) or the injected mass (red). (b) Measured uncertainty on the Higgs boson mass in pseudo-experiments as a function of the measured signal strength μ for different injected values of μ.

8.3.3.3 Dependence of the coverage on μ

While keeping the coverage constant, having an higher value of μ leads to a more accurate measurement of the mass. The distribution of the measured mass becomes then narrower while increasing μ. The coverage as a function of the signal strength is checked using the second definition given in Section 8.3.3.1. For this study, 60000 pseudo-experiments with a mass of 126 GeV and signal strengths of 1 and 1.8 are generated, using the full 2011 dataset and a subset of the 2012 dataset corresponding to 13 fb^{-1}.

For the injected value $\mu = 1$, Figure 8.9(a) shows the integrated coverage as a function of the mean value of the measured μ. The coverage is about 59% for $\hat{\mu} = \mu_{injected} = 1$, which is well under the expected coverage of 68% for Gaussian distributions. The coverage decreases even more when going to higher values of $\hat{\mu}$. Integrating over all $\hat{\mu} > 0$ leads to a global coverage of $63 \pm 0.2\%$.

An under-coverage is then observed for $\mu = 1$, which increases with $\hat{\mu}/\mu_{injected}$, that can be understood as the breaking of the Gaussian feature when large background fluctuations arise and bias the measurement of the strength parameter. In this case, the statistical uncertainty on the mass is artificially reduced, while the distribution does not become narrower. The coverage becomes then insufficient.

The same study is done in bins of $\hat{\mu}/\mu_{injected}$ of size 0.1, and for the two values of the strength parameter $\mu = 1$ and $\mu = 1.8$. Figure 8.9(b) illustrates this test. The correlation emphasized above is again observed and an under-coverage at $\hat{\mu}/\mu_{injected} = 1$ is also noticed for both values of μ, and is worse for the lowest one (64.1 ± 0.4 % and 66.0 ± 0.4 % respectively for $\mu = 1$ and $\mu = 1.8$). Repeating the same study with other values of μ, this appears to be a global feature: the coverage becomes closer to 68% at $\hat{\mu}/\mu_{injected} = 1$ when increasing μ.

Assuming the Standard Model, and given the value of the strength parameter measured in the analysis $\hat{\mu} \sim 1.6$, the coverage is found to be only $\sim 55 \pm 1$ %. Assuming instead a value of the strength parameter similar to the one observed, one finds a coverage of about $\sim 66 \pm 1$ %

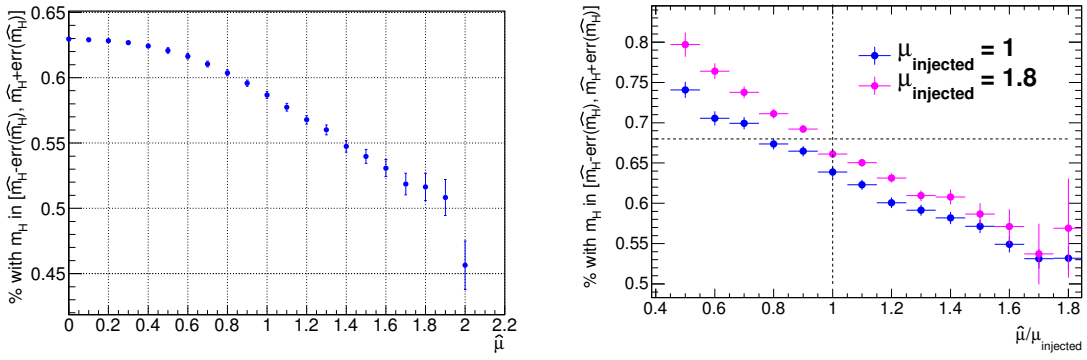

(a) (b)

Figure 8.9: (a) Integrated coverage as a function of the mean value of the measured μ for pseudo-experiments with $\mu = 1$. (b) Coverage as a function of bins of the mean value of the measured μ for pseudo-experiments with $\mu = 1$ (blue line) and $\mu = 1.8$ (pink line). The horizontal dashed line corresponds to the coverage of 68%.

8.3.3.4 Calibration of the statistical uncertainty

The coverage observed is far from that expected for a Gaussian error, and has to be corrected, by inflating the statistical uncertainty.

A Gaussian function is assumed, with width σ. The integral of the Gaussian function in the window $[-\sigma, +\sigma]$ should give 68% of the full integral. In other words, using the Inverse Erf function [3], one gets $\frac{1}{\sqrt{2}} \times \frac{1}{Erf^{-1}(68\%)} = 1\ \sigma$.

The statistical uncertainty for the mass measurement is assumed to be distributed in such a Gaussian function, and the value of σ' that gives the coverages measured previously is calculated using the Inverse Erf function, replacing the value 68% by the coverage really observed. This leads for example to the modified widths $\sigma' = 1.32\ \sigma$ and $\sigma' = 1.05\ \sigma$ for the coverage of 55% and 66% respectively.

Assuming the Standard Model, and Gaussian statistical uncertainties, the width of this Gaussian function should then be inflated by around 1.32 to give the correct coverage of 68%, implying also that the statistical uncertainty on the mass measurement should be inflated by the same amount. If instead a Higgs-like boson with a cross section times branching ratio similar to the observed one is assumed, then the inflation factor would be much smaller, around 1.05. Figure 8.10(a) shows the correction factor on the statistical uncertainty as a function of the ratio $\hat{\mu}/\mu_{injected}$ and for the two different hypotheses of μ.

These factors are used to correct the statistical uncertainty of the mass. The study presented in Section 8.3.3.2 and whose result is illustrated in Figure 8.8(b) is performed again, for the two different μ. The statistical uncertainty on the mass with and without the correction are compared in Figure 8.10(b).

Before the correction, the trend noticed in Figure 8.8(b) is seen again. More precisely, the uncertainty on the mass behaves as a $1/\mu$ function. After the correction, the correlation between the uncertainty and μ is a bit flatter, and the curves for the different hypotheses of μ are not anymore overlaid. This new trend behaves more like a $1/\sqrt{\mu}$ function.

[3] The function $Erf(z)$ gives the normal probability for an event to be included in the window $[-z,+z]$.

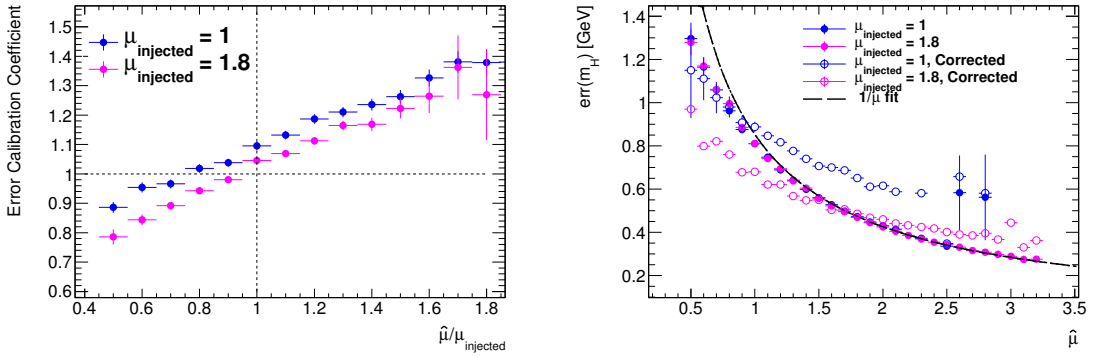

(a) (b)

Figure 8.10: (a) Correction factor for the statistical uncertainty due to an under-coverage as a function of the ratio $\hat{\mu}/\mu_{injected}$ for two different injected signal strength: $\mu = 1$ (blue) and $\mu = 1.8$ (pink). (b) Statistical uncertainty on the mass measurement as a function of the measured signal strength for two different injected signal strength: $\mu = 1$ (blue) and $\mu = 1.8$ (pink); before (full circles) and after (empty circles) the correction of the statistical uncertainty.

8.3.3.5 Checks of the error calibration chain

A Neyman construction [280] is made in order to check the full calibration chain of the statistical uncertainty obtained with the standard fitting procedure.

This frequentist method allows to construct an interval of confidence level $\alpha\%$, such that the probability this interval contains the true value of the measured quantity is precisely $\alpha\%$. This corresponds then to the coverage probability defined previously.

The construction is made using pseudo-experiments generated with $\mu = 1$ and $m_H = 125, 126, 127, 128$ GeV. They are then fitted with the standard procedure to obtain the values of $\hat{\mu}$ and $\hat{m}_H$. Figure 8.11 shows such a construction. The best fitted signal strength is selected in the range $1.1 < \hat{\mu} < 1.3$.

The uncertainty on the mass δm_H derived from this method and indicated with a red arrow in this figure, amounts to around 800 MeV. From Figure 8.10(b), one can note that the statistical uncertainty on the mass for $\mu = 1$ and $\hat{\mu} \sim 1.2$, before correction, was around 680 MeV whereas it was 800 MeV after correction. The Neyman construction gives then directly the corrected statistical uncertainty on the mass.

The check has been repeated with various ranges for the $\hat{m_H}$ and the resulting uncertainty on the mass always corresponds to the corrected one in Figure 8.10(b). The Neyman construction gives then an unbiased measurement of the statistical measurement, assuming Gaussian errors. It validates also the calibration of the uncertainty carried previously.

8.4 Checks on the diphoton invariant mass

8.4.1 Electronic calibration: LAr cell miscalibration

For the cells in the electromagnetic calorimeter, the transition between the medium and high gain occurs for cluster transverse energy of around 60 GeV. The proportion of cells with a medium gain in the $H \to \gamma\gamma$ channel is then expected to be higher than in the $Z \to ee$ one. In case of mis-calibration of the medium and/or high gain cells, the inter-calibration coefficients would correct for such effect. But as they are performed with the $Z \to ee$ channel and given the

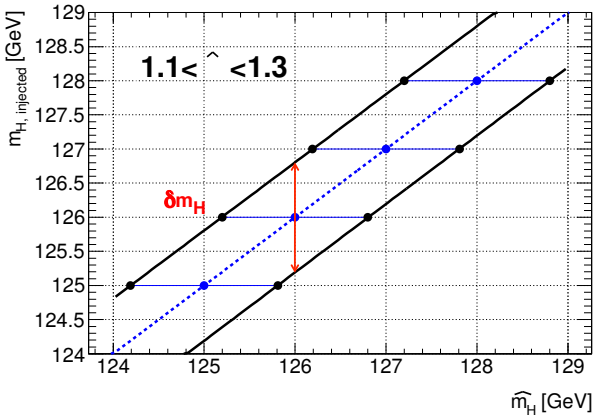

Figure 8.11: Neyman construction for the statistical uncertainty on the mass measurement with pseudo-experiments for $\mu = 1$ and $m_H = 125, 126, 127, 128$ GeV. The result of the fit for a given mass is depicted by the blue dots and the dashed blue line corresponds to the linear fit of these points. The blue horizontal lines corresponds to the interval around the averaged $\hat{m_H}$ that contains 68% of the distribution of $\hat{m_H}$. The uncertainty on the mass δm_H is indicated with a red arrow.

different proportion of high/medium gain cells, the effect would be not completely corrected by the in-situ calibration.
For a $Z \to ee$ sample, the lineshape for the events having all their cells in high gain and the events having at least one cell in the medium gain are compared. A distortion is observed between the two lineshapes due to the implicit higher kinetic selection in the second case. When comparing the peak positions between high and medium gains for data and MC samples a difference of 0.2% is identified and assumed to fully come from the LAr cell mis-calibration.

As around 2/3 of the cells in the $H \to \gamma\gamma$ channel are in the medium gain, and assuming that all the cells in the $Z \to ee$ channel are in the high gain, the final uncertainty due to cell gain difference of calibration is simply assumed to be 0.15% ($2/3 \times 0.2\%$) on the diphoton invariant mass. This number is taken as an uncertainty on the peak position.

8.4.2 Calibration of converted photons

A further energy calibration for converted photons is applied in the analysis, both in data and in the simulation, depending on the conversion radius (see Section 7.2). The impact of this additional calibration on the diphoton invariant mass is investigated.

Using simulation samples of the $H \to \gamma\gamma$ process, for a mass of 125 GeV, the peaks of the diphoton invariant mass with and without this dedicated correction are extracted from the signal model fit. The fitted values are compared, for each category of the analysis. The main difference arises in the transition region. This is expected as this is where the amount of material is largest and the conversion rate is highest. A weighted average is made of the differences observed in each category, giving a value of 70 MeV.

A similar test is performed on the data with the diphoton events selected as described in Chapter 7. The additional correction for converted photons is not applied in the data, keeping only the standard calibration described in Chapter 5. The excess in the data is fitted with a

signal model where this correction is applied. The value extracted from this test differs from the nominal result by about 70 MeV (correction applied both in data and MC). This effect, representing the full effect of the correction, is quite small and neglected in the following.

8.4.3 Conversion fraction

The MC-based calibration of the electromagnetic particles is done independently for electrons, converted photons and unconverted photons (see Chapter 5). Reconstructing an unconverted photon as a converted one would give a biased energy. The energy would be over-estimated as bigger corrections for energy loss in dead material would be applied. Unconverted photons can be wrongly reconstructed as converted when for example a random track matches by chance a photon cluster in the electromagnetic calorimeter.

The conversion fraction in the MC and in the data have been compared, as a function of p_T and η. The agreement depends on these two quantities, and is worst for $\eta > 2.3$ and for $p_T < 40$ GeV (discrepancy of about 10%) In this region, an unconverted photon mistakenly reconstructed as a converted one would have its energy biased by about 2.5%. Then an upper bound has been put on the effect on the mass value

$$\frac{\delta m}{m} \sim \frac{1}{2} \cdot \frac{\delta E_1}{E_1} \cdot \frac{\delta E_2}{E_2},$$

giving then:

$$\delta m \sim 126.6 \times 0.5 \times 0.1 \times 0.025\ GeV = 0.16\ \text{ GeV}.$$

This study can be refined to take into account the proportion of events in the problematic regions. For the moment a systematic uncertainty of 0.16 GeV is used.

8.4.4 Presampler scale

The uncertainty on the presampler energy scale was estimated in 2010 to be around 5% in the barrel and 10% in the endcaps, from the data to MC ratio of the presampler energy for electrons coming from the $Z \to ee$ decay. These numbers are propagated to an uncertainty on the peak position in the $H \to \gamma\gamma$ channel (see Chapter 7). In reality, a direct measurement of the presampler energy scale presented in Chapter 5 has shown that the discrepancy between the data and the MC is rather 15% in the endcap region.

This discrepancy is on average corrected with the *in situ* calibration presented in Chapter 5, which is obtained for electrons with $p_T = 40$ GeV, average p_T of the electrons coming from the Z decay. The bias induced by the fact that photons with different p_T are used is evaluated, using a $H \to \gamma\gamma$ simulation at 125 GeV. With respect to the bias induced with the 10% uncertainty on the presampler scale, a difference of 0.05% is found, which is taken as an uncertainty coming from the presampler scale uncertainty.

8.4.5 Relative calibration of layer 1 and 2

The relative calibration of the layer 1 and 2 has been shown to be different from what is expected in MC simulation in Chapter 5. This difference averages -3% in the barrel and +5% in the endcap.

As in the case of the presampler scale, such difference is corrected on average with the in-situ calibration which is obtained for electrons at 40 GeV. The bias induced by the fact that photons with different p_T are used is evaluated, using a $H \to \gamma\gamma$ simulation at 125 GeV.

This bias on the diphoton invariant mass for each η-dependent category is shown in Table 8.1. The peak position in each category is estimated with a Crystal Ball fit. The effects in the various categories are weighted by the corresponding relative significances, that are given in the last column of the table. The final global effect on the mass amounts to 0.2% using these weights.

Table 8.1: Biases on the diphoton invariant mass due to a bias of -3% ($+5\%$) in the barrel (endcap) for the nine η-dependent categories and the associated significances

Category	$\delta m_{\gamma\gamma,CB}$ [%]	Significance [$\log(1+S/B)$]
Inclusive	0.12	
1	0.31	0.05
2	0.36	0.15
3	0.09	0.02
4	0.11	0.06
5	0.15	0.04
6	0.20	0.15
7	0.04	0.02
8	0.07	0.05
9	-0.02	0.01

8.4.6 Angle reconstruction

A check of the impact of the primary vertex (PV) reconstruction on the peak position is made by quantifying the variations of the $H \to \gamma\gamma$ peak in MC samples and of the $Z \to ee$ peak in MC and data samples for different choices of the PV:

- (0,0,0) : the primary vertex is considered to be at the centre of the detector.
- Track: the direction of the electrons tracks from $Z \to ee$ events is used to reconstruct the η direction and then the primary vertex.
- Pointing: the direction of the electrons is reconstructed thanks to the longitudinal segmentation of the calorimeter (position of the cluster in the first and second layer of the calorimeter).
- PV0: the primary vertex having the highest sum of p_T^2 is selected.
- MLP: MVA method which uses only cluster information. This method takes as input the pointing, the sum of p_T^2, the sum of p_T and the $\Delta\phi$ between the diphoton system and the vertex direction.

Test on $H \to \gamma\gamma$ MC samples The $H \to \gamma\gamma$ invariant mass in MC samples is computed following the formula given in Equation 7.1, using the different methods described previously for the reconstruction of the primary vertex. The resulting invariant masses are all compatible, although the resolution deteriorates when going from the MVA method to the simple pointing for example.

Test on $Z \to ee$ MC and data samples To test the impact of the PV reconstruction in the data, $Z \to ee$ events are used. As above, the Z invariant mass is computed using the different PV reconstruction methods, both in data and MC. As expected from the previous check, the invariant masses are all compatible in the MC. However, small deviations are observed between data and MC for the different methods, as seen in Table 8.2 which gives the ratios between the peaks positions in data and MC. The maximal deviation, amounting to 0.03% (translating into 40 MeV uncertainty for a Higgs boson mass of 126 GeV), is taken as an uncertainty coming from the reconstruction of the primary vertex.

Table 8.2: Data to MC ratio of the $Z \to ee$ invariant mass for various PV reconstruction methods.

	Tracks	MLP	PV0	Pointing	(0,0,0)
m_{data}/m_{MC}	1.0054	1.0054	1.0052	1.0055	1.0055

Test on pseudo-experiments A test is performed on pseudo-experiments in order to decorrelate systematic and statistical effects when measuring the mass of the resonance with different choices of the primary vertex. Using pseudo-experiments simulating the background and signal distributions in the $H \to \gamma\gamma$ channel allows to get rid of the systematic effects. The number of signal and background events are drawn at random in a Poisson distribution around the number expected from the statistical model. Many pseudo-experiments are run, and the mass is fitted with two definitions of the PV in each of these experiments, and the distribution of the mass difference for these two definitions is built. Two different comparisons are done: between the nominal and the pointing PV choices, and between the nominal and the (0,0,0) PV choices. In the two cases, the distribution of the mass difference is centred around 0, demonstrating that the choice of the primary vertex does not bias the mass measurement. However the statistical uncertainties derived from the width of the mass difference distributions are very different: 400 and 700 MeV respectively for the first and second case. In the first case, the statistical uncertainty is similar to the one expected for a mass measurement with the number of events used. In the second one, the choice of the (0,0,0) largely broadens the invariant mass distribution. The result is a statistical uncertainty with is much larger, coming from background fluctuations under the signal peak.

8.5 Consistency checks for the mass measurement

8.5.1 Influence of the Background Models and Fit Ranges

8.5.1.1 Influence of the Background Model choice

The background model was described in Section 7.6.3. The model chosen is such that it minimizes the number of signal extracted from a signal plus background fit on MC samples. The parameters of the models are directly fitted in the data.

The influence of a particular background model choice on the value of the fitted mass both on the data and on pseudo-experiments, and both in inclusive and categorized analysis is tested. This is performed by changing the model and comparing the resulting mass with the one obtained with the nominal function.

The models tested for the inclusive analysis are:

I1) A 3th order Bernstein polynomial instead of the nominal 4th order,

I2) A simple exponential instead of the nominal 4th order Bernstein.

And for the categorized analysis:

C1) Replace the usual functions used for the different categories by *less* flexible functions: the quadratic exponential used in categories 1,5,9 and the 4th order Bernstein used in categories 3,7 are replaced by a 2nd order Bernstein,

C2) Replace the usual functions used for the different categories by *more* flexible functions: the quadratic exponential used in categories 1,5,9 and the 4th order Bernstein used in categories 3,7 are replaced by a 5th order Bernstein,

C3) The nominal functions are used but the signal region $115 < m_{\gamma\gamma} < 130$ GeV is excluded.

The mass of the resonance observed in data is fitted with the combined signal+background fit, with the background modified as explained before. Modifying this model leads to shifts in the measured mass that are reported in Table 8.3.

Table 8.3: Shifts of the mass fitted on the data with the different background models, with respect to the nominal model.

Model	Shift (MeV)
I1	+10
I2	-10
C1	+30
C2	-100
C3	-6

No large bias is observed in data (the largest is of the order of 100 MeV which is below the statistical uncertainty). No additional systematic is then taken from this test.

The data are not free from fluctuations in the whole mass range, and the results found previously could be sensitive to a particular configuration of the invariant mass distribution for a given dataset.

A similar study has been repeated using pseudo-experiments. Background events are drawn at random around one of the models described previously and fitted with the nominal function, to mimic what happens when data are fitted.

No shift of the mass larger than 100 MeV for any of the models is found, confirming the insensitivity of the mass measurement with respect to the background model. However, an uncertainty of 0.1%, corresponding to the maximal deviation observed in these pseudo-experiment studies, is conservatively added.

8.5.1.2 Dependence to the fit range

The impact of the fit range on the peak position is also tested using the 2012 dataset, and the inclusive analysis. The nominal range for fitting the signal is $100 < m_H < 160$ GeV. In this test, two different reduced fit ranges are tested:

- $110 < m_H < 150$ GeV
- $115 < m_H < 135$ GeV

To improve the fit stability, the strength parameter μ is constrained to positive values.

The observed values in the two reduced fit ranges and in the nominal case are the following ones:

- $[100, 160]$ GeV : $m_H = 126.68 \pm 0.66$ GeV
- $[110, 150]$ GeV : $m_H = 126.62 \pm 0.58$ GeV
- $[115, 135]$ GeV : $m_H = 126.59 \pm 0.68$ GeV

Reducing the fit range leads to a variation of the peak position which decreases by 90 MeV at most. This can be explained by statistic fluctuations in the background parametrization. However, this variation is small enough to be neglected.

8.5.2 Signal model choice

In the current analysis a unique signal parametrization is used for all production processes. The impact of this choice is studied, comparing the shapes and peak positions of the Higgs boson signal in MC at the mass $m_H = 125$ GeV, for different processes. This is performed by merging the categories of the analysis into the four following ones: low p_{Tt} Higgs boson, high p_{Tt} Higgs boson, central photons and non-central photons. The invariant mass distributions for the main gluon fusion process and for the other ones have quite different shapes coming mainly from kinetic arguments (the processes other than ggH have a higher Higgs boson p_T which improves the resolution a little). From Table 8.4 one can notice that the peak positions between the vector boson fusion (VBF) and ggH are in good agreement. For the other processes, there are larger differences ($\sim$ 100-200 MeV). These sizeable differences do not contribute a lot in the total mass measurement, because of the low fraction of these events in the data.

Table 8.4: Peak position in GeV of a MC Higgs boson signal at 125 GeV, for different production processes.

Process	ggH	VBF	ttH	WH	ZH
Central categories	124.66±0.02	124.65±0.02	124.85±0.06	124.79±0.05	124.80±0.06
Not central categories	124.63±0.03	124.65±0.02	124.63±0.11	124.81±0.08	124.67±0.09
Low $p_{T,t}$ categories	124.61±0.03	124.66±0.02	124.67±0.09	124.72±0.07	124.75±0.07
High $p_{T,t}$ categories	124.66±0.03	124.62±0.03	124.86±0.06	124.85±0.06	124.81±0.06

8.5.3 Categorized vs. inclusive analysis

The introduction of analysis categories improves the signal significance in the presence of a SM Higgs boson due to the differences in the expected signal-to-background ratios (S/B) and the mass resolution between the categories. This argument also translates to the mass measurement. The mass determination in the inclusive dataset, i.e. without categories, is expected to yield a consistent central value but larger uncertainties. However the categorization could also cause a bias in the mass measurement. This should be verified in case the photon energy scale, S/B or the mass resolution are not correctly estimated.

Performing the mass measurement in the inclusive analysis and categorized analysis, one obtains consistent central values, as expected. The total uncertainty on this measurement is however 15 to 25 % smaller for the categorized analysis compared to the inclusive one.

8.5.4 Consistency checks inside the categories of the analysis

Using the various categories, consistency checks can be performed. One can test the dependence of the mass value with respect to:

- The conversion status of the photons by comparing categories with both unconverted photons, UC, (1,2,3,4) vs categories where at least one photon is converted, CV, (5,6,7,8,9). The numbering corresponds to the one defined in Section 7.3.
- The detector region comparing categories where both photons are in the central part of the detector ($\eta < 0.8$, categories 1, 2, 5, 6) vs categories where at least one photon is not in the central part (3,4,7,8,9)
- The Higgs boson p_{Tt} comparing categories where the diphoton system has a low p_{Tt} (< 60 GeV, categories 1,3,5,7) versus categories with high p_{Tt} (> 60 GeV, categories 2,4,6,8).
- The production process comparing VBF-tagged categories (2 jets high-mass, categories 10 and 11) versus the other categories (1 to 9 and 12, 13, 14). The VH-tagged categories can not be tested alone due to the small signal.

The results of the mass measurement for these four specific comparisons are found in Table 8.5 and the corresponding likelihood ratios in Figure 8.12. The profiled values of the signal strength and of the nuisance parameter related to the resolution, θ are also given with their uncertainty obtained with the MINUIT processor MINOS [281]. The value of θ gives an idea of how much deviates the fitted resolution with respect to the nominal one. It can be seen as the number of standard deviations with respect to the nominal value (this can be approximated: $\sigma_{\mathrm{fitted}} = \sigma_{\mathrm{nom}}(1 + \delta\theta)$, with δ the systematic uncertainty on the resolution).

Table 8.5: Best fitted values of mass m_H, strength parameter μ and nuisance parameter related to the resolution θ for the different categories.

Categories	m_H (GeV)	μ	θ
VBF categories	125.57 ± 0.54 (stat) ± 0.72 (syst)	2.06 ± 0.69	-0.31 ± 0.87
ggH + VH categories	127.15 ± 0.25 (stat) ± 0.69 (syst)	1.64 ± 0.34	-1.01 ± 0.71
UC categories	127.03 ± 0.36 (stat) ± 0.81 (syst)	1.66 ± 0.44	-0.76 ± 0.89
CV categories	126.89 ± 0.47 (stat) ± 0.67 (syst)	1.75 ± 0.53	-0.56 ± 0.86
Central categories	127.19 ± 0.54 (stat) ± 0.63 (syst)	1.12 ± 0.43	-0.48 ± 0.9
Forward categories	126.35 ± 0.32 (stat) ± 0.84 (syst)	2.32 ± 0.52	-0.60 ± 0.76
Low p_{Tt} categories	127.29 ± 0.37 (stat) ± 0.69 (syst)	1.76 ± 0.43	-0.42 ± 0.97
High p_{Tt} categories	$126.29^{+0.52}_{-0.94}$ (stat) $^{+0.80}_{-1.29}$ (syst)	$1.69^{+0.63}_{-0.55}$	-0.49 ± 1.12

A 1 σ tension is observed between VBF and other production process categories (the VBF-tagged categories have on average a lower mass). A tension of the same size is also observed between low and high p_{Tt} categories (the high p_{Tt} categories have on average a lower mass value). These two tensions are probably correlated as the high p_{Tt} regime tends to select more VBF events (see Figure 7.5). For all the other categories, a good compatibility of the mass measurement is observed, suggesting a good understanding of the detector energy response and the photon energy calibration. As expected, the categories having both photons in the central part of the detector or at least one converted photon get the smallest systematic uncertainties.

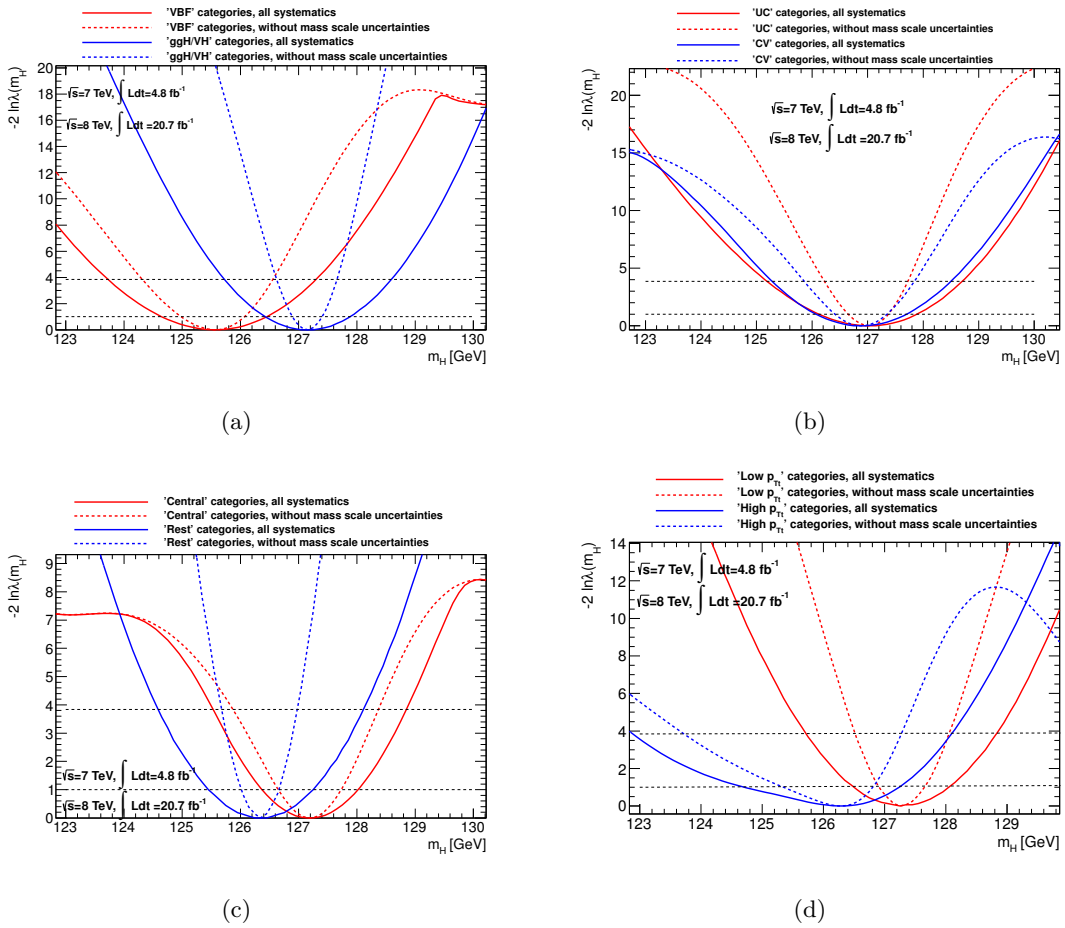

Figure 8.12: Evolution of the likelihood $-2\ln\lambda$ for ggH/VH (blue) vs VBF (red) tagged categories (a), Converted (blue) vs Unconverted (red) tagged categories (b), Central (red) vs Rest (blue) tagged categories (c), and Low (red) vs High (blue) p_{Tt} tagged categories (d), as a function of the Higgs boson mass hypothesis. The dashed lines show the likelihood ratio when the systematic uncertainties related to the peak position are fixed to their profiled value.

One can notice that the nuisance parameter related to the mass resolution is more pulled in the ggH/VH-tagged categories than in the VBF ones, more in the unconverted than converted categories, and more in the forward than central categories.

8.5.5 Excluding events around the transition region

The category with the worst sensitivity and mass resolution is the one where at least one photon is converted and close to the barrel-endcap transition ($1.3 < |\eta| < 1.75$, excluding the region $1.37 < |\eta| < 1.55$, category C9, see Section 7.3). The energy measurement in this region is affected by the large amount of material in front of the calorimeter which is rapidly varying as a function of η and could then be largely biased.

A check is performed removing this category from the measurement. No significant difference is observed with respect to the nominal case where these events are included. This is expected as this category is also the one that has the smallest weight in the combination of the different

categories, due to its poor mass resolution.

8.5.6 Production process strength parameters

In the statistical model used in the $H \to \gamma\gamma$ analysis, the signal strength of the five main production processes are parametrized with five parameters μ_{X_i} which are all required to be equal to 1

$$\mu_{ggH} = \mu_{ttH} = \mu_{VBF} = \mu_{ZH} = \mu_{WH} = 1.$$

An additional global signal strength μ is used to test the deviation of the number of signal events observed with respect to the one expected from the Standard Model (see Chapter 7).

To test the dependence of the mass measurement to this specific choice, another model is built where the global signal strength is fixed at 1 while the signal strength per production process are free in the likelihood and fitted. To help the fit convergence, a simplification based on physical arguments is introduced. Only two signal strengths are kept, one for the Higgs boson coupling to bosons ($\mu_{bosons} = \mu_{VBF} = \mu_{ZH} = \mu_{WH}$) and one for the coupling to fermions ($\mu_{fermions} = \mu_{ggH} = \mu_{ttH}$)

With this new parametrization, the mass measurement is performed and compared to the nominal measurement. This comparison is shown in Figure 8.13, using the full 2011 dataset and a subset of the 2012 dataset corresponding to 13 fb^{-1}. One can see that modifying the parametrization of the signal strength has no impact on the peak position nor on its width.

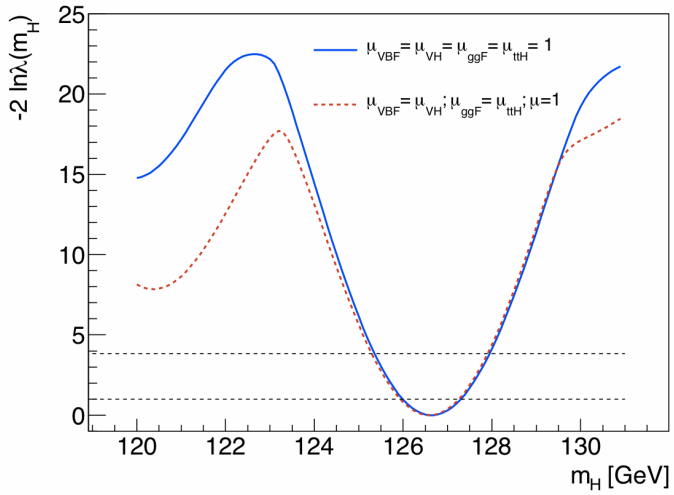

Figure 8.13: Comparison of the likelihood $-2\ln\lambda(\mathrm{m_H})$ for two different models of the signal strength: $\mu_{ggH} = \mu_{ttH} = \mu_{VBF} = \mu_{ZH} = \mu_{WH} = 1$ and the global parameter μ is fitted (blue) and $\mu_{ggH} = \mu_{ttH}$; $\mu_{VBF} = \mu_{ZH} = \mu_{WH}$ are fitted and $\mu = 1$ is fixed (red, dashed line).

8.5.7 Further consistency checks for converted photons

The calibration of the electrons and photons has been described in Chapter 5. At the MC level, three sets of calibration parameters are derived for the electrons and the converted and unconverted photons. In the in-situ calibration, the same corrections are applied to these three types of particles. A small inconsistency in the energy response between the single and double track conversions has been measured in 2012 using radiative $Z \to \mu\mu$ decays [157]. To assess the impact of such a discrepancy in the mass measurement and to test more deeply the validity

of the extrapolation of the electron scale factors to converted or unconverted photons, special categories [4] have been built with the following criteria:

- Both photons are unconverted (UC)
- One photon is unconverted and the other is converted with a single-track (CV 1-track)
- One of the photons is converted with a double-track (CV 2-tracks) and the other is indifferent

Additional categories with two single-track conversions or two double-track conversions were also tried, but they appear to be too poorly populated to be statistically significant.

With these new categories, the full analysis has to be rerun: introduction of new signal and background models specific to the categories, and computation of the systematic uncertainties for each of the categories. In reality, only the uncertainty coming from the photon energy scale are recomputed, because the other systematic have been shown to have a negligible impact on the mass measurement (see Section 8.1).

Figure 8.14 shows the profile likelihood ratio for these three categories in the full mass range and in a smaller region around the signal.

The best fitted mass values inside these three new categories are given below:

- Both photons UC: $m_H = 126.5 \pm 0.5$ (stat) ± 0.7 (syst) GeV
- 1 UC + 1 CV 1-track : $m_H = 127.1 \pm 1.0$ (stat) ± 0.4 (syst) GeV
- 1 CV 2-tracks: $m_H = 127.1 \pm 0.8$ (stat) ± 0.5 (syst) GeV

These mass values are compatible within one standard deviation. The plot in the full mass range allows to see if spurious structures appear outside the signal region. Quite important minima for the two categories with at least one converted photon are present at around 120 GeV (130 GeV) for the 1 CV 2-tracks (1 UC + 1 CV 1-track) category.

This is checked by drawing the variation of the profiled signal strength for these three categories as a function of the tested mass, illustrated in Figure 8.15. The minimum at 120 GeV (130 GeV) in the 1 CV 2-tracks (1 UC + 1 CV 1-track) category is in reality due to a local deficit in the distribution of the diphoton invariant mass, fitted as a signal but with a negative signal strength. On the other hand, the minima found around 126 GeV look more consistent with a real localized excess of events.

The impact of the double-track conversions calibration can also be tested by removing the pathological double-track conversion photons from the selected events. The mass is recomputed without these events and found to be in very good agreement with the nominal value.

8.5.8 Stability with time

In order to test the evolution of the mass with the time three subsets are built and the mass measurement with these data are compared. These datasets correspond to the full 2011 dataset and to the 2012 dataset divided in two smaller sets corresponding to approximately the periods February-June and July-September 2012 with a integrated luminosity of 5.9 fb^{-1} and 7.1 fb^{-1} respectively. These two datasets are called in the next figures "pre-ICHEP" and "post-ICHEP" respectively The results of the mass measurement from these three datasets are shown in Figure 8.16 and given below:

[4] These categories are not used in the analysis, they were specially built for this check.

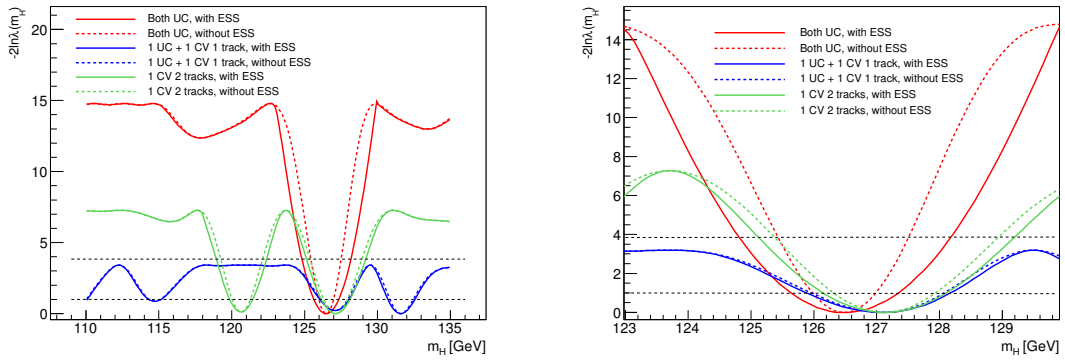

(a) (b)

Figure 8.14: Evolution of the likelihood $-2\ln\lambda$ as a function of the Higgs boson mass m_H in the range [110, 135] GeV (a) and [123, 130] GeV (b), for three different categories: both photons unconverted (red), one photon is unconverted and the other is converted with a single-track (blue) and one of the photons converted with a double-track and the other indifferent (green). The dataset used corresponds to a fraction of the full 2012 dataset. The dashed curves refer to the case where the nuisance parameters related to the energy scale systematics are fixed to their profiled value.

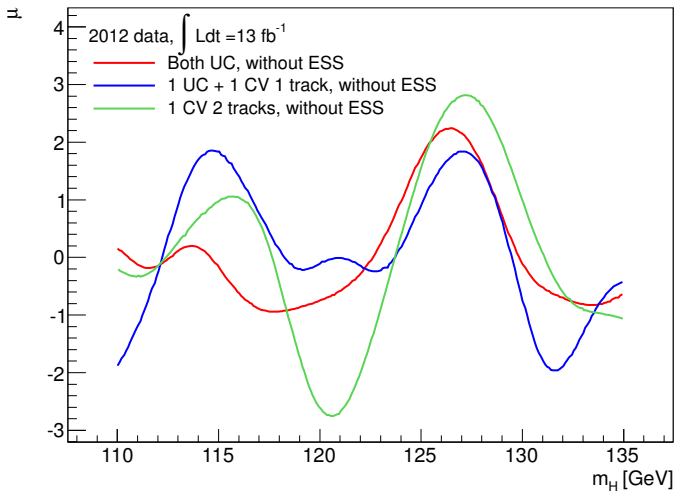

Figure 8.15: Profiled signal strength as a function of the tested mass m_H for three different categories: both photons unconverted (red), one photon is unconverted and the other is converted with a single-track (blue) and one of the photons converted with a double-track and the other indifferent (green). The dataset used corresponds to a fraction of the full 2012 dataset.

- 2011 data: $m_H = 126.24 \pm 0.78$ GeV
- 2012 data, Feb. to June: $m_H = 126.77 \pm 0.80$ GeV
- 2012 data, July to Sep.: $m_H = 126.64 \pm 0.86$ GeV

In Figure 8.16(a), the profile likelihood is shown in the full mass range in order to check the presence of common spurious structures outside the signal regions. No recurrent anomalies can be seen. Figure 8.16(b) shows a closer view of the previous figure, allowing to check that for these three datasets the compatibility of the minima of the profile likelihood is very good, below one standard deviation.

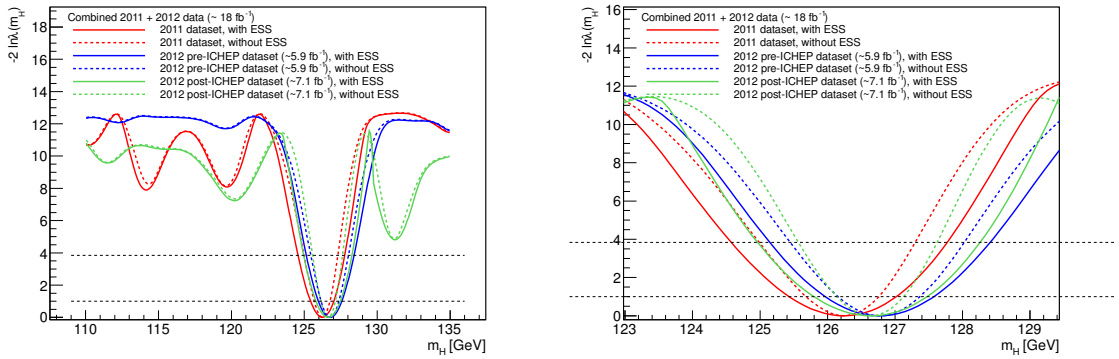

(a) (b)

Figure 8.16: Evolution of the likelihood $-2\ln\lambda$ as a function of the Higgs boson mass m_H in the range [110, 135] GeV (a) and [123, 130] GeV (b), for the three datasets: full 2011 data (red), 2012 data, February to June (blue) and 2012 data, July to September (green). The dashed curves refer to the case where the nuisance parameters related to the energy scale systematics are fixed to their profiled value.

A last check consists of looking at the stability of the signal strength with respect to the time in the signal region. This is shown in Figure 8.17. This plot shows a good stability of this parameter in time, both in location of the signal and in its size. No other structure with higher strength is noticed along the mass range and the time.

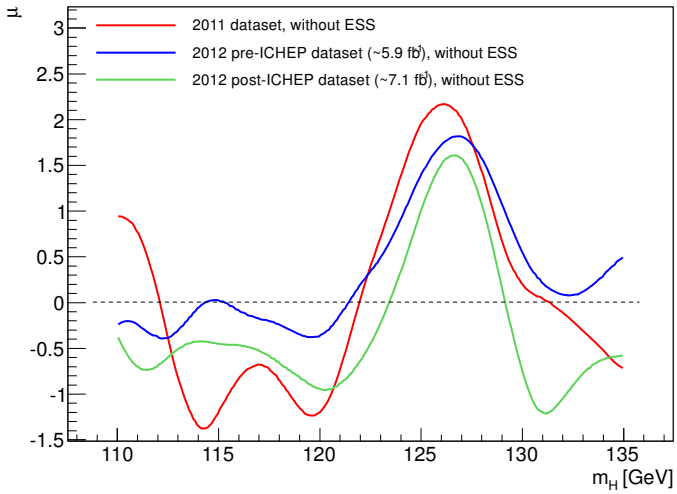

Figure 8.17: Profiled signal strength as a function of the tested mass m_H for three different data periods (see text).

8.5.9 Dependence on the pileup

The pileup effect on the mass measurement has been cross-checked as it is a source of potential bias for the energy scale. For example, it can enhance the wrong matching of a random track to an electromagnetic cluster and lead to a mis-calibration of the unconverted photons as converted ones (see Section 8.4).

Four categories of events, based on the average interactions per bunch crossing μ have been built and the mass was fitted for each of these categories.

No sizeable bias was noticed among the categories within the uncertainties, demonstrating the good stability of the mass measurement with respect to the pileup.

8.5.10 Dependence on the choice of the primary vertex

The impact of the different methods to select the primary vertex on the diphoton invariant mass has been shown in Section 8.4.6. In what follows, the impact of these methods on the resonance mass measurement in data is tested. Three alternative methods are tried, and the comparisons of the resulting mass measurements to the nominal one are given in Table 8.6 (see Section 8.4.6 for the definition of the methods).

Table 8.6: Best fitted values of the mass for different PV reconstruction methods.

	Nominal	Pointing	PV0	(0,0,0)
m_H (GeV)	126.7 ± 0.7	126.6 ± 0.7	126.5 ± 0.8	125.8 ± 0.7

Except for the (0,0,0) method, the mass value is rather stable with respect to the choice of primary vertex. A shift of the order of 200 MeV is observed for the PV0 method, but this shift is within the statistical uncertainty. The large shift of around -900 MeV observed in the (0,0,0) method is rather compatible with the statistical uncertainty of 700 MeV expected for such choice (see Section 8.4.6). The distribution of the diphoton invariant mass and the associated signal+background fit for the nominal and (0,0,0) case are shown in Figure 8.18. The diphoton candidates are clearly redistributed with this last choice, modifying the shape and position of the peak around 126 GeV. This explains the large shift measured for the mass. Taking the centre of the detector as the primary vertex is a rather extreme choice and the rather large bias that this induces is not so large as to imply a problem.

8.5.11 Dependence on the $\cos(\theta^*)$ angle

In Section 7.4.3, an interference effect between the continuum background $gg \to \gamma\gamma$ and the resonance $gg \to H \to \gamma\gamma$ has been highlighted. This interference is destructive so that the signal yield is reduced by 3% in average. In addition a shift of the peak of the resonance due to this interference was reported as being expected by different authors [250, 255]. The size of the shift depends on the Higgs boson width and is predicted to be around 100-200 MeV for the Standard Model Higgs boson at around 126 GeV.

A test of a possible shift of the peak due to this interference is described here. The interference is mainly sensitive to the angle between one of the photons and the proton-proton beam-axis in the Higgs boson Center of Mass frame, θ^*, in the Collins-Spoper frame. More precisely, at LO, the strength of the interference increases when $|\cos(\theta^*)|$ approaches 1. Above $|\cos(\theta^*)| = 0.7$, the NLO terms have also to be taken into account. This can also be translated into a dependence

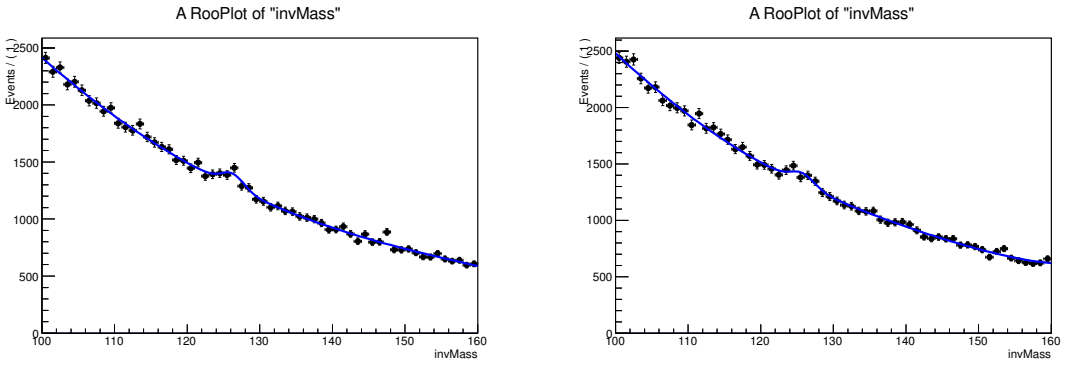

(a) Nominal PV

(b) (0,0,0) PV

Figure 8.18: Distribution of the diphoton invariant mass of the events selected in a subset of the 2012 data for two different choices of the primary vertex: the nominal primary vertex (a) and the centre of the detector (0,0,0) (b). The blue line corresponds to the signal+background fit of the mass distribution.

on the photon pseudorapidity as seen in Section 7.4.3: in the central region, the interference is expected to be smaller than in more forward regions. This study can be then compared to the one presented in Section 8.5.4.

The dependence of the fitted mass value with respect to different values of this angle is tested. Four categories (C1 to C4) are made on the basis of the value of $\cos(\theta^*)$: [-1, -0.5, 0, 0.5, 1].

The two categories C1 and C4 are the ones expected to be the most sensitive to the interference and then to an hypothetical shift of the peak whereas C2 and C3 are control categories.

The fitted mass values found for the four categories are the following ones:

- C1: $m_H = 126.5 \pm 1.5$ GeV
- C2: $m_H = 126.5 \pm 0.8$ GeV
- C3: $m_H = 126.9 \pm 1.1$ GeV
- C4: $m_H = 127.0 \pm 0.9$ GeV

The distribution of the diphoton invariant mass in the window 100-160 GeV and the signal+background fit are shown in Figure 8.19 for the four categories. There is no obvious dependency of the mass value with $\cos(\theta^*)$ and no obvious difference between the categories C1, C4 and C2, C3. The positive $\cos(\theta^*)$ have slightly larger values of the mass, by around 400-500 MeV. This difference is not significant given the large uncertainties on the mass values.

With the data accumulated in 2011 and 2012 and due to the large uncertainties on the photon energy scale, it seems impossible to see a bias in the peak position as expected from the interference effect. This test may be repeated with a larger sample of data, when the uncertainty on the mass measurement will be significantly reduced.

An independent cross-check has however been performed with more categories of $\cos(\theta^*)$: $[-1, -0.85, -0.7, -0.4, -0.1, 0.2, 0.5, 0.8, 1]$. This study also showed a stability of the mass measurement with the angle, within the uncertainties [185].

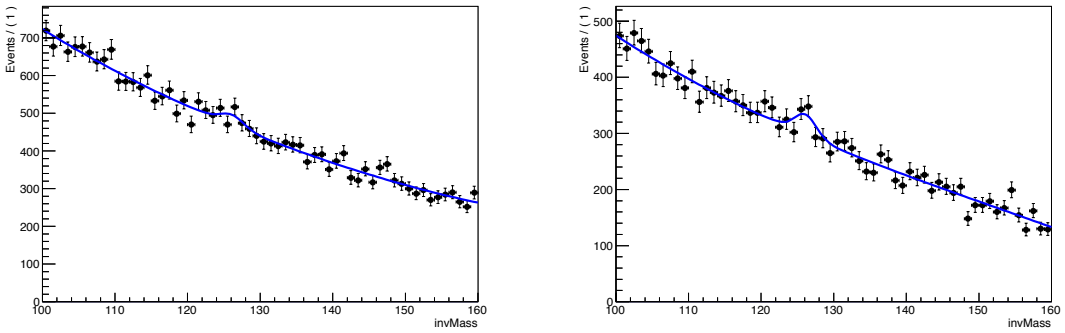

(a) $-1 < \cos(\theta^*) < -0.5$

(b) $-0.5 < \cos(\theta^*) < 0$

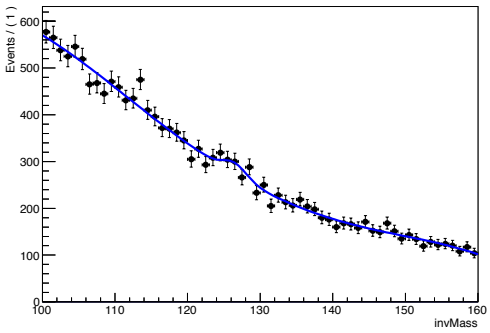

(c) $0 < \cos(\theta^*) < 0.5$

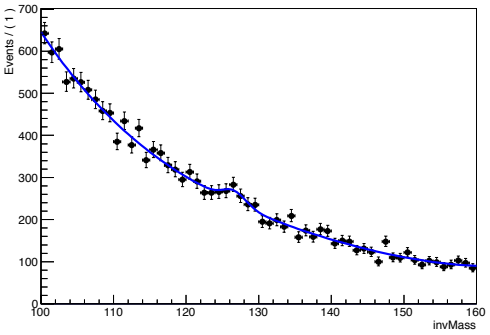

(d) $0.5 < \cos(\theta^*) < 1$

Figure 8.19: diphoton invariant mass distribution for the events selected in the analysis and categorized in bins of $\cos(\theta^*)$.

8.6 Signal resolution effects

The excess observed in the diphoton invariant mass is fitted with a signal model where the resolution is fixed (see Section 7.5). In this model, the resolution comes from the Crystal Ball width and it is fixed to the values fitted in the MC simulating the $H \to \gamma\gamma$ process. In this MC a smearing correction to the photon energy is applied. This smearing correction comes from the comparison of the $Z \to ee$ invariant mass resolution in data and MC samples (see Section 5.3.6). The different constant terms between data and MC arises from various effects: material mis-modeling, multiple scattering modeling, lateral leakage, non-uniformities of the energy response or layer mis-calibration for example. Applying the smearing correction extracted from $Z \to ee$ to photons from the Higgs boson decay could lead to a bias in the $H \to \gamma\gamma$ invariant mass resolution. Indeed, the electron multiple scattering modeling for example which is at the origin of an increase of the constant term in 2012 (see Chapter 5), should not increase the resolution of the photon energy. Another example is the material mis-modeling which is expected to have a larger effect on the electron than photon resolution.

8.6.1 Impact on the peak position

The impact on the peak position of fitting with a different resolution that the nominal one is tested. The study is done with the full 2011+2012 dataset and with the analysis presented in the previous chapter.

The width of the Crystal Ball is modified and takes its values in the range $[0.8, 1.2]$ times the nominal resolution with steps of 0.05 or 0.1 depending on the study. The signal observed in data is fitted with a signal model where the resolution changes as described above, and the resulting mass measurement is compared to the nominal case.

The result is shown in Figure 8.20(a). The best fitted value of the mass, $\hat{m_H}$, in data is quite stable when the resolution with which the peak is fitted varies. The error bars shown in this figure corresponds to the total systematic uncertainty on the mass measurement. These uncertainties are correlated between the different points of the figure.

This feature is not stable with respect to the time: taking a subset of the 2012 dataset with 13 fb^{-1}, a different result is found, as illustrated in Figure 8.20(b). The best fitted value of the mass, $\hat{m_H}$, as well as its uncertainty in data increase with the resolution with which the peak is fitted. For 40 % increasing of the resolution, the best mass value and its uncertainty increase by about 0.5 % and 28 % respectively.

The uncertainty on the resolution is about $\pm 20\%$ (see Chapter 7), leading to an uncertainty on the peak position of $\sim \pm 200$ MeV $\sim 0.15\%$. A 0.15% systematic uncertainty on the peak position from the uncertainty on the resolution was initially taken as an additional uncertainty for the mass measurement.

However, the observation of the dependence of this effect with the time led to more refined studies to understand its origin. Following this, the additional uncertainty on the mass measurement coming from the uncertainty on the resolution was removed.

To assess the effect, two studies are made:

- The first one uses 200 pseudo-experiments, generated with a mass of 126 GeV and with two different strength parameters: $\mu = 1$ and $\mu = 2$. The statistic used corresponds to the full 2011 dataset as well a subset of the 2012 dataset amounting to 13 fb^{-1}. Each pseudo-experiments is generated with the nominal resolution, and is fitted with a different one as was done for the data. For each resolution tried, the average of the 200 masses extracted from these fits is done. The evolution of the best fit averaged mass as a function of the resolution used in the fit appears to be very flat.

- The second one uses an Asimov dataset (see Section 7.9) for each strength parameter hypothesis $\mu = 1$ and $\mu = 2$. This pseudo-data corresponds to the same integrated luminosity as the one described above. As in the previous case, these Asimov events are generated with the nominal resolution and fitted with a different one. Once again the best fit mass is constant with respect to the resolution used to perform the fit. This is illustrated in Figures 8.20(c) and 8.20(d)

The best fitted mass, $\hat{m_H}$, is stable in both studies. This suggests that the specific dataset, with a particular configuration of events, leads to the dependence on resolution observed in Figure 8.20(b).

8.6.2 Impact on the strength parameter

In the likelihood ratio defined in Equation 8.2 the parameter of interest, m_H, is replaced by the signal strength, μ. In this way, the impact of the mis-modeling of the signal resolution on the signal strength can also be checked. The same study as described in the previous section is repeated. In Figure 8.21(a), one can see that enlargement of the signal resolution increases the best fit signal strength, $\hat{\mu}$. The size of the effect is quite large: $\hat{\mu}$ increases by $\sim 10\%$ for a 40% increase of the resolution.

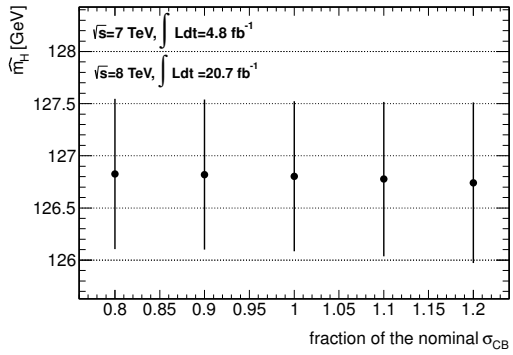

(a) Full dataset

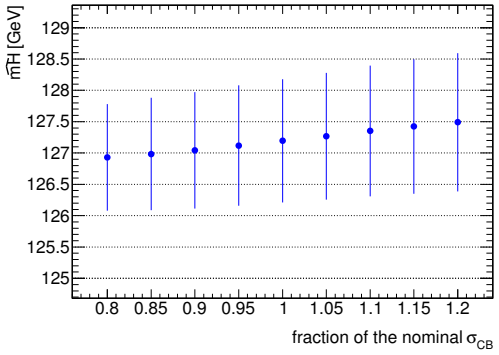

(b) Data subset

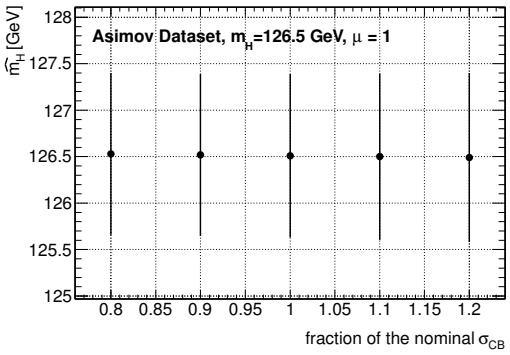

(c) Asimov dataset $\mu = 1$

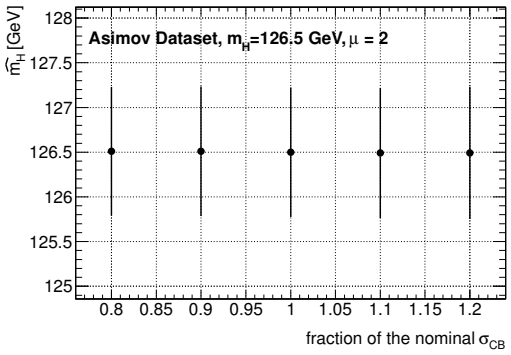

(d) Asimov dataset $\mu = 2$

Figure 8.20: Best fitted value of the peak position when varying the width of the Crystal Ball in the signal parametrisation, using the full data (a), a subset of the data (b), and using toys simulated with a strength parameter of 1 (c) and 2 (d).

A test is done using Asimov datasets to decorrelate systematic effect and specific configurations of the data.

As seen in Figures 8.21(b) and 8.21(c), a dependence of the signal strength on the resolution used for the fit is found for these datasets with $\mu = 1$ and $\mu = 2$. Similar results are found using pseudo-experiments.

The size of the effect is comparable to what is found in data: for a 40% increase in resolution, an increase of 17% and 10% is measured for $\mu = 1$ and $\mu = 2$ respectively. The data are closer to the $\mu = 2$ hypothesis in term of size of the effect, in agreement with the direct measurement of μ in data which is also closer to 2. As the resolution is fixed during the fit, an increase of its value leads to an increase of the signal integrated. If the resolution chosen to fit the signal is too large, this leads to an overestimation of the number of events in the peak and then of the the signal strength.

8.6.3 Impact on the nuisance parameter related to the resolution

The systematic uncertainty on the resolution is taken into account through the use of a nuisance parameter in the likelihood. The systematic uncertainty is implemented in the statistical framework through the parameter K_σ which takes the form

$$K_\sigma = e^{\theta\sqrt{ln(1+\delta^2)}}, \tag{8.4}$$

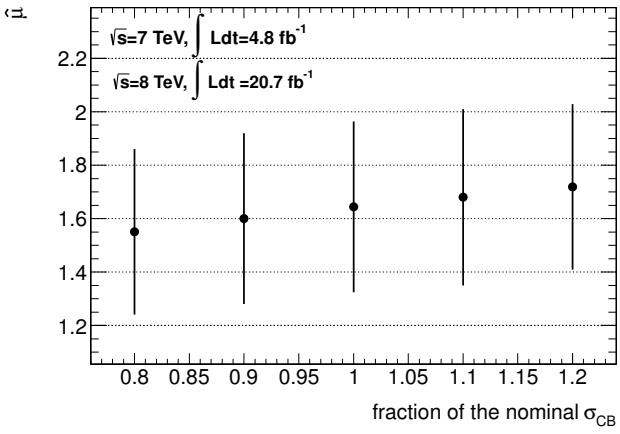

(a) Data

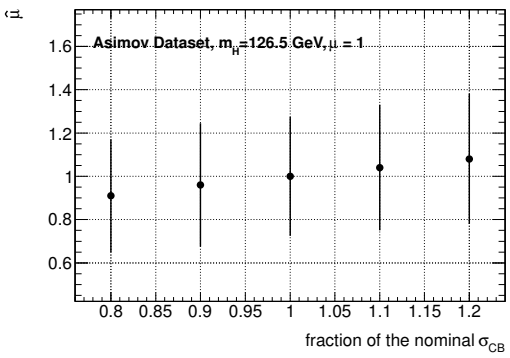

(b) Asimov dataset $\mu = 1$

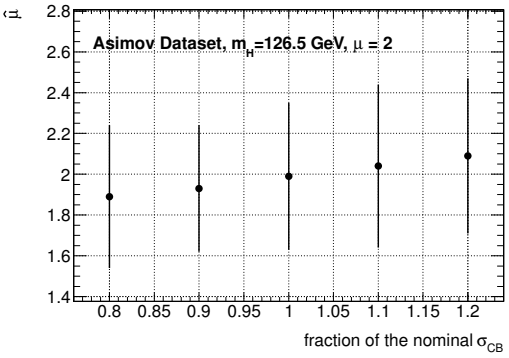

(c) Asimov dataset $\mu = 2$

Figure 8.21: Best fit value of the strength parameter when varying the width of the Crystal Ball in the signal parametrisation, in data (a) and using an Asimov dataset with $\mu = 1$ (b) and $\mu = 2$ (c).

with δ the uncertainty value on the mass resolution and θ the nuisance parameter related to the resolution, constrained with a Gaussian function of width 1 in the likelihood (see Section 7.8.3).

The resolution is written as

$$\sigma = \sigma_{nom}.K_\sigma \;\; = \;\; \sigma_{nom} e^{\theta\sqrt{ln(1+\delta^2)}}, \tag{8.5}$$

with σ_{nom} the nominal mass resolution.

This nuisance parameter is expected to deviate from its nominal value 0 when the resolution used in the fit is different from that in the data.

The signal model used in the fit is modified as described the previous section, with a varying resolution. The value of the nuisance parameter related to the resolution is extracted from the fit of the data with the likelihood described in Section 8.1. Its dependence on the resolution used in the signal model is illustrated in Figure 8.22(a).

A study is done using Asimov datasets generated with the nominal resolution and fitted with the varying resolution. The statistic used corresponds to the full Run I dataset. The two hypotheses $\mu = 1$ and $\mu = 2$ are tested and the result is shown in Figures 8.22(b) and 8.22(c).

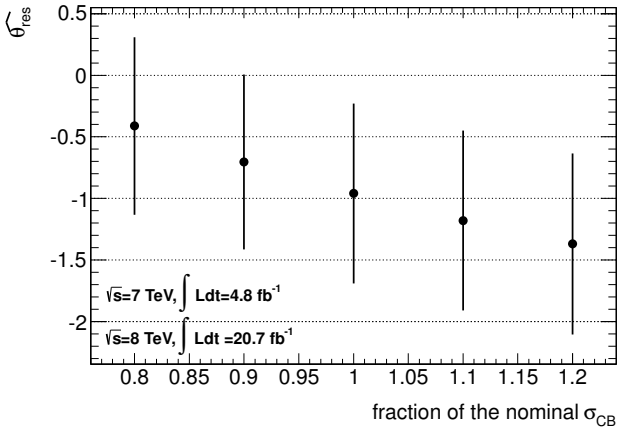

(a) Data

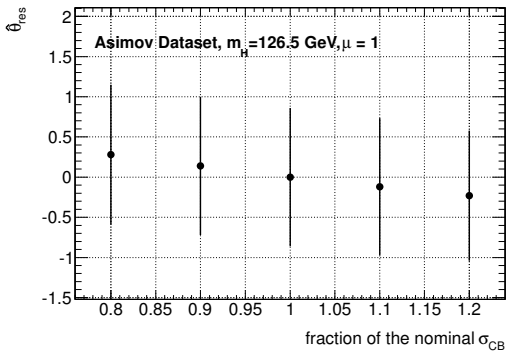

(b) Asimov dataset $\mu = 1$

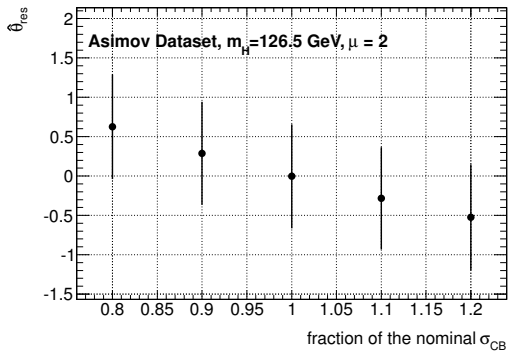

(c) Asimov dataset $\mu = 2$

Figure 8.22: Evolution of the central value of the nuisance parameter associated to the resolution as a function of the Crystal Ball width used to fit the mass. The dataset used are the data (a), an Asimov dataset, with $m_H = 126.5$ GeV and $\mu = 1$ (b) or $\mu = 2$ (c).

The trend observed in the Asimov dataset is as expected for both μ hypotheses: the deviation of θ_{res} from its nominal value (referred to as the "pull" in the following) is minimum when fitting with the nominal resolution and increases when fitting with a different resolution. For a resolution varying between 0.8 and 1.2 times the nominal one, the nuisance parameter takes values within ± 0.3 and ± 0.6 for $\mu = 1$ and $\mu = 2$ respectively. The larger pull measured in the $\mu = 2$ case can be understood as an effect of the reduction of the statistical error that gives more penalty when fitting with a wrong resolution. This leads to a higher pull of the nuisance parameter to correct this.

In the data, the pull of the nuisance parameter associated to the resolution at the nominal resolution is not minimal. The value measured is rather ~ -1. The points are fitted with a first order polynomial function, and the minimal deviation of the nuisance parameter is found for a resolution of $\sim 0.6 \times \sigma_{nom}$. This indicates an overestimation of the photon resolution in the data the investigation of which in more detail is described in Section 8.6.4.

In Figure 8.23, a comparison between the fitted resolution, $\hat{\sigma}$, (derived from Equation 8.4) and the nominal one is made as a function of the resolution used to fit the signal, for the two

Asimov datasets. For $\mu = 2$, the resolution fitted is closer to the nominal one than for $\mu = 1$. The fact that the points in this figure depart from the dashed line $x = y$, is due the uncertainty on the mass resolution.

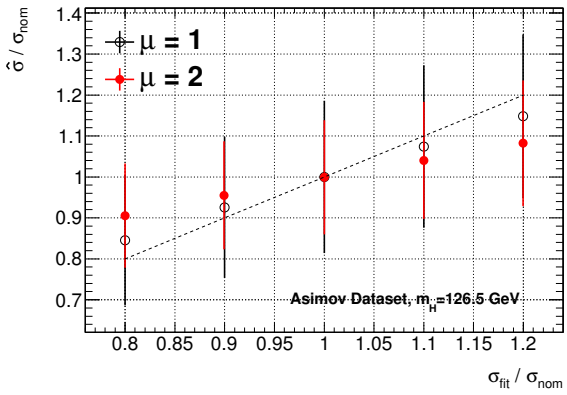

Figure 8.23: Ratio of the fitted resolution over the nominal one as a function of the ratio of the resolution used in the fit over the nominal one, for two Asimov dataset generated with $\mu = 1$ (black open circle) and $\mu = 2$ (red dots) and a mass of 126.5 GeV, for a statistic corresponding to the full Run I dataset.

8.6.4 Validation of the mass resolution

With the 2011 and 2012 datasets, there is sufficient data to perform a direct measurement of the resolution of the observed resonance, using the formula given in Equation 8.4.
In this equation, the nuisance parameter related to the mass resolution θ is normally constrained with a Gaussian function. To perform the measurement of the resolution, the Gaussian constraint is removed.

In Table 8.8, the best values of the mass, strength parameter and nuisance parameter θ with and without the constraint on θ are detailed. The consequences of removing the constraint on the nuisance parameter θ are:

- A slight increase of the mass value,
- An increase of the nuisance parameter related to resolution, θ,
- A decrease by 10-15% of the best fit of μ.

8.6.4.1 Validation for the inclusive analysis

With these numbers, one can measure the resolution using Equation 8.4. The value of the resolution for the inclusive 2012 analysis is

$$\sigma = \sigma_{nom}.(0.79^{+0.21}_{-0.17}) = 1.38^{+0.37}_{-0.30} \text{ GeV},$$

with σ_{nom} corresponding to the nominal resolution given in Table 7.7.
The resolution measured in data is around 20 % smaller than the nominal one. Fitting the signal with 20 % over-estimation of the resolution, leads to an over-estimation of the signal

Table 8.7: Best fitted values of mass, strength parameter and nuisance parameter related to the resolution, with different configurations.

Configuration	Constraint on θ	$\hat{m_H}$	$\hat{\mu}$	$\hat{\theta}$
2011 Inclusive	Yes	126.32 ± 1.07	$2.16^{+0.91}_{-0.84}$	-0.08 ± 1.02
2011 Categorized	Yes	126.24 ± 0.89	$2.17^{+0.76}_{-0.68}$	-0.25 ± 1.01
2012 Inclusive	Yes	126.71 ± 0.81	1.91 ± 0.36	-0.52 ± 0.73
2012 Inclusive	No	126.73 ± 0.81	1.77 ± 0.37	-1.14 ± 1.14
2012 Categorized	Yes	126.91 ± 0.76	1.59 ± 0.33	-0.86 ± 0.70
2012 Categorized	No	126.95 ± 0.74	1.47 ± 0.32	$-1.64^{+0.95}_{-1.03}$
2011 + 2012 Categorized	Yes	126.79 ± 0.72	1.64 ± 0.32	-0.96 ± 0.69
2011 + 2012 Categorized	No	126.85 ± 0.71	1.50 ± 0.21	-1.84 ± 0.96

strength, following studies on data and pseudo-experiments detailed in Section 8.6.2. This overestimation is expected to be about 5%. In Table 8.8, a reduction of $\sim 7\%$ of the central value of the best fit of the signal strength is seen when removing the constraint on θ, in agreement with the previous statement.

8.6.4.2 Validation in separated categories

The measurement of the mass, signal strength and nuisance parameter related to the resolution were given in Table 8.5. The values of these quantities when the nuisance parameter is unconstrained are given in Table 8.8.

Table 8.8: Best fitted values of mass, strength parameter and nuisance parameter related to the resolution θ, for detector and conversion based categories, when the constraint on θ is removed.

	$\hat{m_H}$ [GeV]	$\hat{\mu}$	$\hat{\theta}$
UC categories	126.23 ± 0.77	$1.34^{+0.44}_{-0.39}$	$-2.98^{+1.7}_{-1.98}$
CV categories	$126.89^{+0.84}_{-0.79}$	1.59 ± 0.59	$-1.16^{+2.22}_{-3.84}$
Central categories	-	-	-
Rest categories	126.47 ± 0.92	$2.07^{+0.58}_{-0.48}$	-1.54 ± 1.26

The UC category has a large negative value of $\hat{\theta}$, implying a large discrepancy of the measured resolution with respect to the nominal one. Photons in this category are most dissimilar to electrons and the extrapolation of the electron constant term to this category could be the origin of the disagreement.

For the Central category the fit did not converge properly after the removing of the constraint. The resulting resolutions are:

$$\sigma_{UC} \sim 0.55 \times \sigma_{nom,UC} \ ; \ \sigma_{CV} \sim 0.80 \times \sigma_{nom,CV} \ ; \ \sigma_{rest} \sim 0.75 \times \sigma_{nom,rest}$$

There is clearly an inconsistency for the categories of type Unconverted: indeed, the measured resolution is less than the smallest achievable resolution assuming a perfect detector with a null constant term.

The observations suggest a combined effect of an overestimation of the resolution due to the extrapolation of the constant term and of an upward fluctuation of the number of events in the signal region.

8.7 Summary of the checks and validations

In the previous sections, sources of potential biases for the mass measurement coming from the statistical method, the reconstruction of the diphoton invariant mass or the analysis has been discussed in detail. Underestimates of the uncertainty on the mass measurement and biases on the signal strength measurement have also been noted. In Chapter 5, sources of potential biases for the mass measurement that are not specific to the $H \to \gamma\gamma$ analysis have been also noticed. Finally in Chapter 7 a model for the photon energy scale uncertainty depending on the categories has been established.

The potential biases on the mass measurement have been translated into additional energy scale uncertainties and are summarized in Table 8.9. The previous sections and Chapter 5 provides more details.

These additional uncertainties on the peak position complete the model built for the $H \to \gamma\gamma$ analysis.

Table 8.9: Additional mass scale uncertainties added to the 2012 uncertainty on peak position due to energy scale uncertainties. These uncertainties are common to all categories.

Source of uncertainty	Uncertainty on m_H
In situ Method	±0.3%
Material mismodeling	±0.3%
Presampler energy scale	±0.1%
Conversion fraction	±0.13%
Lateral leakage: $e \to \gamma$	±0.1%
Lateral leakage: energy dependence	±0.02%
LAr cell gain mis-calibration	±0.15%
E_1/E_2 inter-calibration	±0.2%
Primary vertex	±0.03%
Background model	±0.1%
Total	±0.54%

All these uncertainties are added quadratically and a new nuisance parameter is built for this, completely uncorrelated with the five other parameters dedicated to the uncertainty on the peak position. This new nuisance parameter is also constrained with a Gaussian function with unit width. This is a preliminary model, that does not take into account the correlations, and that is not separately defined in the various categories: for most of the uncertainties listed below, a strong dependence to the category is expected. This model is being refined, while the source of uncertainties are better understood.

The undercoverage of the statistical uncertainty on the mass described in Section 8.3.3 requires the inflation of the statistical uncertainty by a factor that depends on the true value of μ. Choosing the observed value of μ the inflation factor is 1.05.

8.8 Impact of the final mass scale uncertainties

The uncertainty on the peak position has different sources as described in Section 7.8.4. In addition an extra uncertainty has been added to account for extra biases on the mass measurement due to other sources. Figure 8.24 shows the breakdown of the four main sources of Mass Scale Systematic (MSS). From this figure, one can deduce the contribution of each of these sources to the total mass uncertainty

$$m_H = 126.79 \pm 0.24\,(\text{stat.}) \pm 0.41\,(\text{mat.}) \pm 0.41\,(\text{meth.}) \pm 0.15\,(\text{PS}) \pm 0.38\,(\text{other MSS})\ \text{GeV},$$

where "stat." corresponds to the statistical error, and where "mat", "meth.", "PS", and "other MSS" correspond to the contribution of the material mis-modeling, the uncertainty on the in-situ calibration procedure, the uncertainty on the presampler scale and the various other uncertainties on the peak position coming from the sources described in this chapter, respectively.

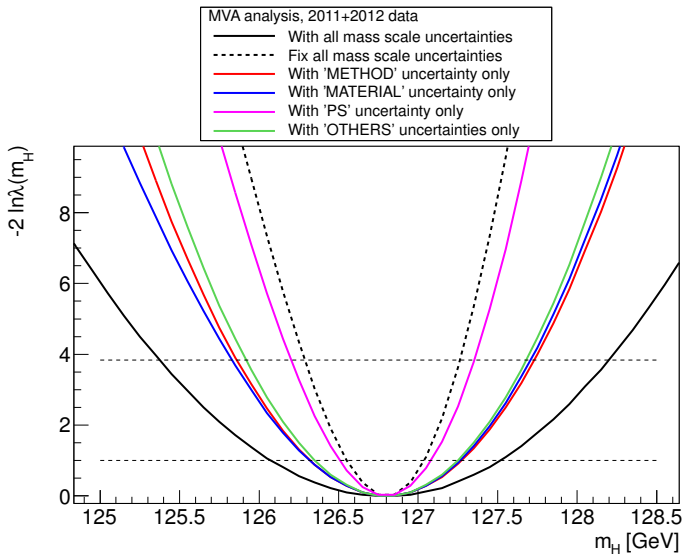

Figure 8.24: Evolution of the likelihood $-2\ln\lambda$ with the Higgs boson mass hypothesis, for the mass measurement. The various curves show the contribution of the different sources of uncertainty on the peak position to the total width of the likelihood.

The dominant contribution comes from the method used to extract the calibration coefficients and from the material mis-modeling in the simulation. The uncertainty on presampler scale is at the level of the statistical uncertainty.

The measurement of the mass is then systematics-limited, and more precisely limited by the uncertainty on the photon energy scale.

A statistical uncertainty of around 200 MeV is reached, but the control of the photon energy response with the electromagnetic calorimeter is not perfect and already limits the accuracy on the measurement of the Higgs boson mass. In the future, efforts will be more concentrated on a better understanding of the calorimeter response to improve this measurement. An overview of the work achieved toward this direction has been presented in Chapters 5 and 6.

- From what has been studied in Chapter 5, the method contribution is expected to decrease once the $Z \to ee$ lineshape issue is better understood.

- Various studies have shown that the amount of material in data is well described by the nominal geometry except in some localized places (see Chapter 6). New simulations have been carried with a more reasonable amount of material and will be used to better assess the uncertainty on the peak position due to material effects.

- The model for the extra uncertainties added within one single nuisance parameter, common to all the categories will be refined. Most of the components of this nuisance parameter are in reality uncorrelated and will be treated in this way in the new model. The dependence within the different categories will be checked and taken into account.

- The presampler scale has been measured quite precisely in Chapter 5. Hence the uncertainty from this source will decrease.

The pull of the different nuisance parameters related to the mass scale systematics has been checked at the best fit mass point and their value is given in Table 8.10. No significant deviation at this point is noticed. Their evolution with the Higgs boson mass hypothesis is shown in Figure 8.25: these parameters are not pulled in the signal region, whereas when moving away from this region, they start to be pulled, to allow the fit to catch the signal.

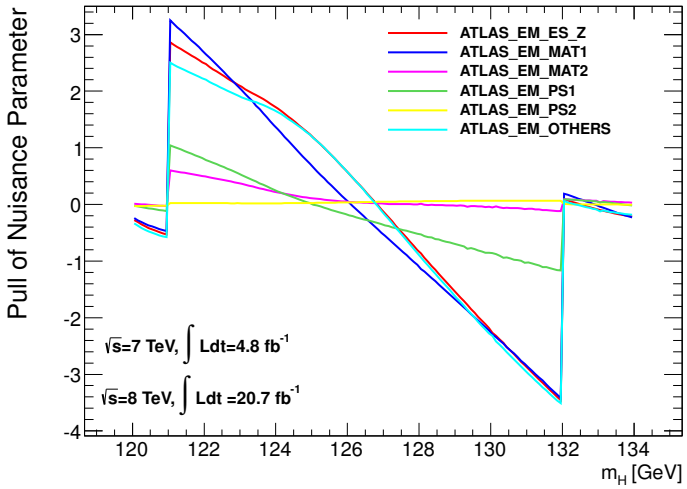

Figure 8.25: Pull of the nuisance parameters related to the mass scale uncertainties as a function of the mass. The parameter ATLAS_EM_ES_Z is related to the uncertainty on the method to extract the calibration coefficients, ATLAS_EM_MAT1 and ATLAS_EM_MAT2 are related respectively to the uncertainties coming from material in the region $\eta < 1.8$ and $\eta > 1.8$, ATLAS_EM_PS1 and ATLAS_EM_PS2 are related respectively to the uncertainties coming from the presampler scale in barrel and endcap and finally ATLAS_EM_OTHERS is related to the additional mass scale uncertainties.

The correlations between the parameters of the likelihood and the variables m_H and μ have been also checked and are shown in Tables 8.11 for the nuisance parameters and 8.12 for the background parametrization parameters. The biggest correlations for m_H are found for the nuisance parameter related to the uncertainty on the peak position coming from the scale extraction method ($\sim -50\%$), the one related to the material mis-modeling for $\eta < 1.8$ ($\sim -46\%$), the one related to the additional systematic uncertainties on the peak position

Table 8.10: Pull of the various nuisance parameter connected to the mass scale uncertainties at the best fit point.

Nuisance parameter	Value
Method	0.018 ± 0.985
Material low η	-0.409 ± 0.968
Material high η	0.017 ± 0.991
PS barrel	-0.329 ± 0.987
PS endcap	0.044 ± 0.994
Others MSS	0.002 ± 0.990

($\sim -51\%$). For μ the biggest correlations are found for the nuisance parameter related to the resolution ($\sim +34\%$), the one related to the Branching ratio and the ggH scale ($\sim -29\%$).

Table 8.11: Correlations between the nuisance parameters of the likelihood and the variables m_H and μ.

Parameter	Correlation with m_H	Correlation with μ
m_H	1	0.045274
μ	0.045274	1
EM_ES_Z	-0.501767	-0.023111
EM_PS_BARR	-0.119437	-0.0331385
EM_PS_EC	0.00765871	0.00340684
EM_MAT_LOW	-0.462807	-0.0363392
EM_MAT_HIGH	-0.0114053	0.00660754
EM_rest	-0.5086	-0.023172
Resolution	-0.0573699	0.339891
Identification	-0.0104833	-0.186229
Energy scale (yield)	-0.000223616	-0.0121445
Material	-0.000778814	-0.00130868
Isolation	0.000602445	-0.0529663
Trigger	0.000615498	-0.0249806
Luminosity 2011	-0.00282827	-0.0131306
Luminosity 2012	0.00440558	-0.182847
Pileup	-0.00515506	-0.022994
JES13	-0.0164092	-0.0532586
MultiJES1	-0.0127557	-0.0415417
MultiJES2	-0.00495624	-0.0186752
JES14	-0.00183338	-0.00255528
JES4	-0.00487818	-0.0203544
JES19	-0.00274189	-0.0111506
MultiJES3	-0.00262524	-0.0115534
JER	-0.00263841	-0.00958726
JVF	0.00024435	0.00612038
UE	-0.0180568	-0.0840402
η^*	-0.00412078	-0.0182896
$\Delta\phi$ model	-0.006258	-0.0283686
Electron Efficiency	0.000427163	-0.000919293
Muon Efficiency	0.000170733	-0.000366595
Branching Ratio	-0.00179756	-0.290923
p_T modeling (ggH)	0.0202132	0.112709
scale ggH	0.0139911	-0.291681
scale ggH 2jets	-0.0155161	-0.0586106
scale ggH 3jets	-0.0239566	-0.107047
scale ggH VHhad	0.000565484	-0.0309627
pdf gg	0.00856474	-0.30383
pdf qq	-0.00355466	-0.0445858
scale VBF	-0.000494949	-0.00230359
scale VH	0.000459028	-0.0040114
scale ttH	0.00077596	-0.00410074
background bias C1	0.00672798	-0.0474693
background bias C2	0.000690657	-0.0217494
background bias C3	0.00125244	-0.055687
background bias C4	-0.000578584	-0.0339568
background bias C5	0.0211511	-0.0267764
background bias C6	-0.00876807	-0.0227881
background bias C7	-0.0090152	-0.036761
background bias C8	-0.00658421	-0.0133684
background bias C9	-0.00521445	-0.0278989
background bias C10	-0.00583105	-0.0274368
background bias C11	-0.0124476	-0.0370241
background bias C12	0.000325293	-0.0117947
background bias C13	0.00143518	-0.00560626
background bias C14	0.00367811	-0.00911533

Table 8.12: Correlations between the background parametrization parameters of the likelihood and the variables m_H and μ.

Parameter	Correlation with m_H	Correlation with μ
a1EP C1 2011	0.000402044	-0.0521118
a1EP C1 2012	-0.00468192	-0.112054
a1EP C5 2011	-0.00661806	-0.0490738
a1EP C5 2012	-0.00381515	-0.0934916
a1EP C9 2011	0.000536746	-0.032934
a1EP C9 2012	0.00140544	-0.0726089
a1 C3 2011	0.00113241	-0.00210247
a1 C3 2012	-0.00476096	0.00180574
a1 C7 2011	0.00940012	-0.00250387
a1 C7 2012	0.00867673	0.00105508
a2EP C1 2011	-0.00109234	0.0499473
a2EP C1 2012	0.00279119	0.107179
a2EP C5 2011	0.0052222	0.0474035
a2EP C5 2012	0.00159532	0.0895985
a2EP C9 2011	-0.000312926	0.0334308
a2EP C9 2012	-0.000417237	0.0734119
a2 C3 2011	-0.00149769	-0.0425225
a2 C3 2012	0.00182871	-0.0933063
a2 C7 2011	-0.00801403	-0.0368042
a2 C7 2012	-0.0102729	-0.0868604
a3 C3 2011	0.000893997	0.0284892
a3 C3 2012	-0.000775078	0.0667168
a3 C7 2011	0.00443793	0.0259543
a3 C7 2012	0.00650089	0.0613763
a4 C3 2011	-2.32484e-05	-0.0205293
a4 C3 2012	-0.00194846	-0.046772
a4 C7 2011	0.00180092	-0.0182893
a4 C7 2012	-0.000255743	-0.0435812
N_{bkg} C10 2011	0.00791652	-0.0391671
N_{bkg} C10 2012	0.00447067	-0.0569992
N_{bkg} C11 2012	0.0148873	-0.0820435
N_{bkg} C12 2012	0.000847427	-0.0334452
N_{bkg} C13 2012	-0.00377426	-0.0390215
N_{bkg} C14 2012	-0.00273105	-0.0568039
N_{bkg} C1 2011	0.000764774	-0.039513
N_{bkg} C1 2012	-0.002594	-0.0921894
N_{bkg} C2 2011	-0.000266008	-0.0177808
N_{bkg} C2 2012	-0.000886396	-0.0498619
N_{bkg} C3 2011	-0.000499798	-0.050013
N_{bkg} C3 2012	-0.00284702	-0.107339
N_{bkg} C4 2011	-0.00024833	-0.0338073
N_{bkg} C4 2012	-0.00222902	-0.0611486
N_{bkg} C5 2011	-0.00398862	-0.0369006
N_{bkg} C5 2012	-0.00144986	-0.0767019
N_{bkg} C6 2011	0.00525127	-0.00582532
N_{bkg} C6 2012	-0.000540647	-0.0434392
N_{bkg} C7 2011	0.00089509	-0.0445949
N_{bkg} C7 2012	-0.00234686	-0.102731
N_{bkg} C8 2011	0.00241504	-0.020083
N_{bkg} C8 2012	-0.00155032	-0.0546482
N_{bkg} C9 2011	8.85475e-05	-0.0306665
N_{bkg} C9 2012	-0.00037041	-0.0673792
slope C10 2011	0.00197348	-0.00133026
slope C10 2012	-0.00272235	0.00470611
slope C11 2012	-0.0034154	0.00362749
slope C12 2012	-0.00131703	-0.000474422
slope C13 2012	-0.00264708	-0.0139669
slope C14 2012	-0.00153896	0.0062155
slope C2 2011	-0.00129194	-0.00551558
slope C2 2012	-0.00351865	-0.00327659
slope C4 2011	-9.0587e-05	0.00023546
slope C4 2012	0.00116713	-0.000112801
slope C6 2011	0.000370316	-0.00128413
slope C6 2012	-0.00403512	-0.00810936
slope C8 2011	-0.00178334	-0.000601639
slope C8 2012	-0.00058568	0.00046469

Conclusion

This thesis presents studies of the energy response of photons and electrons in ATLAS and its impact on the analysis of the $H \to \gamma\gamma$ channel. The reconstruction of the photon energy and subsequently the diphoton mass is one of the critical elements of this analysis which relies largely on the reconstruction of a narrow resonance on top of a continuously falling background. The diphoton channel has played an instrumental role in the design of the ATLAS calorimeter. This design and the quality of the calorimeter construction has allowed this channel to play a leading role in the discovery of the Higgs boson at a mass of approximately 125.6 GeV. Using the diphoton channel and the improved understanding of the photon energy response, the mass of the Higgs boson has been measured with a 0.5% precision.

An algorithm to discriminate misidentified photons from calorimeter cells noise from real photons candidates has been designed. This algorithm is efficient in removing residual sporadic noise, but has a dependence on the photon transverse momentum. Additional variables have been investigated and one has been found to be independent of the transverse momentum, while keeping a high efficiency.

The electron and photon energy response calibration has been tested using an alternative method based on the Jacobian peak. This test has demonstrated a good understanding of the electron energy response in the calorimeter. The standard calibration has also been improved, through a new calorimeter layer calibration. This study has shown that the presampler is mis-calibrated by about 15% in the endcaps, and that the strip and middle layers are relatively mis-calibrated by about -3% in the barrel.

The uniformity of the energy response along the azimuthal angle has been studied using electrons. Structures have been found, understood and corrected. Apart from small residual effects, the uniformity in this plane has been shown to be good and to have a minor contribution to the total constant term. The stability of the energy response with respect to time and pileup has also been checked and found to be under control with fluctuations smaller than 0.1%.

A study of the $Z \to ee$ lineshape that is used to extract the constant term has been done. Small inaccuracies have been found but did not totally solve the disagreement between the observed and simulated lineshapes. The origin of such discrepancy is imputed to at least two sources: the material mis-modeling upstream of the calorimeter and the presampler mis-calibration. The material budget upstream of the calorimeter has been probed using longitudinal shower shapes methods. This study highlighted various small simulation issues, that have been subsequently corrected. In addition it has been shown that the primary uncertainty on the amount of material upstream of the calorimeter was largely overestimated. Using this method, new, more realistic uncertainties have been derived.

The $H \to \gamma\gamma$ channel has been used for the search and thereafter the mass measurement of the Higgs boson. The impact of the interference between the signal produced through the gluon fusion mode and background has been evaluated and found to reduce the signal yield by 2.3%

on average at the mass of 125 GeV. A model for the energy scale systematic uncertainties, that takes into account the various correlations, has been designed for this analysis. This leads to an average systematic uncertainty on the signal peak position of about 0.5%.

Finally, after the validation of the method, the mass has been measured in this channel and found to be: $m_H = 126.8 \pm 0.2$ (stat) $\pm$ 0.7 (syst) GeV. The systematic part of the error is already dominant. From the various validation tests performed, a small underestimation of the statistical uncertainty has been seen, and a small bias on the signal strength measurement has been noted. A correlation between the signal resolution and the signal strength has been also reported.

A combined measurement of the Higgs boson mass in the $H \to \gamma\gamma$ and $H \to 4l$ channels gives the following value: $m_H = 125.5 \pm 0.2$ (stat) $^{+0.5}_{0.6}$ (sys) GeV which provide a measurement as precise as 0.5% and compatible with the CMS result [282].

Bibliography

[1] F. Englert and R. Brout. Broken symmetry and the mass of gauge vector mesons. *Phys. Rev. Lett.*, 13:321, 1964.

[2] Peter W. Higgs. Broken symmetries, massless particles and gauge fields. *Phys. Lett.*, 12:132, 1964.

[3] Peter W. Higgs. Broken symmetries and the masses of gauge bosons. *Phys. Rev. Lett.*, 13:508, 1964.

[4] Peter W. Higgs. Spontaneous symmetry breakdown without massless bosons. *Phys. Rev.*, 145:1156, 1966.

[5] G. S. Guralnik, C. R. Hagen, and T. W. B. Kibble. Global conservation laws and massless particles. *Phys. Rev. Lett.*, 13:585, 1964.

[6] T. W. B. Kibble. Symmetry breaking in non-Abelian gauge theories. *Phys. Rev.*, 155:1554, 1967.

[7] Steven Weinberg. A model of leptons. *Phys. Rev. Lett.*, 19:1264, 1967.

[8] A. Salam. *Elementary Particle Theory.* Almqvist and Wiksell, Stockholm, 1968.

[9] S. L. Glashow. Partial symmetries of weak interactions. *Nucl. Phys.*, 22:579, 1961.

[10] Georges Aad et al. Observation of a new particle in the search for the Standard Model Higgs boson with the ATLAS detector at the LHC. *Phys.Lett.*, B716:1–29, 2012.

[11] Serguei Chatrchyan et al. Observation of a new boson at a mass of 125 GeV with the CMS experiment at the LHC. *Phys.Lett.*, B716:30–61, 2012.

[12] Georges Aad et al. Measurements of Higgs boson production and couplings in diboson final states with the ATLAS detector at the LHC. *Submitted to Phys.Lett.B, CERN-PH-EP-2013-103*, 2013.

[13] Georges Aad et al. Evidence for the spin-0 nature of the Higgs boson using ATLAS data. *Submitted to Phys.Lett.B, CERN-PH-EP-2013-102*, 2013.

[14] Serguei Chatrchyan et al. Study of the Mass and Spin-Parity of the Higgs Boson Candidate Via Its Decays to Z Boson Pairs. *Phys.Rev.Lett.*, 110:081803, 2013.

[15] An update of combined measurements of the new Higgs-like boson with high mass resolution channels. *ATLAS-CONF-2012-170*, Dec 2012.

[16] Combined measurements of the mass and signal strength of the higgs-like boson with the atlas detector using up to 25 fb^{-1} of proton-proton collision data. *ATLAS-CONF-2013-014*, Mar 2013.

[17] Study of the spin of the new boson with up to 25 fb^{-1} of ATLAS data. *ATLAS-CONF-2013-040*, Apr 2013.

[18] E. Noether. Invariant variation problems. *Transport Theory and Statistical Physics*, 1:186–207, 1971.

[19] Jean Iliopoulos. Introduction to the Standard Model of the Electro-Weak Interactions. *2012 CERN Summer School of Particle Physics, Angers*, France, 2012.

[20] W. Heisenberg. Zur theorie des ferromagnetismus. *Zeitschrift fr Physik*, 49(9-10):619–636, 1928.

[21] M. Baker and S. L. Glashow. Spontaneous breakdown of elementary particle symmetries. *Phys. Rev.*, 128:2462–2471, Dec 1962.

[22] Yoichiro Nambu. Quasiparticles and Gauge Invariance in the Theory of Superconductivity. *Phys.Rev.*, 117:648–663, 1960.

[23] Yoichiro Nambu. Axial vector current conservation in weak interactions. *Phys. Rev. Lett.*, 4:380–382, Apr 1960.

[24] Y. Nambu and G. Jona-Lasinio. Dynamical model of elementary particles based on an analogy with superconductivity. i. *Phys. Rev.*, 122:345–358, Apr 1961.

[25] Y. Nambu and G. Jona-Lasinio. Dynamical model of elementary particles based on an analogy with superconductivity. ii. *Phys. Rev.*, 124:246–254, Oct 1961.

[26] J. Goldstone. Field theories with superconductor solutions. *Il Nuovo Cimento*, 19(1):154–164, 1961.

[27] Jeffrey Goldstone, Abdus Salam, and Steven Weinberg. Broken symmetries. *Phys. Rev.*, 127:965–970, Aug 1962.

[28] F. Halzen and A.D. Martin. *Quarks and leptons: an introductory course in modern particle physics*. Wiley, 1984.

[29] Abdelhak Djouadi. The anatomy of electro-weak symmetry breaking. I: The Higgs boson in the Standard Model. *Phys. Rept.*, 457:1, 2008.

[30] Duane A. Dicus and Vishnu S. Mathur. Upper bounds on the values of masses in unified gauge theories. *Phys. Rev. D*, 7:3111–3114, May 1973.

[31] Benjamin W. Lee, C. Quigg, and H. B. Thacker. Weak interactions at very high energies: The role of the higgs-boson mass. *Phys. Rev. D*, 16:1519–1531, Sep 1977.

[32] William J. Marciano and Scott S.D. Willenbrock. Radiative corrections to heavy Higgs scalar production and decay. *Phys.Rev.*, D37:2509, 1988.

[33] T.P. Cheng, E. Eichten, and Ling-Fong Li. Higgs Phenomena in Asymptotically Free Gauge Theories. *Phys.Rev.*, D9:2259, 1974.

[34] K.G. Wilson and John B. Kogut. The Renormalization group and the epsilon expansion. *Phys.Rept.*, 12:75–200, 1974.

[35] J. Ellis, J.R. Espinosa, G.F. Giudice, A. Hoecker, and A. Riotto. The Probable Fate of the Standard Model. *Phys.Lett.*, B679:369–375, 2009.

[36] Manfred Lindner, Marc Sher, and Helmut W. Zaglauer. Probing Vacuum Stability Bounds at the Fermilab Collider. *Phys.Lett.*, B228:139, 1989.

[37] Gino Isidori, Giovanni Ridolfi, and Alessandro Strumia. On the metastability of the standard model vacuum. *Nucl.Phys.*, B609:387–409, 2001.

[38] Greg W. Anderson. New cosmological constraints on the Higgs boson and top quark masses. *Phys.Lett.*, B243:265–270, 1990.

[39] Peter Brockway Arnold and Stamatis Vokos. Instability of hot electroweak theory: bounds on m_H and m_t. *Phys.Rev.*, D44:3620–3627, 1991.

[40] J.R. Espinosa and M. Quiros. Improved metastability bounds on the standard model Higgs mass. *Phys.Lett.*, B353:257–266, 1995.

[41] Giuseppe Degrassi, Stefano Di Vita, Joan Elias-Miro, Jose R. Espinosa, Gian F. Giudice, et al. Higgs mass and vacuum stability in the Standard Model at NNLO. *JHEP*, 1208:098, 2012.

[42] M.J.G. Veltman. The Infrared - Ultraviolet Connection. *Acta Phys.Polon.*, B12:437, 1981.

[43] M.B. Einhorn and D.R.T. Jones. The Effective potential and quadratic divergences. *Phys.Rev.*, D46:5206–5208, 1992.

[44] Christopher F. Kolda and Hitoshi Murayama. The Higgs mass and new physics scales in the minimal standard model. *JHEP*, 0007:035, 2000.

[45] ALEPH Collaboration et al. Precision Electroweak Measurements and Constraints on the Standard Model. *CERN-PH-EP-2010-095*, 2010.

[46] J. Alcaraz et al. Precision Electroweak Measurements and Constraints on the Standard Model. *CERN-PH-EP-2007-039*, 2007.

[47] M. Baak, M. Goebel, J. Haller, A. Hoecker, D. Ludwig, et al. Updated Status of the Global Electroweak Fit and Constraints on New Physics. *Eur.Phys.J.*, C72:2003, 2012.

[48] M. Baak, M. Goebel, J. Haller, A. Hoecker, D. Kennedy, et al. The Electroweak Fit of the Standard Model after the Discovery of a New Boson at the LHC. *Eur.Phys.J.*, C72:2205, 2012.

[49] H. M. Georgi, S. L. Glashow, M. E. Machacek, and Dimitri V. Nanopoulos. Higgs bosons from two-gluon annihilation in proton-proton collisions. *Phys. Rev. Lett.*, 40:692, 1978.

[50] M. Spira, A. Djouadi, D. Graudenz, and P. M. Zerwas. Higgs boson production at the LHC. *Nucl. Phys.*, B453:17, 1995.

[51] S. Dawson. Radiative corrections to Higgs boson production. *Nucl.Phys.*, B359:283–300, 1991.

[52] A. Djouadi, M. Spira, and P.M. Zerwas. Production of Higgs bosons in proton colliders: QCD corrections. *Phys.Lett.*, B264:440–446, 1991.

[53] Robert V. Harlander and William B. Kilgore. Next-to-Next-to-Leading Order Higgs Production at Hadron Colliders. *Phys. Rev. Lett.*, 88:201801, 2002.

[54] Charalampos Anastasiou and Kirill Melnikov. Higgs boson production at hadron colliders in NNLO QCD. *Nucl. Phys.*, B646:220, 2002.

[55] V. Ravindran, J. Smith, and W. L. van Neerven. NNLO corrections to the total cross section for Higgs boson production in hadron-hadron collisions. *Nucl. Phys.*, B665:325, 2003.

[56] Robert V. Harlander and Kemal J. Ozeren. Finite top mass effects for hadronic Higgs production at next-to-next-to-leading order. *JHEP*, 11:088, 2009.

[57] Simone Marzani, Richard D. Ball, Vittorio Del Duca, Stefano Forte, and Alessandro Vicini. Higgs production via gluon-gluon fusion with finite top mass beyond next-to-leading order. *Nucl.Phys.*, B800:127–145, 2008.

[58] Alexey Pak, Mikhail Rogal, and Matthias Steinhauser. Finite top quark mass effects in NNLO Higgs boson production at LHC. *JHEP*, 1002:025, 2010.

[59] Stefano Catani, Daniel de Florian, Massimiliano Grazzini, and Paolo Nason. Soft gluon resummation for Higgs boson production at hadron colliders. *JHEP*, 0307:028, 2003.

[60] U. Aglietti, R. Bonciani, G. Degrassi, and A. Vicini. Two-loop light fermion contribution to Higgs production and decays. *Phys. Lett.*, B 595:432, 2004.

[61] Stefano Actis, Giampiero Passarino, Christian Sturm, and Sandro Uccirati. NLO electroweak corrections to Higgs boson production at hadron colliders. *Phys. Lett.*, B 670:12, 2008.

[62] Charalampos Anastasiou, Radja Boughezal, and Frank Petriello. Mixed QCD-electroweak corrections to Higgs boson production in gluon fusion. *JHEP*, 0904:003, 2009.

[63] LHC Higgs Cross Section Working Group. Handbook of LHC Higgs Cross Sections: 1. Inclusive Observables. *CERN-2011-002*, CERN, Geneva, 2011.

[64] M. Ciccolini, Ansgar Denner, and S. Dittmaier. Strong and electroweak corrections to the production of Higgs + 2jets via weak interactions at the LHC. *Phys.Rev.Lett.*, 99:161803, 2007.

[65] Mariano Ciccolini, Ansgar Denner, and Stefan Dittmaier. Electroweak and QCD corrections to Higgs production via vector-boson fusion at the LHC. *Phys.Rev.*, D77:013002, 2008.

[66] Paolo Bolzoni, Fabio Maltoni, Sven-Olaf Moch, and Marco Zaro. Higgs production via vector-boson fusion at NNLO in QCD. *Phys.Rev.Lett.*, 105:011801, 2010.

[67] V. Del Duca, W. Kilgore, C. Oleari, C. Schmidt, and D. Zeppenfeld. Higgs + 2 jets via gluon fusion. *Phys.Rev.Lett.*, 87:122001, 2001.

[68] Shireen Gangal and Frank J. Tackmann. NLO Uncertainties in Higgs + 2 jets from Gluon Fusion. *Phys.Rev.*, D87:093008, 2013.

[69] John M. Campbell, R. Keith Ellis, and Ciaran Williams. Hadronic production of a Higgs boson and two jets at next-to-leading order. *Phys.Rev.*, D81:074023, 2010.

[70] Tao Han and S. Willenbrock. QCD correction to the $pp \to WH$ and ZH total cross-sections. *Phys.Lett.*, B273:167–172, 1991.

[71] Oliver Brein, Abdelhak Djouadi, and Robert Harlander. NNLO QCD corrections to the Higgs-strahlung processes at hadron colliders. *Phys.Lett.*, B579:149–156, 2004.

[72] M.L. Ciccolini, S. Dittmaier, and M. Kramer. Electroweak radiative corrections to associated WH and ZH production at hadron colliders. *Phys.Rev.*, D68:073003, 2003.

[73] O. Brein, M. Ciccolini, S. Dittmaier, A. Djouadi, R. Harlander, et al. Precision calculations for associated WH and ZH production at hadron colliders. *Physics at TeV colliders. Proceedings, Workshop, Les Houches, France, May 26-June 3, 2003*, 2004.

[74] W. Beenakker, S. Dittmaier, M. Kramer, B. Plumper, M. Spira, et al. Higgs radiation off top quarks at the Tevatron and the LHC. *Phys.Rev.Lett.*, 87:201805, 2001.

[75] W. Beenakker, S. Dittmaier, M. Kramer, B. Plumper, M. Spira, et al. NLO QCD corrections to t anti-t H production in hadron collisions. *Nucl.Phys.*, B653:151–203, 2003.

[76] S. Dawson, L. H. Orr, L. Reina, and D. Wackeroth. Next-to-leading order qcd corrections to $pp \to tth$ at the cern large hadron collider. *Phys. Rev. D*, 67:071503, Apr 2003.

[77] S. Dawson, C. Jackson, L.H. Orr, L. Reina, and D. Wackeroth. Associated Higgs production with top quarks at the large hadron collider: NLO QCD corrections. *Phys.Rev.*, D68:034022, 2003.

[78] Pavel M. Nadolsky, Hung-Liang Lai, Qing-Hong Cao, Joey Huston, Jon Pumplin, et al. Implications of CTEQ global analysis for collider observables. *Phys.Rev.*, D78:013004, 2008.

[79] A.D. Martin, W.J. Stirling, R.S. Thorne, and G. Watt. Parton distributions for the LHC. *Eur.Phys.J.*, C63:189, 2009.

[80] Richard D. Ball, Luigi Del Debbio, Stefano Forte, Alberto Guffanti, Jose I. Latorre, et al. A first unbiased global NLO determination of parton distributions and their uncertainties. *Nucl.Phys.*, B838:136–206, 2010.

[81] Stefano Forte and Graeme Watt. Progress in the Determination of the Partonic Structure of the Proton. 2013.

[82] Pdf4lhc - recommendation for lhc cross section calculations. `http://www.hep.ucl.ac.uk/pdf4lhc`, 2013.

[83] A.D. Martin, W.J. Stirling, R.S. Thorne, and G. Watt. Uncertainties on α_S in global PDF analyses and implications for predicted hadronic cross sections. *Eur.Phys.J.*, C64:653–680, 2009.

[84] Federico Demartin, Stefano Forte, Elisa Mariani, Juan Rojo, and Alessandro Vicini. The impact of PDF and alphas uncertainties on Higgs Production in gluon fusion at hadron colliders. *Phys.Rev.*, D82:014002, 2010.

[85] John R. Ellis, Mary K. Gaillard, and Dimitri V. Nanopoulos. A Phenomenological profile of the Higgs boson. *Nucl. Phys.*, B106:292, 1976.

[86] LHC Higgs Cross Section Working Group, A. David, A. Denner, M. Duehrssen, M. Grazzini, et al. LHC HXSWG interim recommendations to explore the coupling structure of a Higgs-like particle. *CERN, LHCHXSWG-2012-001*, 2012.

[87] Han-qing Zheng and Dan-di Wu. First-order qcd corrections to the decay of the higgs boson into two photons. *Phys. Rev. D*, 42:3760–3763, Dec 1990.

[88] A. Djouadi, M. Spira, J.J. van der Bij, and P.M. Zerwas. QCD corrections to $\gamma\gamma$ decays of higgs particles in the intermediate mass range. *Physics Letters B*, 257(12):187 – 190, 1991.

[89] S. Dawson and Russel P. Kauffman. QCD corrections to the higgs-boson decay $H \to \gamma\gamma$. *Phys. Rev. D*, 47:1264–1267, Feb 1993.

[90] U. Aglietti, R. Bonciani, G. Degrassi, and A. Vicini. Master integrals for the two-loop light fermion contributions to $gg \to H$ and $H \to \gamma\gamma$. *Phys. Lett.*, B 600:57, 2004.

[91] Giuseppe Degrassi and Fabio Maltoni. Two-loop electroweak corrections to the Higgs-boson decay H $\to \gamma\gamma$. *Nucl. Phys.*, B 724:183, 2005.

[92] L. Resnick, M.K. Sundaresan, and P.J.S. Watson. Is there a light scalar boson? *Phys.Rev.*, D8:172–178, 1973.

[93] E. Braaten and J. P. Leveille. Higgs-boson decay and the running mass. *Phys. Rev. D*, 22:715–721, Aug 1980.

[94] N. Sakai. Perturbative quantum-chromodynamic corrections to the hadronic decay width of the higgs boson. *Phys. Rev. D*, 22:2220–2223, Nov 1980.

[95] Takeo Inami and Takahiro Kubota. Renormalization group estimate of the hadronic decay width of the higgs boson. *Nuclear Physics B*, 179(1):171 – 188, 1981.

[96] Manuel Drees and Ken-ichi Hikasa. Heavy-quark thresholds in higgs-boson physics. *Phys. Rev. D*, 41:1547–1561, Mar 1990.

[97] J. Fleischer and F. Jegerlehner. Radiative corrections to higgs-boson decays in the weinberg-salam model. *Phys. Rev. D*, 23:2001–2026, May 1981.

[98] D. Yu. Bardin, B.M. Vilensky, and P. Kh. Khristova. Calculation of the Higgs boson decay width into fermion pairs. *Sov.J.Nucl.Phys.*, 53:152–158, 1991.

[99] A. Dabelstein and W. Hollik. Electroweak corrections to the fermionic decay width of the standard higgs boson. *Zeitschrift fr Physik C Particles and Fields*, 53(3):507–515, 1992.

[100] Bernd A. Kniehl. Radiative corrections for $H \to ff(\gamma)$ in the standard model. *Nuclear Physics B*, 376(1):3 – 28, 1992.

[101] Benjamin W. Lee, C. Quigg, and H.B. Thacker. Weak Interactions at Very High-Energies: The Role of the Higgs Boson Mass. *Phys.Rev.*, D16:1519, 1977.

[102] Thomas G. Rizzo. Decays of Heavy Higgs Bosons. *Phys.Rev.*, D22:722, 1980.

[103] Wai-Yee Keung and William J. Marciano. HIGGS SCALAR DECAYS: $H \to W^{+-}X$. *Phys.Rev.*, D30:248, 1984.

[104] G. Pocsik and T. Torma. On the Decays of Heavy Higgs Bosons. *Z.Phys.*, C6:1, 1980.

[105] A. Bredenstein, Ansgar Denner, S. Dittmaier, and M.M. Weber. Precise predictions for the Higgs-boson decay $H \to WW/ZZ \to$ 4leptons. *Phys.Rev.*, D74:013004, 2006.

[106] A. Bredenstein, Ansgar Denner, S. Dittmaier, and M.M. Weber. Radiative corrections to the semileptonic and hadronic Higgs-boson decays $H \to WW/ZZ \to$ 4fermions. *JHEP*, 0702:080, 2007.

[107] Oliver Sim Brning, Paul Collier, P Lebrun, Stephen Myers, Ranko Ostojic, John Poole, and Paul Proudlock (Eds.). *LHC Design Report*. CERN, Geneva, 2004.

[108] M Bajko et al. Report of the task force on the incident of 19th september 2008 at the LHC. Technical Report LHC-PROJECT-Report-1168. CERN-LHC-PROJECT-Report-1168, CERN, Geneva, Mar 2009.

[109] Lyndon Evans and Philip (Eds.) Bryant. LHC machine. *JINST*, 3(08):S08001, 2008.

[110] ATLAS Collaboration. The ATLAS Experiment at the CERN Large Hadron Collider. *JINST*, 3:S08003, 2008.

[111] The CMS Collaboration. The CMS experiment at the CERN LHC. *Journal of Instrumentation*, 3(08):S08004, 2008.

[112] The LHCb Collaboration. The LHCb detector at the LHC. *Journal of Instrumentation*, 3(08):S08005, 2008.

[113] The ALICE Collaboration. The ALICE experiment at the CERN LHC. *Journal of Instrumentation*, 3(08):S08002, 2008.

[114] O. S. Bruning (Ed.) et al. LHC design report. Vol. I: The LHC main ring. CERN-2004-003-V-1.

[115] C. Wyss. The LHC magnet programme: From accelerator physics requirements to production in industry. *CERN-LHC-PROJECT-REPORT-429*, pages 207–211, 2000.

[116] K. Schindl. The injector chain for the LHC. *CERN-PS-99-018-DI*, pages 47–52, 1999.

[117] M. Benedikt, (Ed.), P. Collier, (Ed.), V. Mertens, (Ed.), J. Poole, (Ed.), and K. Schindl, (Ed.). LHC Design Report. 3. The LHC injector chain. CERN-2004-003-V-3.

[118] Jorg Wenninger. The LHC machine, GIF School, 2012. `http://indico.lal.in2p3.fr/conferenceTimeTable.py?confId=1821`.

[119] Luminosity public plots. `https://twiki.cern.ch/twiki/bin/view/AtlasPublic/LuminosityPublicResults`, 2012.

[120] ATLAS Collaboration. *ATLAS Inner Detector: Technical Design Report, 1.* Technical Design Report ATLAS. CERN, Geneva, 1997.

[121] ATLAS Collaboration, S Haywood, L Rossi, R Nickerson, and A Romaniouk (Eds.). *ATLAS Inner Detector: Technical Design Report, 2.* Technical Design Report ATLAS. CERN, Geneva, 1997.

[122] ATLAS Collaboration, Norbert Wermes, and G Hallewel (Eds.). *ATLAS Pixel Detector: Technical Design Report.* Technical Design Report ATLAS. CERN, Geneva, 1998.

[123] ATLAS Collaboration. ATLAS Pixel Detector electronics and sensors. *Journal of Instrumentation*, 3(07):P07007, 2008.

[124] ATLAS Collaboration. The barrel modules of the ATLAS Semiconductor Tracker. *Nuclear Instruments and Methods in Physics Research Section A: Accelerators, Spectrometers, Detectors and Associated Equipment*, 568(2):642 – 671, 2006.

[125] ATLAS Collaboration. The ATLAS Semiconductor Tracker End-Cap Module. *Nuclear Instruments and Methods in Physics Research Section A: Accelerators, Spectrometers, Detectors and Associated Equipment*, 575(3):353 – 389, 2007.

[126] ATLAS Collaboration. The Silicon Microstrip sensors of the ATLAS Semiconductor Tracker. *Nuclear Instruments and Methods in Physics Research Section A: Accelerators, Spectrometers, Detectors and Associated Equipment*, 578(1):98 – 118, 2007.

[127] The ATLAS TRT collaboration. The ATLAS Transition Radiation Tracker (TRT) proportional drift tube: design and performance. *Journal of Instrumentation*, 3(02):P02013, 2008.

[128] ATLAS Collaboration. Inner Detector Pictures. `http://www.atlas.ch/photos/inner-detector.html`.

[129] V. Radaka and W.J. Willis. Liquid Argon ionization chambers as total absorption detectors. *Nucl.Instrum.Meth.*, 120:221–236, 1974.

[130] ATLAS Electromagnetic Liquid Argon Endcap Calorimeter Group. Construction, assembly and tests of the atlas electromagnetic end-cap calorimeters. *Journal of Instrumentation*, 3(06):P06002, 2008.

[131] Bernard Aubert et al. Performance of the ATLAS electromagnetic calorimeter end-cap module 0. *Nucl.Instrum.Meth.*, A500:178–201, 2003.

[132] M.L. Andrieux, B. Belhorma, A. Belymam, D. Benchekroun, R. Cherkaoui, et al. Construction and test of the first two sectors of the ATLAS barrel liquid argon presampler. *Nucl.Instrum.Meth.*, A479:316–333, 2002.

[133] *ATLAS liquid-argon calorimeter: Technical Design Report.* Technical Design Report ATLAS. CERN, Geneva, 1996.

[134] N.J. Buchanan, L. Chen, D.M. Gingrich, S. Liu, H. Chen, et al. Design and implementation of the Front End Board for the readout of the ATLAS liquid argon calorimeters. *JINST*, 3:P03004, 2008.

[135] ATLAS Collaboration. https://twiki.cern.ch/twiki/pub/AtlasPublic/LArCaloPublicResultsDetStatus/Stability_2012_note.pdf, 2013.

[136] Karsten Kneke and the ATLAS collaboration. A new data format for the commissioning phase of the ATLAS detector. *Journal of Physics: Conference Series*, 219(3):032047, 2010.

[137] Data summary. https://atlas.web.cern.ch/Atlas/GROUPS/DATAPREPARATION/DataSummary, 2012.

[138] B Trocm, J Levque, M Majewski, R McPherson, and O Simard. The monitoring and data quality assessment of the ATLAS liquid argon calorimeter. Technical Report ATL-LARG-INT-2013-004, CERN, Geneva, Jul 2013.

[139] E. Laisné. *Performances of the electromagnetic calorimeter and search for new gauge bosons in the dielectron channel with the ATLAS experiment*. PhD thesis, 2012.

[140] P Bernat, C Collard, D Fournier, and M Kado. Measurement of the drift time in the ATLAS barrel electromagnetic calorimeter using cosmic muon data. Application to the Calorimeter uniformity of response. Technical Report ATL-COM-LARG-2009-024, CERN, Geneva, Jul 2009.

[141] Jet cleaning. https://twiki.cern.ch/twiki/bin/viewauth/AtlasProtected/HowToCleanJets2011, 2011.

[142] Q Buat, J Leveque, N Lorenzo Martinez, F Polci, and B Trocme. Definition of the photon cleaning procedure for 2011 data. Technical Report ATL-COM-PHYS-2012-134, CERN, Geneva, Feb 2012.

[143] Expected photon performance in the ATLAS experiment. *ATL-PHYS-PUB-2011-007*, 2011.

[144] Huong Lan TRAN. Q-factor studies. https://indico.cern.ch/contributionDisplay.py?contribId=1&confId=240809, 2013.

[145] W Lampl, S Laplace, D Lelas, P Loch, H Ma, S Menke, S Rajagopalan, D Rousseau, S Snyder, and G Unal. Calorimeter clustering algorithms: Description and performance. *ATL-LARG-PUB-2008-002*, 2008.

[146] ATLAS Collaboration. Electron and photon reconstruction and identification in ATLAS: expected performance at high energy and results at 900 GeV. *ATLAS-CONF-2010-005*, 2010.

[147] ATLAS Collaboration. Improved electron reconstruction in ATLAS using the Gaussian Sum Filter-based model for bremsstrahlung. *ATLAS-CONF-2012-047*, 2012.

[148] Electron efficiency measurements, ATLAS public results. https://atlas.web.cern.ch/Atlas/GROUPS/PHYSICS/EGAMMA/PublicPlots/20120611/ElectronEfficiency2012/ATL-COM-PHYS-2011-783/index.html, 2012.

[149] Measurements of the photon identification efficiency with the ATLAS detector using 4.9 fb^{-1} of pp collision data collected in 2011. *ATLAS-CONF-2012-123*, 2012.

[150] S. Agostinelli et al. GEANT4, a simulation toolkit. *Nucl. Instrum. Meth.*, A506:250, 2003.

[151] D. Banfi, L. Carminati, and L. Mandelli. Calibration of the ATLAS electromagnetic calorimeter using calibration hits. *ATL-LARG-PUB-2007-012*, 2007.

[152] E Nebot and J Del Peso. Electron energy reconstruction for the em endcap calorimeter using calibration hits. Technical Report ATL-LARG-INT-2008-001. ATL-COM-LARG-2008-005, CERN, Geneva, May 2008.

[153] G. Aad et al. Expected Performance of the ATLAS Experiment - Detector, Trigger and Physics. I: Performances. 2009.

[154] D Banfi, L Carminati, J del Peso, N Kerschen, L Mandelli, D Nebot, and E Paganis. The measurement of the energy of electrons and photons in the atlas electromagnetic calorimeters. Technical Report ATL-PHYS-INT-2010-038, CERN, Geneva, Apr 2010.

[155] Ruggero Turra, C Meroni, and M Fanti. *Energy calibration and observation of the Higgs boson in the diphoton decay with the ATLAS experiment*. PhD thesis, Milano U., Jan 2013. Presented 18 Feb 2013.

[156] Electron energy scale in situ calibration and performances. Technical Report ATL-COM-PHYS-2011-263, 2011.

[157] Supporting note for the 2011 EM calibration analysis. Technical Report ATL-COM-PHYS-2012-1473, 2012.

[158] Torbjorn Sjöstrand, Stephen Mrenna, and Peter Skands. PYTHIA 6.4 physics and manual. *JHEP*, 0605:026, 2006.

[159] Torbjorn Sjöstrand, Stephen Mrenna, and Peter Z. Skands. A Brief Introduction to PYTHIA 8.1. *Comput. Phys. Commun.*, 178:852, 2008.

[160] S. Alioli, P. Nason, C. Oleari, and E. Re. A general framework for implementing NLO calculations in shower Monte Carlo programs: the POWHEG BOX. *JHEP*, 1006:043, 2010.

[161] Performance of the ATLAS Electron and Photon Trigger in p-p Collisions at $\sqrt{s} = 7$ TeV in 2011. *ATLAS-CONF-2012-048*, 2012.

[162] N Besson, M Boonekamp, G Gaycken, H Martinez-Bruzual, and K Muller. Measurement of the transverse momentum distribution of z/γ^* bosons in proton-proton collisions at $\sqrt{s}$ = 7 tev with the ATLAS detector: Update with 4.7 fb^{-1} of the previous measurement at this energy. Technical Report ATL-COM-PHYS-2013-117, CERN, Geneva, Feb 2013.

[163] H Bauchemin et al. Measurement of the cross section for jets produced in association with z bosons. Technical Report ATL-COM-PHYS-2011-141, CERN, Geneva, Feb 2011.

[164] N. Besson and M. Boonekamp. Determination of the Absolute Lepton Scale Using Z Boson Decays. *ATL-PHYS-PUB-2006-007*, 2005.

[165] Nathalie Besson, Maarten Boonekamp, Esben Klinkby, Sascha Mehlhase, and Troels Petersen. Re-evaluation of the LHC potential for the measurement of m_W. *Eur.Phys.J.*, C57:627–651, 2008.

[166] ATLAS Collaboration. Electron performance measurements with the ATLAS detector using the 2010 LHC proton-proton collision data. *Eur. Phys. J.*, C72:1909, 2012.

[167] ATLAS Collaboration. Performance of the electronic readout of the ATLAS liquid argon calorimeters. *Journal of Instrumentation*, 5(09):P09003, 2010.

[168] C. Collard, D. Fournier, S. Henrot-Versill, and L. Serin. Prediction of signal amplitude and shape for the ATLAS electromagnetic calorimeter. *ATL-LARG-PUB-2007-010*, 2007.

[169] T. Skwarnicki. Ph.d. thesis. *DESY-F31-86-02*, page Appendix E, 1986.

[170] M. Oreglia. Ph.d. thesis. *SLAC-R-0236*, page Appendix D, 1980.

[171] J. Gaiser. Ph.d. thesis. *SLAC-R-0255*, page Appendix F, 1982.

[172] Calibrated $z \rightarrow ee$ mass, atlas public results. `https://atlas.web.cern.ch/Atlas/GROUPS/PHYSICS/EGAMMA/PublicPlots/20110512/CalibratedZee/ATL-COM-PHYS-2011-1637/index.html`, 2011.

[173] Aharrouche et al. Response uniformity of the ATLAS liquid argon electromagnetic calorimeter. *Nuclear Instruments and Methods in Physics Research A*, 582:429–455, November 2007.

[174] ATLAS Collaboration. Readiness of the ATLAS Liquid Argon Calorimeter for LHC Collisions. *Eur. Phys. J.*, C 70:723, 2010.

[175] J-B Blanchard, J Bremer, C Fabre, V Filimonov, P Puzo, L Serin, and A Talyshev. Performance of the cryogenic regulation and the monitoring system of the liquid argon calorimeter temperature. Technical Report ATL-COM-LARG-2010-003, CERN, Geneva, Jan 2010.

[176] Jean-Baptiste Blanchard and L Serin. *Asymétrie de charge et mesures angulaires des bosons W dans lexpérience ATLAS auprès du LHC*. PhD thesis, LAL, Orsay, 2011. Presented 12 Sep 2011.

[177] X Ruan, D Fournier, S Jin, and Z Zhang. Drift time measurement in the ATLAS Liquid Argon Barrel Electromagnetic Calorimeter using Collision Events. Technical Report ATL-COM-LARG-2011-039, CERN, Geneva, Oct 2011.

[178] Inter-module correction tool. `https://espace.cern.ch/atlas-egamma/egamma-2011/Lists/Calibration/DispForm.aspx?ID=35`, 2011.

[179] P. Langacker. *Neutrinos in Physics and Astrophysics: From* 10^{-33} *to* 10^{+28} *cm ; TASI 98, Boulder, Colorado, USA, 1-26 June 1998*. World Scientific Publishing Company Incorporated, 2000.

[180] Georges Aad et al. Measurement of the inclusive $W^{\pm}$ and Z/gamma cross sections in the electron and muon decay channels in *pp* collisions at $\sqrt{s} = 7$ TeV with the ATLAS detector. *Phys.Rev.*, D85:072004, 2012.

[181] Alexander L. Read. Linear interpolation of histograms. *Nucl. Instrum. Meth.*, A 425:357, 1999.

[182] V Arnal, D Fournier, L March, J del Peso, J Toth, and JB de Vivie. Measurement of non-uniformity from sagging deformations in the ATLAS electromagnetic end-cap calorimeter. Technical Report ATL-COM-LARG-2011-013, CERN, Geneva, Sep 2011.

[183] Marco Guzzi, Pavel Nadolsky, Edmond Berger, Hung-Liang Lai, Fredrick Olness, et al. CT10 parton distributions and other developments in the global QCD analysis. *SMU-HEP-10-11*, 2011.

[184] F.D. Aaron et al. Combined Measurement and QCD Analysis of the Inclusive $e^{\pm}$-p Scattering Cross Sections at HERA. *JHEP*, 1001:109, 2010.

[185] Private communication. Jean-Baptiste de Vivie.

[186] Private communication. V. Ivantchenko and J. Apostolakis.

[187] Seltzer-berger bremsstrahlung model. `http://indico.cern.ch/getFile.py/access?contribId=3&sessionId=0&resId=0&materialId=slides&confId=216433`, 2012.

[188] Offline calibration tool. `https://twiki.cern.ch/twiki/bin/viewauth/AtlasProtected/CalibrationHitOffline`, 2013.

[189] Private communication. Remie Hanna.

[190] Particle Data Group, K. Beringer, et al. Review of particle physics. *Phys. Rev.*, D86:010001, 2012.

[191] E. Rutherford. The Scattering of α and β Particles by Matter and the Structure of the Atom. *Philos. Mag*, 6, 1911.

[192] W.R. Leo. *Techniques for nuclear and Particle Physics Experiments*. Springer-Verlag, Lausanne, 1987.

[193] Atomic nuclear properties. `http://pdg.lbl.gov/2012/AtomicNuclearProperties`, 2012.

[194] M.J. Berger and S.M. Seltzer. *Tables of Energy Losses and Ranges of Electrons and Positrons*. National Aeronautics and Space Administration Report NASA-SP-3012, Washington, 1964.

[195] M.J. Rossi. *High Energy Particles*. Prentice-Hall, Inc., Englewood Cliffs, NJ, 1952.

[196] Walter R. Nelson, Theodore M. Jenkins, Richard C. McCall, and Joseph K. Cobb. Electron-induced cascade showers in copper and lead at 1 gev. *Phys. Rev.*, 149:201–208, Sep 1966.

[197] ATLAS Collaboration. A study of the material in the ATLAS Inner Detector using secondary hadronic interactions. *J. Instrum.*, 7:P01013. 41 p, Oct 2011.

[198] Atlas public results, hadronic interactions. `http://atlas.web.cern.ch/Atlas/GROUPS/PHYSICS/IDTRACKING/PublicPlots/ATL-COM-PHYS-2013-336`, 2013.

[199] Mapping the material in the ATLAS Inner Detector using secondary hadronic interactions in 7 TeV collisions. *ATLAS-CONF-2010-058*, 2010.

[200] G Aad et al. Track reconstruction efficiency in $\sqrt{s} = 7$ tev data for tracks with $p_t > 100$ Mev. Technical Report ATL-PHYS-INT-2011-001, CERN, Geneva, Jan 2011.

[201] HM Gray, G Gorfine, M Limper, and A Salzburger. Using the SCT Extension Efficiency to Probe Material between the Pixel Detector and the SCT. Technical Report ATL-COM-PHYS-2010-100, CERN, Geneva, Feb 2010.

[202] Photon Conversions at $\sqrt{s}$ = 900 GeV measured with the ATLAS Detector. *ATLAS-CONF-2010-007*, (ATLAS-CONF-2010-007, ATLAS-COM-CONF-2010-007), 2010.

[203] Public plots for conversions studies. `https://atlas.web.cern.ch/Atlas/GROUPS/PHYSICS/EGAMMA/PublicPlots/20110216/ATL-COM-PHYS-2011-120/index.html`, 2011.

[204] Study of the Material Budget in the ATLAS Inner Detector with K^0_S decays in collision data at $\sqrt{s}$=900 GeV. (ATLAS-CONF-2010-019, ATLAS-COM-CONF-2010-019), 2010.

[205] Probing the material in front of the ATLAS electromagnetic calorimeter with energy flow from $\sqrt{s}$ = 7 TeV minimum bias events. *ATLAS-CONF-2010-037*, 2010.

[206] M Kuna, C Gabaldon, F Hubaut, and P Pralavorio. Study of material in front of the EM calorimeter with high p_T electron shower shapes and tracks. Technical Report ATL-PHYS-INT-2008-026. ATL-COM-PHYS-2008-081, CERN, Geneva, Jun 2008.

[207] Jacques Colas, C de La Taille, R. Lafaye, N. Massol, Pascal Pralavorio, et al. Crosstalk in the ATLAS Electromagnetic Calorimeter. 1999.

[208] J Labbe and R Ishmukhametov. Crosstalk Measurements in the Electromagnetic Calorimeter during ATLAS Final Installation. Technical Report ATL-LARG-INT-2009-004. ATL-COM-LARG-2008-012, CERN, Geneva, Dec 2008.

[209] Fabrice Hubaut, Pascal Pralavorio, Bouchra Dekhissi, Jamal Eddine Derkaoui, Abderrahman El-Kharrim, et al. Crosstalk in production modules of the Electromagnetic Endcap Calorimeter. *ATL-LARG-2003-012*, 2003.

[210] Private communication. Guillaume Unal.

[211] Private communication. Daniel Fournier.

[212] Private communication. Oleg Fedin.

[213] Private communication. Patricia Ward.

[214] Oleg Fedin. Investigations at $\eta \sim 1.7$. `https://indico.cern.ch/getFile.py/access?contribId=2\&resId=0\&materialId=slides\&confId=199852`, 2012.

[215] Patricia Ward. Sct forward cryostat cooling. `https://indico.cern.ch/materialDisplay.py?contribId=2\&materialId=slides\&confId=221198`, 2012.

[216] ATLAS Collaboration. Search for the Higgs boson in the diphoton final state with 38 pb^{-1} of data recorded by the ATLAS detector in proton-proton collisions at $\sqrt{s}$=7 TeV. *ATLAS-CONF-2011-025*, 2011.

[217] ATLAS Collaboration. Search for the Higgs Boson in the Diphoton Channel with the ATLAS Detector using 209 pb^{-1} of 7 TeV Data taken in 2011. *ATLAS-CONF-2011-085*, 2011.

[218] Georges Aad et al. Search for the Standard Model Higgs boson in the two photon decay channel with the ATLAS detector at the LHC. *Phys.Lett.*, B705:452–470, 2011.

[219] ATLAS Collaboration. Search for the Standard Model Higgs boson in the diphoton decay channel with 4.9 fb^{-1} of ATLAS data at $\sqrt{s}$=7TeV. *ATLAS-CONF-2011-161*, 2011.

[220] Georges Aad et al. Search for the Standard Model Higgs boson in the diphoton decay channel with 4.9 fb^{-1} of pp collisions at $\sqrt{s}$ = 7 TeV with ATLAS. *Phys.Rev.Lett.*, 108:111803, 2012.

[221] ATLAS Collaboration. Observation of an excess of events in the search for the Standard Model Higgs boson in the gamma-gamma channel with the ATLAS detector. *ATLAS-CONF-2012-091*, 2012.

[222] ATLAS Collaboration. Observation and study of the Higgs boson candidate in the two photon decay channel with the ATLAS detector at the LHC. *ATLAS-CONF-2012-168*, Dec 2012.

[223] ATLAS Collaboration. Measurements of the properties of the Higgs-like boson in the two photon decay channel with the ATLAS detector using 25 fb^{-1} of proton-proton collision data. *ATLAS-CONF-2012-168*, Mar 2013.

[224] HSG1 Working Group. Signal studies in $H \to \gamma\gamma$ search with 4.9 fb^{-1} of 7 TeV data. Technical Report ATL-COM-PHYS-2012-501, CERN, Geneva, May 2012.

[225] HSG1 Working Group. Signal studies in $H \to \gamma\gamma$ search with 8 TeV data. Technical Report ATL-COM-PHYS-2012-755, CERN, Geneva, Jun 2012.

[226] ATLAS Collaboration. Converted photon calibration tool. `https://twiki.cern.ch/twiki/bin/viewauth/AtlasProtected/ConvertedPhotonCalibrationTool`, 2011.

[227] S Laplace and JB de Vivie. Calorimeter isolation and pile-up. Technical Report ATL-COM-PHYS-2012-467, CERN, Geneva, May 2012.

[228] ATLAS Collaboration. Public results: Calorimeter isolation with topoclusters versus pile-up. `https://atlas.web.cern.ch/Atlas/GROUPS/PHYSICS/EGAMMA/PublicPlots/20120404/TopoIsolation/ATL-COM-PHYS-2012-362/index.html`, 2012.

[229] Muon reconstruction efficiency in reprocessed 2010 LHC proton-proton collision data recorded with the ATLAS detector. *ATLAS-CONF-2011-063*, (ATLAS-CONF-2011-063, ATLAS-COM-CONF-2011-068), 2011.

[230] Matteo Cacciari, Gavin P. Salam, and Gregory Soyez. The Anti-k(t) jet clustering algorithm. *JHEP*, 0804:063, 2008.

[231] Matteo Cacciari and Gavin P. Salam. Pileup subtraction using jet areas. *Phys.Lett.*, B659:119–126, 2008.

[232] Georges Aad et al. Performance of Missing Transverse Momentum Reconstruction in Proton-Proton Collisions at 7 TeV with ATLAS. *Eur.Phys.J.*, C72:1844, 2012.

[233] ATLAS Collaboration. Performance of Missing Transverse Momentum Reconstruction in ATLAS with 2011 Proton-Proton Collisions at $\sqrt{s}$ = 7 TeV. *ATLAS-CONF-2012-101*, 2012.

[234] ATLAS Collaboration. Performance of Missing Transverse Momentum Reconstruction in ATLAS studied in Proton-Proton Collisions recorded in 2012 at 8 TeV. *ATLAS-CONF-2013-082*, Aug 2013.

[235] ATLAS Collaboration. Expected performance of the ATLAS experiment: detector, trigger and physics. *CERN-OPEN-2008-020*, 2008.

[236] David L. Rainwater, R. Szalapski, and D. Zeppenfeld. Probing color singlet exchange in Z + two jet events at the CERN LHC. *Phys.Rev.*, D54:6680–6689, 1996.

[237] HSG1 Working Group. Selection for $H \to \gamma\gamma$ analysis supporting note, for Moriond 2013. Technical Report ATL-COM-PHYS-2013-093, CERN, Geneva, Jan 2013.

[238] Andreas Hoecker, Peter Speckmayer, Joerg Stelzer, Jan Therhaag, Eckhard von Toerne, and Helge Voss. TMVA: Toolkit for Multivariate Data Analysis. *PoS*, ACAT:040, 2007.

[239] HSG1 Working Group. Supporting note for coupling measurements in diphoton channel, for Moriond 2013. Technical Report ATL-COM-PHYS-2013-094, CERN, Geneva, Jan 2013.

[240] Simone Alioli, Paolo Nason, Carlo Oleari, and Emanuele Re. NLO Higgs boson production via gluon fusion matched with shower in POWHEG. *JHEP*, 0904:002, 2009.

[241] Paolo Nason and Carlo Oleari. NLO Higgs boson production via vector-boson fusion matched with shower in POWHEG. *JHEP*, 1002:037, 2010.

[242] A. Djouadi, J. Kalinowski, and M. Spira. HDECAY: A Program for Higgs boson decays in the standard model and its supersymmetric extension. *Comput.Phys.Commun.*, 108:56–74, 1998.

[243] LHC Higgs Cross Section Working Group, S. Dittmaier, C. Mariotti, G. Passarino, and R. Tanaka (Eds.). Handbook of LHC Higgs Cross Sections: 2. Differential Distributions. *CERN-2012-002*, 2012.

[244] A. Sherstnev and R. S. Thorne. Parton distributions for LO Generators. *Eur. Phys. J*, C55:553, 2008.

[245] Nansi Andari and Louis Fayard. *Observation of a BEH-like boson decaying into two photons with the ATLAS detector at the LHC*. PhD thesis, Orsay, LAL, Sep 2012. Presented 26 Sep 2012.

[246] Beam spot public results. `https://twiki.cern.ch/twiki/bin/view/AtlasPublic/BeamSpotPublicResults#2011_2012_pp_Collisions`, 2011-2012.

[247] Daniel de Florian, Giancarlo Ferrera, Massimiliano Grazzini, and Damiano Tommasini. Transverse-momentum resummation: Higgs boson production at the Tevatron and the LHC. *JHEP*, 1111:064, 2011.

[248] Lance J. Dixon and M. Stewart Siu. Resonance continuum interference in the diphoton Higgs signal at the LHC. *Phys. Rev. Lett.*, 90:252001, 2003.

[249] Duane A. Dicus and Scott S. D. Willenbrock. Photon pair production and the intermediate-mass higgs boson. *Phys. Rev. D*, 37:1801–1809, Apr 1988.

[250] Stephen P. Martin. Shift in the LHC Higgs diphoton mass peak from interference with background. *Phys.Rev.*, D86:073016, 2012.

[251] Z. Bern, A. De Freitas, and Lance J. Dixon. Two loop amplitudes for gluon fusion into two photons. *JHEP*, 0109:037, 2001.

[252] John Collins and Davison Soper. Angular distribution of dileptons in high-energy hadron collisions. *Physical Review D*, 16:2219–2225, 1977.

[253] R.J. Fries. Angular distribution of Drell-Yan pairs in p + A at LHC. 2002.

[254] Private communication. Lance Dixon.

[255] Lance J. Dixon and Ye Li. Bounding the Higgs Boson Width Through Interferometry. *Submitted to Phys. Rev. Lett.*, 2013.

[256] Stephen P. Martin. Interference of Higgs diphoton signal and background in production with a jet at the LHC. 2013.

[257] HSG1 Working Group. Background Studies for the Search of Higgs Boson Decaying to Two Photons with 4.9 fb^1 of 7 TeV data with the ATLAS Experiment. Technical Report ATL-COM-PHYS-2012-515, CERN, Geneva, May 2012.

[258] HSG1 Working Group. Background Studies for the Search of Higgs Boson Decaying to Two Photons with 8 TeV data. Technical Report ATL-COM-PHYS-2012-754, CERN, Geneva, Jun 2012.

[259] T. Gleisberg et al. Event generation with SHERPA 1.1. *JHEP*, 0902:007, 2009.

[260] T. Binoth, J.P. Guillet, E. Pilon, and M. Werlen. A Full next-to-leading order study of direct photon pair production in hadronic collisions. *Eur.Phys.J.*, C16:311–330, 2000.

[261] Johan Alwall, Michel Herquet, Fabio Maltoni, Olivier Mattelaer, and Tim Stelzer. MadGraph 5 : Going Beyond. *JHEP*, 1106:128, 2011.

[262] Torbjorn Sjostrand, Patrik Eden, Christer Friberg, Leif Lonnblad, Gabriela Miu, et al. High-energy physics event generation with PYTHIA 6.1. *Comput.Phys.Commun.*, 135:238–259, 2001.

[263] Georges Aad et al. Improved luminosity determination in pp collisions at $\sqrt{s} = 7$ TeV using the ATLAS detector at the LHC. *Submitted to Eur. Phys. J. C, CERN-PH-EP-2013-026*, 2013.

[264] The Luminosity Group. Preliminary Luminosity Determination in pp Collisions at $\sqrt{s} =$ 8 TeV using the ATLAS Detector in 2012. Technical Report ATL-COM-LUM-2012-013, CERN, Geneva, Nov 2012.

[265] A. Denner, S. Heinemeyer, I. Puljak, D. Rebuzzi, and M. Spira. Standard Model Higgs-Boson Branching Ratios with Uncertainties. *Eur. Phys. J.*, C71:1753, 2011.

[266] ATLAS Collaboration. Jet energy measurement with the ATLAS detector in proton-proton collisions at $\sqrt{s} = 7$ TeV. *Submitted to Eur. Phys. J.* **C**, 2011.

[267] G. Cowan, K. Cranmer, E. Gross, and O. Vitells. Asymptotic formulae for likelihood-based tests of new physics. *Eur. Phys. J.*, C71:1554, 2011.

[268] Abraham Wald. Tests of Statistical Hypotheses Concerning Several Parameters When the Number of Observations is Large. *Transactions of the American Mathematical Society*, 54(3):426–482, November 1943.

[269] S. S. Wilks. The Large-Sample Distribution of the Likelihood Ratio for Testing Composite Hypotheses. *The Annals of Mathematical Statistics*, 9(1):60–62, 1938.

[270] I. Asimov. *The Complete Stories:Franchise*. Number vol. 1. Doubleday, 1990.

[271] J. Stirling. *Methodus differentialis: sive tractatus de summatione et interpolatione serierum infinitarum*. Typis Gul. Bowyer; impensis G. Strahan, 1730.

[272] HSG1 Working Group. Statistics studies for $H \to \gamma\gamma$ search in the full 2011 dataset. Technical Report ATL-COM-PHYS-2012-732, CERN, Geneva, Jun 2012.

[273] HSG1 Working Group. Statistics studies for $H \to \gamma\gamma$ search with 2012 dataset and combined results with the full 2011 dataset. Technical Report ATL-COM-PHYS-2012-757, CERN, Geneva, Jun 2012.

[274] The ATLAS Collaboration. Frequentist limit recommendations. `https://twiki.cern.ch/twiki/pub/AtlasProtected/StatisticsTools/Frequentist_Limit_Recommendation.pdf`.

[275] Lorenzo Moneta, Kevin Belasco, Kyle S. Cranmer, S. Kreiss, Alfio Lazzaro, et al. The RooStats Project. *PoS*, ACAT2010:057, 2010.

[276] J. Back et al. A User's Guide to the RooFit Tools Package for Unbinned Maximum Likelihood Fitting. BaBar Analysis Document N18, Version 12, June 21, 2001.

[277] W Verkerke and D Kirkby. The roofit toolkit for data modeling. Technical Report physics/0306116, SLAC, Stanford, CA, Jun 2003.

[278] ATLAS Collaboration. Observation of an excess of events in the search for the Standard Model Higgs boson in the $H \to ZZ^{(*)} \to 4\ell$ channel with the ATLAS detector. *ATLAS-CONF-2012-092*, Jul 2012.

[279] Marc Paterno. Calculating efficiencies and their uncertainties. *FERMILAB-TM-2286-CD*, 2004.

[280] J. Neyman. *Outline of a Theory of Statistical Estimation Based on the Classical Theory of Probability*. Philosophical transactions of the Royal Society of London. A. Mathematical and physical sciences. Royal Society, 1937.

[281] F. James. *MINUIT - Function Minimization and Error Analysis - Reference Manual*. CERN Program Library Writeup D506, 2000.

[282] Serguei Chatrchyan et al. Observation of a new boson with mass near 125 GeV in pp collisions at sqrt(s) = 7 and 8 TeV. *JHEP*, 06:081, 2013.

Remerciements - Acknowledgements

Tout d'abord, je tiens à remercier Achille Stocchi pour m'avoir accueillie dans le master NPAC, cela a rendu possible cette thèse et a confirmé une passion naissante pour la physique des particules. Je le remercie aussi ainsi que Guy Wormser pour m'avoir ensuite accueillie au Laboratoire de l'Accélérateur Linéaire. Je le remercie finalement de faire partie de mon jury de thèse.

I would like to warmly thanks Markus Schumacher and Christopher Seez for giving me the honour of accepting to be my referees. Thanks very much Chris for your very helpful and numerous comments.

Je remercie Laurent Serin, Daniel Fournier et Jean-Baptiste de Vivie, avec qui j'ai eu l'immense chance de travailler à un moment ou à un autre de la thèse. Vous m'avez beaucoup apporté, merci d'avoir été patients avec moi. Je remercie Maarten Boonekamp pour le formidable travail que nous avons pu faire ensemble. J'ai trouvé cela très stimulant de travailler en ta compagnie, merci de m'avoir tant appris. Merci aussi d'avoir accepté de faire partie de mon jury.

Je remercie Quentin Buat avec qui j'ai travaillé en début de thèse. Ton amitié et ton enthousiasme ont été très bénéfiques pour moi. J'ai adoré les moments où nous refaisions le monde, à la caféteria du CERN, autour d'une tisane à la menthe. Florian Teischinger, thanks very much for your collaboration in the past two years. I have really appreciated working with you.

Je remercie Jessica Lévêque, Benjamin Trocmé et Isabelle Wingerter pour m'avoir fait découvrir et aimer le suivi de la qualité de prise de données dans le calorimètre à argon liquide. Merci beaucoup pour votre aide Jessica et Benjamin pendant ces longues semaines de shift où vous étiez toujours prêts à répondre à n'importe quelle question. Merci à Isabelle pour les croissants et les cerises le dimanche matin, en salle de shift. Merci pour ta gentillesse.

Je remercie Jean-Baptiste Blanchard, qui loin de m'en vouloir pour une histoire de frigo, m'a techniquement énormément apporté. Merci d'avoir consacré du temps pour ca, je te dois beaucoup. Je retourne les même remerciements à Sébastien Binet, pour m'avoir dispensé son aide et m'avoir fait profiter de son impressionnante connaissance du C++. Merci d'avoir ét'e un bon professeur.

Je remercie chaleureusement Guillaume Unal pour avoir répondu si efficacement à mes nombreuses questions tout au long de la thèse. Il semble quil n'y ait pas de limites à ta connaissance, merci pour de m'en avoir fait profité à tout moment.

I would like to thanks Lance Dixon for his help about theoretical questions and for the interesting discussions. Thanks you so much for having accepted to be part of my thesis committee.

Merci à tous les membres du groupe ATLAS, et notamment Sophie Henrot-Versille, Laurent Duflot, RD Schaffer, Marc Escalier, Lydia et Louis Fayard, Jana Schaarschmidt, Nikola Makovec, Patrick Puzo pour votre soutien et vos conseils et pour certains d'entre vous votre relecture du manuscrit.

Je voudrais remercier Stéphane Plaszczynski qui a parrainé cette thèse. Merci pour ton soutien dans les moments difficiles.

Pauline Bernat, merci beaucoup pour ton amitié et ton soutien, ainsi que tous tes conseils dans ce passage de relais. Je veux remercier Driss Charfeddine, Samah Khalek et Lan Huong mes compagnons de route. Merci Lan pour ta gentillesse et tes bons plats asiatiques, merci Driss pour les longues discussions enrichissantes, merci Samah pour ta générosité et tes bons plats libanais. Il semblerait que je n'ai jamais mangé autant de bonnes choses qu'en thèse. Courage, c'est bientôt votre tour ! Merci à Marthe Teinturier, ma collocataire de bureau pendant une année, j'ai adoré discuter avec toi et tes conseils m'étaient très précieux. Merci à Nancy Andari, tu m'as prise sous ton aile quand je suis arrivée au labo, je t'en suis très reconnaissante.

Je remercie Geneviève Gilbert, Annie Huguet, Dominique Longieras, Francoise Maréchal, Isabelle Vauleon et Cristelle Berezaie pour leur efficacité et leur gentillesse. Merci Geneviève pour ta générosité et ta bonne humeur constantes.

J'ai une pensée émue pour une certaine conseillère d'orientation du lycée qui m'assurait sans en démordre que le métier de physicien n'existait pas. Je ne compte plus le nombre d'entre eux que j'ai pu rencontrer durant ma thèse.

J'aimerais maintenant tout spécialement remercier mon directeur de thèse, Marumi Kado. La quantité de choses que tu m'as apportée ne pourrait se décrire sur une seule page. Merci de m'avoir donné la chance de faire cette thèse. Merci de m'avoir dédié de ton temps malgré ton emploi du temps extrêmement chargé. Merci pour les discussions, pour tes bonnes idées, pour m'avoir aidée à me faire une place dans la collaboration ATLAS. Merci aussi de m'avoir appris à être indépendente, cela me servira toujours.

Et enfin je voudrais remercier du fond du coeur mes proches. María, mi hermanita querida, muchas gracias por todo, te quiero tanto. Gracias por tener siempre fe en mi. Merci à ma mère pour m'avoir autrefois encouragée à suivre mes rêves et à ma petite soeur Galadriel pour les bons moments de notre enfance.

Merci infiniment à Dominique, Didier, Sylvain, Floor, Fanny, David, Simon, Pauline et Raphnin. Vous m'avez toujours soutenue et cru en moi, vous êtes comme une famille pour moi.

Nicolas, je voudrais te dédier cette thèse. Tu es ici celui qui a le plus contribué à son accomplissement. Ta prévenance, ton soutien, ton écoute, ta disponibilité, tes conseils, ton humour, tes petits plats, ta complicité, ta générosité, tes sacrifices, ta bienveillance, en un mot ton amour, m'ont permis de ne jamais flancher même dans les moments les plus difficiles. Tu m'as toujours aidée à garder un équilibre essentiel au bon déroulement de la thèse. Merci mille fois de m'avoir toujours encouragée et fait confiance. Je te dois tout, merci d'être à mes côtés.